Development of Multiscale Models for the Performance of the Gas and Oil Seals in Rotary Engines

by

Mathieu Picard

B. Ing., Mechanical Engineering,
Université de Sherbrooke, 2009

M.Sc.A., Mechanical Engineering,
Université de Sherbrooke, 2011

Submitted to the Department of Mechanical Engineering
in Partial Fulfillment of the Requirements of the Degree of

Doctor of Philosophy in Mechanical Engineering

at the
MASSACHUSETTS INSTITUTE OF TECHNOLOGY

June 2014

Signature redacted

Signature of Author: _____
Department of Mechanical Engineering
May 22, 2014

Signature redacted

Certified by: _____
Dr. Tian Tian
Principal Research Engineer, Department of Mechanical Engineering
Thesis Supervisor

Signature redacted

Certified by: _____
Professor John B. Heywood
Chairman, Ph.D. Thesis Committee
Department of Mechanical Engineering

Signature redacted

Accepted by: _____
Professor David E. Hardt
Chairman, Committee on Graduate Studies
Department of Mechanical Engineering

Development of Multiscale Models for the Performance of the Gas and Oil Seals in Rotary Engines

by

Mathieu Picard

Submitted to the Department of Mechanical Engineering on May 22, 2014
in Partial Fulfillment of the Requirements of the Degree of
Doctor of Philosophy in Mechanical Engineering

Abstract

Rotary engines offer higher power density, fewer parts and lower vibrations than conventional reciprocating piston engines. However, rotary engines are more difficult to seal because of the rotor shape which leads to higher gas leakage and oil consumption resulting in lower efficiency and higher emissions. In order to address this problem, this thesis presents a set of multiscale models to assess rotary engine performances by estimating gas leakage, oil consumption, wear and friction.

An oil seal multiscale model is developed to estimate internal oil consumption guided by oil transport visualization experiments carried using a laser-induced fluorescence technique. A finite element beam model is used to predict the clearance between the oil seals and the side housing for each crank angle in the cycle. From seal-housing clearance, oil transport through the oil seals is calculated using a control volume approach. The main mechanism leading to internal oil consumption is outward scraping of the oil seals due to a lack in conformability of the seals to the distorted side housing, especially next to the intake and exhaust ports.

A set of multiscale models are developed for the performance of the apex and side seals. The models are formulated to couple gas flow to the dynamics and deformation of the seals while accurately describing the interfaces between the seals and their profile and groove. The models are used to predict apex and side seal behavior and understand the mechanisms leading to gas leakage. The main leakage mechanisms identified are leakage through (1) the corner seal clearance, (2) the spark plug holes, (3) the flanks of the seals at high speed, and (4) the side piece corner for the apex seals and at the ends of the side seals. The apex seal model shows good agreement with experiments, especially for the pressure in the apex seal groove.

It is the first time such comprehensive models are developed for rotary engines and they will be valuable tools to help design more efficient and environment-friendly rotary engines.

Thesis Supervisor:
Dr. Tian Tian

Thesis Committee:
Prof. John B. Heywood (Committee Chair)
Prof. Douglas P. Hart

To my wife Émilie,

Acknowledgements

I would first like to thank my advisor, Dr. Tian Tian, for his guidance throughout this project. I have learned a great deal from the way he looks at problems and his patience and perseverance at making sure he fully grasps the physics of a problem. I also enjoyed the time spent with him hearing about his vision. I would also like to thank my committee members, Prof. John B. Heywood and Prof. Douglas P. Hart, for making sure I always question my findings.

I would like to thank Mazda Motor Corporation for funding this work and for their continuous technical support and experimental data. A special thanks to Dr. Nishino for guiding this project and Hiroyuki Hidaka for carrying the experiments with the 2D LIF engine. I would also like to thank Benoist Thirouard, Steve Przemitzki, and Eric Senzer for their expertise and help on the 2D LIF engine.

I would to thank my fellow labmates for the heated discussions and the good time spent together, Camille, Yang, Kai, Yuan, Tianshi, Pasquale, Eric, Dallwoo, Zachary, Qing, Renze, Justin, Kevin, Wen, Felipe, Yujun, Mike, Grace, and Mark. A special thanks to Camille Baelden for his help with the model and his advice on my research.

I would also like to thank my friends and family for their support and their patience. Last, but certainly not least, I would like to thank my wife Émilie for her love and support throughout this endeavor.

Table of Contents

List of Figures

List of Tables

Chapter 1

Introduction

Rotary engines provide higher power density, lower vibrations and lower part count than piston engines. However, sealing has always been an issue with rotary engines. Sealing performance is typically worse than piston engines, and this for all four sealing performance indicators: gas leakage, wear, friction, and oil consumption. Sealing performance has been improved over the years, but there is still a need for improvement, especially with the always more stringent emission standards. Progress in improving sealing in rotary engines is limited by the lack of a method to quantify the sealing performance indicators. This thesis presents a set of multiscale models that can predict gas leakage, wear, friction and oil transport by coupling dynamics of the deformable seals to detailed description of the contact between the parts along the cycle. The focus of the work presented is to assess the main function of each seal, namely oil transport for the oil seals and gas leakage for the gas seals.

1.1 Motivation

The Wankel rotary engine consists of a triangular rotor that rotates around an eccentric which changes the size of the combustion chamber over a cycle, creating the thermodynamic Otto cycle. The engine architecture leads to higher power density because all the chambers are going through a power stroke every revolution and the engine can spin faster than most piston engines. The eccentricity of the crankshaft being smaller, the rotary engine also generates fewer vibrations. Another advantage is that the rotary engine has only one moving part, the rotor, and does not require valve train as the ports are opened and closed by the rotor itself.

The rotary engine today is mainly known because Mazda has taken advantage of the high power density in its sports cars, the latest being the RX-8 with the RENESIS engine [1]. Over the years,

the rotary engine has also been tried and used in various applications, including airplanes [2], motorcycles [3], helicopters [4], tractors [5], chainsaws [6], portable generators [7] and others . Recently, in addition to Mazda planning to launch production of rotary engines again, there is a renewed interest for rotary engines as range extenders for electric vehicles [8] and unmanned aerial vehicles [9].

The drawback of the rotary engine configuration is that a triangular rotor is harder to seal than a cylindrical piston. Sealing the gases requires a seal on each of the edges and a connection at all the vertices (Fig. 1.1). In addition, oil seals are needed to prevent crankcase oil to reach the combustion chamber. This large number of seals and their peculiar shape are responsible for the rotary engine reputation of leaking oil and gas. Every aspect of the sealing is challenging and needs improvement. Specifically, the four targets are the reduction of: (1) gas leakage, (2) wear, (3) oil consumption, and (4) friction.

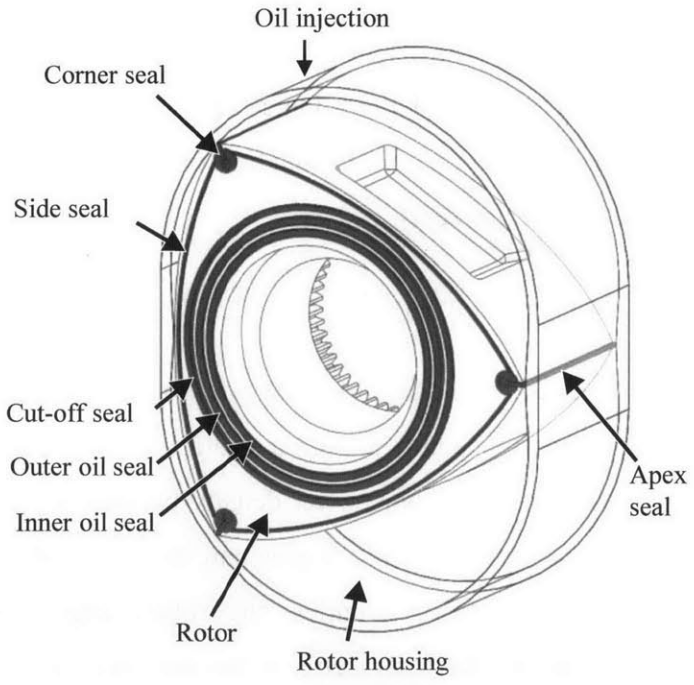

Fig. 1.1 Rotary engine seals

Gas leakage reduces engine thermodynamic efficiency by reducing the peak pressure in the combustion chamber. This effect is similar to the blowby effect in piston engines except

worsened by the many more gaps. An additional problem of gas leakage is the increase of hydrocarbon emissions. This is especially true for rotary engines as gases can leak from the combustion chamber to the leading chamber before combustion. The leading chamber being connected to the exhaust port, the unburnt hydrocarbons can leak directly into the exhaust port and increase hydrocarbon emissions (Fig. 1.2). Gases can also leak from the apex seal groove to the side of the rotor through the corner seal clearance (Fig. 1.3). The side of the rotor being connected to exhaust port for most of the cycle (Fig. 1.4), this leakage mechanism also increases hydrocarbon emissions. Similarly, gases can leak through the side seals to the side of the rotor, which increases unburnt gas flow to the exhaust port (Fig. 1.5). Those leakage mechanisms, and others, are described in more details in the gas seal chapters. In order to reduce gas leakage and hydrocarbon emissions, it is critical to be able to quantify those mechanisms to effectively improve design of gas seals.

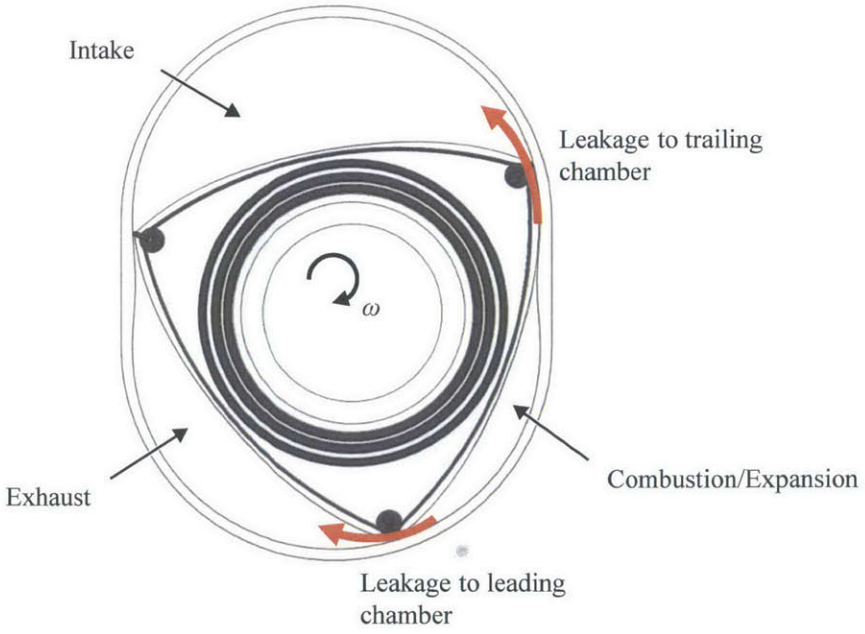

Fig. 1.2 Gas leakage from high pressure chamber to leading and trailing chambers

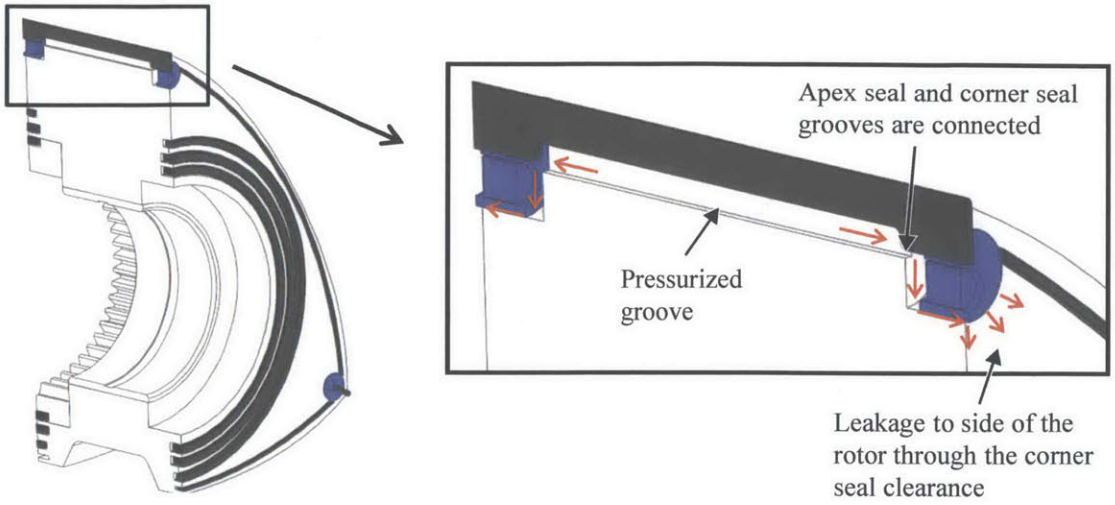

(a) Rotor section view (b) Close-up view on the apex and corner seals

Fig. 1.3 (a) Rotor section view and (b) leakage from the apex groove to the rotor side

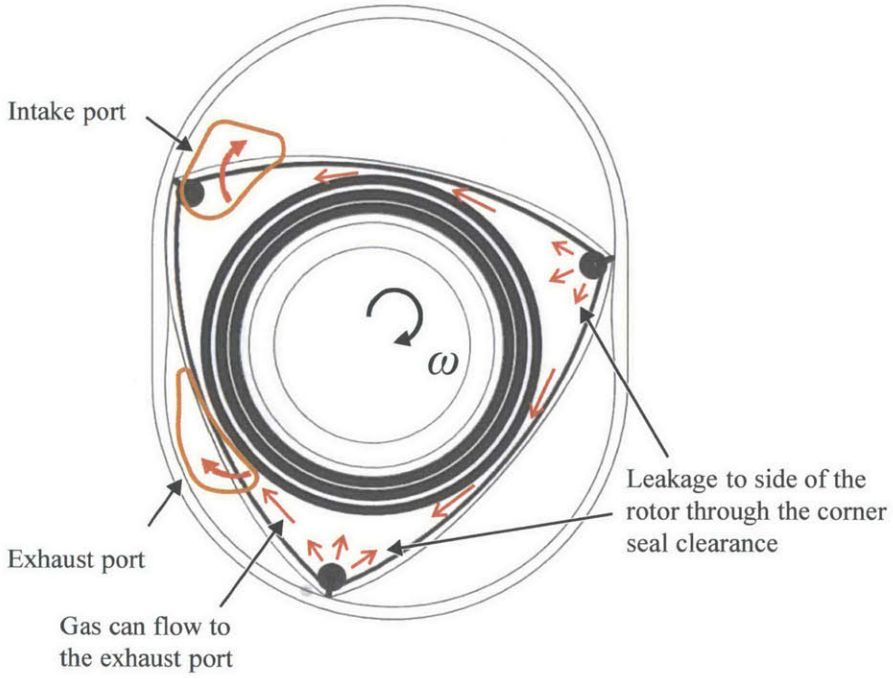

Fig. 1.4 Corner seal gas leakage path to the intake and exhaust ports

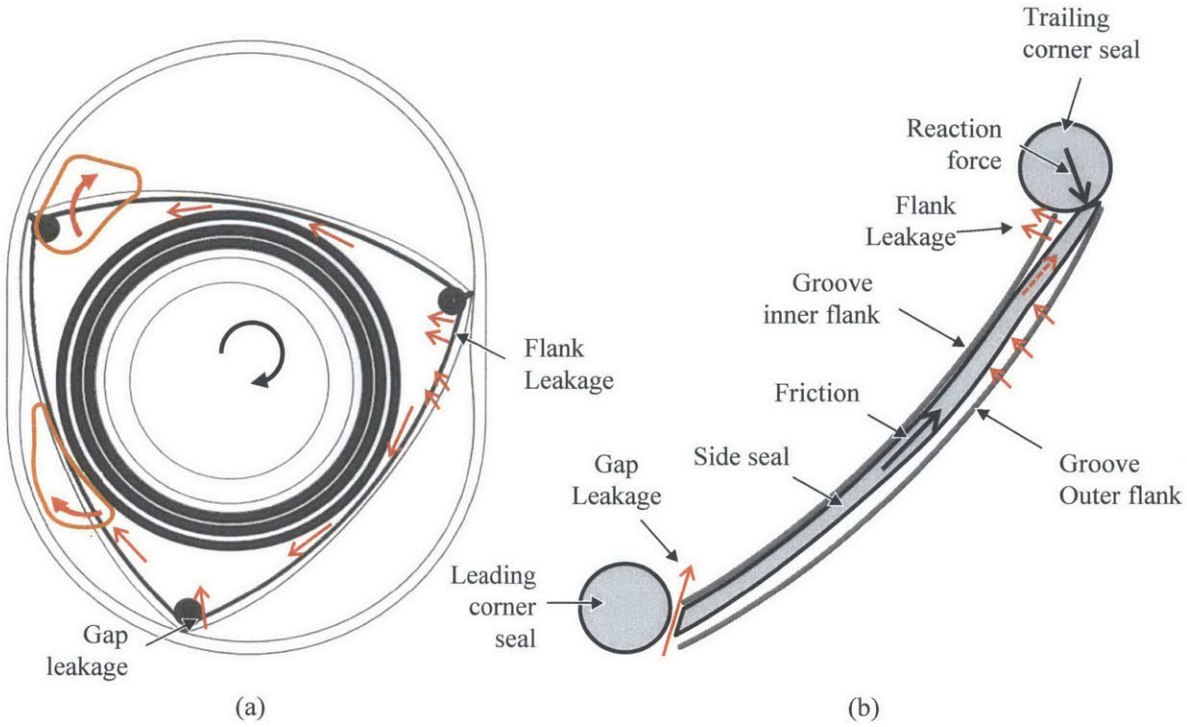

Fig. 1.5 (a) Position of the side seal leakage for high pressure in the combustion chamber and (b) mechanisms leading to side seal leakage

Wear of the apex seal has always been one of the major problem of rotary engines. The apex seal experience extreme lubrication conditions. The angle with the apex seal is varying throughout the cycle, sweeping 25-30 degrees on both sides. This constraints the apex profile to have a small radius of curvature, which results in a very sharp barrel shape from a lubrication standpoint. Therefore the hydrodynamic pressure ability of the apex seal is limited and it relies mainly on the metal-to-metal contact to support the load from the groove gas pressure. Furthermore, a large portion of the rotor housing is a combustion chamber wall which leads to rapid evaporation of the oil present. The apex seal profile is thus expected to be in starved condition when the load is maximal. In order to reduce apex seal wear, it is important to know the contact pressure between the seal profile and the rotor housing as well as the effect of oil presence.

Oil consumption must be maintained at a low level for all engines as it leads to catalyst poisoning and hydrocarbon emissions. In particular, oil consumption is a problem for rotary engines as oil leaks through the oil seals and oil needs to be injected to lubricate the gas seals. Those two oil consumption mechanisms contribute about equally to oil consumption. While it

seems reasonable to assume that all the oil injected is eventually consumed, it is less clear what causes internal oil consumption. There is therefore plenty of room for oil consumption reduction through a better understanding of the system. While it is difficult to predict the value of oil consumption, even for piston engines, identifying and quantifying the oil transport mechanisms is of great interest to an engine designer.

Friction reduction is one of the main targets of piston engine manufacturers at this point. While friction is higher for rotary engines due to the number of seals, friction reduction comes after gas leakage, wear and oil consumption in priority. Nevertheless, being capable of predicting friction losses is advantageous when designing the seals.

1.2 Background

The rotary engine was first developed by Wankel at NSU in the 1950s. The technology was then licensed to Curtiss-Wright, Togo Kogyo and others. This rapidly increasing interest for the rotary engine led to an increasing amount of research in the 1960s and beginning of 1970s. This can be seen by the number of technical papers published per year on the rotary engine by the Society of Automotive Engineers (SAE) (Fig. 1.6). While scientific literature on the rotary engine can also be found elsewhere, SAE technical publications provide a good picture of the evolution in rotary engine research and development interest over the years. After the oil crisis of 1973, the interest in the rotary engine declined, to be renewed again in the 1980s and beginning of 1990s by interest from the NASA for aviation [10] and John Deere for larger engines [5] with a focus on performance and combustion (e.g. [11,12]). After that period, literature is scarce and further development where mainly conducted at Mazda with the results being the RENESIS engine summarized by Okhuba [1]. The complete history of the rotary engine starting from its early development is described by Norbye [13] and Hege [14], and an insider view is given by Max Bentele in its autobiography [15]. The remaining of the background information presented here focuses on the sealing system. For a complete description of the engine kinematics and working principle, the reader is referred to Ansdale [16] and Yamamoto [17].

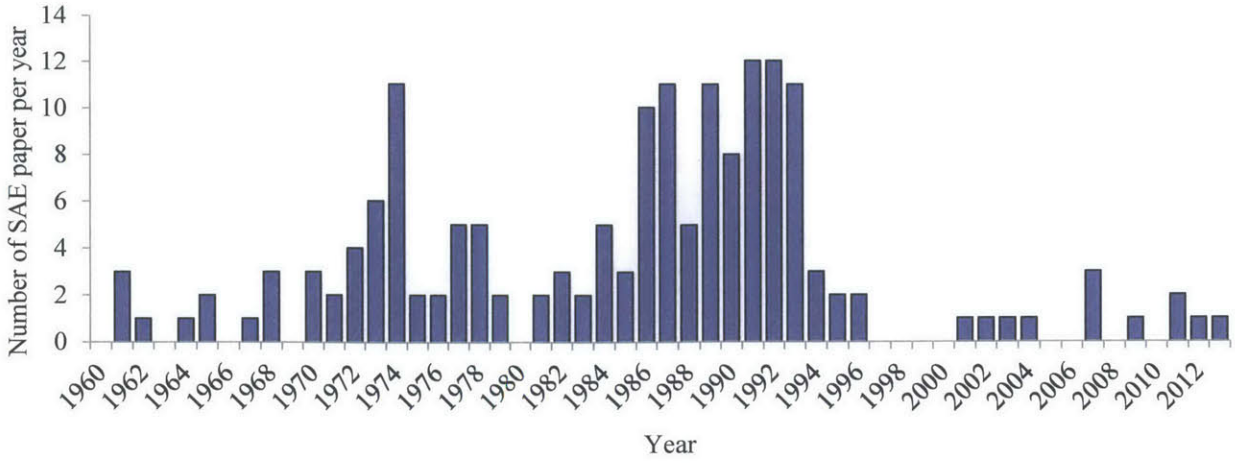

Fig. 1.6 Number of SAE technical papers concerning the Wankel rotary engine published per year from 1960 to 2013

The apex seals have always been one of the most critical parts in rotary engines. It is not surprising that development of apex seals is one of the subjects that have received the most attention by the engineers working on rotary engines. The main problems that were encountered are: (1) wear of the profile, (2) loss of contact with the rotor housing, (3) gas leakage and (4) friction. Those problems, except for gas leakage, have been addressed both empirically and by modeling of the apex seal dynamics. Gas leakage has not been addressed directly from the dynamics of the apex seals, but rather from an overall leakage area per cell. Gas leakage is therefore treated separately from the apex seals. The last subject discussed in the following sub-sections is oil consumption. As emission standards forcing oil consumption to a low level are relatively new, there is a minimum amount of research that has been done to try to fully understand this problem in rotary engines.

1.2.1 Apex Seals

Design of gas seals have been an important challenge in the development of rotary engines. Even Max Bentele himself, who was in charge of the rotary engine early development at Curtiss-Wright, said in 1958 that he didn't see insurmountable problems to the rotary engine but "the gas seals may take some time to develop" [15]. Over the first few years, the sealing system changed rapidly, to converge towards a design that is similar to what is still used today (Fig. 1.7) [18]. Further improvements are reported afterwards, but the general architecture remains the same. For example, Shimamura [19] reports a reduction of raw hydrocarbons from 8.5-9.5 to 6.5-7.5 g/mile

by improving gas sealing, including reducing the clearance of the apex seal side piece (Fig. 1.8). Among a few configurations that have been tried it is worth mentioning the 3-piece configuration that was used in the Mazda RX-7 (Fig. 1.9) [20] and the idea of making recess on both sides of the seal to allow the groove pressure to remain at the same level than the pressure in the combustion chamber [21].

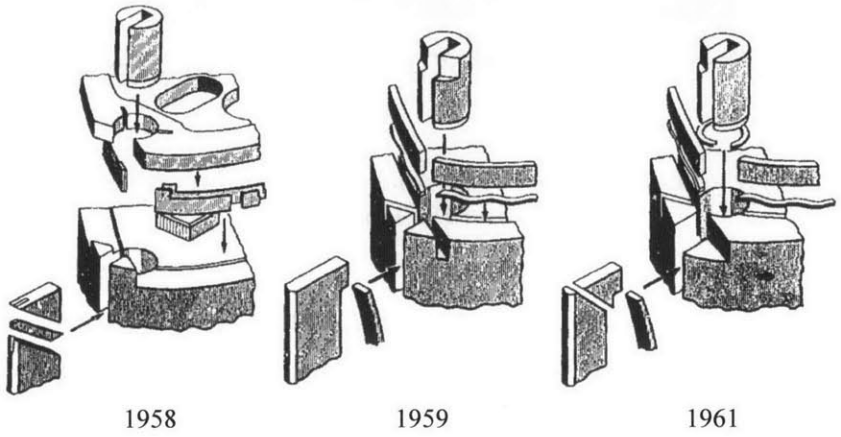

Fig. 1.7 Chronology of Curtiss-Wright sealing grid development [18]

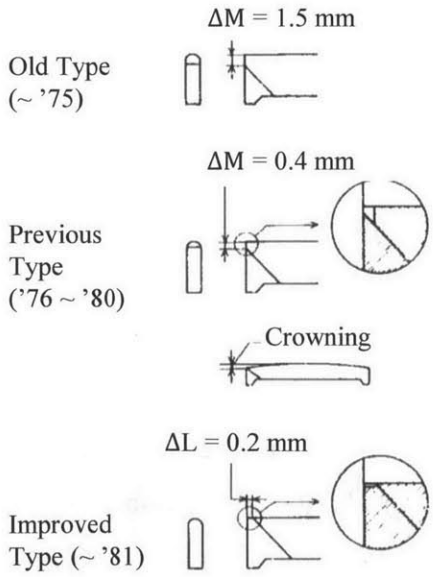

Fig. 1.8 Evolution of the side piece [19]

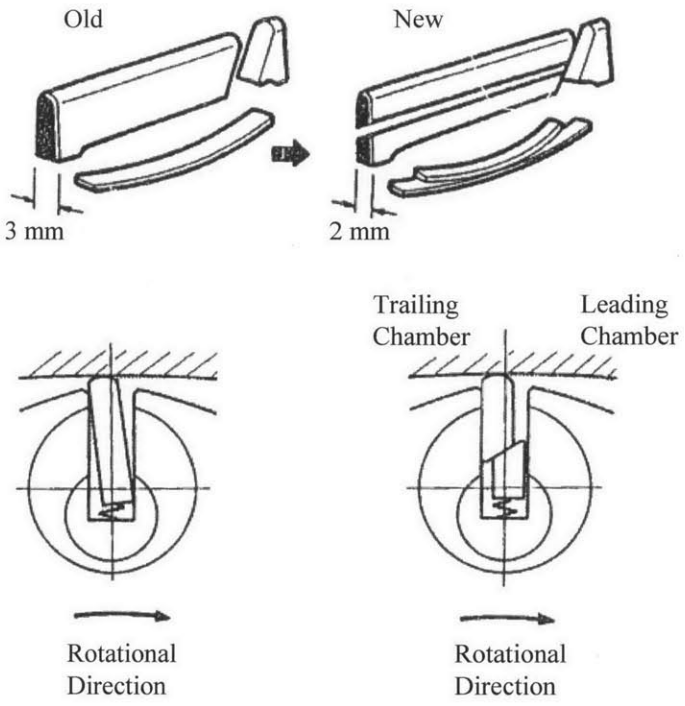

Fig. 1.9 Two-piece and three-piece apex seals [20]

Apex seal dynamics was studied experimentally by Matsuura et al. [22,23] who reported the understanding of the transition from one groove flank to the other. However, seal lift-off that can cause leakage and rotor housing chatter marks [24], was not observed. Seal lift-off is predicted by the dynamics model developed by Knoll et al. [25]. This model, as well as other apex dynamics models [26–28], can predict the seal dynamics, the reaction forces and friction. However, these models consider only the cross-section of the seal and neglect seal deformation or variation of the clearance for gas flow along the seal. They therefore fail to quantify gas leakage as a function of seal geometry and engine operating conditions.

Additionally to the friction losses predictions from the models discussed, apex seal friction has also been studied experimentally. A lubricated coefficient of friction of 0.05 has been reported by Revankar [29] and Muroki reported a dry friction coefficient of about 0.1 for a coated seal and 0.4 for a non-coated seal [30]. As friction has been studied both by modeling and experiments and friction breakdown for the seals is discussed in a few articles (e.g. [31,32]), friction is not the main focus of the work presented in this thesis even if it can be predicted by

the model presented. Nevertheless, general figures are given for friction losses associated with the different seals.

Wear of the apex seals have been studied empirically from a lubricant standpoint (e.g. [33,34]) and from a material and coating standpoint (e.g. [24,29]). Van Basshuysen et Wilmers [35] have shown that it is possible to obtain a wear rate on the same order as piston engine rings. Concerning coatings, the final version chosen by Mazda is electron beam chilling to obtain a sufficient depth of penetration in the apex profile [36]. Although the apex dynamics models presented in the literature can predict the reaction force with the housing, prediction of an estimate of wear rate distribution of the apex is not reported to the author's knowledge.

1.2.2 Gas Leakage

Gas leakage has been evaluated by Eberle and Klomp [37] by changing the leakage area in a performance model assuming isentropic flow through an orifice and comparing with experimental data. They concluded that the best fit with experimental data was an area of 2 mm^2/cell, which results in an increase of 4-6 % of fuel consumption due to leakage. They also concluded from experiments that 1/4 to 1/3 of this leakage was due to the side seals, while the remaining to the apex seals. Danieli et al. [38] used a smaller value of leakage area of 1 mm^2/cell taken from their measurements of the engine clearances that also gave a good fit with experiments. This value of 1 mm^2/cell was also used by Norman [39] and Roberts et al. [40] in their model, while Sierens et al. used 0.9 mm^2/cell [41]. While those models relate leakage to performance, they fail to relate to the dynamics of the apex and side seals.

1.2.3 Oil Consumption

Even though oil consumption of the rotary engine have always been higher than piston engines, it only became a problem relatively recently because of consumer satisfaction and emission standards. Nowadays, consumers are reluctant to add oil in their engine as it looks if the engine was of poor quality. Oil consumption also poisons catalytic converters and increases hydrocarbon emissions, which makes it harder for rotary engines to satisfy emission standards at a reasonable cost. Oil consumption can be split into internal oil consumption, the oil leaking

from the crankcase to the combustion chamber, and metered oil, the oil injected to lubricate the gas seals. In both cases, publications are rare.

A few configurations of oil seals have been tried in the early stage of development (e.g. [18,42,43]), but the design quickly evolved to the current configuration, which was satisfactory until recently. One of the few modifications to the oil seals was to add a coating that reduces the coefficient of friction with the side housing [44].

Oil has been injected to lubricate the gas seals since the first rotary engine configuration. The current configuration has three injectors, one for each side to lubricate the gas seals and one in the center for the apex seal. The strategy to determine the amount of metered oil needed for a given engine operating condition is to reduce the amount of oil until the apex seal temperature increases above a certain threshold that is assumed to be when to seal experience boundary contact [45]. Electronic control has helped to reduce metered oil compared to mechanically controlled injectors. Nevertheless, there is still room for improvement with a better understanding of the seal-housing and seal-groove contact.

1.3 Thesis Objectives and Approach

The main objective of this thesis is to develop multiscale models that relate seal design to sealing performance. In particular, the main objective for the oil seals is to identify the dominant oil transport mechanisms and quantify the oil consumption trends as a function of seal geometry and operating conditions. For the gas seal, the main objective is to quantify the different gas leakage mechanisms. For all the seals, the models must be capable of estimating wear rate by calculating asperity contact pressure and calculating friction.

In order to understand oil transport in the engine, visualization experiments are carried. Those experiments help guiding the development of oil transport through the oil seals. They also allow understanding oil transport around the gas seals on the side of the rotor. Gas leakage to the side of the rotor can also be observed indirectly, which helps to validate gas leakage mechanisms predicted from the gas seal models.

The oil seal model calculates the conformability of the seal to the distorted side housing using a beam finite element model. Based on the seal clearance, a control volume approach is used to calculate the oil transport over a few engine revolutions until the outward scraping of the outer oil seal converges. The oil passed the outer oil seal is used as an indicator of internal oil consumption. The main mechanism leading to internal oil consumption is the lack of conformability of the oil seals because of the shape of the rotor housing, especially close to the intake and exhaust ports.

The apex seal is also modeled with a dual-grid beam finite element method, but also includes dynamics. The model formulation is adapted from the methods developed by Tian et al. [46] and Baelden and Tian [47] for piston rings dynamics. All the dominant forces on the seal and main leakage mechanisms are included. Forces are formulated to be compatible with this numerically stiff problem. Pressure in the groove and general apex position shows good agreement with experiments. From model prediction, the main leakage mechanisms occur through (1) the corner seal clearance, (2) the leading spark plug hole, and (3) the seal flanks. The two first mechanisms are independent of apex seal design and they can be solved by a better sealing around the corner seal and by reducing the leading spark plug hole diameter. On the other hand, flank leakage needs to be addressed through seal design changes.

One of the strategy to reduce apex seal flank leakage is to use a three-piece configuration. This strategy is evaluated by a multi-body model. Although it increases the number of parts, the three-piece configuration seems to have the capability to eliminate the opening of the low-pressure flank that is seen at high speed for the two-piece apex seal.

The set of models is completed by a side seal model that is formulated similarly to the apex seal model, except using a curved beam finite element model instead of a straight beam model. At low speed, gas leakage is mainly caused by (1) the contact with the trailing corner seal and (2) the gap with the leading corner seal. Those mechanisms agree with the oil patterns on the rotor observed from visualization experiments. At high speed, body force is large enough to tilt the seal and flank leakage is increased.

Chapter 2

Visualization of Oil Transport Mechanisms

Improvement of the oil seals and reduction of metered oil have always been supported only by indirect empirical evidences. In this thesis, a method of oil transport visualization is used for a first time for rotary engines, based on a 2D laser-induced fluorescence (LIF) technique adapted from piston engines [48]. Oil transport mechanisms are identified from the center of the rotor to the combustion chamber, both for internal oil consumption and metered oil. Results from the experiments guide the development of the oil seal model and allow a better use of the metered oil to lubricate the gas seals.

2.1 Objectives

The objective of the 2D LIF experiments is to identify and understand the dominant oil transport mechanisms in rotary engines. This objective is subdivided in two sub-objectives: (1) understand how oil can pass the oil seals to become internal oil consumption, and (2) understand how well metered oil is used to lubricate the gas seals. A better understanding of those mechanisms will help designing a better sealing system to reduce oil consumption while maintaining low wear and friction.

2.2 Experimental Setup

The description of the experimental setup is taken from a journal article by the author [49]. For oil transport visualization, a single rotor engine is used (RENESIS [1]), for which the central housing is replaced by a sapphire window. Unless otherwise specified, experiments are carried under firing condition at 50 % load. As shown in Fig. 2.1, the beam of a YAG laser (SOLO III, 50 mJ/pulse, 15 Hz x 2 heads) is expanded and reflected towards the engine with a beam splitter. Light is absorbed by a die placed in the oil. The dyes chosen are pyrromethene 567 and

rhodamine 640 percholate to minimize the effect of temperature on the overall dye properties [50]. Light is then reemitted by the dyes. Reemitted light is filtered to filter out the laser reflections and keep only the light emitted by the dies at 570 nm. The image is captured by a camera (ProEM: 512B, resolution 512x512). The complete optical assembly is mounted on a platform that can translate in two directions to capture any desired position on the sapphire window. The area available for visualization and a cut view of the rotor and seals are shown in Fig. 2.2. Most of the side of the engine can be spanned, except for the bearing mount on the right bottom and the intake and exhaust ports modified to be machined in the sapphire window.

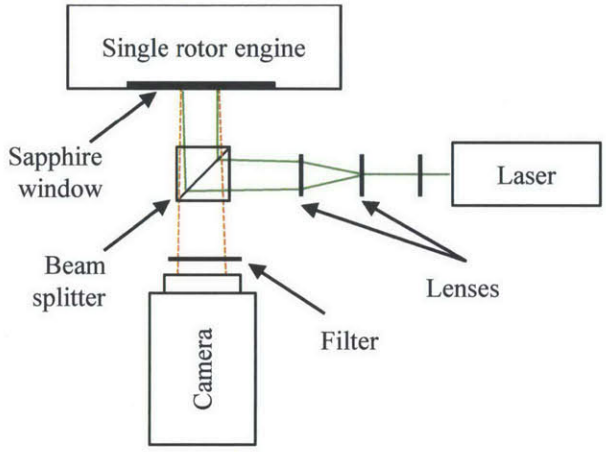

Fig. 2.1 Schematic of the 2D LIF experimental setup

Laser and camera are timed with the rotor rotation to capture one image per rotor revolution at the desired crank angle (CA). A movie is recorded and the evolution of the oil pattern can be observed over time. Rotor land oil accumulation is varying rapidly and images at different CA provide insight about the rotor land accumulation and release mechanism. However, outside the inner oil seal, the oil film is typically thin which leads to typical oil displacement from one image to the other of a fraction of a millimeter. This leads to the conclusion that an image of the oil accumulation pattern is approximately the same captured at any crank angle of the same revolution. This means that, except for the rotor land, only one image of a given position of the rotor needs to be captured and there is no need to sweep all crank angles. This reduces significantly the time involved for oil transport observations. Furthermore, as the oil displacement is small for a revolution, an image shows adequately the oil accumulation and the

corresponding movie is used to determine the direction of the flow. In this thesis, direction of the flow is represented with arrows on the pictures when needed.

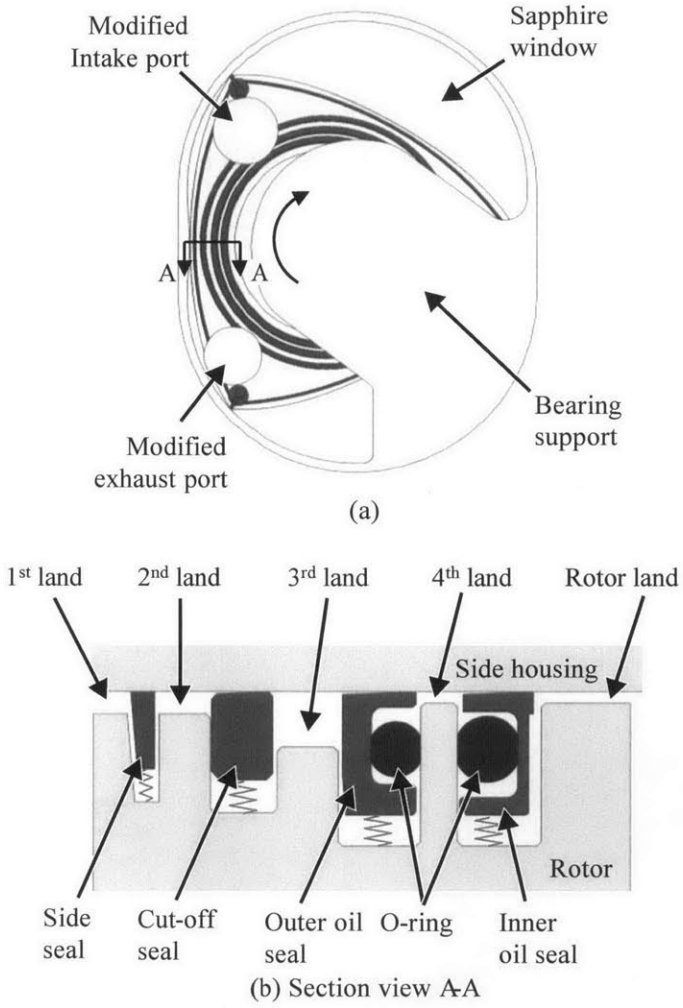

Fig. 2.2 (a) Side view of the engine showing the available area for visualization and (b) section view of the seals

Figures 2.3 and 2.4 show the typical oil accumulation pattern seen on the rotor around the gas seals and oil seals for mass production specifications. Those images show that even if some oil flow can be seen with mass production specifications, oil film thickness is small, on the order of only a few microns. Those images illustrate the challenge of understanding oil transport and reducing oil consumption of the engine, as the amount of oil in the engine is already small. In order to increase the amount of oil and better understand oil transport, oil seal geometry and

injection rate are changed. For the oil seals, three different configurations are tested using different nominal seal contact width, as discussed in section 2.5. Injection rate is also increased for oil flow around the gas seals. Injection frequency of the side injectors and the center injector can be controlled independently. Changing specification of the seals and injection rate changes the amount of oil, but does not seem to change the general behavior of oil transport as can be seen by a close inspection of images taken with the mass production specifications; scraping can be seen on oil seals and oil flow pattern around the gas seals is similar.

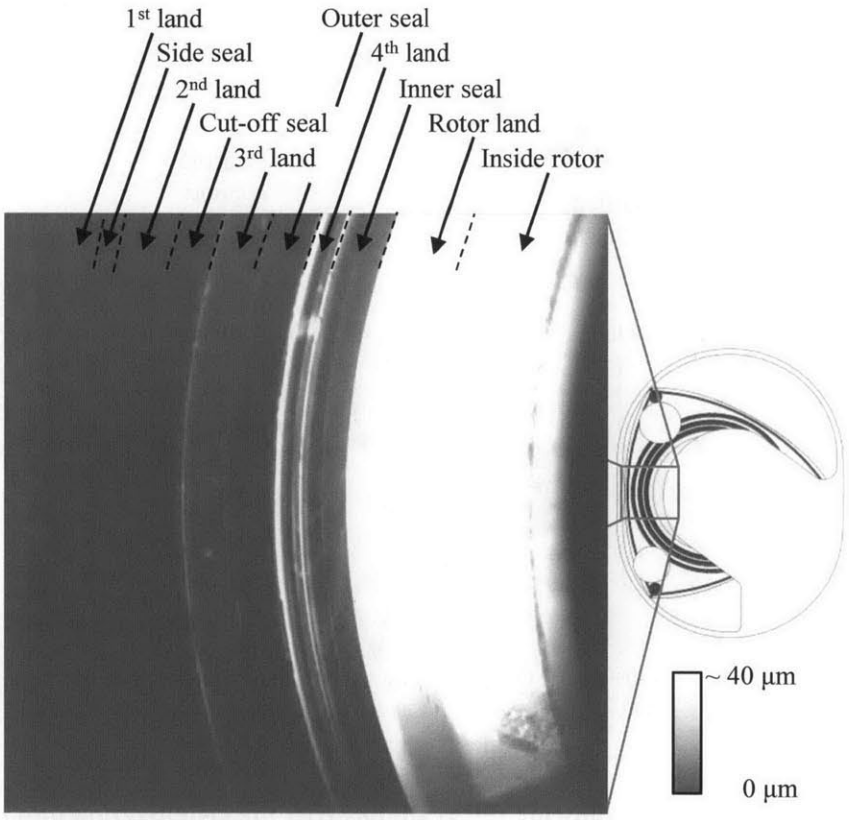

Fig. 2.3 Oil seals and cut-off seal 2D LIF image with mass production specifications

2.3 Overall Rotor Side Oil Transport

From an analysis of the experimental data, the oil transport mechanisms are identified from the center of the rotor to the combustion chamber (Fig. 2.5). Oil first accumulates in the rotor land during inward motion. Some of this oil is allowed to pass the inner oil seal which scrapes some oil to the 4th land. The oil accumulated in the 4th land must be recycled to the housing as the grooves of both oil seals are sealed by O-rings. A similar process occurs for the outer oil seal. Oil

that passes the outer seal is eventually scraped to the rotor and pushed outward by body force. The oil then mixes with the metered oil supply in 2nd land. Finally, oil passes the side seal and reaches the combustion chamber

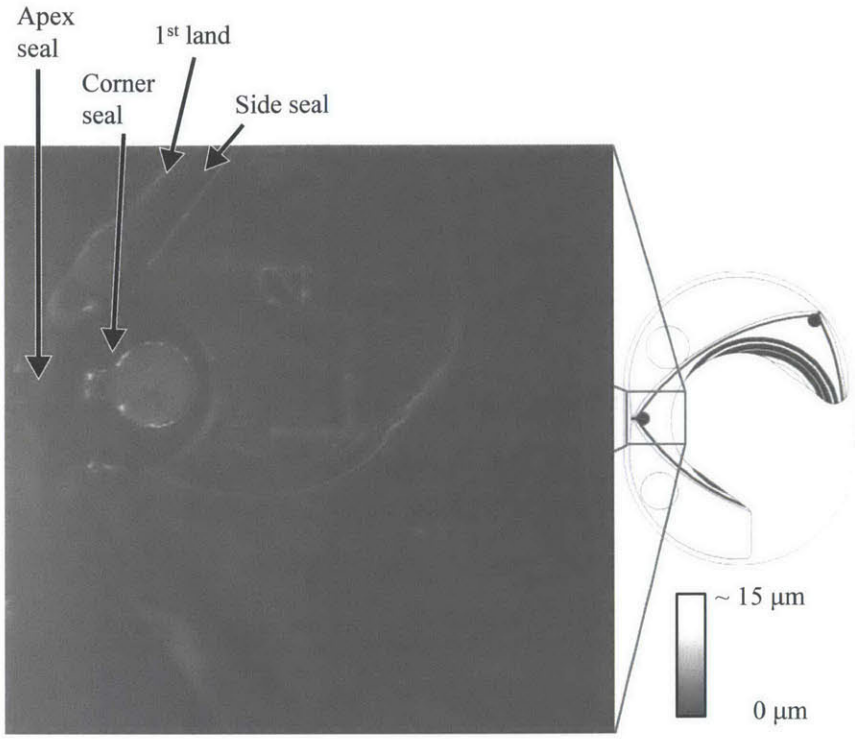

Fig. 2.4 Gas seal oil transport 2D LIF image with mass production specifications

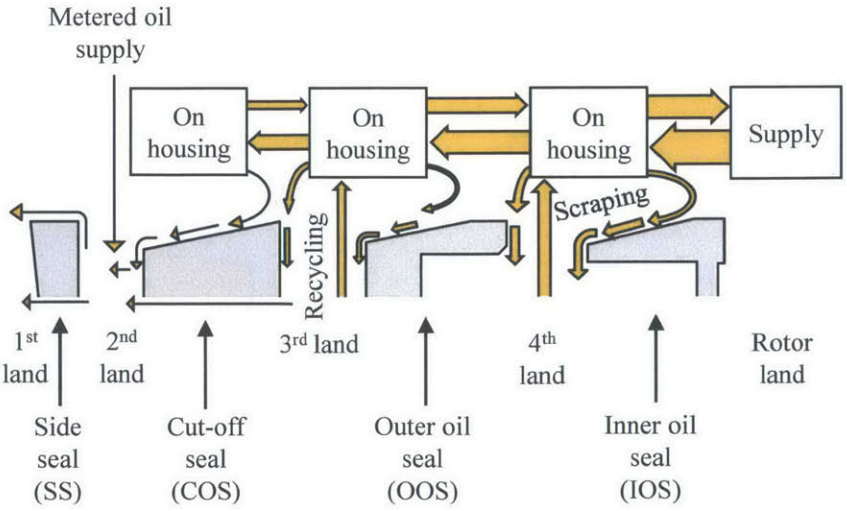

Fig. 2.5 Step-by-step oil transport from the center of the rotor to the combustion chamber

The following sections detail the oil transport mechanisms, the experimental evidences gathered and order of magnitude calculations, starting from inside the rotor to the combustion chamber, in order: (1) the rotor land, (2) the oil seals and cut-off seals, and (3) the gas seals.

2.4 Rotor Land

It is important to understand the mechanism of oil accumulation and release in the rotor land as it determines the supply to the oil seals. In other words, this mechanism determines the boundary conditions at the inner radius of the inner seal clearance with the side housing. First, it determines if the inside of the inner seal is in a fully-flooded or starved condition. Second, it determines the pressure at the inner seal inner radius that can lift the seal.

The rotor land accumulation and release mechanism starts with oil that accumulates in the rotor land during inward motion, mainly due to the oil splashed on the housing (Fig. 2.6). Inertia also contributes to accumulation by pushing oil inside the rotor land during the first part of inward motion. This accumulation generates a pressure near the inner seal that can lift the seal. When radial velocity changes direction, oil is released from the gap and pressure goes back to the atmospheric level.

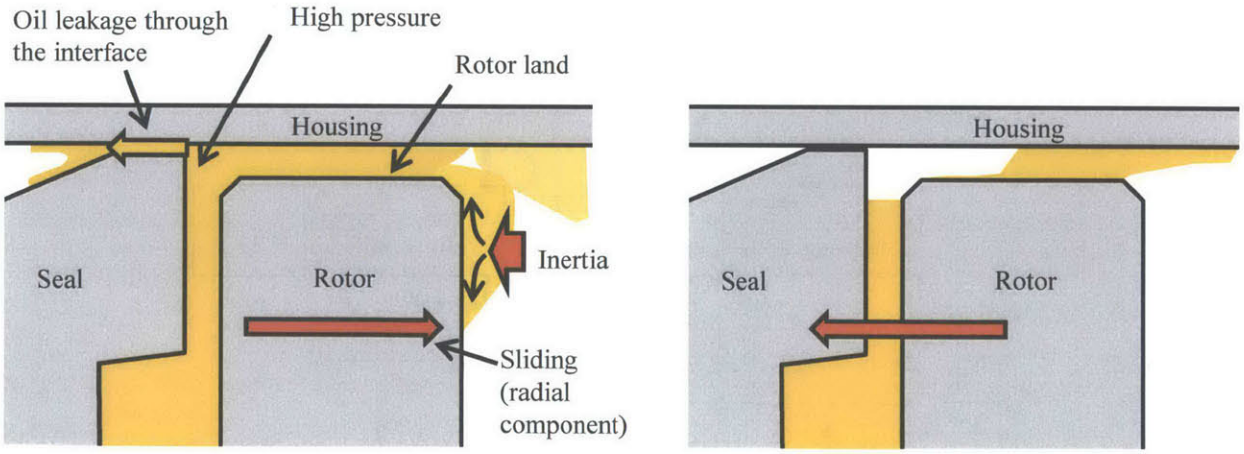

(a) Oil-in from rotor and housing due to sliding and inertia

(b) Oil-out from rotor and housing mainly due to sliding

Fig. 2.6 (a) Accumulation during inward motion and (b) release during outward motion

2.4.1 Accumulation and Release

The complete accumulation and release process can be subdivided in four steps, located on Fig. 2.7. A small portion of the inner seal is followed around a cycle and the rotor land accumulation and release is divided between (a) to (d). Events taking place during those steps are shown in Fig. 2.8:

(a) Outward inertia contributes to the oil supply inside the rotor.

(b) During the first part of inward motion, this oil is pushed inside the gap and some oil is also supplied from a sporadic distribution on the housing.

(c) Oil distribution gets more consistent as the rotor approaches the most inside position.

(d) Finally, oil is dragged out of the rotor land when motion direction reverses.

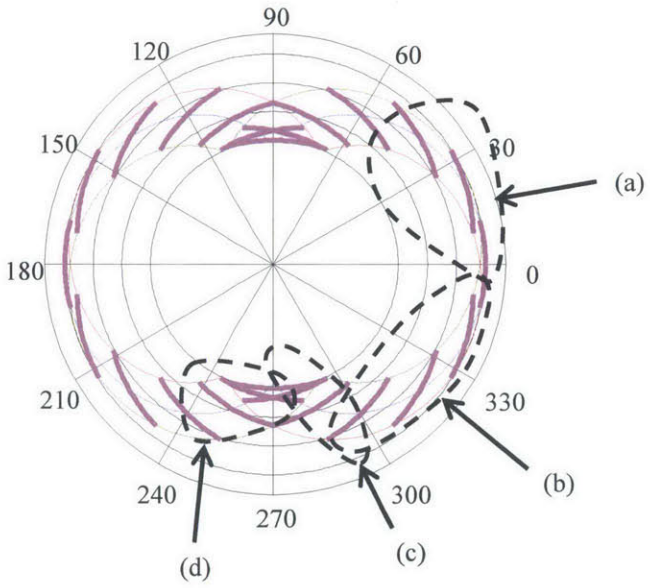

Fig. 2.7 Position of a small portion of the inner seal over a cycle

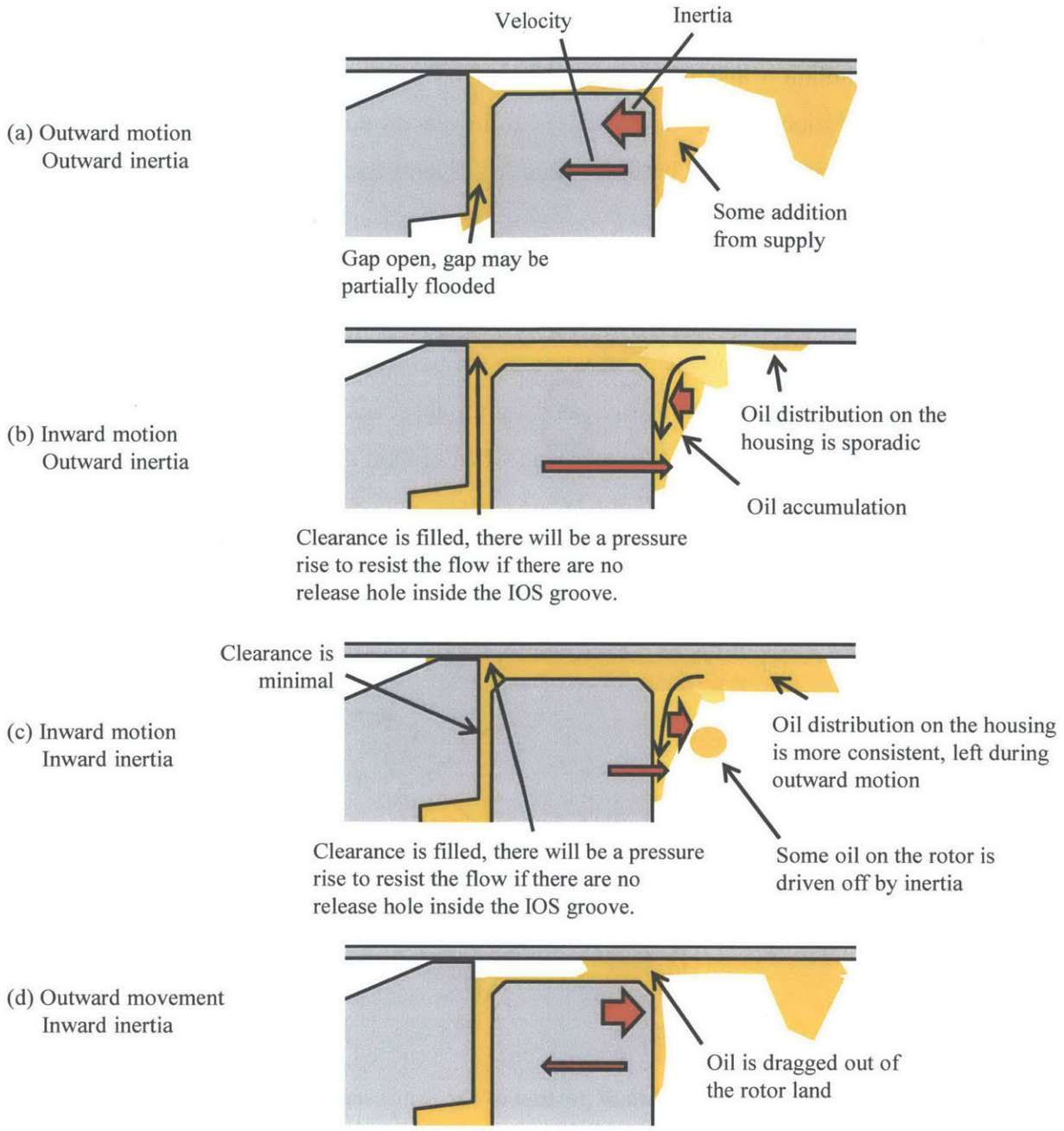

Fig. 2.8 Rotor land accumulation evolution over a cycle

Experiments with the 2D LIF engine confirm this accumulation process, as shown in Fig. 2.9. Accumulation in the rotor land can be seen where the color is continuous. The zones where shade is varying are likely to have oil on the rotor and on the housing, but with air between the two. Accumulation is small at the most outside position of the inner seal (Fig. 2.9a). Oil then accumulates and completely fills the rotor land before reaching the most inside position.

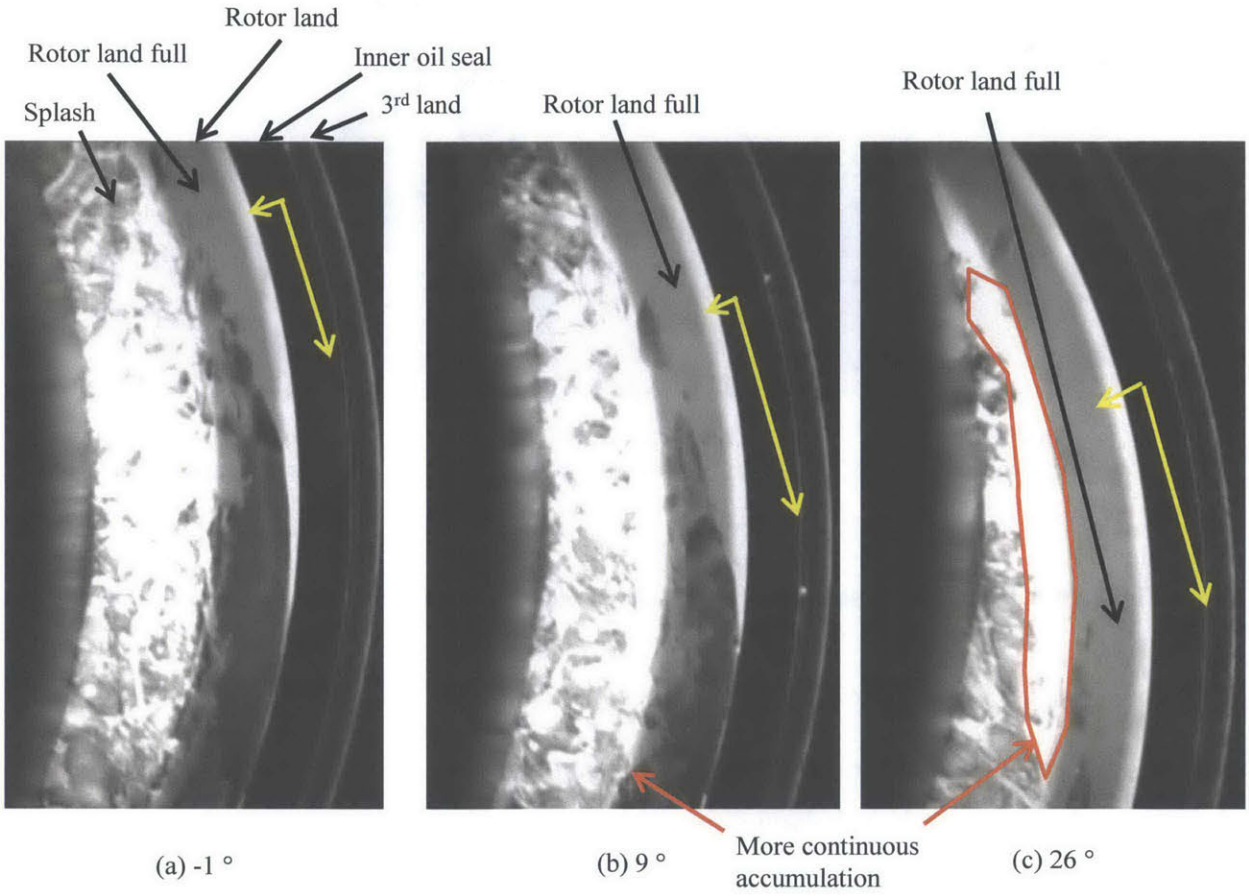

Fig. 2.9 Accumulation seen on the 2D LIF engine at 3000 rpm without drain holes

It has been observed experimentally that oil supply to the housing changes as a function of engine condition, as shown in Fig. 2.10. This is in part due to the activation of the rotor cooling jet. Further investigation is needed to fully understand this relation.

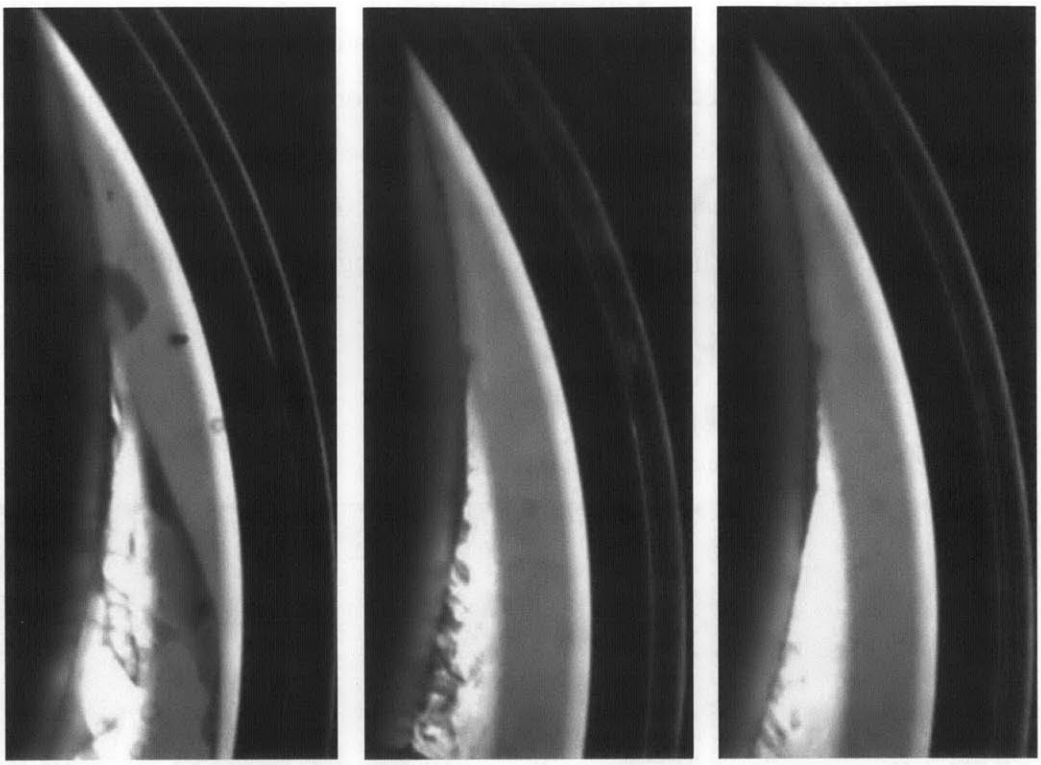

(a) Motored 1000 rpm
High intake pressure

(b) Motored 3000 rpm
Low intake pressure

(c) Motored 3000 rpm
High intake pressure

Fig. 2.10 Accumulation seen on the 2D LIF at 50° CA for different engine conditions

2.5 Oil Seals and Cut-Off Seal

Oil seals are the main barrier between the oil supply in the crankcase and the combustion chamber. Understanding their behavior is essential to reduce oil consumption. The 2D-LIF engine experimental setup provides a unique capability to observe the oil transport around those seals.

In this section, understanding of oil transport mechanisms through the oil seals is first given based on the experiments. The main mechanism for oil to pass the oil seals is scraping, a process by which oil is transported outward due to the eccentric motion of the rotor. Another important effect is the recycling of the oil accumulated between the inner and outer seal to the side housing because both grooves are sealed by O-rings.

Experimental evidences are then presented to support the claims about oil transport understanding. Mass production specifications show small oil film thickness and it is difficult to analyze oil transport mechanisms. Therefore, large contact land width on both oil seals is used to increase the oil film thickness. This allows a significant increase in oil transport and makes it easier to describe the complete path from the center of the rotor to outside the gas seal. A core assumption in all the analyses and models is that the injected oil cannot find its way back to the crankcase, and hence does not affect the oil transport around the oil seals. This assumption is validated by changing the oil injection and comparing the oil pattern at small and high injection rates. The last part of this section is dedicated to a quantitative analysis of the images that calculates the total scraping rate of both the inner and outer seals.

2.5.1 Understanding of Oil Transport Mechanisms

Oil has to go through the complete process to become internal oil consumption, as shown in Fig. 2.11. Oil starts from the oil supply for the rotor journal bearing and rotor cooling inside the inner oil seal (1). Oil is allowed to pass under the inner oil seal by the motion of the seal (2) and is left on the housing between the inner and outer seals (4). Oil can also be pushed through the interface by pressure generated by the oil accumulation between rotor land and housing (3). This pressure-driven flow goes partly on the housing (3a) and partly on the taper (3b).

Once oil is on the housing, it can be scraped by the inner oil seal (6) and pushed by inertia on the taper towards the 4^{th} land (7). Since there is no mechanism to drain the oil from the 4^{th} land volume, oil has to be recycled (8) back to the housing in steady state. Outer oil seal also scrapes inward (9) directly into the 4^{th} land volume. This oil is also recycled to the housing.

From (4), oil is allowed to pass under the outer seal (10) and is left on the housing. Most of the oil finds its way back under the seal (11), part of it is pushed out of the reach of the outer seal (13) and part of it is scraped by the outer seal, and pushed out by inertia on its taper (14). There is no clear mechanism that brings back the oil after being pushed (13) or scraped (15). Thus, this oil travels towards hot regions, evaporates and burns in the combustion chamber. These flows (13 and 15) are considered to be internal oil consumption.

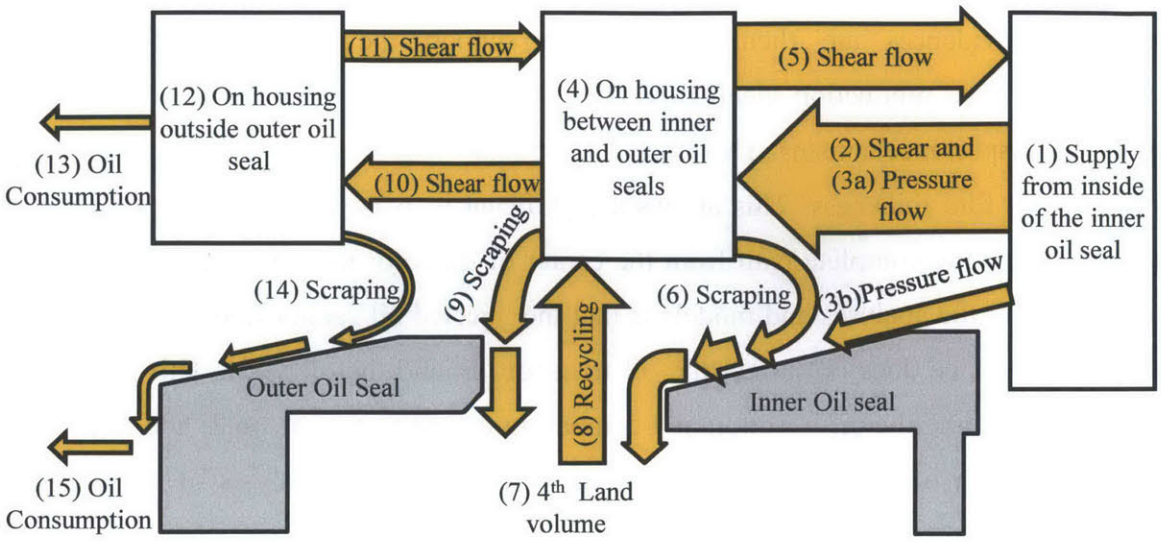

Fig. 2.11 Representation of the internal oil consumption process

2.5.1.1 Scraping Mechanism

Scraping is a mechanism of oil transfer from the housing to the taper of the oil seal. Scraping of the inner oil seal can be divided in steps as shown in Fig. 2.12. To illustrate the process, the scraping sequence starts with a piece of the inner oil seal at its most inner position assuming the housing is dry outside the inner oil seal (1). The seal first moves outward and oil is supplied to the housing (2). The seal then moves inward, leaving a given thickness of oil on the housing (4). When the seal moves outward again, if the clearance is smaller than during outward motion, the scraped oil either directly flows to the taper of the seal or accumulates between the taper and the housing (6). When the seal changes direction, oil separates and some of it stays on the housing and some stays on the taper (7). Once on the taper, oil experiences inertia and shear from the air (8). Finally, oil reaches the 4^{th} land (9). For the outer oil seal, the only difference is that the supply to the housing comes from oil left on the housing by the inner oil seal and is smaller than the supply from the center of the rotor and the bridged oil from the rotor land.

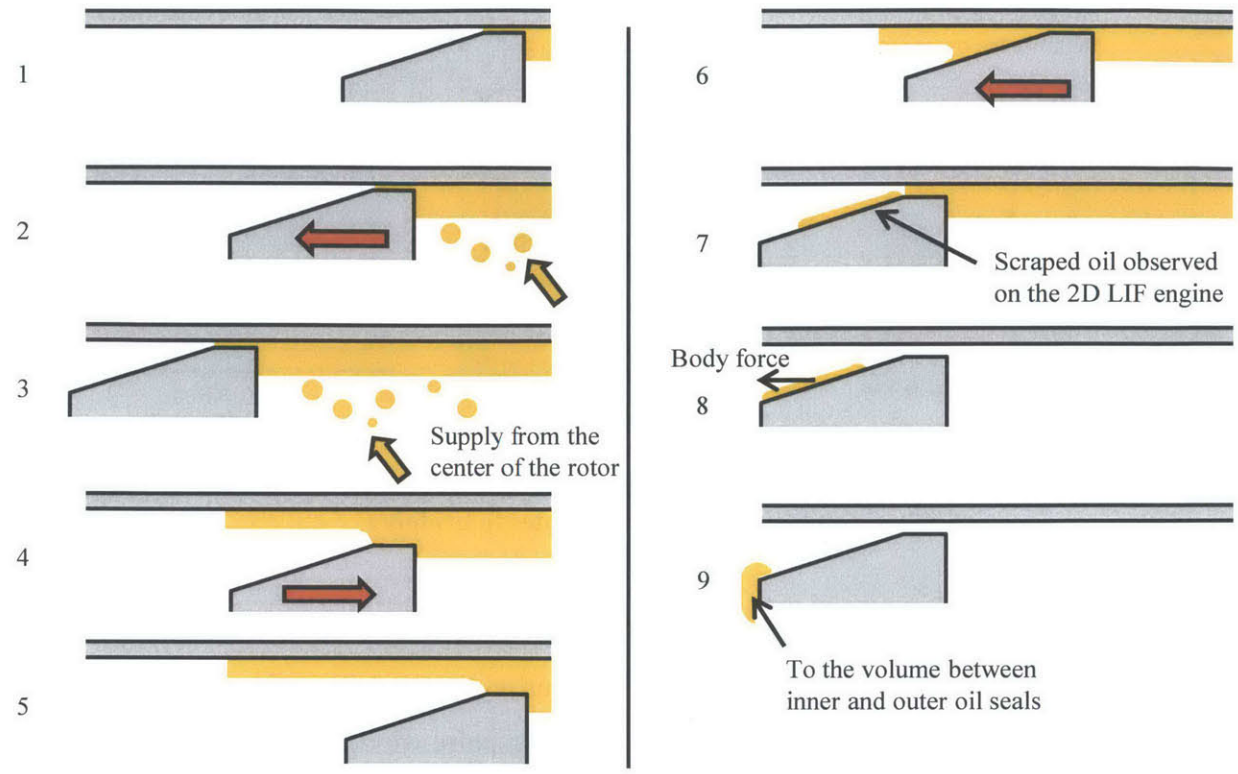

Fig. 2.12 Scraping process

In sum, scraping is caused by an asymmetry between inward and outward motion. If the clearance between the seal and the housing always remains the same, no oil transport occurs. However, if the clearance is different, oil is transported by seal motion.

2.5.1.2 Fourth Land Oil Motion and Recycling

Oil from the inner seal taper and scraped inward by outer seal fills the 4^{th} land. Once the oil accumulation reaches a certain level, oil is recycled to the housing. When body force points outward, oil is pushed against outer seal until it bridges to the housing. When bridging happens, surface tension contributes to recycling oil to the housing. Secondary motion also contributes to bridging by reducing the clearance between the rotor and the housing.

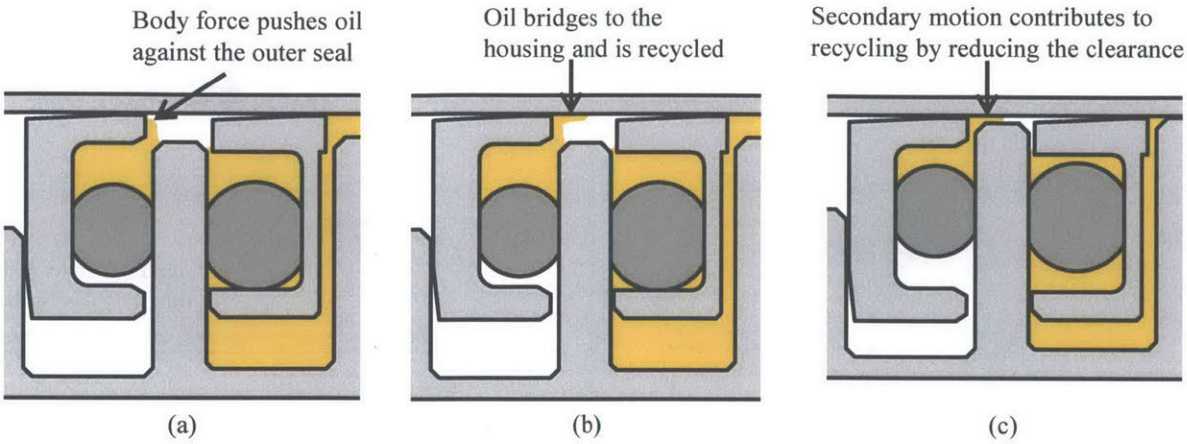

Fig. 2.13 Oil recycling: (a) oil is pushed by body force, (b) oil bridges to the housing, and (c) secondary motion contributes to bridging

2.5.2 Experiments with Mass Production Specifications

Oil transport is small for mass production specifications on the 2D LIF engine setup. This is due to an already well-designed oil seal system and to the sapphire window which is flatter than the actual housing. The resulting small film thickness is therefore difficult to capture and analyze. The center of the engine and the rotor land are both full of oil, as shown in Fig. 2.15. Some scraping is observed on most regions of the inner seal. Oil accumulation is observed in the 4th land. Outer seal scraping is only seen in one location, and the film thickness is small.

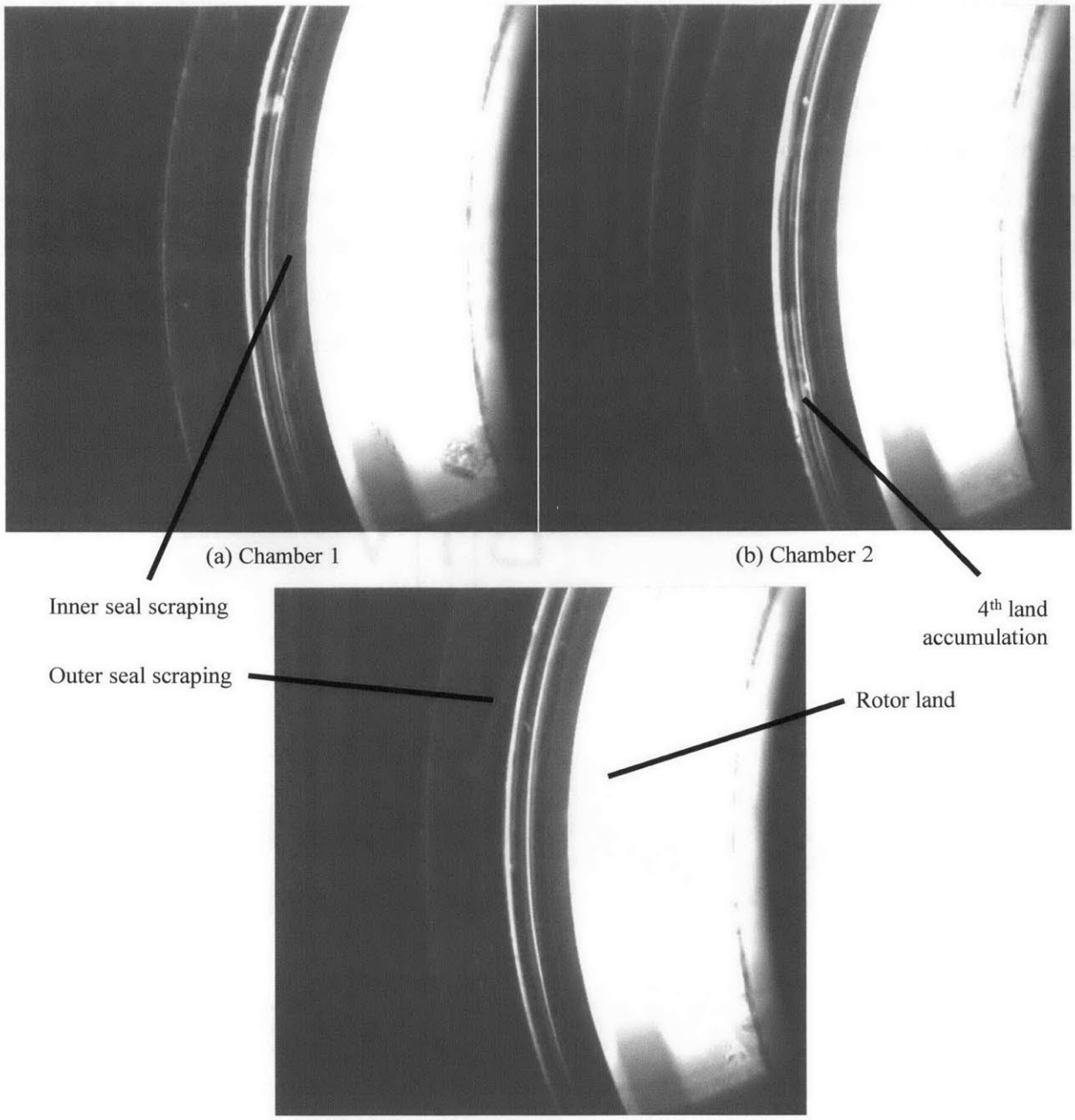

Fig. 2.14 Oil distribution with mass production specifications, 3000 rpm

2.5.3 Oil Path at Large Contact Width

Inner and outer oil seals were both replaced with larger contact width to increase the oil film thickness between the housing and the seals as they move inward and outward. Although this is an undesirable design, this setup illustrates clearly the oil path from inside to outside, as shown in Fig. 2.15 taken at a speed of 3000 rpm. The rotor land filling pattern is unchanged from the

mass production specification. Oil seals are both scraping oil, and oil accumulates in the 3rd and 4th lands. Oil scraping is also observed on the cut-off seal, as its interface pressure is higher than the oil seals and therefore its interface clearance is smaller. Oil can also pass under the cut-off seal, by leaking between the seal and groove inner flank, then in the groove under the seal, and finally leaking between the seal and groove outer flank. This effect is shown in Fig. 2.16 where the oil passed the cut-off seal is significantly larger than the cut-off seal scraping rate. Oil that is scraped and oil that has passed under the cut-off seal is then pushed outside on the rotor by body force. Finally, oil passes under the side seal and reaches the chamber, where it can be thrown off or evaporated.

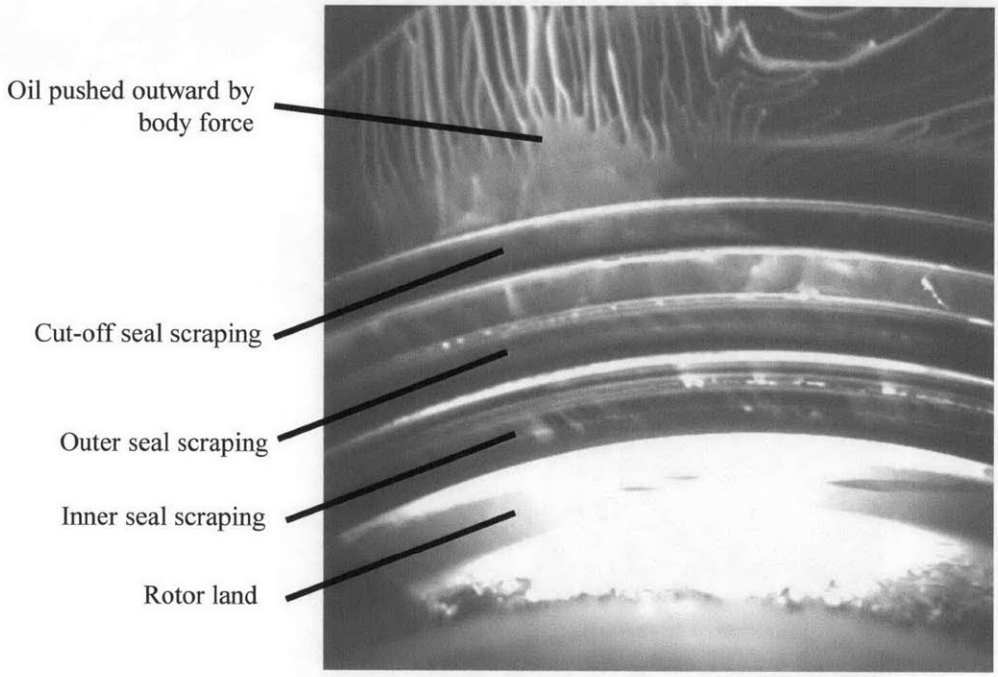

Fig. 2.15 Oil path from inside to outside with oil seal large contact width, 3000 rpm

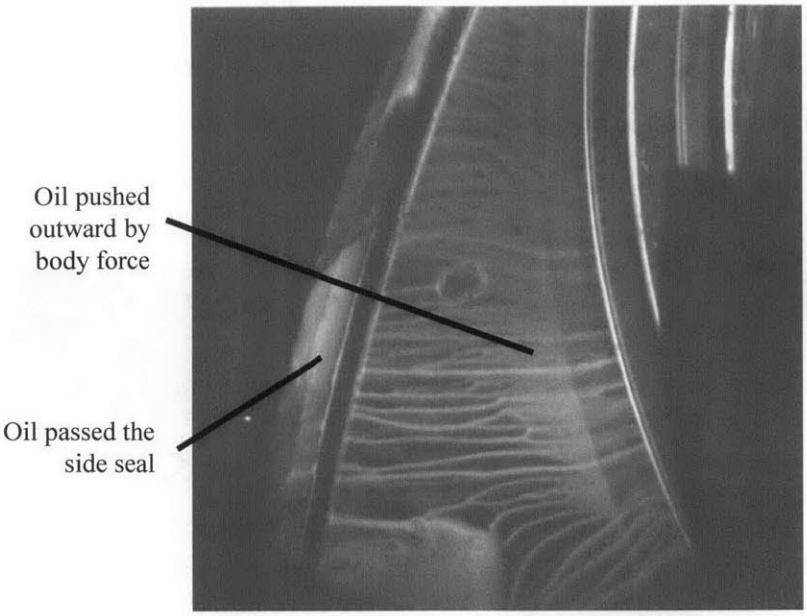

Fig. 2.16 Oil path showing oil passing under the cut-off seal and the side seal, 3000 rpm

At low speed, oil transport is significantly different as surface tension becomes significant compared to body force, as shown in Fig. 2.17 taken at a speed of 1000 rpm. Scraping is observed for all seal, but at a slower rate. Also, oil passage under the cut-off seal is small, even for a large accumulation in the 3rd land.

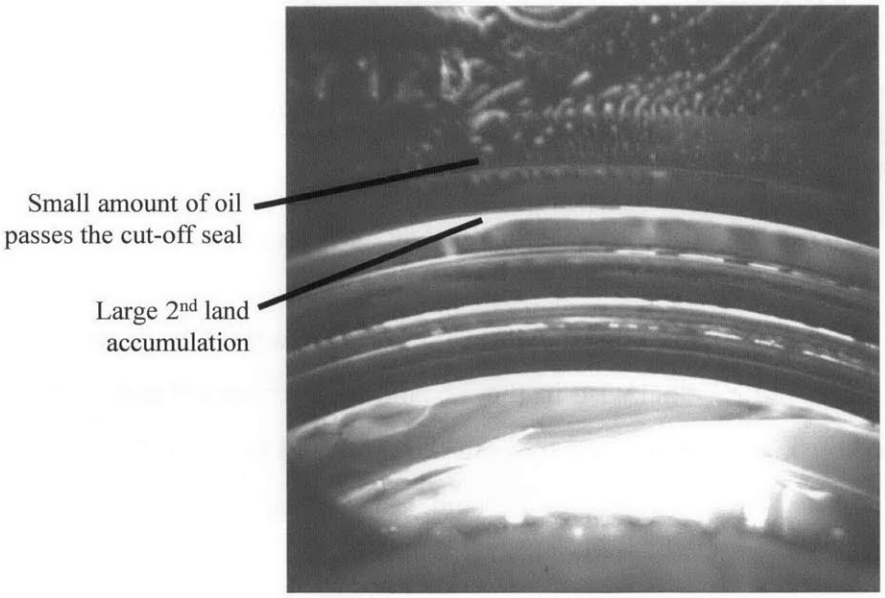

Fig. 2.17 Oil transport for large oil seal contact width, 1000 rpm

Oil transport pattern is similar around the circumference of the oil and cut-off seals, except in the region of the cut-off seal gap, as shown by a comparison of the three chambers in Fig. 2.19. The cut-off seal gap is causing a large accumulation in the 3rd land due to a flow of gas entraining the oil.

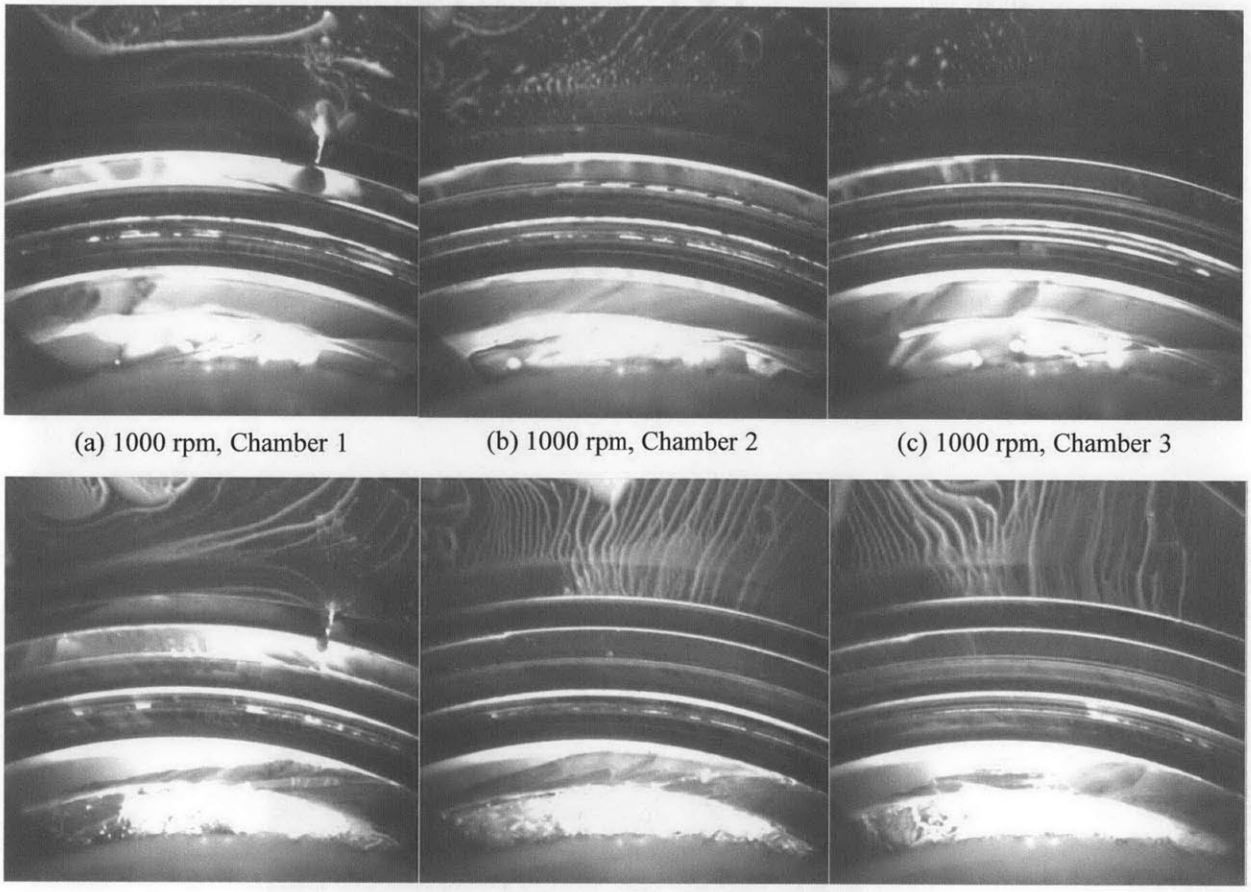

(a) 1000 rpm, Chamber 1 (b) 1000 rpm, Chamber 2 (c) 1000 rpm, Chamber 3

(d) 3000 rpm, Chamber 1 (e) 3000 rpm, Chamber 2 (f) 3000 rpm, Chamber 3

Fig. 2.18 Cut-off seal gap effect on oil transport

Oil transport around the cut-off seal gap is shown in Fig. 2.19. Gas flow drags oil to the 3rd land across the gap. Oil is transported clockwise in the 3rd land by the rotation and bridges with the housing. Once on the housing, oil is scraped by both the outer and the cut-off seals. Oil scraped by the outer seal is returned by body force to 3rd land. Oil scraped outward by the cut-off seal next to the gap is brought back to 3rd land by gas flow through the gap. To escape this cycle, oil has to travel further clockwise, as shown in Fig. 2.19a. From that location, oil can pass the cut-

off seal and is pushed by body force towards the side seal without being brought back to the 3rd land by gas flow.

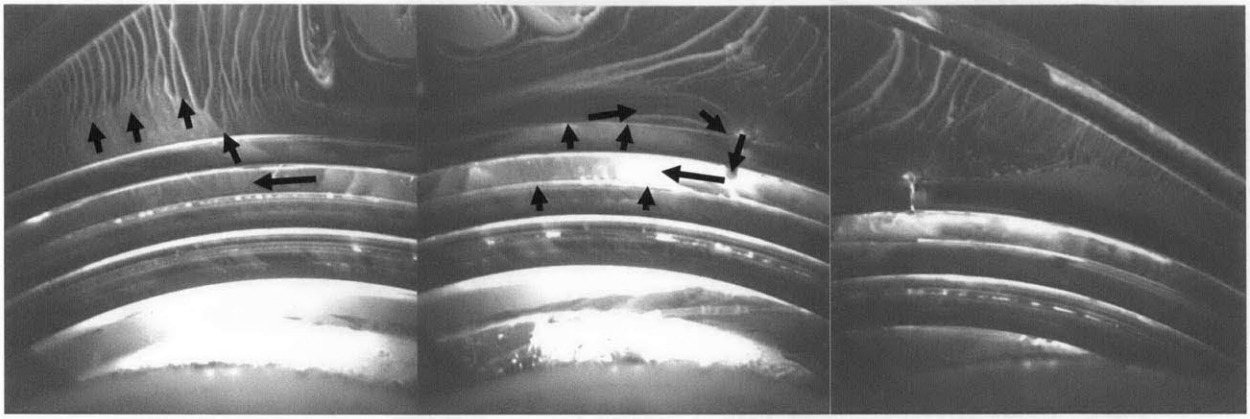

(a) 215 CA (b) 255 CA (c) 300 CA

Fig. 2.19 Oil transport around the cut-off seal gap, 3000 rpm

The oil transport mechanisms seen with a large amount of oil seems to also occur with mass production specifications, but at a slower rate which makes it difficult to observe. The large contact width experiments thus allow understanding better oil transport to improve the design of the oil seals and cut-off seal.

2.5.4 Effect of Metered Oil

A core assumption is metered oil does not change the oil transport around the gas seals. To validate this assumption the injection rate was taken from 0.526 Hz and 0.196 Hz for center injection and side injection to 2 Hz for both. As shown in Fig. 2.20, the change in injected oil does almost no change in the 3rd land accumulation, while the accumulation pattern on the rotor near the corner seal is changed by a larger amount of oil. Those experiments confirm that metered oil should not find its way toward the crankcase and oil transport around the oil seals can be treated independently.

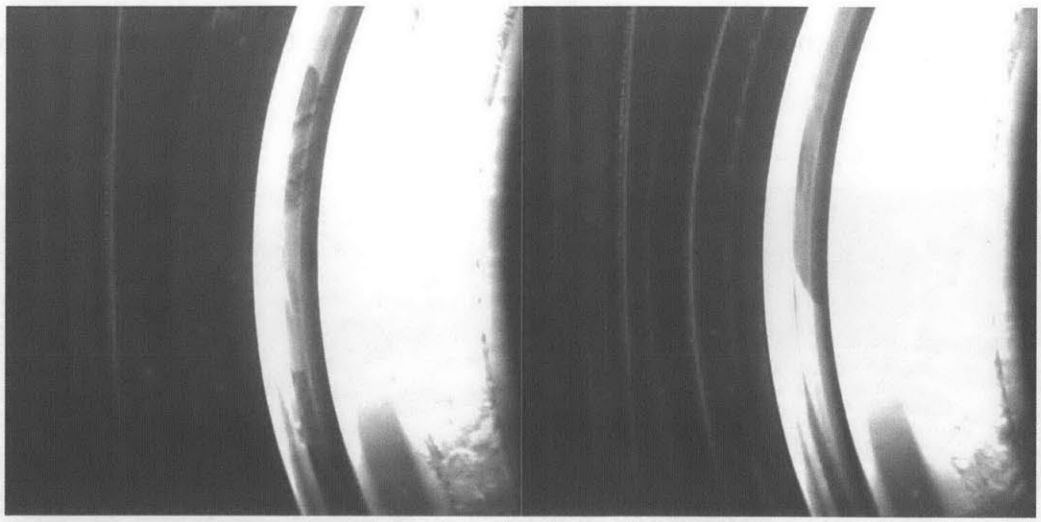

(a) 180 CA, slow oil injection (b) 180 CA, fast oil injection

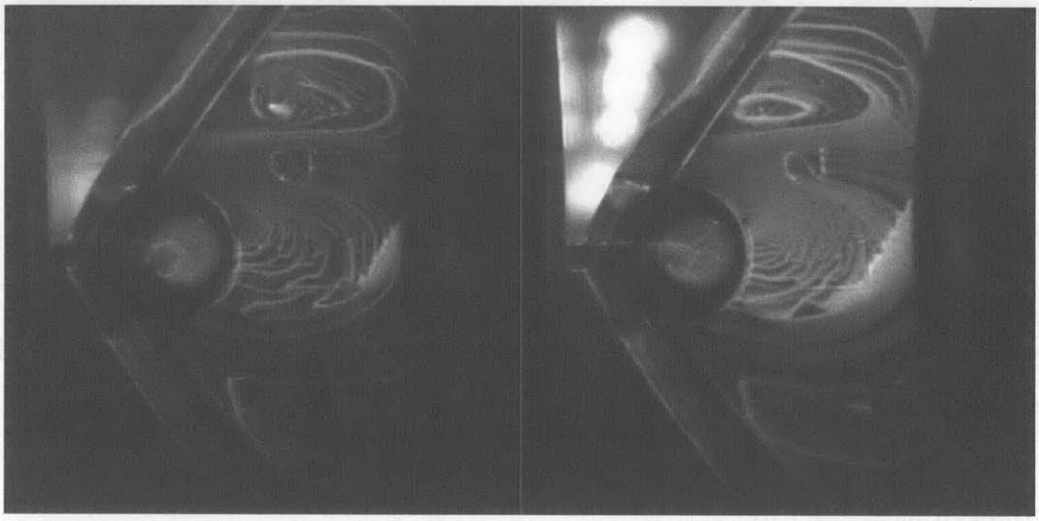

(c) 0 CA, slow oil injection (d) 0 CA, fast oil injection

Fig. 2.20 Effect of metered oil injection rate on oil transport around the oil seals

2.5.5 Quantitative Analysis of Scraping

Quantifying oil film thickness based on LIF images requires a proper calibration. The optimum solution would be to have an in situ calibration by having reference oil film thickness near the measurement at all time. This approach is attempted by using the calibration marks on the seal. However, it is not guaranteed that the calibration marks are full of oil and therefore the calibration gives inconsistent results. Instead, the calibration is done at a specific time when the taper of a seal is full, using the known angle of the seal taper. The calibration results in about 4 $I_3/\mu m$, where I denotes the measured intensity in bit from 0 to 255 and the subscript 3 denotes the

bit shift (LUT) used during the image acquisition. As one bit is shifted for every change in LUT, the value must be multiplied by two for every decrease of LUT, for example 1 I_5 = 2 I_4 = 4 I_3. This is a somewhat imperfect unit as the calibration with oil film thickness varies depending on the remaining dye concentration, the power of the laser, and the location on the image. It has been found that the calibration seems to hold within an acceptable error margin (~ ± 25 %) for the analyzed videos, as long as the measurement is not taken along the edges of the image. This calibration also assume a linear relation between the oil film thickness and the intensity, which has been validated by Thirouard [50], as long as measurement does not approach saturation. Finally, the lowest intensity on a given image is assumed to be the noise level and is attributed the zero oil film thickness value.

In this section, the calibration is first explained in more details, and is used to quantify the overall scraping rate of different oil seal configuration.

2.5.5.1 Oil Film Thickness Calibration

Calibration was first attempted using the calibration marks on the oil seals. The calibration mark used is a shallow groove on the seal taper along the circumferential direction. The first step is to draw a line along the radial direction and plot the intensity value along this line across the oil seal pack, as shown in Fig. 2.21. A zoom on the calibration mark region shows that the number of point taken by the measurement is limited and does not represents fully the shape of the calibration mark. Lines are drawn over the graph to reconstruct the shape of the mark. From those marks, it can be seen that the intensity measurement from the surface to the deeper portion of the valley is 40 I_3. Measurements show a depth of 16 μm. This would result in a sensitivity of 2.5 I_3/μm, which is below the expected value and varies significantly for every image used for calibration. This suggests that the calibration mark could not be full and the resulting measured oil film thickness can be smaller than expected, as shown in Fig. 2.22. A calibration mark with a rectangular profile might give better results, but is also probably harder to manufacture.

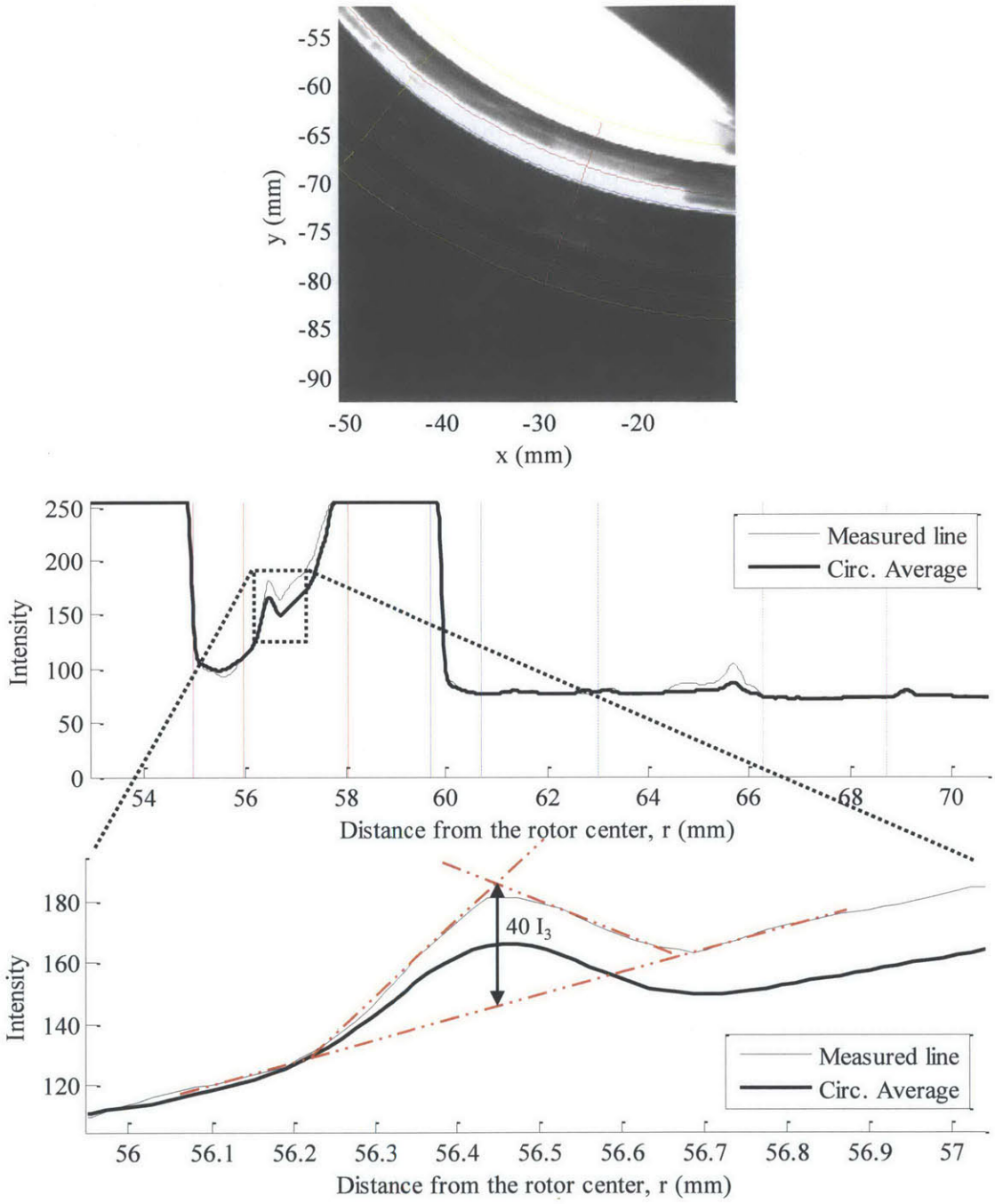

Fig. 2.21 Oil film thickness calibration attempt using calibration marks on inner oil seal

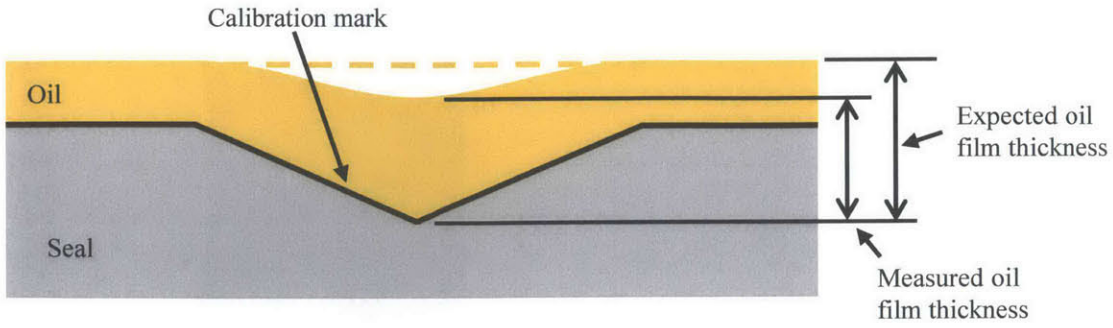

Fig. 2.22 Difference between expected and measured oil film thickness using calibration marks

The taper part of the seal is used as the calibration feature. When the taper is full, the intensity signal measured along the line is linearly increasing with radius, as shown in Fig. 2.23. Two points are taken to calculate the slope, which is the required calibration parameter. The advantage of this method is that the feature is already on the system and does not need any supplemental manufacturing. The two main disadvantages are: (1) generally, only the oil seals with a large contact width cause sufficient scraping to fill the taper part, and (2) the calibration must be made with a few images and conserved for the other images or experiments where the taper is not full. Nevertheless, the taper method gives a calibration that can be used for a first estimation of the oil film thickness.

The summary of the measured sensitivity based on the taper method are presented in Table 2.1, for the images shown in Fig. 2.23 and Fig. 2.24. A reasonable value for the sensitivity is 4 $I_3/\mu m$. This value is used for quantifying the scraping rate on the seals.

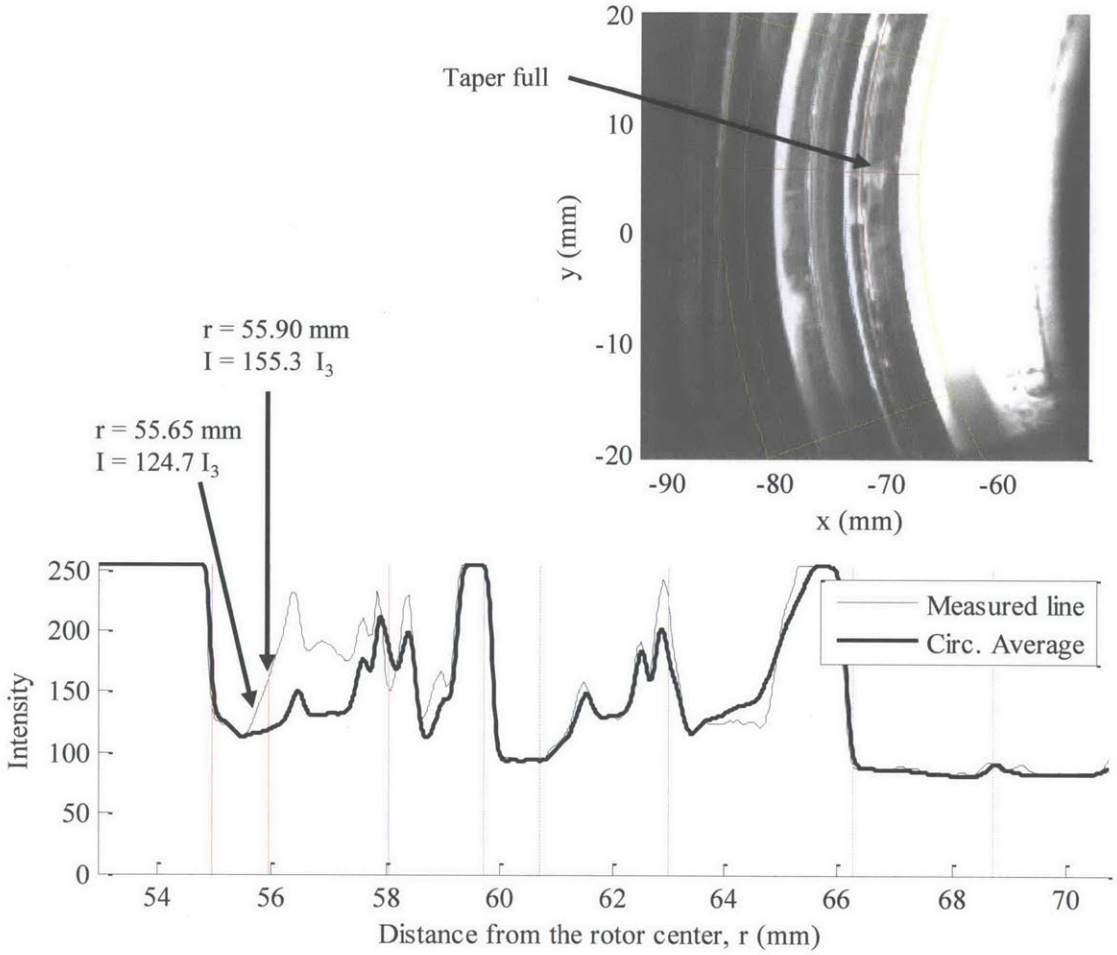

Fig. 2.23 Oil film thickness calibration using the taper full of oil

Table 2.1 Summary of sensitivity from the taper method

Image	Large contact width seal	Speed (rpm)	Sensitivity ($I_3/\mu m$)
Fig. 2.23	Inner and outer	3000	4.3
Fig. 2.24a	Inner and outer	3000	4.0
Fig. 2.24b	Inner and outer	3000	3.9
Fig. 2.24c	Inner only	3000	3.9

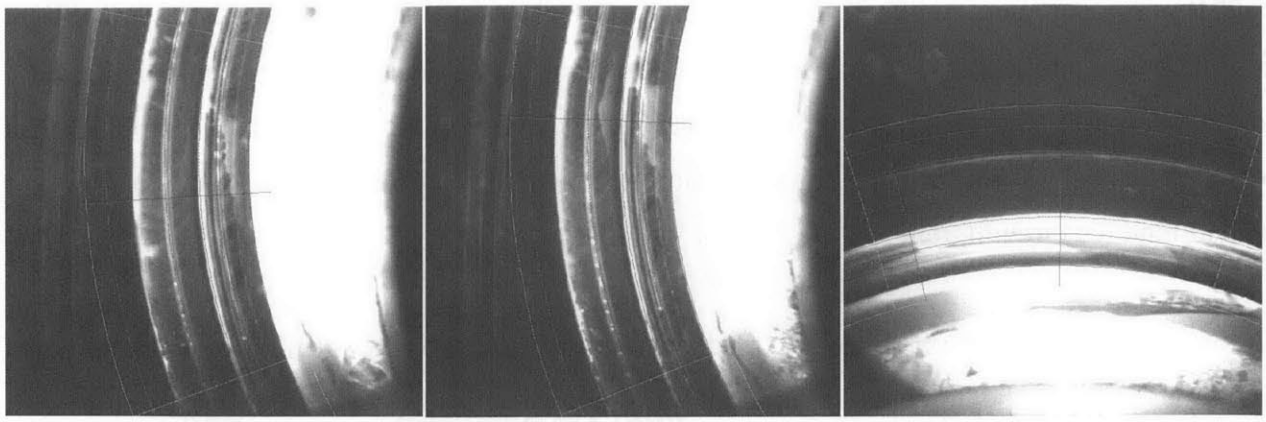

(a) (b) (c)

Fig. 2.24 Image for sensitivity calibration with the taper method

2.5.5.2 Scraping rate

Total scraping rate of the inner and outer seal is calculated for three different configurations: (1) mass production specifications, (2) large contact width for the inner seal, and (3) large contact width for both seals. The film thickness effective average is calculated for 18 regions of 20° each to span the entire seal circumference, as shown in Fig. 2.25. Since the flow rate is a function of the cube of the film thickness, the effective average film thickness ($\bar{h}_{eff}$) is defined as:

$$\bar{h}_{eff} = \left[\frac{1}{\theta_2 - \theta_1}\int_{\theta_1}^{\theta_2} h^3 d\theta\right]^{1/3} \tag{2.1}$$

in which h is the local film thickness, and θ_1 and θ_2 are the starting and ending angle of the region in the rotor reference frame. The effective average can then be used to calculate the scraping volume flow rate (Q) of the seal for the given region, based on a locally fully-developed flow:

$$Q = \frac{\bar{h}_{eff}^3}{3\mu}\rho\omega_R^2 R\,[(\theta_2 - \theta_1)R] \tag{2.2}$$

in which μ and ρ are the oil viscosity and density taken here to be 0.005 Pa·s and 800 kg/m^3, ω_R is the angular velocity of the rotor which is 3 times slower than the crankshaft angular velocity,

and R is measurement radius on the rotor. Since the centrifugal acceleration has a symmetrical variation around the value of $\omega_R^2 R$, this value can be taken as the average acceleration around a rotor revolution, and thus is used to calculate the average flow rate. The total accumulation in each land is calculated similarly, by integrating the oil film thickness from one seal to the other and around the circumference.

A summary of the total scraping rate, land accumulation and average oil film thickness is given in Table 2.2 for the three configurations. The effective average oil film thickness is also illustrated in Fig. 2.26 and Fig. 2.27. The images that were used for those calculations are shown in Fig. 2.28, Fig. 2.29, and Fig. 2.30. For the mass production specifications, there is only one important scraping region for the inner seal, image (p), and the scraping rate of the outer seal is very small.

For the inner seal large contact width configuration, the inner seal scraping rate is very large, and can be seen on all the images. As the contact width of the inner seal is larger, the oil film thickness left after its passage is larger than the outer oil seal clearance. Outer seal is then scraping oil inward and oil accumulates in the 4th land region. The large accumulation rate generates a large recycling rate to the housing which is then scraped outward by the inner seal and seen on its taper. As a large amount of oil is trapped, the scraping rate of the inner seal is large. The outer seal scraping is increased by this accumulation compared to the mass production specifications as expected, but it increases only by a factor of ten while the inner seal scraping is increased by a factor of about a hundred.

When both oil seals are modified with a larger contact width, the scraping rate of both seals is in the same order of magnitude. In this case, the cut-off seal clearance is the smallest of the three seals, and the cut-off seal start scraping both inward and outward, generating accumulation in the 3rd land. This oil is recycled to the housing and then scraped outward by the outer seal. Fourth land accumulation is more similar to mass production configuration than to inner seal large contact width configuration, and so is the inner seal scraping. These experiments suggest that the scraping rate of the inner seal is largely affected by the 4th land accumulation and the outer seal scraping is affected by the 3rd land accumulation.

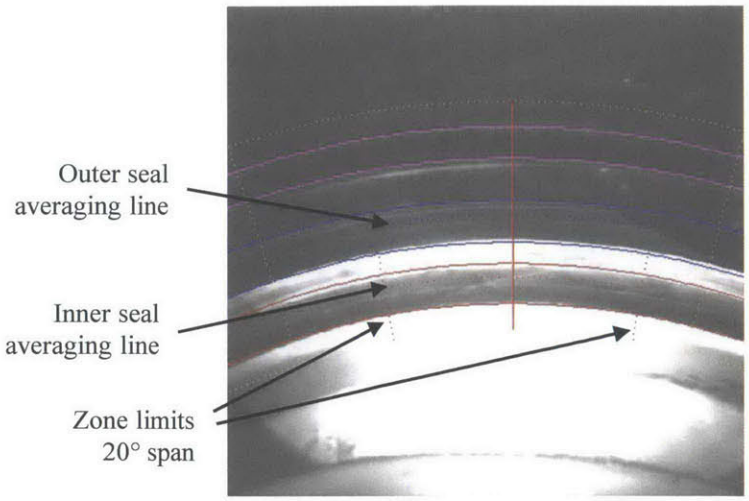

Fig. 2.25 Zone limits and lines along which oil film thickness effective average is calculated

Table 2.2 Summary of scraping rate and effective oil film thickness distribution

		Mass Prod. Specifications		Large contact width for inner seal		Large contact width for both seals	
		Inner seal	Outer seal	Inner seal	Outer seal	Inner seal	Outer seal
Total scraping rate (mL/h)		3.71	0.08	412.13	0.75	20.85	34.98
Land accumulation (mm^3)		21.88 (4^{th} land)	3.27 (3^{rd} land)	95.46 (4^{th} land)	4.55 (3^{rd} land)	27.72 (4^{th} land)	25.24 (3^{rd} land)
Location (°)	**Image**	**Effective average film thickness (μm)**					
0-20	(a)	2.20	0.35	11.36	0.84	2.68	8.17
20-40	(b)	4.70	1.26	21.56	1.85	8.94	9.81
40-60	(c)	2.36	0.60	12.45	2.05	5.56	6.62
60-80	(d)	2.05	0.61	24.03	1.90	7.91	9.06
80-100	(e)	4.44	1.24	28.24	2.16	8.14	9.66
100-120	(f)	4.13	1.73	15.52	2.68	5.68	9.65
120-140	(g)	2.47	0.44	12.17	1.29	1.59	6.71
140-160	(h)	2.45	1.13	44.45	2.42	2.00	7.39
160-180	(i)	1.90	0.94	13.76	2.69	1.94	5.48
180-200	(j)	2.11	0.99	10.56	1.64	3.85	4.15
200-220	(k)	3.69	1.23	22.19	2.99	15.53	7.70
220-240	(l)	2.26	1.18	20.02	2.54	6.69	10.01
240-260	(m)	0.96	0.87	14.73	1.19	4.24	12.43
260-280	(n)	2.45	1.09	16.74	3.46	12.88	14.21
280-300	(o)	5.01	0.58	15.52	3.23	8.17	8.70
300-320	(p)	10.16	0.59	10.42	2.03	5.98	7.88
320-340	(q)	3.84	1.45	13.62	3.54	5.07	5.81
340-360	(r)	2.67	1.91	16.10	2.73	3.19	7.14

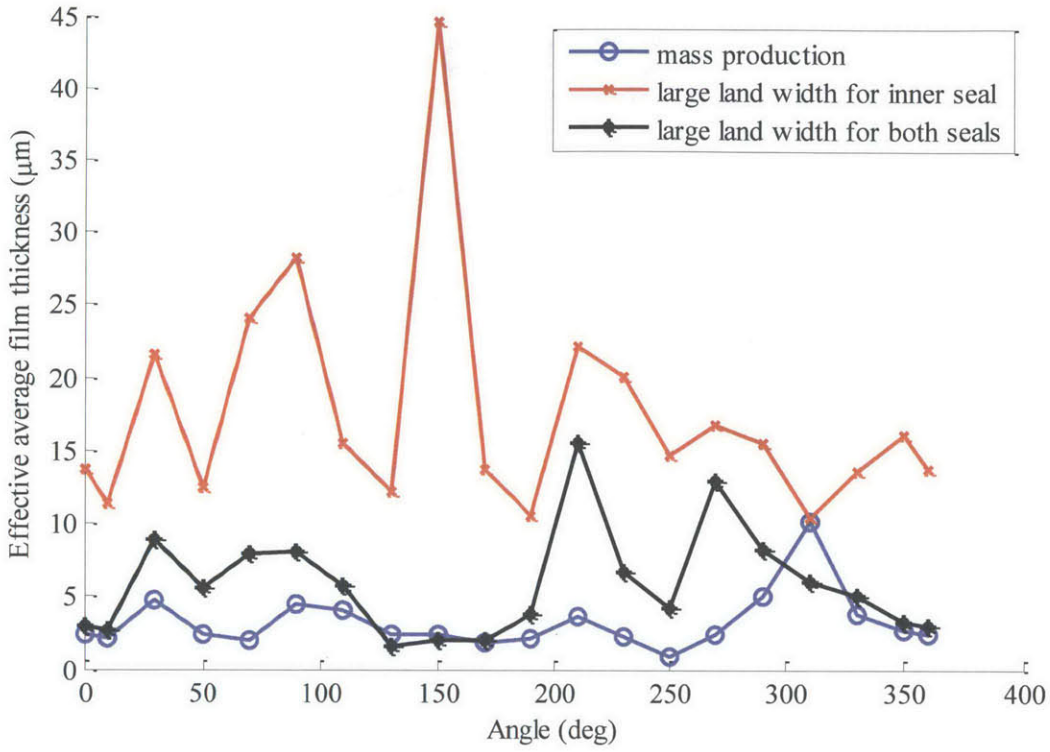

Fig. 2.26 Oil scraping distribution on the inner seal taper

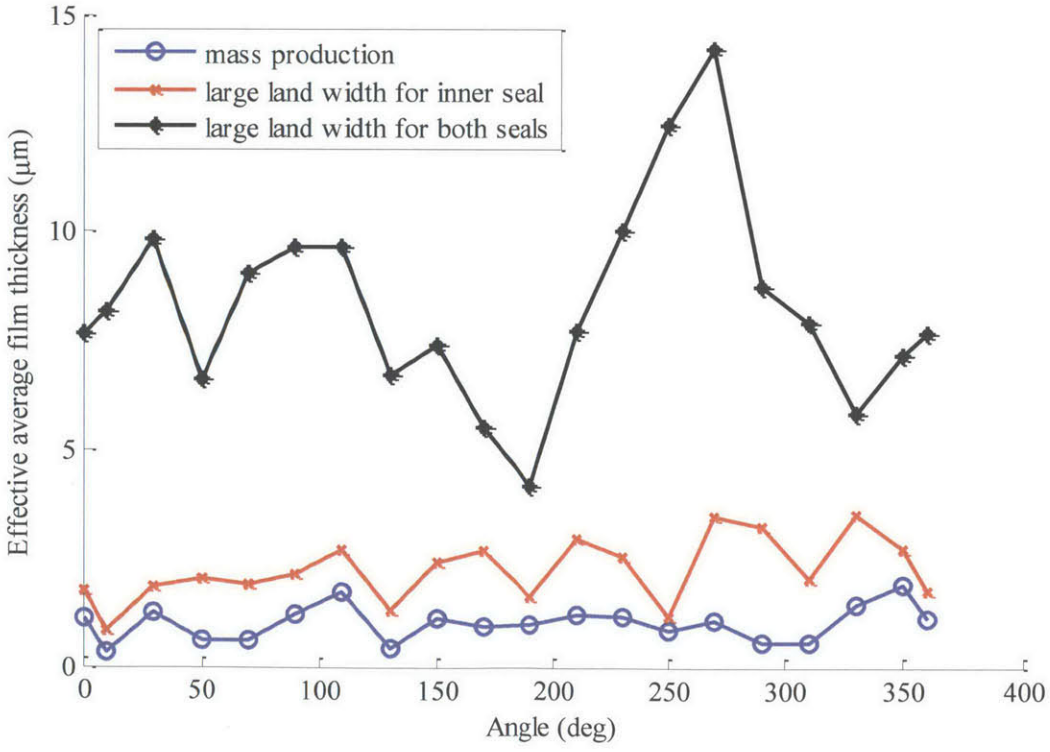

Fig. 2.27 Oil scraping distribution on the outer seal taper

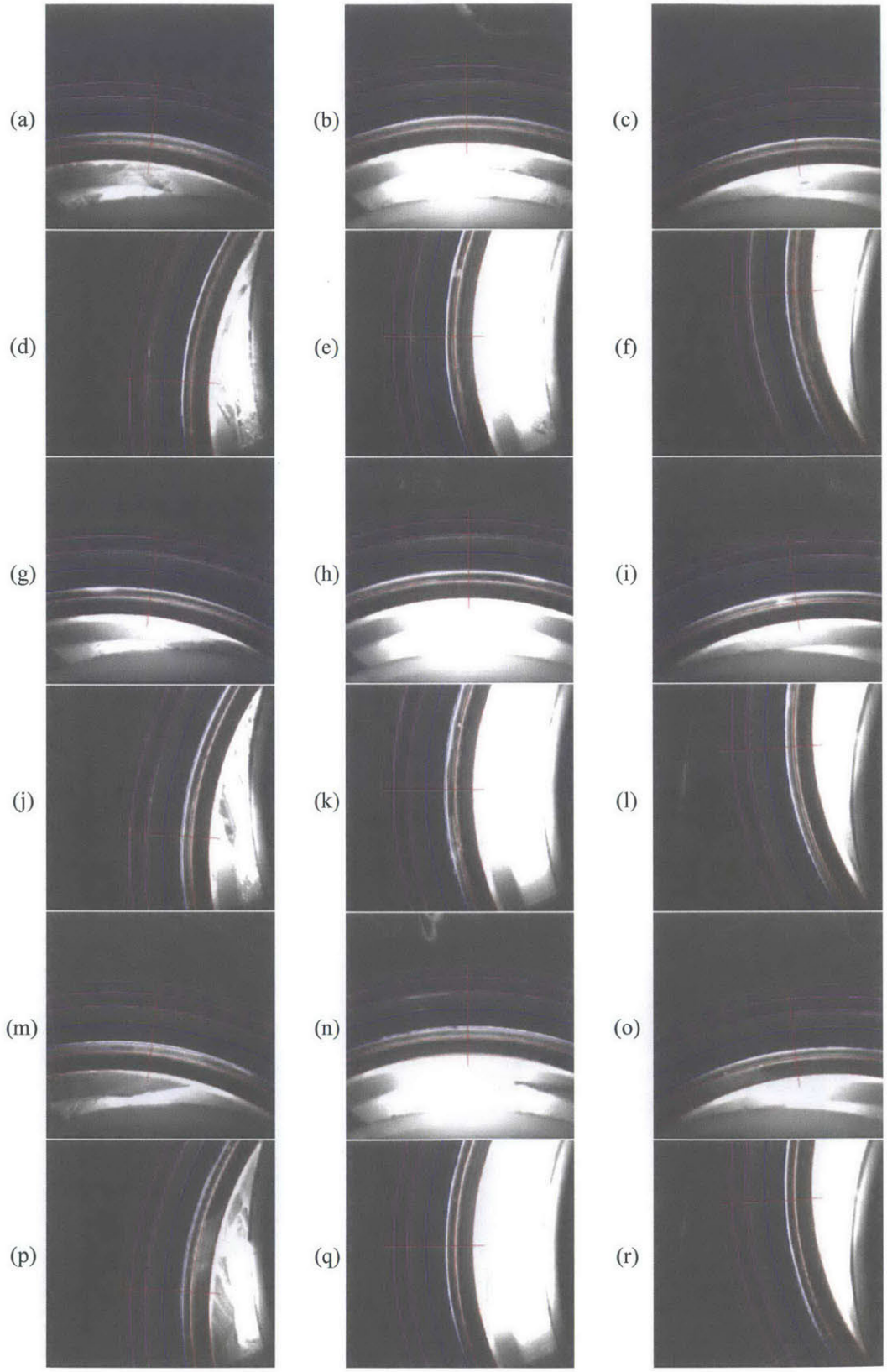

Fig. 2.28 Scraping distribution for mass production specification

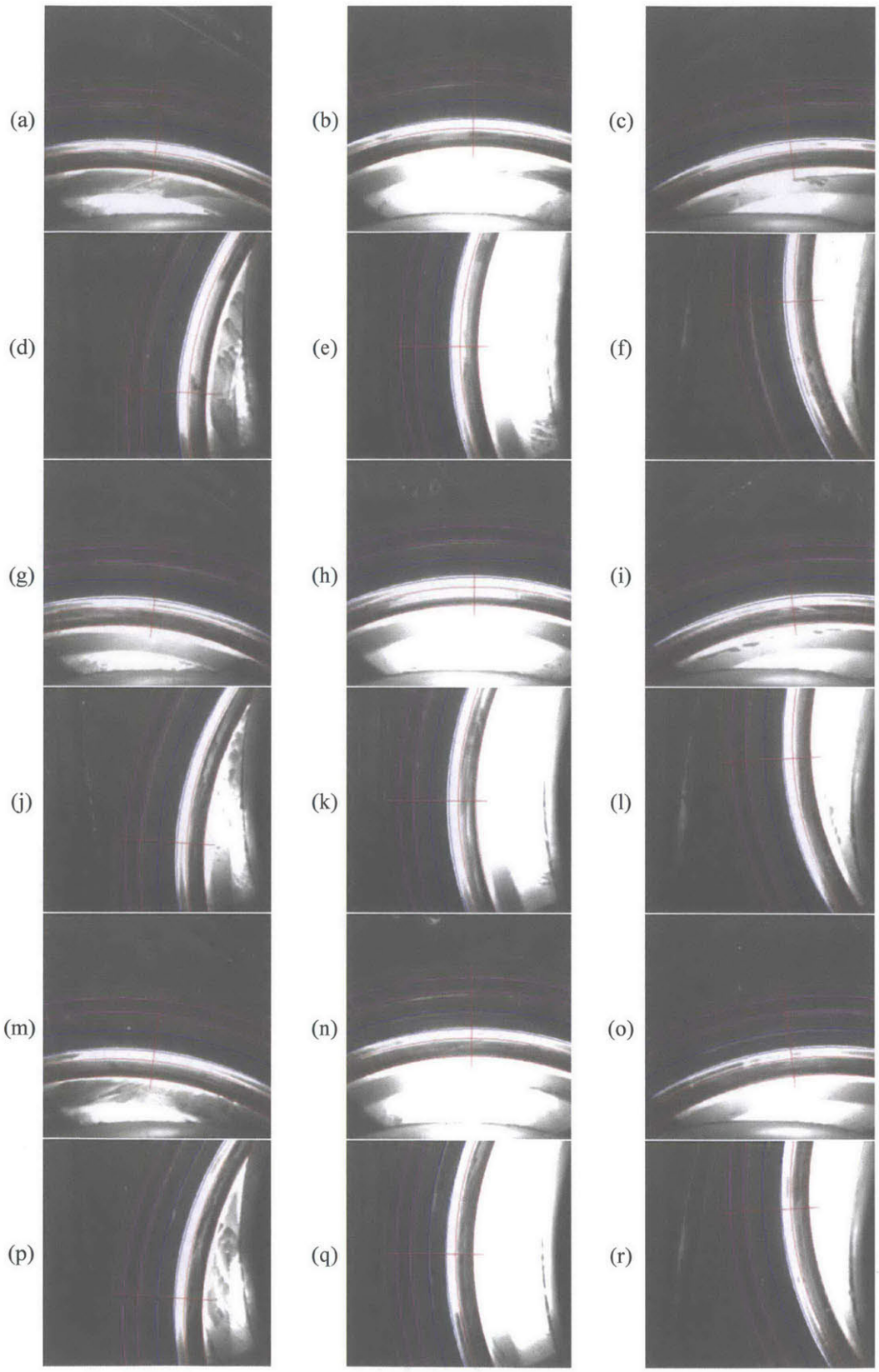

Fig. 2.29 Scraping distribution for large contact width inner seal

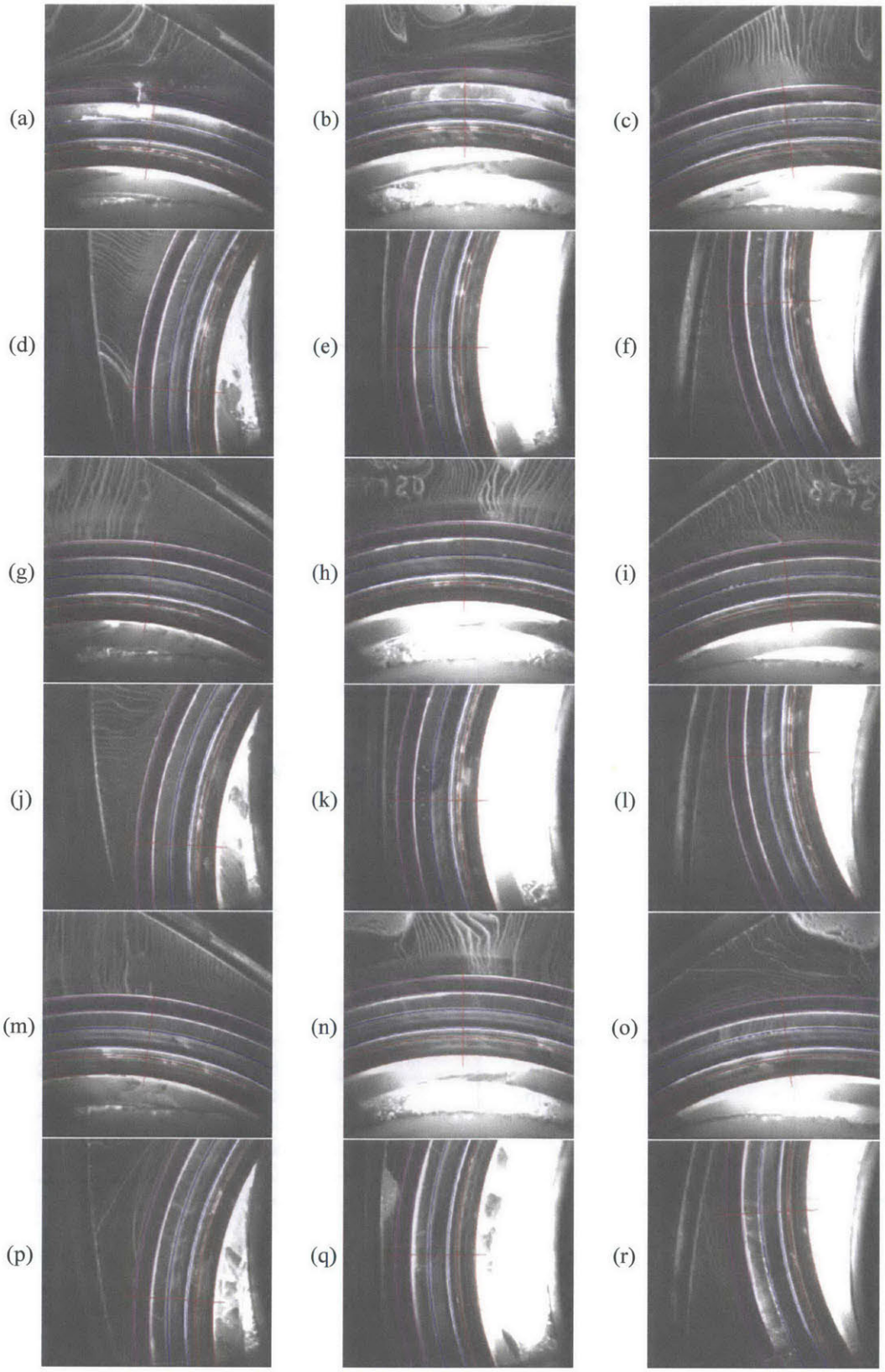

Fig. 2.30 Scraping distribution for large contact width for both oil seals

As a summary, the oil transport for the three different setups is shown in Fig. 2.14. The main difference is that the seal with the highest pressure, and thus the lowest clearance is scraping inward. In the mass production specification case, the inner seal scrapes inward and thus the behavior of the system is adequate. In the case where the inner seal has a large contact width, the outer seal starts scraping inward, filling the 4th land. Finally, when the two oil seals have large contact width, the cut-off seal scrapes inward and fill both the 3rd and 4th lands.

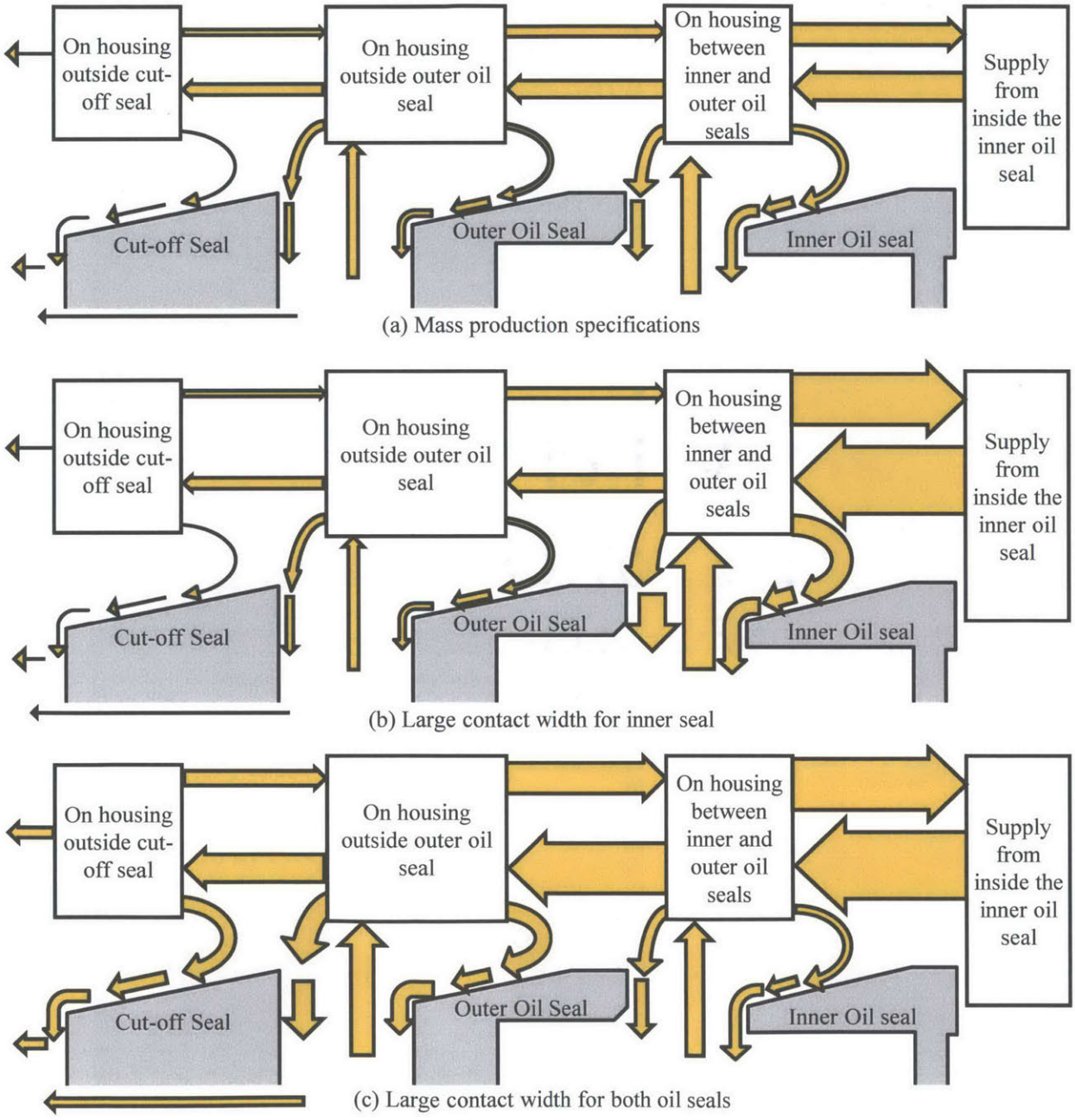

Fig. 2.31 Oil transport comparison between the three oil seal configurations

2.5.6 Conclusions for Oil Seals and Cut-Off Seal Oil Transport

Although the sapphire window distortion is different from the actual side housing, the 2D-LIF engine provides important information on the oil seals and cut-off seal behavior:

1. Inner seal scraping is increasing with an increase in 4th land accumulation.
2. Outer seal scraping is increasing with an increase in 3rd land accumulation.
3. Once oil is scraped outward by the cut-off seal or has passed under the cut-off seal, oil is pushed on the rotor by body force towards the side seal.
4. The mass production relative contact pressure of the seals is appropriate, because scraping of the inner seal is larger than the outer seal, and outer seal scraping is larger than cut-off seal scraping.
5. Reducing the inner seal contact pressure without reducing the outer seal contact pressure generates a large inward scraping of the outer seal and a large 4th land accumulation. An increase in outward scraping of the outer seal is also observed
6. Reducing contact pressure of both oil seals without reducing the cut-off seal contact pressure results in catastrophic internal oil consumption, as the cut-off seal is scraping inward and the accumulation in 3rd land becomes large. There is no barrier to avoid oil consumption when oil reaches 3rd land. Hence, future reduction of spring forces and change of seal design need to ensure decreasing order of seals' scraping ability from inner seal to cutoff seal.
7. Gas exchange around the cut-off seal gap generates a circular pattern of oil transport.

2.6 Gas Seals Oil Transport Visualization

Gas seals are sealing the chamber from one another and from the side of the rotor. To limit amount of wear, the gas seals need to be adequately lubricated. Experiments with the LIF setup allow observing oil transport around those seals and provide information about the distribution of oil in the different regions. Oil distribution patterns also give indirect understanding of gas leakage for the side seals and the corner seals.

Oil pattern seen on the rotor is a competition between five mechanisms:

1. Body force, mainly the centrifugal fictitious force pushing oil outward

2. Shear from rotation, air shear stress caused by the relative motion between the rotor and the housing, pushing the oil in direction opposed to rotation
3. Gas leakage drag, entrainment by gas leakage next to gas seals
4. Oil viscous resistance
5. Surface tension

The three first mechanisms are driving the oil to move, while the two last mechanisms are restraining oil motion. In this section, the general oil pattern caused by those mechanisms on the rotor is first discussed, followed by a comparison of the magnitudes of the different mechanisms.

2.6.1 Oil Pattern

The LIF setup is currently limited to one image every rotor revolution. The motion between two subsequent images is therefore a result of oil motion during a complete revolution. A droplet of oil can thus move in both directions during a rotor revolution, but the motion perceived from the LIF images is unidirectional. This phenomenon is illustrated in Fig. 2.32. Fortunately, the motion is slow enough for most of the regions on the rotor, so the resulting direction can be determined.

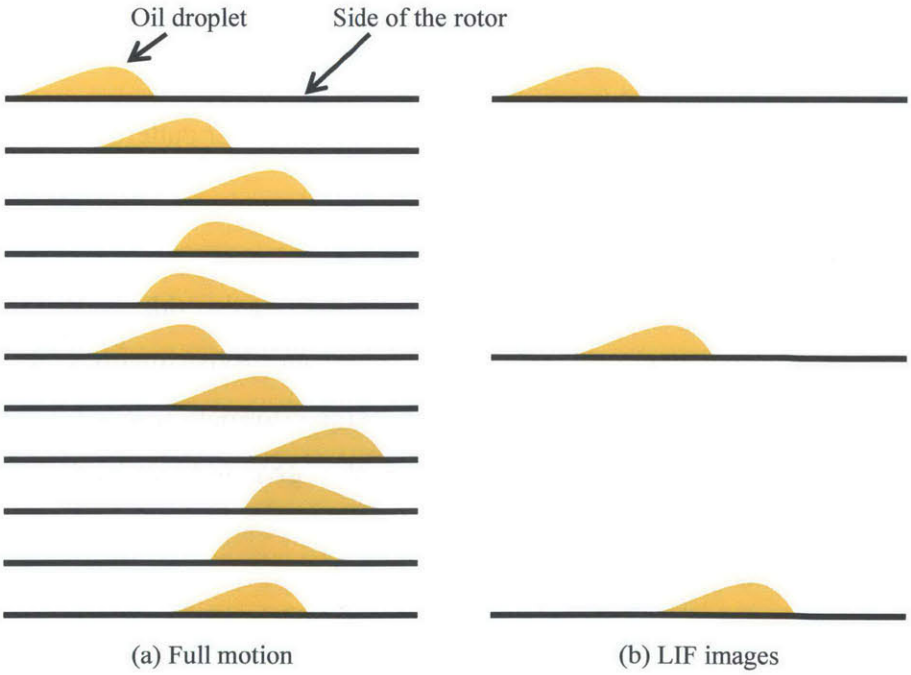

Fig. 2.32 Difference between the complete motion and the motion perceived from the LIF images

Oil pattern on the side of the rotor provides information on oil transport, and indirectly on gas transport. Oil film thickness for mass production specification is small, which makes it difficult to see and analyze, as shown in Fig. 2.33. It is still possible to see oil being dragged by the gas flow against body force. The phenomena are easier to see for the 2 Hz side injection frequency case, as shown in Fig. 2.34. On both sides of the corner seal, gas flow drags the oil inward. On the leading side of the corner seal (on the right side of the corner seal in Fig. 2.34), gas flow drags oil inward in a region of a width similar to the corner seal radius. This is due to the opening of the side seal inner flank caused by the contact with the corner seal. On the trailing side of the corner seal, oil is dragged in a narrow region by the gas leaking between the corner seal and the side seal. For both sides, gas flow seems to be stopped by the cut-off seal and turn circumferentially, dragging the oil with it. Outside those regions, oil is pushed outward by body force and reaches the side seal, completing the circular patterns. Finally, oil finds its way under the side seal, and some is thrown off in the chamber. Some oil is also seen leaking out of the corner seal clearance.

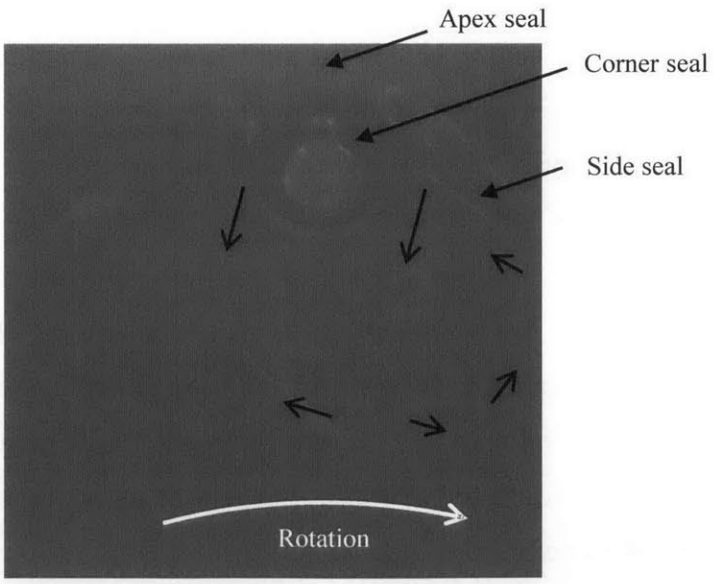

Fig. 2.33 Oil pattern on the rotor for mass production specifications

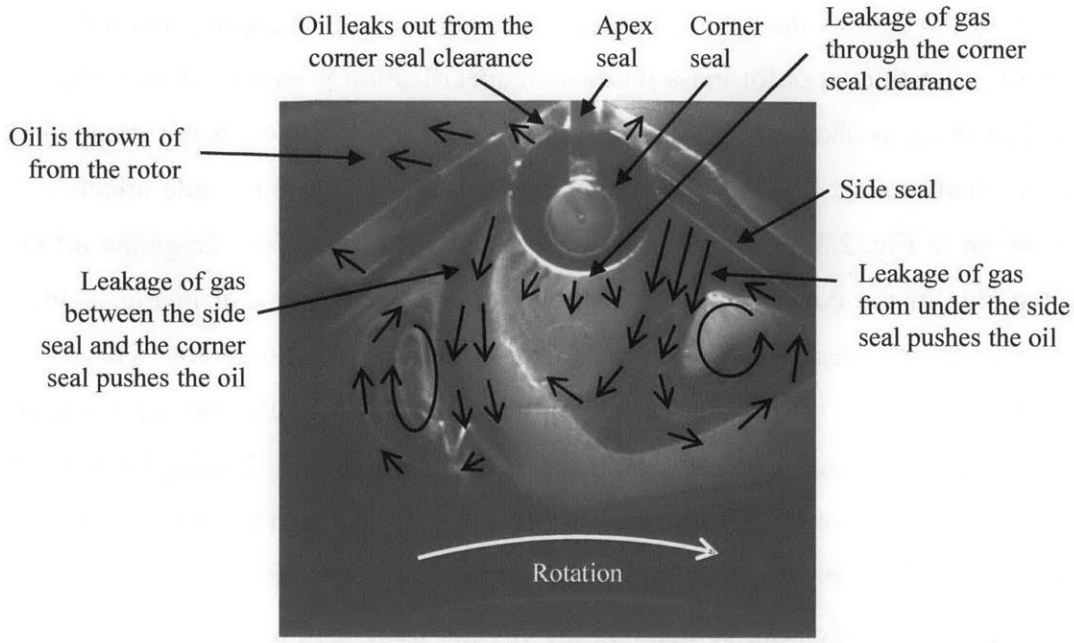

Fig. 2.34 Oil pattern on the rotor for a side injection frequency of 2 Hz

2.6.2 Scaling of Oil Transport Mechanisms

A comparison of the magnitude of the different driving mechanisms allows for a better understanding of the LIF videos, which in turns can guide design improvements. The approach to compare the mechanisms in this section is to use the lubrication approximation and neglect surface tension. Those approximations allow calculating the velocity of the oil film for the three driving mechanisms: body force, shear from rotation and gas leakage drag. As the momentum equation is linear under lubrication approximation, the solutions can be superposed, and the resulting total velocity is the sum of the velocities induced by the three mechanisms. The velocities can then be compared to estimate in which conditions a mechanism dominates over the others. Finally, with the velocity known, the lubrication approximation is validated. Surface tension is also compared to body force to assess in which conditions surface tension would be important, and the oil velocity calculated would be changed.

The variables and values of the different parameters used in this section are defined in Table 2.3. Unless otherwise specified, nominal values are used for calculations and graphs are plotted from minimum to maximum values.

Table 2.3 Properties and dimensions for scaling of the oil transport mechanisms

Property/Dimension	Unit	Variable	Min.	Nominal	Max.
Oil viscosity	Pa·s	μ		0.005	
Oil density	kg/m^3	ρ		800	
Oil surface tension coeff.	N/m	σ		0.02	
Air viscosity	Pa·s	μ_g		1.8×10^{-5}	
Oil film thickness	μm	h_f	1	10	30
Puddle length	mm	L		10	
Rotational velocity	krpm	$krpm$	1	3	9
Rotor angular velocity	rad/s	ω_R	35	105	314
Characteristic radius (2nd land)	mm	R_c		75	
Air velocity from leakage	m/s	V	1	10	100

2.6.2.1 Body Force

The parabolic velocity profile resulting from body force is shown in Fig. 2.35.

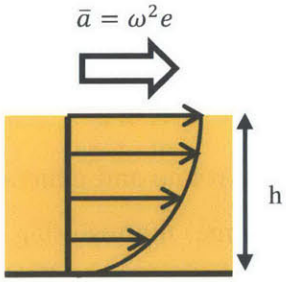

Fig. 2.35 Velocity profile due to body force

From lubrication theory, the average film velocity due to body force ($\bar{u}_B$) is:

$$\bar{u}_B = \frac{h_f^2}{3\mu}\rho\bar{a} \tag{2.3}$$

in which $\bar{a}$ is the average centrifugal acceleration over a cycle. Replacing the acceleration by its value yields the order of magnitude for the velocity due to body force:

$$\bar{u}_B \sim \frac{h_f^2}{3\mu}\rho\omega_R^2 R_c \tag{2.4}$$

The velocity of the film in mm/s is plotted in Fig. 2.36 against oil film thickness and rotational speed to give an order of magnitude. The oil velocity for the 2D LIF engine is about 1-10 mm/s. This is slow enough to see the displacement of the oil film from one image to the other.

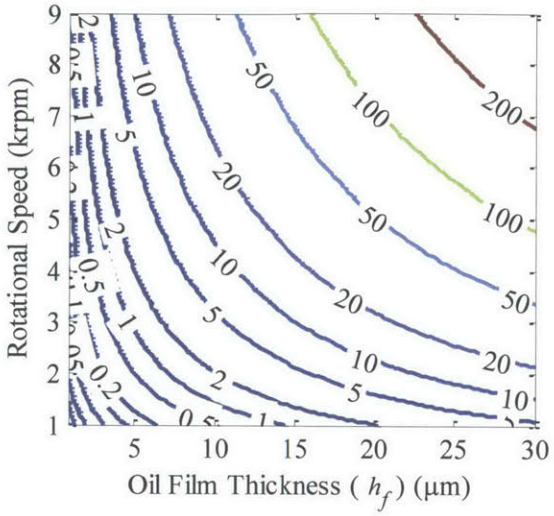

Fig. 2.36 Average film velocity (mm/s) as a function of film thickness and rotational speed

2.6.2.2 Shear from Rotation

The rotation of the rotor causes the air to rotate and generates a shear force on the oil. Changing reference frame to the rotor reference frame, the resulting linear velocity profiles for air and oil are shown in Fig. 2.37.

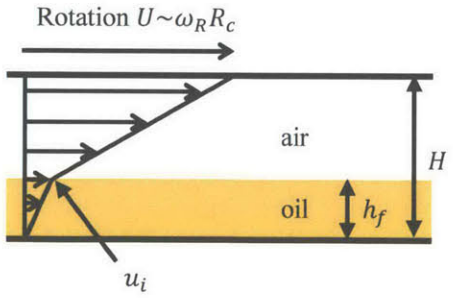

Fig. 2.37 Velocity profiles for oil and air on the rotor reference frame (oil velocity is exaggerated for illustration)

As viscosity of the oil is much larger than air viscosity, the velocity at the interface is much smaller than the rotation velocity and can be neglected when calculating the shear force at the

air-oil interface. At the interface, the oil and air shear stress are the same. Replacing by the respective shear stress values yields:

$$\frac{\mu\, u_i}{h_f} = \frac{\mu_g U}{H - h_f} \tag{2.5}$$

in which u_i is the velocity at the interface. Replacing for the rotor velocity and noting that the average velocity is half the velocity at the interface yields:

$$\bar{u}_S \sim \frac{1}{2}\frac{\mu_g}{\mu}\frac{h_f \omega_R R_c}{(H - h_f)} \tag{2.6}$$

A comparison of the velocities from shear and body force reduces to:

$$\frac{\bar{u}_S}{\bar{u}_B} \sim \frac{3}{2}\frac{\mu_g}{h_f(H - h_f)\rho\omega_R} \tag{2.7}$$

This relation is plotted in Fig. 2.38. For an important film thickness, the body force dominates. Only at low speed and low film thickness, body force and shear from rotation effects are on the same order.

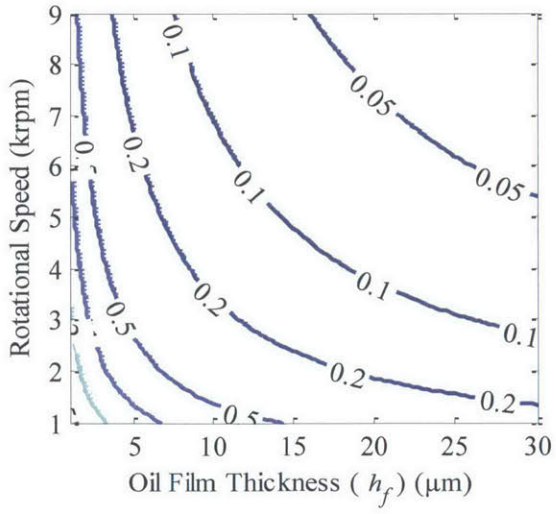

Fig. 2.38 Velocity from shear divided by velocity from body force as a function of oil film thickness and rotational speed

2.6.2.3 Gas Leakage Drag

Oil can also be dragged from gas leaking from the high pressure chamber, as shown in Fig. 2.39.

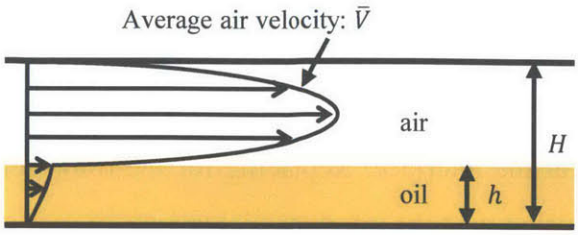

Fig. 2.39 Velocity profiles of oil and air due to gas leakage drag

Again, the air velocity is much larger than the oil velocity, so the interface velocity can be neglected for the air velocity calculation. From lubrication theory, the average oil velocity caused by the drag ($\bar{u}_D$) can be expressed as a function of the pressure gradient (dP/dx) and the shear stress at the interface (τ_i):

$$\bar{u}_G = \frac{h_f^2}{3\mu}\left(-\frac{dP}{dx}\right) + \frac{h_f}{2\mu}\tau_i \tag{2.8}$$

The pressure gradient can be calculated from the air flow, approximating the flow to be fully developed:

$$\bar{V} \sim \frac{(H-h_f)^2}{12\mu_g}\left(-\frac{dP}{dx}\right) \tag{2.9}$$

The shear stress is found by a force balance on a small control volume, and is given by:

$$\tau_i = \frac{(H-h_f)}{2}\frac{dP}{dx} \tag{2.10}$$

Combining yields:

$$\bar{u}_G \sim \frac{\mu_g}{\mu}\frac{h_f \bar{V}}{(H-h_f)}\left(\frac{4h_f}{(H-h_f)} + 3\right) \tag{2.11}$$

The first term is due to the pressure gradient and the second term to the shear stress at the wall. It results that the shear stress term is at least 3 times larger than the pressure term. Neglecting the pressure term, a simple expression can be used to compare velocity from drag to velocity from body force:

$$\frac{\bar{u}_G}{\bar{u}_B} \sim \frac{9\mu_g \bar{V}}{(H - h_f)h_f \rho \omega_R^2 R_c} \tag{2.12}$$

A comparison between the average velocities from drag compared to the velocity from body force is shown in Fig. 2.40. At low gas leakage speed (~ 1 m/s), body force dominates. At high gas speed (~ 100 m/s), drag dominates, except at high rpm. At moderate gas speed (~ 10 m/s), the two effects are on the same order around 3000 rpm, from moderate to large film thickness.

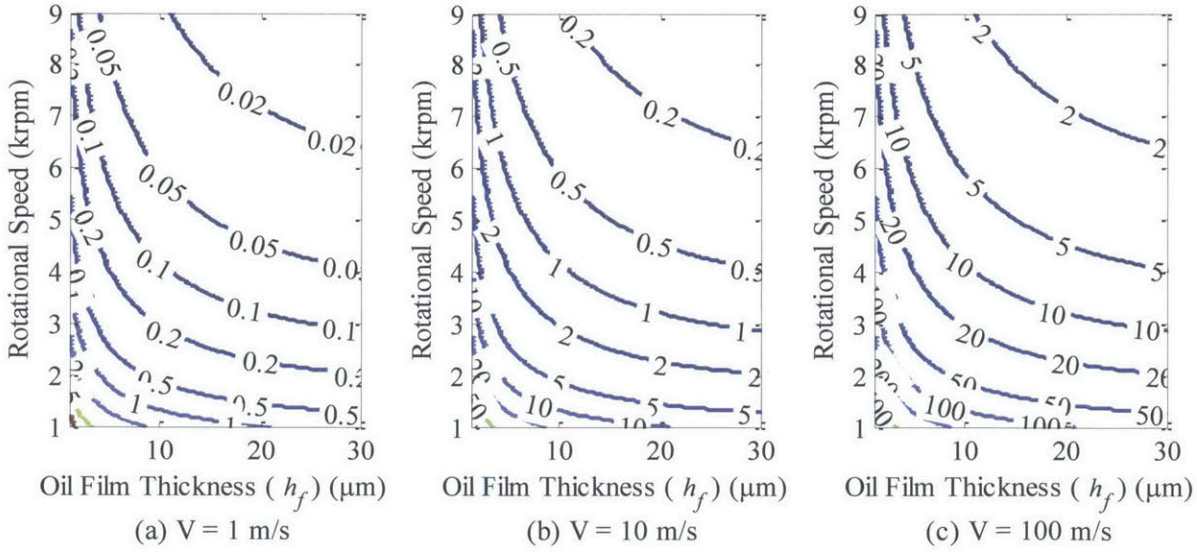

Fig. 2.40 Velocity from drag divided by velocity from body force as a function of oil film thickness and rotational speed

2.6.2.4 Approximation validation

Knowing the velocity, the lubrication approximation can be validated. The worst case is for the largest speed and largest film thickness. Using the velocity from body force, the two criteria are met:

$$\left(\frac{h}{L}\right)^2 \sim 10^{-5} \ll 1$$
$$Re_L\left(\frac{h}{L}\right)^2 \sim 10^{-5} \ll 1 \tag{2.13}$$

The surface tension force can be compared to body to verify when it should be considered. The net surface tension force on a droplet is caused by the difference between the receding and advancing angles (θ_r and θ_a). Assuming the difference between the two cosine functions is around 0.1, the ratio of surface tension force to body force is given by:

$$\frac{F'_{sur.\ tension}}{F'_{body\ force}} \sim \frac{\sigma(\cos(\theta_r) - \cos(\theta_a)}{\rho L h \omega_R R_c} \sim \frac{0.1\sigma}{\rho L h \omega_R R_c} \tag{2.14}$$

A contour plot of the comparison between surface tension and body force is shown in Fig. 2.41. It shows that surface tension is much smaller than body force for most conditions. Inertia and surface tension can be on the same order of magnitude for thin and short oil droplets at low speed. Finally, combining the results of this section it can also be determined that surface tension plays a negligible role near the gaps.

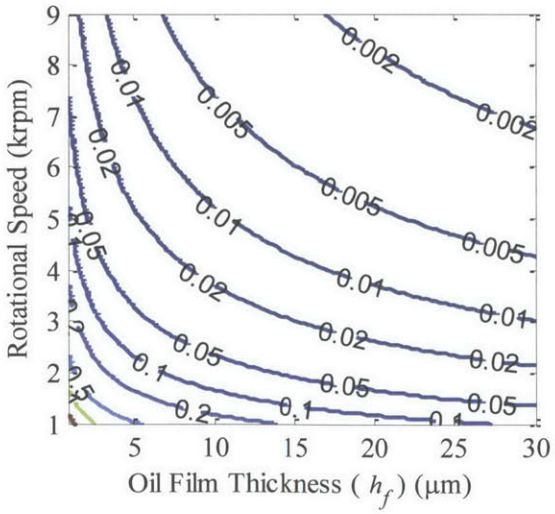

Fig. 2.41 Surface tension force divided by body force as a function of oil film thickness and rotational speed

2.6.2.5 Mechanisms seen on LIF engine

To illustrate the effect of the different mechanisms, the experiments with 2 Hz center injection is chosen because it has sufficient amount of oil to be seen properly on the image, while it is not too flooded to change the pattern on the rotor significantly. It can be seen in Fig. 2.42 that at 1000 rpm, surface tension plays an important role and forms droplets and streaks, while at 3000 rpm it is more entirely streaks. Gas leakage drag clearly dominates near the gaps, and body force away from the gaps. There is no clear evidence of the shear from the rotation as expected from the scaling analysis.

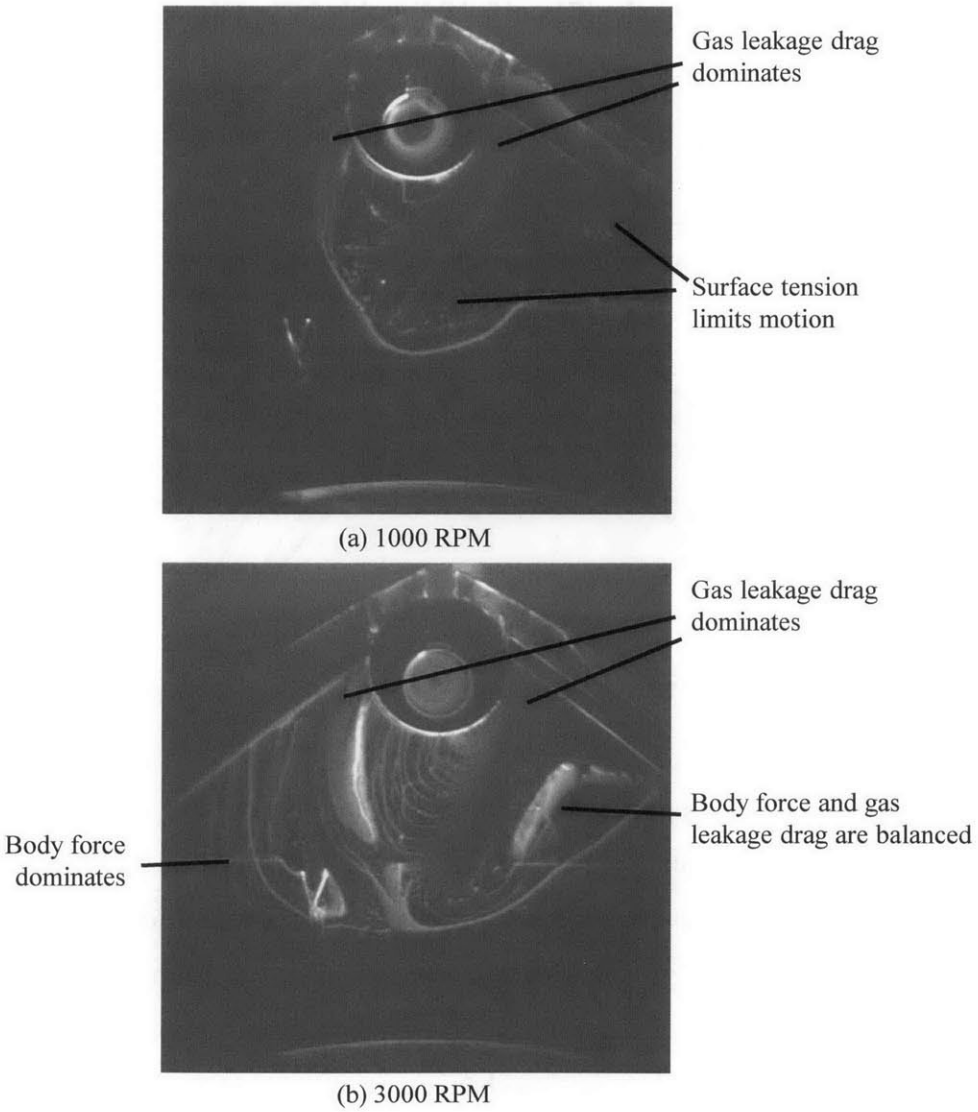

Fig. 2.42 Oil transport mechanisms seen on a 2 Hz center injection experiment

2.6.3 Conclusions for Gas Seal Oil Transport

Experiments with the 2D-LIF engine combined with simple scaling provide an insightful tool to understand oil and gas transport on the side of the rotor, as illustrated in Fig. 2.43:

1. Oil is dragged with gas in the side and corner seal clearances.
2. Oil is dragged inward on the side of the rotor.
3. Away from the gaps, the body force dominates and pushes the oil towards the side seals which lubricates them.
4. The shear from the air due to the rotation of the rotor does not influence significantly oil transport.
5. Oil surface tension can be significant for small droplet at low speed, limiting the motion of the oil on the side of the rotor.

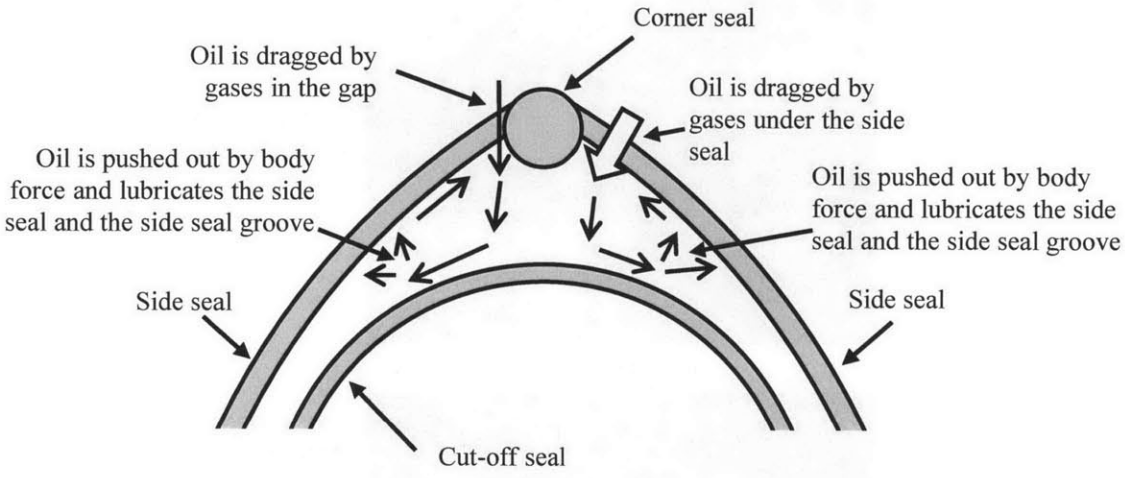

Fig. 2.43 Oil transport summary around the gas seals

2.7 Conclusions

A laser-induced fluorescence technique is used to visualize oil transport on the side of the rotor during engine operation. The dominant oil transport mechanisms are identified and estimated with first order calculations. Oil transport leading to internal oil consumption starts from inside the rotor with the rotor land accumulation and release mechanism. Oil seals are the main barrier for internal oil consumption and the main mechanism for oil to pass them is scraping. Once pass the outer oil seal, there is no mechanism to bring the oil back to the crankcase. Oil scraped by the cut-off seal accumulates on the rotor and is pushed outward by body force on the 2nd land where

it meets the metered oil brought to the rotor side by gas leakage. The oil is then pushed toward the side seals, lubricates the side seal grooves and is finally thrown into the combustion chamber.

The next chapter presents a model to predict internal oil consumption based on the understanding of the oil transport mechanisms developed from the 2D LIF engine.

Chapter 3

Oil Transport Model for the Oil Seals

This chapter presents a model to estimate internal oil consumption of the rotary engine from seal design and operating conditions. The model is based on a curved beam finite element model developed for piston rings. Based on the clearance with the side housing, oil transport is calculated during a few cycles using a control volume approach. The main mechanism for internal oil consumption identified by the model is the lack of conformability of the oil seals to the distorted side housing, which leads to outward scraping. From a parametric study, the most beneficial approach in reducing internal oil consumption is increasing seal compliance. A first order comparison of the model to experimental results show that predicted internal oil consumption is higher than expected, but in the right order of magnitude.

3.1 Oil Seal Model Formulation

The main objective of the oil seal cycle model is to quantify oil transport mechanisms by an accurate description of the seal-housing interaction. The model goal is also to give an estimation of the main lubrication performance indicators, namely:

- Oil consumption
- Friction power
- Wear, by quantifying the contact pressure distribution.

Inputs needed for the model to generate those outputs are shown in Fig. 3.1, as well as other main outputs generated by the model.

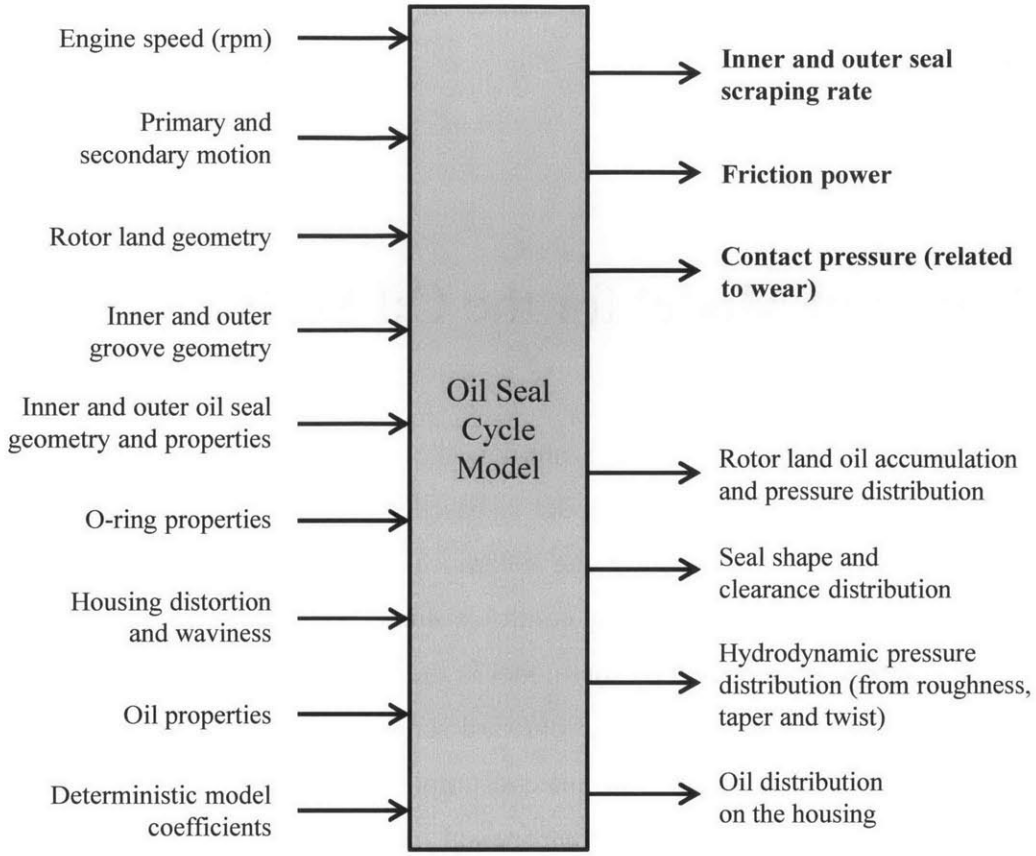

Fig. 3.1 Inputs and outputs of the cycle model

3.1.1 Model Overview

Complete engine revolution is subdivided in a given number of steps of a few crank angle each. For every step, the model can be subdivided into four main stages, as shown in Fig. 3.2:

(1) The position of the seals in the plane (x, y), to locate the seals in the radial direction relative to its groove. This radial position is computed to balance body force, O-ring compression force and groove reaction force if applicable.

(2) Spring force, O-ring friction force and groove friction force in the axial direction (z) are calculated from secondary motion.

(3) Seal deformation and interface pressure are solved simultaneously.

(4) Oil transport is estimated based on interface clearance.

The four stages are repeated for every step in the cycle. Few revolutions are needed until the system reaches steady state.

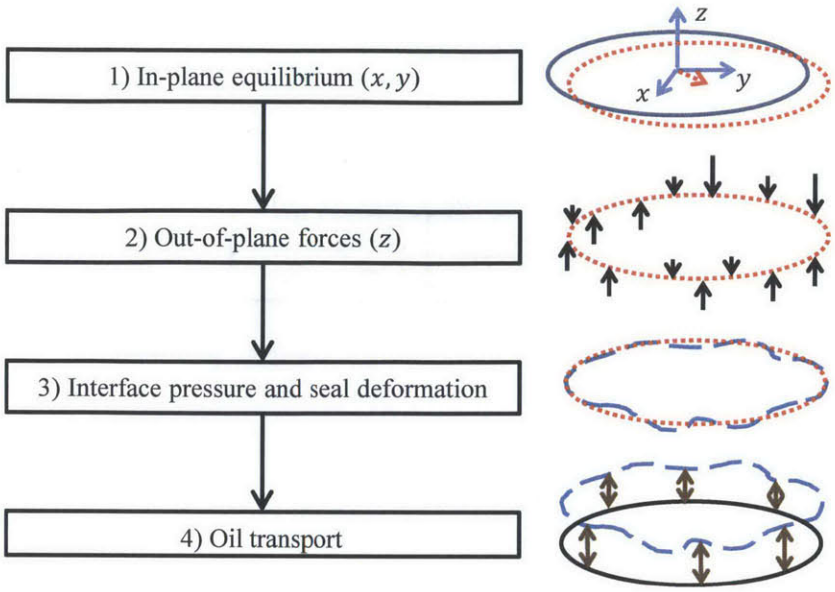

Fig. 3.2 Cycle model main stages

Many interactions take place between the stages, as shown in Fig. 3.3. Inputs and outputs are also related to the different stages.

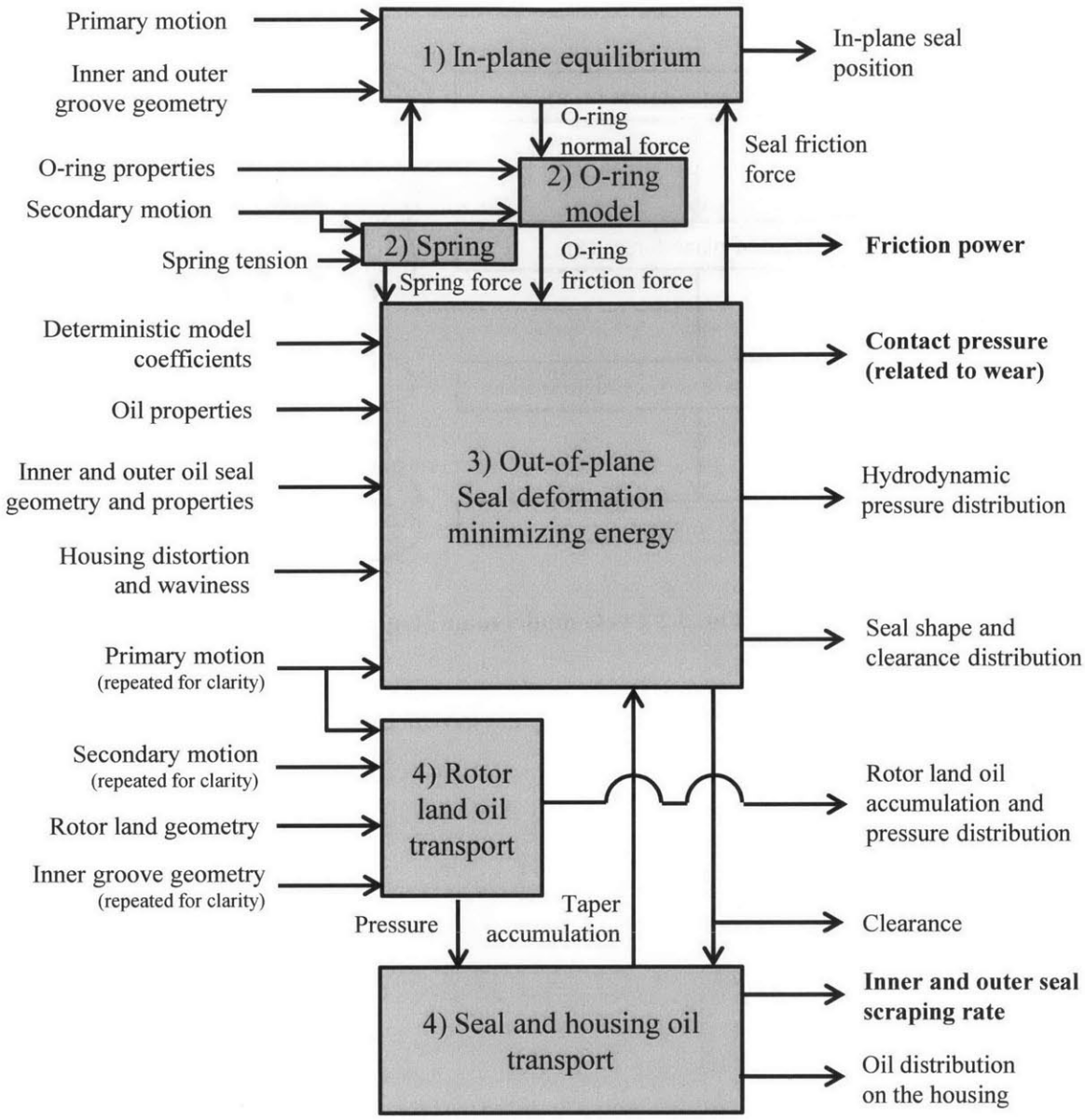

Fig. 3.3 Complete flowchart of the oil seal model

3.1.2 Approximations

The first main approximation is that seal equilibrium can be solved as quasi-steady. Due to the O-ring acting as a spring, the displacement of the seal is slow and its acceleration relative to its groove is small compare to the rotor acceleration. This approximation is validated in section 3.1.11.

Second, seal deformation is small compared to secondary motion. Therefore, the seal deformation is neglected when calculating spring force. This approximation is also validated in section 3.1.11.

Third, all flows are approximated as fully viscous. Effect of fluid acceleration compared to viscous forces can be neglected since, for the rotor land:

$$\mathrm{Re}_L \left(\frac{h}{L}\right)^2 \equiv \frac{\mu U L}{\rho}\left(\frac{h}{L}\right)^2 \sim 0.04 \tag{3.1}$$

This value would be even lower for the seal-housing interface. Capillary effect can be neglected since, for the rotor land:

$$\mathrm{Ca} \cdot \left(\frac{L}{h}\right) \equiv \frac{\mu U}{\sigma}\left(\frac{L}{h}\right) \sim 125 \tag{3.2}$$

This shows that the forces from viscous effect are much greater than the forces from capillary effect. This value would be on the same order or larger for the seal-housing interface and the taper.

Fourth, it is assumed that the hydrodynamic pressure generated by roughness, taper and tilt can be superposed linearly. Although it is realistic to assume that superposing those effects increases hydrodynamic pressure generation, it might not be a simple addition. Nevertheless, this approach allows investigating the effect of those parameters on internal oil consumption.

Fifth, inside the inner oil seal is assumed to be always fully flooded. This is a conservative approximation since internal oil consumption can only be over-estimated by this approximation. If the housing is in starved condition, oil passing the inner oil seal would be smaller than the value predicted by the model, as shown in section 3.2.5.6. This could be the case for large housing distortion.

Sixth, for the roughness and tilt effects, the oil volume flow rate at the seal-housing interface is approximated by the Couette flow term only, which is much larger than the pressure term. A small correction for the taper pressure is included.

Specific approximations for sub-models are discussed in their respective section.

3.1.3 Housing Distortion and Secondary Motion

Before discussing the formulation of the model further, there are two important inputs to the model that need further description: side housing distortion and secondary motion. Both of them were given to the author from results of analysis carried on the real engine configuration.

Side housing distortion is obtained from a finite element analysis of the engine housing including the tightening from the bolts and the thermal gradients. The available results to the author are: (1) 1500 rpm mechanical distortion only, or bolt tightening only, (2) 1500 rpm full load, including the temperature gradient, and (3) 7500 rpm full load. Those results are available for all four housings in the engine: the front housing (FH), the intermediate front housing (IMHF), the intermediate rear housing (IMHR), and the rear housing (RH). The front housing distortion at 7500 rpm full load is shown in Fig. 3.4. The largest distortion is seen next to the exhaust port where there is a large valley parallel to the port. It should be noted that although those distortion should be representative, they have not been validated experimentally.

Secondary motion of the rotor is defined as the real motion of the rotor including the deflection of the parts and the motion due to the clearance between the different parts. Rotor secondary motion is obtained from a finite element analysis of the crankshaft with the two rotors. The only available data is at maximum speed, 9000 rpm, and full load. It is however not critical as secondary motion of the rotor has a small impact on internal oil consumption compared to housing distortion.

It should be noted that the model is flexible and can be used for any side housing distortion or secondary motion of the rotor. The available data are used in the section results to assess the performance of the oil seals.

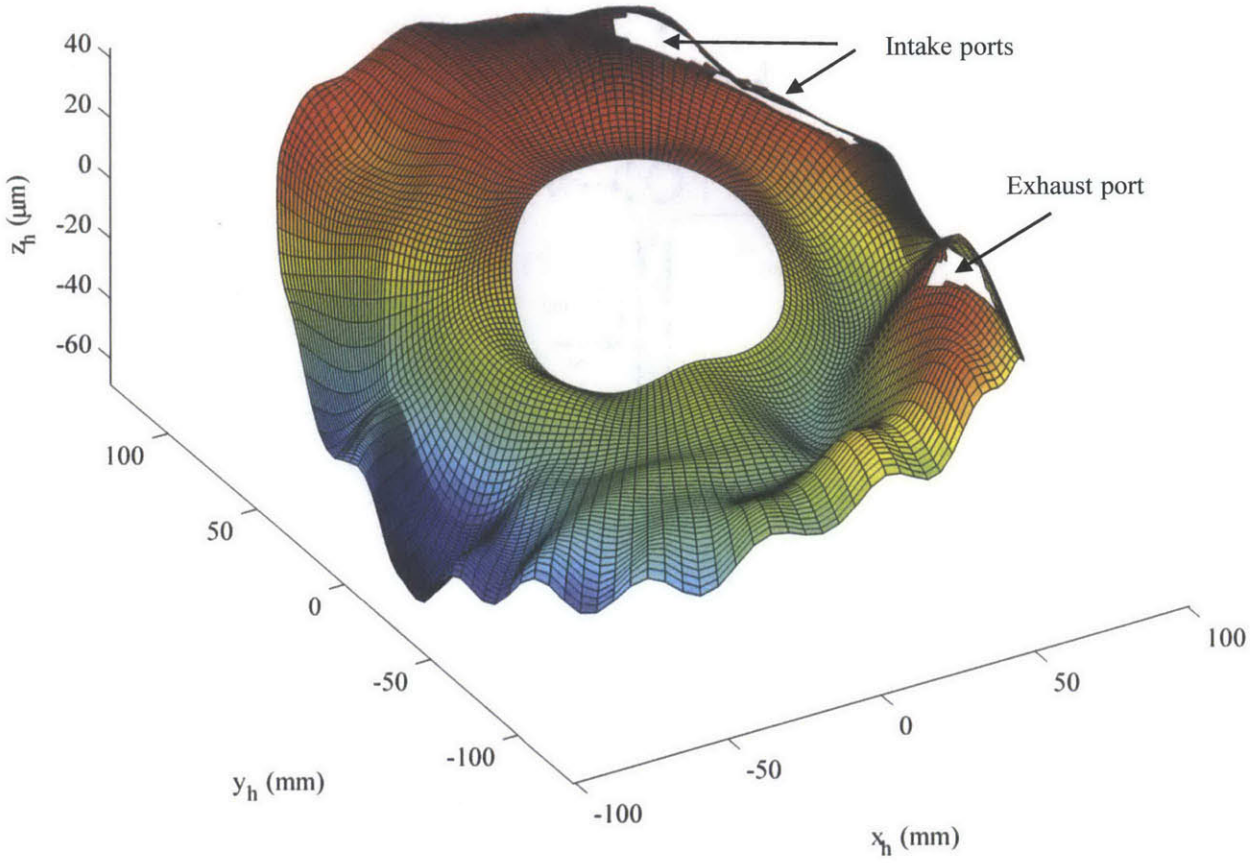

Fig. 3.4 Front housing distortion at 7500 rpm full load

3.1.4 Forces on the Seal

Dominant forces on the seal are all taken into account in the models. A cut view free-body diagram presents those forces in Fig. 3.5. In the r-θ plane, the O-ring acts as a spring that balances rotor land pressure and fictitious forces caused by primary and secondary motion of the rotor due to centrifugal, Coriolis, angular and relative accelerations (shown in Fig. 3.6). Friction forces from the interface and the taper part are also included. Reaction force of the groove is included if the radial displacement is large enough for the seal to touch the groove.

Along the z direction, spring tension is balanced by seal deformation and pressure generated at the interface by roughness, tilt, taper and rotor land pressure. As discussed in section 3.1.2, the three effects of hydrodynamic pressure generation at the interface are linearly superposed. Friction forces from relative motion with the O-ring and the groove are also included.

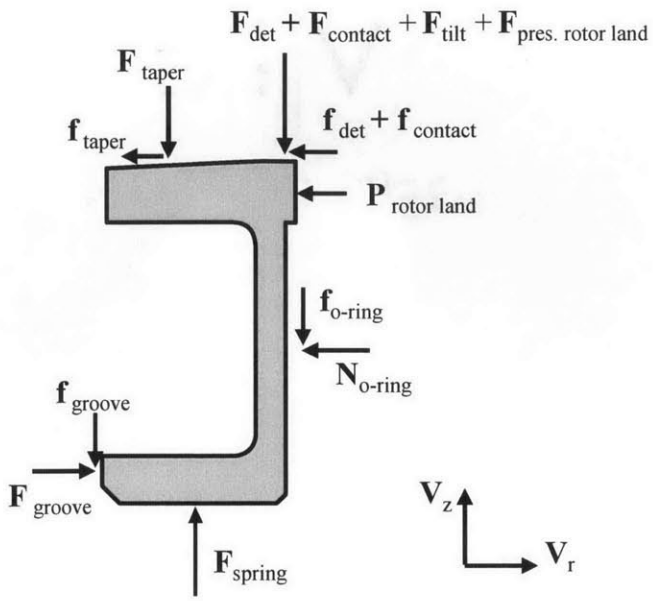

Fig. 3.5 Cut-view free-body diagram inner seal

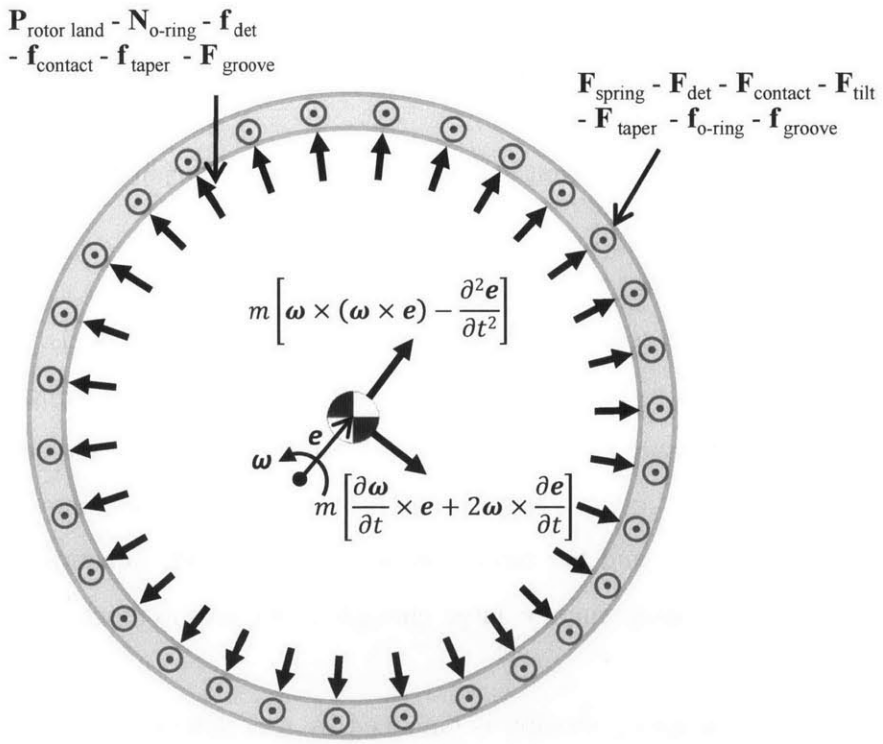

Fig. 3.6 Top view free-body diagram showing fictitious forces from primary and secondary motion

The next subsections describe the formulation of the different forces on the seal.

3.1.4.1 Asperity Contact Pressure

Asperity contact pressure is calculated from the Greenwood-Tripp model [51]. This model can be simplified to [52]:

$$P_{contact} = P_c\left(z - \frac{h}{\sigma_p}\right)^{K_c} \tag{3.3}$$

where P_c, z and K_c are constants calculated from surface topography, h is the interface clearance and σ_p is the standard deviation of roughness on the plateau area. Asperity contact friction is calculated from contact pressure as:

$$f_{contact} = C_{fc}\, A\, P_{contact} \tag{3.4}$$

where C_{fc} is the asperity contact friction coefficient and A is the contact surface. Unless otherwise specified, the constants taken to evaluate contact pressure and friction are taken from Chen [52] and are given in Table 5.1.

Table 3.1 Asperity contact and friction coefficients

Constant	Value
σ_p	0.046 μm
P_c	1.267×10^5 Pa
z	4.8
K_c	6.804
C_{fc}	0.15

3.1.4.2 Asperity Hydrodynamic Pressure and Friction

Hydrodynamic pressure generated by roughness is discussed in details in Appendix A and can be summarized by a correlation based on the deterministic model:

$$P_{hydro} = \frac{\mu V}{\mu_0 V_0} a_p\left(P_h + P_\gamma \sin(\gamma - \phi_\gamma) + P_\beta \beta\right)\left(\frac{h}{\sigma_p}\right)^{-K_h - K_\beta \tan(\beta)}\left(\frac{h_s}{h}\right)^{-K_{p1} + K_{p2}\left(\frac{h_s}{\sigma_p}\right)} \tag{3.5}$$

where μ and V are the actual viscosity and velocity, μ_0 and V_0 are the reference viscosity and velocity, h_s is twice the oil film thickness on the housing, β is the angle between seal and relative velocity, and $a_p, P_h, P_\beta, K_h, K_\beta, P_\gamma, \phi_\gamma, K_{p1}$ and K_{p2} are surface and seal dependent constants from the hydrodynamic deterministic model. This correlation takes into account the surface anisotropy, the effect of the seal orientation and the oil supply on the housing.

Hydrodynamic friction can be summarized by the following correlation:

$$f_{hydro} = \frac{\mu V}{h}\left(C_{f1} + C_{f2}\exp\left(-C_{f3}\frac{h}{\sigma_p}\right)\right)\left(\frac{h_s}{h}\right)^{K_{f1}+K_{f2}\left(\frac{h_s}{\sigma_p}\right)} \tag{3.6}$$

where $C_{f1}, C_{f2}, C_{f3}, K_{f1}$ and K_{f2} are constants from the deterministic model. This correlation takes into account the supply of oil on the housing, but neglect surface and seal orientation.

Unless otherwise specified, the constants taken to evaluate hydrodynamic pressure and friction due to roughness are given in Table 3.2. Values for hydrodynamic pressure generation are correlated from the housing surface. Values related to the oil supply on the housing are taken directly from Chen [52], and are marked with a star in Table 3.2.

Table 3.2 Hydrodynamic pressure and friction coefficients

Constant	Value
σ_p	0.046 μm
μ_0	0.005 Pa·s
V_0	3 m/s
a_p	1
P_h	3.9×10^7 Pa
P_γ	1.64×10^7 Pa
ϕ_γ	109°
P_β	1.06×10^7 Pa/rad
K_h	2.39
K_β	0.072
K_{p1}	1.2918*
K_{p2}	1.1080*
C_{f1}	0.828
C_{f2}	1.269
C_{f3}	1.412
K_{f1}	0.2655*
K_{f2}	0.0311*

3.1.4.3 Taper Hydrodynamic Pressure and Friction

Contribution from the taper to the hydrodynamic pressure generation can be modeled as a flat housing moving at the radial velocity in the seal reference frame, as shown in Fig. 3.7.

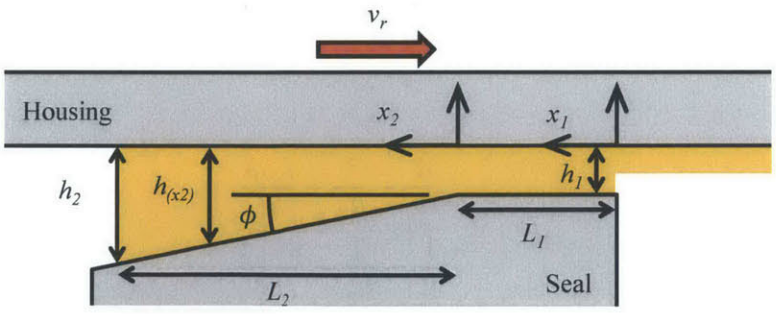

Fig. 3.7 Variable definition for hydrodynamic pressure generated by the taper

Due to the large difference in typical length scale, pressure generation can be modeled as 1D (same arguments as for the rotor land in section 3.1.4.5). This allows neglecting the circumferential pressure variation. Circumferential velocity can also be neglected since the variation in clearance is much smaller than in the radial direction. Finally, the squeezing term is

neglected since the variation in clearance along the radial motion is small compared to the angle of the taper. For the straight part, 1D lubrication Reynolds' equation reduces to:

$$q_1 = \frac{h_1^3}{12\mu}\left(\frac{dP_1}{dx_1}\right) + \frac{v_r h_1}{2} \tag{3.7}$$

where q_1 is the flow per unit length along the circumference, and is defined positive following velocity direction. For the taper part, 1D Reynolds equation reduces to:

$$q_2 = \frac{h^3}{12\mu}\left(\frac{dP_2}{dx_2}\right) + \frac{v_r h}{2} \tag{3.8}$$

where v_r is the radial velocity.

The boundary conditions are the following:

(a) Pressure on both sides ($x_1 = 0$ and $x_2 = L_2$) is atmospheric. Atmospheric pressure is taken to be zero, since it does not generate any net force.

(b) Pressure in the center is the same for both sides ($P_{(x_1=L_1)} = P_{(x_2=0)}$).

(c) The flow is constant across both parts.

Assuming the angle is small, the flow can be solved using both equations and applying boundary conditions:

$$q = v_r \frac{\frac{1}{h_1} - \frac{1}{h_2} + \frac{L_1\phi}{h_1^2}}{\frac{1}{h_1^2} - \frac{1}{h_2^2} + \frac{2L_1\phi}{h_1^3}} \tag{3.9}$$

The pressure distribution for the flat part is linear:

$$P_1 = \frac{6\mu x_1}{h_1^2}\left(\frac{2q}{h_1} - v_r\right) \tag{3.10}$$

For the taper part, the pressure distribution is sketched is Fig. 3.8 and is expressed as:

$$P_2 = \frac{6\mu}{\phi}\left(\frac{1}{h} - \frac{1}{h_2}\right)\left[v_r - q\left(\frac{1}{h} - \frac{1}{h_2}\right)\right] \tag{3.11}$$

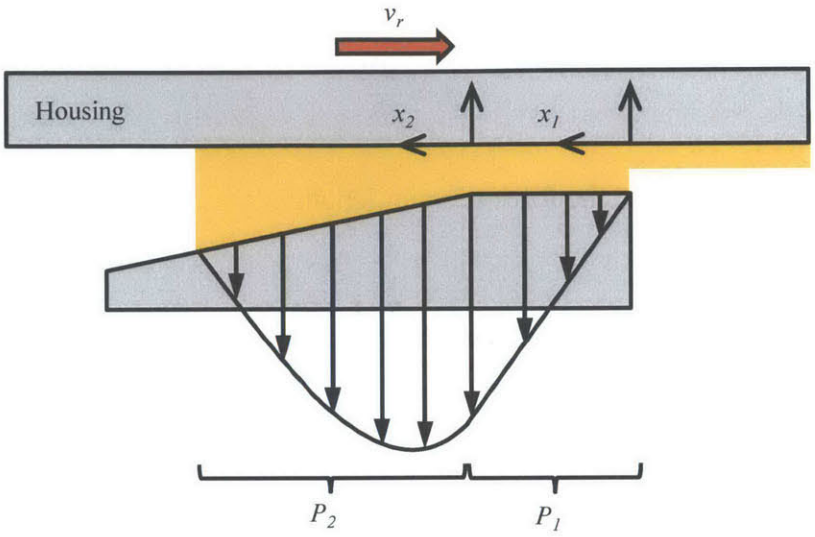

Fig. 3.8 Sketch of hydrodynamic pressure generated by the taper

Integrating the pressure distribution, the force per unit length (F') of the flat part is:

$$F_1' = \frac{3\mu L_1^2}{h_1^2}\left(\frac{2q}{h_1} + v_r\right) \tag{3.12}$$

Similarly for the taper part:

$$F_2' = \frac{6\mu}{\phi^2}\left[v_r\left(\ln\frac{h_2}{h_1} - \frac{L_2\phi}{h_2}\right) - q\left(\frac{1}{h_1} - \frac{1}{h_2} + \frac{L_2\phi}{h_2^2}\right)\right] \tag{3.13}$$

For the friction, only the taper is considered, since the friction of the flat part is already taken into account with the roughness effect. The first effect of friction is the projection of the pressure force due to the taper angle:

$$F_{f,pres}' = F_2'\phi \tag{3.14}$$

The second effect is the shear from the oil. The Couette term only is considered, and the velocity is the total velocity (v), the combination of radial and circumferential. The Poiseuille flow contribution is much smaller than the Couette flow contribution mainly because the circumferential velocity is larger than the radial velocity, and the Poiseuille flow term is only in the radial direction. The shear is given by:

$$\tau = \frac{\mu v}{h} \tag{3.15}$$

Integrating the shear stress to get the force per unit length:

$$F'_{f,shear} = \frac{\mu v}{\phi}\left[\ln\frac{h_2}{h_1}\right] \tag{3.16}$$

3.1.4.4 Tilt Hydrodynamic Pressure

Pressure generated by the tilt of the seal is calculated similarly to the taper pressure, with the 1D Reynolds' equation. The pressure profile is sketched in Fig. 3.9 and can be computed with equation (3.11) by taking L_1 to zero for the volume flow rate in equation (3.9). The tilt angle is defined as positive as shown in Fig. 3.9. A positive tilt has a beneficial effect on oil consumption since it generates more pressure during outward motion and let more oil to pass toward the crankcase. However, a negative tilt has a detrimental effect on oil consumption since it reduces the clearance during outward motion and enhances outward scraping.

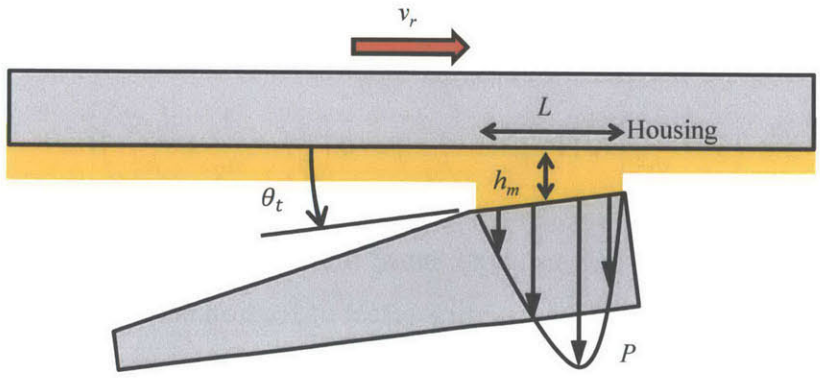

Fig. 3.9 Hydrodynamic pressure generated by seal tilt

Force per unit length is calculated as a function of the mean height (h_m) by integrating the pressure distribution:

$$F' = \frac{6\mu v_r}{\theta_t}\left[\frac{1}{\theta_t}\ln\frac{\left(h_m + \frac{\theta_t L}{2}\right)}{\left(h_m - \frac{\theta_t L}{2}\right)} - \frac{L}{h_m}\right] \tag{3.17}$$

in which θ_t is the seal tilt angle. When combining the pressure generation contributions, the mean height (h_m) is used as the clearance height (h) for the roughness effect and as the straight part clearance height (h_1) for the taper contribution.

Pressure contribution from the tilt and the taper could be calculated altogether in future investigations. This approach, however, allows more flexibility for the parametric study. Contribution to friction by the tilt is neglected in the model.

3.1.4.5 Rotor Land Pressure without Drain Holes

Pressure generated during inward motion is dictated by three mechanisms: relative motion between rotor and housing, squeezing due to secondary motion and body force (respectively U, w, and a in Fig. 3.10).

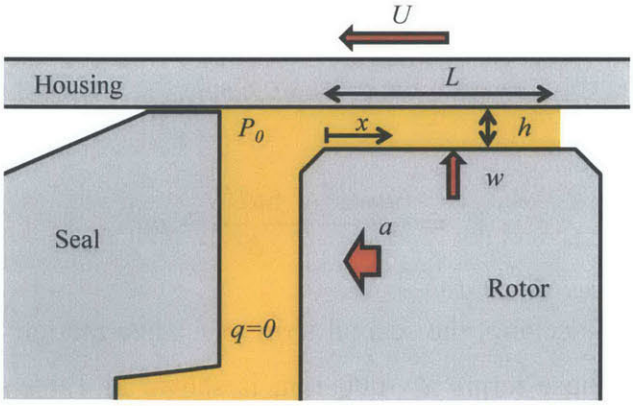

Fig. 3.10 Pressure generation inside the inner seal without drain holes

Lubrication approximation holds in this case since $Re_L(h/L)^2 \sim 0.04$, which is much smaller than unity. Circumferential pressure variation is also neglected due to the difference in

characteristic lengths for pressure variation. The characteristic length radially is the rotor land and circumferentially the radius, which gives a ratio between the two terms of $(R/L)^2 \sim 30$ in the 2D lubrication Reynolds equation. Therefore the difference in pressure due to circumferential flow is small compared to the pressure generated along x.

Considering those approximation and the three mechanisms for pressure generation, 1D Reynolds equation reduces to:

$$\frac{dq}{dx} - w = 0 \tag{3.18}$$

where q is the volume flow rate per unit length, x is the distance from the inner seal, and w is the squeezing velocity. We can assume that the flow to the groove is zero, since there is no release mechanism in the groove in the absence of drain holes. Based on this assumption, the flow rate becomes:

$$q = -\frac{Uh}{2} + \frac{h^3}{12\mu}\left(-\frac{dP}{dx} - \rho a\right) = wx \tag{3.19}$$

where U is the relative velocity between the rotor and the housing, h is the rotor land clearance, μ and ρ are oil viscosity and density, a is the centrifugal acceleration and L is the length of oil accumulation. U, a and w are defined positive as shown in Fig. 3.10. Integrating and taking the gauge pressure inside the rotor to zero, the pressure inside the seal (P_0) is:

$$P_0 = \frac{6\mu w L^2}{h^3} + \frac{6\mu UL}{h^2} + \rho aL \tag{3.20}$$

The first term is due to squeezing, the second term to relative motion and the last term to body force. A comparison of those terms at 3000 rpm is shown in Table 3.3. Pressure terms from squeezing and relative motion are on the same order and are much larger than the body force term. Furthermore, body force is pointing inward and thus reducing the pressure at the end of inward motion, where the accumulation is the largest. It can thus be expected that pressure at the inner radius of the inner seal is mainly generated by sliding and squeezing.

Table 3.3 Pressure terms order of magnitude comparison

Parameter	Order of magnitude		Comment
rpm	3000	rpm	
μ	0.01	Pa·s	
ρ	800	kg/m³	
L	10	mm	
h	100	μm	
U	5	m/s	
w	0.03	m/s	1/3 of secondary motion at 9000 rpm
a	1500	m/s²	$a \sim \omega^2 e$
$P_{squeeze}$	180	kPa	$P_{squeeze} = \frac{6\mu w L^2}{h^3}$
$P_{rel.\ motion}$	300	kPa	$P_{rel.\ motion} = \frac{6\mu U L}{h^2}$
$P_{inertia}$	12	kPa	$P_{inertia} = \rho a L$

Rotor land pressure contributes in lifting the seal away from the housing. In the model, the average pressure on the seal contact width is approximated as half the rotor land pressure as the pressure gradient is almost linear from inside the seal to outside the contact width.

3.1.4.6 Rotor Land Pressure with Drain Holes

Drain holes can be added in the inner oil seal groove to return oil accumulated to the crankcase. In the presence of drain holes, the same mechanism are taking place, but the pressure is reduced by a flow to the groove (q_g), as shown in Fig. 3.11. If the drain holes are big enough, the pressure in the groove can be approximated as atmospheric.

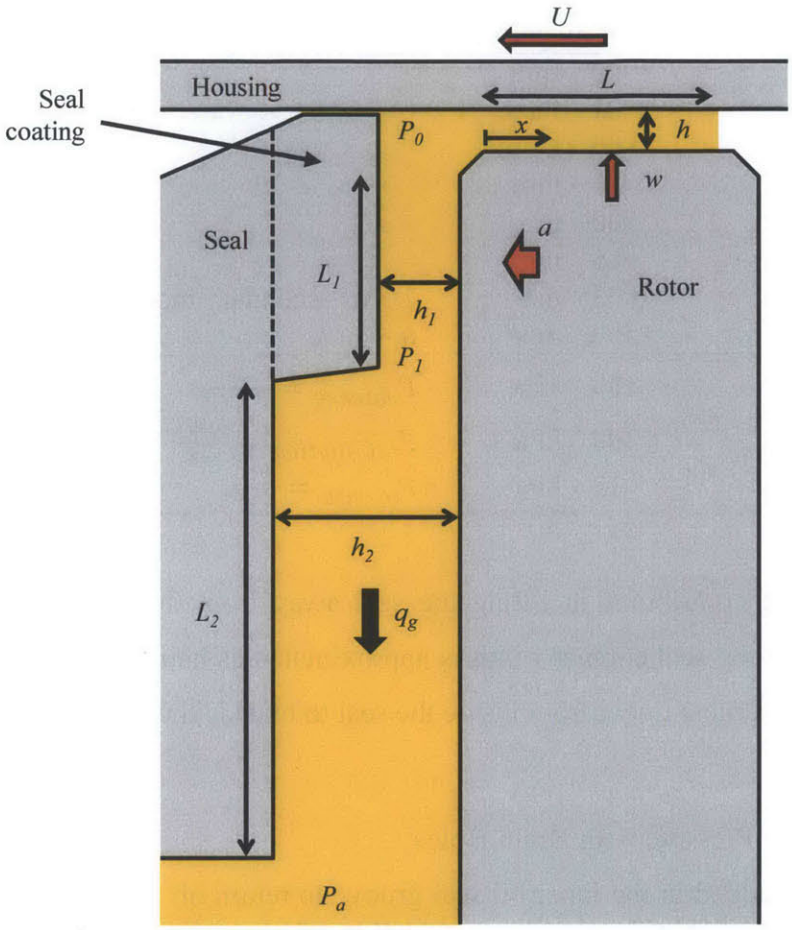

Fig. 3.11 Pressure generation inside the inner seal with drain holes in the groove

Equation (3.19) becomes:

$$q = -\frac{Uh}{2} + \frac{h^3}{12\mu}\left(-\frac{dP}{dx} - \rho a\right) = wx - q_g \tag{3.21}$$

The volume flow rate is dictated by the pressure inside the inner seal and the viscous resistance due to the small clearance between the seal and the groove. The major resistance comes from the clearance between the seal coating and the groove (h_1, L_1). Volume flow rate for that resistance can be expressed as a function of P_0 and P_1:

$$q_g = \frac{h_1^3}{12\mu}\frac{(P_0 - P_1)}{L_1} \tag{3.22}$$

where h_1 and L_1 are the clearance and length of the gap between the seal coating and the groove. Similarly, volume flow rate for the rest of the seal can be expressed as:

$$q_g = \frac{h_2^3}{12\mu}\frac{P_1}{L_2} \tag{3.23}$$

where h_2 and L_2 are the clearance and length of the gap between the the seal and the groove Equations can be solved altogether and pressure expressed inside the inner seal as:

$$P_0 = \frac{\frac{6\mu w L^2}{h^3} + \frac{6\mu U L}{h^2} + \rho a L}{1 + \frac{L/h^3}{L_1/h_1^3 + L_2/h_2^3}} \tag{3.24}$$

The numerator shows the same terms as in the absence of flow to the groove. However, the denominator is a function of the geometry. For the minimum clearance and the rotor land geometry given in Table 3.3, the denominator is 1.6. Therefore the pressure generated by squeezing and relative motion can still be important if the gap is small while the accumulation is large.

3.1.4.7 O-ring Squeezing Force and Friction

O-ring is modeled as a linear spring, with a contact friction due to relative axial motion, as shown in Fig. 3.12.

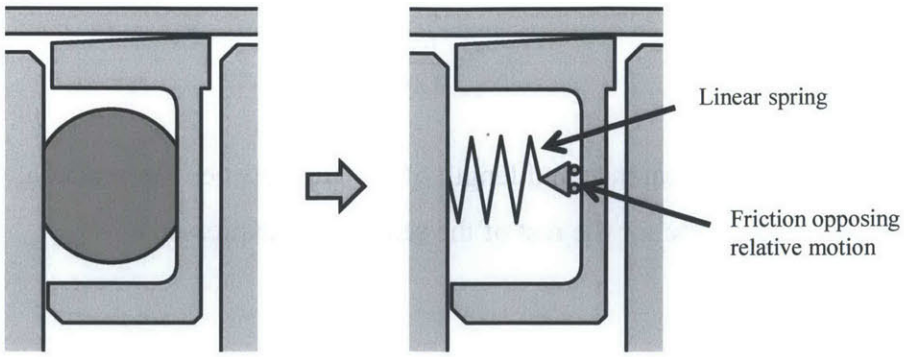

Fig. 3.12 Simple model for the O-ring normal reaction force and friction force

O-ring normal force per unit length (F_o') is calculated by:

$$F_o' = k_l(\delta_0 + \delta(\phi)) \tag{3.25}$$

where k_l is the spring constant per unit length (N/mm²), δ_0 is the initial tightening and $\delta(\phi)$ is the local compression of the O-ring due to seal motion in its groove. This approximation is validated using data from Parker [53], for an average hardness of 70 Shore A and a similar diameter. Since the compression varies from 0 to 0.6 mm, the linear approximation holds, as shown in Fig. 3.13. For this hardness, O-ring spring constant per unit length can be estimated as 4 N/mm².

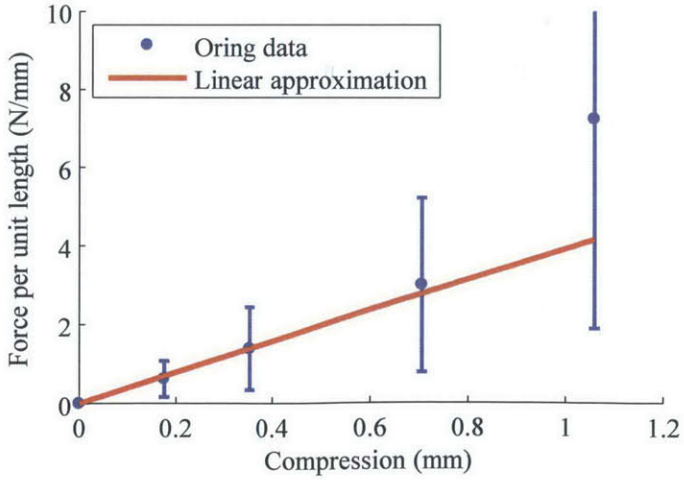

Fig. 3.13 Validation of the linear approximation (data from [53])

Friction force per unit length (f_o') is computed from a boundary contact coefficient and is pointing against relative motion:

$$f_{of}' = C_{of} F_o' \tag{3.26}$$

where C_{of} is the O-ring friction coefficient. From the same data [53], the friction coefficient for this hardness can be estimated to 0.08 for a lubricated seal moving faster than 5 mm/s in one direction. The actual friction coefficient is expected to be lower in the engine since the O-ring can also rotate around itself and translate during oscillatory motion of the rotor. It is still an adequate approximation to evaluate the effect of O-ring friction on internal oil consumption.

3.1.5 In-plane Equilibrium

Seal is displaced until the reacting force of the O-ring balances all other forces: body force, rotor land pressure and friction from the seal-housing interface. Only the rigid body displacement is considered in the plane since the radial deformation is small compared to the rigid body displacement and this deformation does not influence the out-of-plane deformation for a beam. Solution is found by a MATLAB® built-in algorithm. If the displacement is large enough, the displacement is limited by the contact with the groove and a reacting force from this contact is added to balance all the other forces.

3.1.6 Out-of-plane Deformation

The seal deformation model is adapted from a model developed by Baelden [54] for piston rings. The model uses a beam finite element method minimizing energy. The main difference with conventional methods, such as used by Liu [55], is the different discretization for the structure elements and the contact elements. This approach reduces the calculation time by a factor of 10 to 100, which is essential in order to run complete cycles in a reasonable time. The model is detailed for straight beam for the apex seal in section 4.2.12.

The seal is discretized in about 20 elements for the complete circumference. The number of elements needed to adapt to the shape of the surface can vary as a function of housing distortion.

Those structure elements are approximated by 5th order polynomial. About 40 contact points are used on each structure elements to represent accurately the force distribution at the interface.

Deformation energy is calculated by the elastic energy of bending and twisting. Interface work is the product of forces at the seal-housing interface and displacement from the free shape. Total system energy is the combination of both elastic energy and work from the forces at the seal-housing interface. Solution of the overall coupling between force deformation and clearance is found by minimizing total energy using a Newton iterative method. Finally, force distribution at the seal-housing interface can then be calculated from the clearance distribution.

3.1.7 Rotor Land Oil Transport

Pressure inside the inner seal is needed to calculate the oil transport at the seal-housing interface, as discussed in section 3.1.4.5. First, accumulation in the rotor land needs to be known around the complete cycle. For the radial motion, the model assumes a constant oil thickness on the housing, which becomes supply during inward motion. If there are drain holes in the groove, the released flow is calculated as a function of the pressure inside the seal and the gap between the seal and the groove. Based on those two flows, the model tracks the accumulation based on a mass balance for the rotor land. During outward motion, oil accumulation and pressure are taken to be zero.

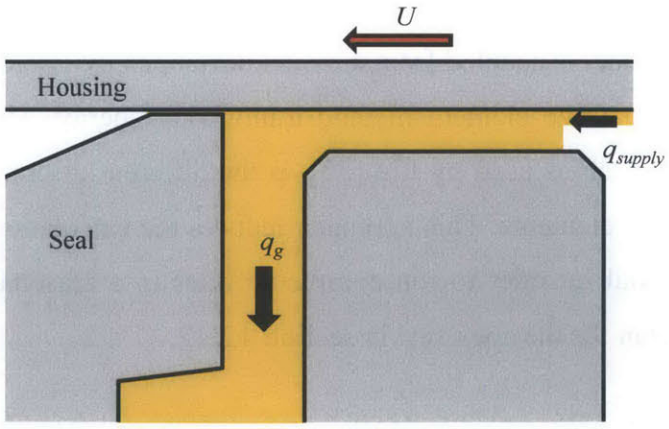

Fig. 3.14 Oil transport in the rotor land due to radial motion

Although the circumferential velocity does not contribute to pressure generation, it redistributes the oil along the circumference by shear, as shown in Fig. 3.15.

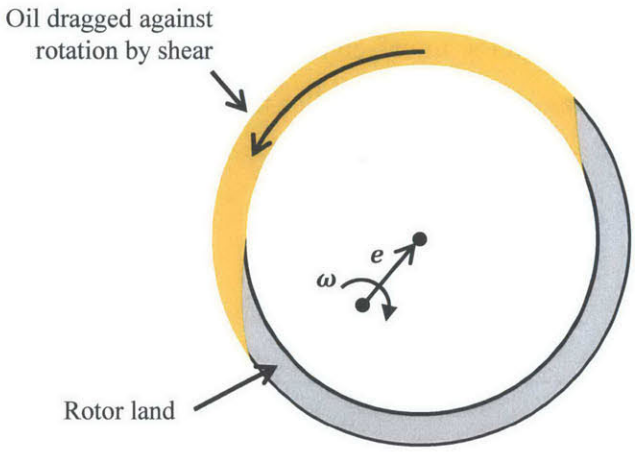

Fig. 3.15 Top view circumferential oil motion in the rotor land due to shear

Flow around the circumference is calculated based on a Couette flow:

$$Q_c = \frac{v_\phi hL}{2} \tag{3.27}$$

where v_ϕ is the circumferential velocity. For every crank angle, the radial flow to the rotor land elements is first calculated. Then, the shear flow redistributes the oil between the rotor land elements.

3.1.8 Seals Oil Transport

The oil transport for the inner and outer oil seals can be determined from interface clearance, rotor land pressure and oil distribution on the housing. During outward motion, both seals behave as shown in Fig. 3.16. The volume flow rate through the seal housing interface is determined by the combination of a shear and a pressure flow. The shear flow, which typically dominates, is calculated from the clearance and the relative velocity. The small contribution by the pressure generated due to the taper is added in the model. Two scenarios can happen depending on the supply from the housing:

(a) The supply from the oil left on the housing previously to the control seal volume can be larger than the flow through the interface. In this case, oil cannot all pass through the interface and part of it accumulates between the taper and the housing. Since the flow generated from body force is small compared to the shear flow, the oil remains in this volume until it can pass through the interface or the motion direction reverses.

(b) The supply from the housing can also be smaller than the flow through the interface. In this case, oil flows from the accumulation through the interface. This is defined as a release from the taper-housing interface.

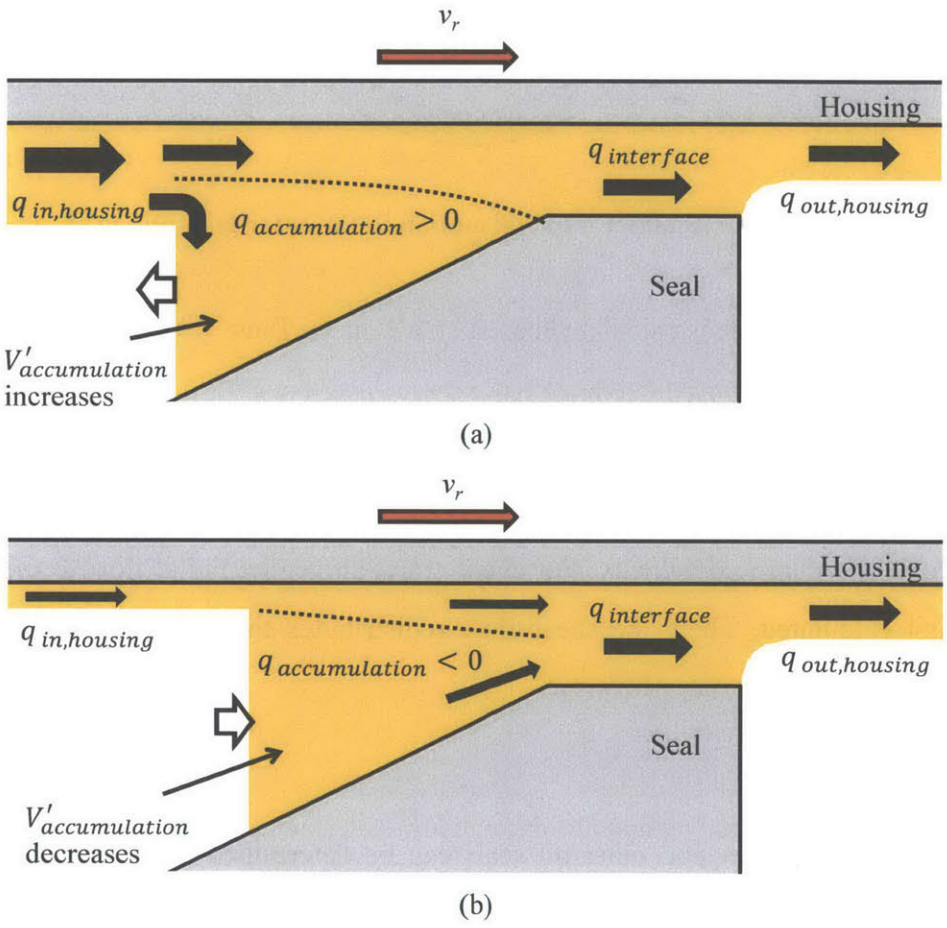

Fig. 3.16 Oil flow and accumulation on the seal during outward motion for (a) large oil film thickness and (b) small film thickness on the housing

The oil accumulation is also redistributed along the seal circumference by a shear flow caused by the circumferential velocity. This flow is taken into account in the model as discussed for the rotor land.

When motion reverses, accumulated oil is released, as shown in Fig. 3.17. For both seals, part of the oil flows on the taper and the remaining oil is left on the housing. The flow rate out of the accumulation is calculated from a Couette flow at the maximum clearance of the accumulation. Once the oil flows to the taper, this oil is assumed to be pushed all the way down to the land and does not come back to the housing, until the recycling process. Separation is a complex phenomenon involving surface tension and cavitation. In this model, separation is simplified by fixing the oil fraction that flows to the taper. For the outer seal, this parameter has no impact on oil consumption since both are considered internal oil consumption. For the inner seal, the fraction selected changes the oil distribution on the rotor and is investigated in section 3.2.5.15. Unless otherwise specified the oil fraction flowing to the taper is fixed to 0.5.

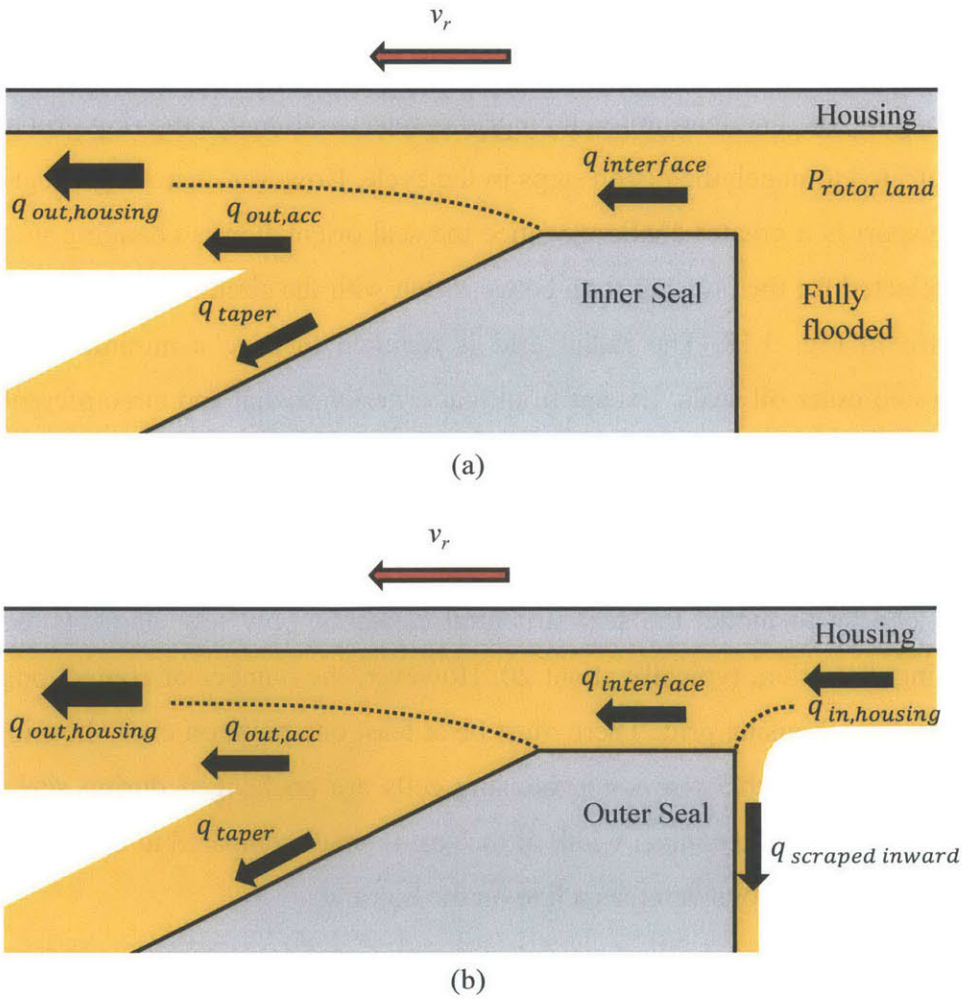

Fig. 3.17 Oil flow and release during inward motion for (a) the inner seal and (b) the outer seal

During inward motion, the inside part of the seals is treated differently. For the inner seal, a fully-flooded condition is generally assumed. The effect of a starved condition is shown in section 3.2.5.6. Pressure from the rotor land also increases oil flow through the interface. For the outer seal, oil supply is calculated from the housing oil distribution. If the supply is greater than the flow through the interface, oil can be scraped by the inside of the seal, defined as inward scraping and shown in Fig. 3.17b.

Recycling process of the 4^{th} land accumulation is a complex phenomenon, again involving surface tension. In the model, oil is recycled evenly between the two seals everywhere body force is pointing outward. Further investigation of oil recycling and separation from the taper would be needed if greater accuracy is required.

3.1.9 Discretization

In the piston engine, the liner circumferential grid is selected to match the ring grid and the axial liner grid is selected to match the piston steps in the cycle. However, matching the grid for rotary engine oil transport is a greater challenge since the seal orientation is changing in the cycle. A polar grid is selected for the housing for a better match with the circular motion and shape of the seals, as shown in Fig. 3.18. The radial grid is required to have a minimum of two points between inner and outer oil seals. Except from that criterion, radial and circumferential grid can be selected to match with housing distortion.

The number of seal structural elements is independent of the housing grid. Since a 5^{th} order polynomial is chosen to model the seal structural elements, only few elements are enough to adapt to housing distortion, typically about 20. However, the number of contact points must be selected to match the housing grid. There must be at least one point on every housing cell along the seal circumference. Otherwise some housing cells are unchanged during seal passage, as shown in Fig. 3.19. Since the contact width of the seal is small compared to the complete motion, the seal control volume is considered as a line on the housing.

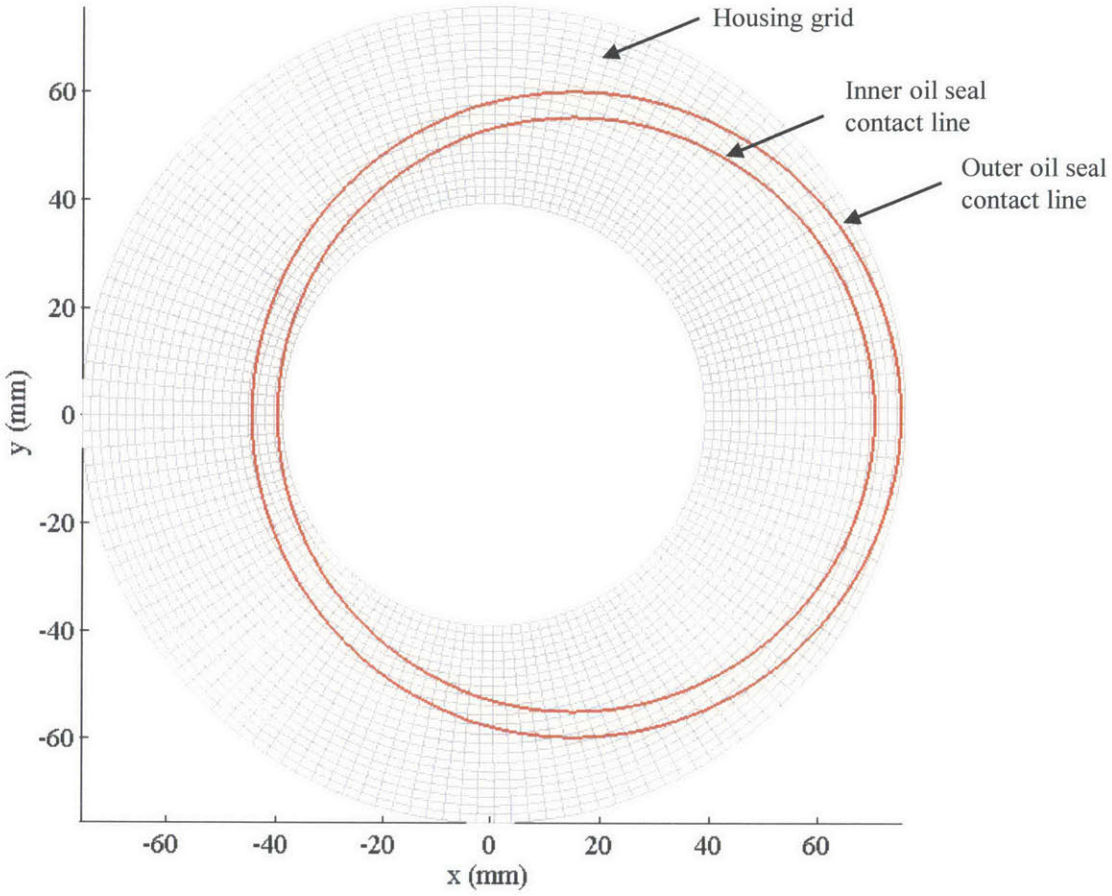

Fig. 3.18 Top view of the housing grid and seal contact lines

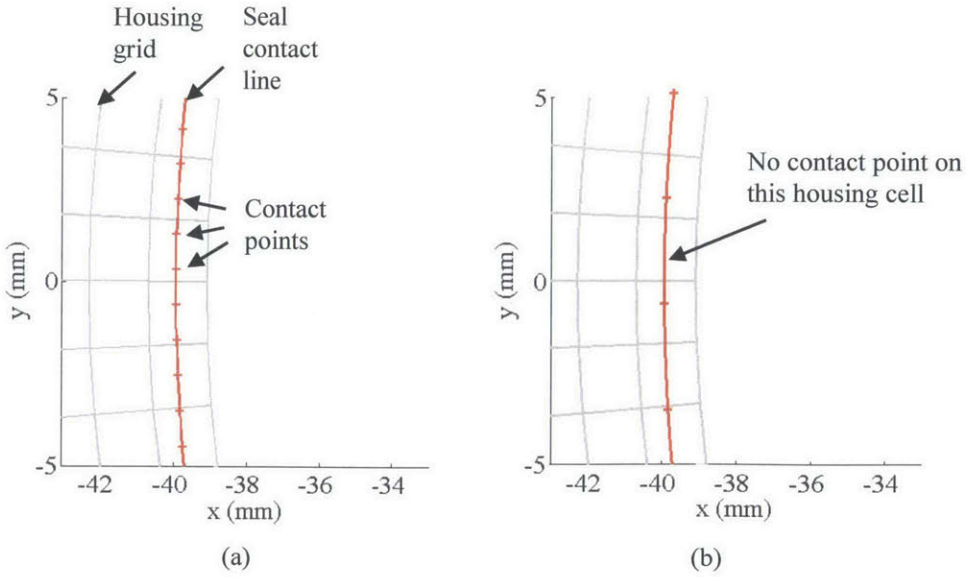

Fig. 3.19 Match of housing grid and seal contact points (a) correct, (b) incorrect

Similarly, crank angle steps must match to housing grid. Otherwise some housing cells are skipped during seal passage, as shown in Fig. 3.20.

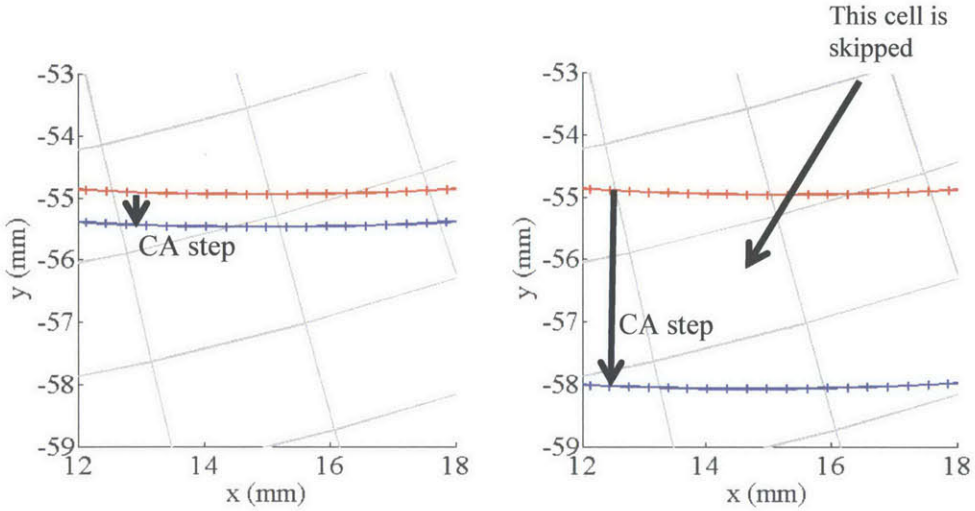

Fig. 3.20 Crank angle step (a) correct, (b) incorrect

Using this discretization scheme, oil transport between housing cells and seal contact elements can be computed. At a given crank angle, a seal contact element of length (Δs) is on a housing cell. During a crank angle step, the seal contact element moves at a radial velocity during a time interval (Δt). The net volume change of the seal control volume is given by:

$$\Delta V_{seal\ C.V.change} = \Delta s \left(Q'_{in,housing} - Q'_{out,housing} \right) \Delta t \tag{3.28}$$

If the net change is positive, oil is added to the seal control volume and is removed from the corresponding housing cell. If the net change is negative, oil is removed from the seal control volume and added to the corresponding housing cell. However, the oil film thickness cannot be changed until the seal has left the cell because it would also change the oil supply to the seal control volume. Therefore, oil film thickness is changed only when the seal leaves the housing cell or changes direction. The same calculation is repeated for every seal contact elements and all crank angle steps for the complete engine revolution. The process is repeated for a few revolutions until the internal oil consumption reaches a steady state, typically 15 to 30 engine revolutions.

3.1.10 Convergence

Four cases representing the range of housing distortion and speed are used to verify convergence:

- Intermediate front housing, 1500 rpm, bolt force distortion only
- Intermediate front housing, 1500 rpm, full load 1500 rpm distortion
- Intermediate front housing, 7500 rpm, full load 7500 rpm distortion
- Rear housing, 1500 rpm, full load 1500 rpm distortion

All cases are tested without considering the pressure from the taper and tilt, and without housing waviness. The baseline discretization is selected to give the best compromise between accuracy and calculation time for those cases and is shown in Table 3.4. This discretization is used for the results shown in the present chapter, unless otherwise specified.

Table 3.4 Baseline discretization of housing, seal and cycle

Housing radial number of cells	23
Housing circumferential number of cells	147
Number of seal structure elements	18
Number of seal contact points	720
Crank angle steps for 3 engine revolutions	540
Engine revolutions to reach steady state	15

3.1.10.1 Steady State

The simulation is started with a given constant oil film thickness on the housing and no recycling from 3rd land. During the few first revolutions, oil is left on the housing in the valleys and recycling increases. Finally, the model usually reaches steady oil consumption after about 15 engine revolutions. The three cases with the intermediate housing are within 2 % of the converged value at 15 engine revolutions, as shown in Fig. 3.21. However, the case with the rear housing is still at about 15 % of the converged value after 15 revolutions. Since the present analysis is mainly about order of magnitude, this error is within the acceptable error margin. For more accurate results one can use 30 engine revolutions.

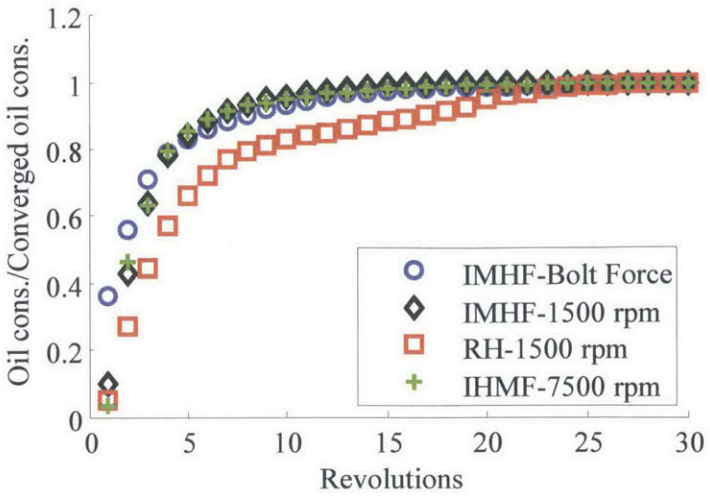

Fig. 3.21 Internal oil consumption convergence to steady state

3.1.10.2 Discretization Convergence

Convergence is studied by changing one of the discretization parameter at the time and comparing internal oil consumption to converged value, as shown in Fig. 3.22. The convergence tests lead to the following conclusions

(a) The number of cells on the housing is the parameter having the most impact. Error is acceptable when there are three cells between inner and outer oil seal, corresponding in this case to 23 cells radially.

(b) The number of structure elements converges quickly and the error on internal oil consumption is small for as low as 12 elements.

(c) The number of contact points on the seal also has a small impact on internal oil consumption as long as it respects the criterion given in section 3.1.9.

(d) The number of crank angle steps can bring a small error if the steps are larger than 2°.

Generally, the error due to discretization is small as long as no cell on the housing is skipped.

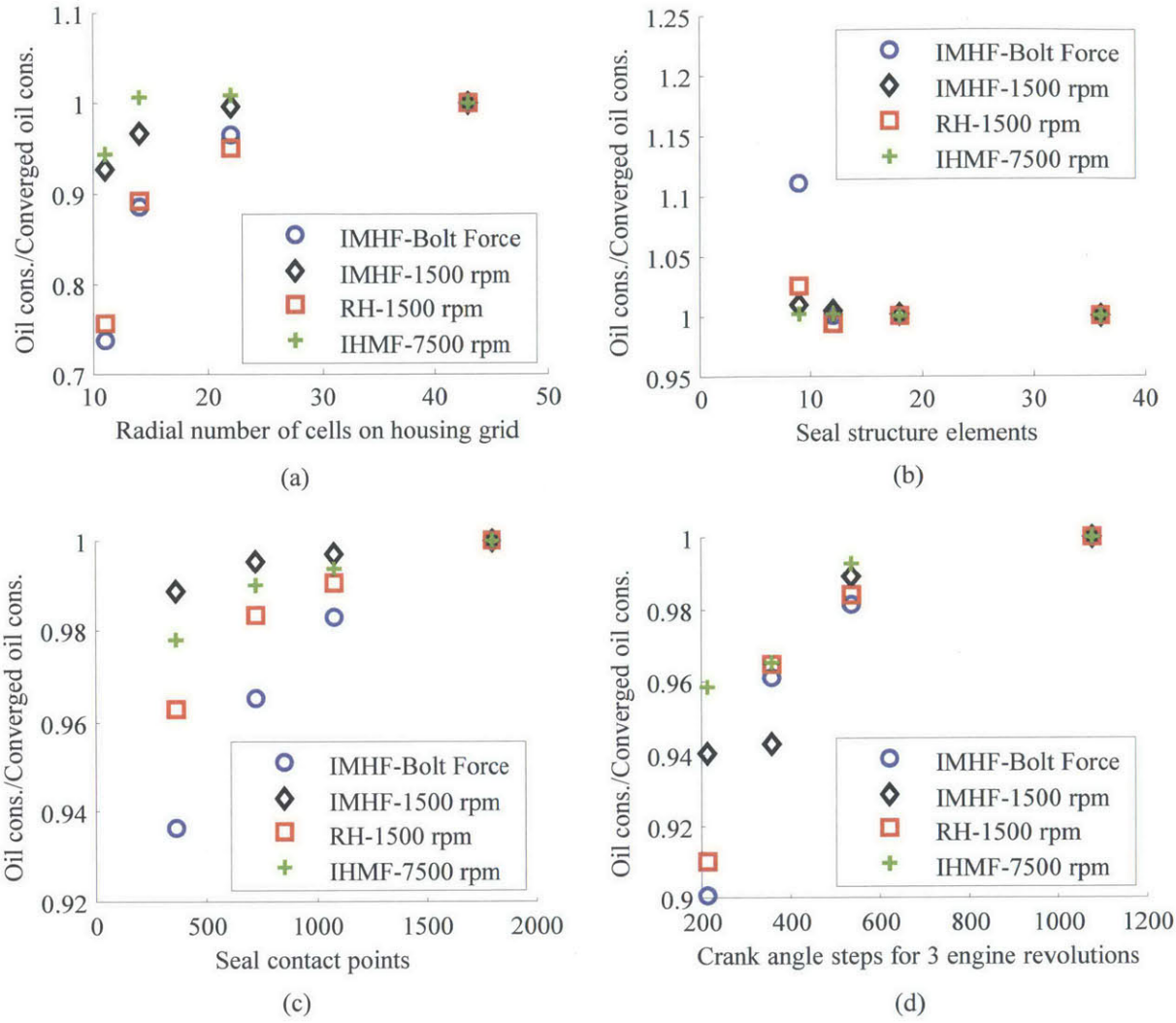

Fig. 3.22 Internal oil consumption convergence for (a) radial grid cells, (b) seal structure elements, (c) seal contact points and (d) crank angle steps

3.1.11 Approximation Validation

The quasi-steady approximation can be validated by comparing the seal relative acceleration or the resulting body force to an appropriate reference. For the out-of-plane acceleration, the body force along z is compared to the spring force. Body force along z is small as it remains below 2 % of the spring force even at high speed, as shown in Fig. 3.23 at 7500 rpm. In the r-θ plane, the relative acceleration between the seal and the groove is compared to the rotor acceleration. At 7500 rpm, the relative acceleration remains below 2 % of the rotor acceleration, as shown in Fig. 3.24. The quasi-steady approximation is therefore valid even at high speed.

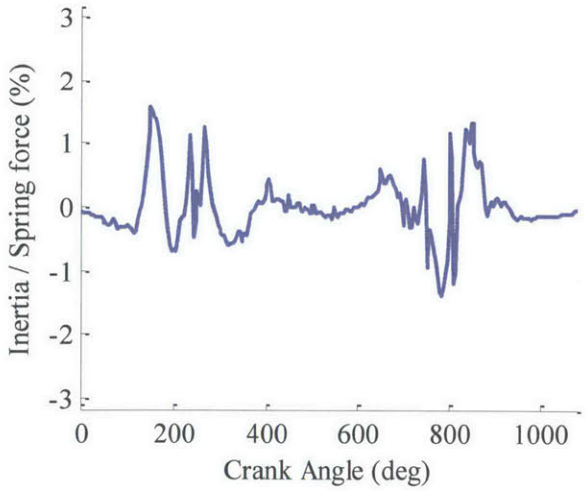

Fig. 3.23 Fictitious force due to the relative motion along z compared to spring force for one element on the seal at 7500 rpm

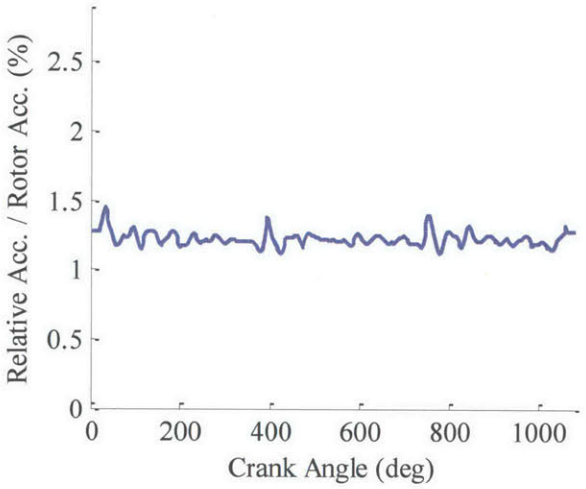

Fig. 3.24 Relative acceleration between the inner seal and its groove compared to the rotor acceleration at 7500 rpm

The second approximation about neglecting variation in spring force due to deformation of the seal is also valid as the spring force variation remains below 0.5 % of the total spring force even with the largest deformation, as shown in Fig. 3.25.

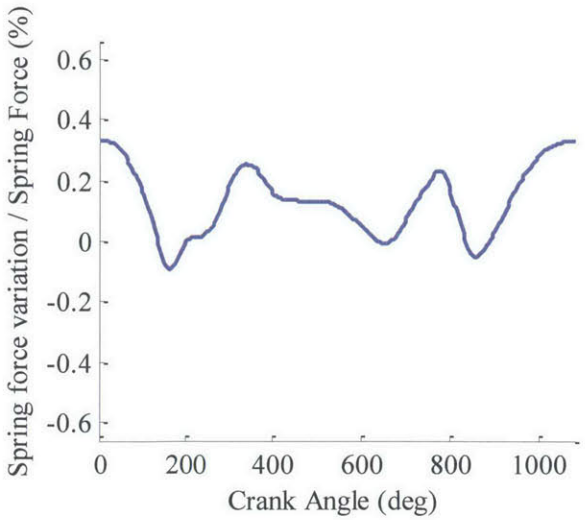

Fig. 3.25 Spring force variation due to seal deformation compared to total spring force for one seal element at 7500 rpm

3.1.12 Oil Seal Model Formulation Summary

A cycle model is presented to calculate the lubrication and internal oil consumption of the inner and outer oil seals. The important forces are included to calculate the clearance between the housing and the seal. The method to track the oil on the lands, seals and housing is explained. Finally, a specific numeric scheme is developed for the kinematics of the rotary engine and its convergence is validated. The next section uses the presented cycle model to calculate internal oil consumption and friction for the current engine configuration and the effect of changing the different important parameters.

3.2 Oil Seal Model Results

Numerous design parameters can be changed, modified, and optimized in the internal consumption cycle model. Before changing those parameters, the current engine configuration is used to develop an understanding of the oil transport mechanisms in the engine and how they are introduced in the model. Two extreme conditions are used to study those mechanisms: low speed and small housing distortion, and high speed and large housing distortion. Figures are used to show kinematics of the grooves, accumulation and pressure in the rotor land, in-plane forces, out-of-plane forces and clearance, and oil transport.

Oil scraping distribution is discussed in the following subsections, in order to show the distortion regions that generates important scraping. Internal oil consumption is then given for the different housing distortions. Friction caused by the seals is also quantified for those conditions. Afterward, transverse waviness is defined and its effect on oil consumption is explained. Finally, a parametric study is performed to show the relative impact of the different mechanisms.

Numeric values given for internal oil consumption are to be taken as an order of magnitude since oil consumption is very sensitive to input parameters. As an example, there can be a factor of more than 20 on internal oil consumption between two housing distortion shapes with the same amplitude. The focus should therefore be on the trends and the relative magnitude between the configurations. Those conclusions aim to support the design process.

3.2.1 Baseline Results

Two extreme conditions are used for the current engine. The first one is somewhat representative of low speed motored condition since the housing distortion is only from the mechanical effect. The second condition represents high speed and high load condition, with a large housing distortion caused by thermal effect.

For both conditions, nominal values of spring forces and dimensions are used. Typical values are used for steel properties: 210 GPa for Young's Modulus and 0.3 for Poisson's coefficient. O-ring linear spring constant is set to 4 N/mm^2 and the friction coefficient to 0.02 to avoid the friction force being larger than the spring force. Coefficients for interface pressure and friction are taken as shown in Table 3.1 and Table 3.2. Oil viscosity and density are set to 0.005 Pa·s and 800 kg/m^3. Oil film thickness is set to 17 μm on the housing from the splash inside the inner oil seal. High speed secondary motion is used for both cases, mainly to determine the direction of the O-ring and groove friction forces. Rotor land nominal clearance is set to 100 μm since the maximum displacement of the rotor land due to secondary motion is about 80 μm. Those conditions are used for all results presented in this chapter, unless otherwise specified.

The two cases are simulated without drain holes to see the effect of the pressure inside the rotor land. The pressure generated from the tilt is not included. The surface anisotropy from the hydrodynamic pressure correlation is set to zero.

3.2.1.1 Low Speed, Small Housing Distortion

The cycle model is run at 1500 rpm. The intermediate front housing with mechanical distortion is used. It is assumed that this distortion would be representative of the motored condition. No waviness is added to the housing distortion.

Results are shown for 280 CA, a representative angle showing the main mechanisms and their relative order of magnitudes. Inner seal groove motion is first presented as a reference for the other results. Results for the rotor land accumulation and pressure generation are then presented since this sub-model is decoupled from the other sub-models in the absence of drain holes. Afterwards, results are shown following the main model stages: in-plane equilibrium, out-of-plane forces and seal deformation, and oil transport. A summary of all forces around the cycle is also given to compare their order of magnitude.

Inner seal groove kinematics is first shown in Fig. 3.26. This information is given from secondary motion and is shown here as a reference for the subsequent results. Graphs are displayed as follows:

(a) shows the out-of-plane position of the groove. The location along z axis is used to calculate the variation in spring force on the seal.

(b) shows the position of the groove from a top view. Along x and y axes, the seal is assumed to follow the groove since the relative motion is small.

(c) shows the direction and relative magnitude of the velocity and acceleration. This information is used in many aspects of the model, such as the interface pressure and friction, the rotor land accumulation and pressure.

(d) shows the out-of-plane velocity of the groove. O-ring and groove friction forces are along this velocity.

(e) and (f) show velocity and acceleration magnitudes.

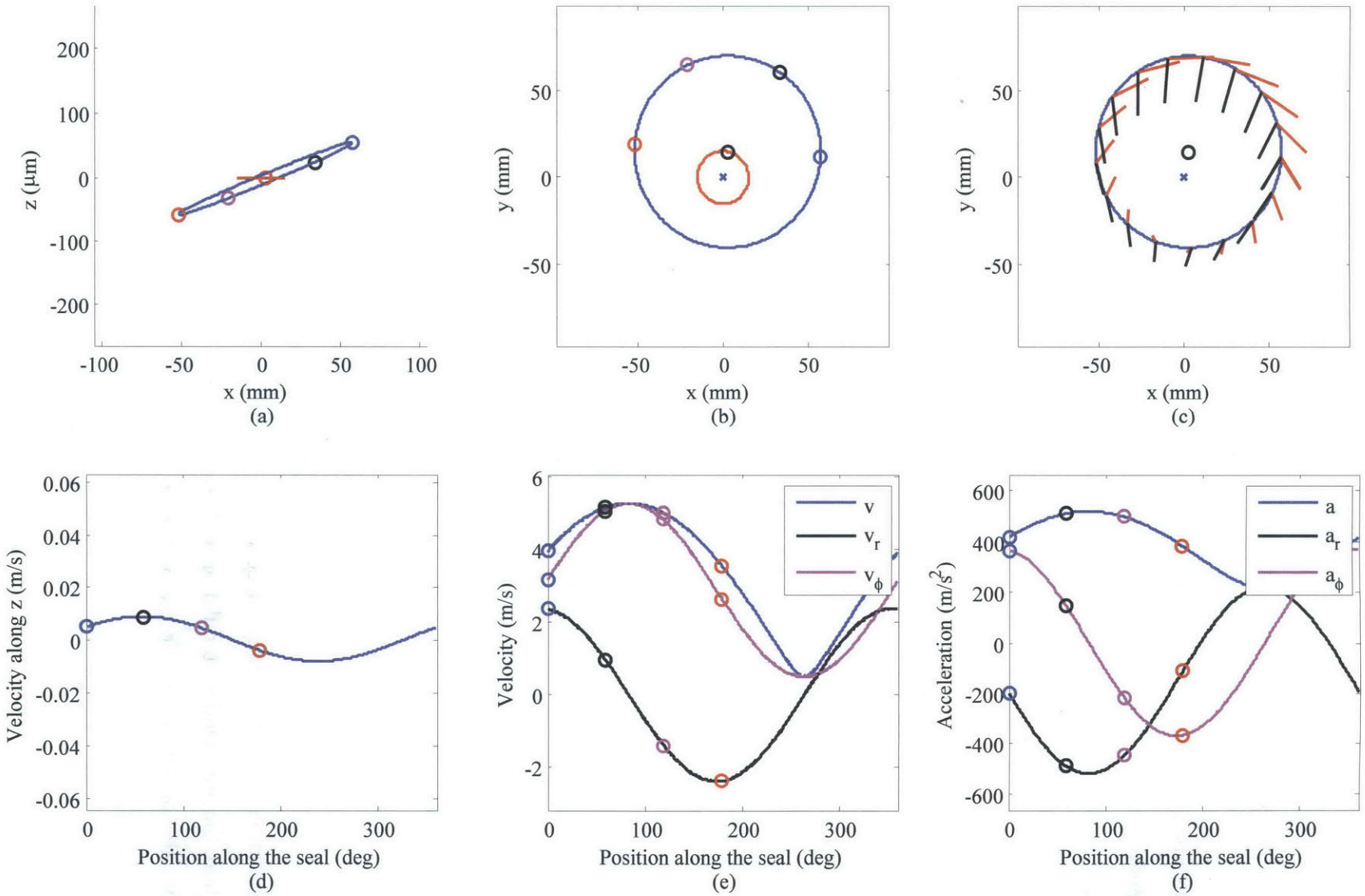

Fig. 3.26 Inner seal groove kinematics at 1500 rpm, 280 CA: (a) out-of-plane position, (b) in plane top view, (c) velocity (red) and acceleration (black) vectors, (d) out-of-plane velocity, (e) radial, circumferential and absolute velocities, and (f) radial, circumferential and absolute accelerations

Results for the rotor land are shown in Fig. 3.27 as an example of a typical accumulation and pressure generation. Data from all crank angles can be extracted from the model. Graphs display oil accumulation, clearance, pressure and flow rate as follows:

(a) shows the shape of the accumulation in the rotor land on a top view of the seal contact line. The shape is similar to experiments with an accumulating region and a zone where the land is full.

(b) shows the length of accumulation. Four points are added at 0, 60, 120 and 180 degrees on the graphs to relate to the 2D top view. From about 90° to 140° on the seal, oil is accumulating. From about 140° to 270°, the rotor land is full and the accumulation length is the same as the rotor land length. After about 270°, the accumulation is set to zero, since this section of the land is moving outward. In reality, the land does not empty immediately, but the pressure generated is zero. There is no interest in tracking the accumulation during outward motion.

(c) shows the volume flow supplied to the rotor land. Since there is no flow to the groove, the net flow rate is the supply from the housing minus the flow pushed out by squeezing due to secondary motion.

(d) shows the clearance between the rotor land and the housing. Due to secondary motion, this clearance varies along the rotor land and around the cycle. In this case, the clearance is minimal where the rotor land is full.

(e) shows the pressure generated from the different mechanisms. The pressure is maximal at the minimum clearance. The pressure generated by the relative motion is the largest effect in this case. Squeezing also contributes to pressure in a smaller importance. However, in some other cases, squeezing effect can be much larger depending on secondary motion. Body force has a negligible impact on pressure at low speed.

(f) shows the total pressure generated and would show the contribution of the two restrictions behind the seal in the presence of drain holes.

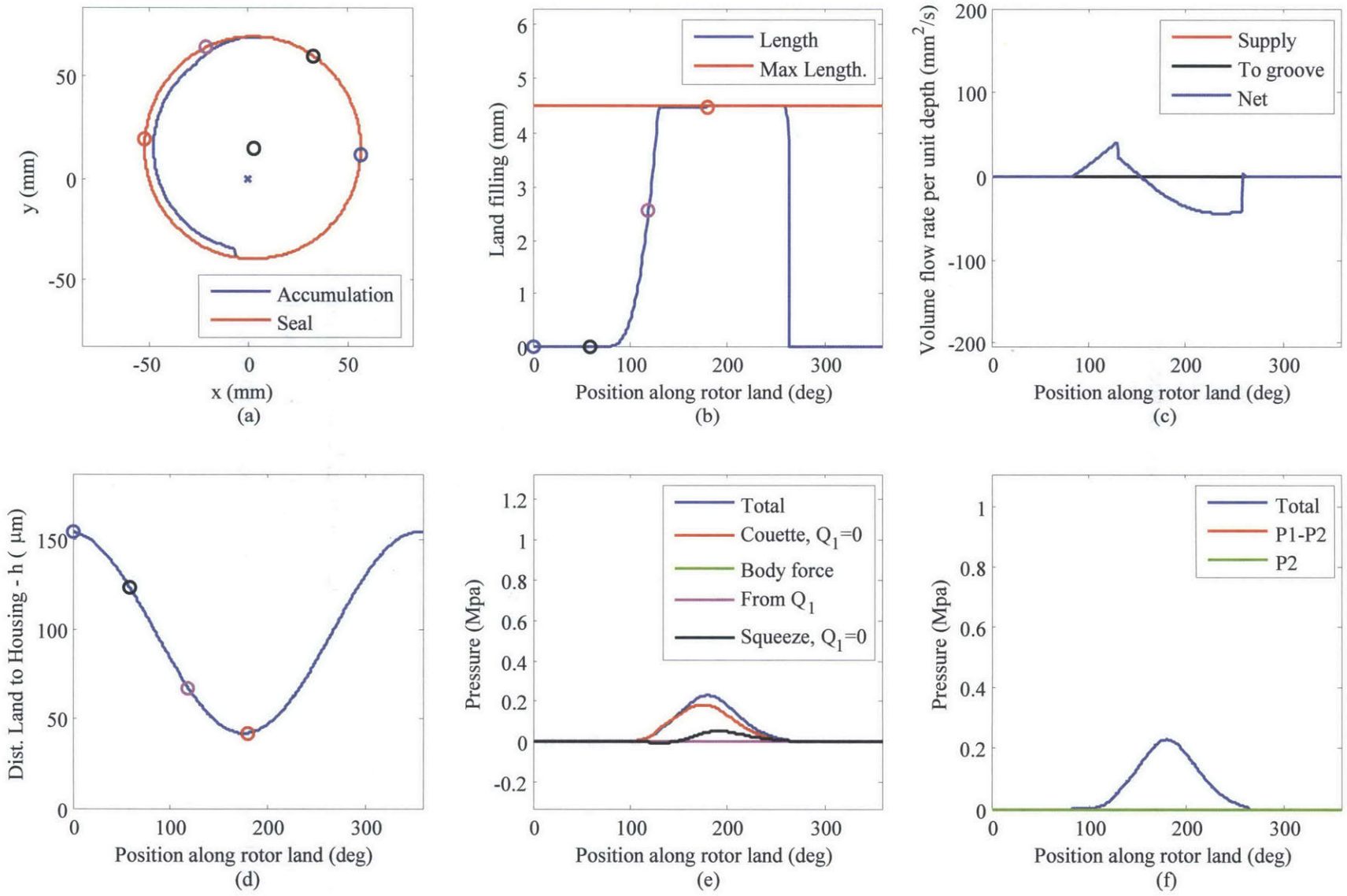

Fig. 3.27 Rotor land accumulation and pressure distribution at 1500 rpm, 280 CA: (a) top view of accumulation inside the inner oil seal, (b) length of the rotor land filled, (c) flow to the land, (d) rotor land clearance distribution, (e) pressure contributions, (f) total pressure

Distribution of in-plane forces for the inner seal is shown in Fig. 3.28. The outer seal force distribution is similar, except there is no pressure inside the seal and the O-ring normal force is in the opposite direction. Graphs on the top row display the distribution in a top view and graphs on the bottom row display the magnitude of those forces. They are divided as follows:

(a) shows the distribution of the friction force at the interface on a top view of the seal contact line. The lines are vectors pointing from the seal to the direction of the force. Friction magnitude varies principally due to clearance and velocity. Friction direction is pointing against the absolute velocity, except for the pressure drag from the taper accumulation which points against the radial velocity. Graph (d) shows the magnitude of the different contributions to friction. Hydrodynamic friction of the flat part varies smoothly along the seal. Contact friction is in the same order of magnitude, but varies more abruptly due to the stiff response of the contact pressure to clearance. Both contributions from the taper accumulation are much smaller than the two first ones.

(b) shows the force distribution on the seal due to rotor land pressure, and graph (e) its magnitude. The force from rotor land pressure is oriented against inward velocity, as expected. This force is dominating in this case.

(c) shows the O-ring normal force, and graph (f) its magnitude. O-ring force is a superposition of the original tightening and the displacement of the seal in its groove. In this case, the compression of the O-ring is sufficient to balance the other forces, mainly from the rotor land pressure. Therefore, the seal does not contact the groove.

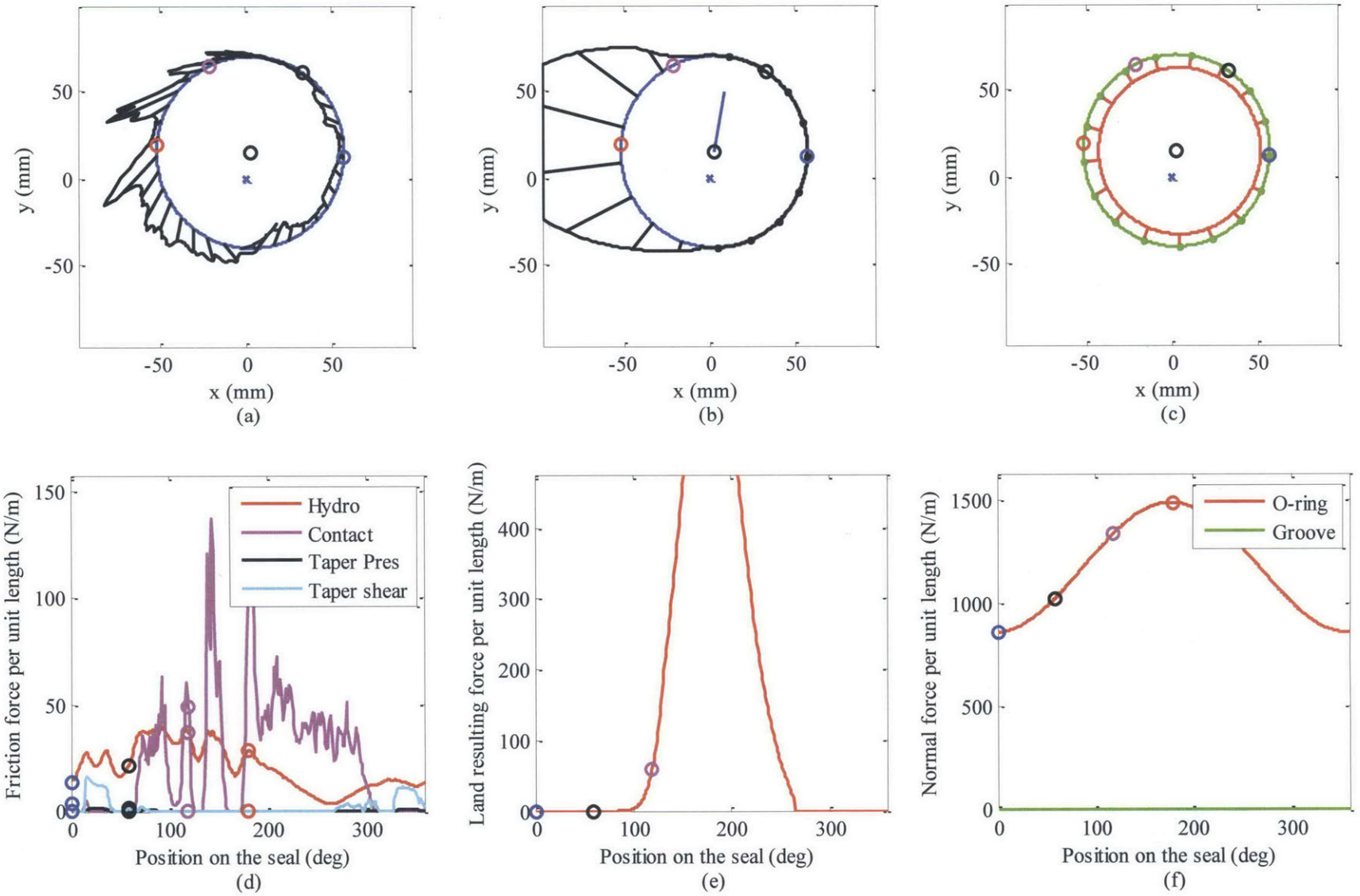

Fig. 3.28 In-plane force distribution for the inner seal at 1500 rpm, 280 CA: (a) Total friction force distribution and direction, (b) Rotor land pressure distribution (black) and body force direction (blue), (c) O-ring and groove reaction forces distribution, (d) friction forces distribution, (e) force distribution from rotor land pressure, and (f) O-ring and groove reaction forces distribution

Distribution of out-of-plane forces, seal deformation and clearance is shown in Fig. 3.29, and is divided as follows:

(a) shows a 3D view of the seal position on the housing. The red line represents the seal contact line, the black line its projection on the housing and the gray surface the housing distortion.

(b) shows the unwrapped housing distortion and seal deformation. Since the housing distortion is small, the seal is roughly following housing distortion.

(c) shows the clearance between the seal contact line and the housing. The seal conformability in this case is relatively good since the clearance variation is small.

(d) shows the force per unit length due to asperity contact. From 300 to 360° and from 0 to 60°, the velocity is high enough for the seal to be mainly supported by hydrodynamic pressure and the contact pressure is only small peaks. From 180 to 300°, velocity is smaller and contact pressure balance an important part of the spring force.

(e) shows the contributions to the hydrodynamic force per unit length at the interface. The main contribution is the pressure generated by roughness and its magnitude is directly related to velocity and clearance. The pressure generated from the accumulation in the taper provides an important contribution for the region moving outward.

(f) shows the forces from the spring, from the O-ring friction and from the rotor land pressure. The spring force is negative, thus pointing towards the surface and shows a small variation due to secondary motion of the rotor. O-ring friction is modeled as contact friction, thus the force is always opposing the relative motion between the seal and the groove. This explains the abrupt change in sign. In this case, the spring dominates and friction does not play an important role in determining the seal-housing clearance.

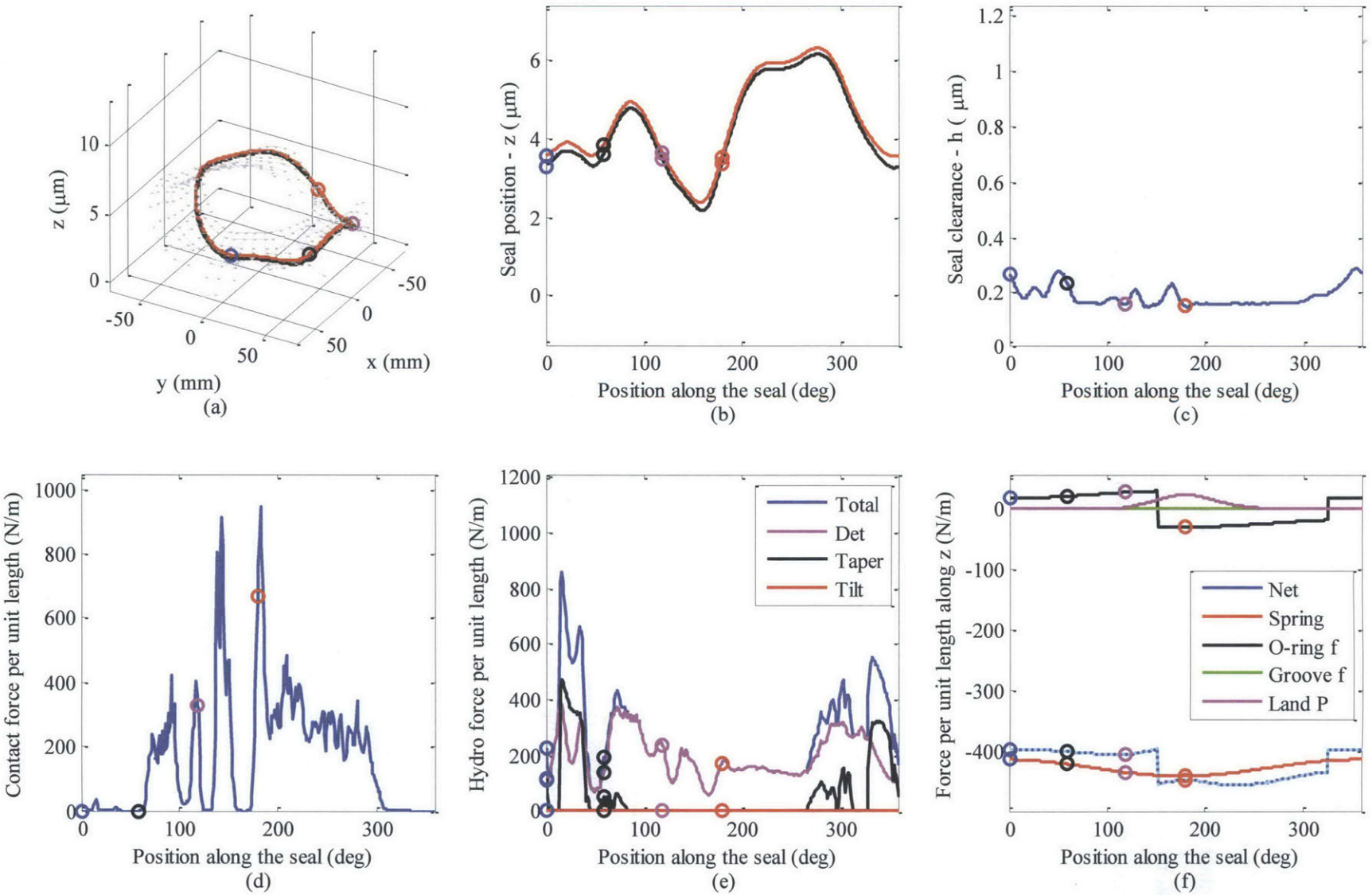

Fig. 3.29 Inner seal out-of-plane forces and position at 1500 rpm, 280 CA: (a) 3D view of conformability, (b) Seal deformation (red) to housing distortion (black), (c) seal clearance, (d) asperity contact distribution, (e) hydrodynamic pressure distribution, and (f) spring and O-ring force distribution

Up to this point, graphs presented are showing distributions on the seal for a specific crank angle. To get a better overview of the cycle, total forces on the seal are shown in Fig. 3.30 as a function of the crank angle:

- Graphs (a) and (b) shows the forces in the plane, along x and y taken in the fixed reference frame on the housing. Contributions from body force and friction are small. Therefore, the O-ring normal force is mainly balancing the force due to the rotor land pressure.
- Graph (c) shows the out-of-place forces, along z. The total spring force is almost constant over the complete cycle. The hydrodynamic pressure from roughness is the main force at the interface, followed by asperity contact pressure and taper pressure. O-ring friction is negligible along z axis. However, it can cause a torque on the seal since it is not applied uniformly along the circumference.

The last step is the calculation of the oil scraped by the seals. This process is illustrated from left to right in Fig. 3.31. The graphs in the first row show a top view of the oil thickness on the housing in μm and the contact lines of the inner and outer seals. The graphs in the second row show an isometric view of the same oil distribution and contact lines. The purple lines on the seals represent the volume of oil scraped and accumulated between the taper and the housing. The solid line is for the inner seal and the dotted line for the outer oil seal. The process can be divided in four steps:

1. During outward motion, the seals approaches a puddle of oil left on the housing, as shown in graphs (a) and (d).
2. Both seals pass the puddle and accumulate oil in their taper region, as shown in graphs (b) and (e). Meanwhile, oil on the housing is reduced by seal passage. In this case, housing distortion is small and the variation in oil film thickness is difficult to perceive.
3. Seals reach the most outward position and motion is reversed. Part of the oil accumulated flows to the taper of the seals.
4. Seals pass the same zone in the opposite direction and oil is left on the housing again, as shown in graphs (c) and (f), waiting to be scraped during the next revolution.

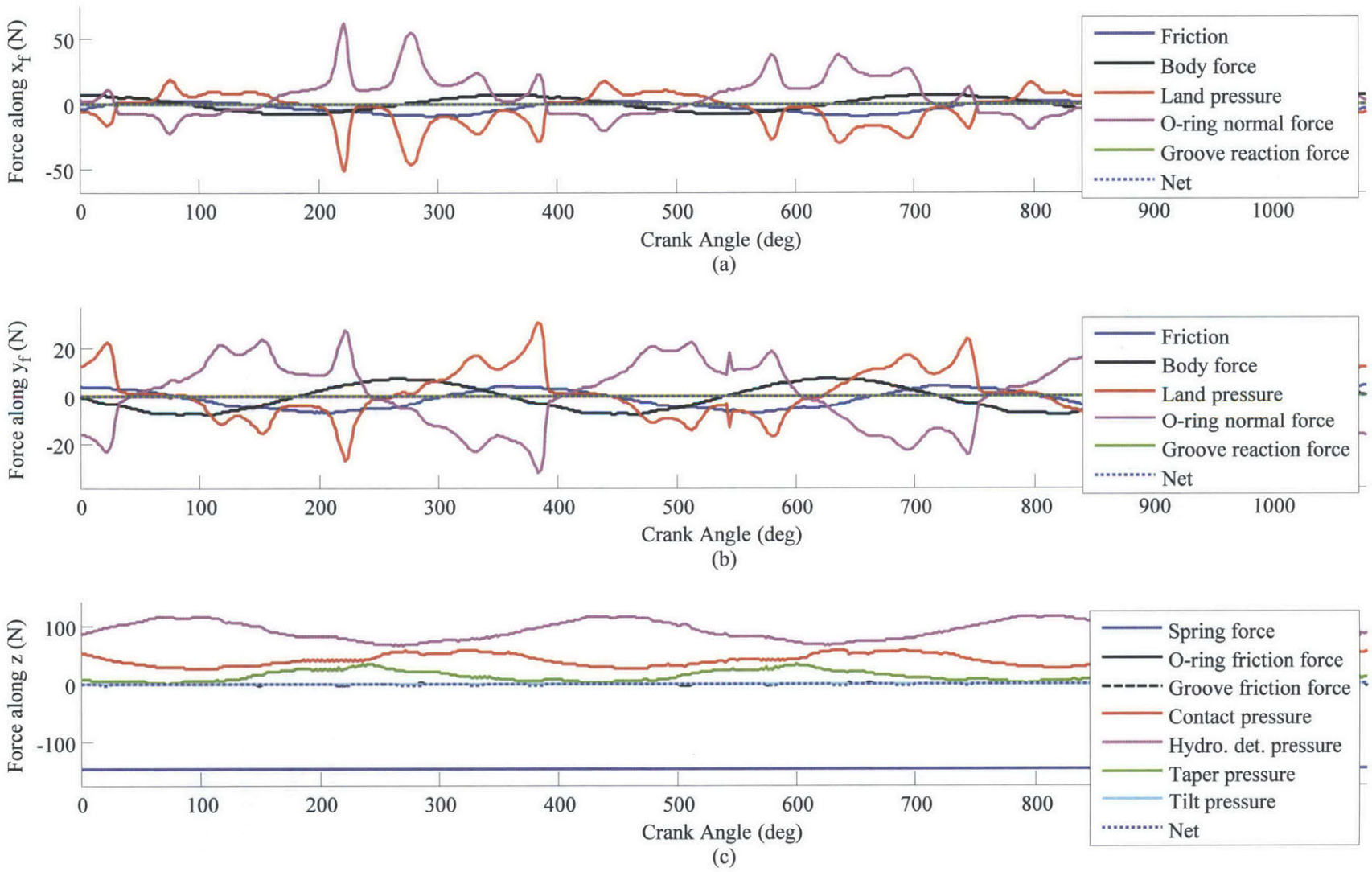

Fig. 3.30 Total forces on the inner seal at 1500 rpm, 280 CA, along (a) x, (b) y and (c) z taken in the housing reference frame

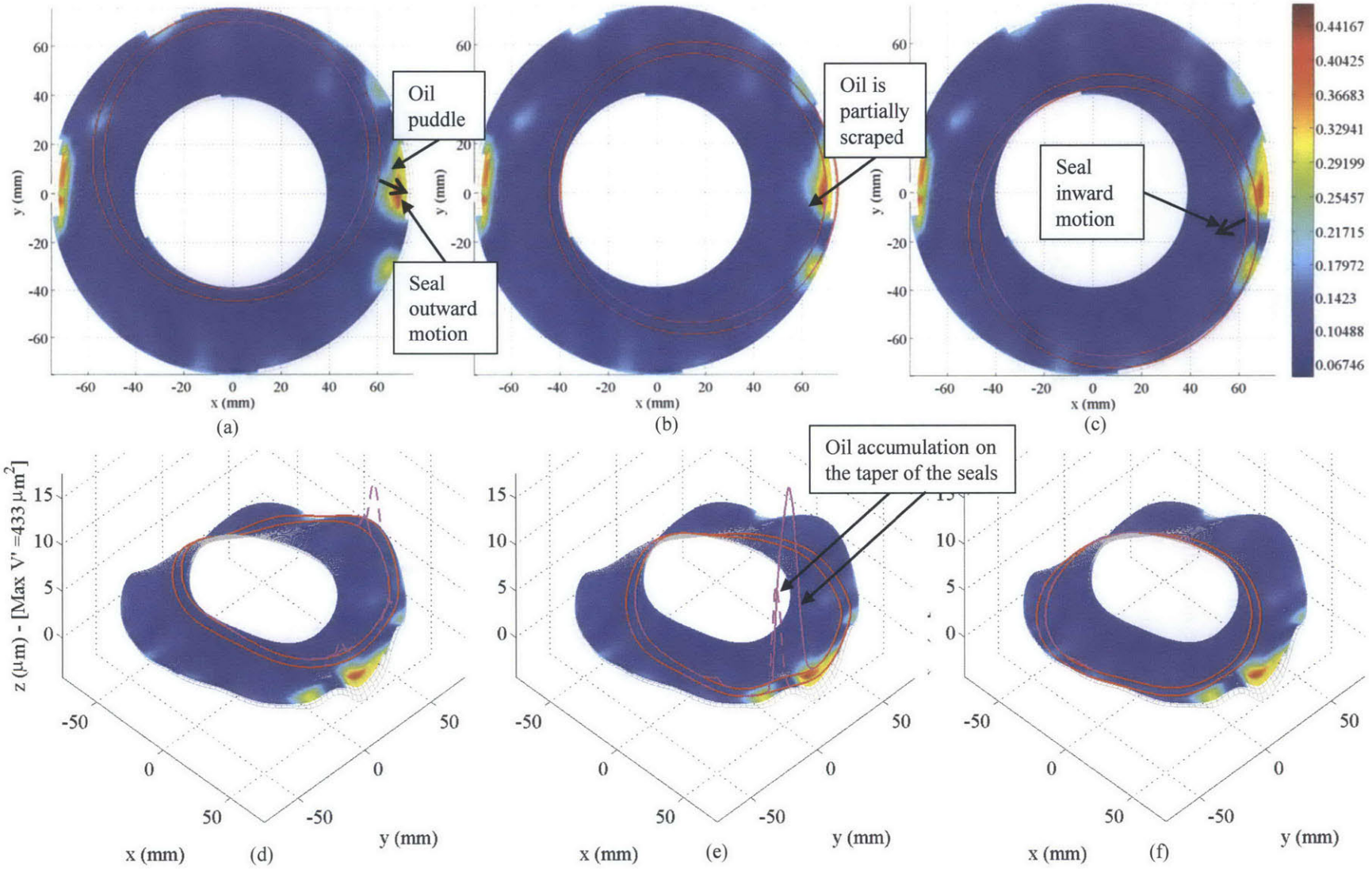

Fig. 3.31 Scraping process at 1500 rpm, shown by oil distribution on the housing (μm), seal position (red lines) and oil accumulated between housing and taper (purple lines, solid for the inner seal and dotted for the outer seal), seen in top view at (a) 276 CA, (b) 356 CA, and (c), 416 CA, and in isometric view at (d) 276 CA, (e) 356 CA, and (f) 416 CA

3.2.1.2 High Speed, Large Housing Distortion

At high speed and large distortion, the relative magnitude of the different forces is changed. The seal cannot conform to the surface, leading to a high scraping rate. To show those effects, the cycle model is run at 7500 with housing thermal distortion. Results are shown in the same order as the low speed case, and only the main differences are highlighted. Results are shown for 744 CA to display the important mechanisms.

For the kinematics, the magnitude of the velocity is increased linearly, but the acceleration is squared leading to important body force, as shown in Fig. 3.32. For the rotor land, the accumulation is similar, as shown in Fig. 3.33. However, the pressure is much greater and dominated by the squeezing mode. For the in-plane forces, the friction is mainly peaks due to the non-uniform contact between the seal and the housing, as shown in Fig. 3.34. The rotor land pressure again has an important contribution. However, in those conditions, body force is also on the same order of magnitude. O-ring and groove reaction forces are oriented to balance those two components. In this case, the seal cannot adapt to the large distortion of the housing, as shown in Fig. 3.35. The clearance can be up to 8 μm, which is 40 times more than the average clearance with small housing distortion. This non-conformability leads to large peaks in both contact and hydrodynamic pressure. It is important to note that the taper part generates more force per unit length than the roughness for the zone moving outward. The taper also contributes more than the asperity contact in supporting the seal, as shown in Fig. 3.36. Finally, the scraping is much more important, as the oil puddle completely disappear on the housing in Fig. 3.37b.

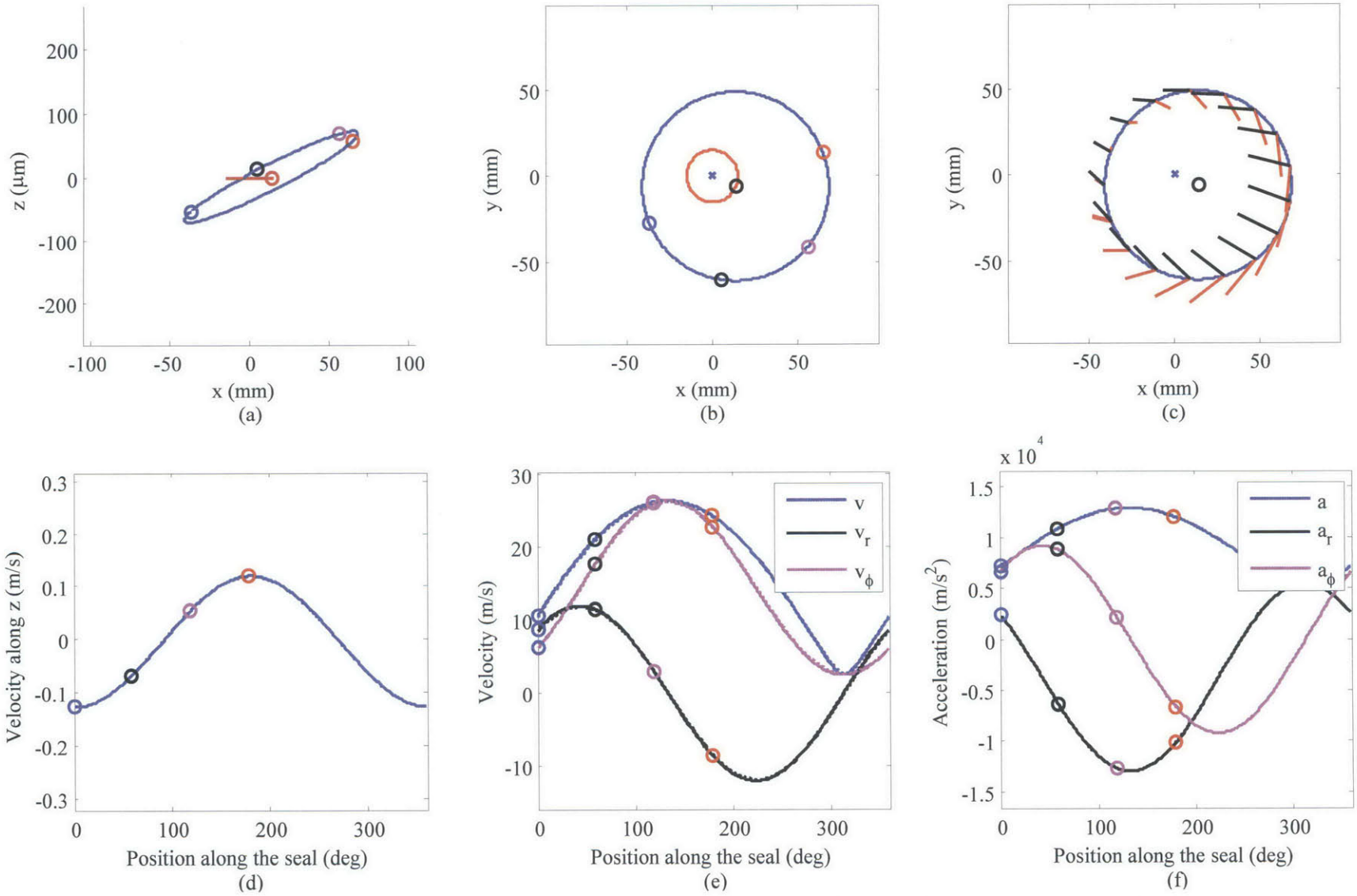

Fig. 3.32 Inner seal groove kinematics at 7500 rpm, 744 CA: (a) out-of-plane position, (b) in plane top view, (c) velocity (red) and acceleration (black) vectors, (d) out-of-plane velocity, (e) radial, circumferential and absolute velocities, and (f) radial, circumferential and absolute accelerations

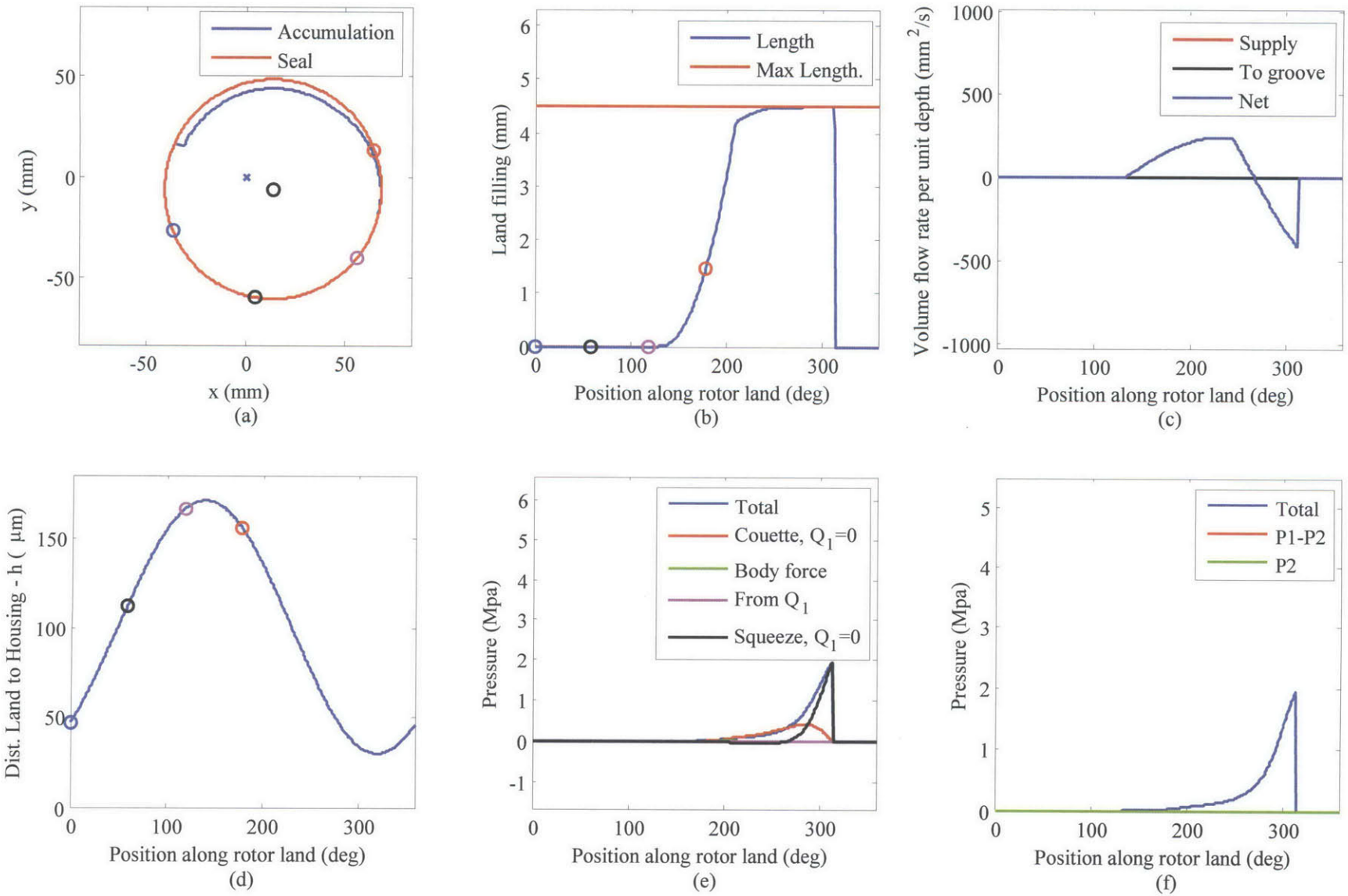

Fig. 3.33 Rotor land accumulation and pressure distribution at 7500 rpm, 744 CA: (a) top view of accumulation inside the inner oil seal, (b) length of the rotor land filled, (c) flow to the land, (d) rotor land clearance distribution, (e) pressure contributions, (f) total pressure

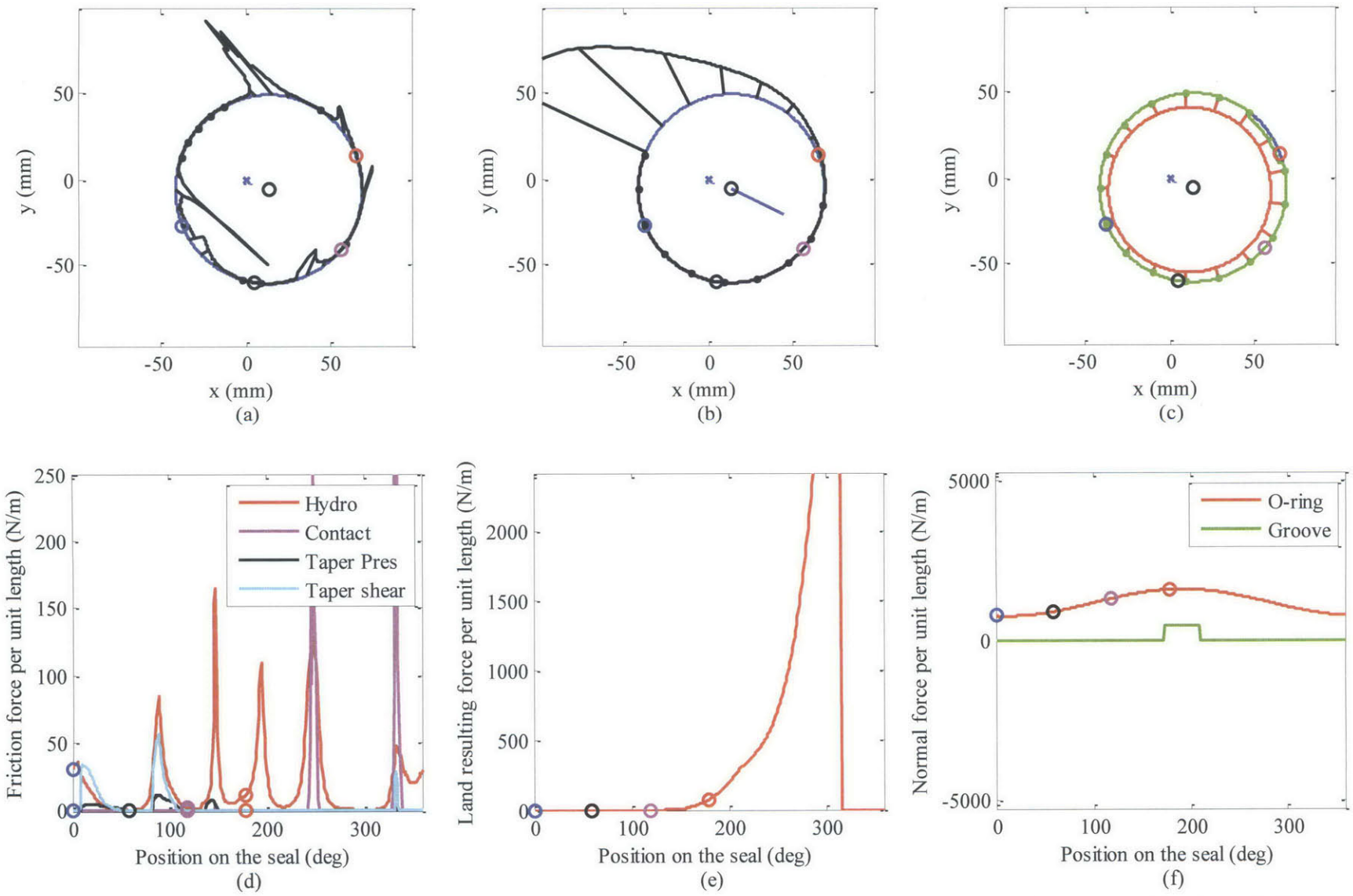

Fig. 3.34 In-plane force distribution for the inner seal at 7500 rpm, 744 CA: (a) Total friction force distribution and direction, (b) Rotor land pressure distribution (black) and body force direction (blue), (c) O-ring and groove reaction force distribution, (d) friction forces distribution, (e) force distribution from rotor land pressure, and (f) O-ring and groove reaction force distribution

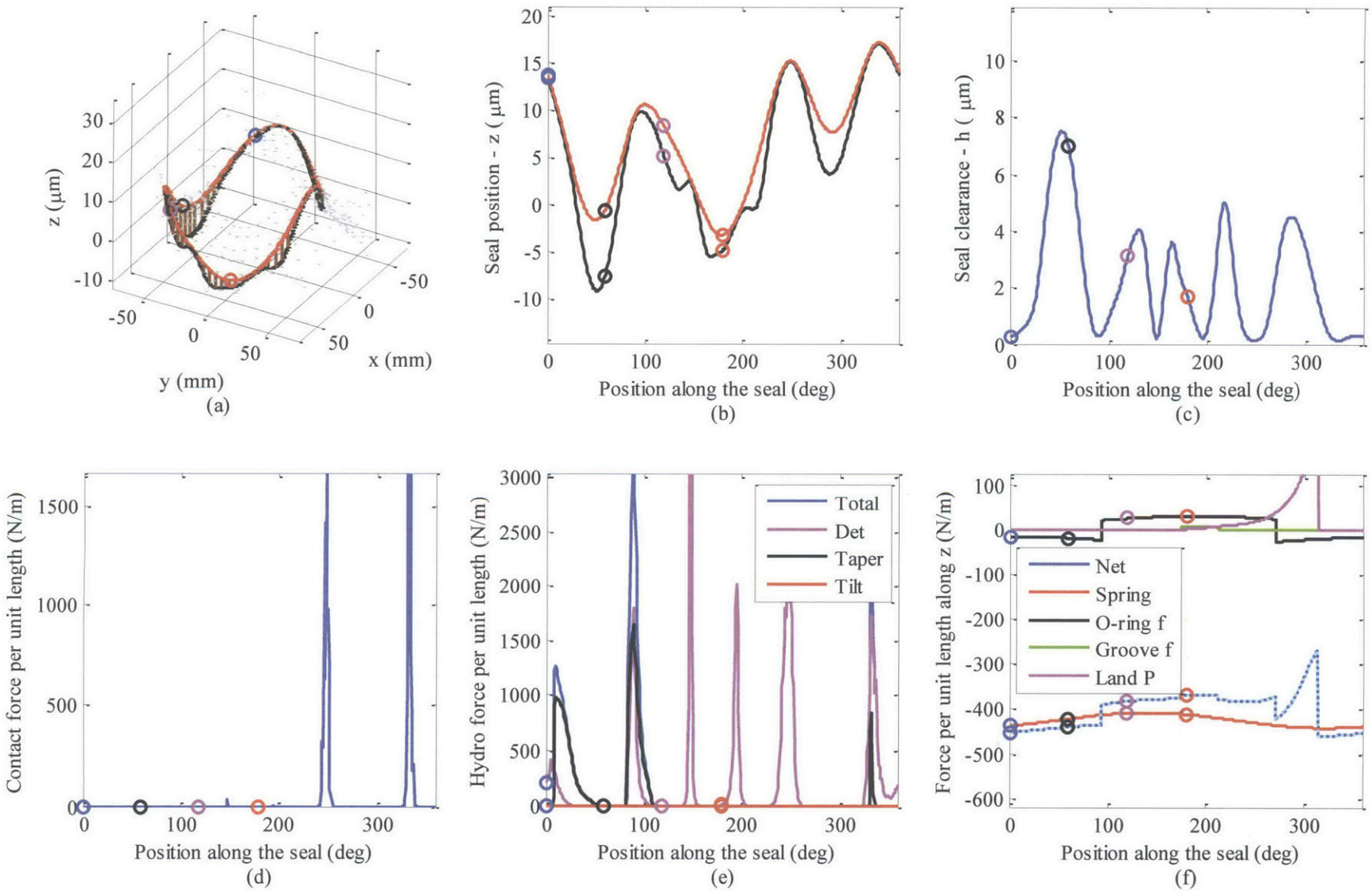

Fig. 3.35 Inner seal out-of-plane forces and position at 7500 rpm, 744 CA: (a) 3D view of conformability, (b) Seal deformation (red) to housing distortion (black), (c) seal clearance, (d) asperity contact distribution, (e) hydrodynamic pressure distribution, and (f) spring and O-ring force distribution

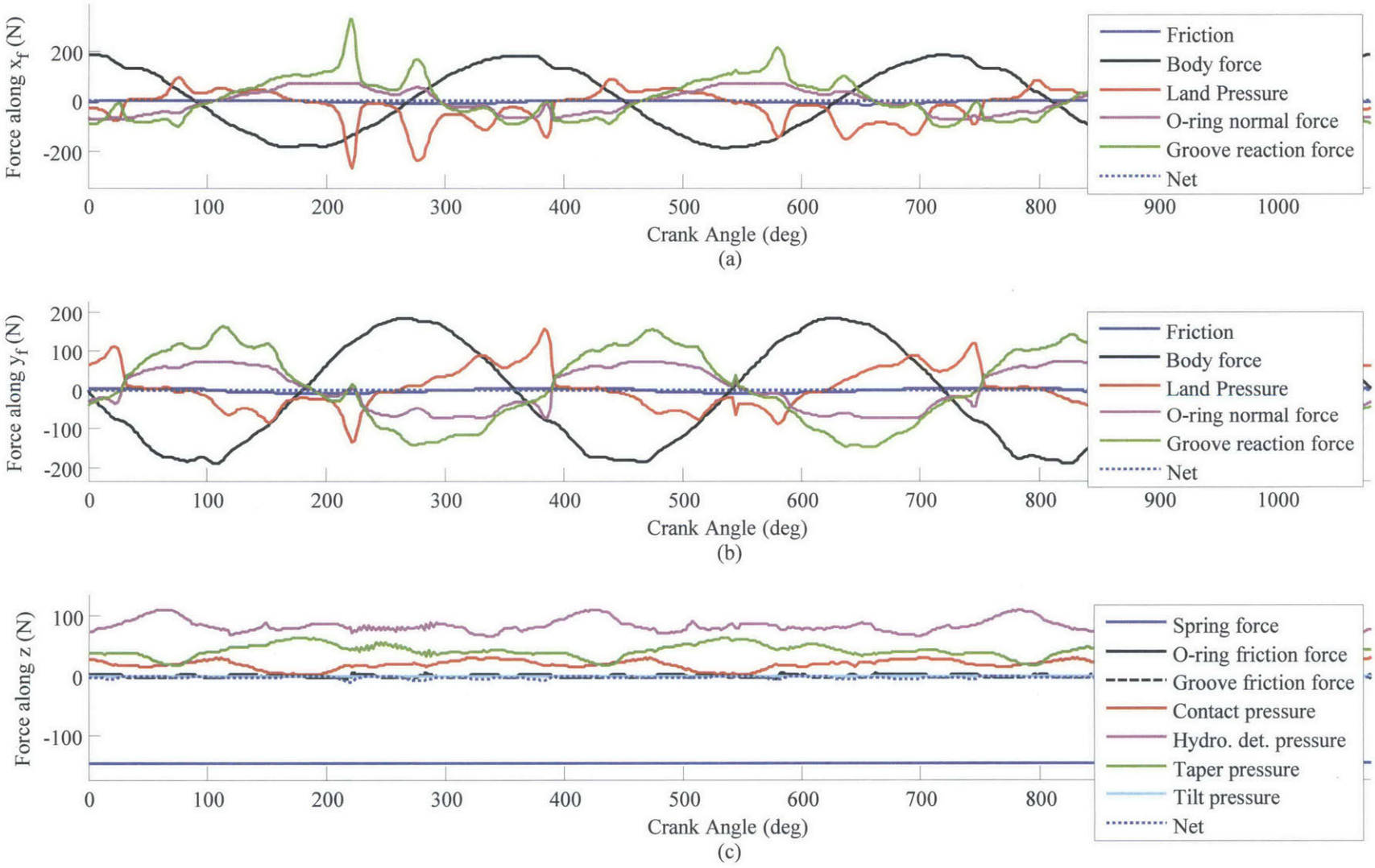

Fig. 3.36 Total forces on the inner seal at 7500 rpm, 744 CA, along (a) x, (b) y and (c) z taken in the housing reference frame

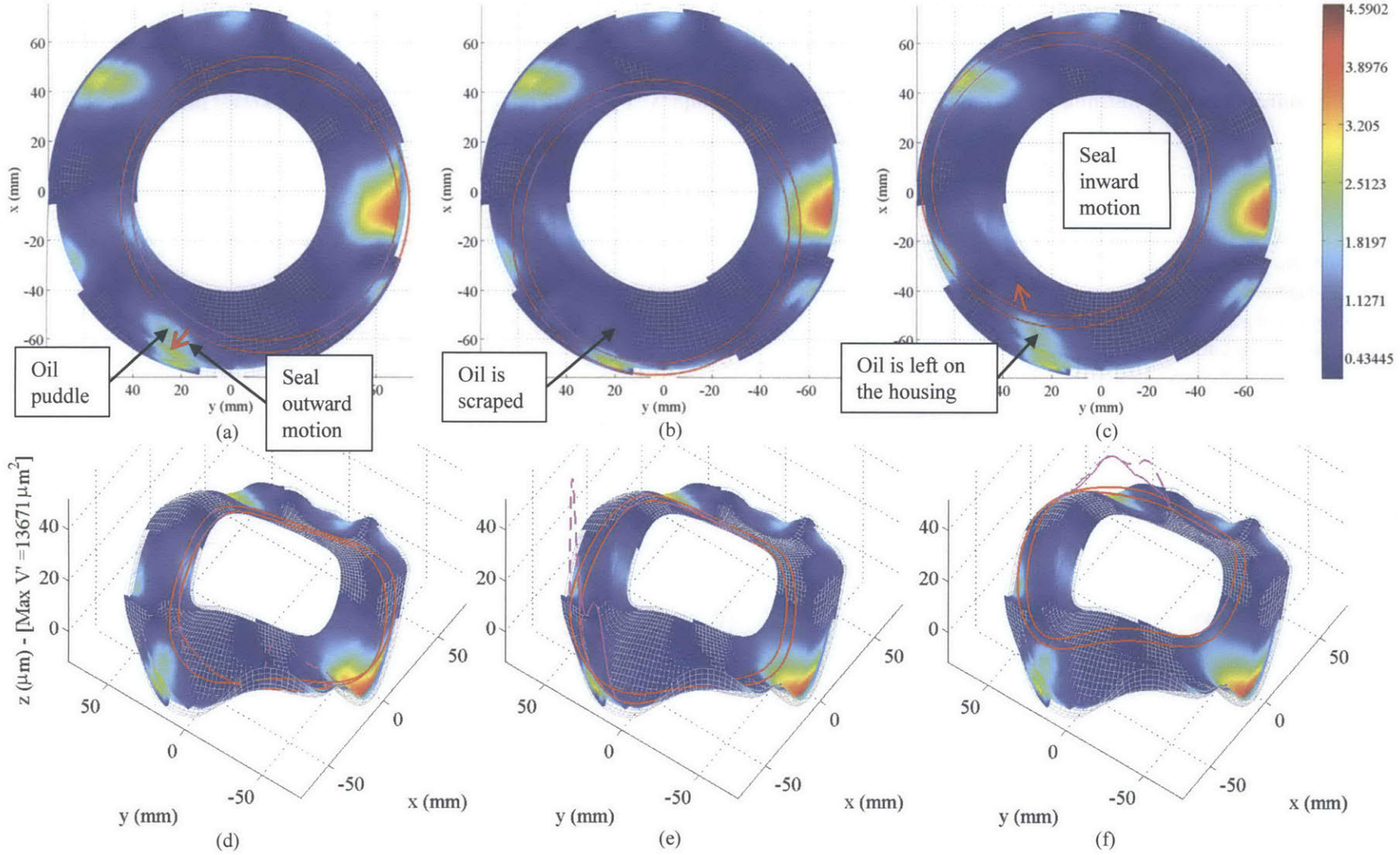

Fig. 3.37 Scraping process at 7500 rpm, shown by oil distribution on the housing (μm), seals position (red lines) and oil accumulated between housing and taper (purple lines, solid for the inner seal and dotted for the outer seal), seen in top view at (a) 112 CA, (b) 192 CA, and (c), 288 CA, and in isometric view at (d) 112 CA, (e) 192 CA, and (f) 288 CA

3.2.2 Scraping

The scraping process due to a clearance asymmetry caused by housing distortion is the main factor for internal oil consumption. Understanding this mechanism and where it occurs is essential to reduce oil consumption. In this section, location of scraping is first shown on the different housing distortions and inner and outer seal scraping are compared.

3.2.2.1 Scraping Distribution

Scraping is highly dependent on the shape and amplitude of housing distortion. To illustrate this principle, Fig. 3.38 shows the thickness of oil distribution scraped per revolution on the different distortions of the rear housing, for both inner and outer seals. A high film thickness means an important amount of oil is scraped at that location. A negative value of scraping would mean that more oil is released from the accumulation between the taper and the housing than oil is scraped at that location. The graphs show the scraping distribution as follows:

(a) shows the distribution of oil scraped by the inner seal with the mechanical distortion. Scraping values are small and scraping is relatively distributed.

(b) shows the distribution for the outer seal with also the mechanical distortion. Maximum scraping value of scraping is higher than for the inner seal, but is concentrated in the top right corner.

(c) shows the distribution for the inner seal with 1500 rpm thermal distortion. Scraping occurs in the same region as for the mechanical distortion, except an important scraping region is added near the exhaust port.

(d) shows the distribution for the outer seal. Scraping values are higher than the inner seal. The exhaust port region is also the main scraping region.

(e) shows the distribution for the inner seal with the 7500 rpm distortion. Exhaust port region scraping dominates.

(f) shows the distribution for the outer seal. Maximum scraping in the exhaust region is about 3 times higher for the outer seal than for the inner seal.

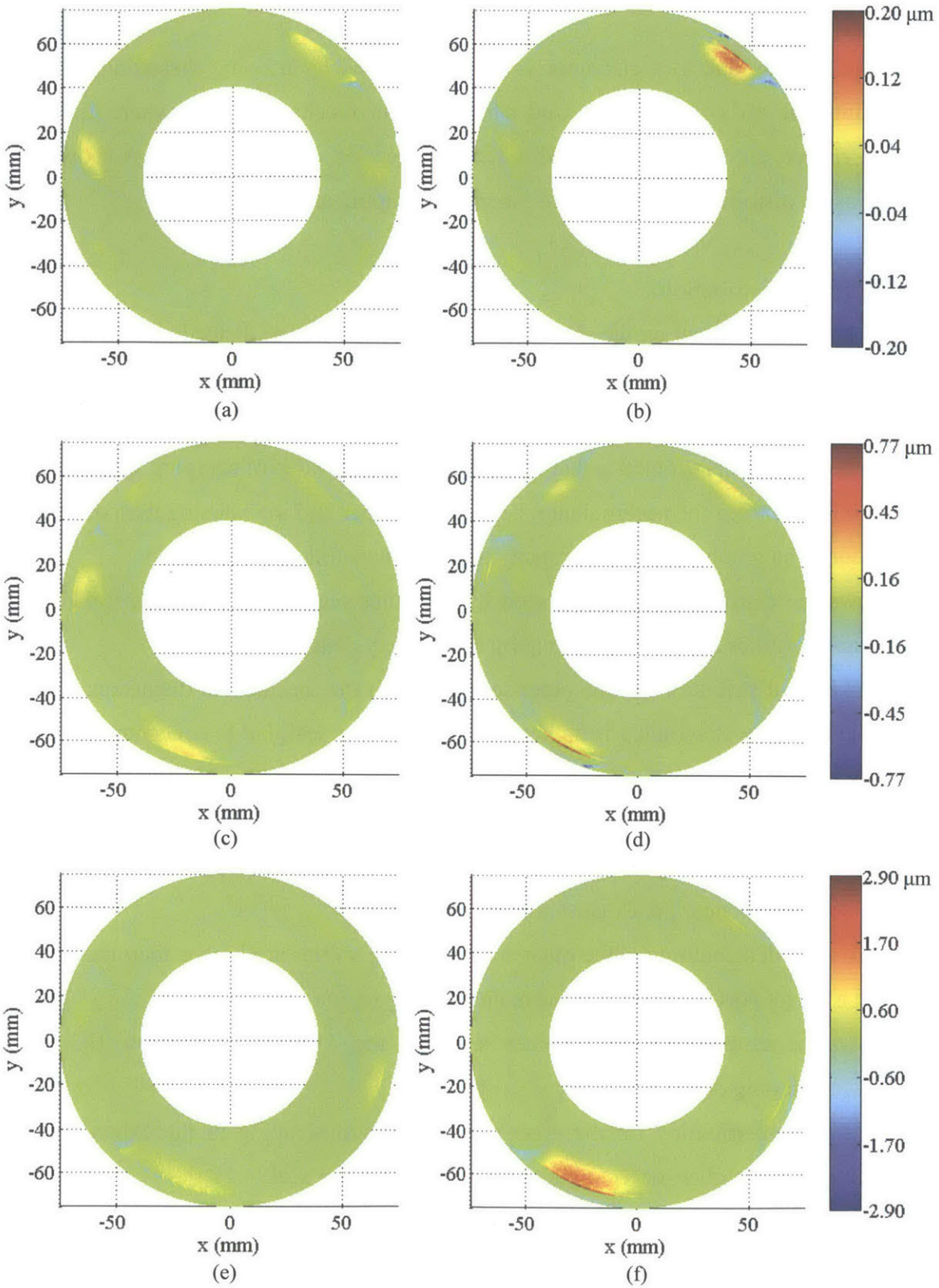

Fig. 3.38 Scraping distribution for the rear housing: with mechanical distortion for (a) inner and (b) outer seals, with 1500 rpm thermal distortion for (c) inner and (d) outer seals, and with 7500 rpm thermal distortion for (e) inner and (f) outer seals

The different housing scraping distributions are compared. Maximum distortion is chosen since it generates maximum scraping. Front and rear housing outer seal scraping is compared in Fig. 3.39. Scraping is mainly occurring in the exhaust port region for both housings. Scraped oil thickness of the front housing is about 1.5 times larger than for the rear housing and the scraping zone is larger. This leads to about 3 times more internal oil consumption for the front housing than for the rear housing.

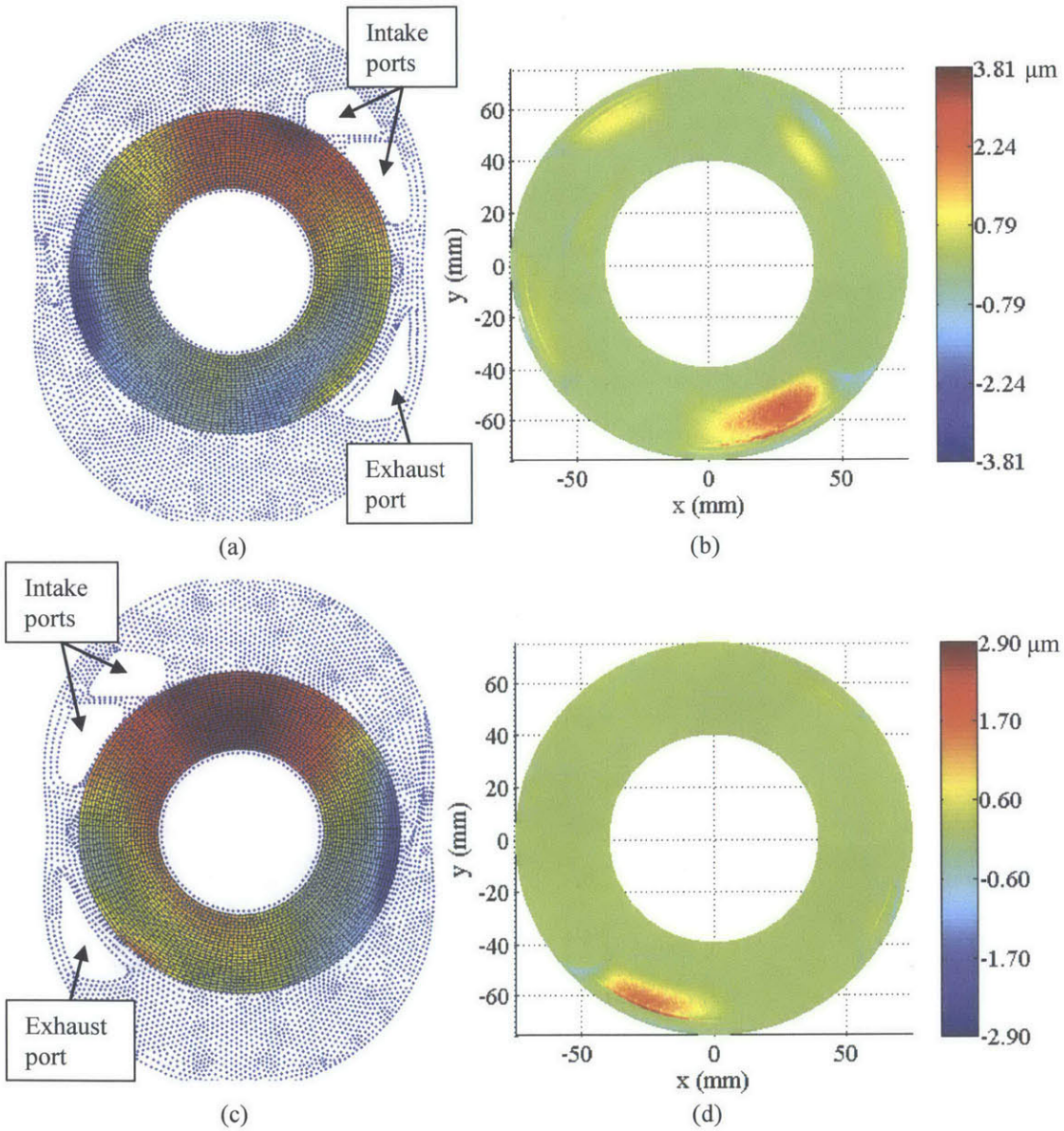

Fig. 3.39 Location of intake and exhaust port and outer seal scraping distribution for (a-b) front housing and (c-d) rear housing with 7500 rpm thermal distortion

Intermediate front and intermediate rear housing outer seal scraping is compared in Fig. 3.40. Although some scraping occurs near the exhaust ports, the main scraping region is near the intake ports. A small scraping region is also observed opposing the intake port. In this case, scraping value and dimension of scraping regions are similar for the two intermediate housings. This leads to similar internal oil consumption for those two housings.

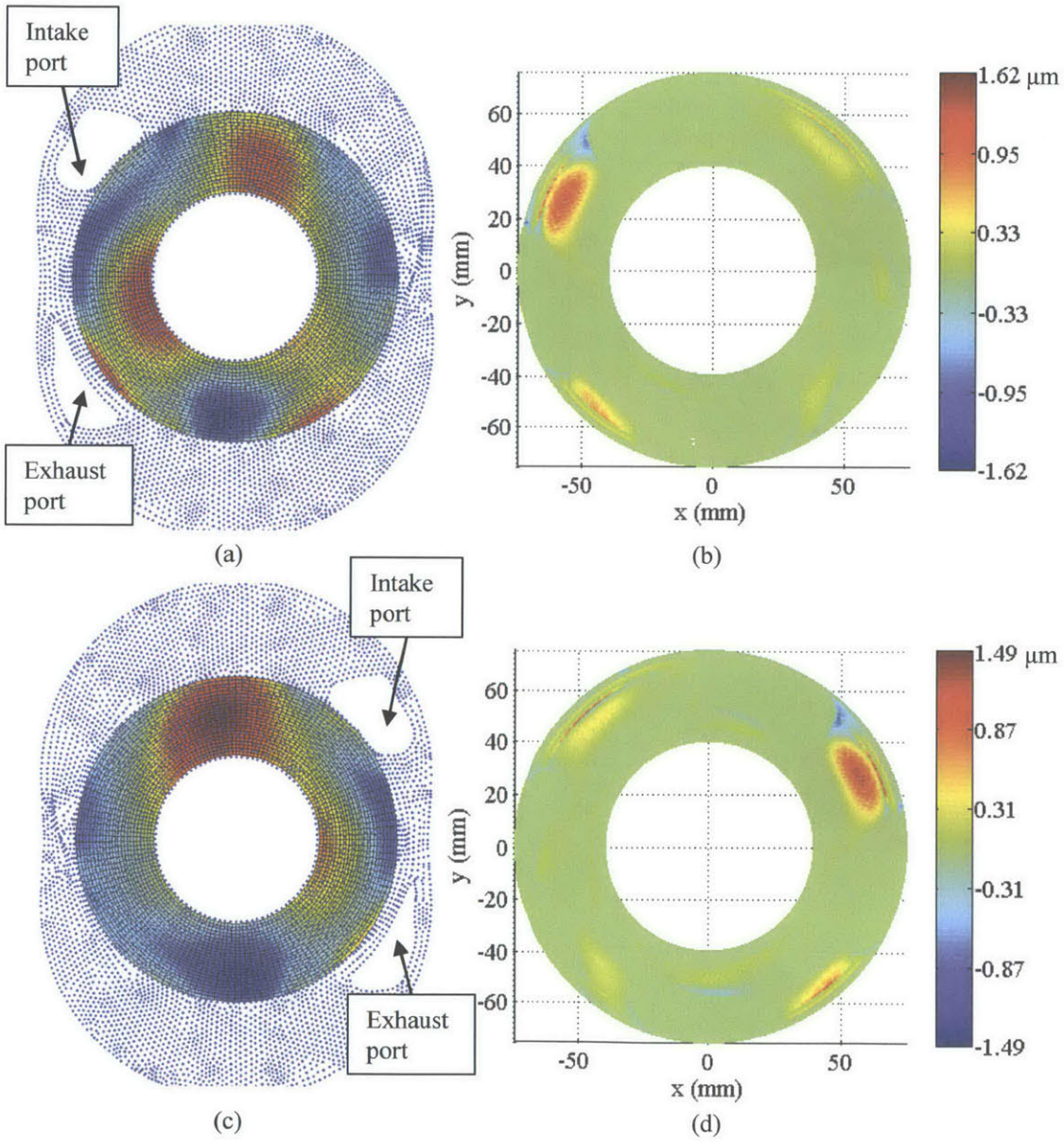

Fig. 3.40 Location of intake and exhaust port and outer seal scraping distribution for (a-b) intermediate front housing and (c-d) intermediate rear housing with 7500 rpm thermal distortion

3.2.2.2 Inner and Outer Seal Scraping

For a well-behaved system, outer seal outward scraping is expected to be much smaller than the inner seal scraping. Outward scraping is defined as the oil scraped when the seals moves outward and flows to the taper of the seal. For the outer seal, this scraping is defined as internal oil consumption. Outward scraping is also expected to be smaller than inward scraping. Inward scraping is defined as the oil scraped during inward motion by the outer seal and flowing to the 4^{th} land.

Average outward and inward scraping of the outer seal is compared to the inner seal scraping, as shown in Fig. 3.41. Outer seal outward scraping is about 50 % of the inner seal scraping for the mechanical distortion. However, for thermal distortions, outer seal outward scraping is higher than inner seal scraping, reaching about 160 %.

Inward scraping of outer seal is relatively constant compared to inner seal scraping. For the mechanical distortion, inward scraping is much higher than outward scraping, meaning that the outer seal prevents an important part of oil consumption. However, for thermal distortions, outer seal does not seem to help reducing oil consumption significantly.

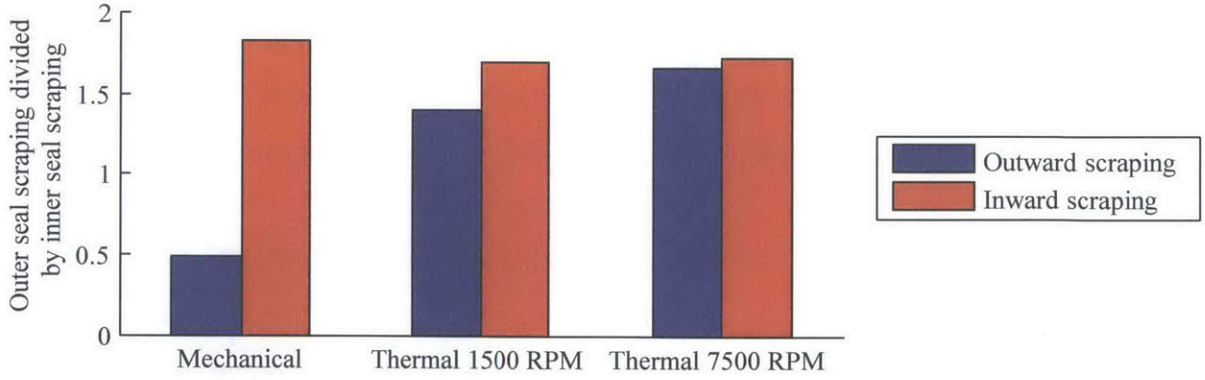

Fig. 3.41 Average inward and outward outer seal scraping compared to inner seal scraping for the three sets of housing distortion

The inward and outward scraping of the outer seal is compared to inner seal scraping for different scaling factor of the front housing mechanical distortion, as shown in Fig. 3.42. Proportion of outer seal outward scraping increases quickly as the amplitude of the distortion

increases. Inward scraping proportion is relatively constant again, varying from 3 to 2 times inner seal scraping as distortion is increased. These results show that as distortion gets larger, the outer oil seal is not capable of reducing internal oil consumption as it scrapes the oil left by the inner oil seal during inward motion.

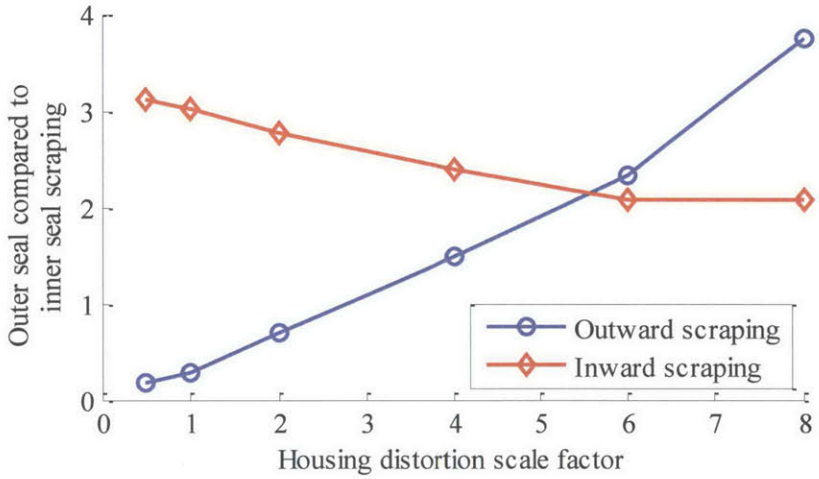

Fig. 3.42 Inward and outward scraping of the outer seal compared to the inner seal scraping against the scale factor of the front housing mechanical distortion

3.2.3 Lubrication Performance

The cycle model is used to estimate internal oil consumption and friction for different housing distortions. For this case, primary motion only is used and the pressure from the tilt is not included. Oil consumption results are shown in Fig. 3.43 for the four housing types. The graphs are shown as follows:

(a) shows oil consumption at 1500 rpm with mechanical distortion only. Seal conformability to the housing is good and the maximum consumption is about 1 mL/hr per side.

(b) shows oil consumption again at 1500 rpm, but including thermal distortion. Both intermediate housings consume more oil than the front and rear housings, due to their larger distortion amplitude.

(c) shows oil consumption at 7500 rpm, with thermal distortion. Front and rear housings show large increase compared to 1500 rpm while intermediate housings a relatively

small increase. Front housing oil consumption is much greater than the others, mainly due to the shape of housing distortion near the exhaust port.

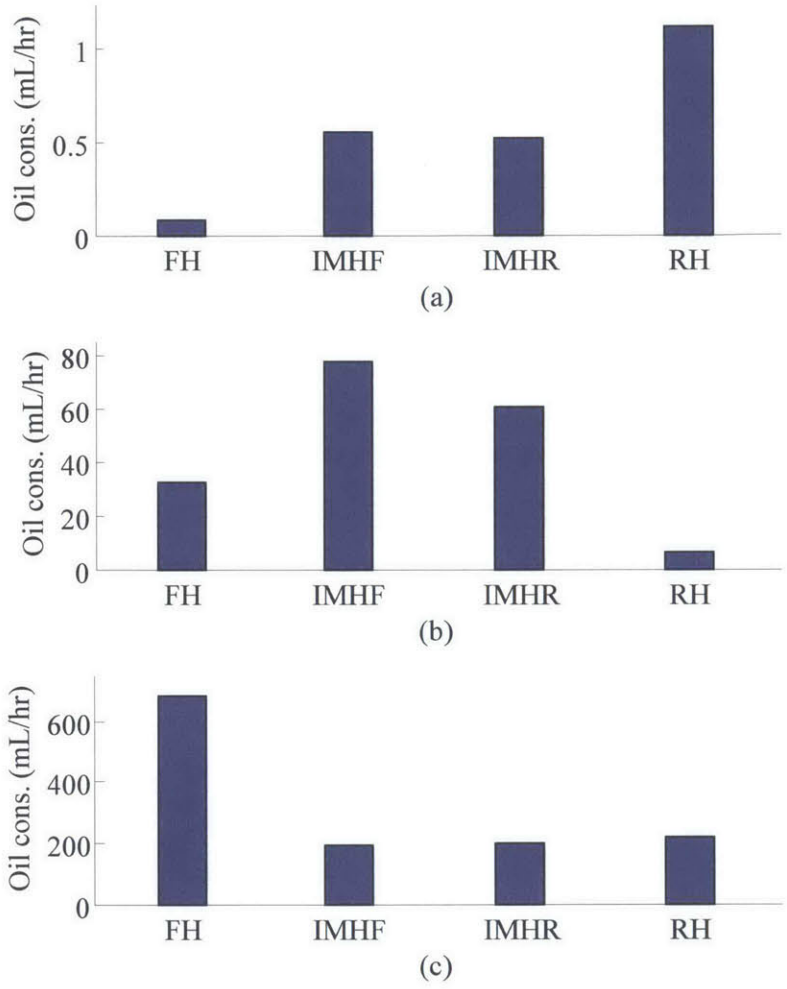

Fig. 3.43 Prediction of internal oil consumption for front housing (FH), intermediate front housing (IMHF), intermediate rear housing (IMHR) and rear housing (RH): (a) mechanical distortion only at 1500 rpm, (b) 1500 rpm, and (c) 7500 rpm

For a given engine condition, the friction power losses of all four housings are very similar. Therefore, the total friction power for the eight seals in the engine is calculated, as shown in Table 3.5. At 1500 rpm, friction power is higher with the thermal housing distortion. This can be explained by the presence of more boundary contact due to the seal non-conformability. From 1500 to 7500 rpm, friction power mainly scales with speed.

Table 3.5 Predicted friction power due to all oil seals for different engine conditions

Housing Distortion	Speed (rpm)	Friction (W)
Bolt-Force	1500	250
1500 rpm	1500	317
7500 rpm	7500	1583

3.2.4 Housing Transverse Waviness Effect

Housing transverse waviness without housing distortion is shown in Fig. 3.44. Straight waves are running across the surface. These waves are potentially left on the housing during the polishing process. Based on roughness measurements, this waviness would have an amplitude of about 1.1 μm or more and a wavelength of about 8 mm. The measurements are made on replicas and the waviness does not seem to appear on the worn housing measured. Nevertheless, waviness is still discussed since it represents an important potential for scraping, and understanding its effect can be useful for certain shapes of housing distortion. Amplitude and wavelength are defined in Fig. 3.45. For this section, wavelength is set to 16 mm to get a better illustration of the effect of housing waviness.

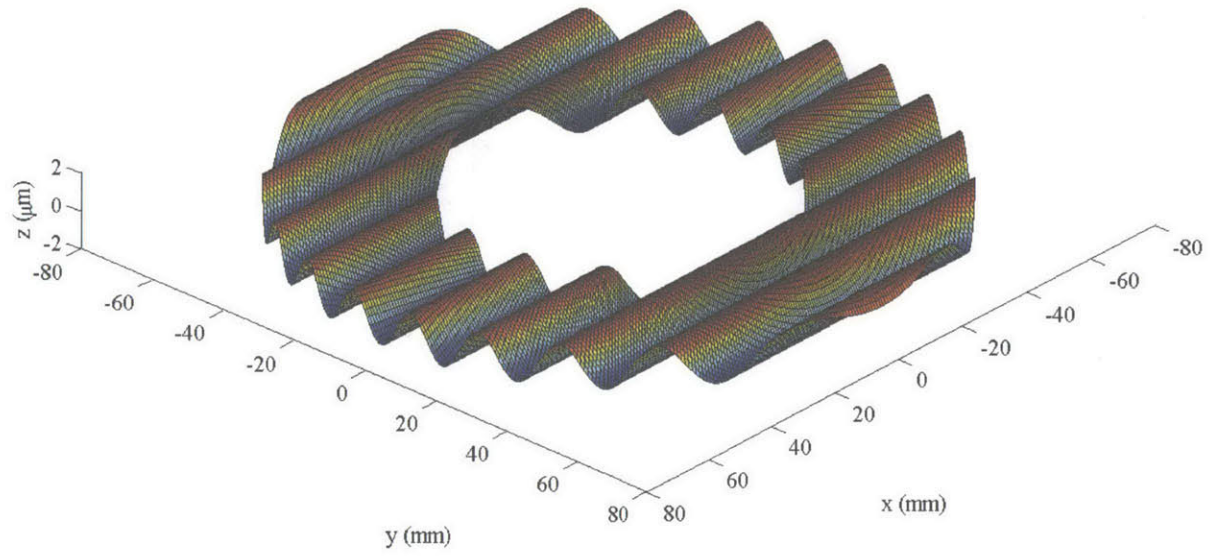

Fig. 3.44 Housing transverse waviness, 1.1 μm amplitude and 16 mm wavelength

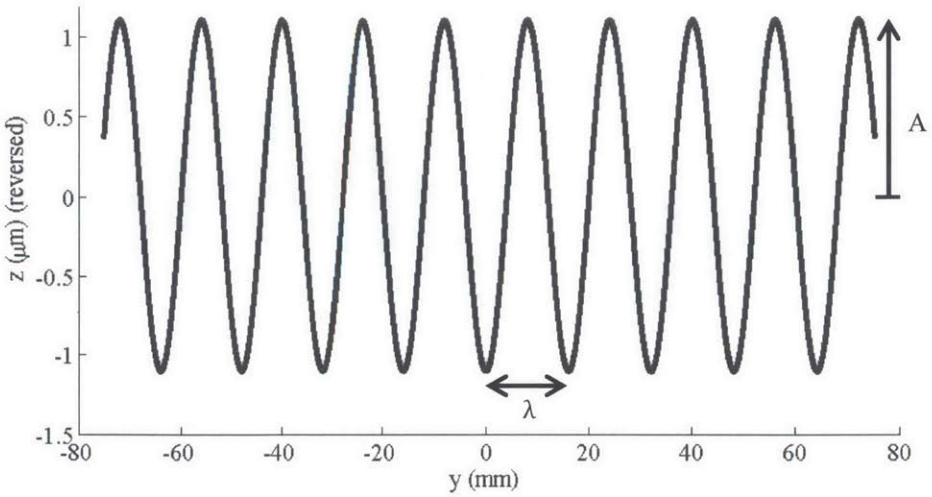

Fig. 3.45 Side view of waviness and definition of wavelength (λ), and amplitude (A)

Since this type of waviness is straight, it is aligned with the seal on the sides of the seals but perpendicular to the seal between those two regions. When the seal is parallel to the waves, it conforms to them. However, when the seal is perpendicular to the waves, it cannot conform and only holds on the peaks. This behavior is shown in Fig. 3.46. Around 0 and 180°, the seal conforms, but everywhere else it is almost flat on top of the waviness peaks.

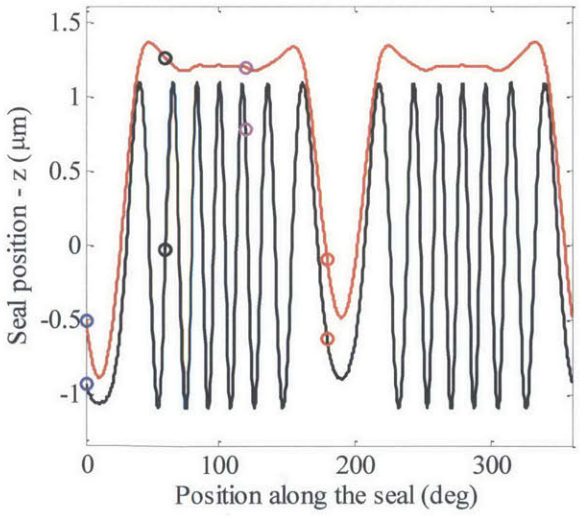

Fig. 3.46 Deformation of the seal to the waviness of the housing

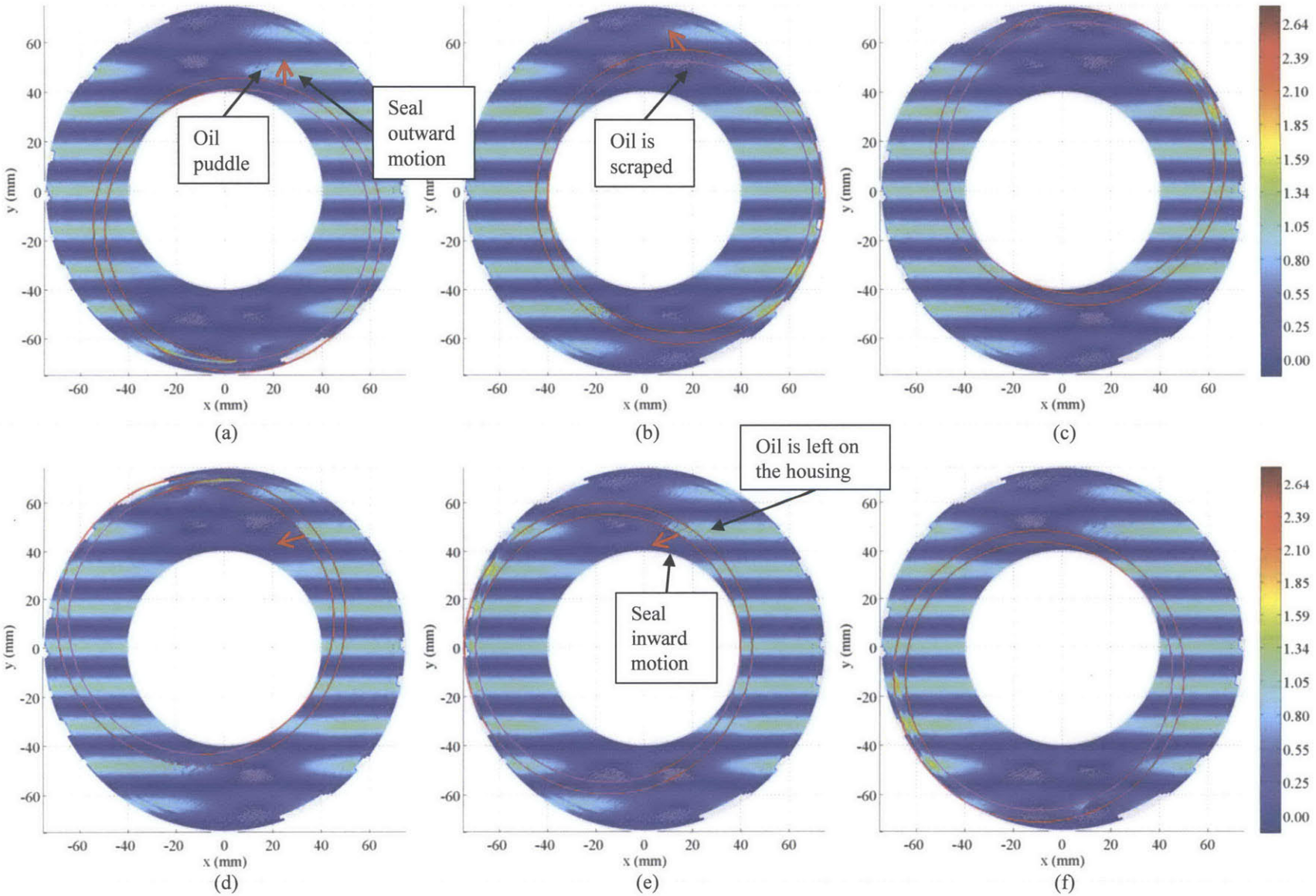

Fig. 3.47 Scraping process for waviness housing distortion shown by a top view of oil distribution (in μm) and contact line of the seals (in red) at: (a) 110 CA, (b) 170 CA, (c) 240 CA, (d) 310 CA, (e) 360 CA, and (f) 410 CA

This situation creates an important potential for outward scraping, as shown by the oil distribution in Fig. 3.47 for a few positions during the cycle:

(a) Seals are located to the right.

(b) When the seals go up, their upper part is parallel to the waves and scrapes the oil from the housing valleys.

(c) The upper part of the seals reaches the most outward position.

(d) When the seals move to the left, they are perpendicular to the waves. Thus, they do not conform to the surface and leave oil in the valleys.

(e) The seals move down, but on the left part of the housing.

(f) Oil is left in the right part of the valleys and is scraped during the next revolution.

3.2.5 Parametric Study

In this section, the effect on oil consumption and friction is studied for the design parameters and engine conditions that influence internal oil consumption. Those effects are presented from the most important to the less, as much as possible, and are listed as follows:

1. Housing distortion
2. Housing transverse waviness
3. Spring tension and seal stiffness
4. Taper angle
5. Rotational speed
6. Inner seal oil supply
7. Housing wear
8. Oil viscosity
9. Rotor land pressure
10. O-ring and groove friction
11. Hydrodynamic pressure from tilt
12. Roughness
13. Surface orientation
14. Seal orientation
15. Oil fraction flowing to the taper

For most of the parameters studied, their effect is evaluated with small and large housing distortions. The parameters are mainly studied at 1500 rpm to match the given housing distortion and the conclusions given are generally independent of speed. The effect of surface anisotropy and seal orientation is however studied at high speed, to better show its impact.

Secondary motion is not explicitly listed, but directly impacts the O-ring friction, groove friction, and rotor land pressure. Secondary motion also changes spring force, but this effect has not shown significant contribution to oil consumption in the current configuration.

For the parametric study, there is no secondary motion, no pressure generated by the tilt and no surface anisotropy unless otherwise specified. Inner seal groove is modeled with drain holes to limit the rotor land pressure. The number of crank angle steps is reduced to 216 for a rotor revolution, in order to minimize calculation time. As discussed in section 3.1.10.2, this discretization leads to an error of less than 10 %, which is acceptable for this parametric study. When transverse waviness is added, the error due to the selected discretization can be up to 20 %, since there are more maxima and minima.

3.2.5.1 Housing Distortion

Housing distortion is the principal source of asymmetry between inward and outward motion and therefore the principal source of scraping. Oil consumption depends on both housing distortion shape and amplitude. Oil consumption is calculated with the cycle model for the 12 housing distortions discussed in section 3.2.3. To isolate the housing distortion effect, engine speed is set to 1500 rpm for all cases. The results are shown in Fig. 3.48. Although it is clear that oil consumption increases with the housing distortion amplitude, oil consumption can greatly differ for a given distortion amplitude. This shows that the shape of housing distortion have even a greater influence than amplitude on internal oil consumption.

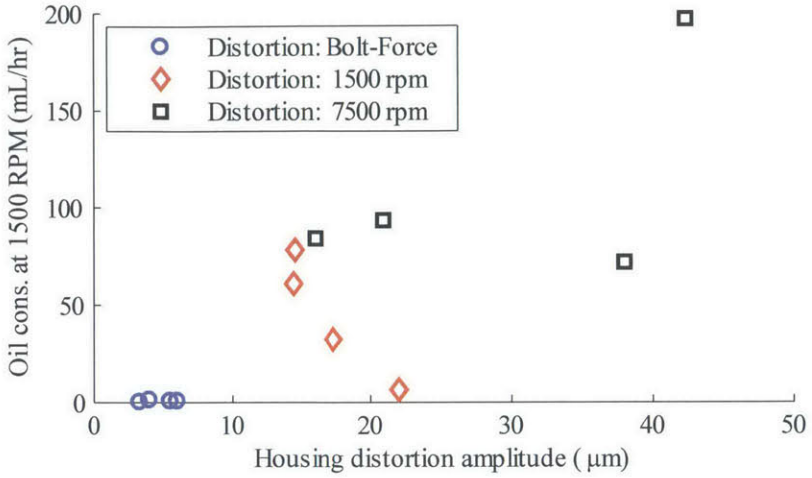

Fig. 3.48 Internal oil consumption as a function of housing distortion amplitude, all 12 conditions ran at 1500 rpm

In order to isolate the effect of the amplitude from the shape, two housing distortion shapes are scaled up and down. Oil consumption as a function of the scaling is shown in Fig. 3.49. Front housing mechanical distortion z position is scaled from 0.5 to 8 times its original distortion amplitude (Fig. 3.49a). Front housing, 1500 rpm distortion is scaled from 0.1 to 2 times its original shape (Fig. 3.49b). Both results show the same trend: under a critical distortion amplitude, oil consumption is almost zero and above this value, oil consumption increases rapidly to an unacceptable level.

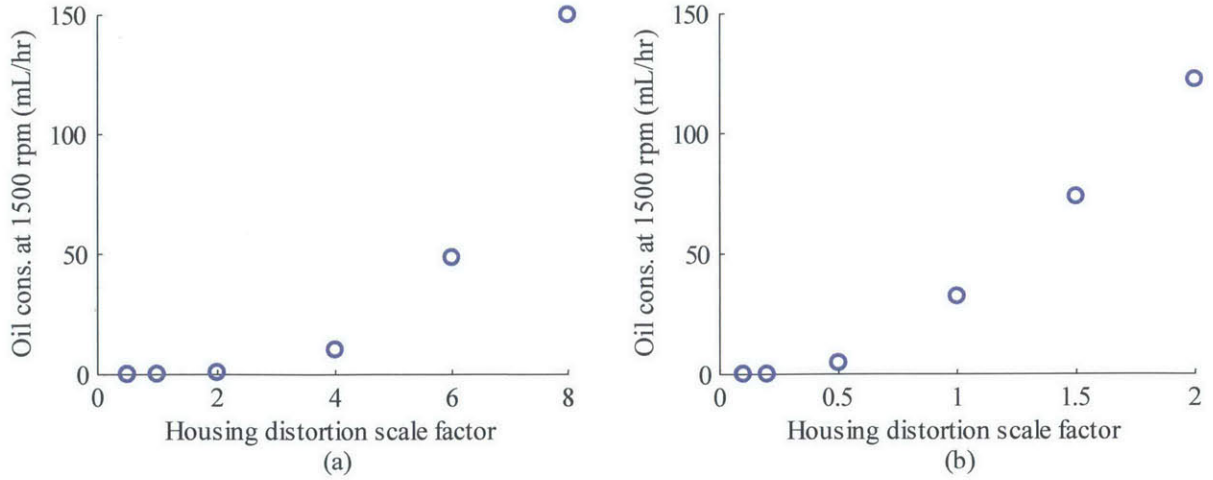

Fig. 3.49 Internal oil consumption as a function of housing distortion scaling: (a) FH mechanical distortion, (b) FH 1500 rpm distortion

3.2.5.2 Transverse Waviness

Amplitude and wavelength of transverse waviness are varied to show their effect on oil consumption, as shown in Fig. 3.50. To isolate this effect, housing is originally taken without distortion before adding transverse waviness. For the 8 mm wavelength, the oil consumption increases slowly as a function of waviness amplitude after a waviness amplitude of 1 μm, since the seal cannot conform to the housing. However, the oil consumption for larger wavelengths continues to increase with amplitude. The more the amplitude increases, the more difference there is between wavelengths for the same amplitude.

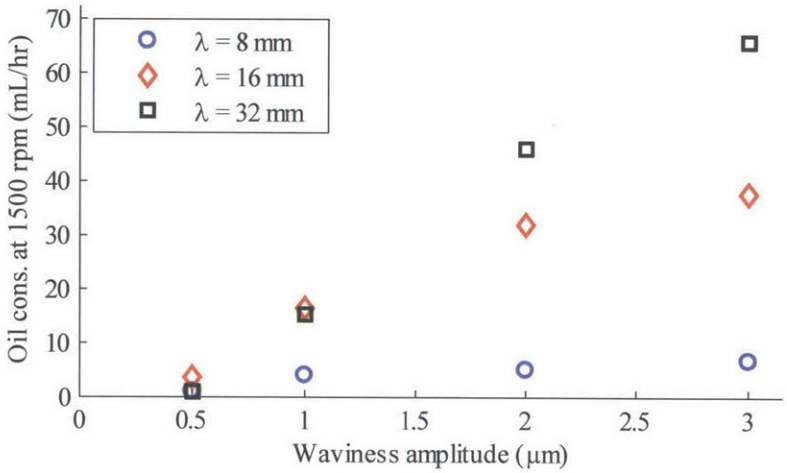

Fig. 3.50 Effect of transverse waviness amplitude and wavelength on internal oil consumption

3.2.5.3 Spring Tension and Seal Stiffness

Spring tension pushes the seal against the housing and the seal conforms more or less to the distortion as a function of its stiffness. Internal oil consumption is therefore greatly affected by spring tension. The spring constant and preload of both seals are scaled altogether to show the effect of this parameter. For the first case, FH-1500 rpm housing distortion is used and waviness is set to an amplitude of 1.1 μm and a wavelength of 8 mm. As shown in Fig. 3.51, oil consumption for the distortion only first increases for very low spring force and then decreases as expected. However, oil consumption for the waviness increases monotonically with spring tension. This can be explained by the fact that the seal do not conform at low spring tension and is mainly flat on the peaks of the waves. Therefore, this reduces the asymmetry between inward and outward motion that generates scraping. As tension increases, the seal scrapes more and

more oil in the valleys. For waviness and housing distortion combined, oil consumption is roughly an addition of the two effects, leading to a minimum value at 4 times the baseline spring forces. This minimum varies as a function of distortion and waviness, and shows the very important trend that oil consumption can increase with spring force.

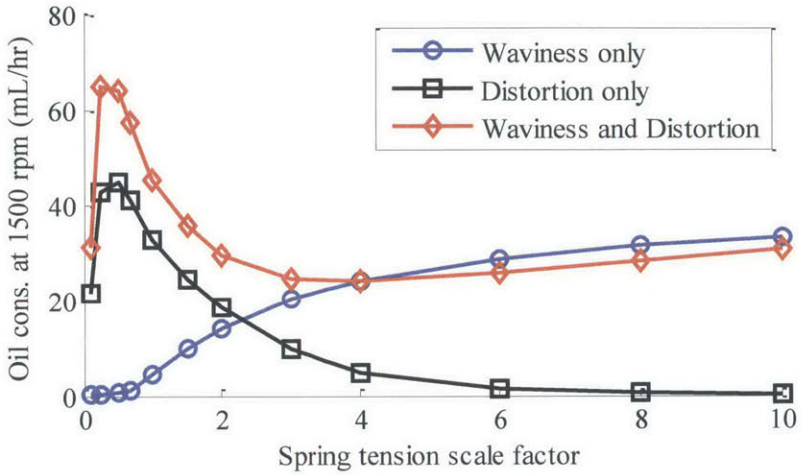

Fig. 3.51 Internal oil consumption as a function of the spring tension scale factor for front housing 1500 rpm distortion

Increasing spring tension has a cost in friction losses, as shown in Fig. 3.52. Friction power increases almost linearly with spring force scale factor. The alternative solution would be to keep the same spring force but lowering seal stiffness. This would have a similar effect on oil consumption without increasing friction. Increasing hydrodynamic pressure generation from the surface would also help reducing friction by increasing the clearance for the same tension.

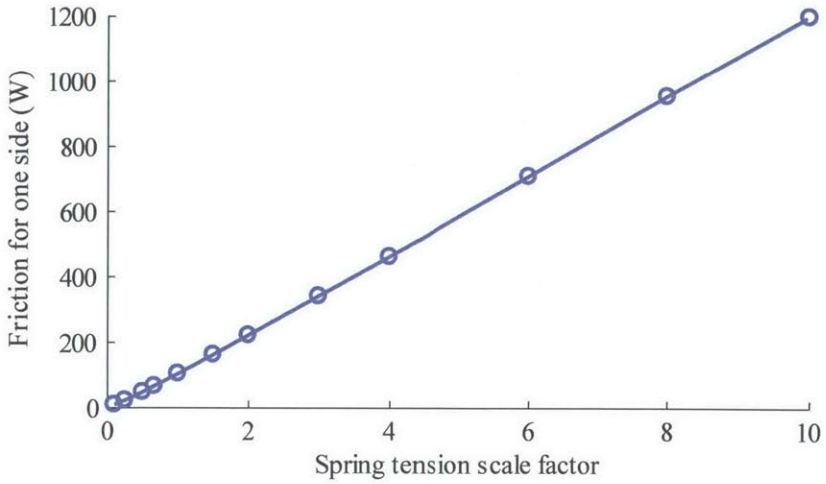

Fig. 3.52 Friction losses power for the combined housing distortion and waviness, FH-1500 rpm distortion

The same procedure is done for the RH-1500 rpm distortion, and the same waviness. As seen in Fig. 3.53, minimum oil consumption is between 1 and 2 times the baseline tension.

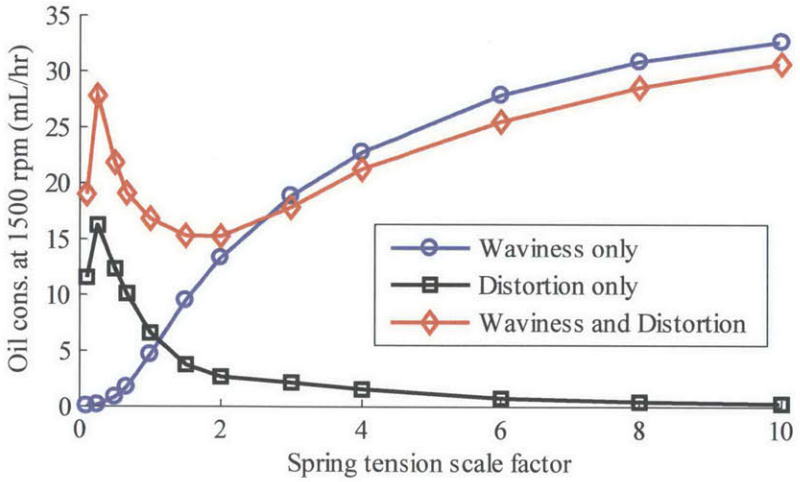

Fig. 3.53 Internal oil consumption as a function of the spring tension scale factor for rear housing 1500 rpm distortion

Seal stiffness effect is studied by scaling the second moment of inertia and the torsion constant of both seals altogether. To compare with the spring tension, internal oil consumption is plotted as a function of the seal compliance, which is defined as the inverse of stiffness. Results are shown in Fig. 3.54 for the front housing and in Fig. 3.55 for the rear housing. The effect is similar to the

spring tension effect. The main difference is that the taper pressure effect remains constant even if seal stiffness is changed. Therefore, at low compliance, or high stiffness, oil consumption increases drastically. As compliance is increased, oil consumption decreases faster than when spring tension is increased. The local minimum for combined waviness and distortion is displaced and is not as clear as for the spring tension effect.

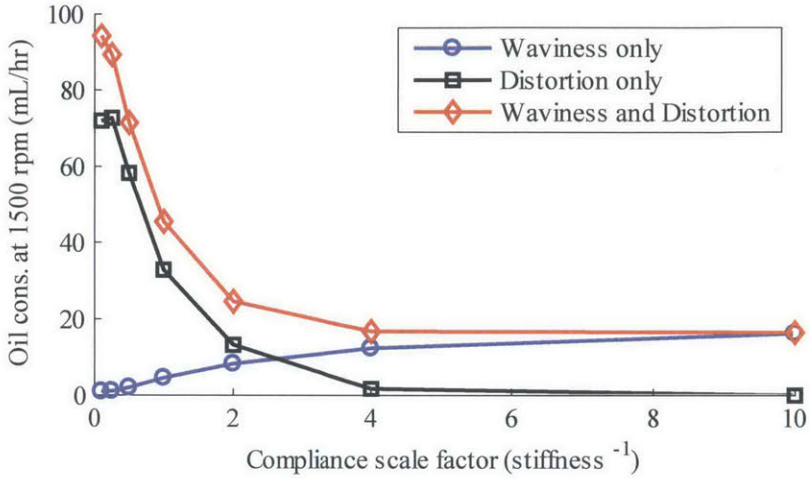

Fig. 3.54 Internal oil consumption as a function of the seal compliance scale factor for front housing 1500 rpm distortion

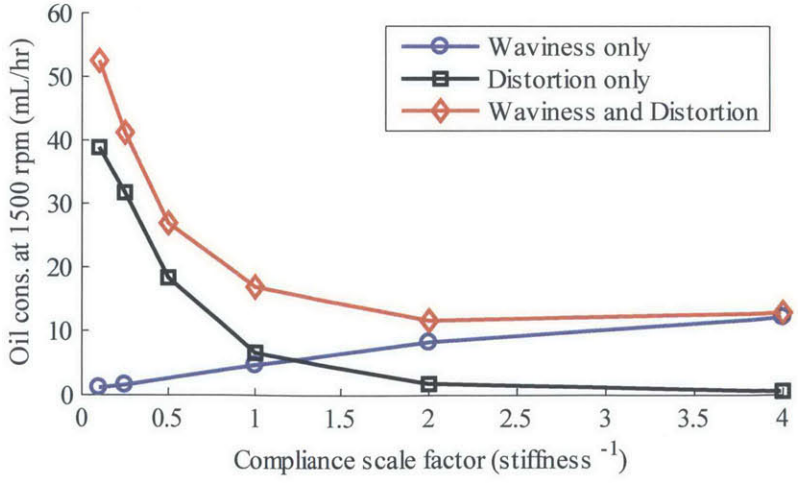

Fig. 3.55 Internal oil consumption as a function of the seal compliance scale factor for front housing 1500 rpm distortion

The outer seal spring tension is varied to estimate its effect on oil consumption, as shown in Fig. 3.56 for the intermediate front housing at 1500 rpm. The cycle model predicts that internal oil consumption decreases to a minimum when the outer seal spring tension is minimal. However, the model does not include large puddles of oil left by the bridging, where the outer seal would act as a safety feature and avoid those puddles to be pushed to the combustion chamber. The model also does not include the accumulation during inward motion that could lead to a fully-flooded condition inside the outer oil seal. In sum, a small tension on the outer oil seal is beneficial, but the minimum limit cannot be determined by the current model.

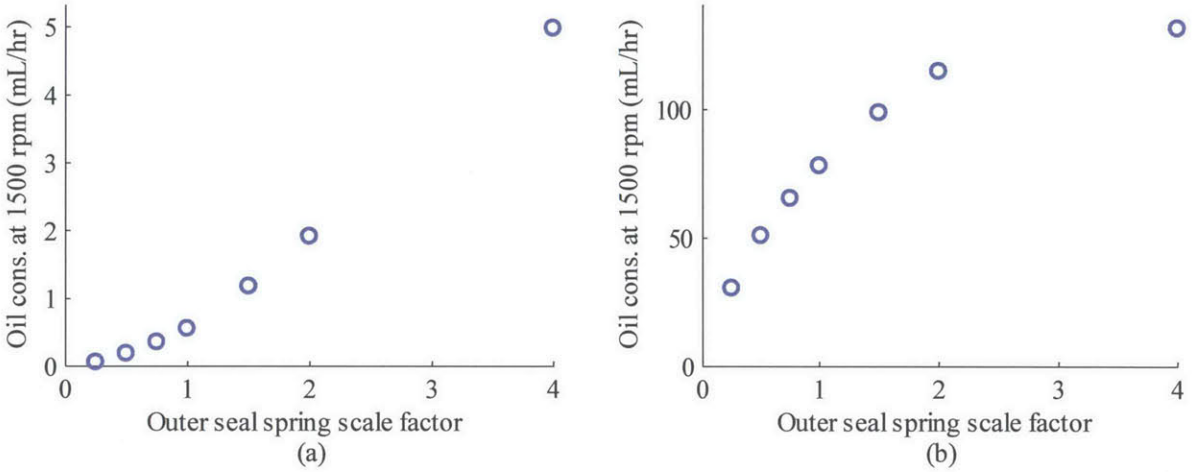

Fig. 3.56 Internal oil consumption as a function of the outer spring force scale factor for intermediate front housing at 1500 rpm with (a) mechanical and (b) thermal distortion

3.2.5.4 Taper Contribution

Pressure generated by the taper contributes in reducing oil consumption by lifting the seal during outward motion allowing oil to be returned inside the inner seal. This is especially true for a seal that is conforming to the surface. However, a non-conforming seal is supported by few contact points and the taper does not generate sufficient pressure to lift the seal. This leads to an undesirable situation where the low oil consumption cases are further reduced, but high oil consumption cases tend to remain as they are. This effect is shown in Fig. 3.57, where the oil consumption reduction by the taper pressure compared to a case without taper is plotted against oil consumption without taper. For low oil consumption, taper contribution almost reduces it to zero. However, for high oil consumption, the reduction is only about 20 %.

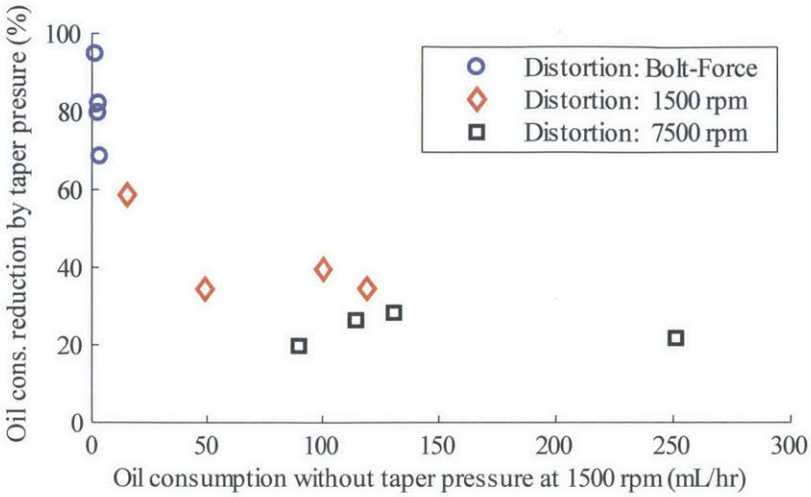

Fig. 3.57 Reduction of internal oil consumption by taper pressure compared to the internal oil consumption without taper at 1500 rpm for all housing distortions

The effect of the taper angle is studied with the intermediate front housing (IMHF) with both mechanical and 1500 rpm thermal distortions. Internal oil consumption is shown for taper angles from 0.5 to 30° in Fig. 3.58. Results above 10° might be slightly off, since the small angle approximation is used. For both distortions, oil consumption decreases significantly for small taper angles. The curve is sharper for the larger distortion. The taper angle should therefore be as small as it is possible to manufacture and maintain an acceptable contact width even with wear. The tilt angle is also a limit. The static tilt is about 0.02° and tilt can reach about 0.05° for large distortion due to the coupling with bending.

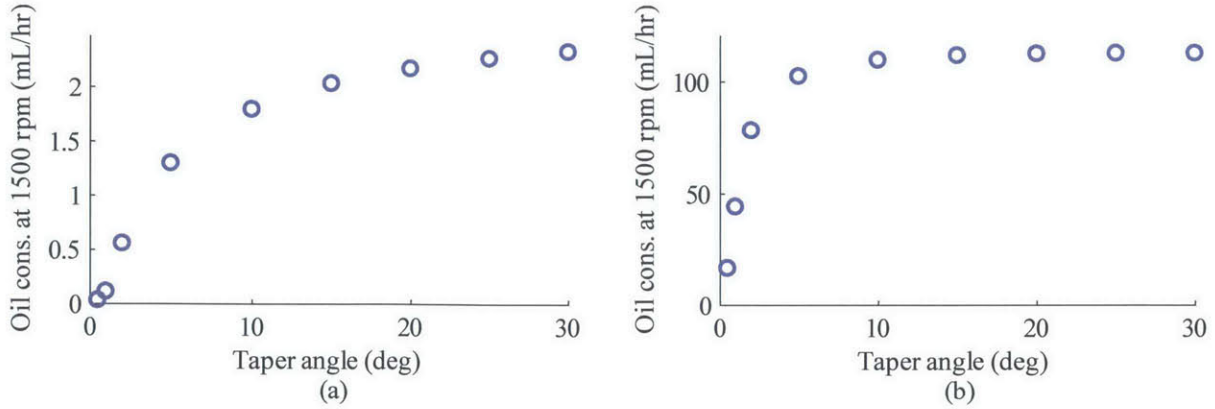

Fig. 3.58 Internal oil consumption against taper angle for the intermediate front housing: (a) mechanical distortion, (b) 1500 rpm thermal distortion

3.2.5.5 Speed

Influence of speed is isolated by calculating internal oil consumption of a given housing distortion at different speeds. The intermediate front housing distortion is used, both mechanical and thermal at 7500 rpm. The results, as shown in Fig. 3.59, are surprising. For the mechanical distortion, oil consumption decreases as the engine speed is increased, meaning that the oil scraped out per revolution decreases faster than speed increases. This can be explained by the taper pressure that gets larger as speed increases, allowing oil to pass under the seals during outward motion. At high distortion, oil consumption first increases at low speed, but then stabilizes at higher speed.

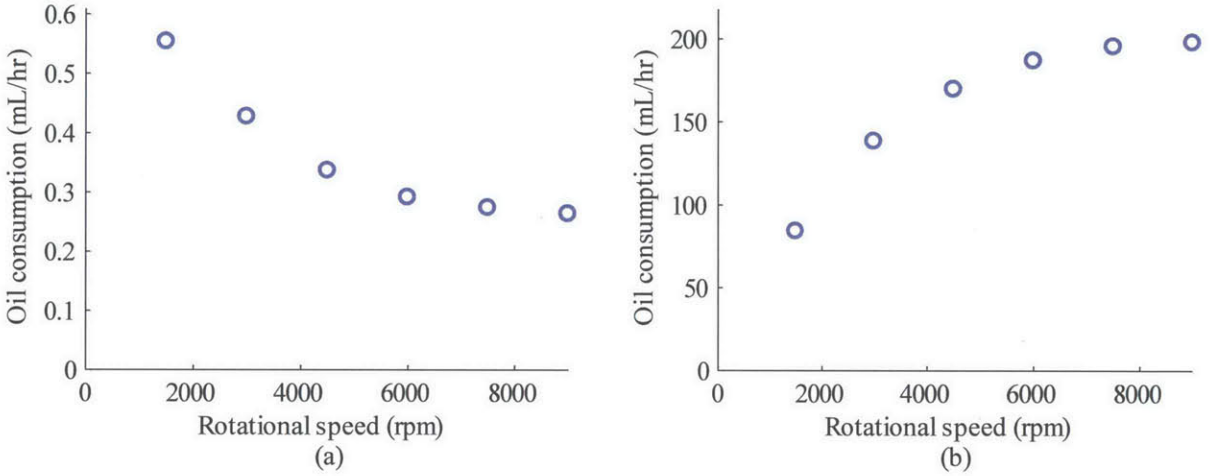

Fig. 3.59 Internal oil consumption against speed for intermediate front housing with: (a) mechanical distortion, and (b) 7500 rpm thermal distortion

Friction power for both seals is shown in Fig. 3.60 for the two cases. Friction of the high distortion case is slightly higher at low speed due to greater boundary contact. As speed increases, friction of the low distortion case gets larger, due to the higher hydrodynamic friction.

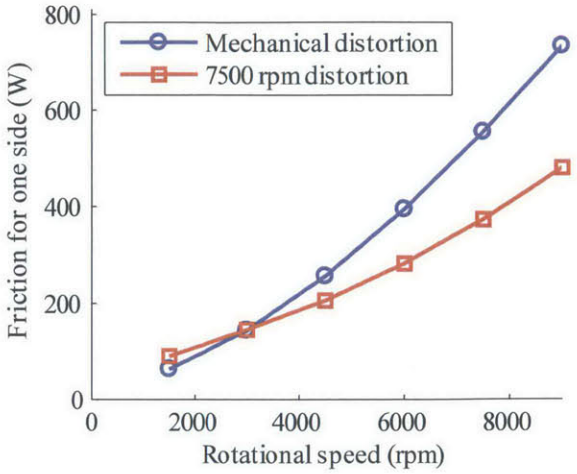

Fig. 3.60 Friction power for both seals for small and large housing distortions

3.2.5.6 Inner Seal Supply

The model assumes the inside of the inner oil seal to be always fully-flooded. However, for large distortion, it might not be the case. The effect of relaxing this boundary condition to a starved condition is shown in Fig. 3.61, using the intermediate front housing thermal distortion. Internal oil consumption is zero if there is no oil supply, as expected. Internal oil consumption increases quickly until about 2 μm oil film thickness and then stabilizes to the fully-flooded condition at about 5 μm, which changes for different distortions.

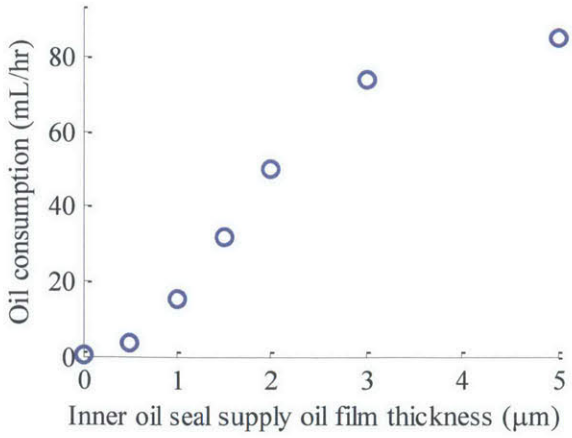

Fig. 3.61 Internal oil consumption against inner seal supply at 1500 rpm with the intermediate front housing thermal distortion

3.2.5.7 Housing Wear

To study the effect of wear on oil consumption a simple wear model is implemented. The model is first run for five rotor revolutions. At the end of each subsequent engine revolution, distortion height is reduced proportionally to asperity contact pressure with an arbitrary coefficient. The model is run for 20 cycles until the maximum wear is about 5 μm, which represents an average wear of about 0.4 μm. That level of wear is unlikely to happen, but shows the trend. Initial distortion is from both the intermediate front and front 1500 rpm thermal distortions. The model is run at 1500 rpm. Oil consumption results are shown in Fig. 3.62 against the maximum height of material removed on the housing. Oil consumption is first dropping linearly with wear and then has a hyperbolic behavior. Housing wear can therefore significantly reduce oil consumption if it reaches a certain level.

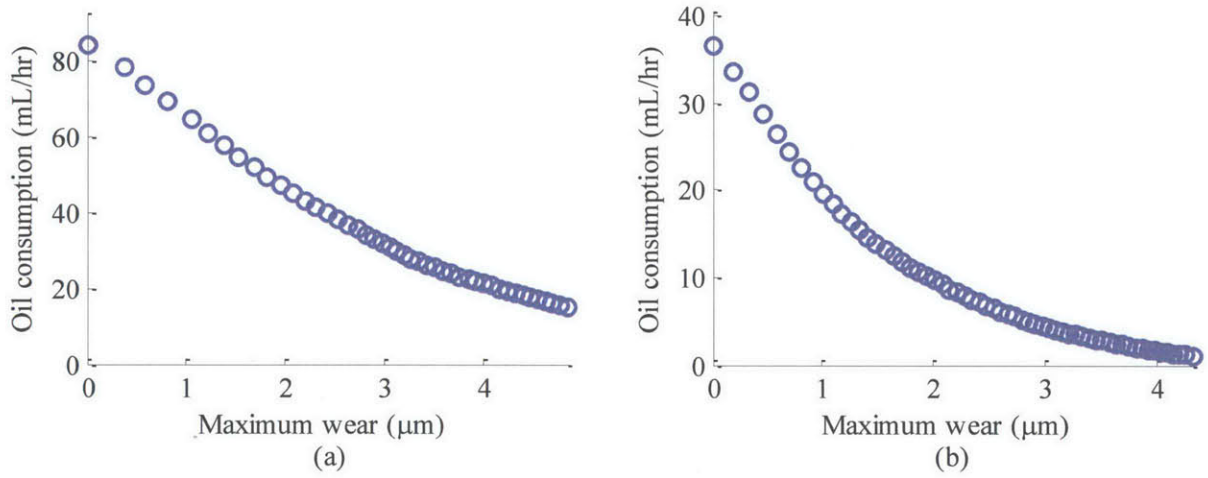

Fig. 3.62 Internal oil consumption against maximum wear at 1500 rpm for thermal distortions of (a) intermediate front housing, and (b) front housing

3.2.5.8 Rotor Land Pressure

Effect of rotor land pressure is studied by varying the amount of oil on the housing inside the inner oil seal from 0 to 33 μm. An oil film thickness of zero results in no pressure inside the rotor land. The intermediate front housing is used with both mechanical and thermal distortions. Both cases are run at low speed and high speed, 1500 and 7500 rpm respectively. Secondary motion is included in this case since it has an important effect on both the relative motion and the squeezing terms of pressure generation. The results of the four cases are shown in Fig. 3.63. At low speed, oil consumption only increases slightly due to rotor land pressure for the chosen

configuration. At high speed, the rotor land pressure increases significantly oil consumption. This is mainly caused by the inner seal lift during inward motion that leaves more oil to pass under the seal. For large oil supply, oil consumption stabilizes as the rotor land fills quickly at the beginning of inward motion.

When there are drain holes in the inner seal groove, the pressure in the rotor land is too small to create any substantial change in oil consumption in the present configuration.

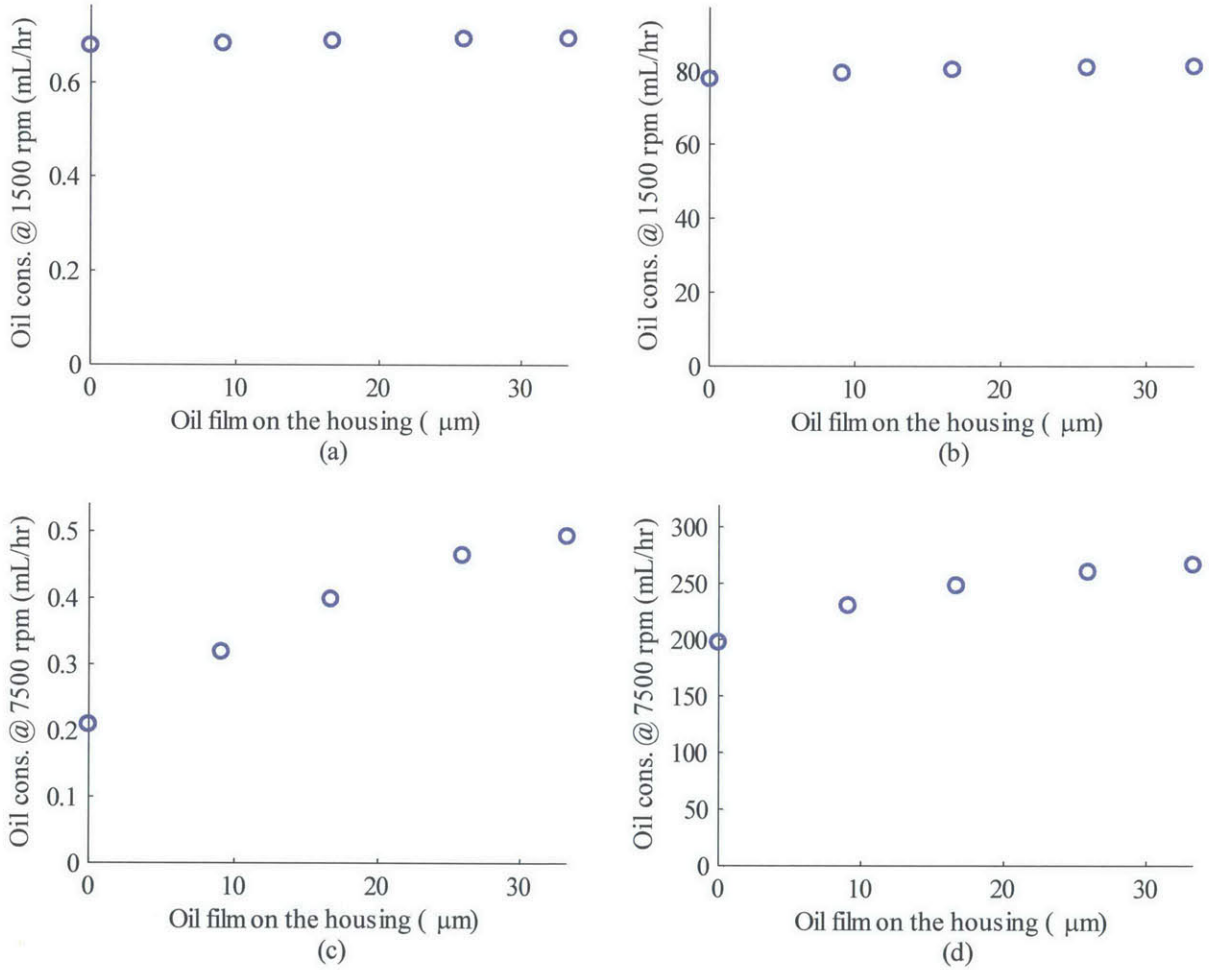

Fig. 3.63 Internal oil consumption against oil film on the housing for the intermediate front housing: (a) at 1500 rpm with mechanical distortion, (b) at 1500 rpm with thermal distortion, (c) at 7500 rpm with mechanical distortion, and (d) at 7500 rpm with thermal distortion

3.2.5.9 O-ring and Groove Friction

O-ring and groove friction forces push the seal towards the housing or reduce the spring force depending on the direction of secondary motion. This effect is studied by setting the friction coefficient of the O-ring-groove interface and the seal-groove interface to the same value. This value is then varied from 0 to 0.1. Internal oil consumption is calculated at 1500 rpm for the intermediate front housing for both mechanical and 1500 rpm thermal distortions. The results are shown in Fig. 3.64. For a well-behaved system such as the small distortion case, oil consumption increases as the friction coefficient increases. For the 7500 rpm thermal distortion, the inward scraping of the outer seal is significantly increased, but the outward scraping and thus oil consumption increases only slightly.

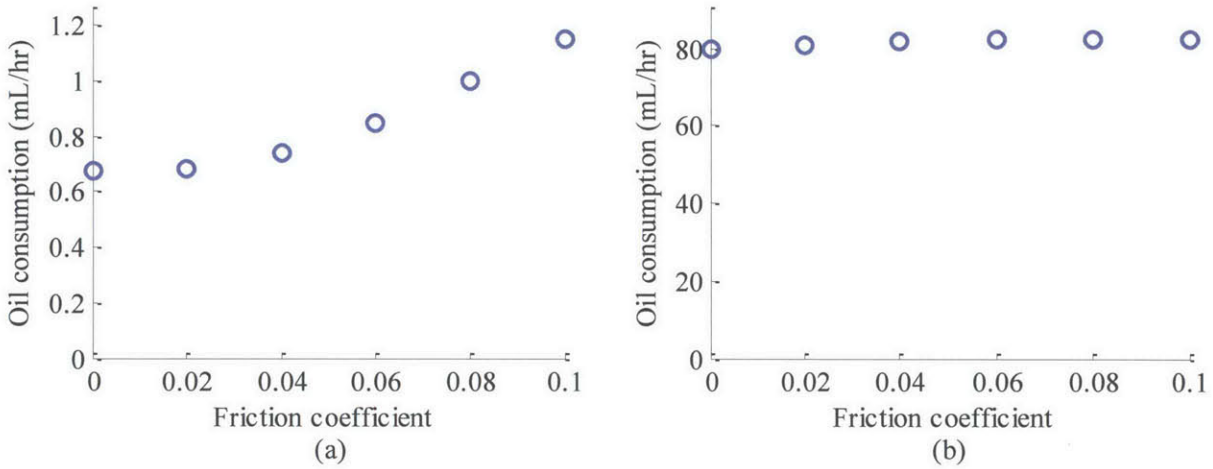

Fig. 3.64 Internal oil consumption against O-ring and groove friction coefficient at 1500 rpm for IMHF: (a) mechanical, and (b) 1500 rpm thermal distortions

3.2.5.10 Oil Viscosity

Oil viscosity effect is calculated at 1500 rpm for the intermediate front housing, both mechanical and 1500 rpm thermal distortion. Internal oil consumption trend is inversely proportional to viscosity, mainly due to increase in taper pressure as viscosity is increased. As expected, the large distortion is less sensitive to viscosity. In sum, decrease in oil viscosity due to increase in temperature can lead to significantly higher oil consumption.

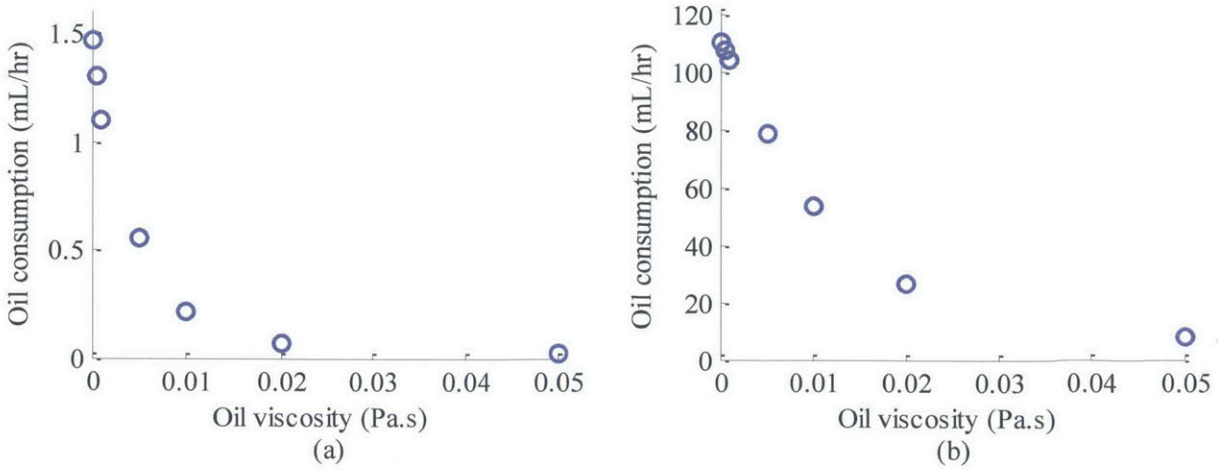

Fig. 3.65 Internal oil consumption against oil viscosity at 1500 rpm for IMHF: (a) mechanical, and (b) 1500 rpm thermal distortions

Concerning friction, the trend is following Stribeck curve behavior, as shown in Fig. 3.66. For a low viscosity, boundary contact is dominant. As viscosity increases, friction reaches a minimum and then increases again due to hydrodynamic friction.

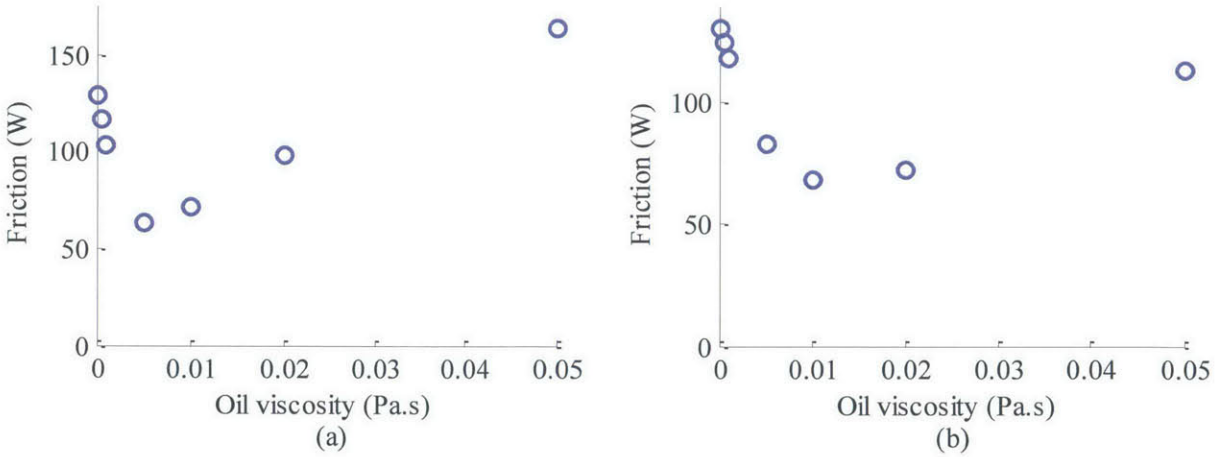

Fig. 3.66 Friction power against oil viscosity at 1500 rpm for IMHF: (a) mechanical, and (b) 1500 rpm thermal distortions

3.2.5.11 Hydrodynamic Pressure from Tilt

The cycle model is run with and without hydrodynamic pressure from the tilt to show its effect on oil consumption. Both the front and intermediate front housing are used, at low and high speed. For the mechanical distortion, oil consumption increases from almost zero to between 10

and 40 mL/hr, as shown in Fig. 3.67a. For thermal distortion, oil consumption is increased of 75 % in average by the hydrodynamic pressure from tilt, as shown in Fig. 3.67b.

This difference in oil consumption is mainly caused by the static negative tilt of the seals. This tilt is created because the spring force is not aligned with the seal-housing contact and generates a torque. Since this tilt is static, the contact part of the seal is probably worn quickly and the pressure generated greatly reduced. Oil consumption given in Fig. 3.67 neglects this wear and is therefore a pessimistic approximation.

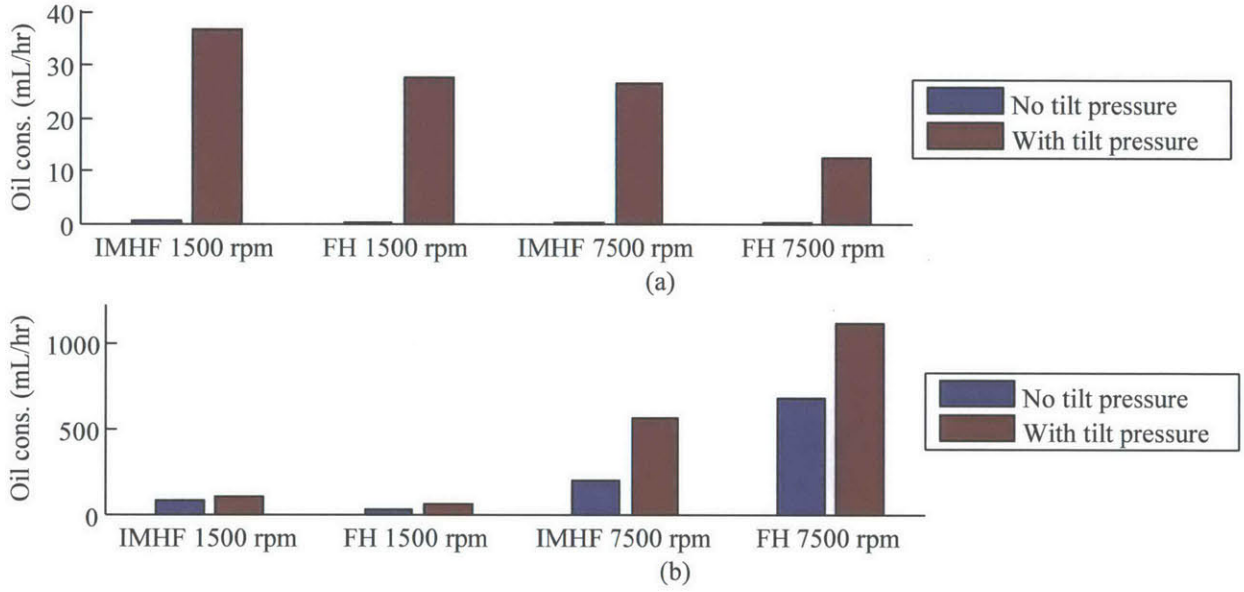

Fig. 3.67 Internal oil consumption with and without tilt pressure for front and intermediate front housing, 1500 and 7500 rpm with (a) mechanical and (b) thermal distortions

3.2.5.12 Roughness

Roughness effect is studied by calculating oil consumption at 1500 rpm for different standard deviations of plateau roughness. As an order of magnitude, the product $P_h \sigma_p^{K_h}$ is kept constant, meaning that the hydrodynamic pressure is the same for a given clearance for any roughness. Taper pressure is also neglected to isolate the roughness effect only. Results are shown in Fig. 3.68 for the front housing mechanical distortion and rear housing 1500 rpm thermal distortion. For small distortion, roughness has an important impact on oil consumption (Fig. 3.68a). Oil consumption first decreases slightly with roughness and then increases significantly. For larger

distortion, roughness influence on oil consumption is relatively small, until roughness reaches a high level (Fig. 3.68a). A small decrease is observed since as roughness increases, more oil can pass under the seal before the seal reaches its most outside position and then oil and accumulation at the taper-housing interface is reduced. For large roughness oil consumption increases rapidly as a function of roughness.

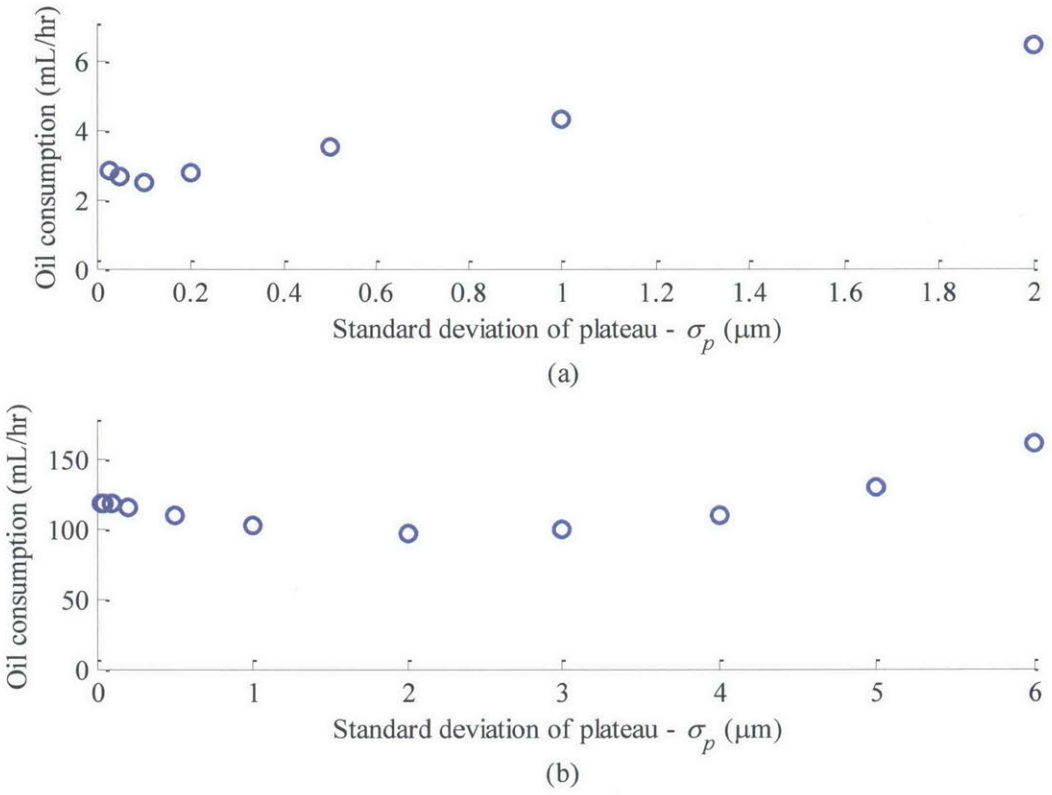

Fig. 3.68 Internal oil consumption at 1500 rpm against roughness for: (a) rear housing mechanical distortion, and (b) front housing 1500 rpm thermal distortion

3.2.5.13 Surface Anisotropy

Surface orientation is studied by varying the anisotropy coefficient (P_γ) in the hydrodynamic correlation from 0 to twice is actual value and the orientation from 0 to 360°. Oil consumption is calculated at 7500 rpm for the intermediate housing, both mechanical and 7500 rpm thermal distortions. Results are shown in Fig. 3.69. For small distortion, surface anisotropy can increase or decrease oil consumption depending on orientation and becomes important at high value of P_γ. For large distortion, the effect remains small compared to the housing distortion effect.

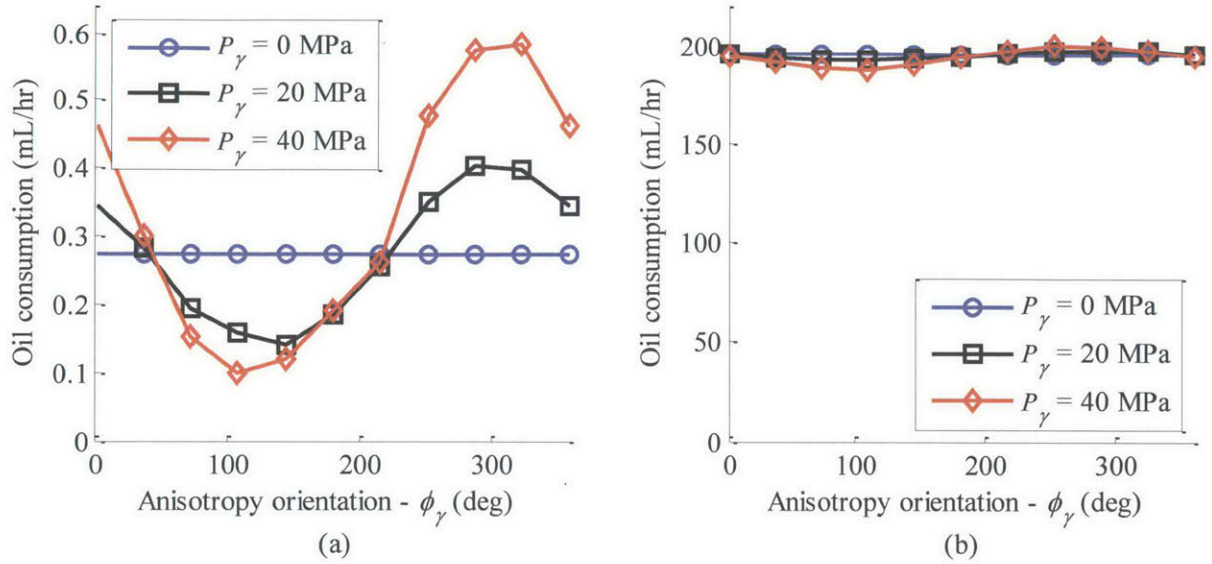

Fig. 3.69 Internal oil consumption as a function of surface anisotropy coefficient and orientation at 7500 rpm for (a) mechanical, and (b) thermal distortion

3.2.5.14 Seal Orientation

Effect of seal orientation is studied by varying the exponent K_β in the hydrodynamic correlation shown in equation (3.5). This constant determines how fast the pressure drops as a function of the seal angle. This effect is studied at 7500 rpm, with the intermediate front housing, both mechanical and 7500 rpm thermal distortions. The results are shown in Fig. 3.70. At low distortion, oil consumption is significantly reduced as K_β is increased. This could be explained by a smaller film at the outer portion of the housing where the velocity of the seals is mainly circumferential. At high distortion, oil consumption is roughly independent of the exponent constant.

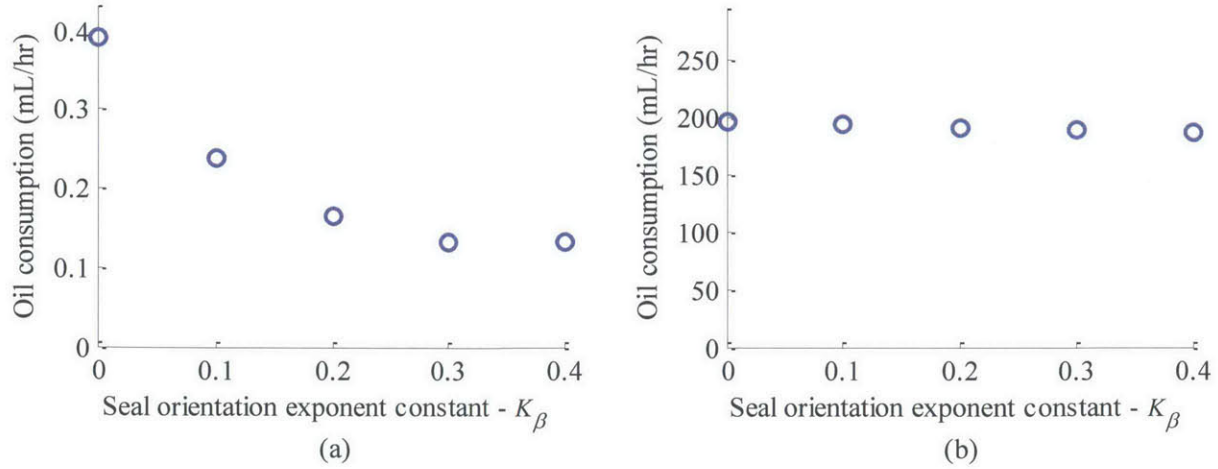

Fig. 3.70 Internal oil consumption against scaling of seal orientation effect at 7500 rpm for the intermediate front housing: (a) mechanical, and (b) 7500 rpm thermal distortions

3.2.5.15 Oil Fraction Flowing on the Taper after Separation

When the seal motion reverses to inward motion, oil accumulated between the taper and the housing separates. The cycle model assumes a fixed fraction of this oil to flow to the taper and the remaining stays on the housing. Oil consumption is calculated by adding the oil flowing to the outer seal taper and the oil pushed outside the area covered by the outer seal. To estimate the impact of this approximation, the fraction of oil flowing to the seal taper is varied from 0.1 to 0.9. The results are shown in Fig. 3.71 for the intermediate front housing, both mechanical and 1500 rpm thermal distortions. In both cases, oil consumption is relatively constant since the increase in outward scraping is balanced by almost the same decrease in oil pushed out of the outer seal area. The arbitrary fraction has therefore a small impact on the final results, and a value of 0.5 is selected to average the error.

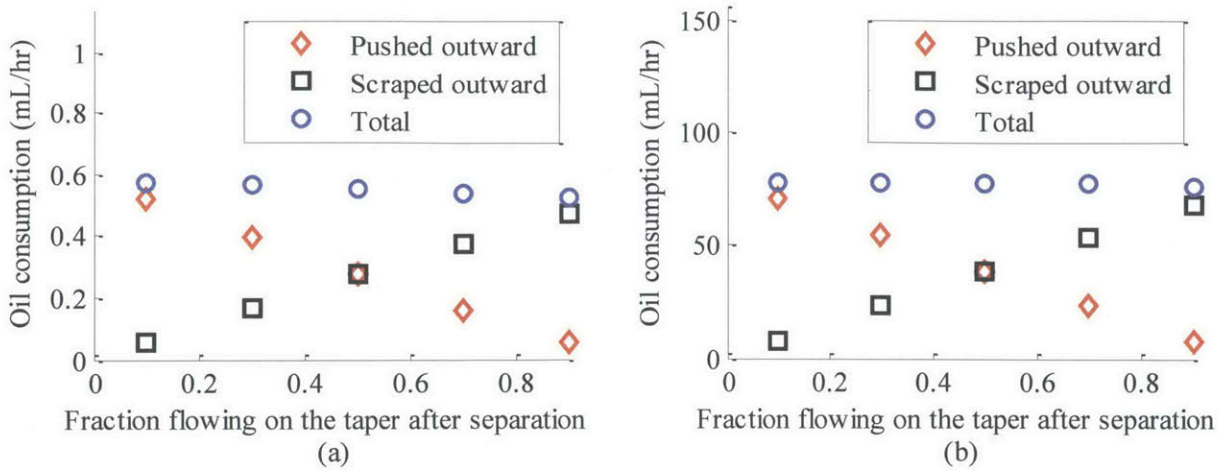

Fig. 3.71 Internal oil consumption against arbitrary fraction of oil flowing to the taper after separation, at 1500 rpm for intermediate front housing: (a) mechanical, and (b) 1500 rpm thermal distortions

3.2.6 Conclusions

This section presents the results of the cycle model for the lubrication and oil transport of the oil seals. Order of magnitude of the different mechanisms is first detailed with a low speed small distortion case and a high speed high distortion case. Scraping distribution on the different housing distortions is shown. Scraping is distributed for mechanical distortions. For thermal distortions, scraping mainly occurs near the exhaust port for the front and rear housings and near the intake port for the intermediate housings. The important oil consumption potential of housing transverse waviness is explained. Finally a parametric study leads to the following conclusions:

1. Housing distortion is the principal source of oil consumption. Both amplitude and shape have an important impact on oil consumption.
2. Concerning transverse waviness, oil consumption increases with an increase in both amplitude and wavelength.
3. For housing distortion only, oil consumption decreases as spring force is increased. For transverse waviness only, oil consumption increases as spring force is increased. When waviness and housing distortion are combined, a minimum value of oil consumption is observed when varying spring force. Reducing stiffness is a better way of reducing oil consumption than increasing spring tension as it does not generate more friction and the beneficial contribution of the taper pressure remains important. Reducing outer seal

spring force only seems to reduce oil consumption, but the optimal value cannot be predicted by the current model.

4. The taper of the seal reduces significantly oil consumption, especially when the seal can conform to the housing.
5. Effect of speed on oil consumption on a time basis (e.g. mL/hr) is smaller than expected due to the taper pressure.
6. Relaxing the inner seal oil supply boundary condition to starve reduces significantly oil consumption.
7. Large housing wear can significantly reduce oil consumption.
8. Rotor land pressure increases oil consumption by lifting the seal during inward motion.
9. O-ring and groove friction increases oil consumption for a good seal-housing conformability.
10. As oil viscosity decreases with temperature, oil consumption increases.
11. Hydrodynamic pressure from tilt increases oil consumption due to the negative static tilt. This effect would be reduced by wear of the seal.
12. Roughness mainly increases oil consumption for conforming seals, but its influence is much smaller than the housing distortion effect for non-conforming seals.
13. Surface anisotropy can increase or decrease significantly oil consumption for conforming seals depending on orientation. However, surface anisotropy influence is small on oil consumption for non-conforming seals.
14. Seal orientation effect reduces slightly oil consumption for conforming seals.
15. Oil fraction flowing to the taper does not influence significantly oil consumption in the presented model.

In sum, the main cause of internal oil consumption is the lack of conformability of the seals to the distorted housing. All the other effects only become important when the oil seals conform to the housing.

3.3 Comparison with Experiments

This section first discusses the current 2D LIF experimental validation. Then a discussion is presented about the comparison between the cycle model and oil consumption measurements.

3.3.1 Experiments with 2D-LIF Engine

The 2D-LIF engine is a powerful tool that allows looking directly to oil transport. Experimental observation of the oil transport mechanisms guided the development of the cycle model. First, the rotor land accumulation and release process is observed. This is an important mechanism since it is the supply for the complete seal pack. Then, the scraping mechanism of the inner seal is observed. It shows that in steady state, oil transport is a steady process with a similar scraping every revolution. The 2D-LIF experiments also show the 4^{th} land fills quickly and remains almost full in steady state. The outer seal scraping is observed for high speed condition. Finally, the 3^{rd} land, between outer and cut-off seal, is mainly dry and no clear mechanism is observed that can bring the oil towards the center.

The next subsection compared the predicted rotor land accumulation to the observed accumulation with the 2D LIF engine. The predicted scraping of the seals is not compared to experiments as the distortion of the sapphire window is smaller than the actual housing distortion.

3.3.1.1 Rotor Land

Accumulation in the rotor land is highly dependent on the oil film thickness on the housing. The model is run with different oil thickness and is compared to experiments. At 3000 rpm, the best fit is 47 μm oil left on the housing for a 100 μm rotor land clearance. The predicted accumulation for this supply is shown by a red line in Fig. 3.72, superposed to a 2D-LIF picture. On the picture, the accumulation can be defined as the zone where the shade is constant. The shape of the accumulation is very similar between model and experiments. Since the oil film thickness is about half the rotor land clearance, it means the rotor land is generally full and the inner oil seal fully-flooded. At 1000 rpm the accumulation shape is not as consistent and it is difficult to compare with the simple accumulation model.

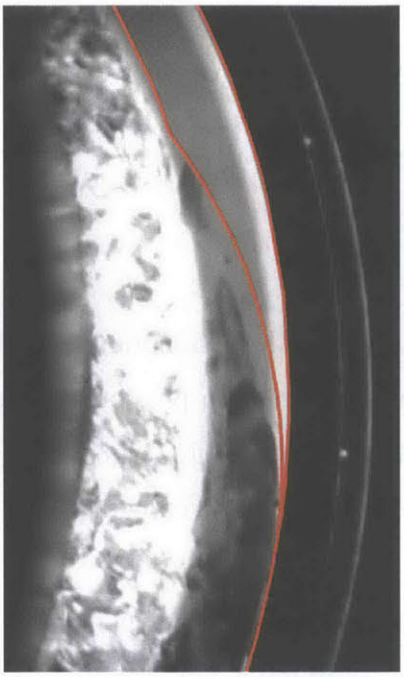

Fig. 3.72 Rotor land accumulation at 3000 rpm, 9 CA, from the 2D-LIF engine compared to the predicted accumulation (red line) for an oil film thickness on the housing of 47 μm

3.3.2 Oil Consumption Measurements

The model is built on robust physics. This means that the predicted behavior concerning oil transport due to distortion should be representative. Nonetheless, it is still interesting to compare to oil consumption measurements. However, oil consumption is very sensitive to input parameters and a perfect fit is not to be expected.

The cycle model is used to predict the total internal oil consumption of the engine at 2000, 3000, and 4500 rpm for both mechanical housing distortion and thermal housing distortion at 1500 rpm. Results from the model are compared to experiments in Table 3.6. Speed effect is not captured, since 1500 rpm housing distortion is used for all cases. The measured oil consumption is between the mechanical and thermal distortions values, which confirms that the predicted oil consumption is on the good order of magnitude. The difference between the thermal distortion oil consumption and the measured oil consumption can be explained by many factors:

(a) Oil consumption is very sensitive to distortion amplitude. As shown in Fig. 3.73, if the housing distortion is half the full load distortion, predicted oil consumption drops to about 50 mL/hr.

(b) Shape of housing distortion is also very important, as shown in section 3.2.5.1.

(c) Wear reduces oil consumption, as shown in section 3.2.5.7, and is not considered here.

(d) Inner oil seal is assumed to be always fully flooded when moving inward. However, this might not be the case for large distortion. This effect can also reduce oil consumption, as shown in section 3.2.5.6.

The results first show that the predicted oil consumption is on the right order of magnitude. The results also show that accurate oil consumption predictions need accurate data, particularly for housing distortion. More importantly, the results with only mechanical distortion show that internal oil consumption can be practically removed with proper housing distortion.

Table 3.6 Relative oil consumption comparison between model and experiments

Speed (rpm)	Relative internal oil consumption		
	Cycle model Mechanical Distortion	Measured (Internal = Total - Metering) Load = 75 to 80 %	Cycle model Thermal distortion at 1500 rpm
2000	0.09	0.54	8.04
3000	0.08	1.00	9.18
4500	0.06	1.94	9.29

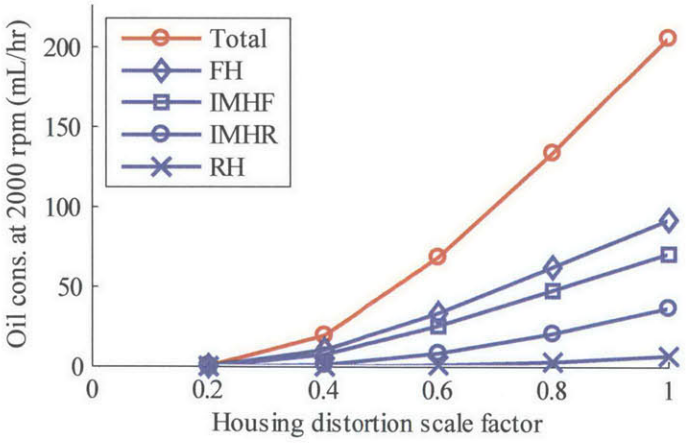

Fig. 3.73 Predicted oil consumption for the complete engine at 2000 rpm as a function of the scale factor applied on 1500 rpm thermal housing distortion

3.3.3 Conclusion

This section compares the cycle model results to measurements. The 2D-LIF engine is a powerful tool for observing oil transport, and has been used for developing the model. The predicted rotor land accumulation pattern show good agreement with experiments, provided that the supply is known. Oil consumption predicted from the model is on the good order of magnitude, but seems to be higher than measured due to pessimistic approximation and possibly housing distortion used as an input.

3.4 Oil Seal Model Summary and Conclusions

A cycle model is developed to estimate internal oil consumption in rotary engines. The cycle model tracks the oil during few engine revolutions in the rotor land, on the housing, and between both seal taper and the housing. The location of the seals in their groove is first computed. The hydrodynamic and asperity contact pressure is then solved simultaneously with the seal deformation to get the seal-housing clearance distribution. Oil transport is solved based on this clearance and the supply inside the inner oil seal. Oil consumption is calculated based on the outward scraping of the outer seal and the oil pushed outside of the outer seal reach.

Results of the cycle model show that the main contribution to oil consumption is the non-conformability of the seal to the distorted housing. Outward scraping is relatively distributed on the housings with mechanical distortion. However, outward scraping for the housing with thermal distortion is concentrated. For the front and rear housings, scraping is concentrated before the exhaust port, while for the two intermediate housings, scraping is concentrated near the intake port. Housing waviness, is also shown to have an important oil consumption potential, and shows that oil consumption can increase with increasing spring tension for certain housing shape. A parametric study supports that oil consumption is created by housing distortion and waviness and that reducing seal stiffness is a good solution to reduce oil consumption. Interface parameters such as roughness, surface orientation and seal orientation also play a role in oil transport but in an order of magnitude smaller than distortion.

Comparison with experiments confirms the predicted rotor land accumulation. The oil consumption predicted by the cycle model is on the good order of magnitude considering that oil consumption is very sensitive to the shape and amplitude of housing distortion.

Chapter 4

Two-Piece Apex Seal Model

Similarly to modeling piston ring dynamics, modeling apex seal dynamics is challenging as the apex seal is free to move laterally in its groove and contacts are highly stiff. Moreover, the straight apex seal (AS) does not have any rotational stiffness compared to curved piston rings that resist uniform tilt. Transitions from one flank of the groove to the other are fast compared to rotor revolution and a time-implicit solver is required.

This chapter first describes how the model is formulated to address these challenges. Predicted performances of the apex seal (AS) are then shown, followed by a comparison with experiments.

4.1 Objectives

The objective of the AS model is to predict AS sealing performance based on engine and component geometry and operating conditions. In particular, the model aims at predicting trends in gas leakage, wear and friction based on a detailed modeling of the seal dynamics and deformation as well as accurate description of the interfaces. Although predicting the correct absolute value of gas leakage, wear and friction is the ultimate goal of such a model, predicting correct trends and their dependency on key parameters is usually enough for a designer to decide how to modify the engine to reach the desired objective. From piston ring modeling experience, accurately predicting gas flow seems feasible so it is the objective of the presented model. On the other hand, predicting wear is difficult and the AS model objective is limited to calculating the distribution of a wear indicator based on asperity contact pressure. The capacity of predicting friction lies somewhere between gas flow and wear predictions. Therefore, the objective for this model is to estimate friction based on realistic friction coefficients. In brief, the objective of the apex seal model is to reach the same level of details in performance predictions as state-of-the art piston models, which includes:

- Calculate dominant forces on the AS and the resulting AS dynamics.
- Predict gas leakage.
- Estimate wear from the contact pressure distribution.
- Estimate friction losses.

4.2 Model Formulation

General inputs and outputs of the two-piece AS model are summarized in Fig. 4.1. The inputs describe engine operating conditions as well as the geometry of the AS, the AS groove, the rotor, and the rotor housing. From those inputs, the model calculates the position of the seal for each crank angle step and returns sealing performances.

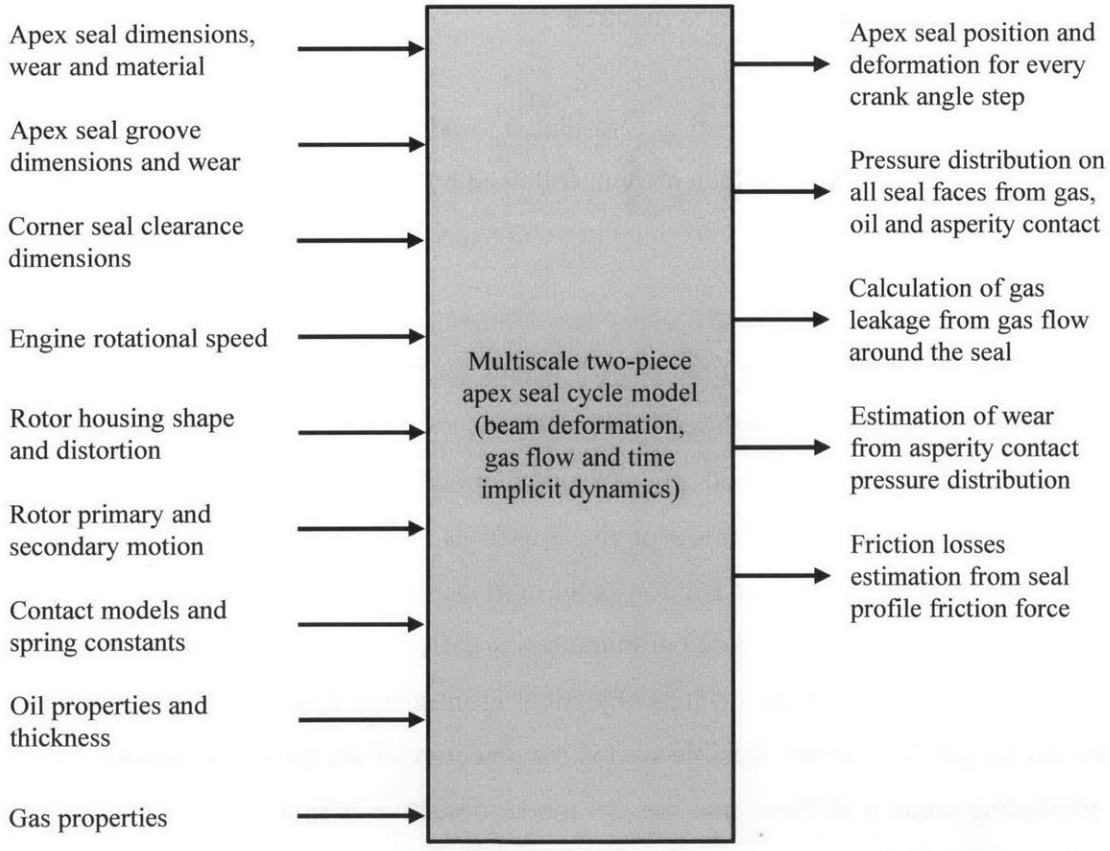

Fig. 4.1 Inputs and outputs of the two-piece apex seal model

The model first discretizes the apex seal in the desired number of beam elements. Each beam elements are subdivided in a number of cross-sections. A reduced number of AS cross-sections

are shown in Fig. 4.2(a). For each crank angle step, the model calculates the position of each seal cross-section according to forces acting on the seal, gas flow, seal stiffness, and seal mass. Displacements of the cross-section are illustrated in Fig. 4.2. Displacements of a given cross-section relative to the reference position are defined in Fig. 4.3: x_g is the lateral displacement, y_g the radial displacement, and α_g the cross-section tilt. From the cross-section displacements all the dominant forces on the seal are calculated (Fig. 4.4). The model then iterates to find the position and deformation of the seal that minimizes energy. From the converged seal position, leakage, wear and friction indicators are calculated.

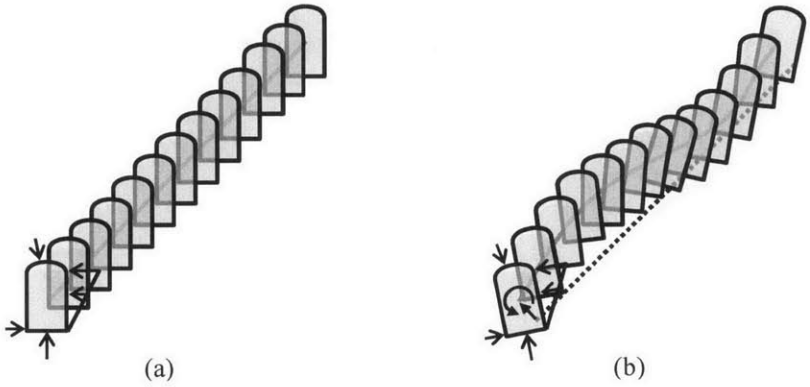

Fig. 4.2 (a) AS discretization and (b) displacement of the cross-sections under applied forces

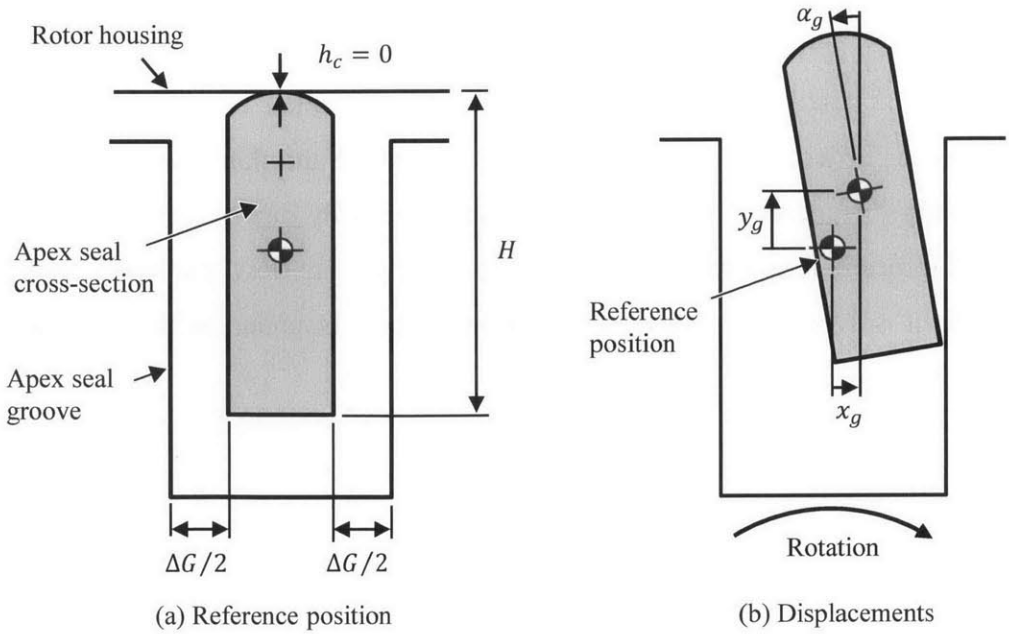

Fig. 4.3 (a) Apex seal reference position at 0 CA with no distortion and no wear (b) displacements of the cross-section compared to its reference position

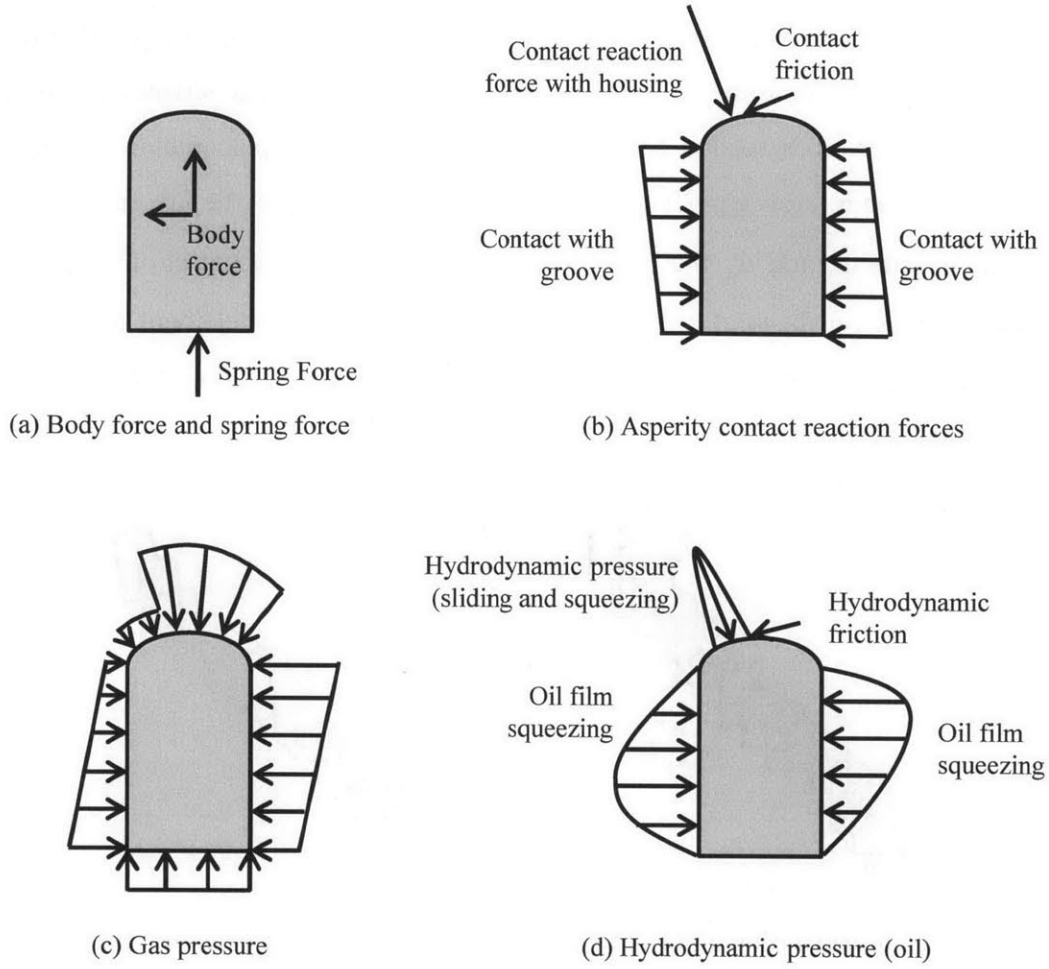

(a) Body force and spring force

(b) Asperity contact reaction forces

(c) Gas pressure

(d) Hydrodynamic pressure (oil)

Fig. 4.4 Dominant forces on the apex seal

The next subsection details the approximations made in the model. Then, the method to calculate the different forces is described. Forces on the sliding surface and flanks are described separately as their geometry differs and the profile has a sliding velocity due to the rotor movement. The description of forces is followed by the method to calculate gas flow, the beam model used, and the time-implicit solver. The model formulation section is ended with a validation of the approximations using sample model results.

4.2.1 Approximations

The first approximation is that all displacements are small. This approximation is justified because seal-groove and seal-housing clearances are small compared to seal dimensions. The maximum lateral displacement ($\Delta G/2$) is 1 % of seal height (H) and the maximum tilt angle

(α_g) is about 2° (see Fig. 4.3 for definition of variables). This approximation allows decoupling the effects of translations and rotation of the seal when calculating clearances.

The second approximation is that the seal cross-section is taken as rigid. Local deformation of the section (δ in Fig. 4.5) is assumed to be small compared to the deformation of the seal as a beam in the lateral direction. This approximation is validated in section 4.2.15 with the maximum value of contact pressure calculated in the model.

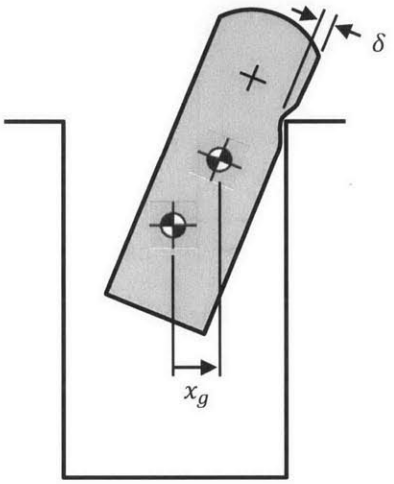

Fig. 4.5 Small deflection of the section (total deflection includes groove flank deformation)

The third approximation is that the gas flow can be described as locally fully-developed for calculating the pressure exerted on the seal. The criterion for neglecting inertia is that the pressure difference to push the flow through the clearance assuming a fully developed must be much larger than the dynamic pressure:

$$\frac{\Delta P_{visc}}{\frac{1}{2}\rho U^2} \gg 1 \tag{4.1}$$

in which ρ is the gas density, U is the average flow velocity across the clearance (Fig. 4.6), and ΔP_{visc} is the pressure difference obtained from a fully-developed pressure-driven flow, for which the volume flow rate per unit length (q_s) is given by a Poiseuille flow between two flat plates:

$$q_s = \frac{h^3}{12\mu_g}\frac{dP}{dx} \sim \frac{(\Delta G)^3}{12\mu_g}\frac{\Delta P_{visc}}{H} \tag{4.2}$$

in which ΔG is the total seal lateral clearance, and μ_g is the gas viscosity.

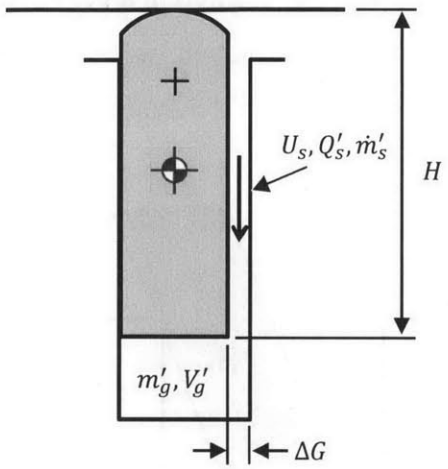

Fig. 4.6 Flow along the groove for fully-developed flow criterion

Replacing flow rate by the average velocity times the clearance ($q_s \sim U\Delta G$), the scale for the pressure difference is obtained:

$$\Delta P_{visc} \sim \frac{12\mu_g UH}{(\Delta G)^2} \tag{4.3}$$

The criterion for neglecting inertia becomes

$$\frac{\Delta P_{visc}}{\frac{1}{2}\rho U^2} \sim \frac{24\mu_g H}{(\rho U\Delta G)\Delta G} \sim \frac{24\mu_g H}{\dot{m}_s'\Delta G} \tag{4.4}$$

in which $\dot{m}_s$ is the mass flow rate per unit length through the clearance ($\dot{m}_s \sim \rho U\Delta G$). The mass flow rate through the clearance can be obtained by assuming the pressure in the groove follows the combustion chamber pressure. Thus the mass flow rate entering the groove is about the same as the change in the mass of gas in the groove:

$$\dot{m}_s' \sim \frac{dm_g'}{dt} \sim V_g' \frac{d\rho}{dt} \sim \frac{V_g'}{RT_g} \frac{dP}{dt} \tag{4.5}$$

in which m_g' is the mass of gas in the groove per unit length, V_g' is the groove volume per unit length, R is the gas constant, T_g is the groove temperature, and the ideal gas law has been used to replace the variation in density by a variation in pressure that can be approximated from the experimental pressure trace. Replacing the mass flow rate in eq. (4.4), the criterion for neglecting inertia becomes:

$$\frac{\Delta P_{visc}}{\frac{1}{2}\rho U^2} \sim \frac{24\mu_g RT_g}{V_g'} \left(\frac{H}{\Delta G}\right) \frac{dP}{dt} \gg 1 \tag{4.6}$$

The final criterion value is on the order of 10 for representative values. The approximation is therefore expected to hold for most cases as the criterion was evaluated for the largest clearance. The gas flow model is therefore satisfactory to calculate the gas pressure distribution on the seal to calculate the net gas forces and moment. However, the flow rate is limited to an isentropic flow through an orifice for proper accounting of the mass flow rate through the gap when calculating leakage to avoid an unphysical situation.

The fourth approximation is that gas temperature is the same as groove temperature. This is justified by the fact that heat transfer with the walls is much larger than the heat capacity of the fluid flowing through the clearance because of the small clearance. This approximation is validated in section 4.2.15 with the maximum clearance and flow rate calculated from the model.

The fifth approximation is to consider all the forces and gas flow to be 1D. This means that the flow of oil and gas along the seal is considered to be small compared to the flow of oil and gas in the lateral and radial directions ($\dot{m}_{axial} \ll \dot{m}_{radial}$ in Fig. 4.7a for the seal profile and $\dot{m}_{axial} \ll \dot{m}_{radial}$ in Fig. 4.7b for the seal flanks). This is justified by the ratio of 15 between the length and height of the seal and that the boundary conditions vary smoothly along the seal. This approximation fails at the two ends of the seal and at the two changes in seal height. This effect is neglected as these regions are small compared to the entire length of the seal.

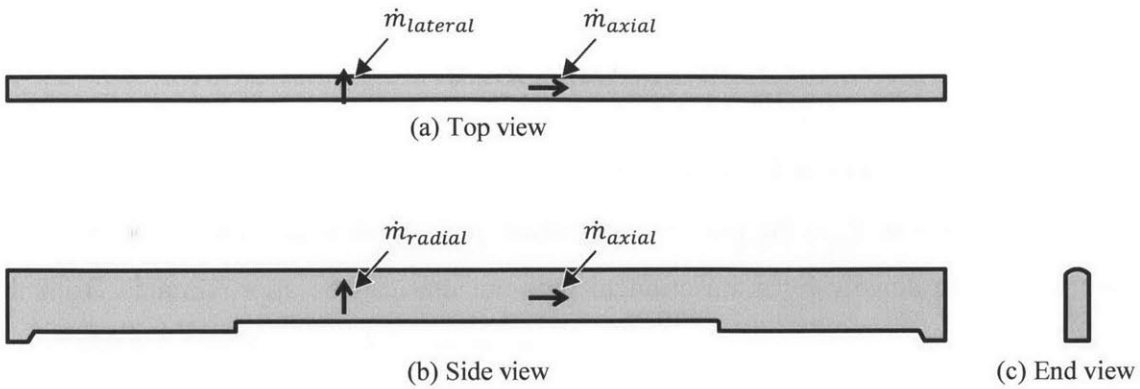

Fig. 4.7 Definition of axial, radial, and lateral mass flow rates for 1D gas flow approximation

The sixth approximation is to consider the pressure in the groove to be uniform. This can be validated by comparing the flow along the groove (Q_s) to the flow pass the seal flank clearance (Q_e) (Fig. 4.8). Assuming fully-developed flow for both, the criterion for this approximation to be valid is given by

$$\frac{Q_s}{Q_e} \approx \frac{L\frac{h_s^3}{12\mu_g}\frac{\Delta P}{H}}{\frac{\pi R_e^4}{8\mu_g}\frac{\Delta P}{L}} = \frac{2h_s^3 L^2}{3\pi R_e^4 H} \ll 1 \tag{4.7}$$

in which L is the AS length, μ_g is the gas viscosity, h_s is the AS flank clearance, H is the AS heigth, R_e is an equivalent radius for the flow channel along the AS groove, and ΔP is a pressure difference which drops out of the scaling. For typical AS geometry, this criterion is on the order of 1/100 which validates the approximation of constant pressure in the groove.

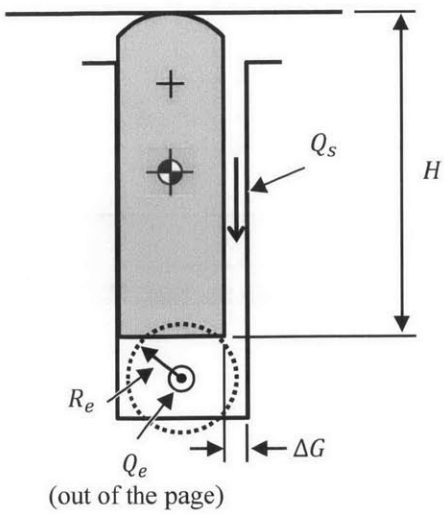

Fig. 4.8 Definition of flow along the flank and along the groove for uniform groove pressure approximation

The seventh and last general approximation is to consider that the variation of leakage has small influence on the leading and trailing pressure chambers taken from experimental data. This approximation is validated in section 4.2.15 by comparing the maximum amount of leakage to the engine mass flow rate.

Approximations specific to the sub-models are given in the respective sub-model section.

4.2.2 Spring Force

Two springs under the seal provide the force needed to maintain the apex seal in contact with the rotor housing when the groove is not pressurized. In the model, the two springs are replaced by localized forces applied at the contact points between the springs and the apex seal (Fig. 4.9). Each force is calculated by:

$$F_{s,k} = \frac{F_{s0,k} - k_{s,k} y_{g,i}}{2} \tag{4.8}$$

in which k is the index of the spring, either 1 or 2, F_{sk} is the force of the kth spring, $F_{s0,k}$ and $k_{s,k}$ are the tension and spring constant of the kth spring, and $y_{g,i}$ is the radial displacement of the cross-section in contact with the end of the kth spring. The radial displacement (y_g) is the

outward relative displacement measured from the seal reference position which is at a fixed distance from the back of the groove.

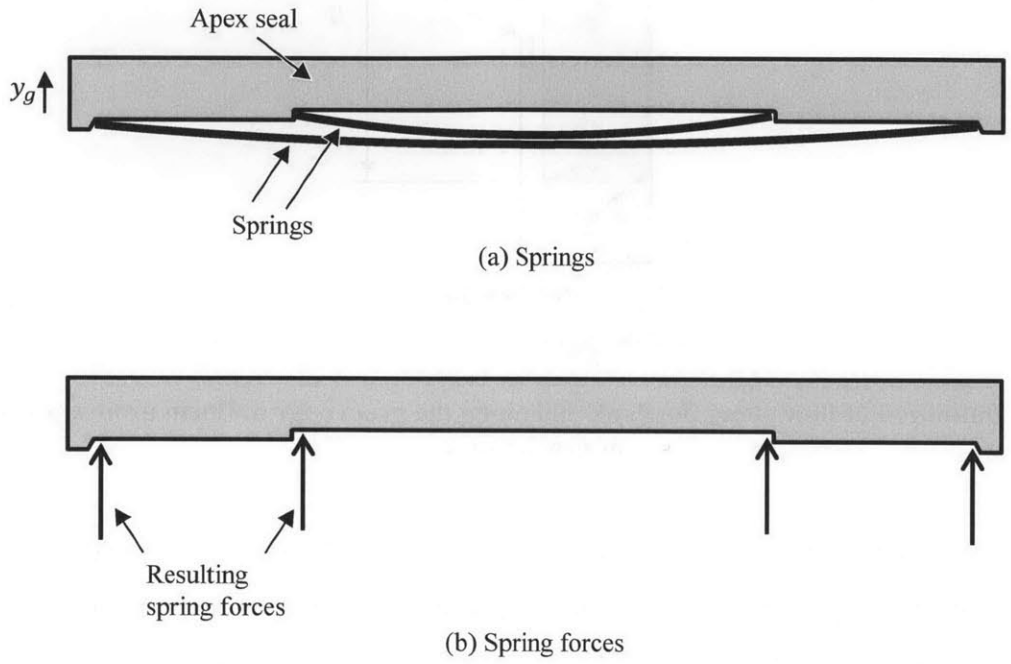

Fig. 4.9 (a) Springs under the apex seal, and (b) resulting local spring forces

4.2.3 Body Force

Body force is calculated from primary and secondary motion of the rotor. Primary motion is taken from the rotor kinematics and is calculated using the rotary engine kinematics. Secondary motion is taken from finite element analysis carried using an assembly of the crankshaft and two rotors. The effect of rotational acceleration is neglected as it is small compared to the other forces.

4.2.4 Profile Asperity Contact Forces and Moment

Profile asperity contact reaction forces and moment on the seal are calculated based on a simple contact model which relates the clearance to the contact pressure.

The first step towards calculating the asperity contact pressure is the description of the profile clearance as a function of the variables of interest, in this case the geometry and displacement of the seal, and the rotor housing surface position (Fig. 4.10).

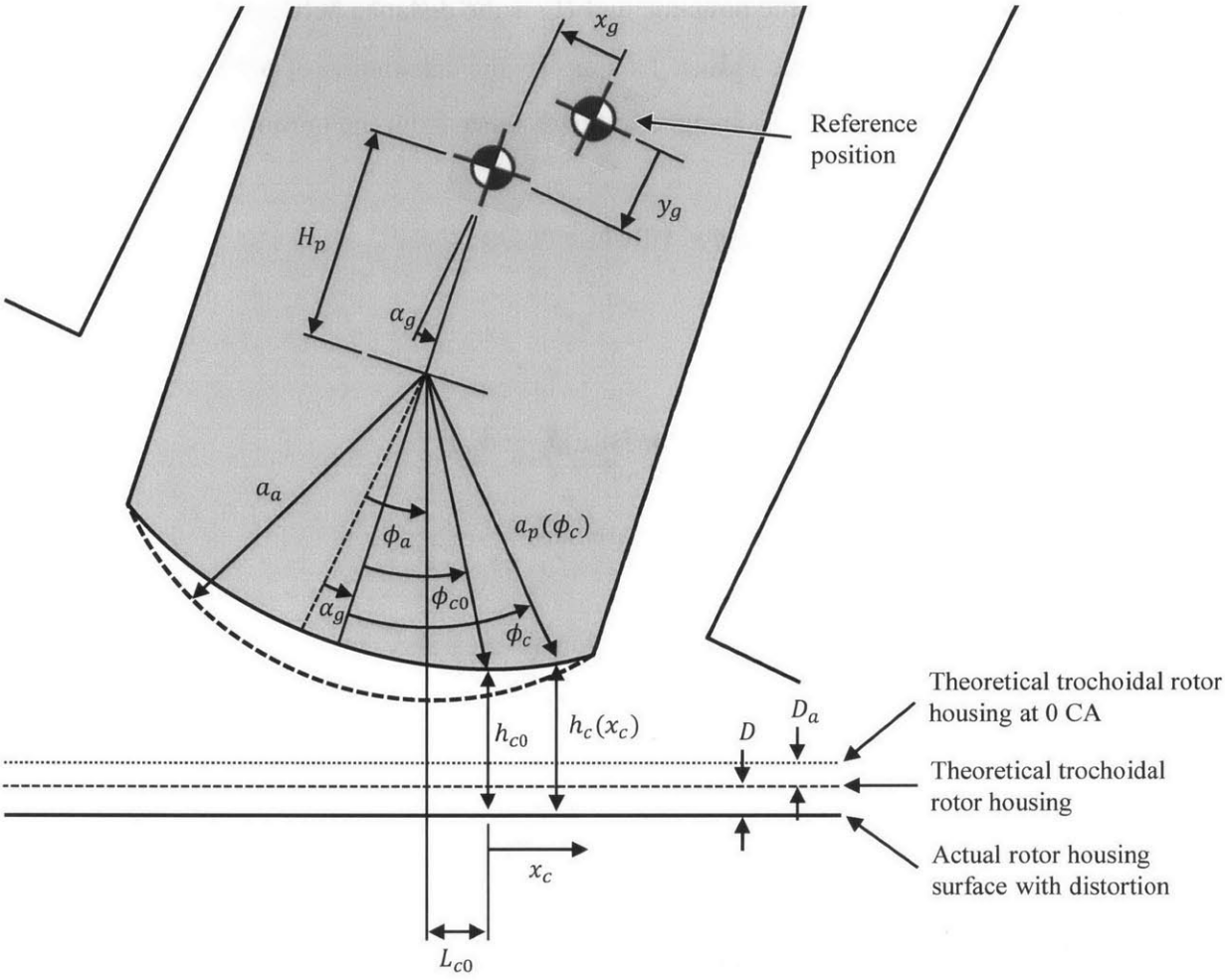

Fig. 4.10 Profile geometry

Under the small displacement approximation, the seal-housing clearance as a function of the position along the profile (ϕ_c) is given by

$$h_c(\phi_c) = D + D_a + a_a - a_p(\phi_c)\cos(\phi_c - \phi_a) - y_g\cos(\phi_a) + x_g\sin(\phi_a) + \alpha_g\left[a_p(\phi_c)\sin(\phi_c - \phi_a) - H_p\sin(\phi_a)\right] \quad (4.9)$$

in which D is the rotor housing displacement due to housing distortion, D_a is the difference between the rotor housing at 0 CA and rotor housing at a given crank angle caused by the difference between the apex seal radius for generating the trochoidal shape and the no-wear actual apex seal radius (a_a), $a_p(\phi_c)$ is the worn actual apex seal radius, ϕ_a is the angle between the seal and a line perpendicular to the housing, and H_p is the distance between the seal center of mass and the center of the seal profile radius. To simplify the calculation of profile pressures and forces, the position along the profile is changed to the distance from the minimum clearance (x_c):

$$x_c = a_p(\phi_c)\sin(\phi_c - \phi_a) - L_{c0} \tag{4.10}$$

in which L_{c0} is defined as

$$L_{c0} = a_p(\phi_{c0})\sin(\phi_c - \phi_a) \tag{4.11}$$

in which ϕ_{c0} is ϕ_c evaluated at the minimum clearance.

Asperity contact pressure is calculated as a function of clearance from the Greenwood-Tripp model the same way as for the oil seals:

$$P_{pc}(x_c) = P_c\left(z - \frac{h_c(x_c)}{\sigma_p}\right)^{K_c} \tag{4.12}$$

in which P_{pc} is the profile contact pressure, σ_p is the plateau roughness standard deviation, and P_c, K_c, and z are constants calculated from the surface topography. Net forces from asperity contact (Fig. 4.11) are calculated by numerically integrating the contact pressure:

$$\begin{aligned} F'_{pc,x_c} &= 0 \\ F'_{pc,y_c} &= \int_{x_{ci}}^{x_{co}} P_{pc}\,dx_c \\ F'_{pc,a_c} &= \int_{x_{ci}}^{x_{co}} x_c P_{pc}\,dx_c \end{aligned} \tag{4.13}$$

in which F_{pc,x_c} and F_{pc,y_c} are the net asperity contact forces per unit length on the profile perpendicular and parallel to the housing, and F_{pc,α_c} is the net asperity contact moment per unit length around the minimum clearance point. Throughout this chapter, F_α is used as the symbol for moments to simplify the vector notation. In the model, the integrals in eqs. (4.13) are evaluated numerically to allow the flexibility of choosing any shape of AS profile. In the remaining of this chapter, all integrals in the final force and moment expressions are evaluated numerically.

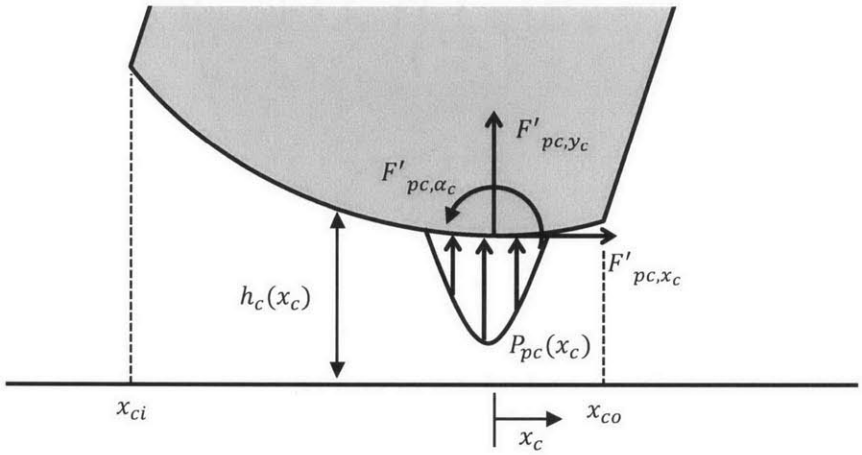

Fig. 4.11 Net forces and moment from asperity contact pressure

Net forces and moment in the center of mass reference frame ($\boldsymbol{F'_{pc,g}}$) are shown in Fig. 4.12 and are calculated from

$$\boldsymbol{F'_{pc,g}} = \boldsymbol{T_{cg}}\, \boldsymbol{F'_{pc,c}}$$

in which

$$\boldsymbol{F'_{pc,g}} = \begin{bmatrix} F'_{pc,x_g} \\ F'_{pc,y_g} \\ F'_{pc,\alpha_g} \end{bmatrix}, \tag{4.14}$$

$$\boldsymbol{T_{cg}} = \begin{bmatrix} -\cos(\phi_a) & \sin(\phi_a) & 0 \\ -\sin(\phi_a) & -\cos(\phi_a) & 0 \\ H_p\cos(\phi_a) + a_{p0}\cos(\phi_{c0} - \phi_a) & -H_p\cos(\phi_a) + L_{p0} & 1 \end{bmatrix},$$

$$\boldsymbol{F'_{pc,c}} = \begin{bmatrix} F'_{pc,x_c} \\ F'_{pc,y_c} \\ F'_{pc,\alpha_c} \end{bmatrix},$$

and

$$L_{p0} = L_{c0} - H_p \sin(\phi_a)$$

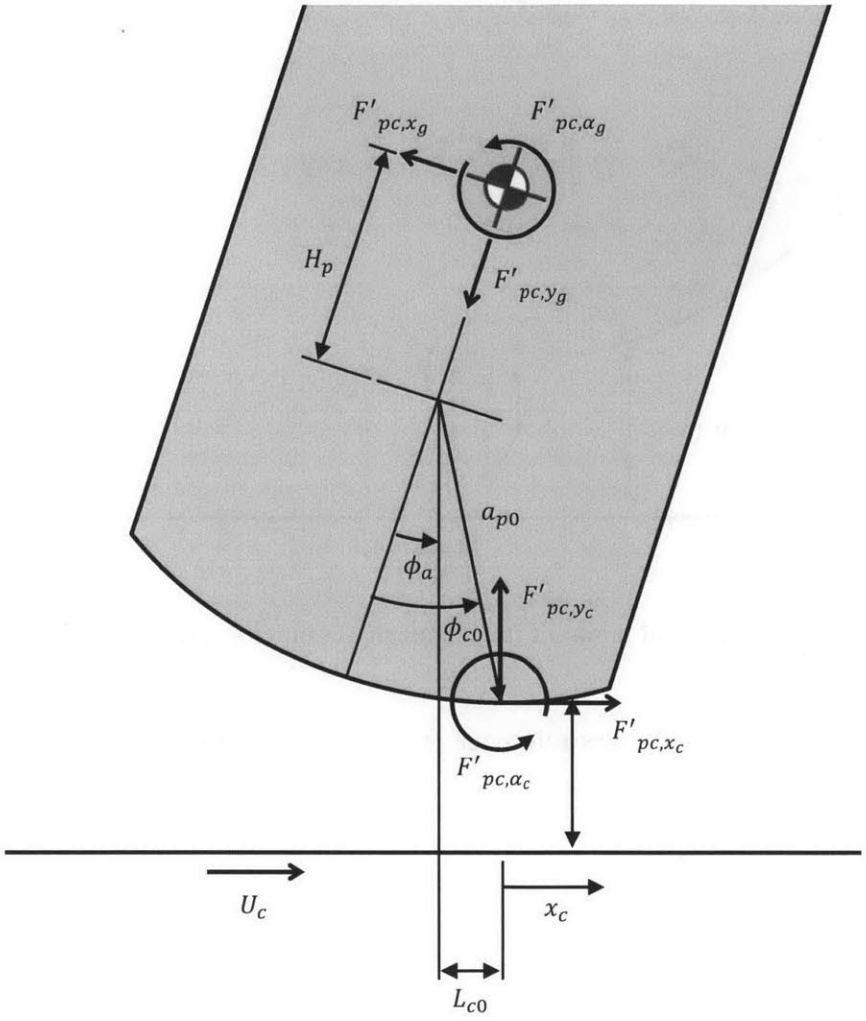

Fig. 4.12 Forces and moment in the center of mass reference frame

Asperity contact shear stress (τ_{pc}) is calculated from the asperity contact pressure and a dry friction coefficient (C_{fc}):

$$\tau_{pc}(x_c) = C_{fc} P_{pc} \tag{4.15}$$

Unless mentioned otherwise, the dry friction coefficient is taken to be 0.15. Net forces and moment per unit length from asperity contact friction are given by

$$f'_{pc,x_c} = \int_{x_{ci}}^{x_{co}} \tau_{pc} dx_c$$
$$f'_{pc,y_c} = 0 \qquad (4.16)$$
$$f'_{pc,\alpha_c} = 0$$

Friction is parallel to the housing and pointing in the positive x_c direction as the relative sliding velocity (U_c) always points in that direction. Friction forces are reported to the center of mass reference frame with the same transformation as forces normal to the housing. The transformation is given by

$$\boldsymbol{f'_{pc,g}} = \boldsymbol{T_{cg}}\, \boldsymbol{f'_{pc,c}} \qquad (4.17)$$

4.2.5 Profile Hydrodynamic Forces and Moment

In presence of lubricating oil on the rotor housing, oil accumulates at the AS profile interface and generates pressure that helps support the radial forces on the AS (Fig. 4.13). As there is no accurate analytical solution to this problem, a semi-analytic method is used. The method used is adapted from Tian's thesis [56] to include the effect of seal-housing relative rotation on hydrodynamic pressure generation. The general strategy is to use a Newton iterative method to find the boundaries of the full-film region that satisfy Reynolds' lubrication equation, mass conservation and boundary conditions. The pressure gradient in the full-film region is then integrated numerically to calculate the net hydrodynamic forces and moment.

Leading and trailing chamber gas pressure needs to be included in the hydrodynamic pressure analysis as it changes the oil pressure by changing the pressure boundary conditions at the ends of oil full-film region. Only in starved condition, where supply is insufficient to maintain a full-film region, that there is a gas flow at the interface. This gas flow is solved analytically in the next section.

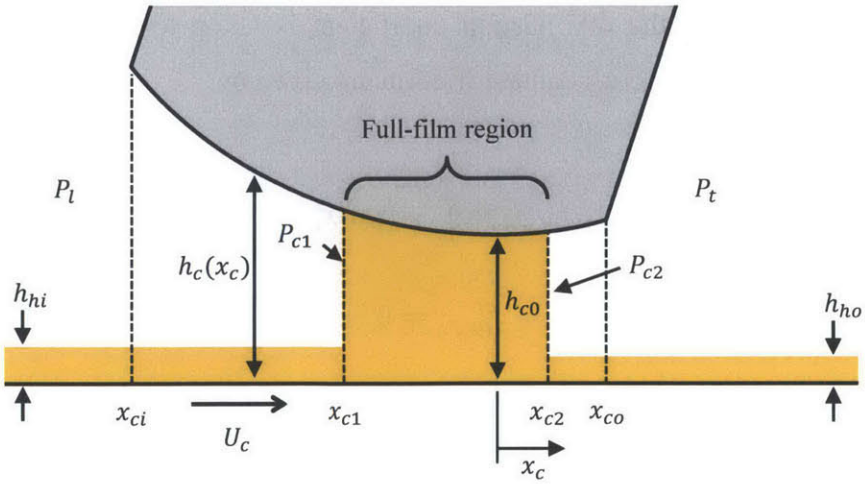

Fig. 4.13 Oil accumulation at the seal-housing interface

The goal is to find the limits of the full-film region (x_{c1} and x_{c2}) that satisfy Reynolds' equation everywhere in the full-film region, mass conservation in the control volume under the seal, and boundary conditions at the two ends of the full-film region. First, Reynolds' 1D lubrication equation is given by

$$\frac{dq_c}{dx_c} = -\dot{h}_c \tag{4.18}$$

in which q_c is the volume flow rate per unit length calculated from Couette and Poiseuille flows, and $\dot{h}_c$ is the time derivative of the profile clearance. Integrating from a location in the full-film region (x_c) to the end of the full-film region (x_{c2}) yields

$$q_c = q_{c2} + \int_{x_c}^{x_{c2}} \dot{h}_c \, dx_c \tag{4.19}$$

in which q_{c2} is the volume flow rate per unit length at the end of the full-film region and is typically given by the Reynolds' conditions, which dictates that the pressure gradient at the outlet must be zero. However, if supply is insufficient, q_{c2} is limited by mass conservation. Those conditions are discussed toward the end of this section. Under lubrication approximation, the volume flow rate can be calculated from a Couette flow and a Poiseuille flow:

$$q_c = -\frac{h_c^3}{12\mu}\frac{dP_{ph}}{dx_c} + \frac{U_c h_c}{2} \tag{4.20}$$

in which P_{ph} is the profile hydrodynamic pressure and μ is the oil viscosity. Replacing in eq. (4.20) and solving for the pressure gradient yields

$$\frac{dP_{ph}}{dx_c} = \frac{12\mu}{h_c^3}\left[\frac{U_c h_c}{2} - q_{c2} - \int_{x_c}^{x_{c2}} \dot{h}_c \, dx\right] \tag{4.21}$$

Integrating over x_c yields the first condition on the full-film limits:

$$P_{c2} - P_{c1} = \int_{x_{c1}}^{x_{c2}} \frac{12\mu}{h_c^3}\left[\frac{U_c h_c}{2} - q_{c2} + \int_{x_c}^{x_{c2}} \dot{h}_c \, dx_c\right] dx_c \tag{4.22}$$

in which the pressure at the ends of the full-film region (P_{c1} and P_{c2}) are given by the pressure in the leading and trailing chambers. Taking the pressure in the leading chamber as the boundary condition at x_{c1} is an appropriate approximation because the viscosity of the oil is much larger than the gas viscosity so the pressure difference between x_{ci} and x_{c1} is small. The same argument applies for the pressure difference between x_{c2} and x_{co}.

In order to find the solution for this equation in the present case, U_c and $\dot{h}_c$ must be related to the seal motion. The relative velocity between the AS profile and the rotor housing (U_c) is calculated from primary and secondary motion of the rotor. The model neglects the effect of relative motion of the AS in its groove, as the AS-groove relative velocity is much smaller than the circumferential apex velocity due to rotor motion. The time derivative of the clearance ($\dot{h}_c$) is calculated by taking the time derivative of eq. (4.9):

$$\dot{h}_c(x_c) = \dot{D} + \dot{D}_a - \dot{y}_g \cos(\phi_a) + \dot{x}_g \sin(\phi_a) + (\dot{\alpha}_g - \dot{\phi}_a)\left[x_c - H_p \sin(\phi_a)\right] \tag{4.23}$$

Cross-terms containing time derivative of the seal-housing angle ($\dot{\phi}_a$) and seal displacement (x_g, y_g, or α_g) are neglected as they are one to two orders of magnitude smaller than the last term. By inspection, one can replace the expression in (4.23) by a translational speed of the seal at the

minimum clearance point ($\dot{h}_{c0}$) and a rotational speed of the seal around the minimum clearance point (ω_{c0}). The time derivation of the profile clearance becomes:

$$\dot{h}_c(x_c) = \dot{h}_{c0} + \omega_{c0} x_c$$

in which

$$\dot{h}_{c0} = \dot{D} + \dot{D}_a - \dot{y}_g \cos(\phi_a) + \dot{x}_g \sin(\phi_a) - \dot{\alpha}_g H_p \sin(\phi_a) \tag{4.24}$$

and

$$\omega_{c0} = \dot{\alpha}_g - \dot{\phi}_a$$

The integral over $\dot{h}_c$ in can be replaced by

$$\int_{x_c}^{x_{c2}} \dot{h}_c \, dx_c = \dot{h}_{c0}(x_{c2} - x_c) - \frac{1}{2}\omega_{c0}(x_{c2}^2 - x_c^2) \tag{4.25}$$

Replacing in eq. (4.22) gives the first error function to be solved for $G_{c1} = 0$:

$$G_{c1} = \int_{x_{c1}}^{x_{c2}} \frac{12\mu}{h_c^3}\left[\frac{U_c h_c}{2} - q_{c2} - \dot{h}_{c0}(x_{c2} - x_c) - \frac{1}{2}\omega_{c0}(x_{c2}^2 - x_c^2)\right] dx_c - (P_{c2} - P_{c1}) \tag{4.26}$$

The second error function is derived from mass conservation and must be solved for $G_{c2} = 0$:

$$G_{c2} = q_{c2} + \int_{x_{c1}}^{x_{c2}} \dot{h}_c \, dx_c + \dot{x}_{c1}(h_{c1} - h_{hi}) - U_c h_{hi} \tag{4.27}$$

in which h_{hi} and h_{ho} are the oil film thicknesses on the rotor housing before and after the seal has passed (Fig. 4.13). In the present model, the oil film thickness supplied to the seal profile (h_{hi}) is assumed to be constant as there is no oil transport model included. The first term of eq. (4.27) is the outflow, the second term is the volume increase due to clearance variation, the third term is the change in volume when x_{c1} varies and the last term is the inflow of oil to the control volume due to seal-housing relative motion. Replacing $\dot{h}_c$ in eq. (4.27) and integrating yields

$$G_{c2} = q_{c2} + \dot{h}_{c0}(x_{c2} - x_{c1}) - \frac{1}{2}\omega_{c0}(x_{c2}^2 - x_{c1}^2) + \dot{x}_{c1}(h_{c1} - h_{hi}) - U_c h_{hi} \quad (4.28)$$

The outlet flow rate is related to oil left on the housing by

$$q_{c2} = \dot{x}_{c2}(h_{c2} - h_{ho}) + U_c h_{ho} \quad (4.29)$$

As discussed, for most conditions, the outlet mass flow rate is given by the Reynolds' condition that imposes a zero pressure gradient at the outlet:

$$\left.\frac{dP_{ph}}{dx_c}\right|_{x_{c2}} = 0 \quad (4.30)$$

This leads to no pressure flow at the outlet and q_{c2} is given by

$$q_{c2} = \frac{U_c h_{c2}}{2} \quad (4.31)$$

In this case, the oil left on the housing (h_{ho}) becomes a dependent variable and could be calculated for oil tracking. However, the outflow must not exceed the supply and q_{c2} is limited by a non-separating condition, given by eq. (4.29) without outflow to the housing:

$$q_{c2} = \dot{x}_{c2} h_{c2} \quad (4.32)$$

The last outlet condition is the case where the end of the full-film region reaches the trailing edge of the seal ($x_{c2} = x_{co}$). In this case, the outlet is fully-flooded, x_{c2} is fixed and q_{c2} becomes the unknown.

Similarly, if the inlet is fully-flooded, x_{c1} is fixed and the equation for G_{c2} becomes irrelevant as the exceeding incoming oil flows to the leading flank of the seal. The effect of the accumulation of oil at the leading edge is not included in the present model.

The different conditions to solve boundaries of the full-film region are summarized in Table 4.1. A first order time discretization is used to calculate time derivatives of x_{c1} and x_{c2} and a Newton method with a globally convergent algorithm is used to find the unknowns.

Table 4.1 Summary of unknowns and equations for profile lubrication

		Inlet condition	
		Partially flooded	**Fully flooded** ($x_{c1} = x_{ci}$)
Outlet condition	**Reynolds' cond.** $\left(\left.\frac{dP_{ph}}{dx_c}\right\|_{x_{c2}} = 0\right)$	Unknowns: x_{c1} and x_{c2} Eqs.: G_{c1} and G_{c2} with $q_{c2} = U_c h_c/2$	Unknown: x_{c2} Eq.: G_{c1} with $q_{c2} = U_c h_c/2$
	No-separation ($h_{ho} = 0$)	Unknowns: x_{c1} and x_{c2} Eqs.: G_{c1} and G_{c2} with $q_{c2} = \dot{x}_{c2} h_{c2}$	Unknown: x_{c2} Eq.: G_{c1} with $q_{c2} = \dot{x}_{c2} h_{c2}$
	Fully-flooded ($x_{c2} = x_{co}$)	Unknowns: x_{c1} and q_{c2} Eqs.: G_{c1} and G_{c2}	Unknown: q_{c2} Eq.: G_{c1}

Once the full-film limits are found, the net forces and moment on the profile due to hydrodynamic lubrication can be calculated. First, the force along x_c is given by

$$F'_{ph,x_c} = P_{c1}(h_{ci} - h_{c1}) + \int_{h_{c1}}^{h_{c2}} P_{ph} dh_c - P_{c2}(h_{co} - h_{c2}) \tag{4.33}$$

in which the first term is the gas contribution from x_{ci} to x_{c1}, the second term is the hydrodynamic pressure, and the last term is the gas contribution from x_{c2} to x_{co}. Integrating by part the second term reduces computing needed by replacing the pressure by the pressure gradient. This leads to a force along x_c given by

$$F'_{ph,x_c} = -P_{c2} h_{co} + P_{c1} h_{ci} - \int_{x_{c1}}^{x_{c2}} h_c \frac{dP_{ph}}{dx_c} dx_c \tag{4.34}$$

In which the pressure gradient is known from eq. (4.21) with the value of the $\dot{h}_c$ integral given by eq. (4.25). Similarly, one can calculate the force along y_c

$$F'_{ph,y_c} = P_{c2}x_{co} - P_{c1}x_{ci} - \int_{x_{c1}}^{x_{c2}} x_c \frac{dP_{ph}}{dx_c} dx_c \tag{4.35}$$

and the moment around the minimum clearance point

$$\begin{aligned} F'_{ph,\alpha_c} = \frac{P_{c2}}{2} x_{co}^2 - \frac{P_{c1}}{2} x_{ci}^2 - \int_{x_{c1}}^{x_{c2}} \frac{x_c^2}{2} \frac{dP_{ph}}{dx_c} dx_c + P_{c2}\left(\frac{h_{co}^2}{2} - h_{co}h_{c0}\right) \\ - P_{c1}\left(\frac{h_{ci}^2}{2} - h_{ci}h_{c0}\right) - \int_{x_{c1}}^{x_{c2}} \left(\frac{h_c^2}{2} - h_c h_{c0}\right) \frac{dP_{ph}}{dx_c} dx_c \end{aligned} \tag{4.36}$$

Hydrodynamic forces and moment are reported to the center of mass reference frame in the same way as the asperity contact forces and moment:

$$\boldsymbol{F'_{ph,g}} = \boldsymbol{T_{cg}}\, \boldsymbol{F'_{ph,c}} \tag{4.37}$$

For friction, hydrodynamic shear stress is given by the velocity gradient at the wall from the pressure flow and the shear flow:

$$\tau_{ph} = \frac{\mu U_c}{h_c} - \frac{h_c}{2}\frac{dP}{dx} \tag{4.38}$$

Friction force is calculated by integrating the shear stress:

$$\begin{aligned} f'_{ph,x_c} &= \int_{x_{c1}}^{x_{c2}} \tau_{ph} dx_c \\ f'_{ph,y_c} &= 0 \\ f'_{ph,\alpha_c} &= 0 \end{aligned} \tag{4.39}$$

The friction forces and moment in the center of mass reference frame are given by

$$f'_{ph,g} = T_{cg} f'_{ph,c} \tag{4.40}$$

4.2.6 Profile Gas Forces and Moment

In starved condition, when the oil supply from the rotor housing is insufficient, the oil film on the housing detaches from the seal (Fig. 4.14). Gas can flow through the profile clearance and the pressure distribution on the AS profile can be calculated from lubrication theory applied to the gas. The approach is similar to the approach to calculate hydrodynamic pressure generation. The main difference is that the limits of the flow are known and corresponds to the edges of the seal profile. This simplifies the analysis significantly as there is no need to use an iterative method as in the hydrodynamic pressure case.

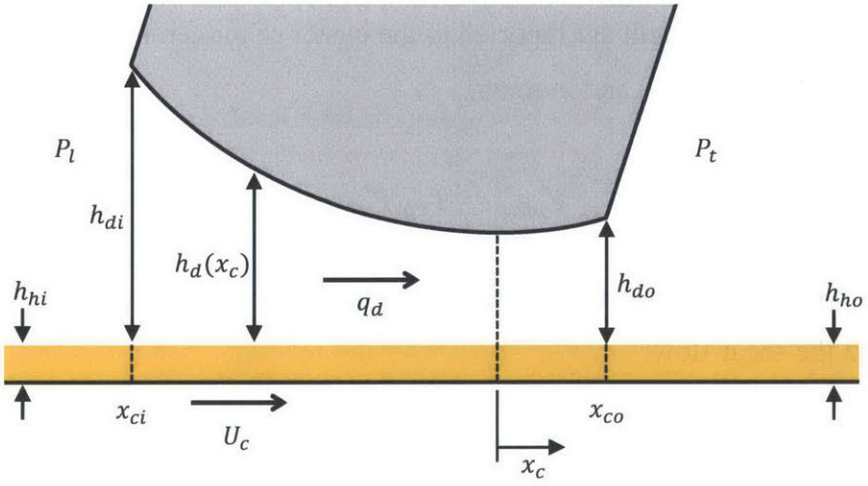

Fig. 4.14 Gas flow in starved condition

In starved condition, the clearance available for gas flow ($h_d(x_c)$) can be approximated by substracting the oil film thickness on the rotor housing to the total profile clearance:

$$h_d(x_c) = h_c(x_c) - h_{hi} \tag{4.41}$$

The oil film is considered a no-slip condition. This approximation is valid because under a pressure-driven flow the oil velocity is small compared to the gas velocity due to a large viscosity difference. Also, the pressure due to sliding and squeezing is neglected when

calculating the pressure distribution as it is much smaller than the typical pressure difference between the chambers. Finally, the gas flow is approximated as incompressible for calculating the force, but the mass flow rate is limited by the compressible flow through an orifice when calculating gas flow for leakage calculation.

Without sliding and squeezing terms, the 1D Reynolds' equation applied to the gas reduces to

$$q_d = -\frac{h_d^3}{12\mu_g}\frac{dP_{pg}}{dx_c} \tag{4.42}$$

in which q_d is the gas volume flow rate through the clearance per unit length, μ_g is the gas viscosity, and P_{pg} is the pressure on the AS profile due to the gas. Rearranging and integrating over x_c yields

$$-12\mu_g q_d J_{d03} = P_{c2} - P_{c1} \tag{4.43}$$

in which

$$J_{d03} = \int_{x_{ci}}^{x_{co}} \frac{1}{h_d^3} dx_c$$

The variable J_{d03} is introduced to replace the integral evaluated numerically. The volume flow rate is then given by:

$$q_d = -\frac{1}{J_{d03}}\frac{(P_{c2} - P_{c1})}{12\mu_g} \tag{4.44}$$

Gas forces and moment are calculated by integrating by part to get integrals of the pressure gradient as is done for the hydrodynamic forces and moment. This leads to

$$F'_{pg,x_c} = -\left(P_{c2}h_{do} - P_{c1}h_{di} - (P_{c2} - P_{c1})\frac{J_{d02}}{J_{d03}}\right)$$

$$F'_{pg,y_c} = P_{c2}h_{do} - P_{c1}h_{di} - (P_{c2} - P_{c1})\frac{J_{d13}}{J_{d03}}$$

$$F'_{pg,\alpha_c} = P_{c2}\left(\frac{x_{co}^2}{2} + \frac{h_{do}^2}{2} + h_{do}h_{d0}\right) - P_{c1}\left(\frac{x_{ci}^2}{2} + \frac{h_{di}^2}{2} + h_{di}h_{d0}\right) - \frac{(P_{c2} - P_{c1})}{J_{d03}}\left(\frac{J_{d23}}{2} + \frac{J_{d01}}{2} - h_{c0}J_{d02}\right) \tag{4.45}$$

in which

$$J_{dnm} = \int_{x_{cl}}^{x_{co}} \frac{x_c^n}{h_d^m} dx_c$$

Friction forces and moment are calculated by integrating shear stress at the wall:

$$f'_{pg,x_c} = -\frac{1}{2}(P_{c2} - P_{c1})\frac{J_{d02}}{J_{d03}}$$

$$f'_{pg,y_c} = 0 \tag{4.46}$$

$$f'_{pg,\alpha_c} = 0$$

Finally, gas forces and moment are reported to the center of mass reference frame by

$$\boldsymbol{F'_{pg,g} = T_{cg}\, F'_{pg,c}} \tag{4.47}$$

and

$$\boldsymbol{f'_{pg,g} = T_{cg}\, f'_{pg,c}} \tag{4.48}$$

4.2.7 Seal Flank Asperity Contact Forces and Moment

The model calculates the forces and moment on both flanks from the asperity contact pressure as a function of clearance. Flank friction force is calculated based on this contact pressure. As the friction force is discontinuous when changing direction, a correction is added to make it

continuous and avoid convergence problem. This section focuses on the description of force and moment calculations for the trailing flank. The method to calculate the forces and moment on the leading flank is briefly described at the end of this section.

The first step is to calculate the trailing seal flank clearance as a function of the seal-groove displacement, geometry and wear (Fig. 4.15). Under small displacement approximation, the trailing flank clearance (h_b) is given by

$$h_b(y_b) = \frac{\Delta G}{2} + x_g - (y_b - H_l)\alpha_g + h_{wb}(y_b) + h_{eb}(y_{eb}) \tag{4.49}$$

in which y_b is the distance from the bottom of the seal to a point on the flank, ΔG is the total seal clearance, H_l is the distance from the bottom of the seal to the center of mass, $h_{wb}(y_b)$ is the wear thickness on the seal trailing flank, and $h_{eb}(y_{eb})$ is the wear thickness on the groove trailing flank. The y-coordinate on the seal (y_b) is related to the y-coordinate on the groove (y_{eb}) by

$$y_{eb} = y_b + H_{ub} \tag{4.50}$$

It should be noted that H_{ub} is a function of y_g and varies throughout the cycle. The groove wear must therefore be interpolated for every iteration to calculate the clearance in eq. (4.49).

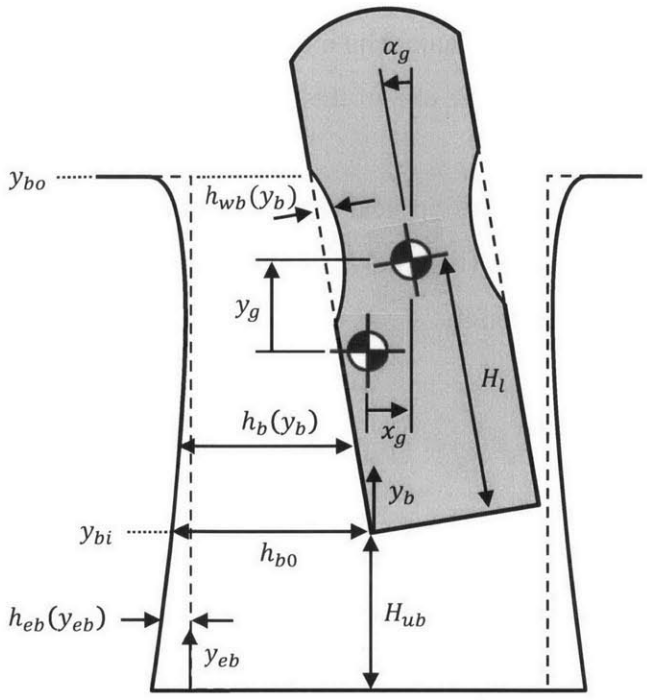

Fig. 4.15 Trailing flank clearance

Asperity contact pressure on the seal trailing flank (P_{bc}) is calculated from the simplified Greenwood-Tripp correlation presented in section 4.2.4. Forces and moment on the seal are calculated in the trailing flank reference frame (Fig. 4.16) by numerically integrating the contact pressure:

$$F'_{bc,x_b} = \int_{y_{bi}}^{y_{bo}} P_{bc} dy_b$$

$$F'_{bc,y_b} = 0 \tag{4.51}$$

$$F'_{bc,\alpha_b} = \int_{y_{bi}}^{y_{bo}} y_b P_{bc} dy_b$$

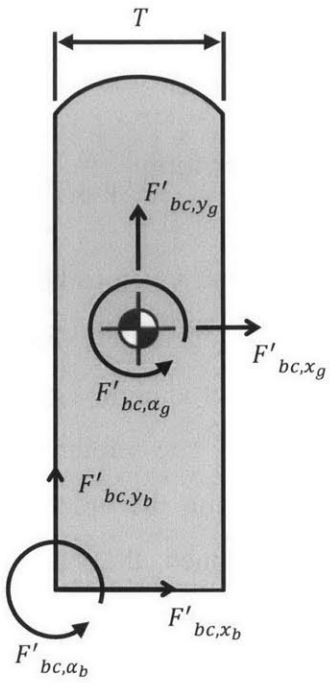

Fig. 4.16 Seal trailing flank and center of mass reference frames

Net forces and moment in the center of mass reference frame ($\boldsymbol{F'_{bc,g}}$) are calculated from

$$\boldsymbol{F'_{bc,g}} = \boldsymbol{T_{bg}}\, \boldsymbol{F'_{bc,b}} \tag{4.52}$$

in which

$$\boldsymbol{T_{cb}} = \begin{bmatrix} 1 & 0 & 0 \\ 0 & 1 & 0 \\ H_l & -T/2 & 1 \end{bmatrix}$$

and T is the seal thickness.

Shear stress on the seal flank is opposed to the seal-groove relative motion and is approximated as

$$\tau_{bc} = -k_{sc} C_{fs} P_{bc}$$

in which

(4.53)

$$k_{sc} = \tanh\left(\frac{\dot{y}_g}{v_{s0}}\right)$$

and C_{fs} is the seal-groove contact coefficient, taken to be 0.15 unless otherwise specified, and v_{s0} is a reference velocity. The variable k_{sc} gives the direction of the velocity and makes the friction force function smooth. As the contact is highly stiff, it is essential that all functions are smooth in order for the model to converge. The reference velocity v_{s0} must be chosen much below the typical radial velocity, which is on the order of 100 mm/s based on the modified trochoid geometry. Unless otherwise mentioned, the value of v_{s0} is taken to be 0.1 mm/s. A hyperbolic tangent function is chosen for k_{sc} as it is a smooth function and it converges rapidly to 1 for positive velocities and -1 for negative velocities (Fig. 4.17).

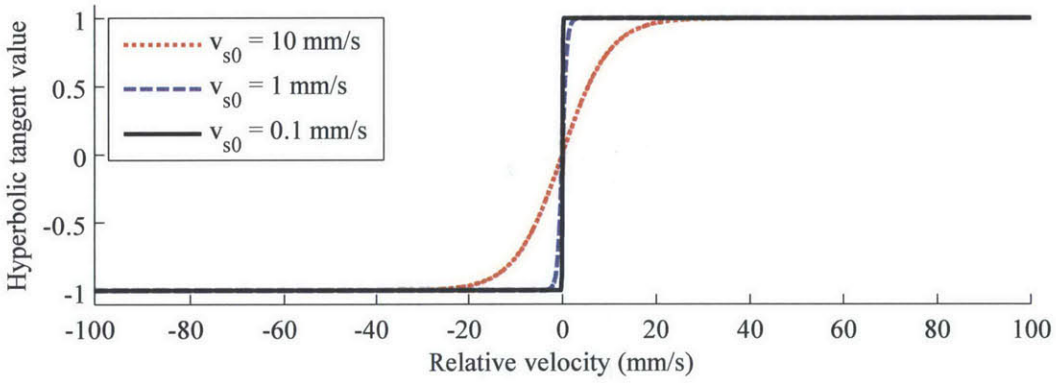

Fig. 4.17 Hyperbolic tangent function for different reference velocities

The friction force is given by numerically integrating the shear stress.

$$f'_{bc,x_b} = 0$$

$$f'_{bc,y_b} = \int_{y_{bi}}^{y_{bo}} \tau_{bc} dy_b \tag{4.54}$$

$$f'_{bc,\alpha_b} = 0$$

The friction forces and moment are reported to the center of mass reference frame using the transformation in eq. (4.52). This completes the calculation of the asperity contact friction forces and moment for the trailing flank.

Leading flank forces and moment are calculated by first changing the expression for clearance (Fig. 4.18):

$$h_b(y_b) = \frac{\Delta G}{2} - x_g + (y_f - H_l)\alpha_g + h_{wf}(y_f) + h_{ef}(y_{ef}) \tag{4.55}$$

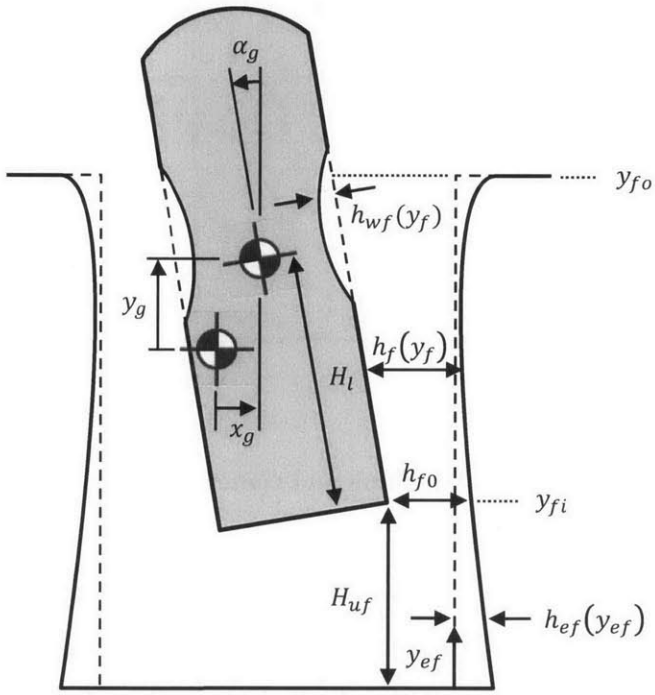

Fig. 4.18 Leading flank geometry.

Forces in the leading flank reference frame are defined by reversing the x-force and the moment (Fig. 4.19). This allows calculating forces and moment on the leading flank also from equations (4.51) and (4.54). However, the transformation matrix from the flank reference frame to the center of mass reference frame must be changed. The forces and moment in the center of mass reference frame are given by

$$\boldsymbol{F'_{fc,g} = T_{fg}\, F'_{fc,f}}$$

in which

$$\boldsymbol{T_{fg}} = \begin{bmatrix} -1 & 0 & 0 \\ 0 & 1 & 0 \\ -H_l & T/2 & -1 \end{bmatrix} \tag{4.56}$$

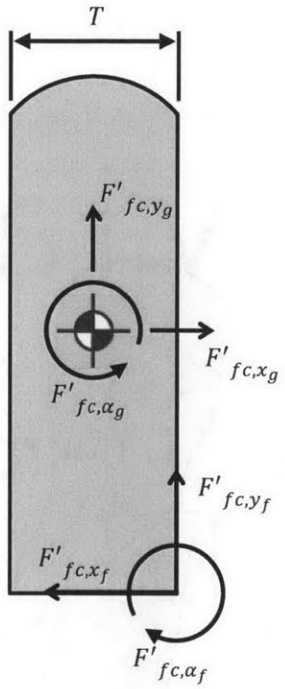

Fig. 4.19 Seal trailing flank and center of mass reference frames.

4.2.8 Seal Flank Hydrodynamic Squeezing Force and Moment

Oil present between the AS flanks and the groove flanks generates hydrodynamic pressure when it is squeezed. This pressure changes the dynamic behavior of the AS and reduces the contact pressure at the AS-groove interface. As a first order approximation, the oil film thickness on the groove flanks is assumed to be uniform (Fig. 4.20) and to remain constant throughout the cycle as oil transport around the AS is not included in the present model. Nevertheless, the oil film thickness on the oil seal flanks (h_g) is an input to the model and the effect of varying it is explored in section 4.3. When the seal is in contact with the oil film, forces and moment are calculated from the hydrodynamic pressure calculated according to 1D Reynolds' equation. As the boundaries of the full-film region are known from seal kinematics, the difference in gas

pressure can be ignored when calculating the pressure due to squeezing of the oil film. The effect of gas pressure can be superposed linearly and is described in section 4.2.9. Finally, a smoothing method is used by modifying the viscosity to avoid discontinuity in the squeezing force when the seal first touches the oil on the flank.

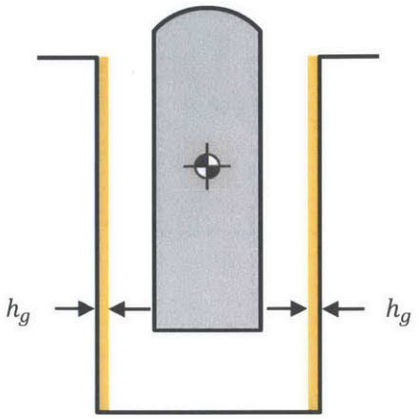

Fig. 4.20 Oil film thickness on the groove flanks.

Again, the first step is to calculate the clearance and determine the boundaries of the full-film region. Trailing flank clearance is given by eq. (4.49). Boundaries of the full-film region are given by two conditions. The first one is that the seal must be in contact with the oil. The second one is imposed by cavitation of the oil. Whenever the oil pressure goes below cavitation pressure, the oil cavitates and no hydrodynamic pressure is generated. In order to simplify this problem, the model assumes that any point on the seal moving away from the groove is in a cavitation state. This region is therefore excluded from the full-film region. An example of full-film boundaries is given in Fig. 4.21. In this case, the lower boundary of the full-film region (y_{b1}) is set by the end of the contact between the seal and the oil on the flank. The upper limit of the full-film region (y_{b2}) is set by the point at which the relative velocity changes direction. Above the y_{b2} line, the oil is assumed to cavitate and this region does not increase nor reduce hydrodynamic pressure.

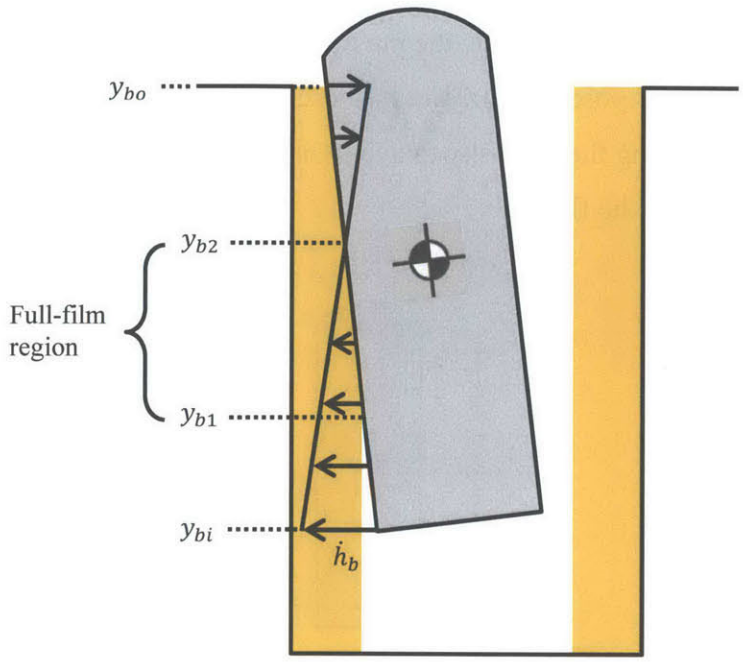

Fig. 4.21 Example of trailing flank full-film boundaries

Neglecting the small radial seal-groove relative velocity, the 1D Reynolds' equation reduces to

$$\frac{d}{dy_b}\left(-\frac{h_b^3}{12\mu_b(h_b)}\frac{dP_{bh}}{dy_b}\right)+\dot{h}_b=0 \tag{4.57}$$

in which P_{bh} is the hydrodynamic pressure on the trailing flank of the seal. The viscosity is taken to be a general function of the clearance to smooth out the transition from no contact to contact with the oil. The time derivative of the trailing clearance ($\dot{h}_b$) is given by taking the time derivative of eq. (4.49):

$$\dot{h}_b(y_b)=\dot{x}_g-(y_b-H_l)\dot{\alpha}_g \tag{4.58}$$

Similarly to the profile clearance time derivative, $\dot{h}_b$ can be expressed as a function of the translational speed of the lowest point ($\dot{h}_{b0}$, see Fig. 4.15) and the rotational speed around that point ($\dot{\alpha}_b$):

$$\dot{h}_b(y_b) = \dot{h}_{b0} - y_b\dot{\alpha}_b$$

in which

$$\dot{h}_{b0} = \dot{x}_g + H_l\dot{\alpha}_g \tag{4.59}$$

and

$$\dot{\alpha}_b = \dot{\alpha}_g$$

Replacing $\dot{h}_b$ in eq. (4.57) and integrating over y_b yields

$$\frac{dP_{bh}}{dy_b} = \frac{12\mu_b(h_b)}{h_b^3}\left(y_b\dot{h}_{bo} - \frac{y_b^2\dot{\alpha}_b}{2} + C_{b1}\right) \tag{4.60}$$

in which C_{b1} is a constant of integration that is found by integrating again over y_b and applying the zero-pressure boundary condition at both ends:

$$C_{b1} = \frac{1}{J_{b03}}\left(-\dot{h}_{b0}J_{b13} + \frac{\dot{\alpha}_b}{2}J_{b23}\right)$$

in which (4.61)

$$J_{bnm} = \int_{y_{b1}}^{y_{b2}} \frac{\mu_b(h_b)\, y_b^n}{h_b^m}\, dy_b$$

Forces and moment are calculated by integrating the pressure and carrying integration by part to get an integral of the pressure gradient explicitly, as shown in eqs. (4.33) and (4.34):

$$F'_{bh,x_b} = -12\left(\dot{h}_{b0}J_{b23} - \frac{\dot{\alpha}_b}{2}J_{b33} + C_{b1}J_{b13}\right)$$

$$F'_{bh,y_b} = 0 \tag{4.62}$$

$$F'_{bh,\alpha_b} = 6\left(\dot{h}_{b0}J_{b33} - \frac{\dot{\alpha}_b}{2}J_{b43} + C_{b1}J_{b23}\right)$$

The last step in calculating the flank hydrodynamic pressure is to set the function for viscosity. If the viscosity is taken to be constant all the way to the maximum oil film thickness, the force is not continuous as a function of clearance. For example, if the seal moves from the leading flank to the trailing flank, it would come in contact with the film at high velocity. So, even for a very small interference between the seal and the oil on the flank, say 1 nm, the hydrodynamic pressure generated would be very large. On the other hand, if the seal is just outside of the oil film, say 1 nm away, there is no hydrodynamic pressure generated. There is therefore a discontinuity in the contact model and the model cannot converge to a solution that satisfies Newton's second law. In a real system, this situation would not occur as the oil film on the flank is not flat to the nanometer level. There would thus be a continuous increase of hydrodynamic pressure as clearance is reduced. To solve this problem, the viscosity can be modified so there is no hydrodynamic pressure generated at a clearance equal to the maximum oil film thickness, but rises rapidly to the value of the nominal oil viscosity. A trigonometric function is chosen to satisfy those conditions:

$$\mu_b(h_b) = \begin{cases} \mu & \text{for } \dfrac{h_b}{h_g} \leq h_\mu^* \\ \mu \cos\left(\dfrac{\pi}{2}\dfrac{\left(\frac{h_b}{h_g} - h_\mu^*\right)}{1 - h_\mu^*}\right)^2 & \text{for } \dfrac{h_b}{h_g} > h_\mu^* \end{cases} \tag{4.63}$$

in which h_μ^* is the value of the normalized clearance at which the viscosity starts to decrease. Unless otherwise specified, h_μ^* is taken to be 0.75. The resulting viscosity as a function of clearance is shown in Fig. 4.22.

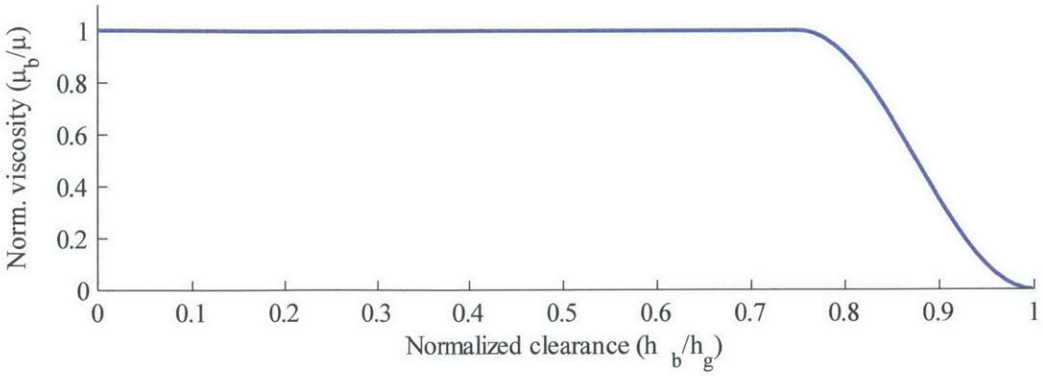

Fig. 4.22 Viscosity as a function of AS flank clearance

The leading flank hydrodynamic pressure is calculated in the same way as for the trailing flank. The only new difference added to the differences mentioned in section 4.2.7 is that the time derivative of the flank clearance must be changed to

$$\dot{h}_f(y_f) = \dot{h}_{f0} - y_f \dot{\alpha}_f$$

in which

$$\dot{h}_{f0} = -\dot{x}_g - H_l \dot{\alpha}_g \tag{4.64}$$

and

$$\dot{\alpha}_f = -\dot{\alpha}_g$$

4.2.9 Seal Flank Gas Force and Moment

In the case where the seal is in contact with the oil, the pressure at the full-film boundaries pressurizes the oil film and increases the hydrodynamic pressure (Fig. 4.23a). As discussed in the previous section, this effect can be added to the squeezing effect as Reynolds' equation is linear. When the seal loses contact with the film, the pressure distribution on the flank can be calculated from the gas flow through the open clearance (Fig. 4.23b), as shown in section 4.2.6 for the AS profile. Modeling the hydrodynamic pressure and the gas pressure independently would create a discontinuity in the forces and moment when the seal either enters the film or leaves the film. One could solve the exact velocity profile of the combined oil and gas flow at the interface by matching their velocity and shear stress at the interface (Fig. 4.24a). However, this would lead to

a cumbersome expression for the pressure gradient and would still require switching between two models. Instead, the apex seal model uses simplified velocity profiles by setting the velocity at the oil-gas interface to zero (Fig. 4.24b). This approximation gives an exact solution for an only-oil film. It also converges rapidly to the exact solution when the gas clearance increases to only a small fraction of the total clearance as the oil can be considered as a wall. Only when the gas film is very small that this simplified model does not lead to the exact solution, but predicts the correct trend, only the numerical constant in the final expression would differ. Furthermore, this situation typically only happens for one time step in a transition from one flank to the other. This simplified velocity profile approximation simplifies the expression for the pressure gradient significantly and makes the forces and moment continuous as a function of clearance.

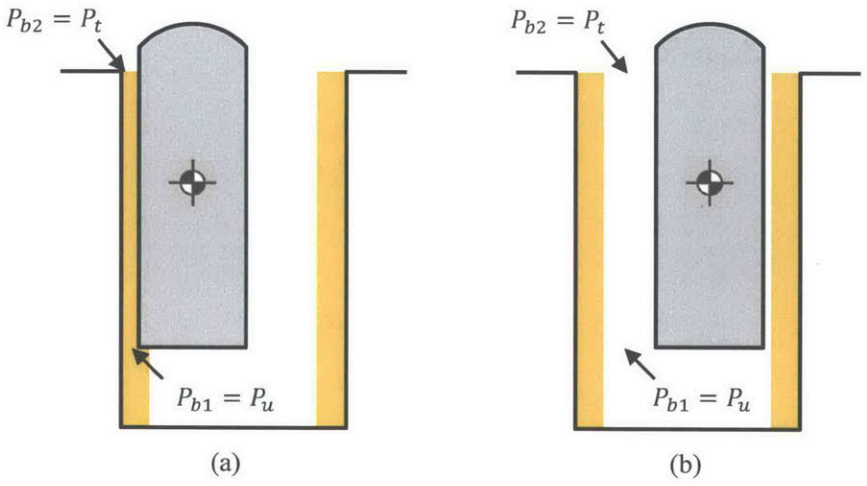

Fig. 4.23 Extreme conditions for flank gas pressure calculation: (a) seal in contact with the oil film and (b) large gas clearance

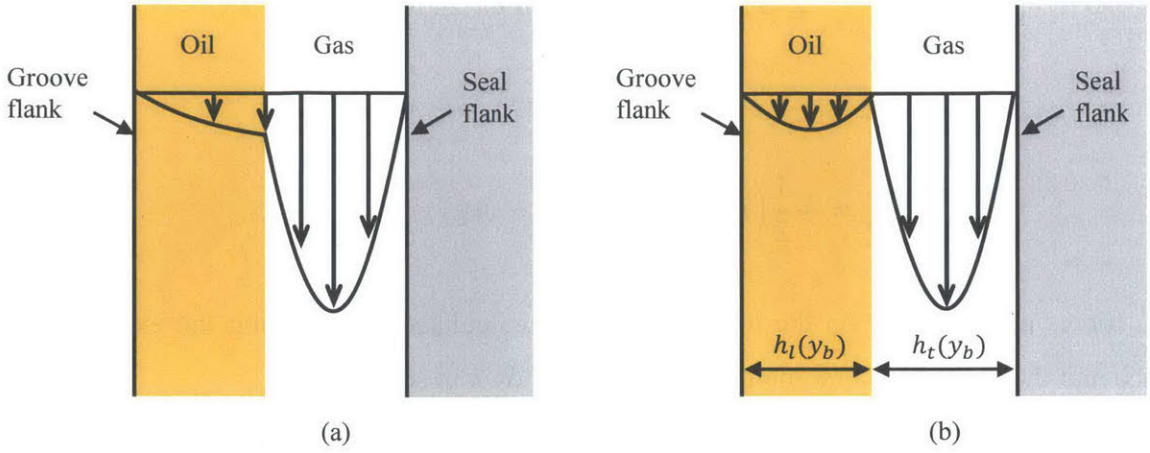

Fig. 4.24 Oil and gas velocity profiles in the seal-groove clearance, (a) exact and (b) simplified.

Under the simplified velocity profile approximation, the total volume flow rate through the interface (q_{lt}) is given by

$$q_{lt} = -\left(\frac{h_l^3(y_b)}{12\mu} + \frac{h_t^3(y_b)}{12\mu_g}\right)\frac{dP_{bg}}{dy_b} \tag{4.65}$$

in which $h_l(y_b)$ is the oil film thickness, h_t is the gas clearance, and P_{bg} is the pressure from the gas pressure effect. A new variable is introduced for the oil film thickness ($h_l(y_b)$) as it can decrease below the maximum oil film thickness on the flank (h_g) when the seal is in contact with the oil film. Assuming a constant total volume flow rate, integrating eq. (4.65) over y_b and applying the boundary conditions on pressure yields

$$q_{lt} = -\frac{P_{b2} - P_{b1}}{12\, J_{lt03}} \tag{4.66}$$

in which

$$J_{ltnm} = \int_{y_{b1}}^{y_{b2}} y_b^n \left(\frac{h_l^m(y_b)}{\mu} + \frac{h_t^m(y_b)}{\mu_g}\right)^{-1} dy_b$$

Again, forces and moment are calculated by integrating the pressure and carrying the integration by part to get an integral of the pressure gradient explicitly, as shown in eqs. (4.33) and (4.34):

$$F'_{bg,x_b} = P_{b2}y_{bo} - P_{b1}y_{bi} - (P_{b2} - P_{b1})\frac{J_{lt13}}{J_{lt03}}$$

$$F'_{bg,y_b} = 0 \tag{4.67}$$

$$F'_{bg,\alpha_b} = -\frac{1}{2}\left(P_{b2}y_{bo}^2 - P_{b1}y_{bi}^2 - (P_{b2} - P_{b1})\frac{J_{lt23}}{J_{lt03}}\right)$$

Finally, forces and moment on the leading flank are calculated by changing the expression for clearance and the x-force and moment directions, as shown in section 4.2.7.

4.2.10 Under-Seal Contact and Gas Forces

Two more forces are applied under the seal in addition to the spring force. First, gas in the groove pushes the seal radially outward. Second, if the seal enters the groove too deep, it compresses the springs completely and hits the bottom of the groove.

Gas force under the seal is calculated by multiplying the pressure under the seal (P_u) by the projected area ($A = T \times L$).

Contact force under the seal is modeled with the simplified Greenwood-Tripp correlation. In most conditions, the contact force under the seal is zero. Only when the seal enters the groove radially more than on the order of 1 mm that the contact force limits its displacement.

4.2.11 Gas Flow Sub-Model

An adequate prediction of gas flow is essential as it allows predicting correctly pressure in the AS groove that strongly impact seal dynamics. An adequate prediction of gas flow also allows predicting gas leakage and evaluating how good a design is at sealing the high pressure gases in the combustion chamber. In most conditions, the flow rate at the interfaces is correctly predicted by lubrication theory, which is used to calculate gas forces. However, for some conditions, the flow predicted by lubrication theory can exceed the flow through an isentropic orifice, which is not a physical situation. The flow through an isentropic orifice is set as the upper limit on mass flow rate.

All the dominant gas paths are considered in the model (Fig. 4.25). Gases can leak from one chamber to the other whenever there is a clearance between the seal profile and the rotor housing. Gases can flow in and out the groove through both flanks of the seal when the seal is not in contact with the oil film. Gases also leaks through the corner seal clearance, the side piece corner and the spark plug holes.

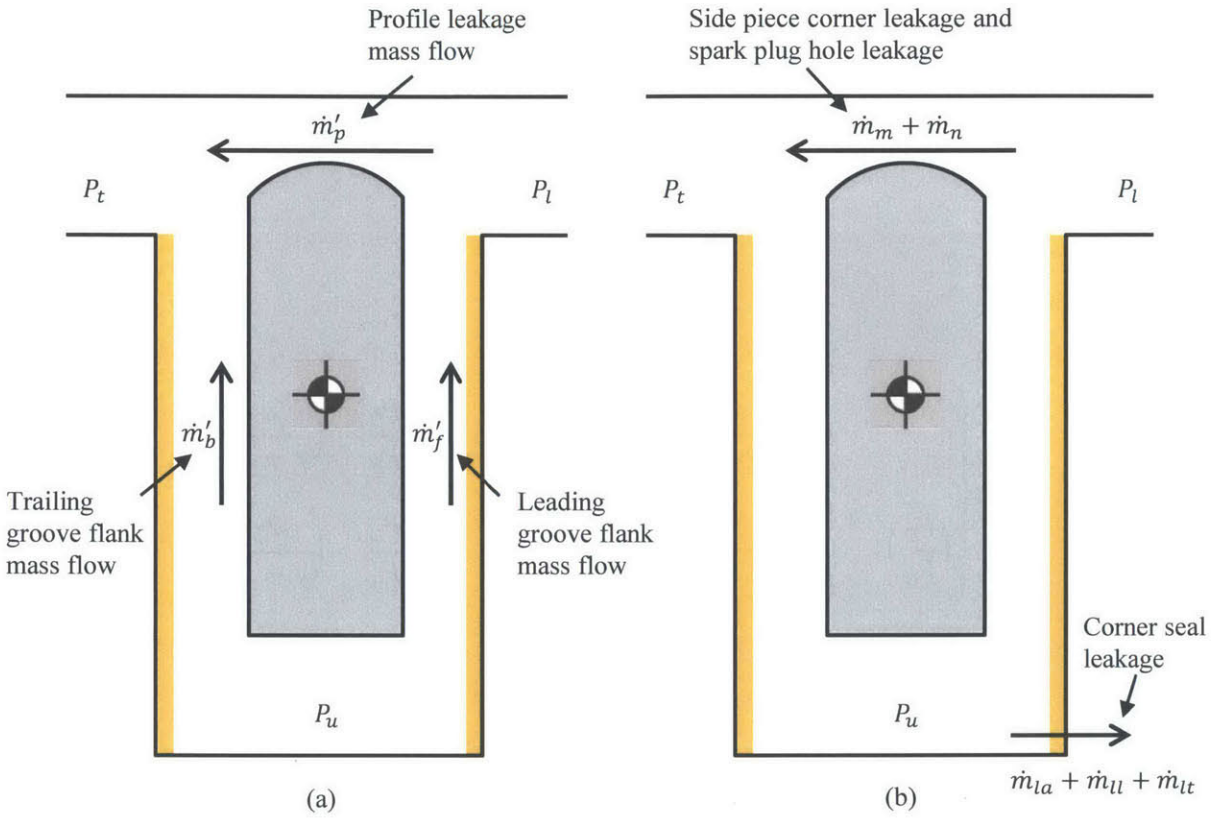

Fig. 4.25 (a) Mass flow rate per unit length around the AS and (b) additional leakage paths considered in the model.

Profile mass flow rate per unit length ($\dot{m}'_p$) is calculated based on the profile volume flow rate (q_d) calculated in eq. (4.44):

$$\dot{m}'_p = \rho_c q_d \tag{4.68}$$

Gas density (ρ_c) is approximated as

$$\rho_c = \frac{P_{c2} + P_{c1}}{2R_g T_g} \tag{4.69}$$

in which R_g is the gas constant and T_g is the groove temperature. Air properties are used throughout this thesis to estimate gas properties. The seal is assumed to be at the same temperature as the groove as they are generally in good thermal contact. The mass rate through the profile is limited to the flow through an isentropic orifice at the minimum clearance. The methodology to calculate an isentropic flow is widely available in the literature. The specific notation is taken from Tian [56]. In this case, the mass flow rate per unit length is given by

$$\dot{m}'_{p,max} = \frac{C_D h_{c0} P_U}{\sqrt{R_g T_U}} f_m$$

in which

$$f_m = \begin{cases} \gamma^{1/2} \left(\frac{2}{\gamma+1}\right)^{\frac{\gamma+1}{2(\gamma-1)}} & \text{for } \frac{P_D}{P_U} \leq \left(\frac{2}{\gamma+1}\right)^{\frac{\gamma}{\gamma-1}} \\ \left(\frac{P_D}{P_U}\right)^{1/\gamma} \left\{ \frac{2\gamma}{\gamma+1} \left[1 - \left(\frac{P_D}{P_U}\right)^{\frac{\gamma-1}{\gamma}} \right] \right\}^{1/2} & \text{for } \frac{P_D}{P_U} > \left(\frac{2}{\gamma+1}\right)^{\frac{\gamma}{\gamma-1}} \end{cases} \tag{4.70}$$

and

$$C_D = 0.85 - 0.25 \left(\frac{P_D}{P_U}\right)^2$$

In eq. (4.70), P_U is the upstream pressure, P_D is the downstream pressure, T_U is the upstream temperature, and γ is the ratio of specific heat. Upstream temperature is taken to be groove temperature. Upstream and downstream pressures alternate between leading and trailing chamber pressures depending on the crank angle. Finally, the first condition for f_m is a choked flow at the minimum section and the second condition for f_m is a subsonic flow with the downstream pressure as the static pressure at the minimum section.

Calculation of flow through the flank clearance is similar to calculation of flow through the profile clearance. Flow rate for force calculation given by eq. (4.65) includes both oil and gas.

The trailing flank volume flow rate of gas must be calculated separately for the gas flow model and is given by

$$q_b = -\frac{P_{b2} - P_{b1}}{12\mu_g J_{t03}}$$

in which (4.71)

$$J_{t03} = \int_{y_{b1}}^{y_{b2}} \frac{1}{h_t^3(y_b)} dy_b$$

Trailing flank mass flow rate per unit length ($\dot{m}_b'$) is given by

$$\dot{m}_b' = \rho_b q_b \tag{4.72}$$

in which gas density (ρ_b) is approximated as

$$\rho_b = \frac{P_{b2} + P_{b1}}{2R_g T_g} \tag{4.73}$$

Trailing flank mass flow rate is also limited to the isentropic mass flow rate through an orifice as given by eq. (4.70) with the clearance h_{c0} replaced by the minimum trailing flank clearance ($h_{b,min}$). The leading flank mass flow rate is calculated in the same way.

For both the leading and trailing flanks, gas flow does not directly mean leakage because part of the gas accumulated in the AS groove during compression and combustion returns to the high pressure chamber during expansion. For flank gas flow, leakage is defined as any flow toward the low pressure chamber.

The AS groove is connected to the corner seal (CS) groove with almost no restriction to the flow (Fig. 4.26). In turn, the corner seal groove exchanges gases with the rotor side and both adjacent chambers through the corner seal clearance (Fig. 4.27). The model approximates those flows as fully-developed flows between two parallel plates limited to the isentropic flow through an orifice (Fig. 4.28). The corner seal clearance is approximated as being uniform around the

circumference. In reality, the position of the corner seal is determined by a force balance that includes the pressure distribution around the corner seal, the friction force with the side housing, and the reaction forces with the two adjacent side seals. The displacement of the corner seal changes the leakage flow rate as the clearance has a higher power than the width in the fully-developed flow rate equation. This effect is neglected in the present model to avoid modeling all the gas seal simultaneously. The calculated leakage flow rate is still expected to be on the right order of magnitude.

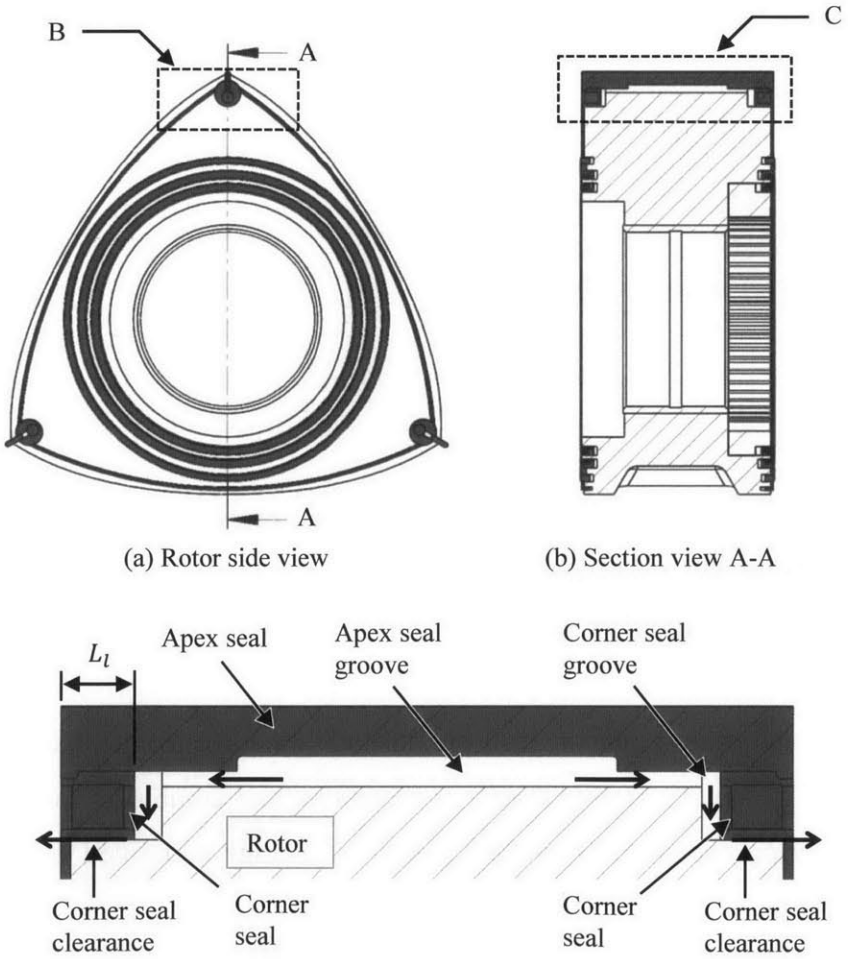

(a) Rotor side view

(b) Section view A-A

(c) Close-up view C of the apex seal, corner seals and their grooves

Fig. 4.26 Connection of apex groove to CS groove and leakage from CS groove to the side of the rotor through CS clearance.

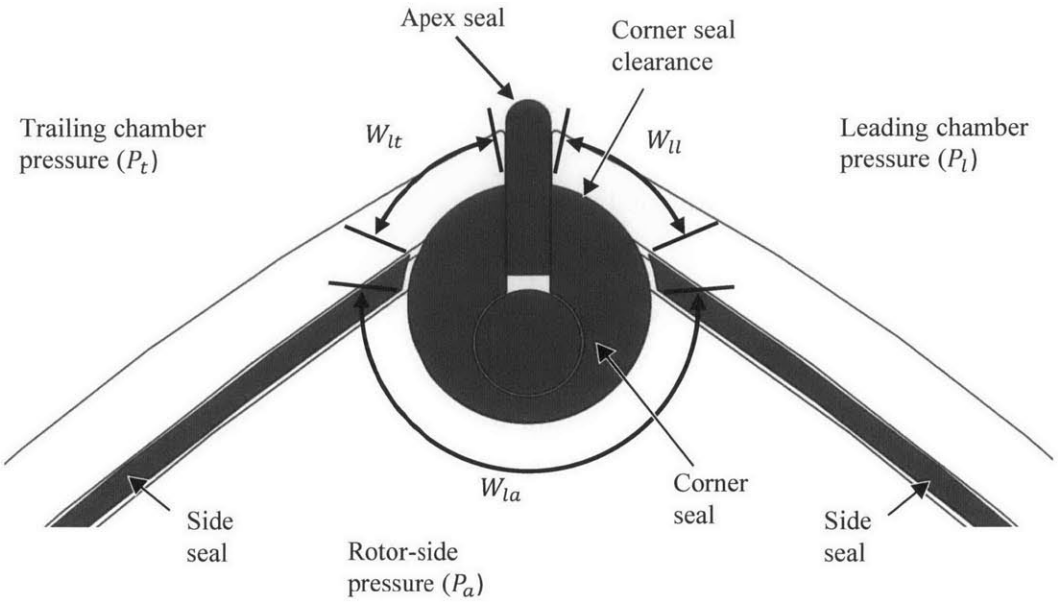

Fig. 4.27 Length of the sections of the CS clearance (close-up view B).

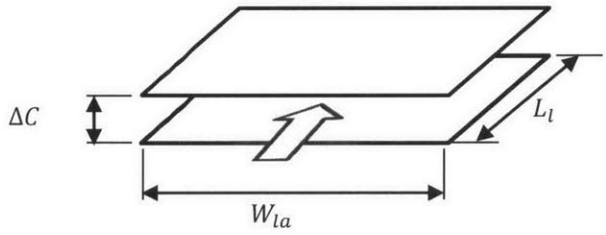

Fig. 4.28 Simplified flow model for the CS clearance.

Assuming a uniform corner seal clearance, the total volume flow rate to the rotor side from the corner seals on both sides of the rotor (Q_{la}) is given by

$$Q_{la} = 2W_{la}\frac{(\Delta C)^3}{12\mu_g}\frac{P_u - P_a}{L_l} \tag{4.74}$$

in which W_{la} is the arc length of the corner seal clearance connected to the rotor side, ΔC is the corner seal clearance, P_a is the pressure on rotor side, and L_l is the length of the corner seal clearance. The pressure on the side of the rotor is approximated as atmospheric as the side of the rotor is connected to either the exhaust or the intake port during most of the cycle.

Leakage mass flow rate to rotor side ($\dot{m}_{la}$) is given by

$$\dot{m}_{la} = \rho_{la} Q_{la} \tag{4.75}$$

in which gas density (ρ_{la}) is approximated as

$$\rho_{la} = \frac{P_u + P_a}{2R_g T_g} \tag{4.76}$$

Again, mass flow rate is limited to an isentropic flow through an orifice. Mass flow rate to the leading chamber ($\dot{m}_{ll}$) and mass flow rate to the trailing chamber ($\dot{m}_{lt}$) are calculated in the same way, but changing the width and using appropriate pressures to calculate density. As is done for flank leakage, leakage through the corner seal clearance is defined as flow toward the low pressure chamber.

The side piece avoids leaving a clearance all along the AS end (Fig. 4.29). However, there is an orifice left open even when the side piece moves to close that clearance. The side piece orifice area (A_m) is approximated to be constant and is taken to be 0.04 mm² unless otherwise specified. Leakage mass flow rate through the side piece orifice is calculated from an isentropic flow through an orifice, as shown in eq. (4.70), between the leading and trailing chambers.

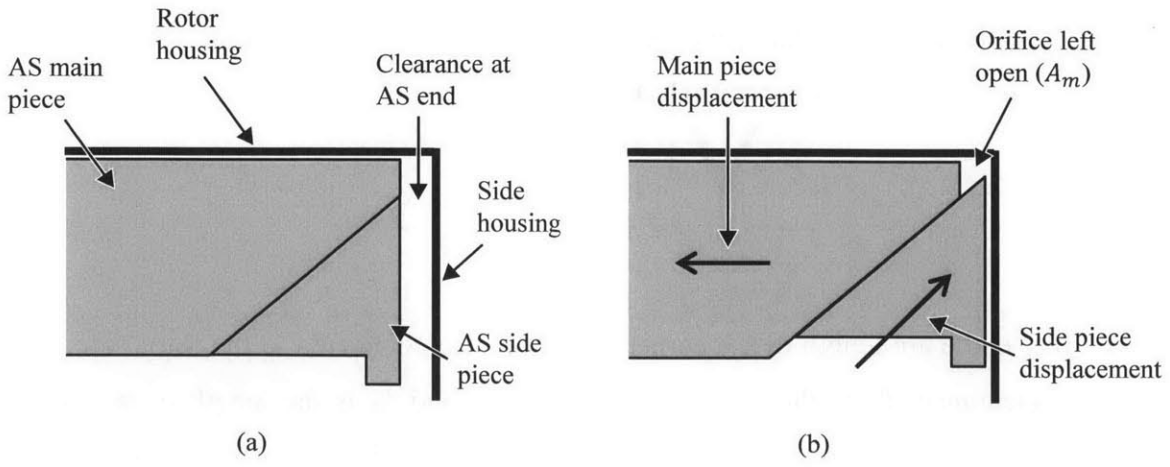

Fig. 4.29 (a) AS end clearance and (b) orifice left once the side piece has closed the AS end clearance

The last leakage path considered is the leakage through the spark plug holes. When the apex seal passes on the leading or trailing spark plug hole, the model calculates the minimum area open for the flow and computes mass flow rate leakage based on an isentropic flow through that area.

4.2.12 Beam Model

The objective of this section is to derive the error function for the seal position and deformation given by the finite element form:

$$\{G_d\} = [K_d]\{X_d\} + [M_d]\{\ddot{X}_d\} - \{F_d\} \tag{4.77}$$

in which G_d is the error vector, X_d is the displacement unknown vector containing all the information necessary to reconstruct the seal displacements (x_g, y_g, and α_g) as a function of the position along the seal (z), $\ddot{X}_d$ is the second derivative of the unknown vector, K_d is the stiffness matrix, M_d is the mass matrix, and F_d is the force vector.

The beam finite element method to derive the error function is adapted from a method invented by Baelden [47] for conformability of piston rings. The method uses coarse beam elements with polynomial interpolation to calculate the displacements on a finer contact grid. This method is the most adapted method to handle the inherent multiscale modeling of the deformable AS dynamics. AS geometry is simpler, when compared to piston rings, as the AS can be modeled as a straight beam so the displacements are decoupled. However, the model has to handle discontinuities in the neutral axis due to section changes (Fig. 4.30). Those discontinuities are handled by introducing two set of nodes: the U-nodes and the X-nodes. U-nodes are the nodes at the end of each beam elements. X-nodes are the intermediate nodes that connect the adjacent beam elements. Values at the X-nodes are the unknowns contained in the unknown vector X_d. From the X-node values, the model can calculate U-node positions and their derivatives from which the shape and position of the seal can be reconstructed. In this section, the lateral displacement (x_g) is first used to show the derivation of the terms of the mass and stiffness matrices and the terms of the load vector. The method is then extended to the radial displacement (y_g) and the section tilt (α_g). Finally, the switch from U-node displacements to X-node values is explained to get to the desired form of the error equation.

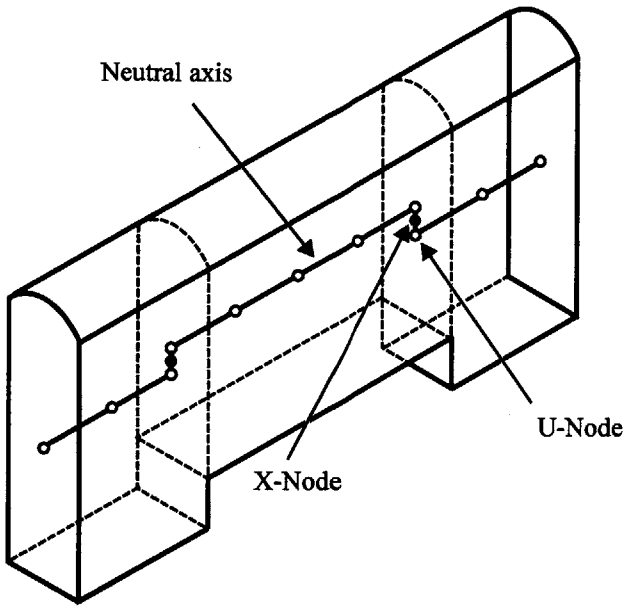

Fig. 4.30 AS neutral axis and difference between X and U nodes.

First, the seal neutral axis is split in a series of beam elements (on the order of 10). For a given element, the lateral displacement (x_g) is given as a function of an isoparametric variable (η), as shown in Fig. 4.31. The isoparametric variable (η) is related to position along the element by

$$z = L_c\eta \tag{4.78}$$

in which L_c is the length of the beam element.

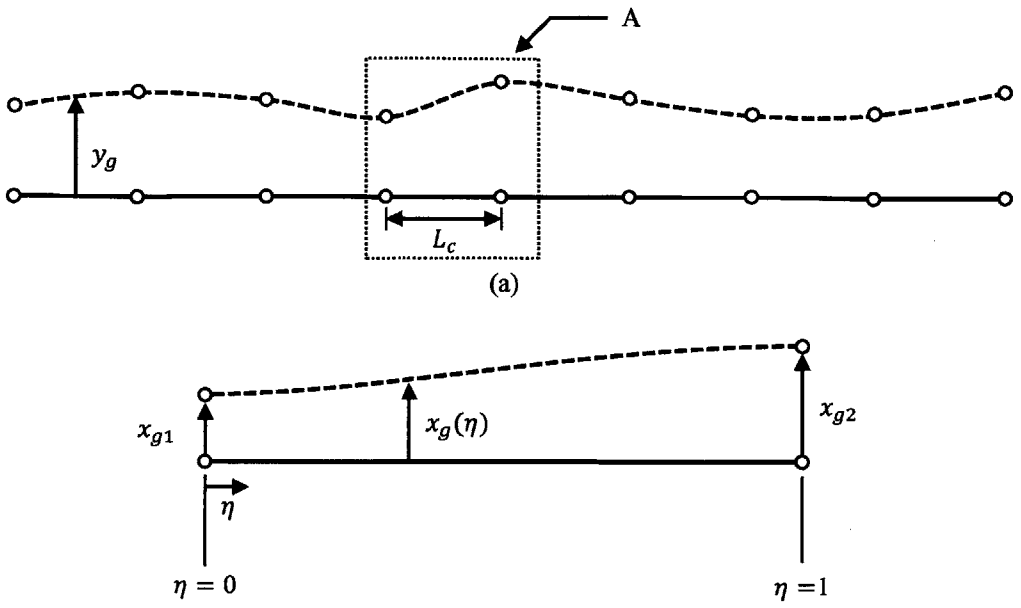

Fig. 4.31 Lateral displacement and close-up view of one beam element

The radial displacement is mainly caused by the bending moment. The shear force of the section generates much smaller displacement and could be neglected in order to only reconstruct the displacement in a single straight beam element. However, the shear force is needed at the neutral-axis discontinuities in order to switch between U-node and X-node values. In order to calculate the shear force locally, the radial displacement is taken to be the sum of the two modes of deformation:

$$x_g(\eta) = x_m(\eta) + x_v(\eta) \tag{4.79}$$

in which x_m is the lateral displacement caused by the bending moment and the rigid-body motion, and x_v is the lateral displacement caused only by the shear force. In order for the bending moment to be continuous at the nodes, x_m is described by Hermite quintic polynomials (N_Q):

$$x_m(\eta) = \sum_{k=1}^{6} N_{Q,k}(\eta) U_{xm,k} \tag{4.80}$$

in which $U_{xm,k}$ refers to the k[th] components of the nodal x_m displacement vector $\{U_{xm}\}$ given by

$$\{U_{xm}\} = \begin{Bmatrix}\{U_{xm}\}_1 \\ \{U_{xm}\}_2\end{Bmatrix} = \left\{x_{m1}, \frac{\partial x_{m1}}{\partial \eta}, \frac{\partial^2 x_{m1}}{\partial \eta^2}, x_{m2}, \frac{\partial x_{m2}}{\partial \eta}, \frac{\partial^2 x_{m2}}{\partial \eta^2}\right\}^T \tag{4.81}$$

in which the subscripts 1 and 2 refer to the first and second nodes of the element respectively, and the superscript T refers to matrix transpose. The vector $\{U_{xm1}\}$ contains the three displacements of the first node and $\{U_{xm2}\}$ the three displacements of the second node. Quintic Hermite polynomials are designed to decompose the displacement within the element in 6 shape functions (Fig. 4.32) and are given by [47]

$$\begin{aligned}
N_{Q,1} &= 1 - 10\eta^3 + 15\eta^4 - 6\eta^5 \\
N_{Q,2} &= L_c(\eta - 6\eta^3 + 8\eta^4 - 3\eta^5) \\
N_{Q,3} &= L_c^2\left(\frac{\eta^2}{2} - \frac{3\eta^3}{2} + \frac{3\eta^4}{2} - \frac{\eta^5}{2}\right) \\
N_{Q,4} &= 10\eta^3 - 15\eta^4 + 6\eta^5 \\
N_{Q,5} &= L_c(-4\eta^3 + 7\eta^4 - 3\eta^5) \\
N_{Q,6} &= L_c^2\left(\frac{\eta^3}{2} - \eta^4 + \frac{\eta^5}{2}\right)
\end{aligned} \tag{4.82}$$

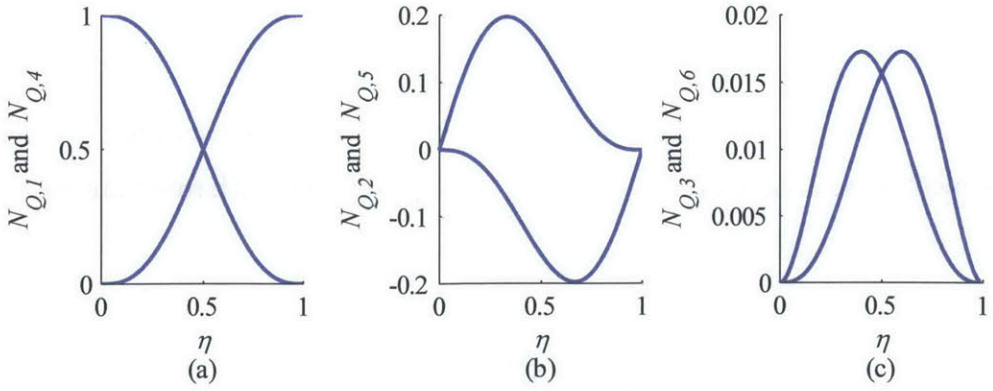

Fig. 4.32 Quintic Hermite polynomials for a unit length element

Hermite cubic polynomials (N_C) are sufficient to get a continous shear force at the nodes. Thus, x_v is described by

$$x_v(\eta) = \sum_{k=1}^{4} N_{C,k}(\eta) U_{xv,k} \tag{4.83}$$

in which $U_{xv,k}$ refers to th k[th] components of the nodal x_v displacement vector $\{U_{xv}\}$ given by

$$\{U_{xv}\} = \begin{Bmatrix} \{U_{xv}\}_1 \\ \{U_{xv}\}_2 \end{Bmatrix} = \left\{ x_{v1}, \frac{\partial x_{v1}}{\partial \eta}, x_{v2}, \frac{\partial x_{v2}}{\partial \eta} \right\}^T \tag{4.84}$$

Cubic Hermite polynomials are constructed to decomposed the displacement within the element in 4 shape functions (Fig. 4.33) and are given by

$$\begin{aligned} N_{C,1} &= 1 - 3\eta^2 + 2 \\ N_{C,2} &= L_c(\eta - 2\eta^2 + \eta^3) \\ N_{C,3} &= 3\eta^2 - 2\eta^3 \\ N_{C,4} &= L_c(-\eta^2 + \eta^3) \end{aligned} \tag{4.85}$$

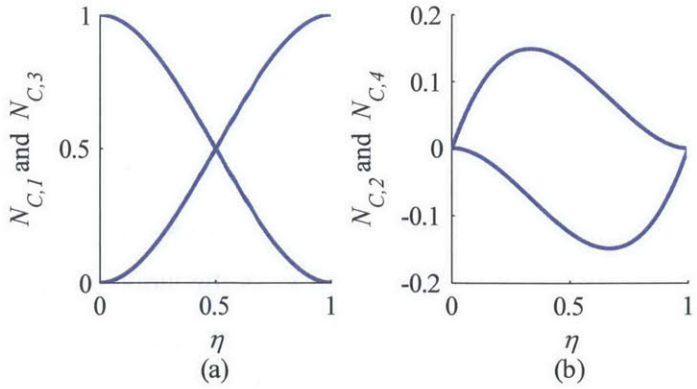

Fig. 4.33 Cubic Hermite polynomials for a unit length element

Stiffness and mass matrices as well as the load vector are derived based on Euler-Lagrange equation, for which the i[th] term is given by

$$\frac{d}{dt}\frac{\partial \mathcal{L}}{\partial \dot{U}_i} - \frac{\partial \mathcal{L}}{\partial U_i} = F_i \tag{4.86}$$

in which $\mathcal{L}$ is the Lagrangian function, U_i is the i[th] displacement, and F_i is the i[th] generalized force obtain from the work done by external forces ($\mathcal{W}$) during a virtual displacement, written as

$$F_i = \frac{\partial \mathcal{W}}{\partial U_i} \tag{4.87}$$

Considering strain energy ($\mathcal{U}$) and kinetic energy ($\mathcal{K}$), the Lagrangian function is given by

$$\mathcal{L} = -\mathcal{U} + \mathcal{K} \tag{4.88}$$

Replacing in eq. (4.86) and rearranging yields

$$0 = \frac{\partial \mathcal{U}}{\partial U_i} + \frac{d}{dt}\frac{\partial \mathcal{K}}{\partial \dot{U}_i} - \frac{\partial \mathcal{W}}{\partial U_i} \tag{4.89}$$

The goal is to derive the expression of those derivatives as a function of the node displacements. First the strain energy for x_g displacement can be written as

$$\mathcal{U} = \int_0^{L_c} \frac{1}{2} M_x(\eta)\kappa_x(\eta)dz + \int_0^{L_c} \frac{1}{2} V_x(\eta)\gamma_x(\eta)dz \tag{4.90}$$

in which M_x is the moment around the y-axis due to x-curvature, κ_x is the projection of the curvature in the x-z plane, V_x is the shear force, and γ_x is the slope due to shear. By definition, the moment and curvature are calculated from the x_m displacements and shear force and shear slope are calculated from x_v displacements. Replacing moment, curvature, shear force and shear slope, and changing integration variable to η yields

$$\mathcal{U} = \frac{EL_c}{2}\int_0^1 I_x\left(\frac{\partial^2 x_m}{\partial\eta^2}\right)^2 d\eta + \frac{k_a G L_c}{2}\int_0^1 A\left(\frac{\partial x_v}{\partial\eta}\right)^2 d\eta \tag{4.91}$$

in which E is Young's modulus, I_x is the section moment of inertia for the x-displacement, k_a is the form factor to calculate shear deflection, G is the shear modulus, and A is the cross-section area. Section properties are left inside the integral so the model is flexible and could admit variable section along the element. Displacements can be replaced by the derivatives of the Hermite polynomials:

$$\mathcal{U} = \frac{E}{2L_c^3}\int_0^1 I_x\left(\sum_{k=1}^{6}\frac{\partial^2 N_{Q,k}}{\partial\eta^2}U_{xm,k}\right)^2 d\eta + \frac{k_a G}{2L_c}\int_0^1 A\left(\sum_{k=1}^{4}\frac{\partial N_{C,k}}{\partial\eta}U_{xv,k}\right)^2 d\eta \tag{4.92}$$

This expression can be rewritten in the form

$$\mathcal{U} = \frac{1}{2}\{U_{xm}\}^T[K_{xm}]\{U_{xm}\} + \frac{1}{2}\{U_{xv}\}^T[K_{xv}]\{U_{xv}\} \tag{4.93}$$

in which $[K_{xm}]$ is the bending stiffness matrix, and $[K_{xv}]$ is the shear stiffness matrix. The terms of the 6x6 bending stiffness matrix are given by

$$K_{xm,ij} = \frac{E}{L_c^3}\int_0^1 I_x\frac{\partial^2 N_{Q,i}}{\partial\eta^2}\frac{\partial^2 N_{Q,j}}{\partial\eta^2}d\eta \tag{4.94}$$

The terms of the 4x4 shear stiffness matrix are given by

$$K_{xv,ij} = \frac{k_a G}{L_c}\int_0^1 A\frac{\partial N_{C,i}}{\partial\eta}\frac{\partial N_{C,j}}{\partial\eta}d\eta \tag{4.95}$$

As the stiffness matrix is symmetrical, taking the derivative of eq. (4.93) with respect to the ith terms of the $\{U_{xm}\}$ displacements yields

$$\frac{\partial\mathcal{U}}{\partial U_{xm,i}} = \sum_j K_{xm,ij}U_{xm,j} \tag{4.96}$$

Similarly, the derivatives of the $\{U_{xv}\}$ displacements are given by

$$\frac{\partial \mathcal{U}}{\partial U_{xv,i}} = \sum_j K_{xv,ij} U_{xv,j} \tag{4.97}$$

Second, the kinetic energy can be written as

$$\mathcal{K} = \frac{L_c}{2} \int_0^1 m'(\dot{x}_m(\eta))^2 d\eta \tag{4.98}$$

in which m' is the AS mass per unit length. The contribution of x_v in the kinetic energy is neglected as it is much smaller than x_m. Replacing the velocity by Hermite polynomials in the expression of the kinetic energy yields

$$\mathcal{K} = \frac{L_c}{2} \int_0^1 m' \left(\sum_{k=1}^{6} N_{Q,k}(\eta) \dot{U}_{xm,k} \right)^2 d\eta \tag{4.99}$$

This expression can be rewritten in the form

$$\mathcal{K} = \frac{1}{2} \{\dot{U}_{xm}\}^T [M_{xm}] \{\dot{U}_{xm}\} \tag{4.100}$$

in which $[M_{xm}]$ is the 6x6 mass matrix for x-displacements, and its terms are given by

$$M_{xm,ij} = L_c \int_0^1 m' N_{Q,i} N_{Q,j} d\eta \tag{4.101}$$

Taking the derivative of eq. (4.100) with respect to the i^{th} terms of the time derivative of the $\{U_{xm}\}$ displacements yields

$$\frac{\partial \mathcal{K}}{\partial \dot{U}_i} = \sum_j M_{xm,ij} \dot{U}_{xm,j} \tag{4.102}$$

Taking the time derivative of eq. (4.102) yields the kinetic energy term in Euler-Lagrange equation

$$\frac{d}{dt}\frac{\partial \mathcal{K}}{\partial \dot{U}_i} = \sum_j M_{xm,ij}\ddot{U}_{xm,j} \tag{4.103}$$

Third, for the load vector, work from external forces can be written as

$$\mathcal{W} = L_c \int_0^1 F'_{x_g} x_g(\eta) d\eta \tag{4.104}$$

in which F'_{x_g} is the sum of the forces along x_g per unit length calculated in sections 4.2.2 to 4.2.9. Splitting x_g into x_m and x_v, and replacing by their respective Hermite polynomial expressions yields

$$\mathcal{W} = L_c \int_0^1 F'_{x_g} \left(\sum_{k=1}^{6} N_{Q,k}(\eta) U_{xm,k} \right) d\eta + L_c \int_0^1 F'_{x_g} \left(\sum_{k=1}^{4} N_{C,k}(\eta) U_{xv,k} \right) d\eta \tag{4.105}$$

This expression can be rewritten in the form

$$\mathcal{W} = \{U_{xm}\}^T \{F_{xm}\} + \{U_{xv}\}^T \{F_{xv}\} \tag{4.106}$$

in which the 6 terms of the x-bending load vector $\{F_{xm}\}$ are given by

$$F_{xm,i} = L_c \int_0^1 F'_{x_g} N_{Q,i} d\eta \tag{4.107}$$

and the 4 terms of the x-shear load vector $\{F_{xv}\}$ are given by

$$F_{xv,i} = L_c \int_0^1 F'_{x_g} N_{C,i} d\eta \tag{4.108}$$

Taking the derivative of eq. (4.106) with respect to the i[th] terms of the $\{U_{xm}\}$ displacements yields

$$\frac{\partial \mathcal{W}}{\partial U_{xm,i}} = F_{xm,i} \tag{4.109}$$

Similarly, the derivatives of the $\{U_{xv}\}$ displacements are given by

$$\frac{\partial \mathcal{W}}{\partial U_{xv,i}} = F_{xv,i} \tag{4.110}$$

All the components are derived for the x-displacements in one element, and can be assembled in the desired error function form based on Euler-Lagrange equation:

$$\{0\} = [K_{xm}]\{U_{xm}\} + [M_{xm}]\{\ddot{U}_{xm}\} - \{F_{xm}\} \tag{4.111}$$

and

$$\{0\} = [K_{xv}]\{U_{xv}\} + [M_{xv}]\{\ddot{U}_{xv}\} - \{F_{xv}\} \tag{4.112}$$

For the y-displacements, $y_g(\eta)$ is splitted a component due to bending ($y_m(\eta)$) and component due to shear ($y_m(\eta)$):

$$y_g(\eta) = y_m(\eta) + y_v(\eta) \tag{4.113}$$

This decomposition is introduced for symmetry between the x and y displacements. Displacement vector are introduced for both components:

$$\{U_{ym}\} = \begin{Bmatrix} \{U_{ym}\}_1 \\ \{U_{ym}\}_2 \end{Bmatrix} = \left\{ y_{m1}, \frac{\partial y_{m1}}{\partial \eta}, \frac{\partial^2 y_{m1}}{\partial \eta^2}, y_{m2}, \frac{\partial y_{m2}}{\partial \eta}, \frac{\partial^2 y_{m2}}{\partial \eta^2} \right\}^T \tag{4.114}$$

and

$$\{U_{yv}\} = \begin{Bmatrix} \{U_{yv}\}_1 \\ \{U_{yv}\}_2 \end{Bmatrix} = \left\{ y_{v1}, \frac{\partial y_{v1}}{\partial \eta}, y_{v2}, \frac{\partial y_{v2}}{\partial \eta} \right\}^T \tag{4.115}$$

Derivation of the mass and stiffness matrices as well as the load vector is the same as for the x-displacements, except the moment of inertia is replaced by I_y and the external force by F'_{y_g}.

For the tilt of the section (α_g), cubic interpolation is sufficient as it guarantee that the torsion is continous at the nodes. Section tilt along the seal is described by

$$\alpha_g(\eta) = \sum_{k=1}^{4} N_{C,k}(\eta) U_{\alpha,k} \tag{4.116}$$

in which $\{U_\alpha\}$ is given by

$$\{U_\alpha\} = \begin{Bmatrix} \{U_\alpha\}_1 \\ \{U_\alpha\}_2 \end{Bmatrix} = \left\{ \alpha_{g1}, \frac{\partial \alpha_{g1}}{\partial \eta}, \alpha_{g2}, \frac{\partial \alpha_{g2}}{\partial \eta} \right\}^T \tag{4.117}$$

Derivation of stiffness and mass matrices as well as load vector is similar to the x and y displacement due to shear (x_v and y_v). The terms of the 4x4 stiffness matrix are given by

$$K_{\alpha,ij} = \frac{G}{L_c} \int_0^1 J_a \frac{\partial N_{C,i}}{\partial \eta} \frac{\partial N_{C,j}}{\partial \eta} d\eta \tag{4.118}$$

in which J_a is the torsion constant. The terms of the 4x4 mass matrix are given by

$$M_{\alpha,ij} = L_c \int_0^1 I'_\alpha N_{C,i} N_{C,j} d\eta \tag{4.119}$$

in which I'_α is the moment of inertia per unit length. Finally, the 4 terms of the load vector are given by

$$F_{\alpha,i} = L_c \int_0^1 F'_{\alpha_g} N_{C,i} d\eta \tag{4.120}$$

Before switching to the X-node values, the mass, stiffness and load matrices must be assembled for a displacement vector containing all the displacements. This combined displacement vector $\{U\}$ contains 24 terms and is given by

$$\{U\} = \begin{Bmatrix} \{U\}_1 \\ \{U\}_2 \end{Bmatrix}$$

in which

$$\{U\}_1 = \begin{Bmatrix} \{U_{xm}\}_1 \\ \{U_{xv}\}_1 \\ \{U_{ym}\}_1 \\ \{U_{yv}\}_1 \\ \{U_{\alpha}\}_1 \end{Bmatrix} \; ; \quad \{U\}_2 = \begin{Bmatrix} \{U_{xm}\}_2 \\ \{U_{xv}\}_2 \\ \{U_{ym}\}_2 \\ \{U_{yv}\}_2 \\ \{U_{\alpha}\}_2 \end{Bmatrix} \tag{4.121}$$

The combined stiffness matrix is given by

$$[K_U] = \begin{bmatrix} [K_U]_{11} & [K_U]_{12} \\ [K_U]_{21} & [K_U]_{22} \end{bmatrix} \tag{4.122}$$

in which the 4 terms are given by

$$[K_U]_{pq} = \begin{bmatrix} [K_{xm}]_{pq} & & & & \\ & [K_{xv}]_{pq} & & & \\ & & [K_{ym}]_{pq} & & \\ & & & [K_{yv}]_{pq} & \\ & & & & [K_{\alpha}]_{pq} \end{bmatrix} \tag{4.123}$$

and the indices p and q run from 1 to 2. The terms of the stiffness matrix of each displacement are obtained by splitting the matrices in four. For example, the terms of the stiffness matrix $[K_{xm}]$ are obtained from

$$[K_{xm}] = \begin{bmatrix} [K_{xm}]_{11} & [K_{xm}]_{12} \\ [K_{xm}]_{21} & [K_{xm}]_{22} \end{bmatrix} \tag{4.124}$$

in which $[K_{xm}]_{pq}$ are 3x3 matrices. The terms of the combined mass matrix are identical to the combined stiffness matrix. The load vector is given by

$$\{F_U\} = \begin{Bmatrix} \{F_U\}_1 \\ \{F_U\}_2 \end{Bmatrix} \tag{4.125}$$

in which the 2 terms are given by

$$\{F_U\}_p = \begin{Bmatrix} \{F_{xm}\}_p \\ \{F_{xv}\}_p \\ \{F_{ym}\}_p \\ \{F_{yv}\}_p \\ \{F_\alpha\}_p \end{Bmatrix} \tag{4.126}$$

Those components can be assembled in the desired error function form for the combined displacements:

$$\{0\} = [K_U]\{U\} + [M_U]\{\ddot{U}\} - \{F_U\} \tag{4.127}$$

To connect the elements the X-node values are defined halfway between the U-node of the previous beam element and the U-node of the following element (Fig. 4.34).

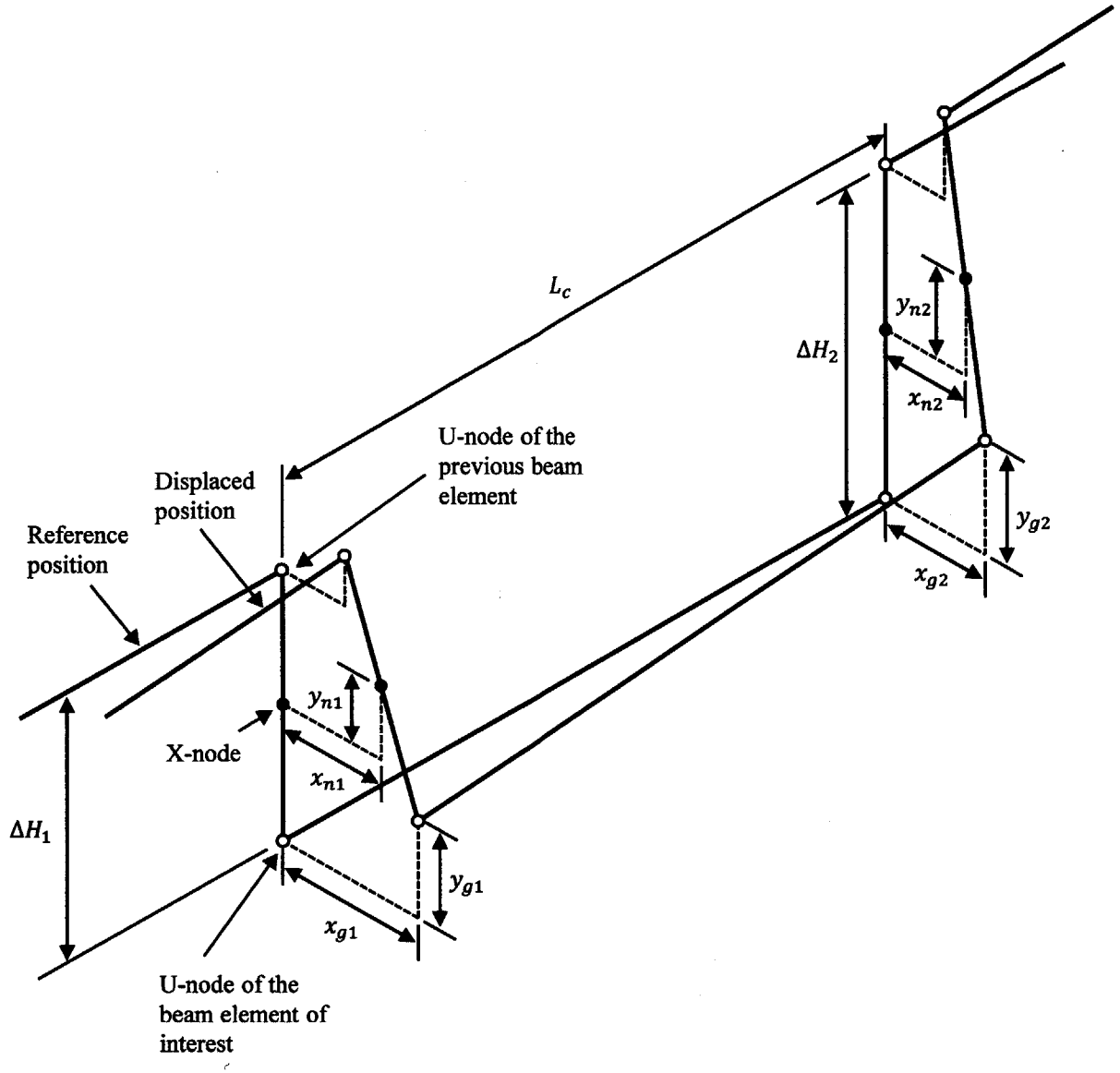

Fig. 4.34 Isometric view of the neutral axis of one beam element for the conversion between U-node and X-node displacements.

The unknown vector X for one beam element is composed of displacements, forces and moments at the first and second X-nodes. The combined unknown vector is given by

$$\{X\} = \begin{Bmatrix} \{X\}_1 \\ \{X\}_2 \end{Bmatrix} \tag{4.128}$$

in which

$$\{X\}_1 = \begin{Bmatrix} \{X_{xmn}\}_1 \\ \{X_{xvn}\}_1 \\ \{X_{ymn}\}_1 \\ \{X_{yvn}\}_1 \\ \{X_{an}\}_1 \end{Bmatrix} \quad ; \quad \{U\}_2 = \begin{Bmatrix} \{X_{xmn}\}_2 \\ \{X_{xvn}\}_2 \\ \{X_{ymn}\}_2 \\ \{X_{yvn}\}_2 \\ \{X_{an}\}_2 \end{Bmatrix}$$

The unknown vector at one node for x-displacements due to bending moment is given by

$$\{X_{xmn}\}_p = \left\{x_{mn,p}, \frac{\partial x_{mn,p}}{\partial \eta}, M_{xn,p}\right\}^T \tag{4.129}$$

in which $x_{mn,p}$ is the x-displacement of the X-node due to bending moment and M_{xn} is the bending moment at the X-node. The subscript can be 1 or 2 and refers to the first or the second node of the beam element of interest. The displacement of the X-node can be related to the displacement of the U-node by

$$x_{mn,p} = x_{m,p} - \alpha_{g,p} \frac{\Delta H_p}{2} \tag{4.130}$$

in which ΔH_p is the height of the discontinuity in the neutral axis between the neighbouring elements and the beam element of interest. Positive directions of ΔH_1 and ΔH_2 are shown in Fig. 4.34. The second term of eq. (4.130) is the difference in x-displacement between the X and U nodes due to twisting and shows one of the reason why the two set of nodes have been introduced. The derivative is approximated to be continuous and

$$\frac{\partial x_{mn,p}}{\partial \eta} = \frac{\partial x_{m,p}}{\partial \eta} \tag{4.131}$$

The second derivative is replaced by the moment at the X-node because it needs to be continuous from one beam element to the other so that the net moment on the node is zero. From a force balance on a node (Fig. 4.35), the moment at the node is given by

$$M_{xn,p} = M_{x,p} = EI_x \frac{\partial^2 x_{m,p}}{\partial \eta^2} \tag{4.132}$$

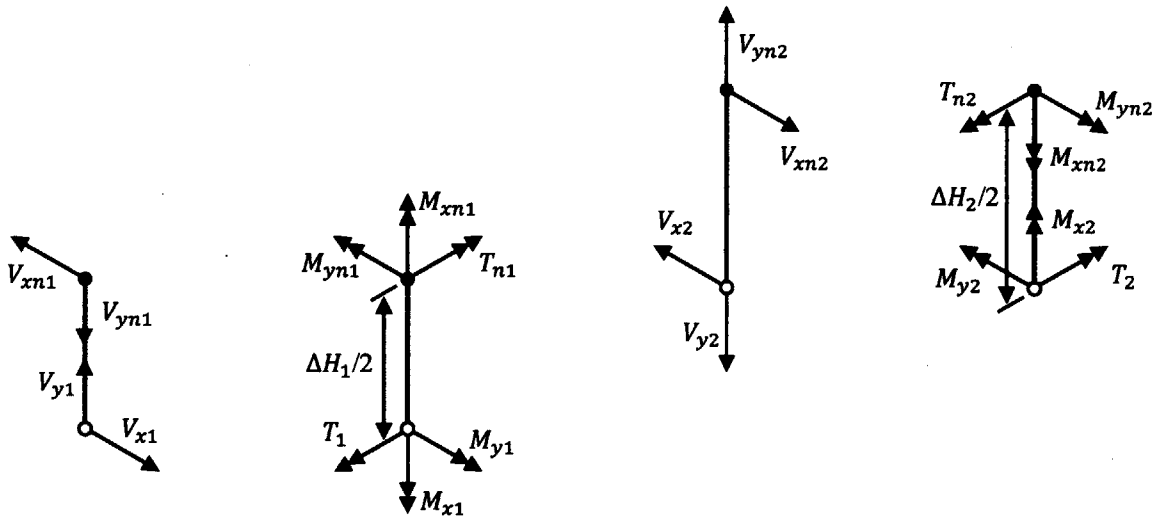

Fig. 4.35 Force and moment balance on the first and second nodes of a beam element

The unknown vector at one node for x-displacements due to shear force is given by

$$\{X_{xvn}\}_p = \{x_{vn,p}, V_{xn,p}\}^T \tag{4.133}$$

in which $x_{vn,p}$ is the x-displacement of the X-node due to shear force and $V_{xn,p}$ is the shear force at the X-node. As the twisting effect is included in x_{mn}, the x-displacement due to shear force is the same for the X-node and the U-node:

$$x_{vn,p} = x_{v,p} \tag{4.134}$$

The shear force at the node is given by

$$V_{xn,p} = V_{x,p} = k_a AG \frac{\partial x_{v,p}}{\partial \eta} \tag{4.135}$$

Similarly, the y-displacements are given by

$$\{X_{ymn}\}_p = \left\{y_{mn,p}, \frac{\partial y_{mn,p}}{\partial \eta}, M_{yn,p}\right\}^T = \left\{y_{m,p}, \frac{\partial y_{m,p}}{\partial \eta}, EI_y \frac{\partial^2 y_{m,p}}{\partial \eta^2}\right\}^T \tag{4.136}$$

and

$$\{X_{ymn}\}_p = \{y_{vn,p}, V_{yn,p}\}^T = \left\{y_{v,p}, k_a AG \frac{\partial y_{v,p}}{\partial \eta}\right\}^T \tag{4.137}$$

The α-displacements are given by

$$\{X_{ymn}\}_p = \{\alpha_{n,p}, T_{n,p}\}^T \tag{4.138}$$

The section tilt is the same at the X and U nodes:

$$\alpha_{n,p} = \alpha_{g,p} \tag{4.139}$$

The torque at the X-node is given by

$$T_{n,p} = T_p + \frac{\Delta H_p}{2} V_{x,p} = GJ_a \frac{\partial \alpha_{v,p}}{\partial \eta} + \frac{\Delta H_p}{2} k_a AG \frac{\partial x_{v,p}}{\partial \eta} \tag{4.140}$$

The transformation from U-displacements to the unknown vector X can be summarized by

$$\{X\} = [T_{UX}]\{U\} \tag{4.141}$$

in which the transformation matrix $[T_{UX}]$ can be decomposed in one matrix for each node:

$$[T_{UX}] = \begin{bmatrix} [T_{UX}]_{11} & [0] \\ [0] & [T_{UX}]_{22} \end{bmatrix} \tag{4.142}$$

and the matrix for each of the two nodes is given by

$$[T_{UX}]_{pp} = \begin{bmatrix} 1 & & & & & & & & & & & & -\frac{\Delta H_1}{2} \\ & 1 & & & & & & & & & & & \\ & & EI_x & & & & & & & & & & \\ & & & 1 & & & & & & & & & \\ & & & & k_aAG & & & & & & & & \\ & & & & & 1 & & & & & & & \\ & & & & & & 1 & & & & & & \\ & & & & & & & EI_y & & & & & \\ & & & & & & & & 1 & & & & \\ & & & & & & & & & k_aAG & & & \\ & & & & & & & & & & 1 & & \\ & & & k_aAG\left(\frac{\Delta H_1}{2}\right) & & & & & & & & & GJ_a \end{bmatrix} \tag{4.143}$$

Under this transformation, the error function for one beam element becomes

$$\{0\} = [K_X]\{X\} + [M_X]\{\ddot{X}\} - \{F_X\}$$

in which

$$[K_X] = ([T_{UX}]^{-1})^T[K_U][T_{UX}]^{-1},$$

$$[M_X] = ([T_{UX}]^{-1})^T[M_U][T_{UX}]^{-1}, \tag{4.144}$$

and

$$\{F_X\} = ([T_{UX}]^{-1})^T\{F_U\}$$

The error function for all the nodes (eq. (4.77)) is assembled by adding the effect of the beam elements on both sides of each node. The unknown vector is given by

$$\{X_d\} = \begin{Bmatrix} \{X\}^{(1)} \\ \{X\}^{(2)} \\ \vdots \\ \{X\}^{(n_e)} \end{Bmatrix} \tag{4.145}$$

in which superscripts refer to the beam element number, and n_e is the number of beam elements used. The global stiffness matrix is given by

$$[K_d] = \begin{bmatrix} [K_U]_{11}^{(1)} & [K_U]_{12}^{(1)} & & & & \\ [K_U]_{21}^{(1)} & [K_U]_{22}^{(1)} + [K_U]_{11}^{(2)} & [K_U]_{12}^{(2)} & & & \\ & [K_U]_{21}^{(2)} & [K_U]_{22}^{(2)} + [K_U]_{11}^{(3)} & & & \\ & & & \ddots & & [K_U]_{22}^{(n_e)} \\ & & & & [K_U]_{21}^{(n_e)} & [K_U]_{22}^{(n_e)} \end{bmatrix} \quad (4.146)$$

The global mass matrix is assembled the same way as the global stiffness matrix. Finally, the global load vector is given by

$$\{F_d\} = \begin{Bmatrix} \{F_X\}_1^{(1)} \\ \{F_X\}_2^{(1)} + \{F_X\}_1^{(2)} \\ \{F_X\}_2^{(2)} + \{F_X\}_1^{(3)} \\ \vdots \\ \{F_X\}_2^{(n_e-1)} + \{F_X\}_1^{(n_e)} \\ \{F_X\}_2^{(n_e)} \end{Bmatrix} \quad (4.147)$$

4.2.13 Solver

The model starts the calculation at 0 CA with the apex in the center of the groove and the apex profile clearance at four times the roughness. It then uses a forward Euler method to calculate the time derivatives and an implicit globally convergent Newton method [57] to find the unknown vector that satisfies the error function. For all the following steps, the model first tries an explicit time step and then iterates to solve the error function. Finally, the detailed gas flow and dynamics results are used to calculate sealing performances, such as gas leakage, friction and wear.

The complete unknown vector is assembled from the node displacements and the gas mass in the groove:

$$\{X_g\} = \begin{Bmatrix} \{X_d\} \\ m_g \end{Bmatrix} \quad (4.148)$$

The equation for all the residuals is given by

$$\{G_g\} = \begin{Bmatrix} \{G_d\} \\ G_{mg} \end{Bmatrix} \tag{4.149}$$

in which the residual of the error function on the mass of gas in the groove is given by a mass balance on the groove volume

$$G_{mg} = \left(\int_0^L -\dot{m}_b' - \dot{m}_f' \, dz \right) - \dot{m}_{la} - \dot{m}_{ll} - \dot{m}_{lt} - \dot{m}_g \tag{4.150}$$

For every time step, the model finds the elements of the unknown vector that results in residuals below a desired convergence criterion which is chosen to insure that the dynamics, gas flow and deformations are correctly solved (Fig. 4.36). The model starts with an explicit time step. For every iteration in the dynamics loop, the model calculates the forces, including iterating to find the force on the AS profile in the lubrication loop. If the residuals are below an acceptable tolerance, the model moves to the next time step. If not, the model recalculate a new set of displacements and mass of gas in the groove based on an optimal step in the direction given by the Jacobian matrix and a length given by the globally convergent algorithm. The Jacobian matrix is derived analytically to greatly accelerate calculations.

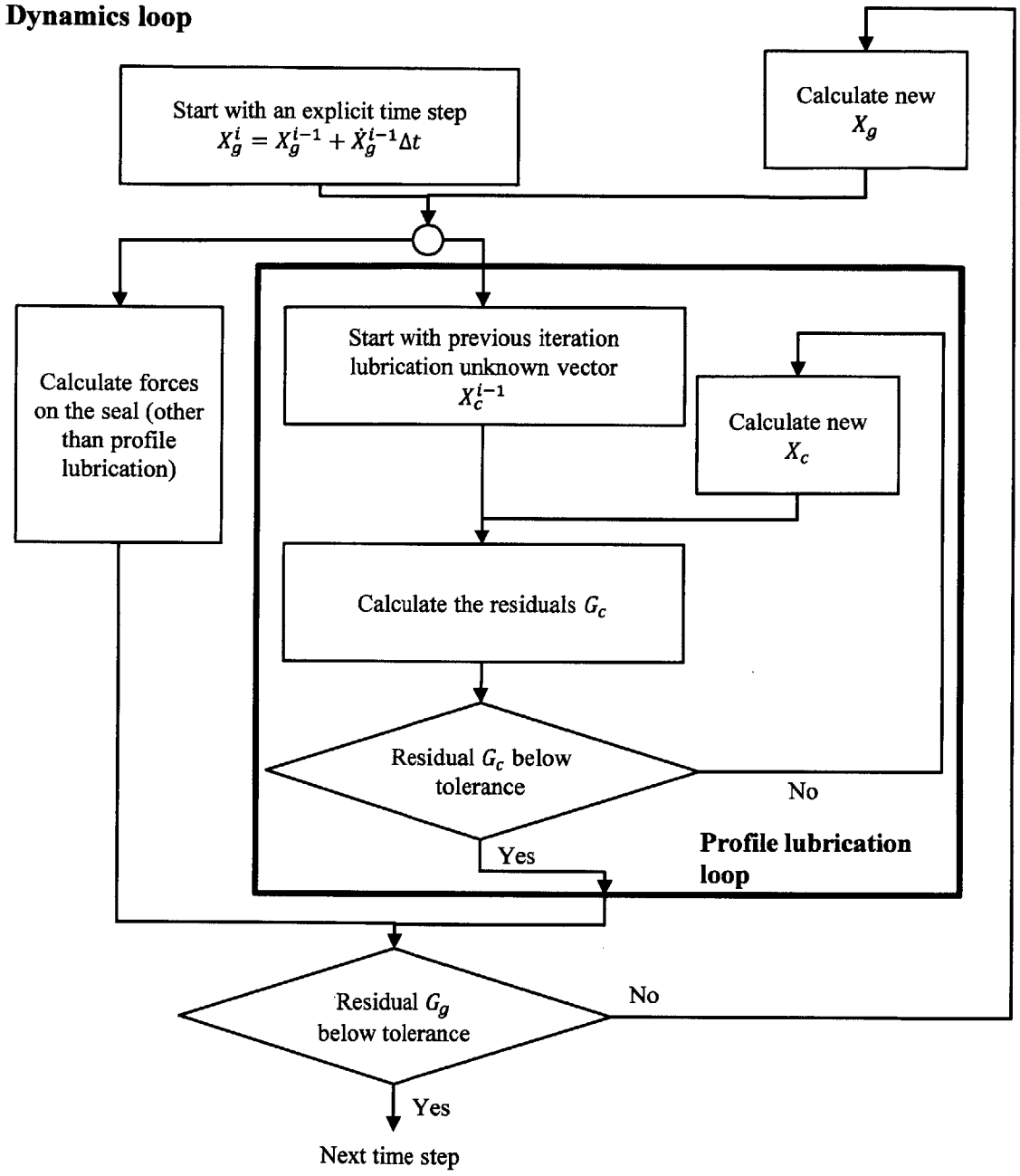

Fig. 4.36 Solver scheme for one time step

4.2.14 Discretization

Time and space needs to be discretized properly in order to calculate dynamics and resulting forces. Time is discretized based on the engine crank angle. A short CA step must be chosen to accurately predict the fast transitions from one groove to the other. A step of 0.1 CA is chosen. Along the seal, the number of beam elements must be about twice the number of local extrema in

the rotor distortion or groove deformation. As there is typically up to 4 local extrema in the rotor housing distortion, 8 beam elements are used. Model predictions show that sealing performances are almost independent of the number of contact points on the seal, which is the number of points used to evaluate the integrals to evaluate the load vector. Ten contact points per beam elements are used to evaluate the forces, which is equivalent to one point every millimeter. However, the number of contact points to evaluate the stiffness and mass matrices must be higher in order to get accurate results. As the stiffness and mass matrices are only calculated once at the beginning of the cycle, computing cost is low and therefore 100 contact points are used. When calculating the forces, the distance along the profile and the flank must also be discretized. As the profile is sharp, a large number of cells are needed to accurately predict the pressure generated close to the minimum clearance. Five hundred cells are used for the entire profile, and the vector is trimmed based on the full-film limits when evaluating the numerical integral for the hydrodynamic forces. The number of cells on the flanks is not as critical and 100 cells are used.

4.2.15 Validation of Approximations

To satisfy the rigid cross-section approximation, the apex should not experience plastic deformation. The maximum contact pressure predicted on the AS is on the order of 200 MPa, both on the profile and on the flank. This maximum pressure is reached in absence of lubricating oil, without wear on the groove and apex flank, and at maximum load and rpm. The deflection caused by the maximum force on the apex should also not generate a deflection much larger than the roughness for the model prediction to be accurate. This deformation can be estimated by calculating the deformation of a cylinder pressed towards a flat plane at the maximum lateral force the AS experiences. The compression (δ) of such a cylinder can be calculated from a Hertzian line contact [58] given by

$$\delta = \frac{4F}{\pi L}\left(\frac{1-\nu^2}{E}\right) \tag{4.151}$$

in which F is the force applied on the AS, L the AS length, and ν is Poisson's ratio. It can be noted that the deformation is independent of the radius of the cylinder, which is convenient in validating the approximation for all AS geometry. Under the maximum force, on the order of

1 kN, the deflection is on the order of 0.1 μm. As this is on the order of the roughness, even for the worst case scenario, the rigid cross-section approximation can be considered valid.

The constant temperature gas flow approximation can be validated by comparing convection to advection, or more specifically, by comparing the heat flow to the walls and the energy carried by the thermal capacity of the gas through the flank clearance. From scaling argument the criterion for the approximation to be valid is given by

$$\frac{h_{conv} A \Delta T}{\dot{m}_s c_p \Delta T} = \mathrm{St} \frac{H}{h_s} \gg 1 \tag{4.152}$$

in which h_{conv} is the convection coefficient, A is the clearance cross-section area, $\dot{m}_s$ is the mass flow rate through the clearance, c_p is the constant-pressure specific heat, ΔT is the temperature difference from inlet to oultet of the channel, St is the Stanton number, H is the height of the AS and h_s is the flank clearance. The Stanton number compares the heat transferred to or from the fluid to the thermal capacity. The criterion in eq. (4.152) also includes a geometric ratio due to the difference in scale between the width and length of the clearance. From model predicted gas flow, the minimum value that this criterion reaches is 100, which valids the approximation of considering the gas to be at the same temperature as the groove.

The last approximation can be validated by comparing the leakage mass flow rate to the engine mass flow rate. At 2000 rpm the total predicted leakage is 5 g/s, which represents 12 % of an engine mass flow rate of 43 g/s estimated from a displacement of 1.3 L and a volumetric efficiency of 1. At 8000 rpm the total predicted leakage is 12 g/s, which represents 7 % of an engine mass flow rate of 174 g/s. It is reasonable to assume that the chamber pressure does not vary significantly enough due to leakage to change the dynamics and gas flow drastically.

4.2.16 AS Model Formulation Conclusions

A model is formulated to predict the deformable AS dynamics coupled to the surrounding gas flow. The model is formulated to take into account the specifics of the rotary engine geometry and kinematics while including the same level of detail as state-of-the-art models for piston

rings. The model considers all the dominant forces including the forces caused by asperity contact, hydrodynamic and gas pressure distribution. Formulation of all forces is designed so they are continuous as a function of clearance and seal tilt. While this feature adds complexity, it is essential to obtain convergence for a wide range of engine geometry and operating conditions. In brief, the model is capable of assessing AS sealing performance, including leakage, wear and friction, for a large number of design parameters.

4.3 Model Predictions

The AS model is capable of predicting dynamics and deformation of the seal coupled to gas transport for a range of engine geometry and operation conditions even if the system is highly numerically stiff. From the detailed results, sealing performance is assessed based on leakage, contact pressure and friction. It is found that for most cases the seal can conform to the distorted groove and to the rotor housing and the effect of groove and housing distortion on leakage is minimal. Apex seal dynamics can therefore be regarded as rigid-body dynamics for most cases, which helps understanding the AS behavior. The main leakage mechanisms are leakage out of the AS groove through the CS clearance and leakage through the spark plug holes. Leakage through the flank clearance increases with speed and reaches a similar level as the two others at high-speed. Concerning wear, oil supply on the rotor housing reduce the wear rate on the profile even for its sharp profile, especially at high-speed. However, even if oil supply decreases friction losses, friction is still dominated by asperity contact friction.

This section first describes the model prediction for low-speed high-load. Those first results are presented for the case with wear on the groove and apex seal flanks because it is more representative of typical operation condition and the AS can find a stable position. The model predictions for a flat AS and groove flanks show seal oscillation and that the flanks would wear rapidly due to large contact pressure at the edges. High-speed predictions are similar to low-speed, except for the opening of the low pressure flank at the end of expansion. Finally, the effect of varying certain parameters is investigated in order to quantify the potential gains on sealing performances.

4.3.1 Low-Speed Predictions

This section details the model predictions for an engine typical geometry at 2000 rpm and at full-load. Wear of the AS and groove are approximated based on measurement made on engine parts after operation. Apex seal dynamics is first explained for the different phases of the cycle. It is then shown that the seal can conform to rotor housing and groove thermal distortion. Therefore, leakage along the seal is small and the other leakage paths dominate. Concerning wear, profile contact pressure and friction predictions show that the amount of oil film thickness on the rotor housing has small influence on profile lubrication due to the sharp profile. Oil film thickness on the groove flanks also has limited effect as the high gas pressure is mainly supported by the asperity contact.

The AS cycle is split in 6 phases based on the pressure in the leading and trailing chambers (Fig. 4.37). The phase changes occur when the pressure in one of the two chambers starts increasing or starts decreasing. In a specific phase of the cycle, the AS position and forces trend remains similar, as shown for example by the seal tilt (Fig. 4.37). Starting from 0 CA, where the apex seal is located between the intake and exhaust ports, the 6 phases are described by:

1. From 0 to ~180 CA, both chambers are at about atmospheric pressure because the leading chamber is connected to the intake port and the trailing chamber is connected to the exhaust port.
2. From ~180 to ~410 CA, leading chamber pressure is rising due to compression and beginning of combustion.
3. From ~410 CA to ~580 CA, leading chamber pressure is decreasing due to expansion. This phase ends when the exhaust ports opens and the leading pressure drops.
4. From ~580 CA to ~770 CA, trailing chamber pressure increases.
5. From ~770 CA to ~940 CA, trailing chamber pressure decreases.
6. From ~940 CA to 1080 CA, both chambers are again at about atmospheric pressure.

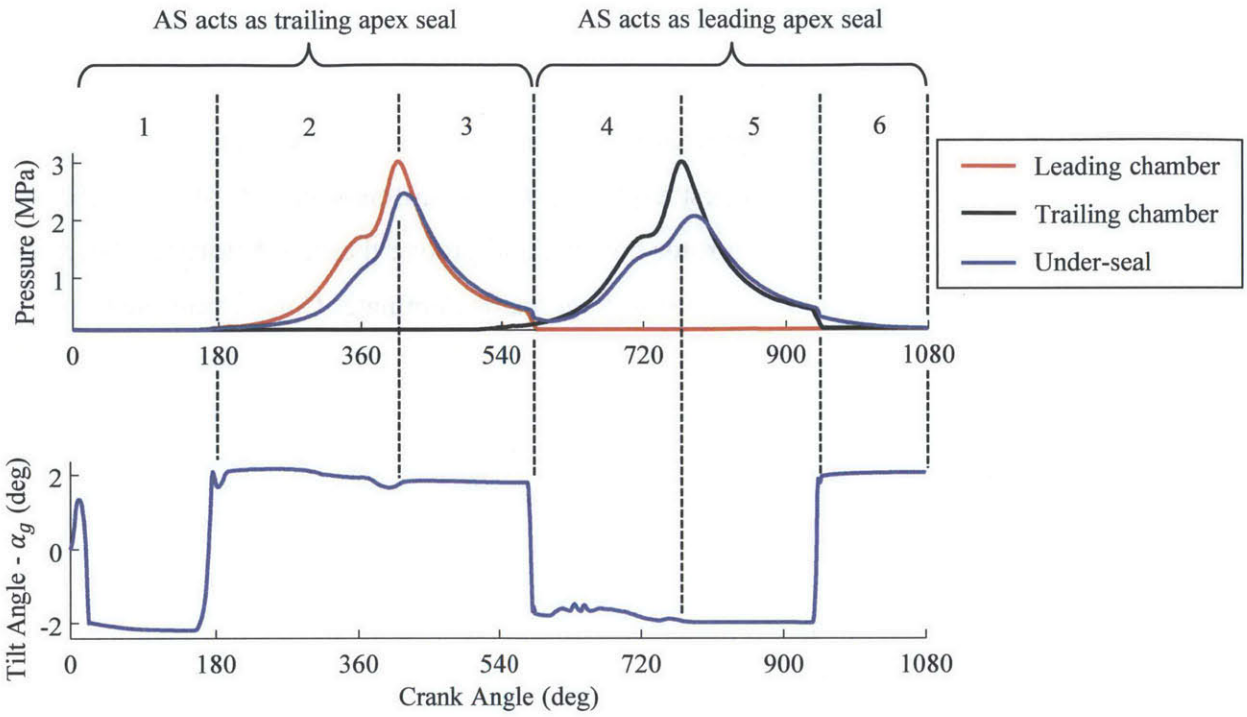

Fig. 4.37 Pressure in the leading and trailing chambers, pressure under the seal and tilt angle of the seal as a function of crank angle at 2000 rpm full-load

Figure 4.37 also shows the predicted pressure in the AS groove under the seal. The under-seal pressure follows the pressure in the combustion chamber with a lag. As the volume in the groove is small, this important lag between the two pressures requires an important restriction of the flow through the flank clearance. Also, in phases 3 and 5, the difference in pressure between the groove and the high-pressure chamber is too small to explain the rapid decay in under-seal pressure if the flow restriction remains similar as for phases 2 and 4. Therefore, the mass of gas accumulated in the groove at high pressure must leak either to the side of the rotor or to the low-pressure chamber. Those effects can be explained by a detailed description of the model predictions in the 6 phases. The position of the seal in the different phases is shown using three different AS cross-sections at different location along the seal (Fig. 4.38). The first one, at $z/L = 0.05$ is inside the corner seal and shows the passage of gas due to increased clearance. The second one, at $z/L = 0.15$ is at the maximum seal height inside the full groove and is the most useful in understanding the forces as this part of the AS always contact with the flanks of the groove. The last one, at $z/L = 0.5$, shows the seal at its minimum height.

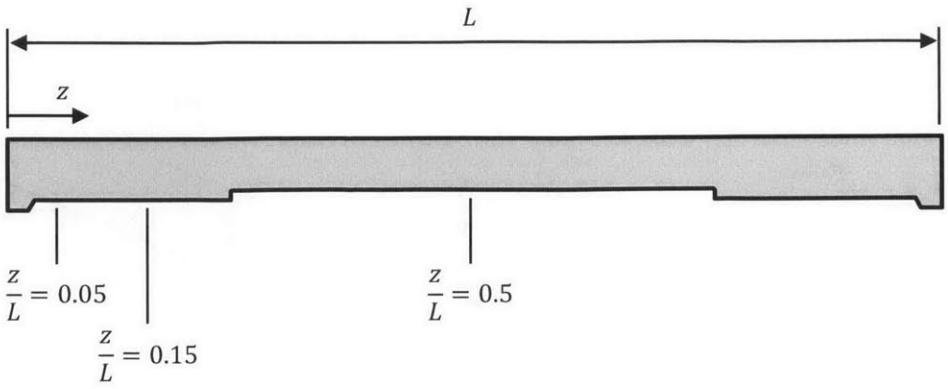

Fig. 4.38 Position along the seal

The position of the seal and the forces applied on the AS are shown in Fig. 4.39 at 90 CA and at $z/L = 0.15$. Positions of the rotor and of the AS of interest are shown in the upper left corner inside the trochoidal rotor housing. Difference between the modified trochoid and the theoretical trochoid is amplified for clarity. Pressures are shown in the lower left corner with markers to indicate the position in the cycle. The center graph shows the cross-section of the AS in its groove with the forces and pressure applied on the seal. The upper right corner graph shows the contact point and contact angle between the AS and the rotor housing. The two graphs in the lower right corner show the clearance of the trailing and leading flanks by stretching the x-direction and zooming on the clearance. For conciseness, explanation and legends are only shown on Fig. 4.39, but they apply to all the following figures using the same format in this chapter.

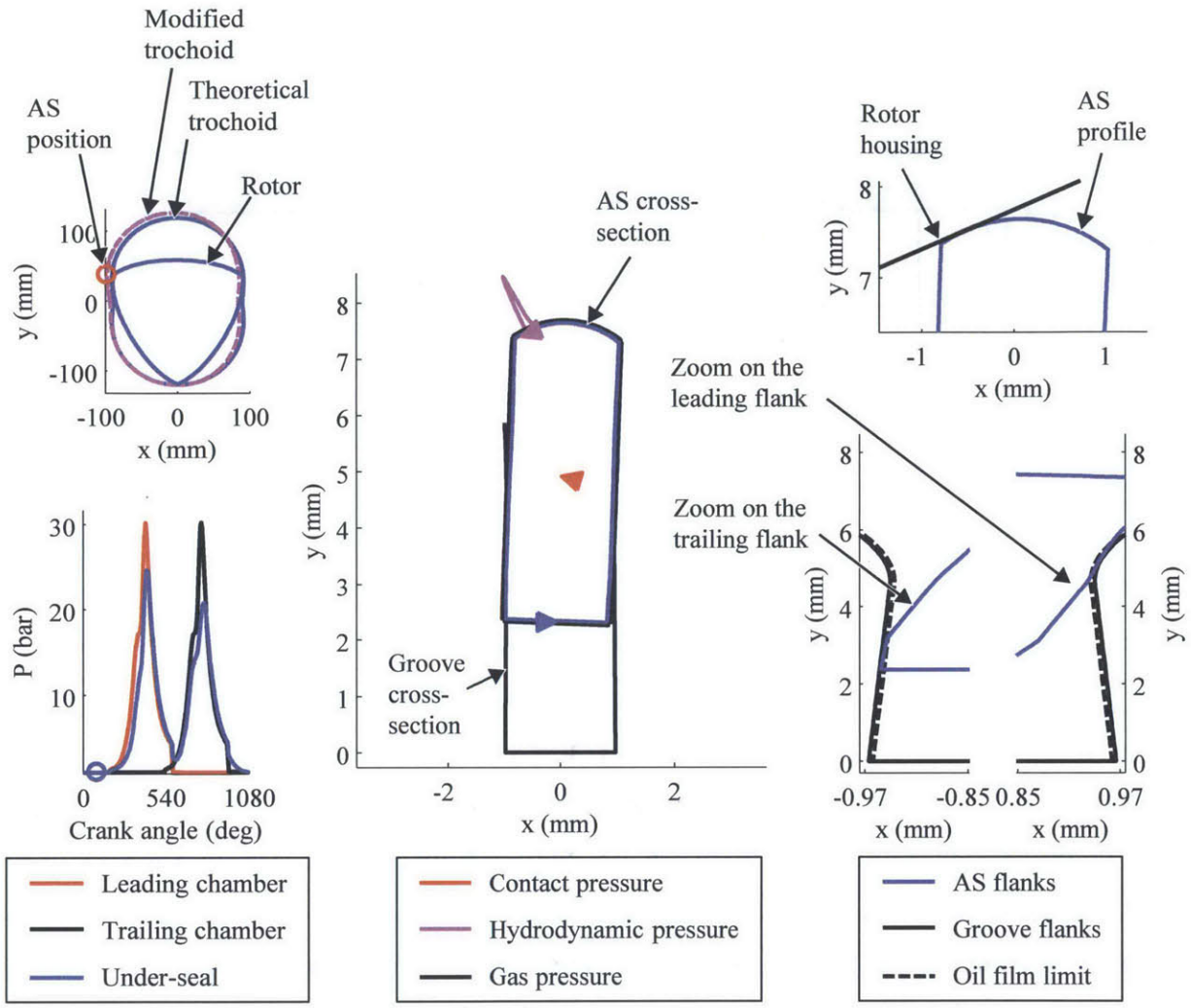

Fig. 4.39 Apex seal position and forces on the cross-section at z/L = 0.15 and at 90 CA

Displacements and forces shown in Fig. 4.39 are typical of phase 1. As there is no net effect of the gases, the tilt of the seal is dictated by the contact angle with the housing. In this case, the AS is tilted clockwise, as the contact with the rotor housing is on the trailing side of the AS profile. Phase 1 is of small interest towards understanding sealing performance because the leakage is small due to small pressure difference and the forces are small leading to negligible wear.

As soon as the pressure starts increasing in the leading chamber, the AS is pushed towards the trailing flank of the groove. All along phase 2, the seal is in contact with the trailing flank and tilted counter-clockwise, but not tilted all the way so there is a small gap at the inner leading corner of the seal where gas can flow through the groove (Fig. 4.40). The difference in pressure

makes the seal tilt, but as it tilts, the contact point with the flank moves upward providing a resisting moment to seal tilting. This results in a stable position of the AS without contacting both flanks. In phase 2, the seal is pushed inward due to the shape of the modified trochoid. This generates a friction force with the trailing flank which contributes in keeping the leading flank open.

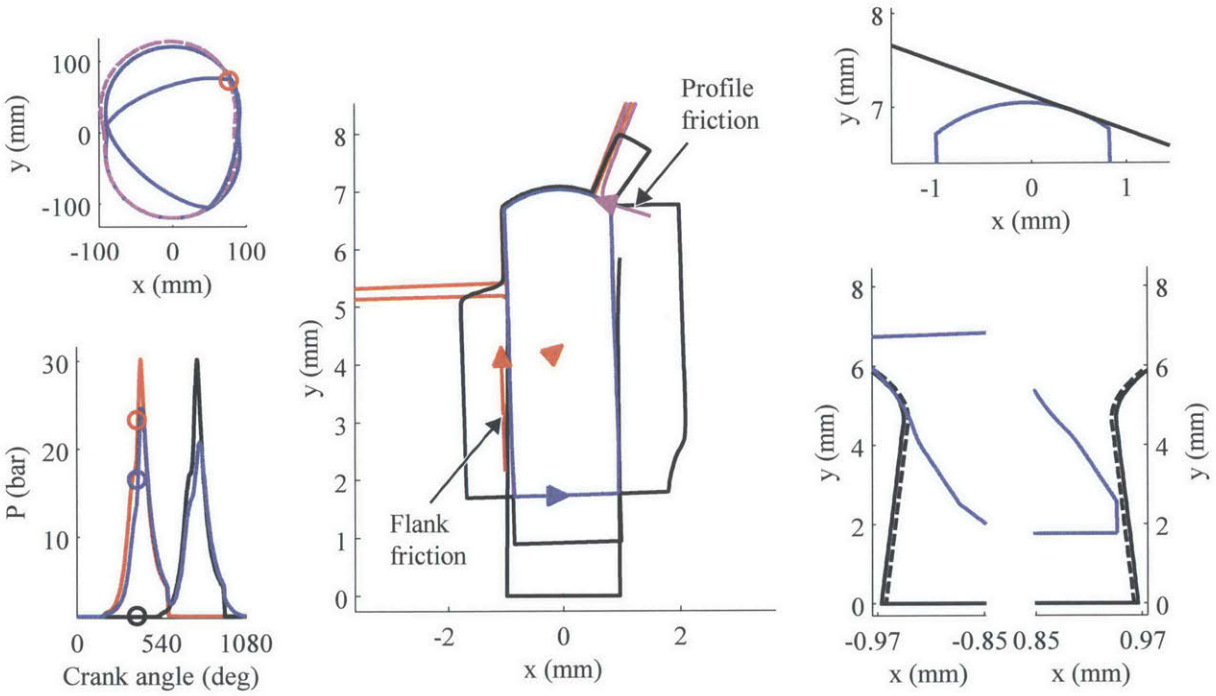

Fig. 4.40 Apex seal position and forces on the cross-section at z/L = 0.15 and at 390 CA

Unlike what would be predicted by a model that would assume a uniform cross-section, the gas mass flow rate through the flank varies along the seal. Inside the corner seal, the AS groove flanks are cut by the presence of the corner seal groove (Fig. 4.41a). This leaves the trailing flank open, even if the seal is completely tilted. The region where the seal is at its maximum height and outside the corner seal (z/L around 0.15) is where the gas flow restriction is maximal (Fig. 4.41b). In this case, the center portion of the seal (Fig. 4.41c) also provides large flow restriction because of the wear that trims the inner corners of the seal.

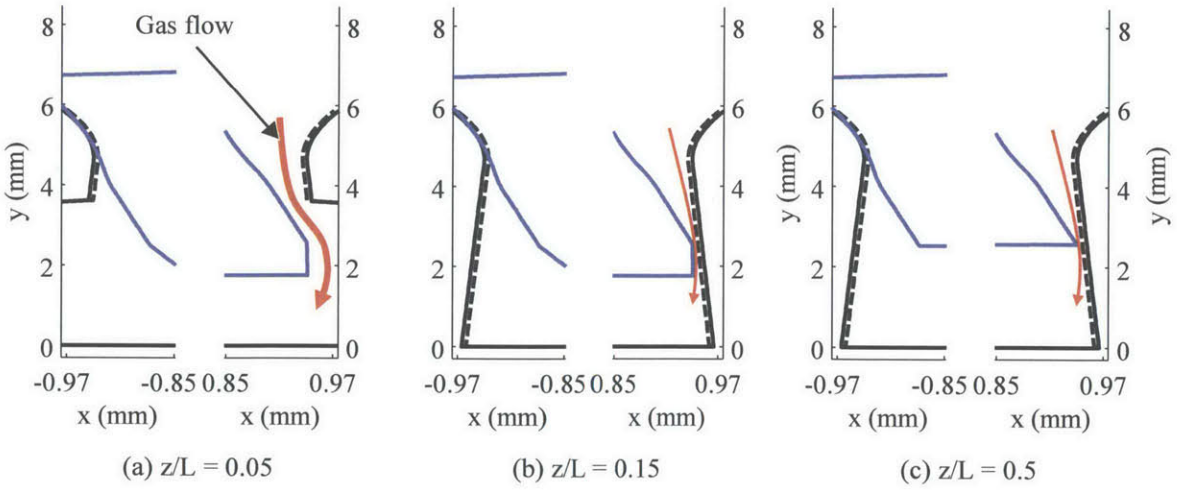

Fig. 4.41 Difference in flank clearance along the seal at 390 CA

During leading chamber expansion, or phase 3, the high under-seal pressure tilts the seal completely and the seal is in contact with both flanks (Fig. 4.42). Under-seal pressure decreases simultaneously with leading chamber pressure by leaking to the rotor side and to the trailing chamber mainly through the corner seal clearance.

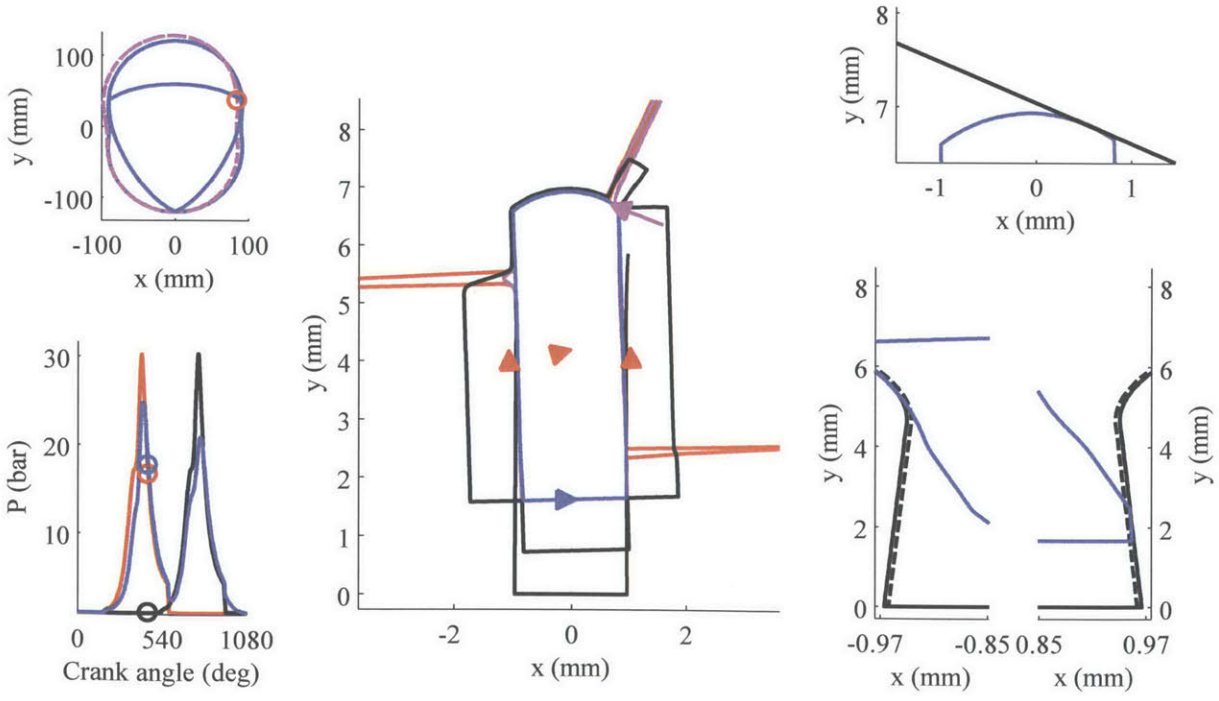

Fig. 4.42 Apex seal position and forces on the cross-section at z/L = 0.15 and at 450 CA

During phase 4, the position of the seal is similar to phase 2, but tilted in the opposite direction (Fig. 4.43). However, the seal motion is outward due to the shape of the modified trochoid. This generates a friction force in the opposite direction which closes the leading flank. The gas can thus only flow through the flank clearance inside the corner seal groove, as shown in Fig. 4.41a. This difference in flank friction direction explains why the pressure under the seal is lower in phase 4 than in phase 2.

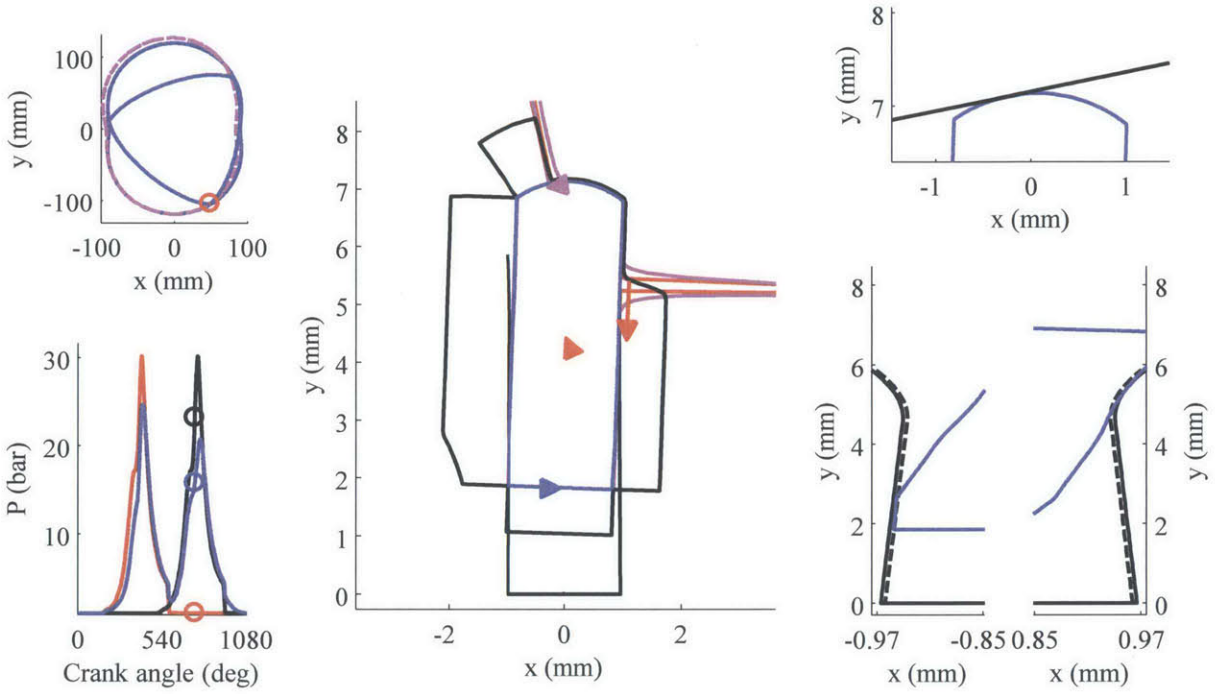

Fig. 4.43 Apex seal position and forces on the cross-section at z/L = 0.15 and at 750 CA

During phase 5, the seal is completely tilted (Fig. 4.44), as during phase 3. Another important difference between the leading and trailing apex is the position of the contact point between the apex profile and the rotor housing. During phase 2 and 3, the contact with the housing is on the leading side of the profile. The gas force on the profile is therefore minimal and the force generated by the pressure under the seal must be balanced by the contact force with the housing. However, during phase 4 and 5, the contact with the rotor housing is centered on the apex seal profile. About half of the force generated by the pressure under the seal is balanced by the gas pressure on the profile and the contact force is significantly reduced.

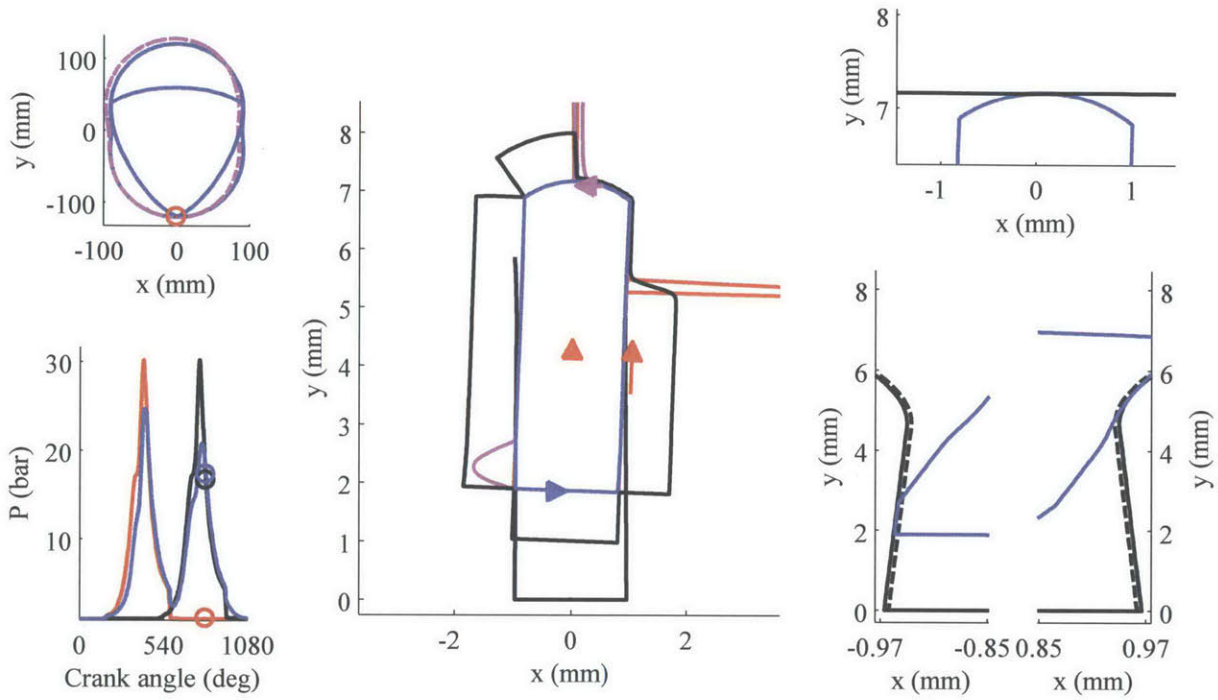

Fig. 4.44 Apex seal position and forces on the cross-section at z/L = 0.15 and at 810 CA

When the exhaust port opens, the seal changes from a complete clockwise tilt to a complete counter-clockwise tilt, and remains in that position until the end of the cycle (Fig. 4.45). The pressure under the seal decreases slowly by leaking to the leading chamber.

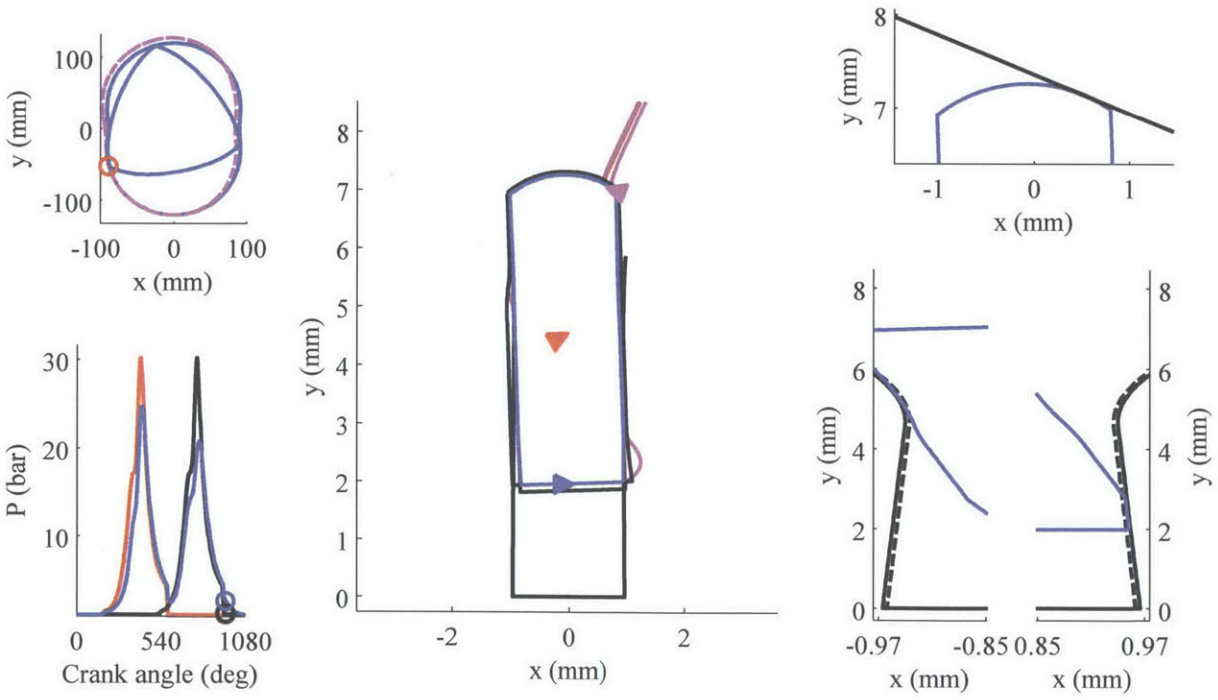

Fig. 4.45 Apex seal position and forces on the cross-section at z/L = 0.15 and at 960 CA

Up to this point, results shown do not include rotor housing distortion. Rotor housing distortion can be included using finite element results of the engine block as an input. The shape of the housing distortion has typically one or two maxima (Fig. 4.46) and its amplitude at low-speed full-load is on the order of 10-30 μm.

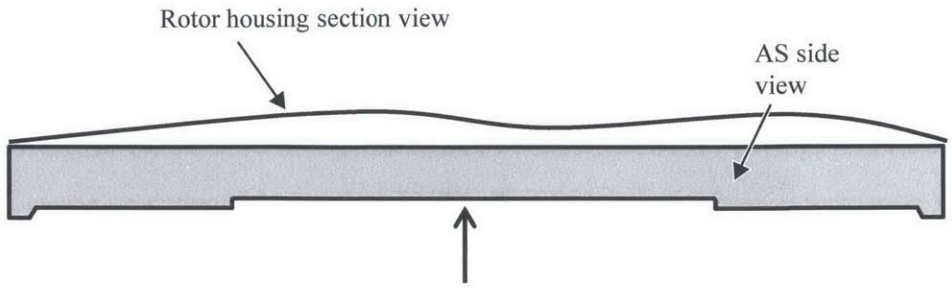

Fig. 4.46 Section-view of typical shape of rotor housing distortion (amplitude is amplified for the illustration)

The AS cannot conform to the rotor housing full-load distortion with only the spring force (Fig. 4.47a). Nevertheless, the seal conforms to housing distortion when pressure in the groove is high (Fig. 4.47b). The leakage caused by the non-conformability of the seal is therefore small. However, the non-conformability can be problematic for oil transport, as oil could be scraped away from the regions where lubrication is critical and a large oil film thickness could be left where lubrication needs are minimal.

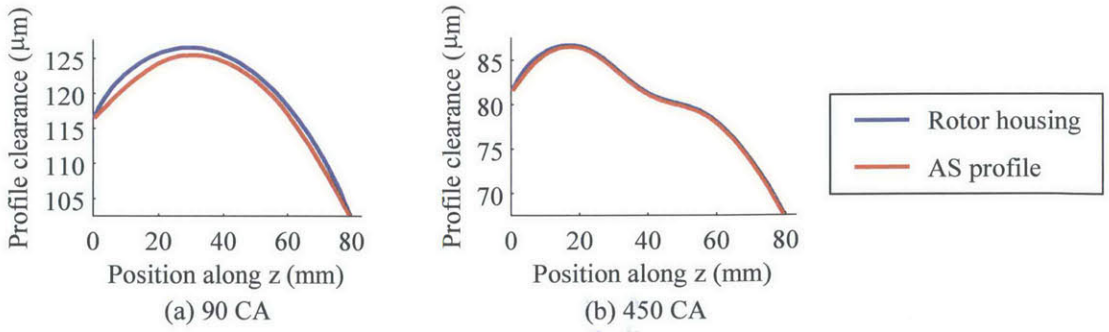

Fig. 4.47 Conformability of the seal to the rotor housing (a) with spring force only and (b) with a pressurized groove

Similarly, the effect of groove distortion can be added as an input to the model taken from finite element results. Typical thermal groove distortion has a parabolic shape when looking at the

apex and its groove from the top (Fig. 4.48) and its amplitude at low-speed high-load is on the order of 10-20 μm.

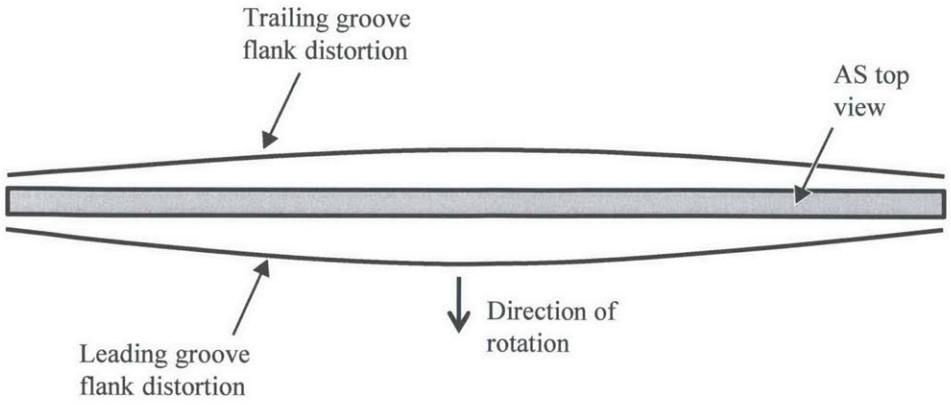

Fig. 4.48 Top view of typical thermal groove distortion

The AS cannot conform to the groove flank when the pressure difference between the chambers is small, as there is only the profile normal and friction forces that push the seal toward the flank (Fig. 4.49a). On the other hand, the seal conforms to the flank when chamber pressure difference is high (Fig. 4.49b). The effect of groove distortion on leakage is therefore small.

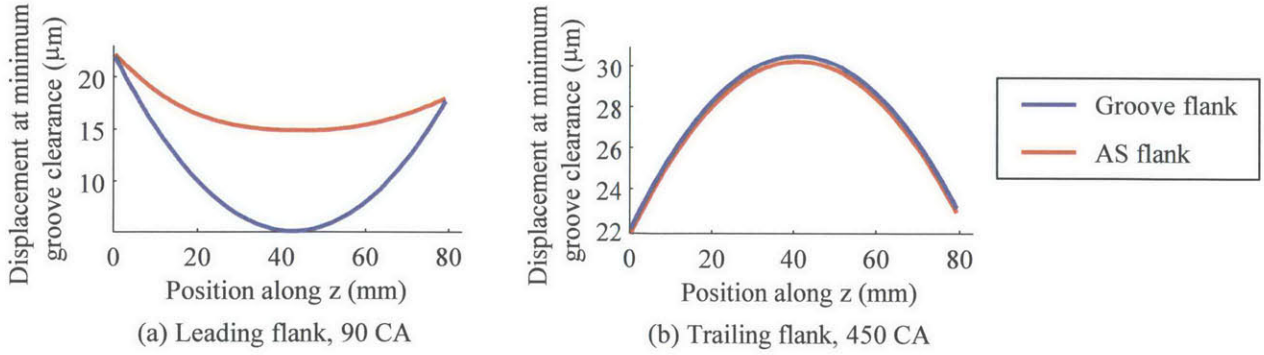

Fig. 4.49 Conformability of the seal to the rotor housing at (a) low chamber pressure difference, and (b) high chamber pressure difference

The first role of the AS is to seal the high pressure chamber. The most important performance indicator is thus the amount of gas leakage to the low pressure chamber and side of the rotor. The leakage rate through the different paths during the cycle is shown in Fig. 4.50, and the total

amount of leakage for those mechanisms is shown in Fig. 4.51. At low speed, leakage through the flank clearances mainly happens during transition from one flank to the other and the gas accumulated under the seal leaks to the low pressure chamber. The leading flank also leaks at the end of the cycle when the seal tilts angle switches. Profile leakage is marginal as the seal can conform to the rotor housing. Side piece corner leaks as a function of the pressure in the high-pressure chamber and is one of the important leakage mechanisms. The groove leaks from the corner seal clearance anytime the groove is pressurized. This leakage mechanism is one of the two most important leakage mechanisms. Finally, leakage through the spark plug holes is the other dominant leakage mechanism for the experimental pressure trace used. Predicted leakage through the leading spark plug hole is large as the hole is large and the time it is opened is important due to the low engine speed. However, it should be noted that the amount of leakage through the leading spark plug is highly function of the pressure difference between the chambers when the seal passes the hole and can vary significantly as a function of when the exhaust port opens.

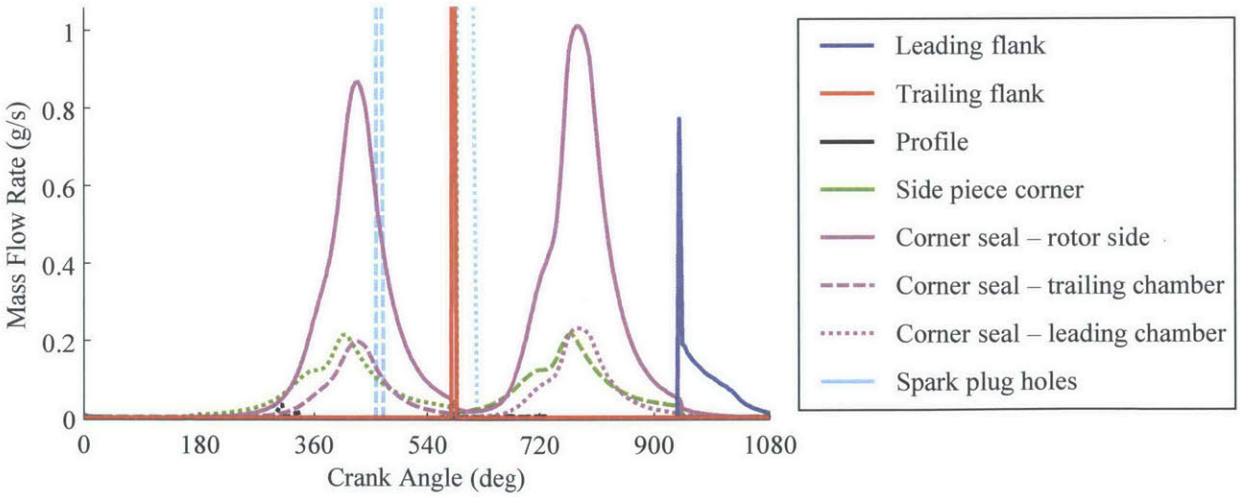

Fig. 4.50 Leakage mass flow rate as a function of crank angle for the different mechanisms at 2000 rpm full-load

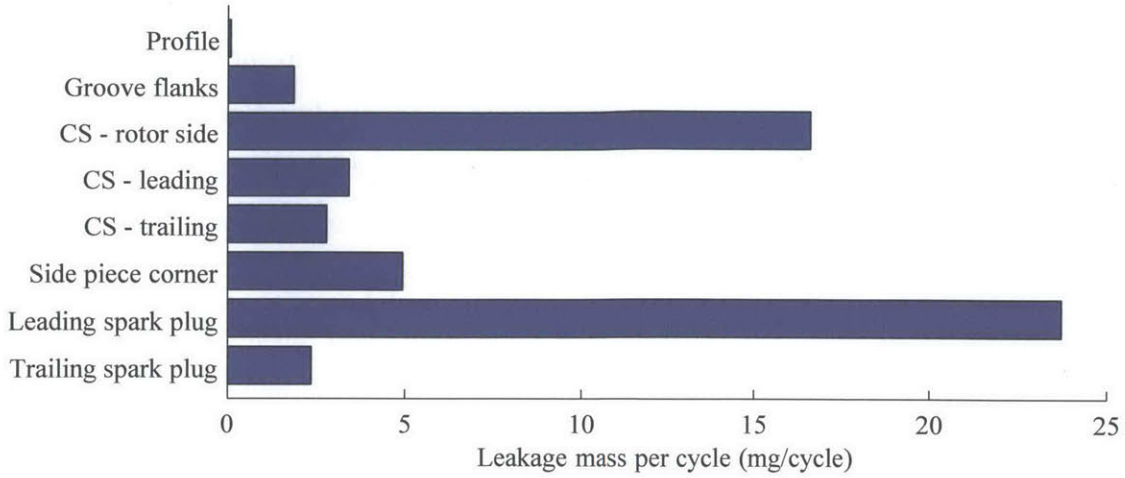

Fig. 4.51 Comparison of the total leakage for the different mechanisms at 2000 rpm full-load

The apex seal must survive, which means that wear must be limited below an acceptable level. Even if wear assessment still remains largely empirical, the model can be used to better understand wear. Adhesive wear rate ($\dot{\delta}_w$) can be related to prediction of the model using a simple wear equation [58]:

$$\dot{\delta}_w = \left(\frac{K_w}{H_w}\right) P_w V_w \tag{4.153}$$

in which K_w is the wear coefficient ranging from 10^{-6} to 10^{-3} depending on the materials and lubrication conditions, H_w is the hardness, P_w is the contact pressure, and V_w is the relative velocity between the two surfaces in contact. Although the wear coefficient is difficult to estimate, the product $P_w V_w$ can be calculated from the model results and gives an indication of the expected relative wear when comparing different position on the seal, lubrication conditions and operating conditions.

The profile contact is sharp from a lubrication standpoint. Therefore, the asperity contact pressure supports a large portion of the radial load, especially for the trailing apex, even in fully-flooded condition (Fig. 4.52). The average reduction of the factor $P_w V_w$ is about 40 % when going from a completely dry condition to a film thickness of 1 μm, which guarantees fully-flooded condition at the leading edge (Fig. 4.53). Effective wear reduction by having oil supply

is expected to be greater than 40 % due to the change of wear coefficient K_w by the presence of oil and additives. It can also be seen that the wear rate is expected to be much higher on the leading side of the profile. This is explained by the difference of the contact point on the profile for the different phases (see Fig. 4.40 and Fig. 4.43).

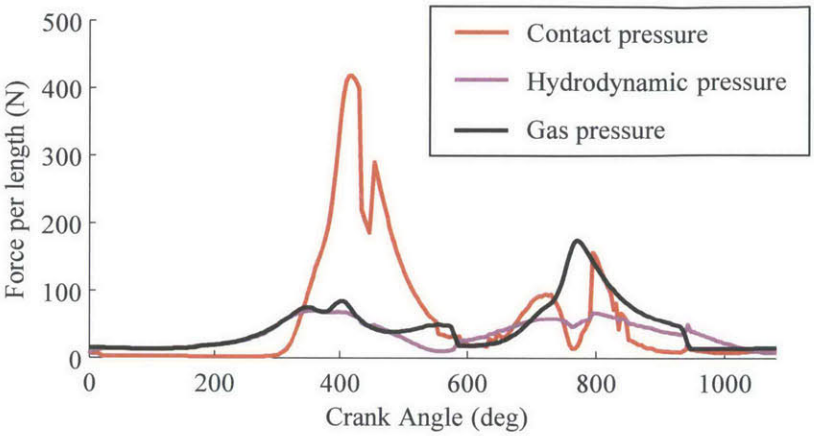

Fig. 4.52 Contact, hydrodynamic and gas pressure on the profile at 2000 rpm full-load

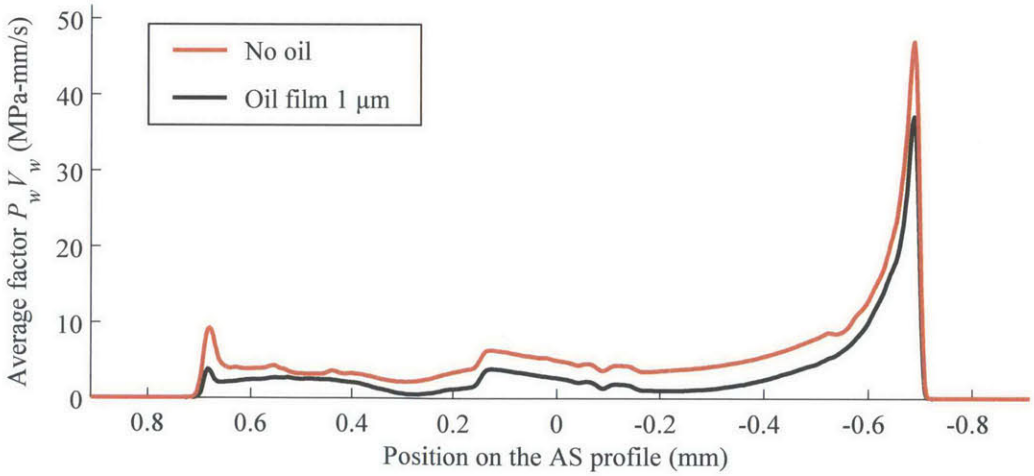

Fig. 4.53 Average wear rate indicator on the profile at 2000 rpm full-load

For the flanks, the relative motion is generated by the variation of clearance with the housing caused mainly by the modified trochoid. The wear on both flanks of the seal is concentrated around the pivot line and at the lowest contact point (Fig. 4.54). It is interesting to note that adding oil as small influence on the trailing flank while reduces significantly wear on the leading flank. This is mainly due to a better groove-seal fit for the leading flank than for the trailing

flank. It should be noted that the groove and seal wear profiles are input to the model and have not been calculated based on predicted contact pressure. Therefore the fit between the seal flank and the groove flank is expected to be better than in those predictions. The key take-away from the flank friction is that the presence of oil can reduce significantly the factor $P_w V_w$.

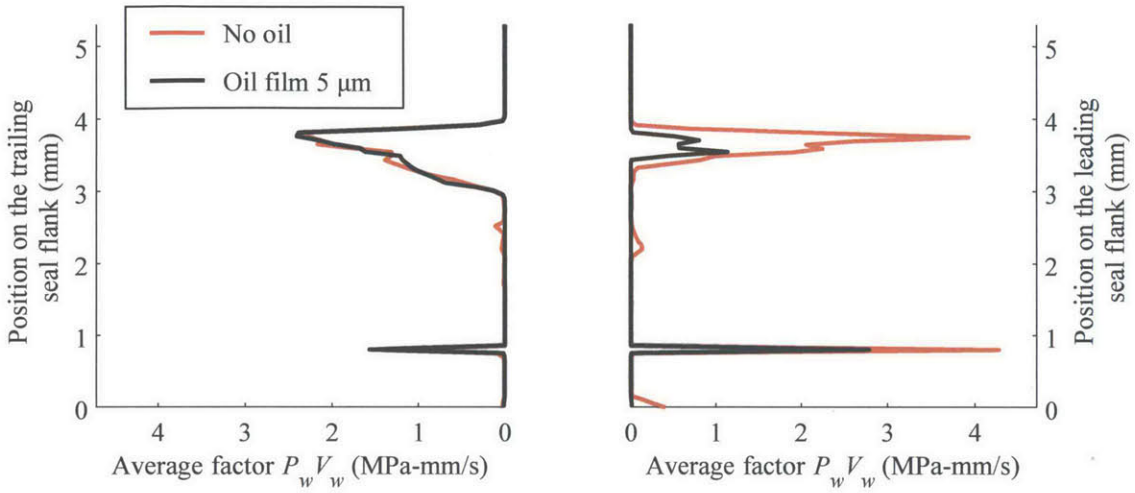

Fig. 4.54 Average wear rate indicator on the AS flanks at 2000 rpm full-load

Once the AS seals and survives, one wish to reduce friction losses. Friction losses of the AS are also calculated from the detailed model results. Without oil supply on the rotor housing, friction power of one AS at 2000 rpm full-load is 108 W. Friction power is reduced by 40 % in fully-flooded condition, down to 66 W. Asperity contact friction accounts for 65 W while hydrodynamic friction accounts for only 1 W. This is again due to the sharp AS profile.

4.3.2 Low-Speed Predictions with Unworn Geometry

In new conditions, without wear on the groove and seal flanks, the location of the contact between the seal and groove flanks cannot vary smoothly and it either occurs at the corners or the entire flank. As a result, the seal oscillates between those two stable positions during most of compression phases (phase 2 and 4 in Fig. 4.55). During phase 2, seal oscillations alternatively open and close the leading flank clearance so more gas can flow to the groove than the case where wear is included (Fig. 4.56). More gas also flows to the groove as the center section leading flank is not closed because the seal only contacts the flank where the seal height is

maximal (Fig. 4.57). For those two reasons, the gas restriction is reduced and the under-seal pressure lag is small (Fig. 4.55).

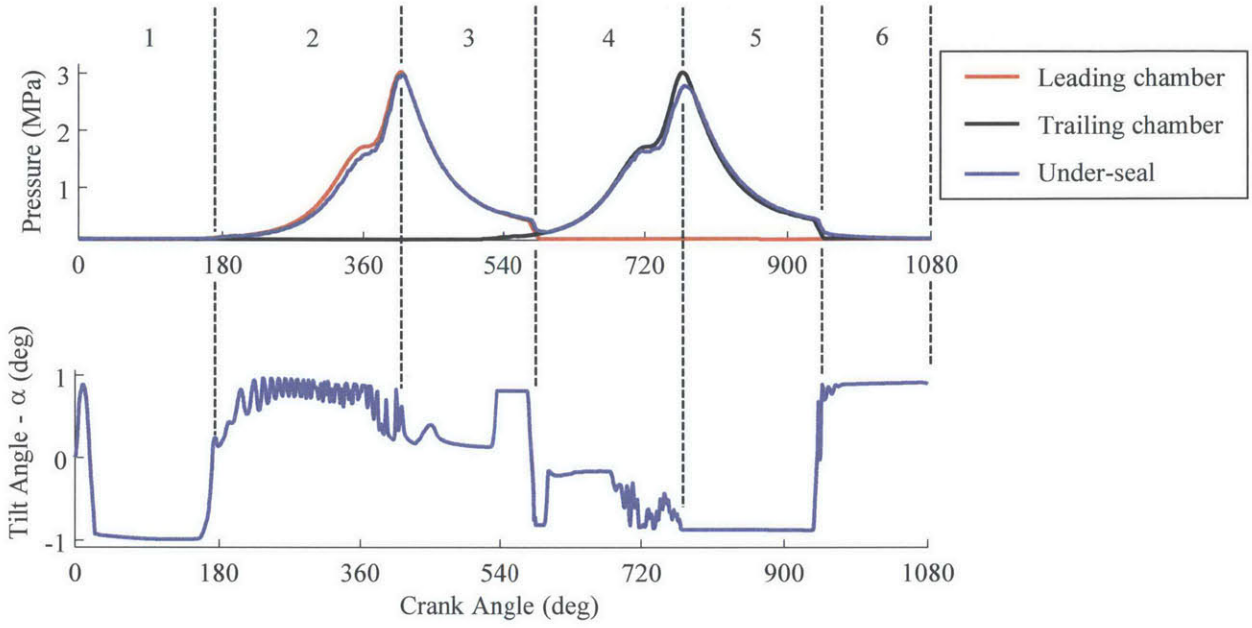

Fig. 4.55 Pressure in the leading and trailing chambers, pressure under the seal and tilt angle of the seal as a function of crank angle at 2000 rpm full-load without seal and groove flank wear

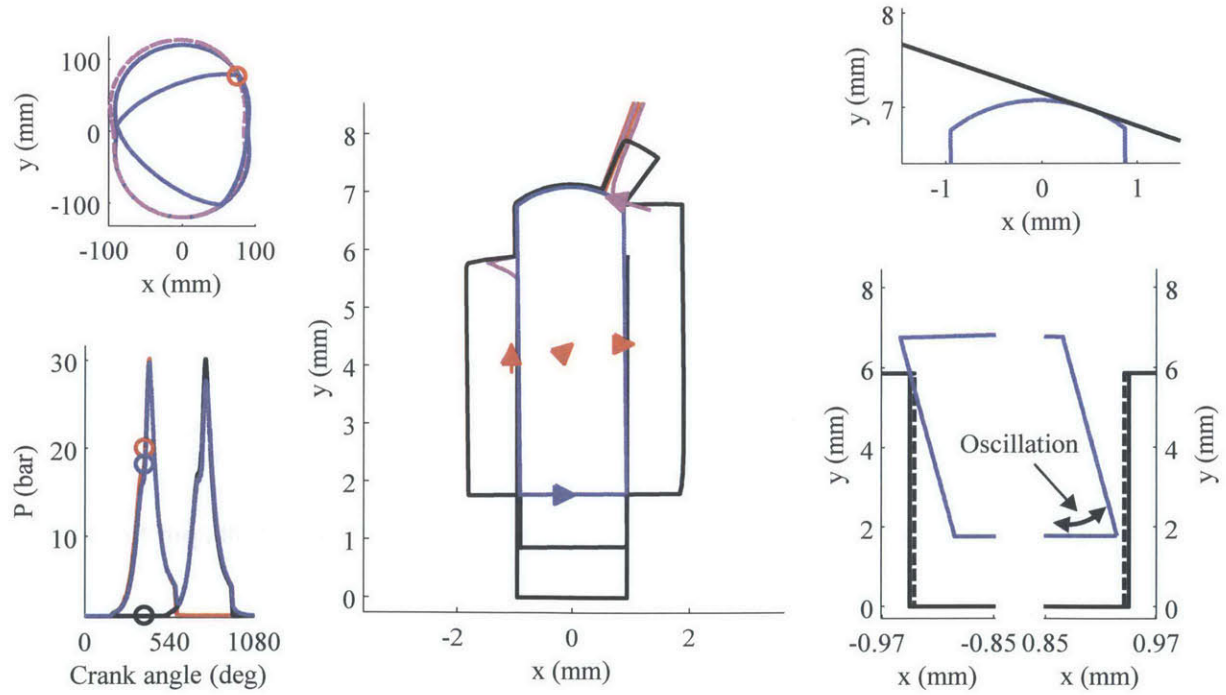

Fig. 4.56 Apex seal position and forces on the cross-section at z/L = 0.15 and at 382.8 CA

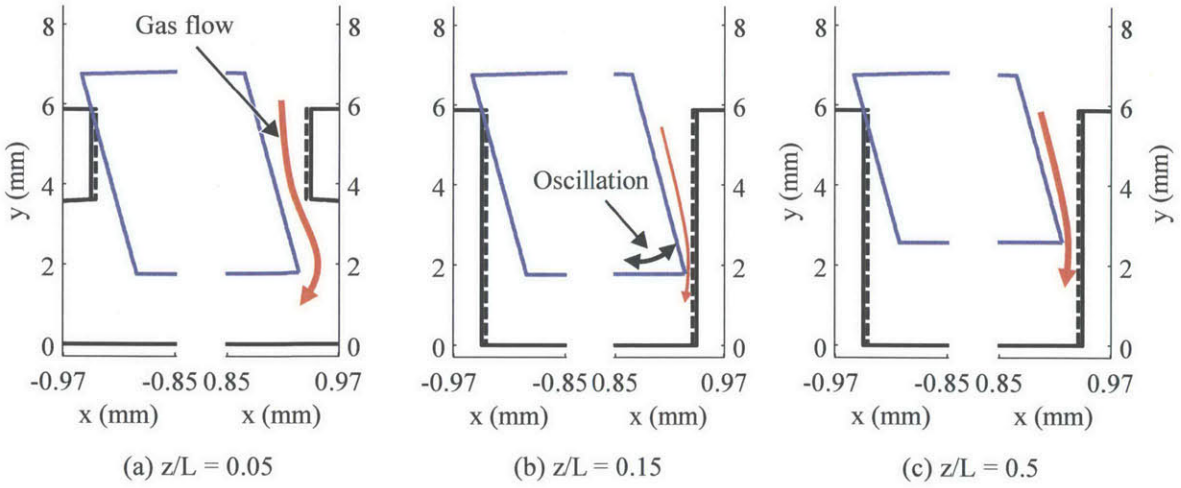

Fig. 4.57 Difference in flank clearance along the seal at 382.8 CA

Due to a local contact pressure between the seal and the groove, the wear rate on the AS flank is high (Fig. 4.58). The wear rate on the groove flanks is even higher as the contact is always on the same line. Therefore, the flanks geometry may change rapidly and modeling the worn flank condition provides better insight on real engine performances, as presented in the previous section.

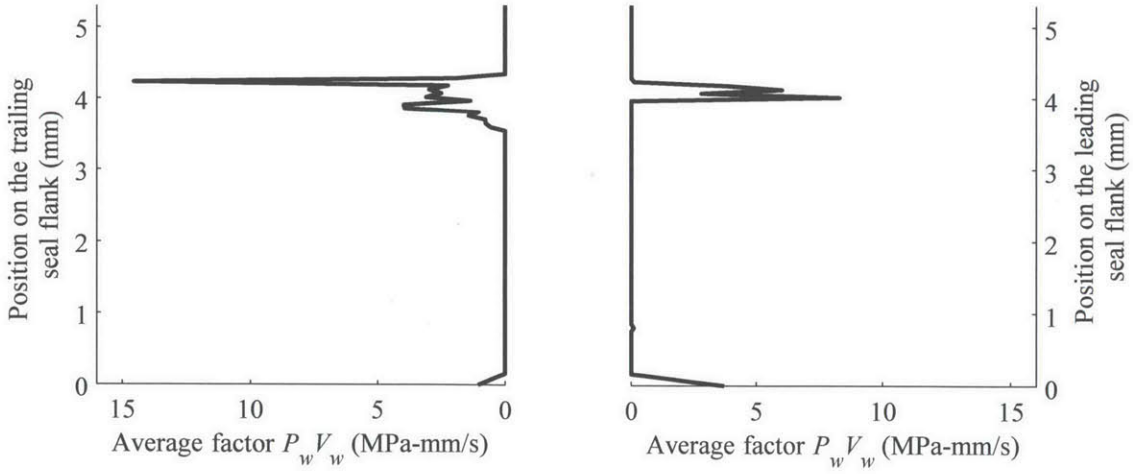

Fig. 4.58 Average wear rate indicator on the AS flanks with 5 µm of oil at 2000 rpm full-load without seal and groove wear

4.3.3 High-speed Predictions

In order to describe the high-speed limit of the AS behavior, the model is used to predict the performances of the AS at 8000 rpm full-load. The main differences compared to low-speed are: (1) gases have less time to flow in and out the groove for the same rotor displacement, (2) the body force of the seal becomes important, and (3) transition from one groove to the other or seal oscillations becomes slower as a function of crank angle. Overall, the slower gas flow as a function of CA is the dominant effect and the under-seal pressure lag becomes more important during compression (Fig. 4.59). It also prevents the groove pressure to decrease as fast as the chamber pressure which leads to increased groove flank leakage. Housing and groove distortions, even if they are larger than at low-speed, do not significantly increase leakage. Corner seal clearance and spark plug leakage are still the most prominent leakage mechanisms, but not as from the others different as is seen at low speed. Also, oil supply for the profile provides more wear and friction reduction than at low-speed.

The cycle is divided in 6 phases, as is done for the low-speed analysis. The general position of the seal is similar to low-speed, except at the end of expansion and when the chamber pressure difference is small (Fig. 4.59). Seal oscillation at the end of expansion opens the low-pressure flank which leads to flank leakage.

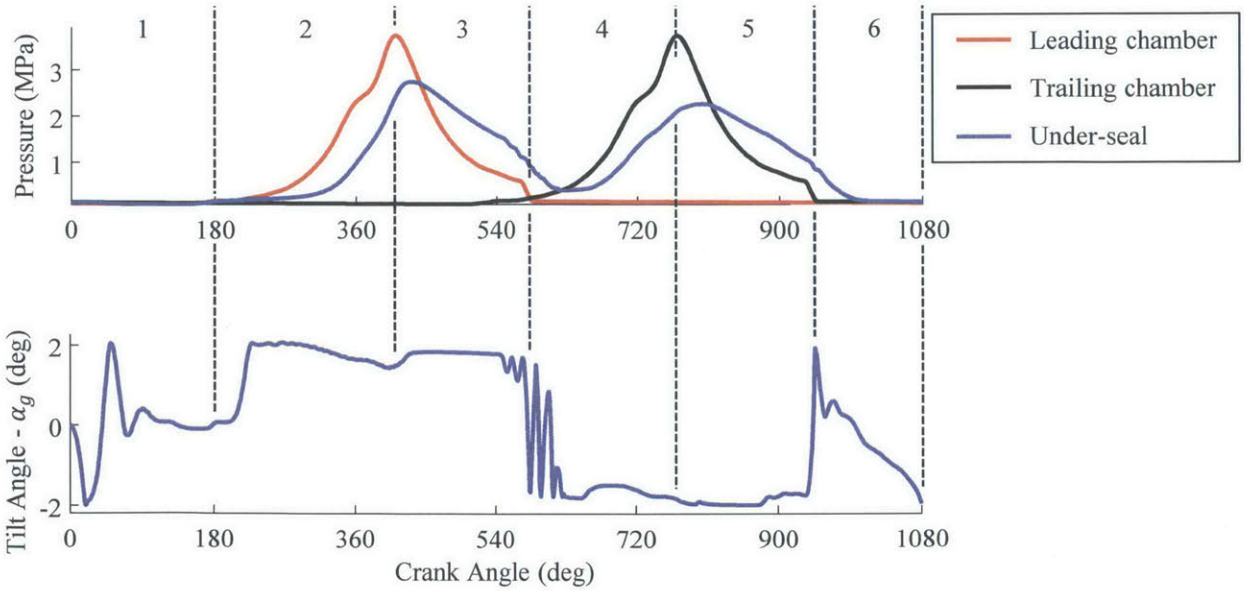

Fig. 4.59 Pressure in the leading and trailing chambers, pressure under the seal and tilt angle of the seal as a function of crank angle at 8000 rpm full-load

When chamber pressure difference is low, the body force dictates the equilibrium that was mostly determined by the reaction force with the rotor housing at low speed. During most of phase 1, the AS is pushed toward the trailing groove flank (Fig. 4.30).

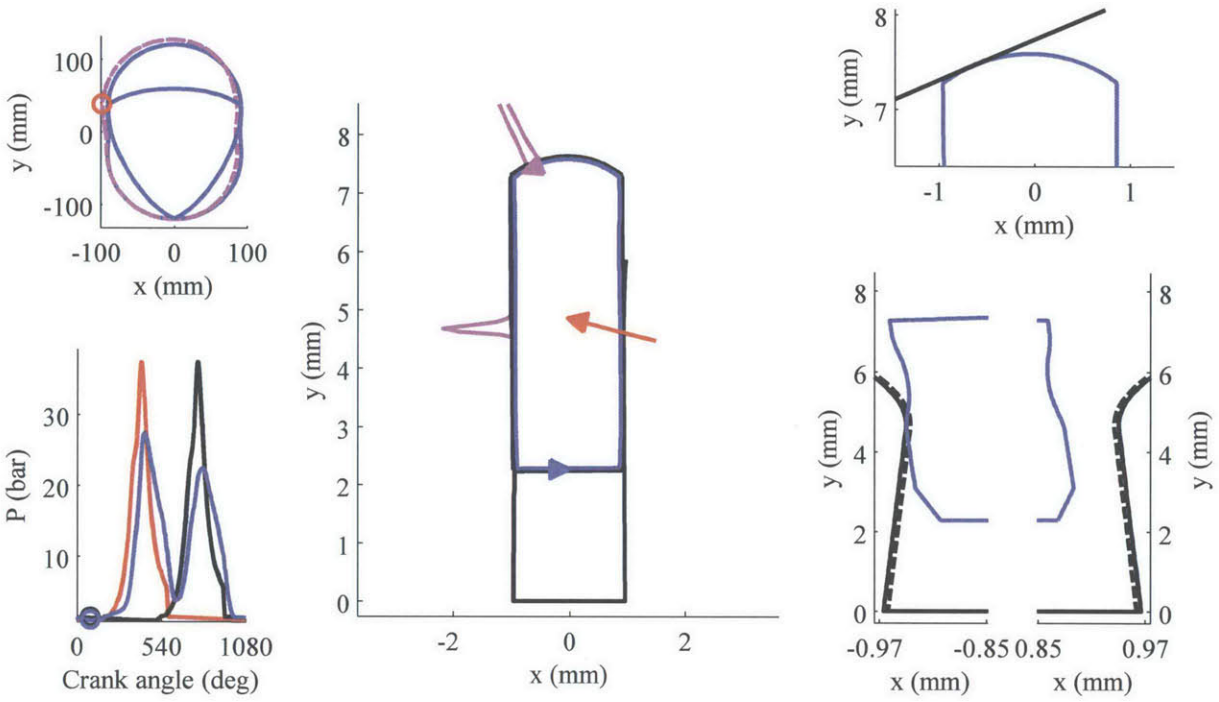

Fig. 4.60 Apex seal position and forces on the cross-section at 8000 rpm, z/L = 0.15 and 90 CA

During phase 2, the AS is partly tilted as at low-speed (Fig. 4.61). However, the leading flank is slightly more open due to a lower pressure in the groove as a result of the larger groove pressure lag.

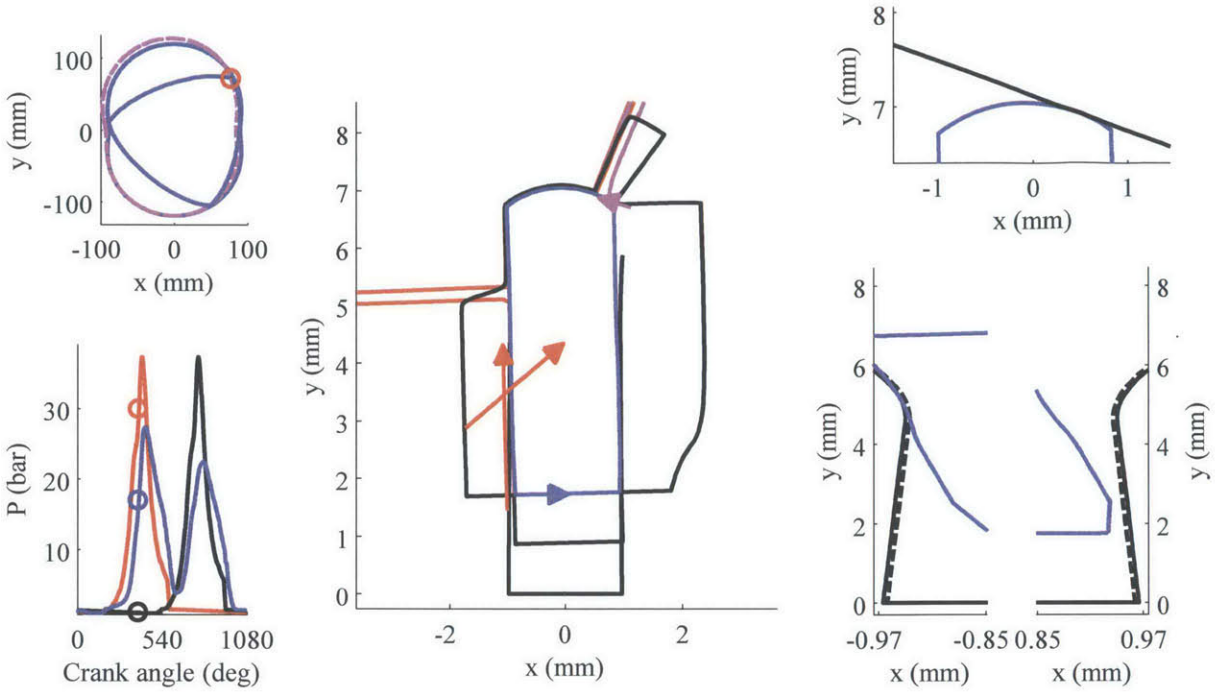

Fig. 4.61 Apex seal position and forces on the cross-section at 8000 rpm, z/L = 0.15 and 390 CA

During most of phase 3, the seal is completely tilted and closes the leading flank clearance.

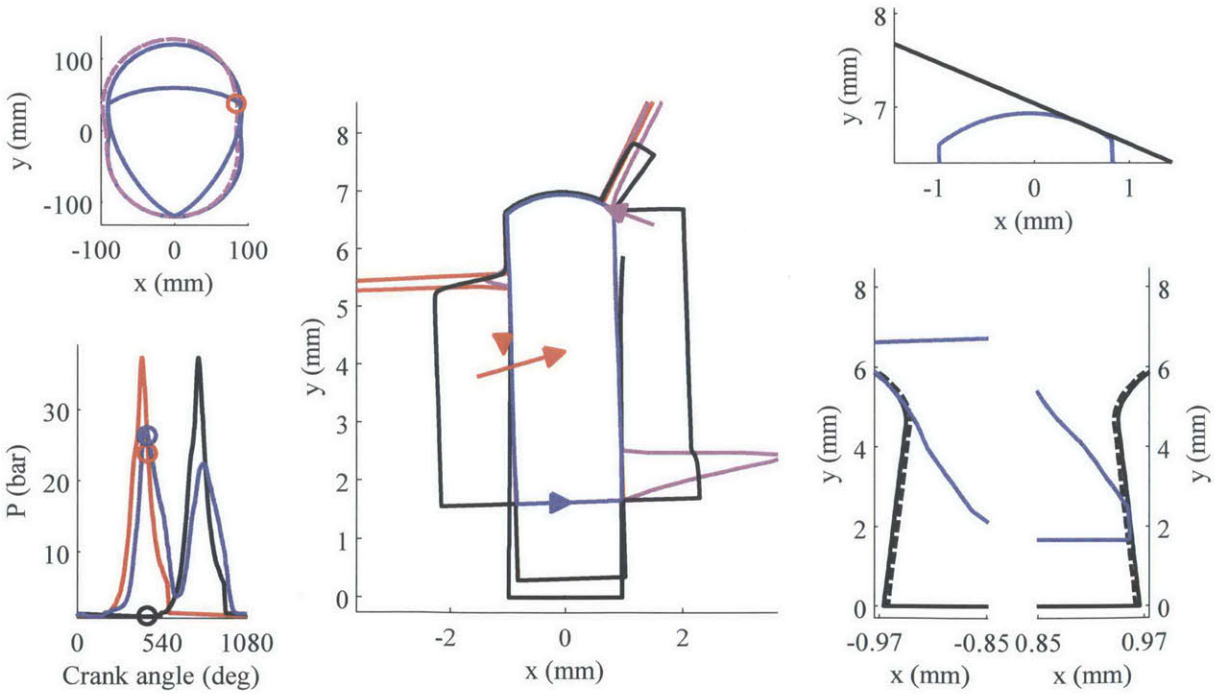

Fig. 4.62 Apex seal position and forces on the cross-section at 8000 rpm, z/L = 0.15 and 450 CA

At the end of expansion, the pressure in the groove is significantly higher than chamber pressure. This opens the trailing flank and the gas under the seal can leak to the trailing chamber (Fig. 4.63). This effect is not seen at low speed because the groove-chamber pressure difference is not large enough.

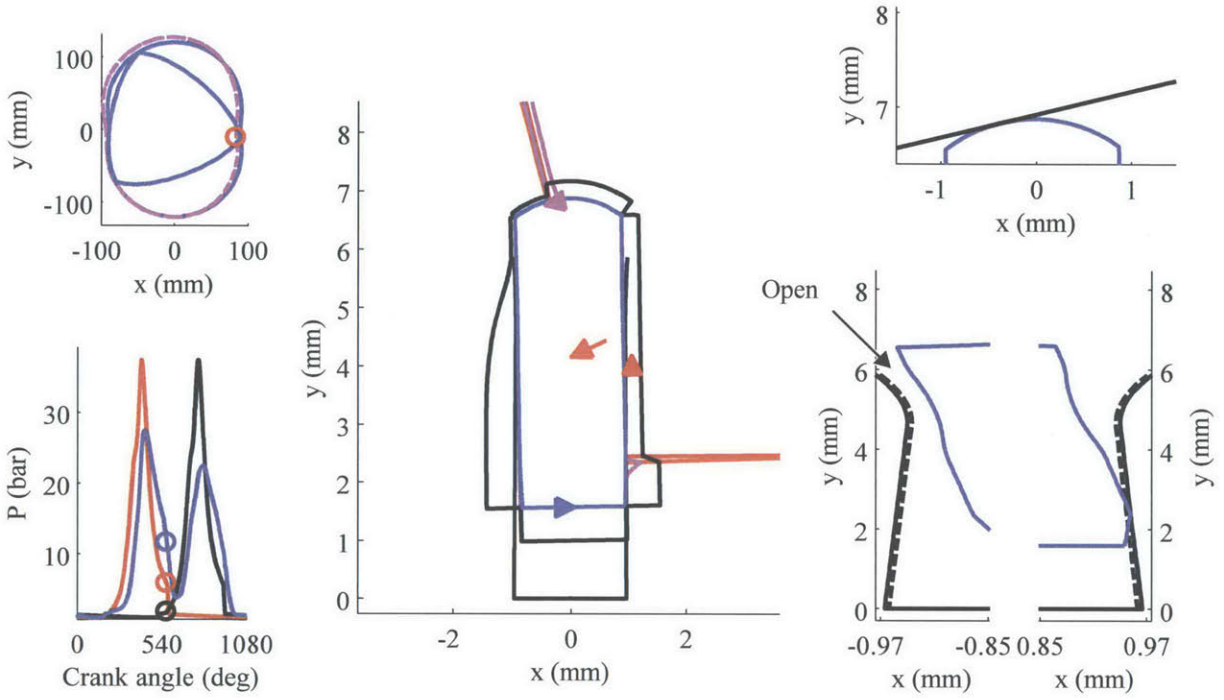

Fig. 4.63 Apex seal position and forces on the cross-section at 8000 rpm, z/L = 0.15 and 570 CA

During phase 4 and most of phase 5, the AS also behaves similarly to its low-speed behavior (Fig. 4.64 and Fig. 4.65).

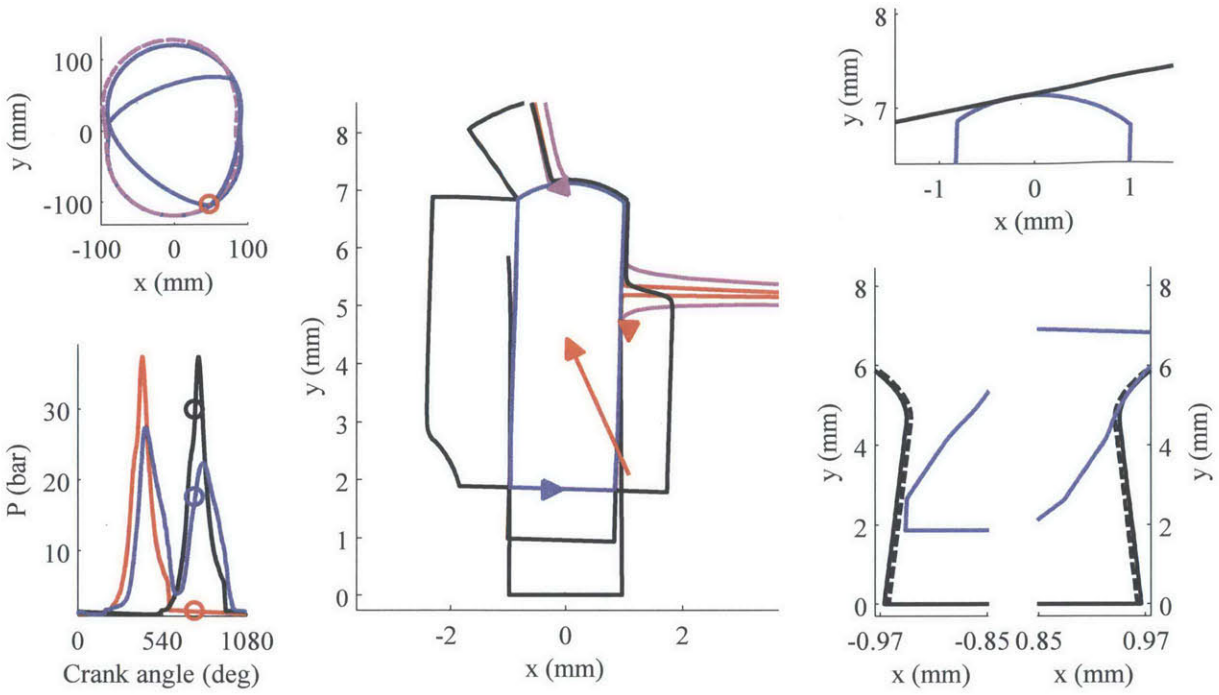

Fig. 4.64 Apex seal position and forces on the cross-section at 8000 rpm, z/L = 0.15 and 750 CA

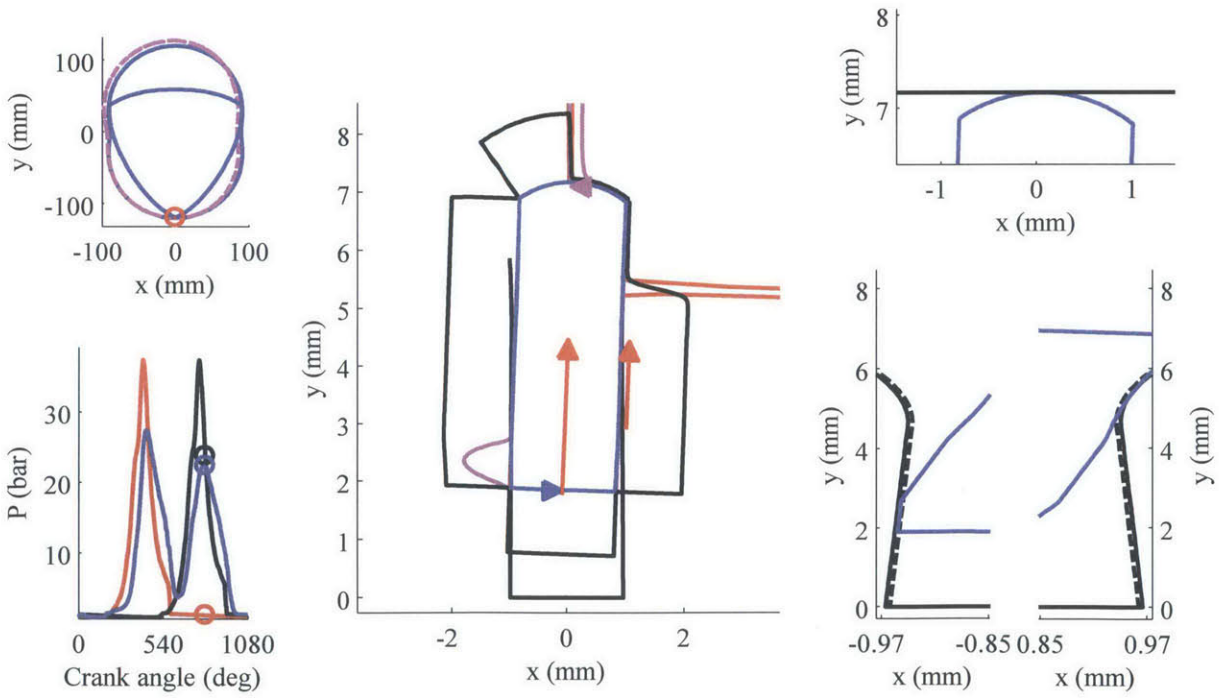

Fig. 4.65 Apex seal position and forces on the cross-section at 8000 rpm, z/L = 0.15 and 810 CA

At the end of phase 5, the groove pressure tilts the seal and opens the trailing edge, similarly to the end of phase 3 (Fig. 4.66).

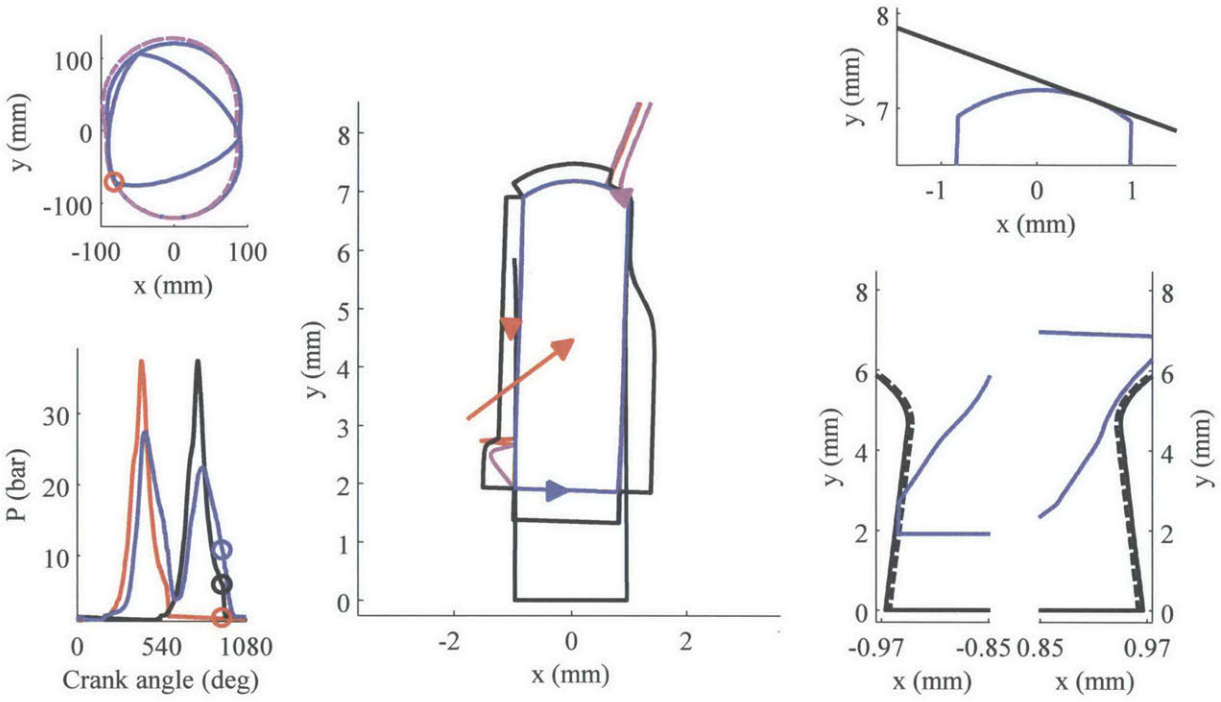

Fig. 4.66 Apex seal position and forces on the cross-section at 8000 rpm, z/L = 0.15 and 930 CA

At the end of phase 6, when the pressure reaches about atmospheric level, the seal is pushed towards the leading side by body force (Fig. 4.67).

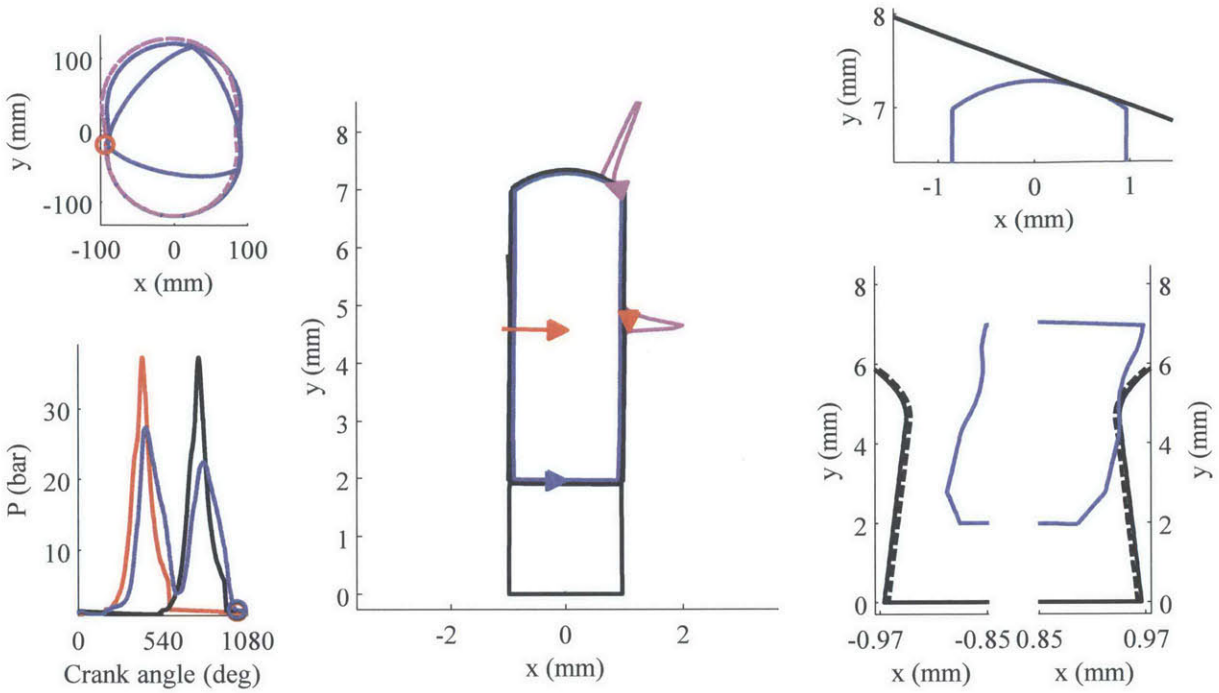

Fig. 4.67 Apex seal position and forces on the cross-section at 8000 rpm, z/L = 0.15 and 1020 CA

Rotor housing distortion has larger amplitude at high speed and also a shape that is more difficult to conform to. Nevertheless, when the pressure in the groove is high, the seal can mostly conform to housing distortion (Fig. 4.68). There is still a small clearance in some conditions, and the leakage is not zero but remains relatively small.

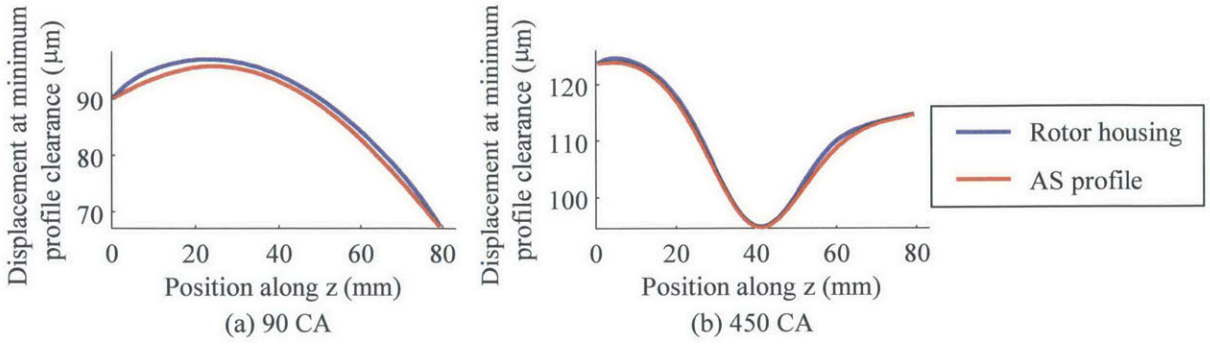

Fig. 4.68 Conformability of the seal to the rotor housing (a) with spring force only and (b) with a pressurized groove

The AS can conform to the groove as the groove distortion has a parabolic shape and its amplitude is not too large (Fig. 4.69).

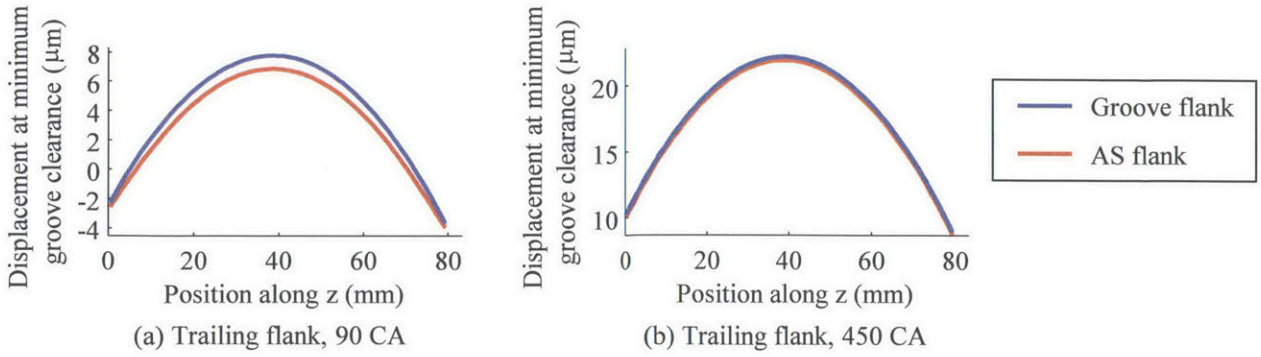

Fig. 4.69 Conformability of the seal to the rotor housing at (a) low chamber pressure difference, and (b) high chamber pressure difference

Corner seal clearance and spark plug leakage remains the most two important leakage mechanisms (Fig. 4.70 and Fig. 4.71). However, flank leakage also becomes an important leakage mechanism due to the opening of the low pressure flank around exhaust port opening.

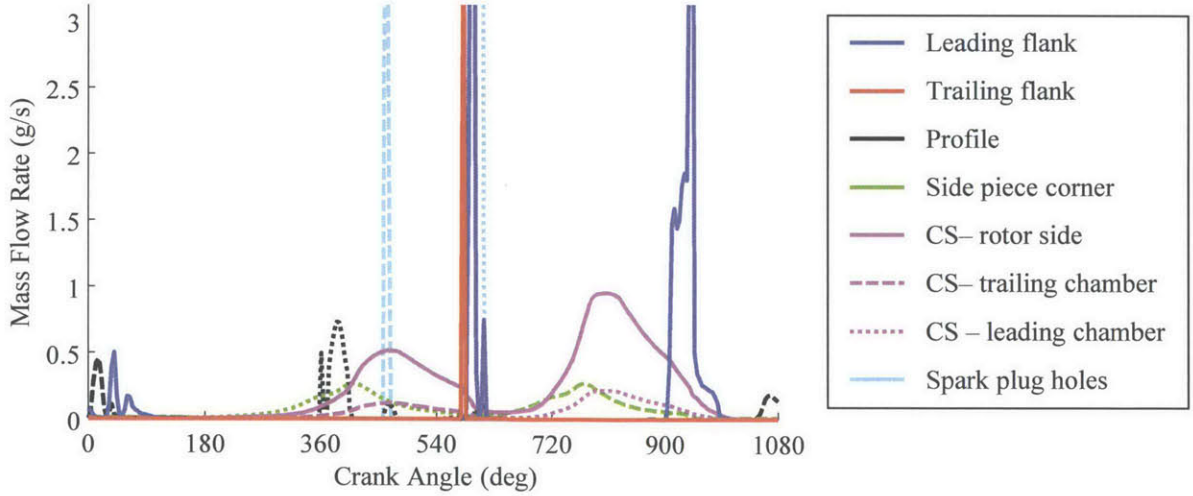

Fig. 4.70 Leakage mass flow rate as a function of crank angle for the different mechanisms at 8000 rpm full-load

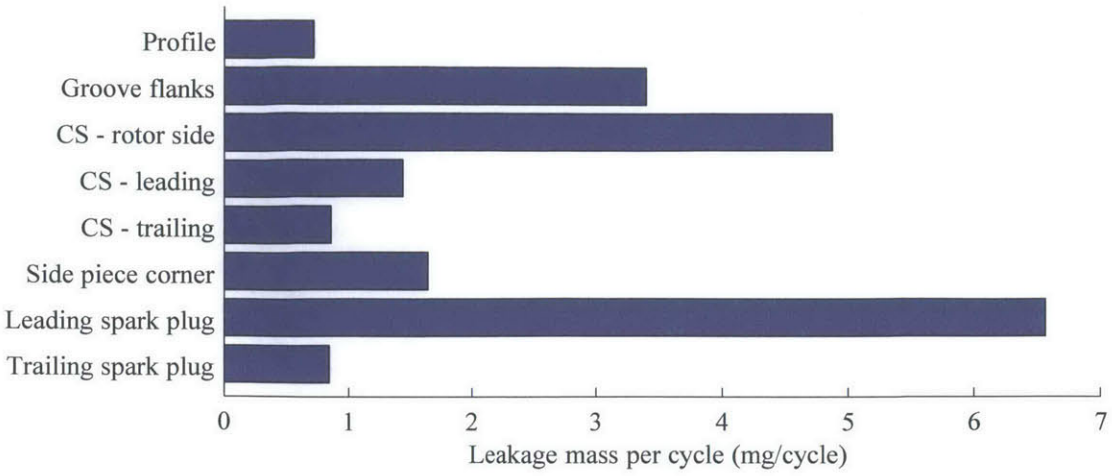

Fig. 4.71 Comparison of the total leakage for the different mechanisms at 8000 rpm full-load

As speed is higher, the hydrodynamic pressure generation ability of the seal profile is significantly increased. About half of the load on the trailing AS is supported by hydrodynamic pressure while the leading AS is mainly supported by hydrodynamic pressure (Fig. 4.72). This higher hydrodynamic pressure generation ability leads to a reduction of 76 % of the factor $P_w V_w$ when adding oil on the housing (Fig. 4.73).

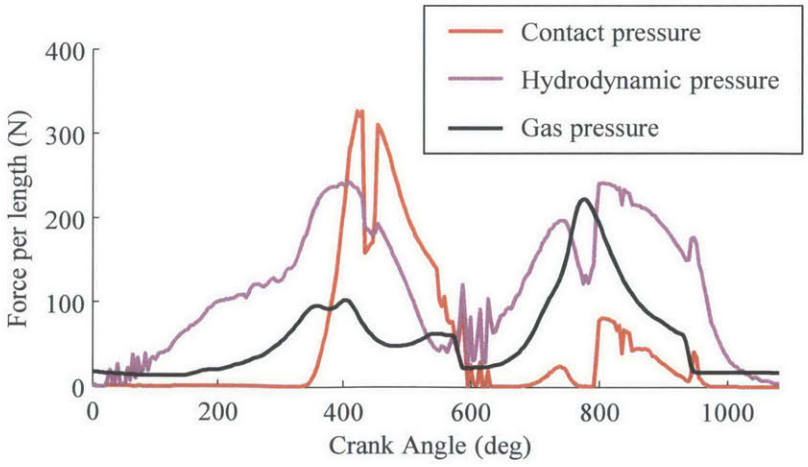

Fig. 4.72 Contact, hydrodynamic and gas pressure on the profile at 8000 rpm full-load

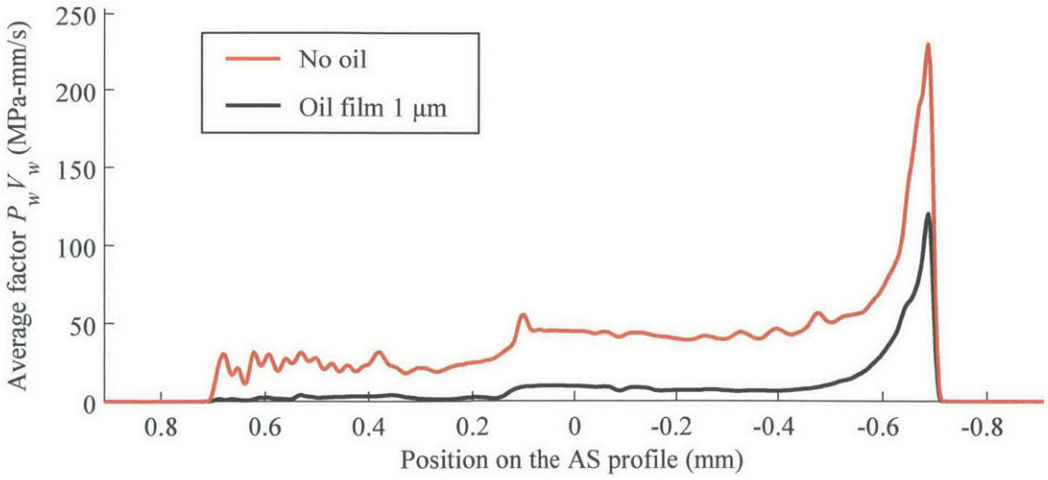

Fig. 4.73 Average wear rate indicator on the profile at 8000 rpm full-load

Flank wear distribution is similar to low speed, except the wear on the inner part of the flanks is increased when compared to the outer part of the flanks.

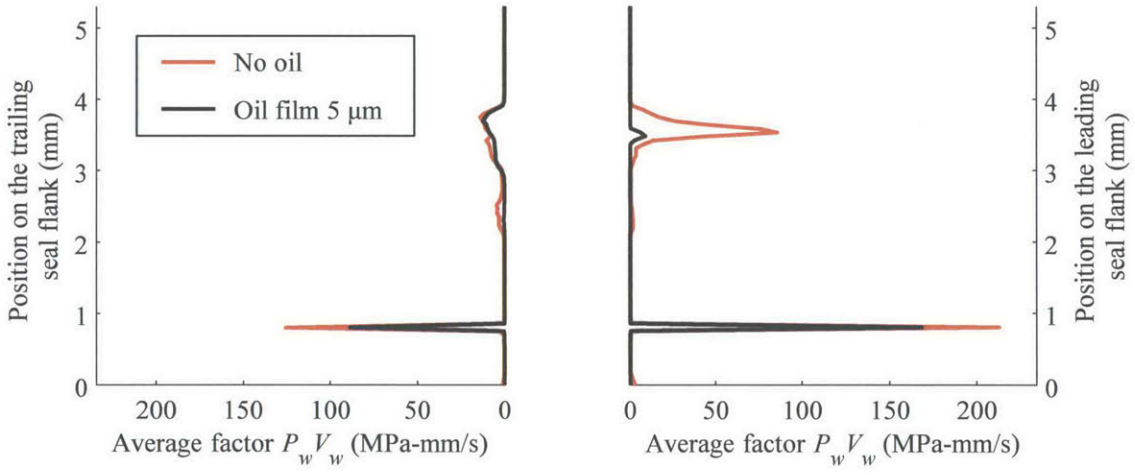

Fig. 4.74 Average wear rate indicator on the AS flanks at 8000 rpm full-load

Friction power of one AS at 8000 rpm full-load is 758 W without oil supply. Friction power is reduced by 74 % in fully-flooded condition, down to 202 W. Asperity contact friction accounts for 184 W while hydrodynamic friction accounts for 18 W.

4.3.4 Effect of Speed on Performance

The comparison between low-speed and high-speed AS sealing performances can be extended to an analysis of the performances as a function of rpm. In order to remove the effect of change in peak pressure as a function rpm, the leakage is presented in equivalent leakage area, which is defined as the isentropic orifice area at groove temperature needed to produce the same leakage as predicted by the different mechanisms. The total CS clearance leakage is the most important leakage mechanism and increases slightly with rpm as the peak pressure increases and then decreases at high rpm as the peak pressure starts to decrease (Fig. 4.75). Leading spark plug leakage varies slightly with rpm as the shape of the pressure trace changes. Flank leakage is low at low speed and increases rapidly between 4000 and 7000 rpm as the low-pressure flank starts to open at the end of expansion, as explained in section 4.3.3. Side piece corner leakage is constant by definition. Trailing spark plug hole leakage is much smaller than leading spark plug leakage and is more or less constant.

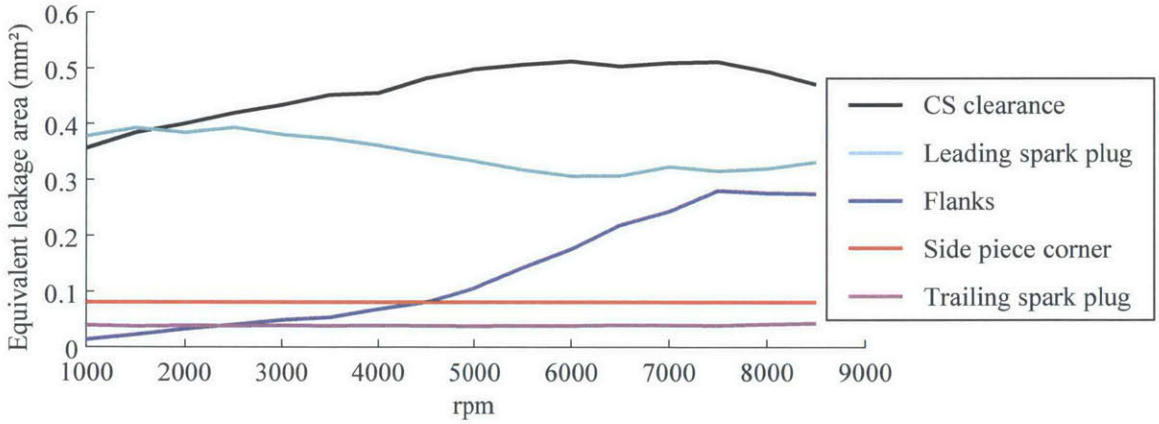

Fig. 4.75 Effective leakage area as a function of rpm at full-load

Friction increases with rpm until peak pressure starts to decrease (Fig. 4.76). Friction also changes from fully asperity contact friction at low-speed to partially hydrodynamic friction at high speed. It is still far from reaching the hydrodynamic regime.

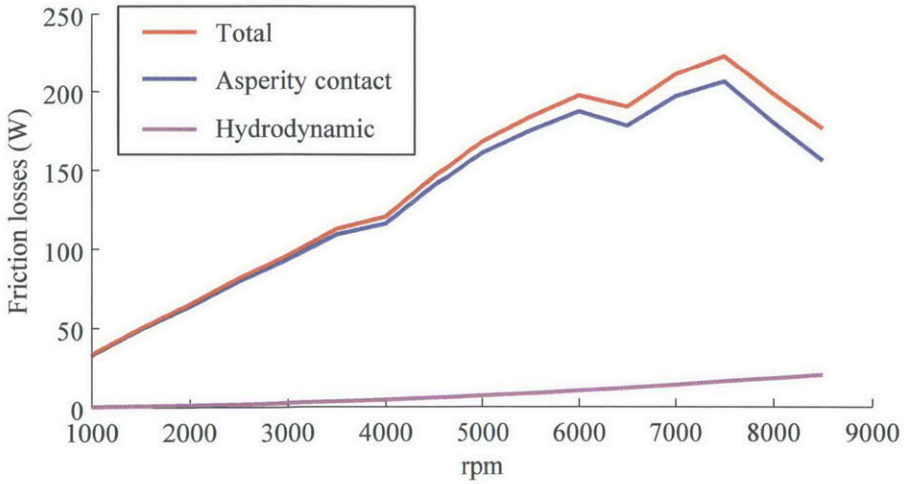

Fig. 4.76 Friction losses for one AS as a function of rpm at full-load

4.3.5 Effect of Corner Seal Clearance

Corner seal clearance leakage is the most important leakage mechanism and is highly dependent on the size of the clearance (Fig. 4.77). As the leakage is a power function of the clearance at small clearance, a small reduction in clearance leads to a large gain. As an example, reducing the clearance from 12 to 9 μm cuts down the leakage by half.

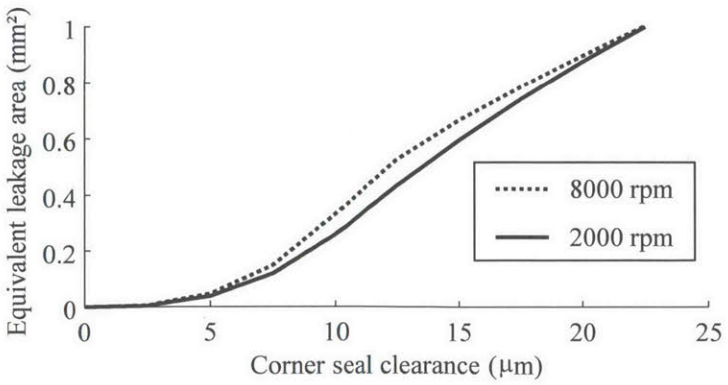

Fig. 4.77 Effect of corner seal clearance on leakage at 2000 and 8000 rpm full-load

4.3.6 Effect of Leading Spark Plug Hole Diameter

Reducing the spark plug diameter also results in an important gain in sealing performance (Fig. 4.78). Reducing the hole to the size of the trailing spark plug hole would make this leakage

mechanism small compared to the other mechanisms. This is however a trade-off with ignition performance.

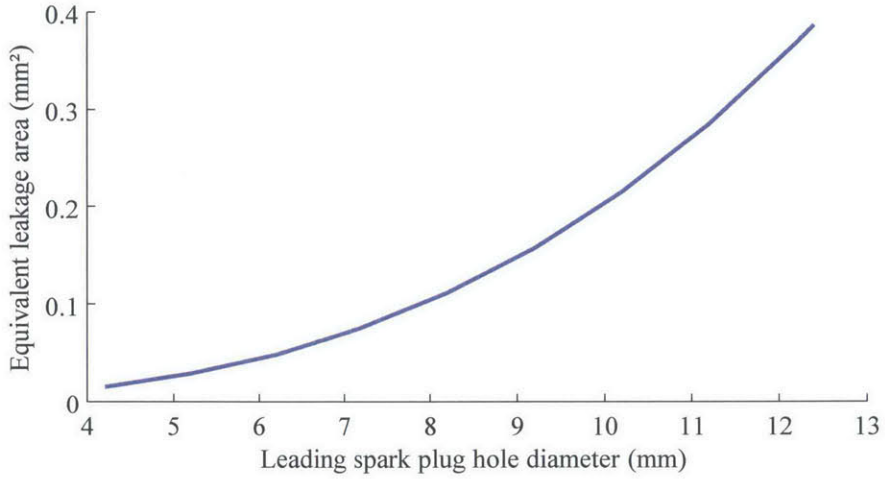

Fig. 4.78 Effect of leading spark plug hole diameter on leakage at 2000 rpm full-load

4.3.7 Effect of Seal Height

The effect of increasing seal height is investigated in order to try to reduce flank leakage. For a seal height 60 % larger than mass production specifications, the general behavior of the AS remains similar and the pressure under the seal is generally higher (Fig. 4.79). Increasing seal height is slightly reduces flank leakage by retarding the increase of flank leakage to a higher speed (Fig. 4.80). On the other hand, the leakage from the CS clearance increases due to the increased under-seal pressure. Simply changing the height of the seal is not enough to reduce leakage at high speed.

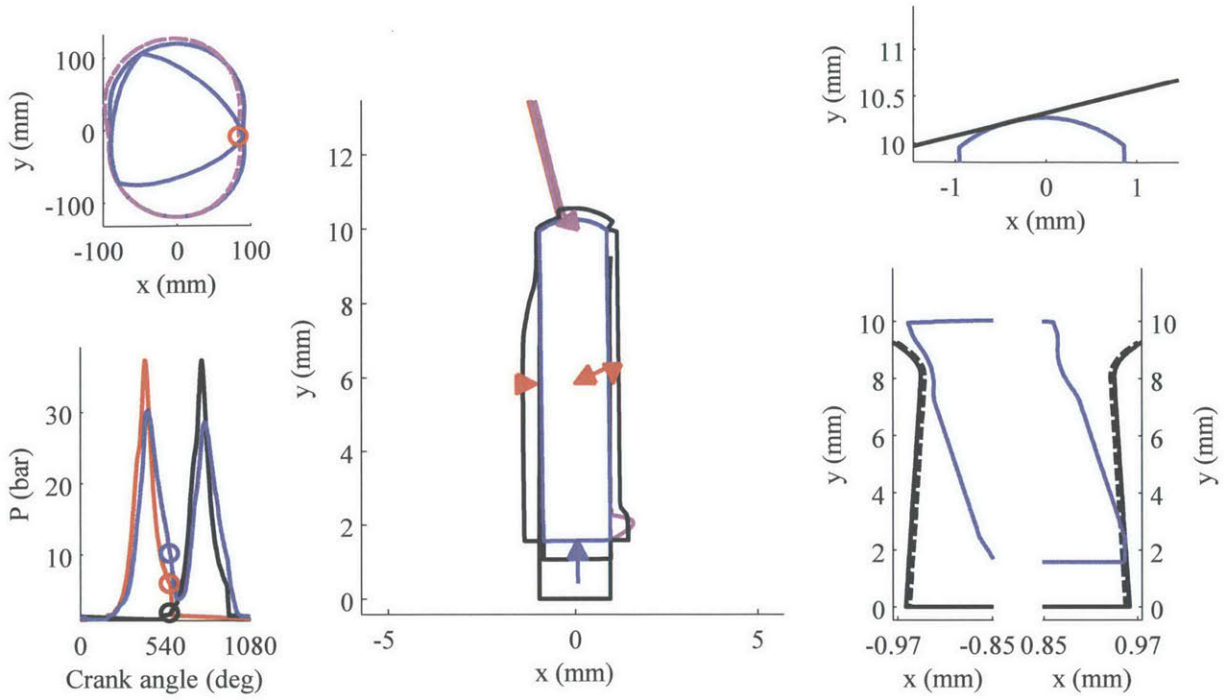

Fig. 4.79 Apex seal position and forces on an extended height AS at 8000 rpm, z/L = 0.15 and 570 CA

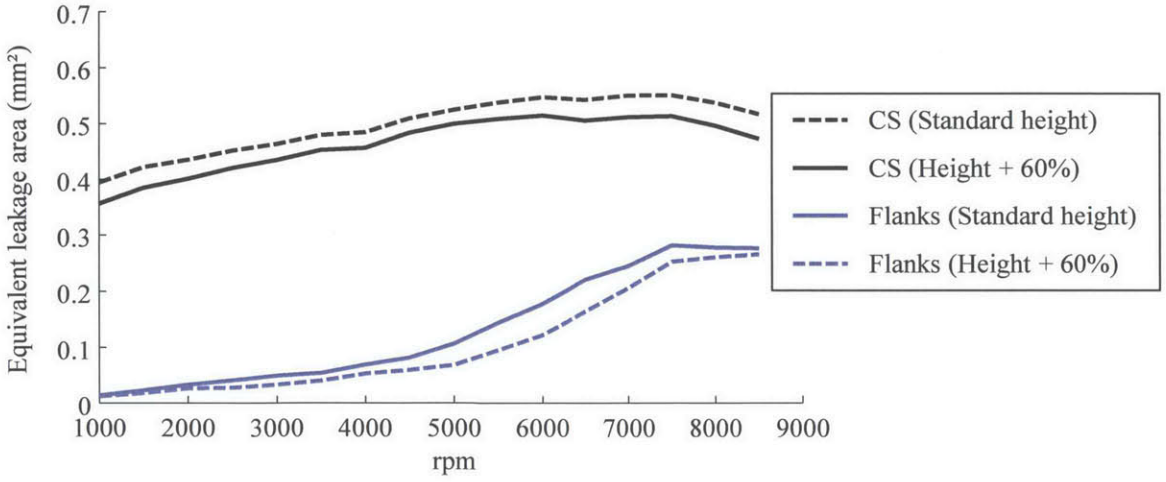

Fig. 4.80 Change in leakage for increased height AS

4.3.8 Conclusions on Model Prediction

The model can robustly predict the coupled AS dynamics and gas flow around the seal in a large range of conditions. The findings on the AS behavior can be summarized by the following conclusions:

1. The apex seal can conform to the distorted housing and groove for most conditions. Therefore, as far as the dynamics and gas leakage are concerned, the apex seal can be modeled as a rigid body with no groove and housing distortions. Doing so can make simplify the input and shorten the preparation time for applications. Nevertheless, it is important to take into account the different heights of the seal and the groove along the seal in order to obtain accurate groove pressure and AS dynamics predictions.
2. Without wear on the seal and groove flanks, the seal oscillates because there is no stable equilibrium position during an important portion of the cycle. As the flanks wear down rapidly, this is not a representative condition and predictions with measured wear give a better understanding of AS behavior.
3. Corner seal leakage is the dominant leakage mechanism and is highly dependent on the size of the clearance.
4. Leakage through the leading spark plug is the second most important leakage mechanism for the experimental pressure trace taken in the presented results.
5. Flank leakage is almost negligible at low speed, but increases rapidly as a function of speed. This is due to the fact that, as speed increases, the gas has less time to flow out of the groove during expansion. The resulting higher groove pressure forces open the low-pressure flank leading to gas leakage.
6. Side piece corner leakage is smaller than the three dominant leakage mechanisms as the leakage area is small.
7. Profile wear rate is reduced of at least 40 to 76 % from 2000 to 8000 rpm due to oil supply when compared to a dry contact. This only accounts for the pressure-velocity term and the effective reduction is expected to be higher due to the reduction in the wear coefficient caused by the presence of the lubricant and additives.
8. Wear rate of the flanks is expected to be significantly smaller in the presence of oil when compared to dry contact. For the shape used in the analysis, the wear rate reduction on

the leading flank is important while the presence of oil on the trailing flank does not significantly reduced wear.

9. Friction losses are dominated by asperity contact friction. Nevertheless, adding oil on the housing decreases friction by 40 to 74 % from 2000 to 8000 rpm. Hydrodynamic friction remains small even at high speed, which means that the contact is still in the beginning of the mixed regime on the Stribeck curve.

4.4 Comparison with Experiments

As a first step toward validating the model, the under-seal pressure and AS position are compared to experimental data. Experimental pressure was obtained from a pressure transducer in the groove while apex position was measured by two inductive sensors, one on top of the groove and one inside the groove both measuring the clearance between the seal and the groove flank (Fig. 4.81). The condition chosen for comparison is 2000 rpm full-load. The predicted under-seal pressure shows good agreement with the measured data (Fig. 4.82). It should be noted that the inputs to the model are the engine specifications, tolerances and measurements without any adjustment.

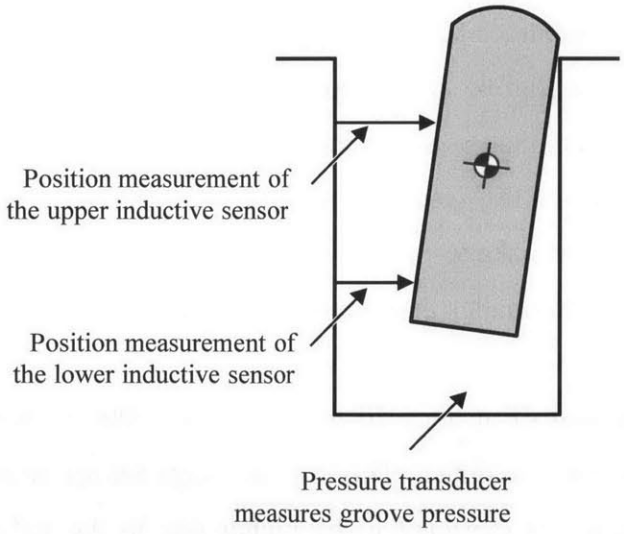

Fig. 4.81 Position of the sensors

The predicted under-seal peak pressure for both seals is similar to experimental data. The predicted under-seal pressure is also similar to experimental data for the expansion phase as well

as for the compression of the trailing chamber. The predicted under-seal pressure differs from experimental data only for the compression phase of the leading chamber. This could be further investigated. Nevertheless, this good agreement between model and experiments shows that the model captures the dominant physics.

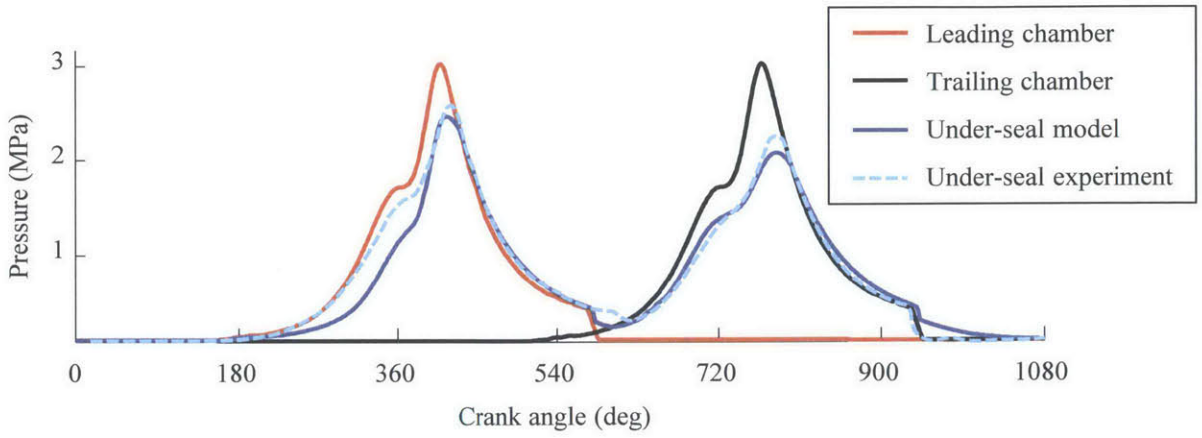

Fig. 4.82 Comparison between predicted and measured under-seal pressure at 2000 rpm full-load

The predicted position of the seal is also compared to the measured position by simulating the lateral displacement at the same location as the upper and lower sensors (Fig. 4.83). It can be seen that the general transitions are correctly predicted. However, there are still secondary effects that do not match, especially for the lower sensor.

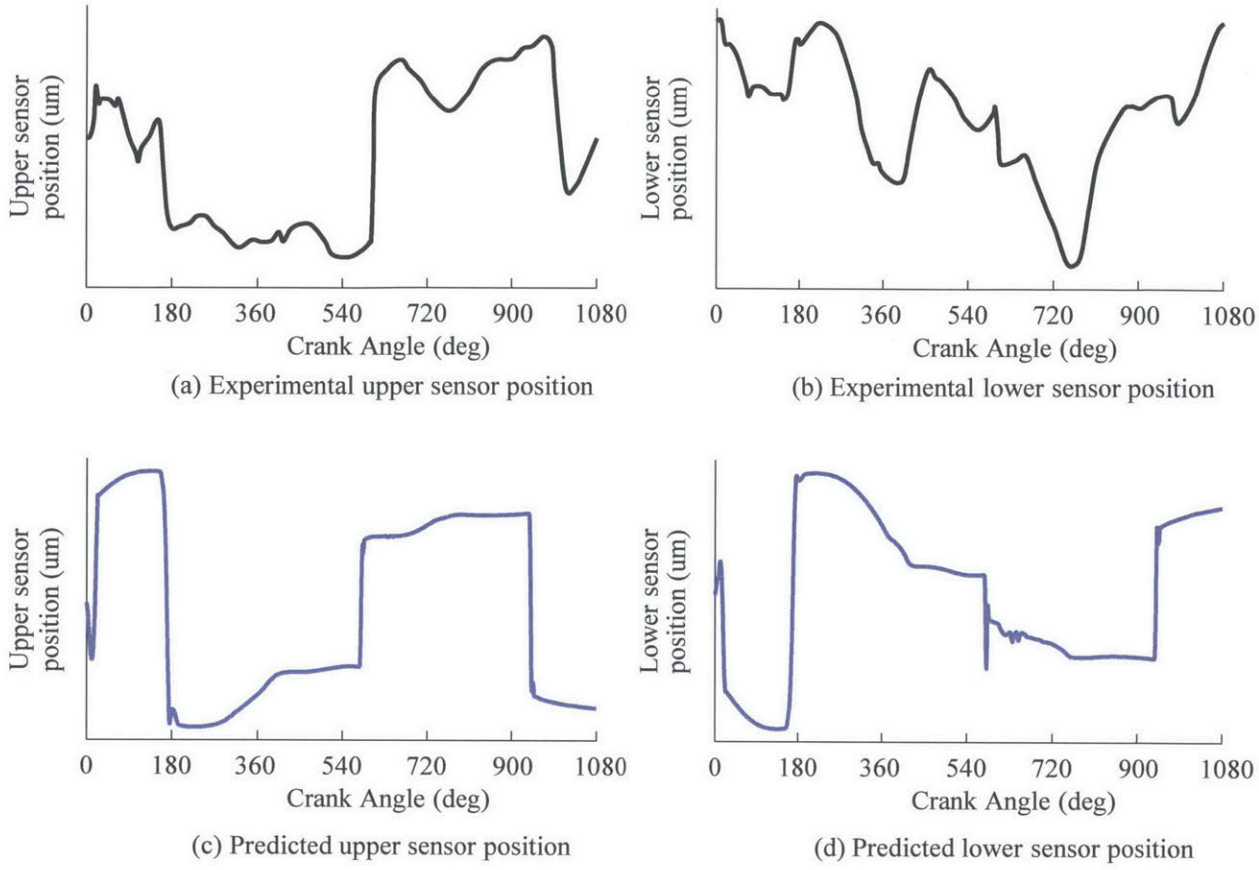

Fig. 4.83 Comparison between measured and predicted AS position at 2000 rpm full-load

In short, even if the model is not fully validated, this first step comparison gives a good level of confidence that the model captures the main AS dynamics and gas flow around it. It also shows that the model can predict dynamics and gas leakage with accurate input data without tuning.

4.5 Two-Piece Apex Seal Model Conclusions

A model is formulated to predict the sealing performance of the two-piece apex seal. After testing the model for a range of different inputs, it is shown that the model is robust thanks to the force formulation that makes the error function continuous. From the model predictions, which show good agreement with experimental results, performances of the AS are assessed by calculating trends in leakage, wear and friction.

Due to the unique configuration of the rotary engine, corner effects dominate leakage. However, it seems possible to reduce corner leakage below an acceptable level by mainly sealing the

corner seal clearance by controlling the gap with a force instead of controlling the geometric tolerances. In seems also reasonable that leakage through the spark plug hole can be reduced below an acceptable level. The seal seems to be flexible enough to conform to the distorted groove and housing. Flank leakage also needs to be reduced. Increasing the under-seal pressure would contribute to reducing flank leakage. The effect of the three-piece configuration on flank leakage is investigated in the next chapter.

Potential reduction in wear and friction is limited as the shape of the AS profile is dictated by engine kinematics. Providing oil supply helps in reducing wear and friction by changing the force balance, from 40 to 76% from low to high speed. Asperity contact still remains an important part of the force that supports the load and dominates friction. Those results do not include the effects of supplying additives and ensuring boundary lubrication rather that dry lubrication, which can potentially be more important effects on reducing wear and friction.

In brief, it seems feasible to reduce leakage, wear and friction below an acceptable level. Oil transport and evaporation assessment would be the next step in the modeling effort in order to determine how much oil supply is needed and what is the best way of supplying this lubricating oil.

Chapter 5

Three-Piece Apex Seal Model

Leakage issues of the two-piece AS seem to be possible to solve by simple design modifications, except for flank leakage that increases above an acceptable threshold as speed increases. This chapter presents a multi-body model to investigate if a three-piece AS can solve the flank leakage problem. Although the model is capable of handling seal deformation, this chapter focuses on rigid-body dynamics and interactions between the two main pieces, as it was shown that the AS can conform to the distorted housing and groove.

From model predictions, the three-piece AS has the potential to significantly reduce flank leakage because the inner piece remains pushed toward the low pressure flank during most of the cycle. Only at high-speed, body force creates oscillation of the trailing apex inner piece creating an important groove pressure lag. Nevertheless, flank leakage is significantly lower for this case when compared to a two-piece AS. In all cases, the clearance between the inner and outer pieces should be kept small to avoid flow along the seal that would equilibrate the pressure on all faces of the inner piece to groove pressure level.

5.1 Objectives

Similarly to the two-piece AS model, the objectives of the three-piece AS model are to predict dynamics and performances of the apex seal. In particular, the three-piece AS model targets at assessing if adding the inner piece can significantly reduce flank leakage. It is expected that other performance indicators, such as the other leakage mechanisms, wear and friction, should be similar to what is seen for the two-piece AS. This chapter therefore focuses on the inner and outer pieces interaction and the understanding of the coupled dynamics of the pieces in order to predict flank leakage.

5.2 Model Formulation

Three-piece AS model formulation is similar to the two-piece AS model. Forces, moments and gas flow on the profile, flanks and under the seal are calculated in the same fashion. A finite element beam model is used for both pieces, and a globally convergent Newton algorithm is used to solve the dynamics of both pieces simultaneously.

The main differences are that the model must consider the displacement of the inner and outer pieces simultaneously (Fig. 5.1) and must calculate forces, moments and gas flow at the interface between the pieces (Fig. 5.2).

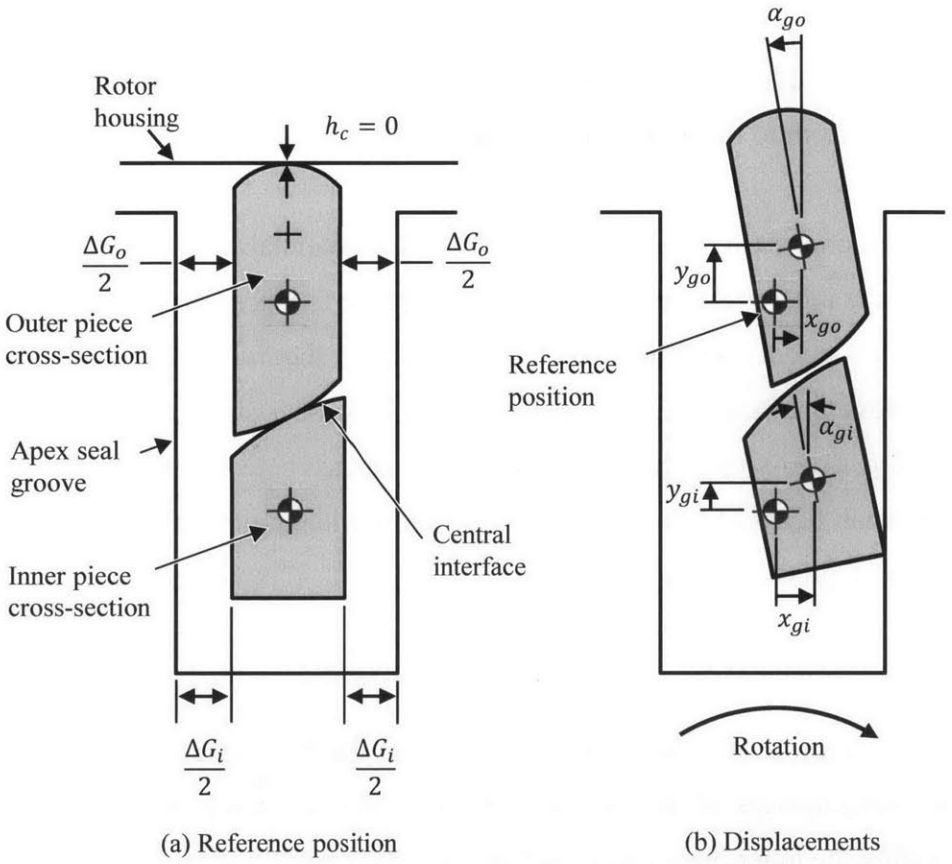

Fig. 5.1 Displacements of inner and outer pieces of the three-piece AS

Asperity contact pressure and shear force are the main interaction between the two pieces. Hydrodynamic pressure generated by oil squeezing is neglected as the two pieces generally remain in contact with each other and therefore their relative velocity remains small when

compared with the velocity at which the seal can hit the flanks of the groove. Gas forces and moment on the two pieces are considered as their contribution can be large. For gas flow at the interface, the values of pressure on both sides of the seal for each cross-section are added as unknowns so the model can calculate the gas flow around the seal as a function of those pressures.

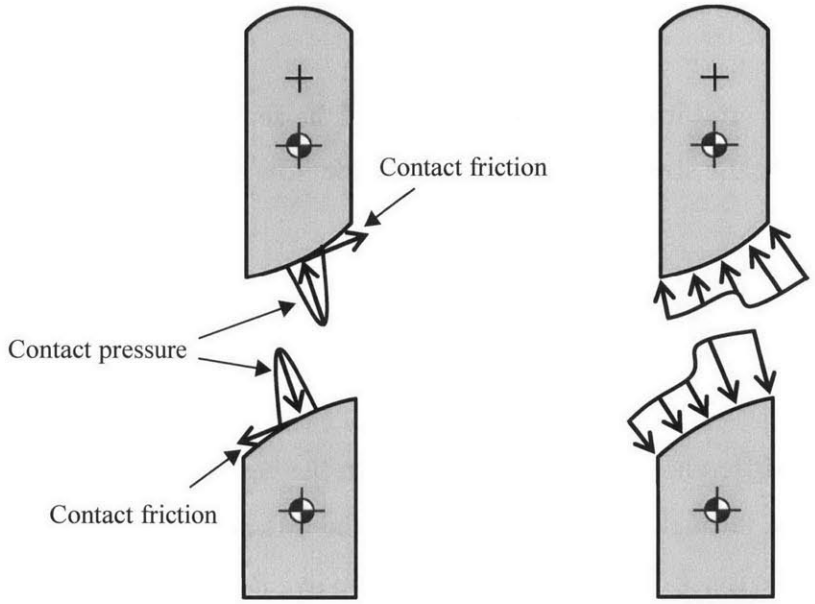

(a) Asperity contact (b) Gas

Fig. 5.2 Asperity contact and gas forces at the interface between the inner and outer pieces

5.2.1 Approximations

All the approximations used in the two-piece AS model still holds for the three-piece AS model. Two additional approximations are added for the central interface between the inner and outer pieces.

First, the hydrodynamic pressure is neglected between the inner and outer pieces. This approximation holds because relative velocity between the two pieces is generally small. Gas flow between the two pieces is still set to zero whenever the minimum central clearance is smaller than the film thickness on the groove flanks. This insures that the gas does not flow preferably flow through the central interface due to the no-oil approximation.

Second, the flow along the central clearance, between the inner and outer pieces, is neglected. A criterion for this approximation to be valid is that the time it takes to fill the cavity from the end of the seal (τ_f) should be small compared to the time scale of pressure variation in the groove (τ_P):

$$\tau_f \ll \tau_P \tag{5.1}$$

The time scale to fill the central interface from the ends of the seal can be approximated by the time it takes to fill a volume the size of the cavity through the flow restriction

$$\tau_f \sim \frac{\Delta m}{\dot{m}} \sim \frac{\left(\frac{\Delta P\, V}{RT}\right)}{\bar{\rho} Q} \sim \frac{\left(\frac{\Delta P\, V}{RT}\right)}{\frac{\bar{P}}{RT}\frac{\Delta P}{r}} \sim \frac{Vr}{\bar{P}} \tag{5.2}$$

in which Δm is the mass difference in the volume between the beginning and end of the filling process, $\dot{m}$ is the flow rate through the restriction, ΔP is the difference in pressure between the end of the seal and the cavity, V is the volume of the cavity, R is the gas constant, T is the temperature of the cavity, $\bar{\rho}$ is the average gas density, $\bar{P}$ is the average gas pressure, and r is the resistance to the flow given for a viscous flow between two parallel plate by

$$r \sim \frac{12\mu_g L}{h^3 W} \tag{5.3}$$

in which μ_g is the gas viscosity, L is the half-length of the seal, h is the average height of the cavity, and W the half-thickness of the seal. The volume can be approximated by a rectangular box of size L, h, and W:

$$V \sim LhW \tag{5.4}$$

Replacing the volume and flow resistance in eq. (5.2) yields the time scale for filling the central interface

$$\tau_f \sim \frac{12\mu_g}{\bar{P}}\left(\frac{L}{h}\right)^2 \tag{5.5}$$

For a pressure of 1 bar, a length of about 40 mm, an approximate height of 40 μm, the time scale is on the order of 2 ms. Considering that groove pressure varies on a time scale on the order of 36 CA, the two time scale are on the same order. The model is therefore only valid for small clearance between the inner and outer pieces. The gas flow along the seal could be added to the model, but a design for which the gas can flow along the central clearance would not be beneficial because pressure in the central clearance would be the same as groove pressure and the inner piece would be useless as the pressure all around it would be the same.

5.2.2 Central Interface Asperity Contact Forces and Moment

Asperity contact forces and moment at the central interface are calculated based on the clearance between the inner and outer pieces using the simplified Greenwood-Tripp relation. Contact friction force is calculated from the contact pressure, a coefficient of friction and the relative velocity between the inner and outer pieces using a smoothing method around changes of velocity direction as is done for flank friction.

The first step towards calculating asperity contact pressure is to calculate the clearance at the central interface. The profile of both pieces is defined using a cut angle between the two pieces (θ_v) and a small deviation from that cut angle (Fig. 5.3). This method is used to allow the flexibility of using a large cut angle while maintaining the small displacement approximation when calculating the clearance (Fig. 5.4).

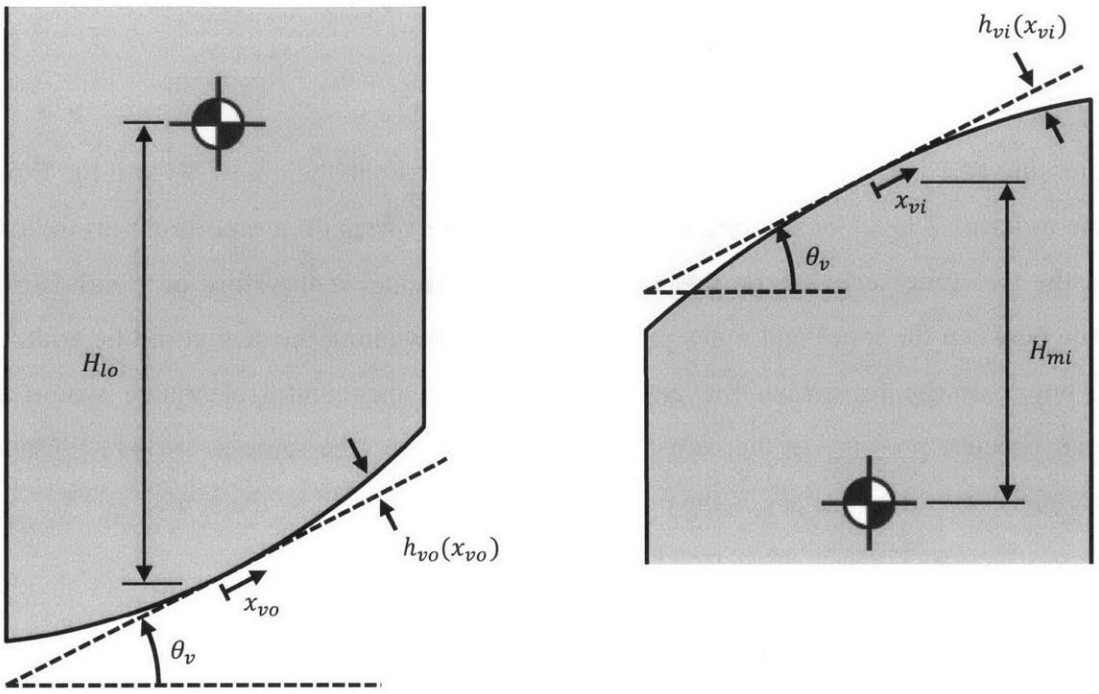

(a) Outer piece (b) Inner piece

Fig. 5.3 Geometry of the inner and outer pieces at the interface

Under the small displacement approximation, the central clearance (h_v) is given by a linear addition of the different contributions

$$h_v(x_{vi}, x_{vo}) = (x_{gi} - x_{go})\, sin(\theta_v) + (-y_{gi} + y_{go})\, cos(\theta_v) - \alpha_{gi}(x_{vi} + L_{vi}) + \alpha_{go}(x_{vo} - L_{vo}) + h_{vi}(x_{vi}) + h_{vo}(x_{vo}) \tag{5.6}$$

in which

$$L_{vi} = H_{mi}\sin(\theta_v),$$

$$L_{vo} = H_{lo}\sin(\theta_v),$$

x_{gi}, y_{gi} and α_{gi} are the lateral, radial, and rotational displacements of the inner piece, x_{go}, y_{go} and α_{go} are the lateral, radial, and rotational displacements of the outer piece, h_{vi} and h_{vo} are the profile clearance of the inner and outer pieces, x_{vi} and x_{vo} are the distances from the center of the inner and outer pieces along the cut line, and H_{mi} and H_{lo} are the distances from the contact point to the section center of the inner and outer pieces.

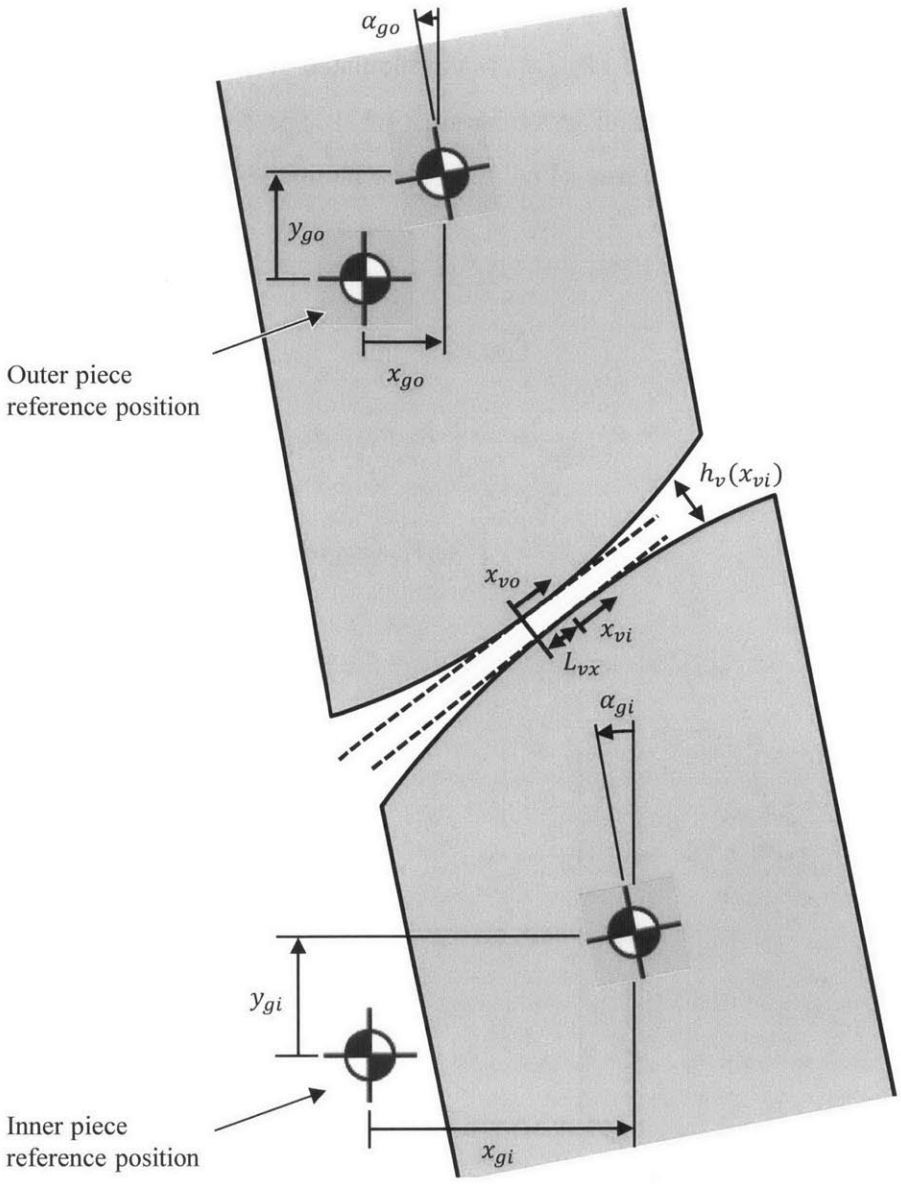

Fig. 5.4 Clearance between the inner and outer pieces

The distance along the inner seal cut line (x_{vi}) is chosen as the reference coordinate to calculate the forces and moments and the coordinate along the outer seal cut line (x_{vo}) can be related to x_{vi} by

$$x_{vo} = x_{vi} + L_{vx}$$

in which (5.7)

$$L_{vx} = (x_{gi} - x_{go})\cos(\theta_v) + (y_{gi} - y_{go})\sin(\theta_v) - (\alpha_{go}H_{lo} + \alpha_{gi}H_{mi})\cos(\theta_v)$$

The central clearance (h_v) becomes a relation of x_{vi} only by using eq. (5.7) and interpolating h_{vo}. The asperity contact pressure ($P_{vc}(x_{vi})$) is calculated from the central clearance and the simplified Greenwood-Tripp relation given in eq. (4.12). The forces and moment on the inner piece in the cut-line reference frame (Fig. 5.5) are calculated by numerically integrating the contact pressure

$$F'_{vci,x_{vi}} = 0$$

$$F'_{vci,y_{vi}} = -\int P_{vc}(x_{vi})dx_{vi} \tag{5.8}$$

$$F'_{vci,\alpha_{vi}} = -\int x_{vi}P_{vc}(x_{vi})dx_{vi}$$

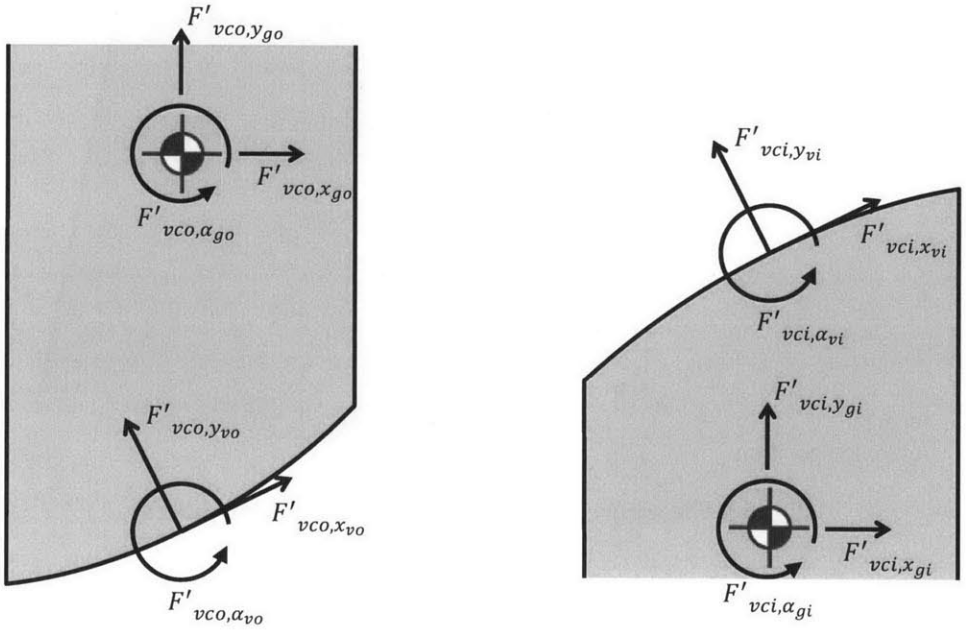

(a) Outer piece

(b) Inner piece

Fig. 5.5 Asperity contact resulting forces and moments on the inner and outer pieces

Forces and moment on the inner piece are transferred to the center of mass reference frame by the transformation

$$\boldsymbol{F'_{vci,gi}} = \boldsymbol{T_{vgi}}\,\boldsymbol{F'_{vci,vi}}$$

in which

$$\boldsymbol{F'_{vci,gi}} = \begin{bmatrix} F'_{vci,x_{gi}} \\ F'_{vci,y_{gi}} \\ F'_{vci,\alpha_{gi}} \end{bmatrix},$$

$$\boldsymbol{T_{vgi}} = \begin{bmatrix} \cos(\theta_v) & -\sin(\theta_v) & 0 \\ \sin(\theta_v) & \cos(\theta_v) & 0 \\ -H_{mi}\cos(\theta_v) & L_{vi} & 1 \end{bmatrix}, \tag{5.9}$$

and

$$\boldsymbol{F'_{vci,vi}} = \begin{bmatrix} F'_{vci,x_{vi}} \\ F'_{vci,y_{vi}} \\ F'_{vci,\alpha_{vi}} \end{bmatrix}$$

To avoid carrying additional numerical integrals, forces on the outer piece ($\boldsymbol{F'_{vco,vo}}$) are calculated as reaction forces and moment to the inner piece forces and moment:

$$\begin{aligned} F'_{vco,x_{vo}} &= -F'_{vci,x_{vi}} \\ F'_{vco,y_{vo}} &= -F'_{vci,y_{vi}} \\ F'_{vco,\alpha_{vo}} &= -F'_{vci,\alpha_{vi}} - F'_{vci,y_{vi}}L_{vx} \end{aligned} \tag{5.10}$$

Forces and moment on the outer piece are transferred to the center of mass reference frame by

$$\boldsymbol{F'_{vco,go}} = \boldsymbol{T_{vgo}}\,\boldsymbol{F'_{vco,vo}}$$

in which

$$\boldsymbol{T_{vgo}} = \begin{bmatrix} \cos(\theta_v) & -\sin(\theta_v) & 0 \\ \sin(\theta_v) & \cos(\theta_v) & 0 \\ H_{lo}\cos(\theta_v) & -L_{vo} & 1 \end{bmatrix} \tag{5.11}$$

Asperity contact shear stress at the interface on the inner piece is calculated using hyperbolic tangent functions of the relative velocity in order to make the friction force smooth around the change in direction:

$$\tau_{vci}(x_{vi}) = -k_{vc} C_{fv} P_{vc}(x_{vi})$$

in which

$$k_{vc} = C_{v0} \tanh\left(\frac{v_{vr}}{v_{v0}}\right) + C_{v1} \tanh\left(\frac{v_{vr}}{v_{v1}}\right), \tag{5.12}$$

C_{fv} is the central interface friction coefficient, and v_{vr} is the relative velocity between the inner and outer pieces. Unless otherwise specified the friction coefficient and the other constants in eq. (5.12) are given in Table 5.1. One hyperbolic tangent function is used so the value of k_{vc} converges rapidly to a value close to 1 for a small relative velocity. The second hyperbolic tangent function is used to extend the range of non-unity k_{vc} to insure the slope calculated for the Newton solver is non-zero for a larger range of relative velocity.

Table 5.1 Constants for central interface friction

Constant	Value
C_{fv}	0.15
C_{v0}	0.95
C_{v1}	0.05
v_{v0}	0.1 mm/s
v_{v1}	1 mm/s

The inner-outer piece relative velocity is given by the time derivative of eq. (5.7)

$$v_{vr} = \dot{L}_{vx}$$

in which

$$\dot{L}_{vx} = (\dot{x}_{gi} - \dot{x}_{go})\cos(\theta_v) + (\dot{y}_{gi} - \dot{y}_{go})\sin(\theta_v) - (\dot{\alpha}_{go} H_{lo} + \dot{\alpha}_{gi} H_{mi})\cos(\theta_v) \tag{5.13}$$

Friction forces and moment on the inner piece ($\boldsymbol{f}'_{vci,vi}$) are calculated by numerically integrating the shear stress:

$$f'_{vci,x_{vi}} = \int \tau_{vci}(x_{vi})dx_{vi}$$

$$f'_{vci,y_{vi}} = 0 \tag{5.14}$$

$$f'_{vci,\alpha_{vi}} = 0$$

Friction forces and moment on the inner piece are transferred to the center of mass reference frame by

$$\boldsymbol{f'_{vci,gi} = T_{vgi} f'_{vci,vi}} \tag{5.15}$$

Finally, friction forces and moment on the outer piece are calculated from the friction forces and moment on the inner piece using the relations given in eq. (5.10) and transferred to the center of mass reference frame by

$$\boldsymbol{f'_{vco,go} = T_{vgo} f'_{vco,vo}} \tag{5.16}$$

5.2.3 Central Interface Gas Forces and Moment

Gas forces and moment on the inner piece are calculated using the same method as for the profile in starved conditions presented in section 4.2.6. The clearance used is the central clearance (h_v) and the pressure on both sides of the central interface are the pressure values introduced specifically for the three-piece model, P_{vf} for the leading flank and P_{vb} for the trailing interface (Fig. 5.6). Gas forces and moment on the inner piece are transferred to the center of mass reference frame using the same transformation as for the asperity contact. Forces on the outer piece are calculated with the same method as described for the inner piece.

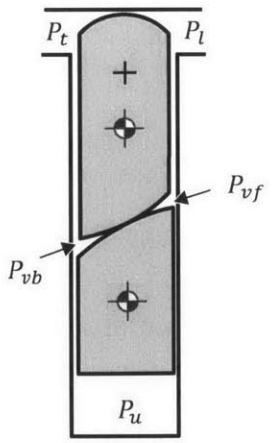

Fig. 5.6 Pressure on both sides of the central clearance

5.2.4 Three-piece AS Gas Flow Sub-Model

The two-piece AS flow sub-model is used to calculate all the individual mass flow rates as a function of the pressure at the ends of each interfaces (see section 4.2.11), including the central interface mass flow rate (Fig. 5.7). The difference from the two-piece model is that the pressure values on both sides of the central interface are added for all cross-sections to the global unknown vector along the mass under the seal. The corresponding added error equations are derived from mass flow conservation on both sides of the seal for all the cross-sections. As discussed in the approximation section, flow from one cross-section to the other is neglected.

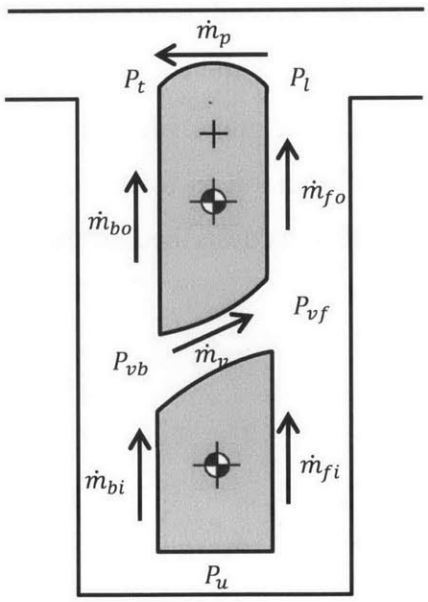

Fig. 5.7 Gas flow around the three-piece apex seal

5.3 Model Predictions

Three-piece AS design space is significantly larger due to a number of new parameters that can be varied. This section focuses on a potentially beneficial geometry to show that the model can predict the dynamics of the three-piece AS. The chosen configuration shows that the flank leakage can significantly be reduced when compared to the two-piece flank leakage. Flank leakage is particularly reduced at high-speed where the low-pressure flank opening phenomenon is almost eliminated. The three-piece configuration seems to be particularly beneficial for the trailing apex. The three-piece configuration also reduces leakage for the leading apex, but body force at high-speed causes a large groove-pressure lag.

The geometry chosen for the performance predictions has a total height about 60% greater than the current two-piece apex seal, a zero degree cut angle, a small barrel on the outer piece central interface but a flat inner piece, and a flank clearance 30 % smaller for the inner piece (Fig. 5.8). Groove wear is approximated based on two-piece groove wear measurements. Apex seal wear is not included as it is yet unknown and does not drastically change seal dynamics.

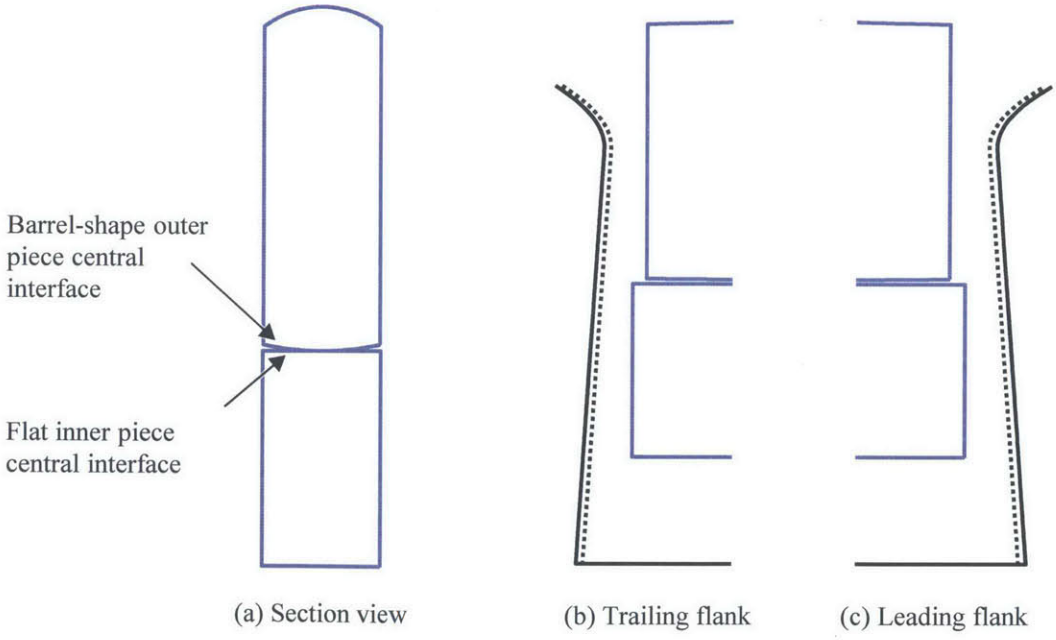

Fig. 5.8 Three-piece geometry used for model predictions

5.3.1 Low-Speed Predictions

At low speed, the tilt of the inner and outer pieces remains small for most of the cycle and consequently the groove pressure is almost the same as the high-pressure chamber (Fig. 5.9). The inner piece remains pushed against the low-pressure flank and keeps the low-pressure side of the central interface at a pressure close to the low-pressure chamber. This limits the tilt of the outer piece due to the net gas moment. Conversely to what could be imagined, the three-piece design does not rely on friction between the inner and outer pieces to keep the outer piece from tilting.

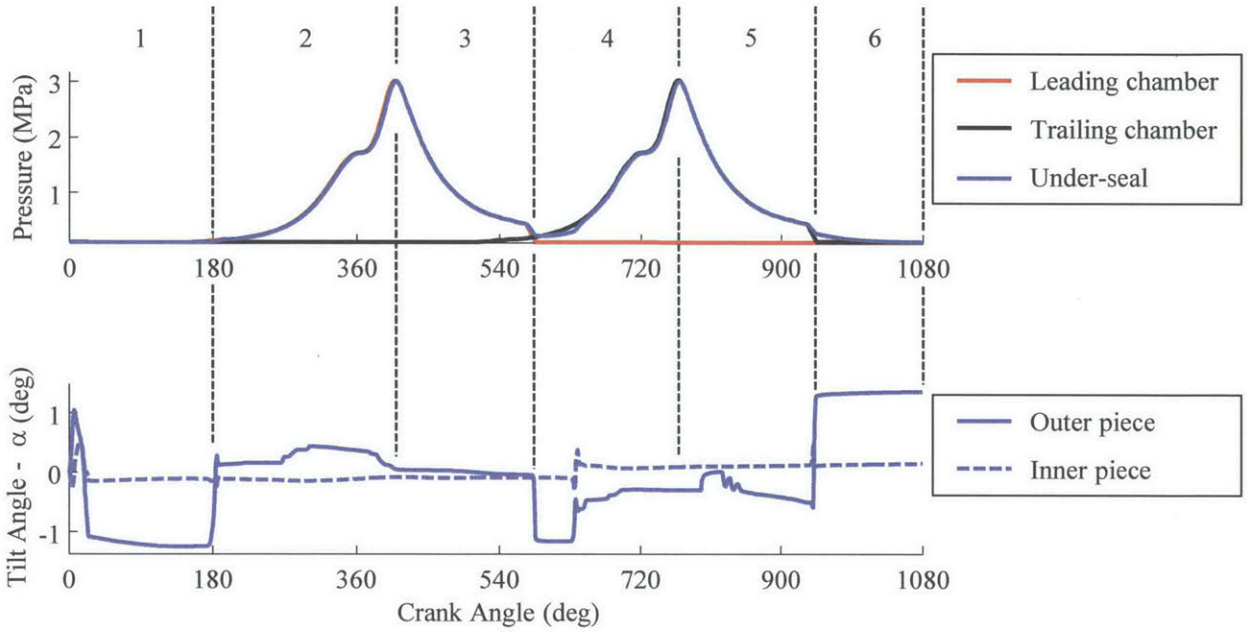

Fig. 5.9 Pressure in the leading and trailing chambers, pressure under the seal and tilt angle of the inner and outer pieces as a function of crank angle at 2000 rpm full-load

The cycle is again subdivided in six phases as is done for the two-piece AS prediction analysis (see section 4.3.1). During phase 1, pressure is low in both chambers and seal position is determined by body force and the profile contact angle with the rotor housing (Fig. 5.10). The outer piece is completely tilted, while the inner piece is pushed towards the groove trailing flank.

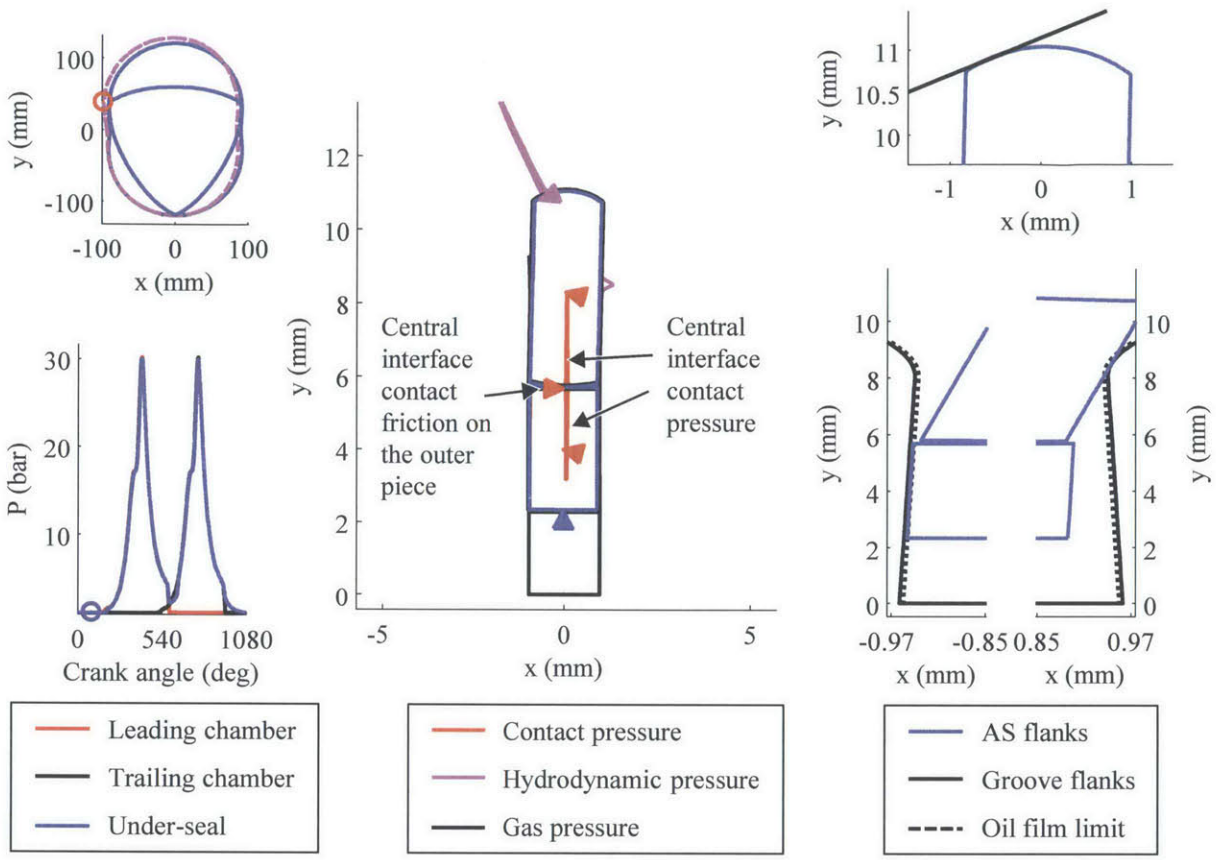

Fig. 5.10 Apex seal position and forces on the cross-section at z/L = 0.15 and at 90 CA

During phase 2, the inner piece seals the groove trailing flank and the central interface (Fig. 5.11). On the trailing side of the minimum clearance, the central interface pressure remains close to atmospheric pressure, while the leading side pressure is close to the leading chamber pressure. The net moment on the outer piece is balanced for a minimum tilt value. This leaves the leading flank completely open and the gas is free to flow to the groove. Groove pressure therefore remains close to the leading chamber pressure as is seen for the top ring of piston engines. It should be noted that the actual pressure on the trailing side of the central clearance is expected to be higher than atmospheric due to flow along the seal. This should not completely change the dynamics as long as the pressure remains significantly lower than the leading chamber pressure.

At low-speed, the seal behavior from phase 3 to 5 is similar to the one observed in phase 2 (Fig. 5.12, Fig. 5.13, and Fig. 5.14). It can be seen that the friction force at the central interface is not

the dominant effect on the outer piece titling as it can be in the opposite direction to the direction that would prevent the outer piece from tilting.

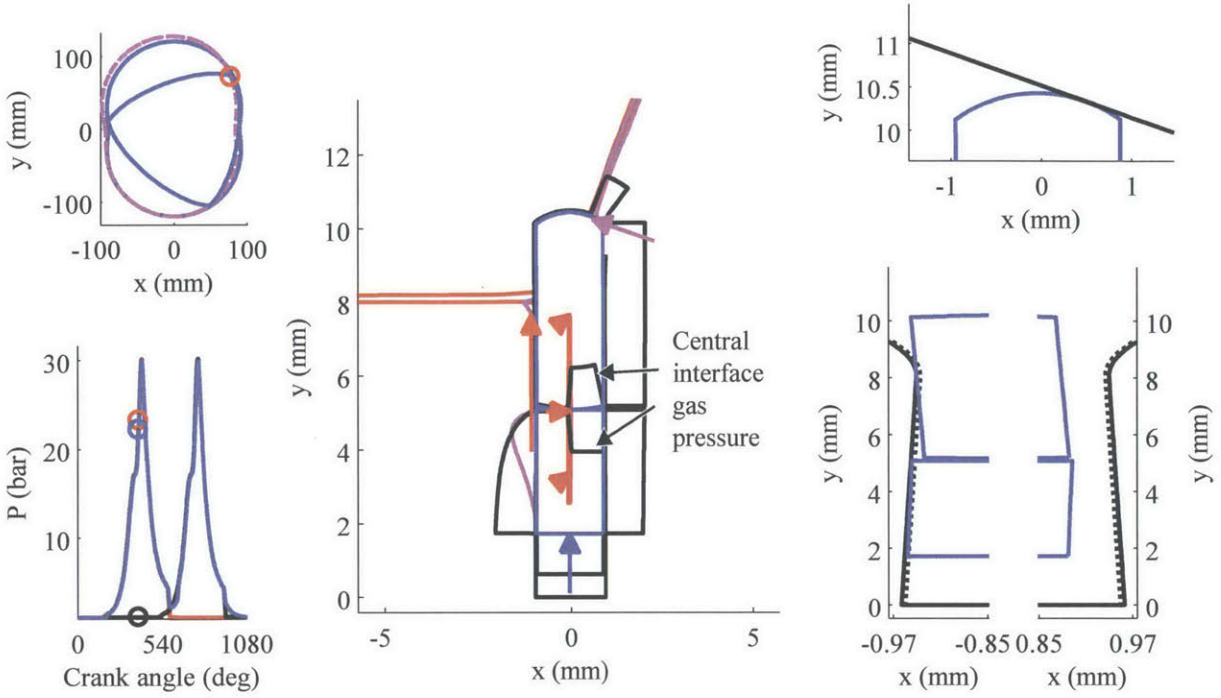

Fig. 5.11 Apex seal position and forces on the cross-section at z/L = 0.15 and at 390 CA

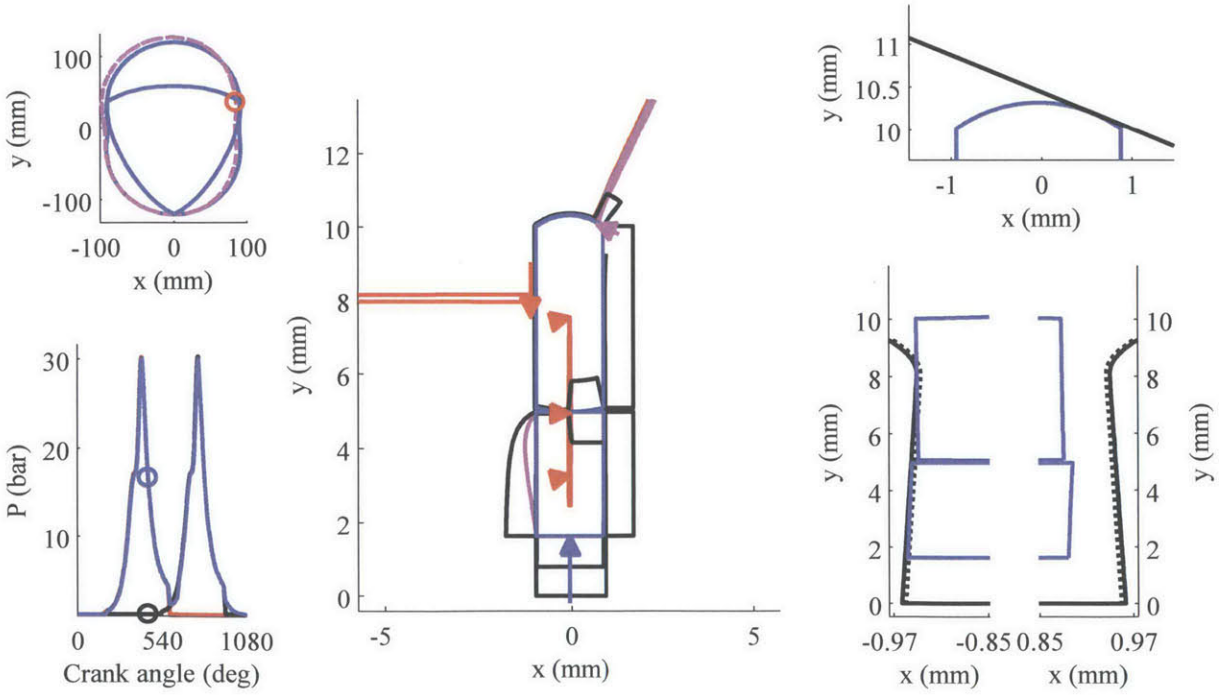

Fig. 5.12 Apex seal position and forces on the cross-section at z/L = 0.15 and at 450 CA

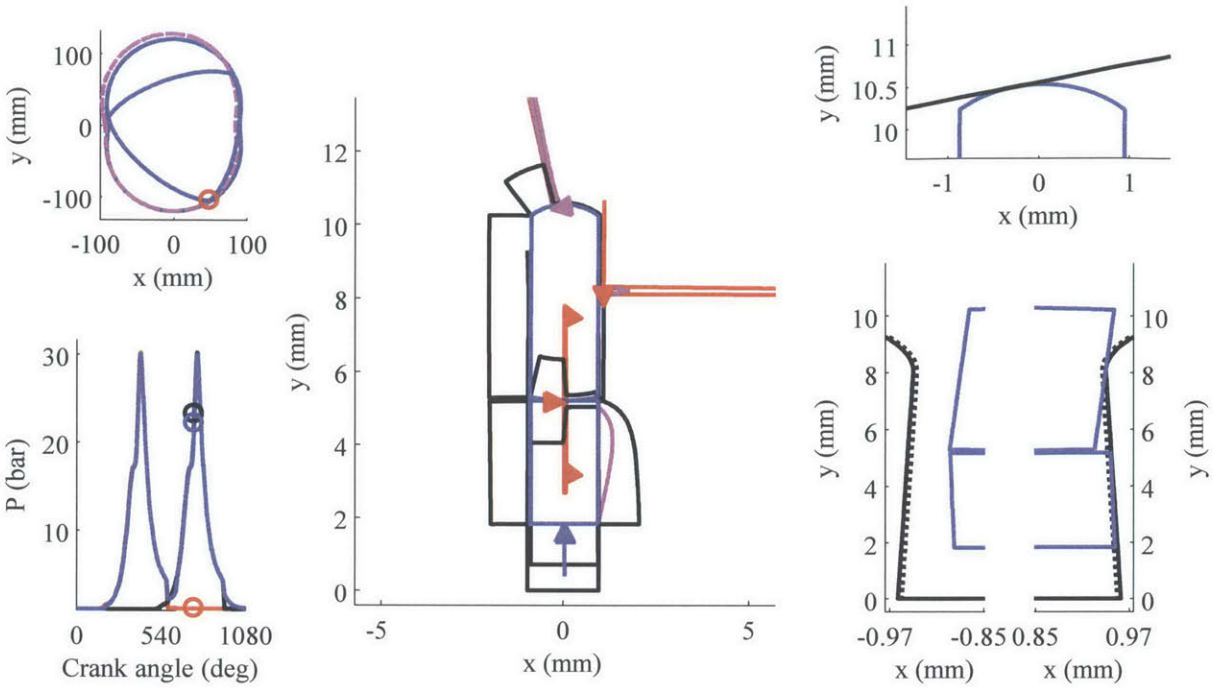

Fig. 5.13 Apex seal position and forces on the cross-section at z/L = 0.15 and at 750 CA

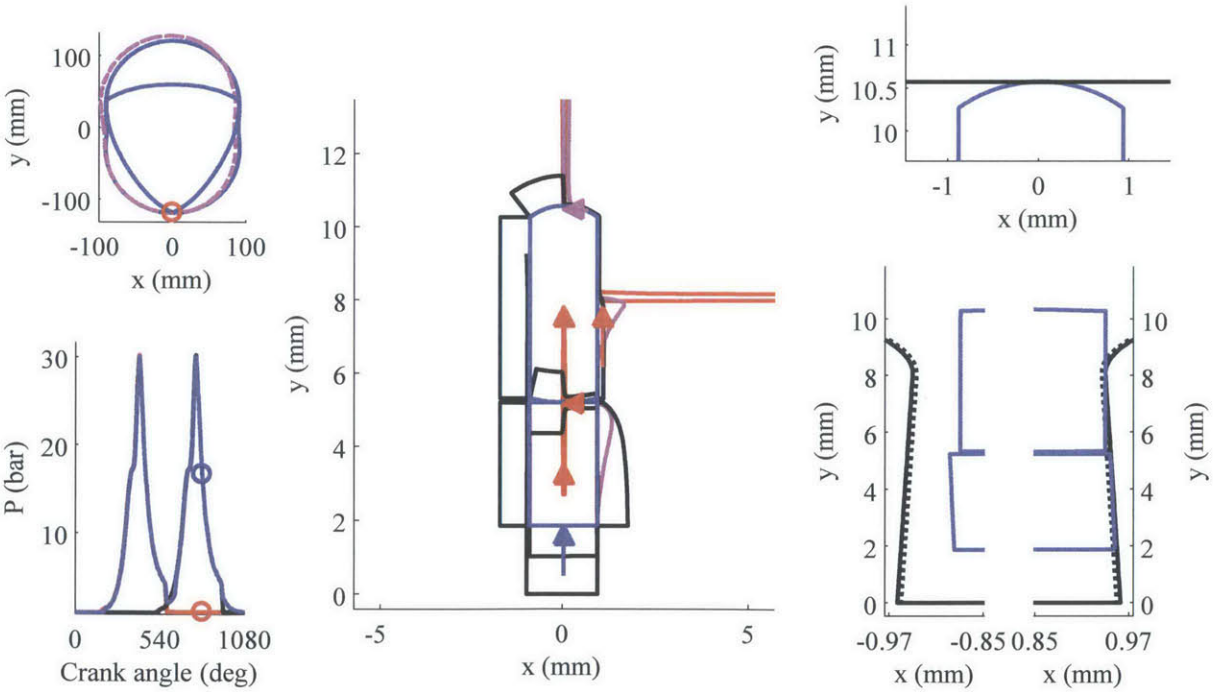

Fig. 5.14 Apex seal position and forces on the cross-section at z/L = 0.15 and at 810 CA

During phase 6, pressure in the chambers is low again and the seal position is similar to the seal position in phase 1, but vertically flipped.

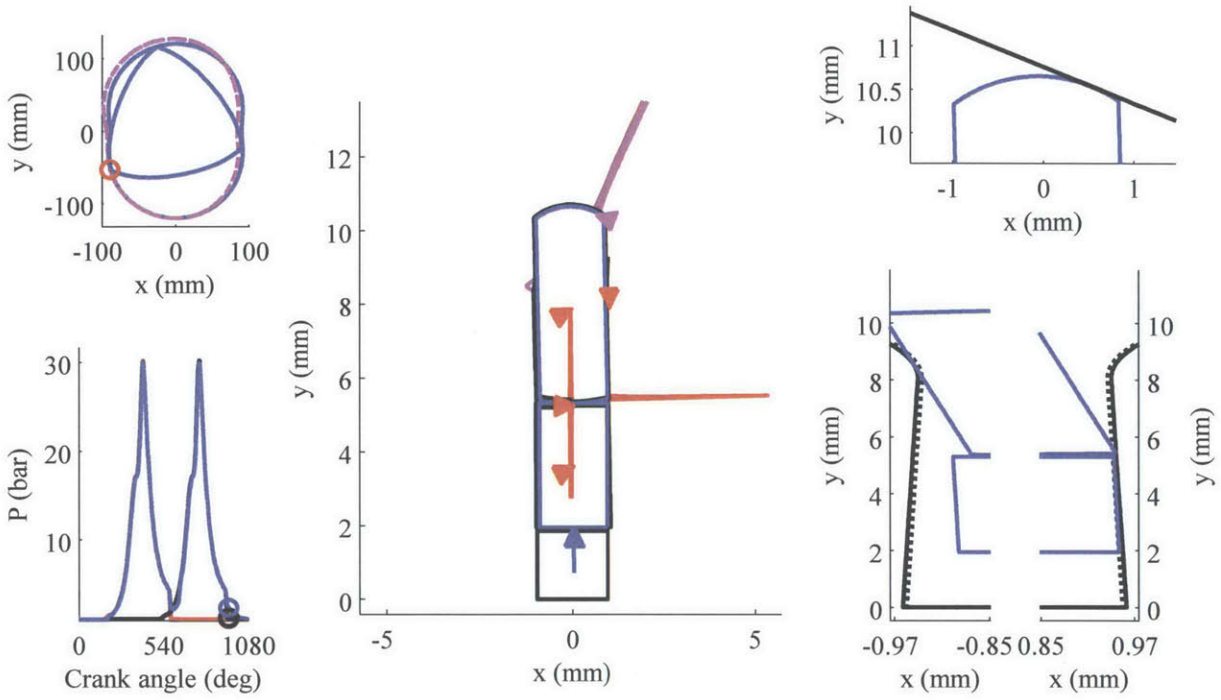

Fig. 5.15 Apex seal position and forces on the cross-section at z/L = 0.15 and at 960 CA

At low speed, the total leakage for the three-piece AS is similar to the total leakage for the two-piece AS (Fig. 5.16). Flank leakage is reduced from the already small level of the two-piece AS. Corner seal leakage is increased due to a larger groove pressure caused by the quasi-absence of pressure lag. It is therefore important to reduce corner seal clearance before using the three-piece configuration in order to decrease total leakage. Side piece corner and spark plug leakage values are identical as they are not influence by the changes in geometry from the two-piece AS to the three-piece AS.

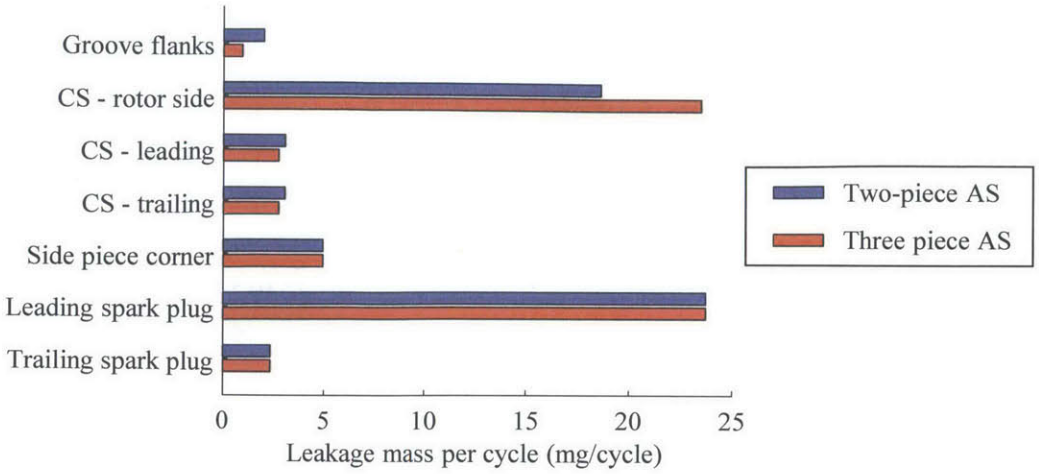

Fig. 5.16 Comparison of the two-piece and three-piece AS mass leakage per cycle at 2000 rpm full-load

5.3.2 High-speed Predictions

At high speed, the model predicts a similar behavior to the low-speed behavior for the trailing apex (Fig. 5.17). This results in a trailing AS pressure lag much smaller than what is seen for the two-piece trailing AS. However, body force prevents the inner piece of the leading AS from sealing the flank and causes an important groove pressure lag. Nevertheless, flank leakage is significantly reduced compared to the two-piece AS.

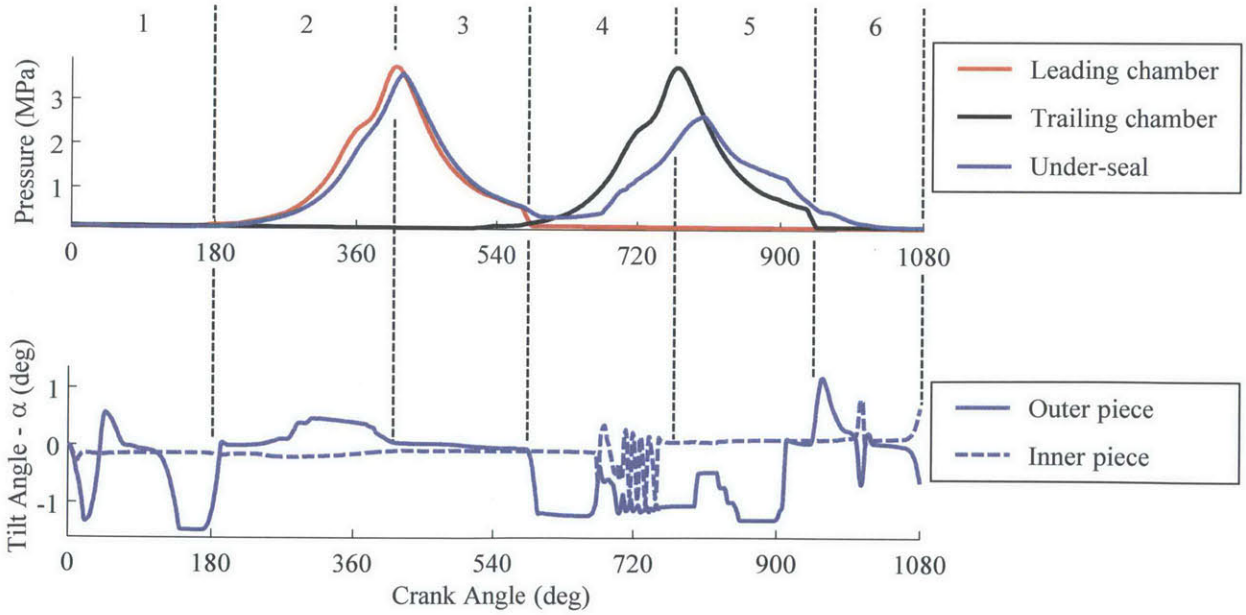

Fig. 5.17 Pressure in the leading and trailing chambers, pressure under the seal and tilt angle of the inner and outer pieces as a function of crank angle at 8000 rpm full-load

During phase 1, seal position is dominated by body force and both pieces are pushed against the groove trailing flank (Fig. 5.18). Phase 2 and 3 seal behavior is similar to the low-speed behavior even if body force is increased (Fig. 5.19 and Fig. 5.20). Pressure lag is still slightly increased due to a shorter amount of time for gas to flow to the groove.

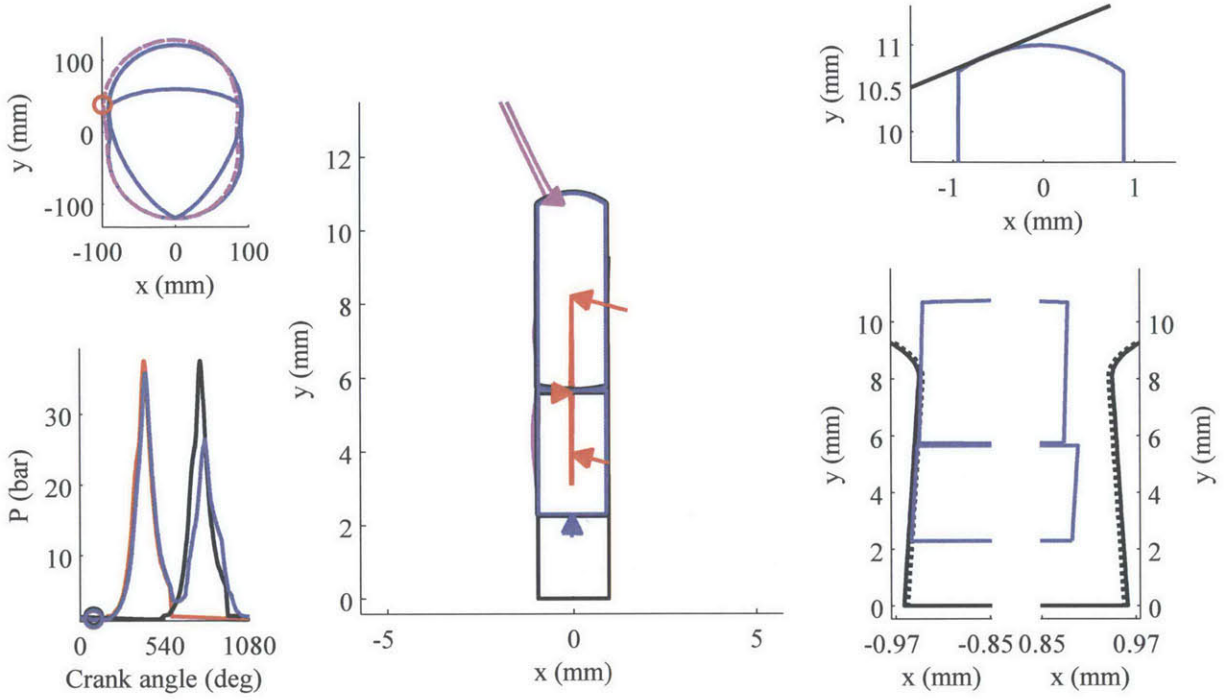

Fig. 5.18 Apex seal position and forces on the cross-section at z/L = 0.15 and at 90 CA

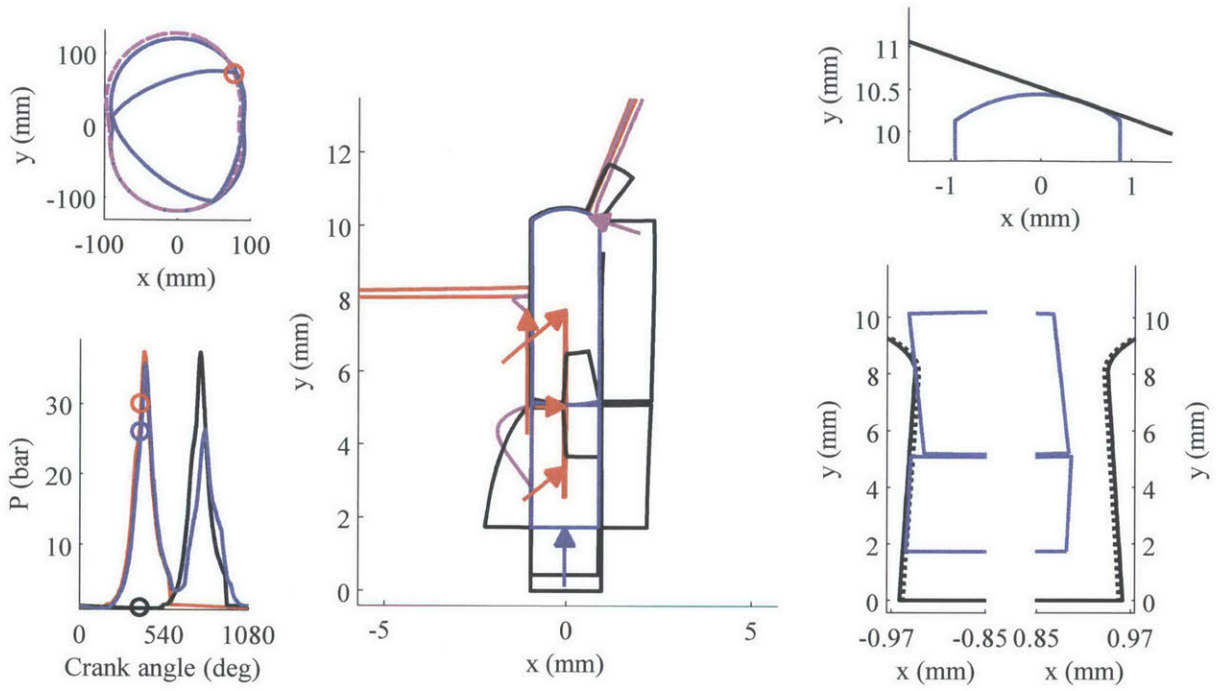

Fig. 5.19 Apex seal position and forces on the cross-section at z/L = 0.15 and at 390 CA

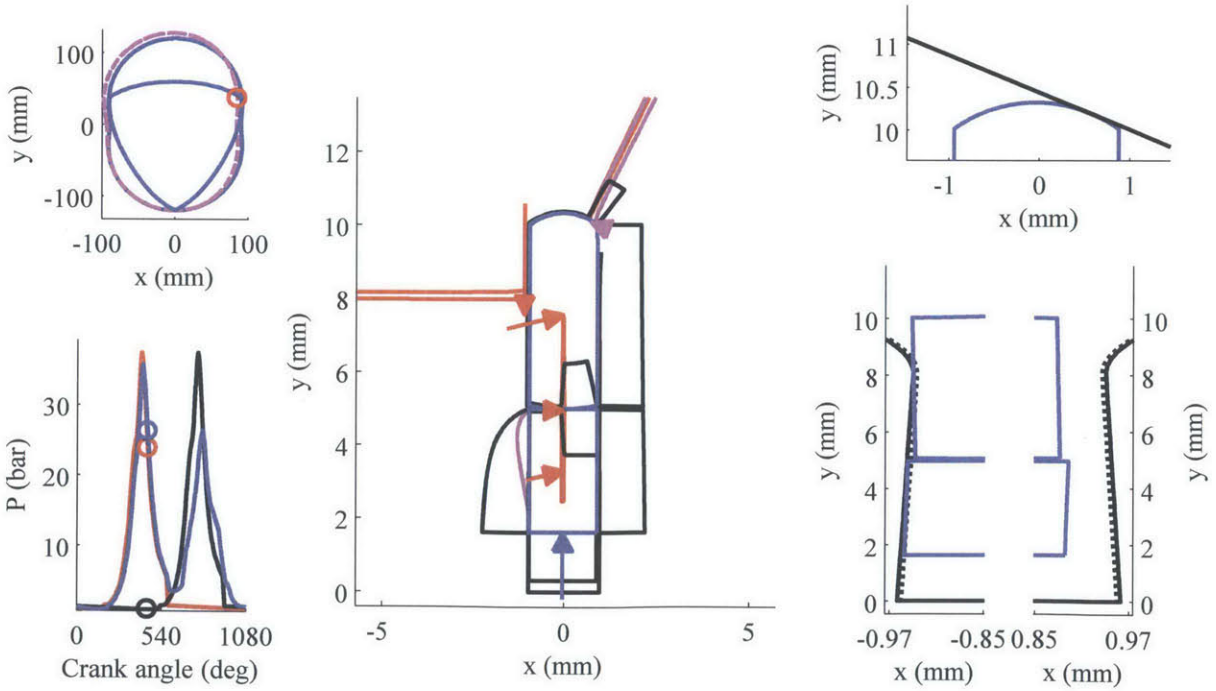

Fig. 5.20 Apex seal position and forces on the cross-section at z/L = 0.15 and at 450 CA

At the beginning of phase 4, body force and groove pressure maintain the inner piece towards the low-pressure flank (Fig. 5.21). This causes both pieces to oscillate, as seen in Fig. 5.17, for about 100 CA. When the inner piece settles down against the leading flank, the pressure on the leading side of the central interface clearance is already significantly higher than atmospheric pressure (Fig. 5.22). In this case, the equilibrium position of the outer piece is almost completely tilted. This creates an important restriction to the flow along the trailing flank and causes an important groove pressure lag.

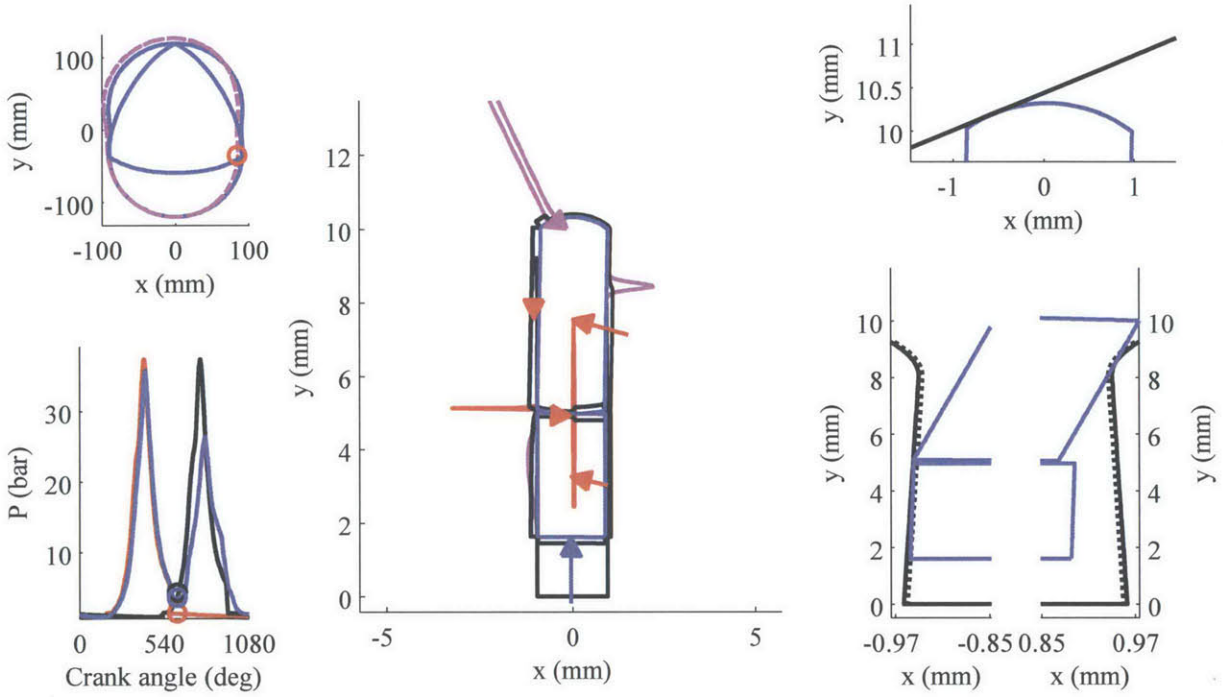

Fig. 5.21 Apex seal position and forces on the cross-section at z/L = 0.15 and at 630 CA

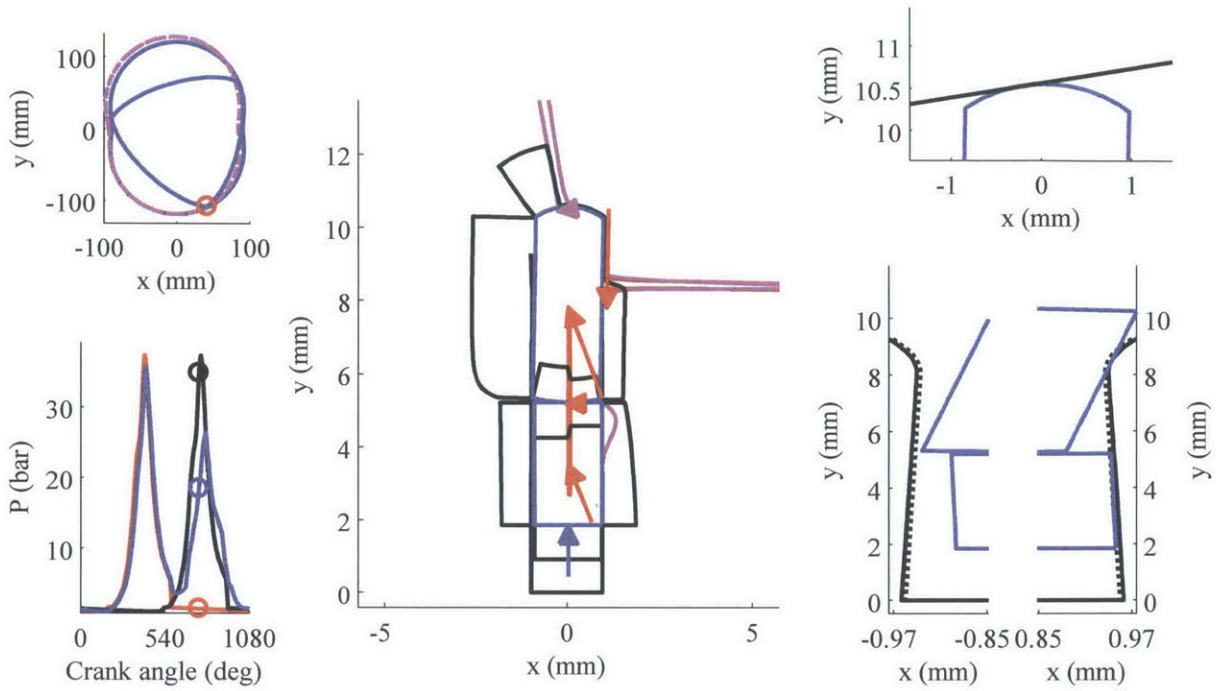

Fig. 5.22 Apex seal position and forces on the cross-section at z/L = 0.15 and at 760 CA

At the beginning of phase 5, the outer piece tilt is small because the central interface pressure is smaller than the trailing chamber pressure (Fig. 5.23). The trailing flank is completely open and gas can flow freely from the groove to the trailing chamber. However, when the trailing chamber pressure decreases to a level close to the central clearance pressure, the outer piece tilts again, closing the gas path to the groove (Fig. 5.24). Shortly after, the leading flank of the outer piece opens, purging the high pressure gas trapped in the central interface clearance (Fig. 5.25). This effect is similar to the flank leakage seen at high-speed for the two-piece AS. However, as the central clearance is not directly connected to the groove, only a small amount of gas is allowed to leak. Once the central clearance is purged, the outer piece is pushed back towards the leading flank and gas can flow from the groove to the trailing chamber (Fig. 5.26).

Finally, seal position in phase 6 is similar to low-speed seal position except that the larger body force prevent the outer piece from being completely tilted (Fig. 5.27).

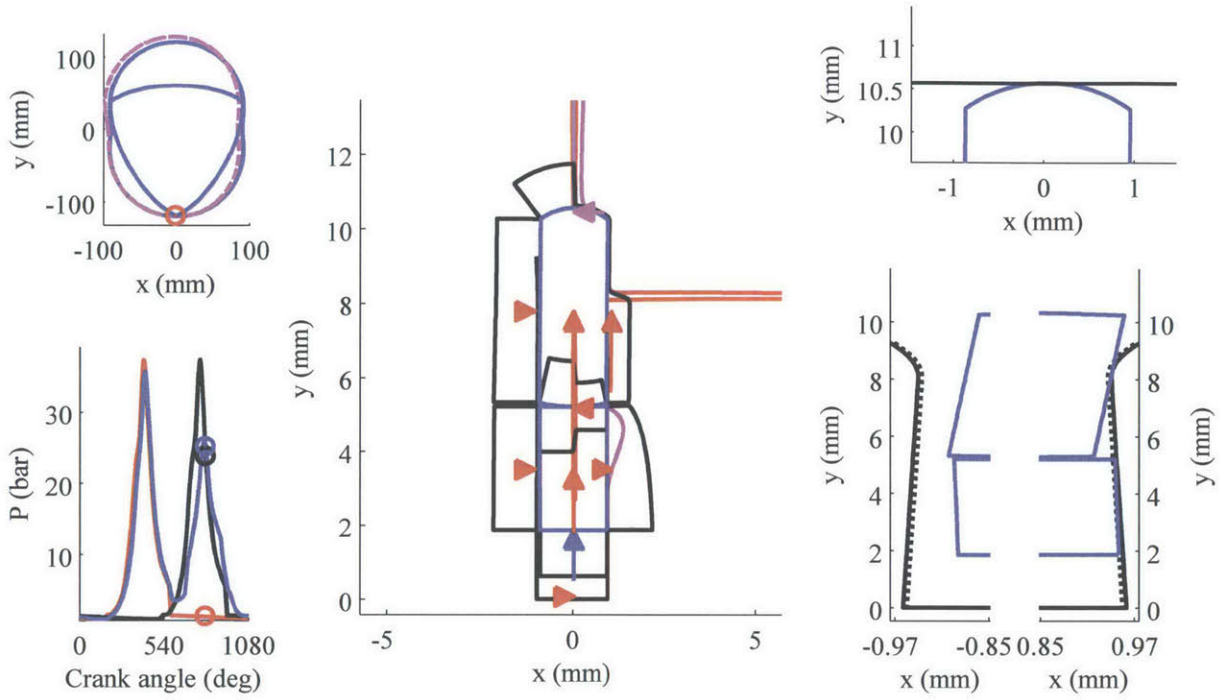

Fig. 5.23 Apex seal position and forces on the cross-section at z/L = 0.15 and at 810 CA

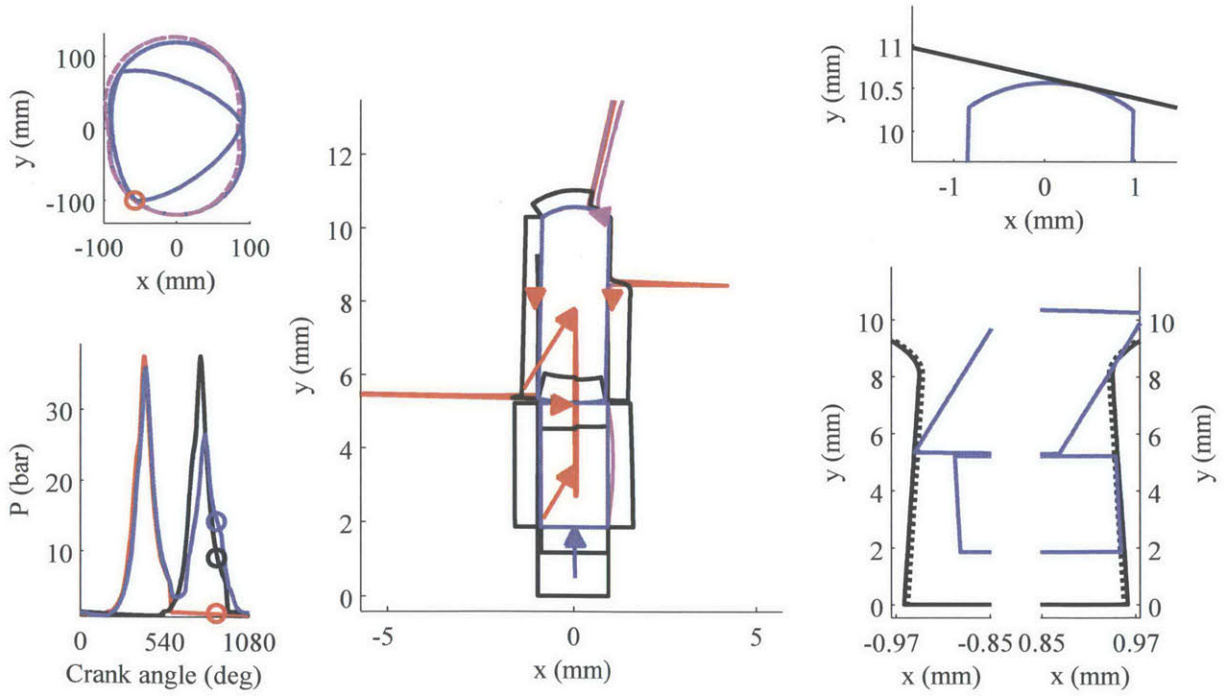

Fig. 5.24 Apex seal position and forces on the cross-section at z/L = 0.15 and at 880 CA

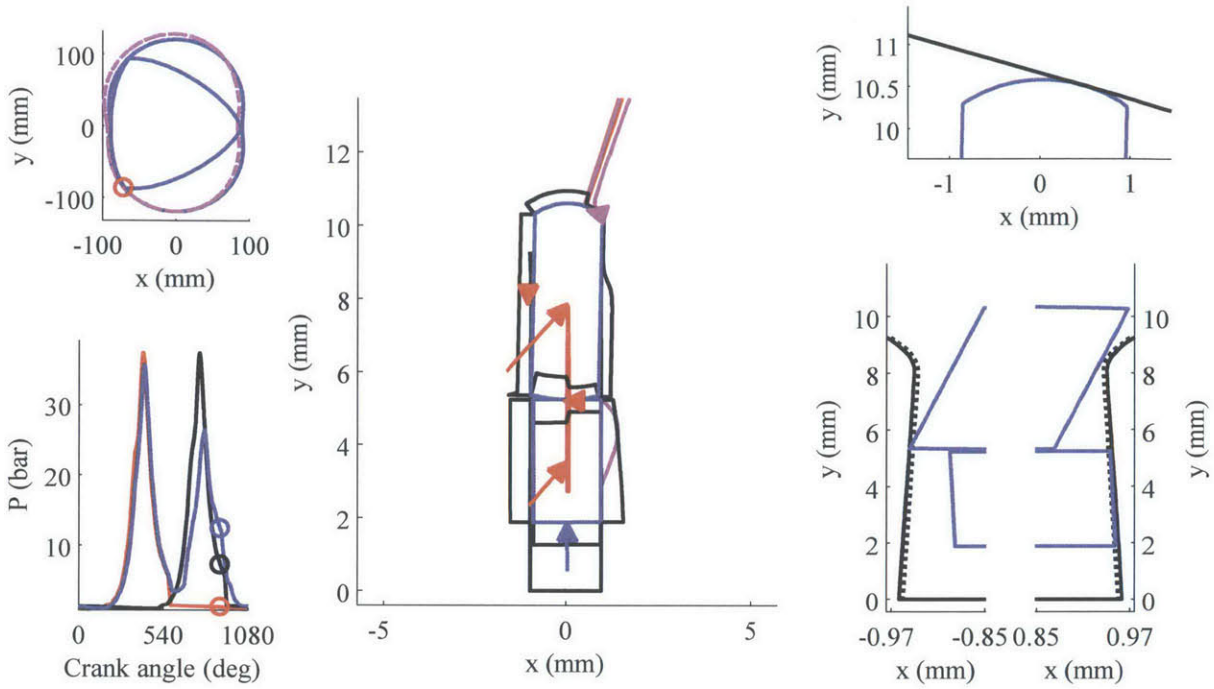

Fig. 5.25 Apex seal position and forces on the cross-section at z/L = 0.15 and at 905 CA

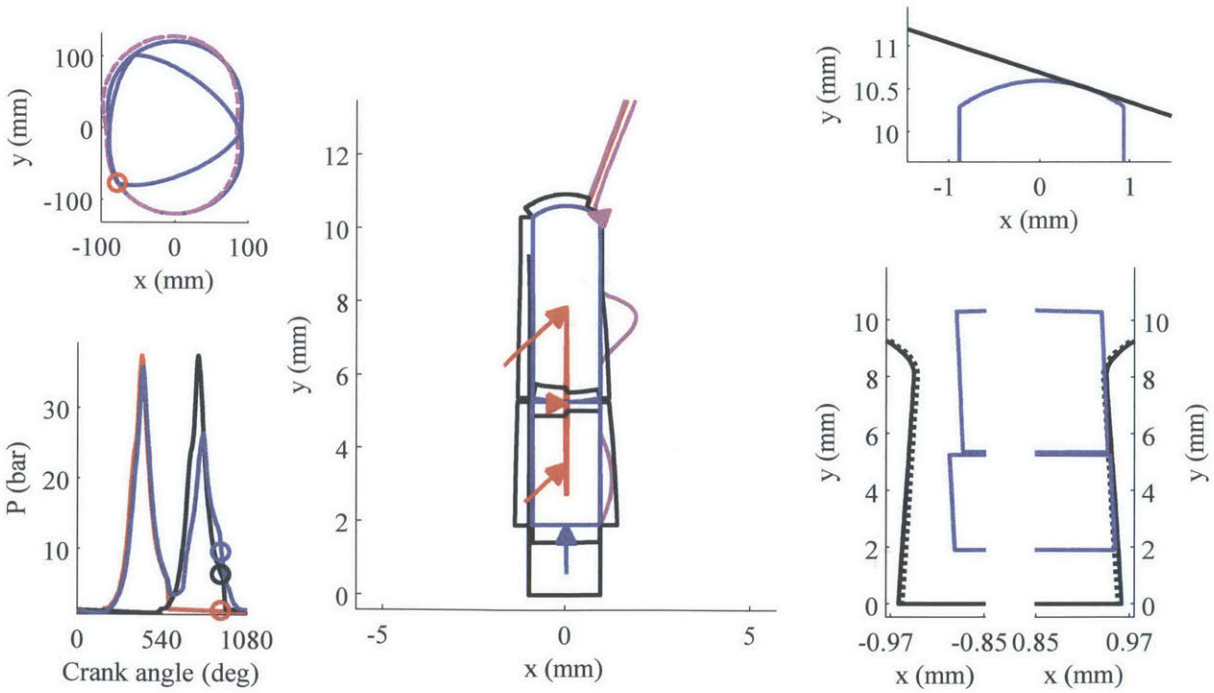

Fig. 5.26 Apex seal position and forces on the cross-section at z/L = 0.15 and at 920 CA

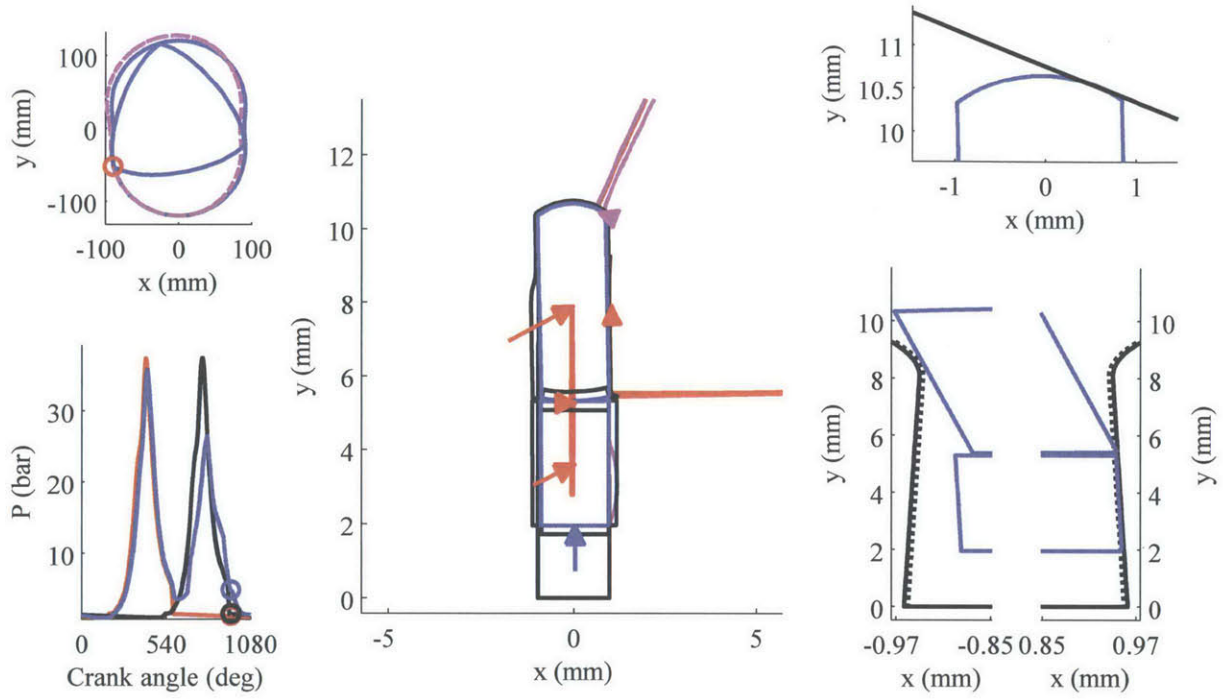

Fig. 5.27 Apex seal position and forces on the cross-section at z/L = 0.15 and at 960 CA

At high speed, flank leakage is significantly reduced due to the suppression of the low-pressure flank leakage mechanisms seen with a two-piece AS (Fig. 5.28). Corner seal leakage is similar to two-piece because of the groove pressure lag for the leading apex.

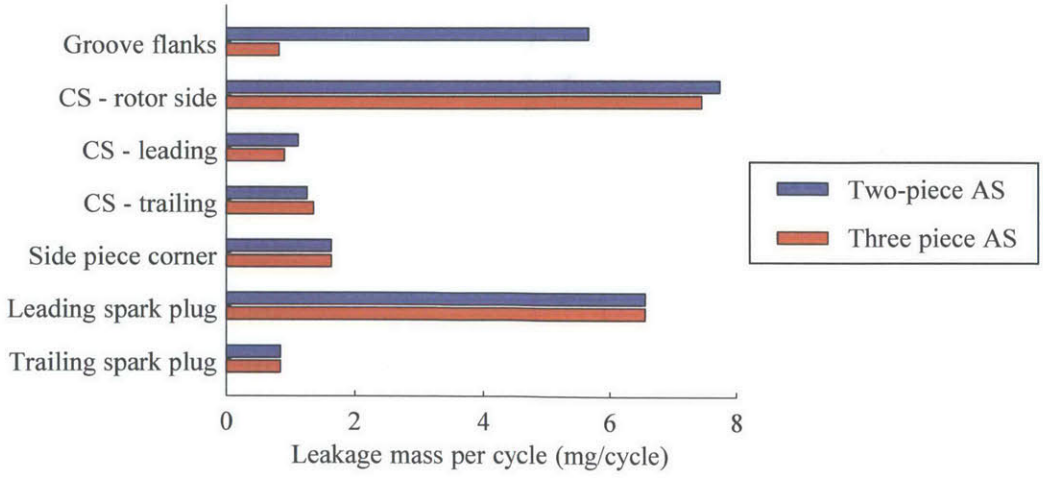

Fig. 5.28 Comparison of the two-piece and three-piece AS mass leakage per cycle at 8000 rpm full-load

5.3.3 Effect of Speed on Gas Leakage

The leakage analysis of the previous sections can be extended to the complete speed range (Fig. 5.29). Corner seal leakage is similar for both the two-piece AS and the three-piece AS. Both configuration have similar flank leakage at low-speed, but the three-piece AS flank leakage remains low for the entire speed while the two-piece AS flank leakage increases rapidly at high speed.

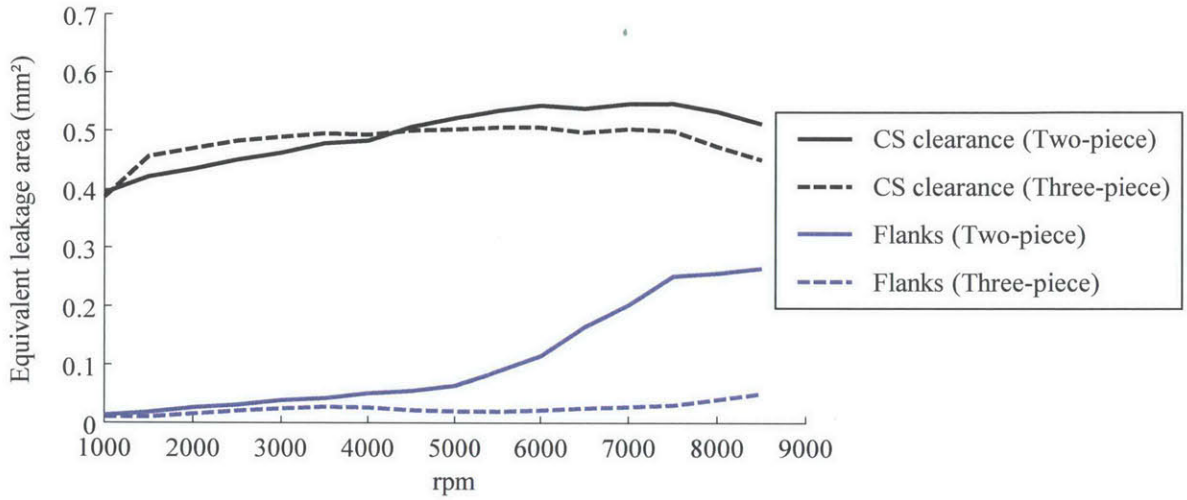

Fig. 5.29 Corner seal and flank leakage for the two-piece AS and three-piece AS as a function of speed

5.3.4 Effect of Central Interface Friction Coefficient on Gas Leakage

As discussed in section 5.3.1, the friction between the inner and outer pieces is not the mechanism that keeps the outer piece from tilting. This is further shown by the fact that the flank leakage is almost constant as a function of the coefficient of friction at the central interface (Fig. 5.30). Even in the limit of a friction coefficient of zero, the flank behavior of the seal is not significantly changed.

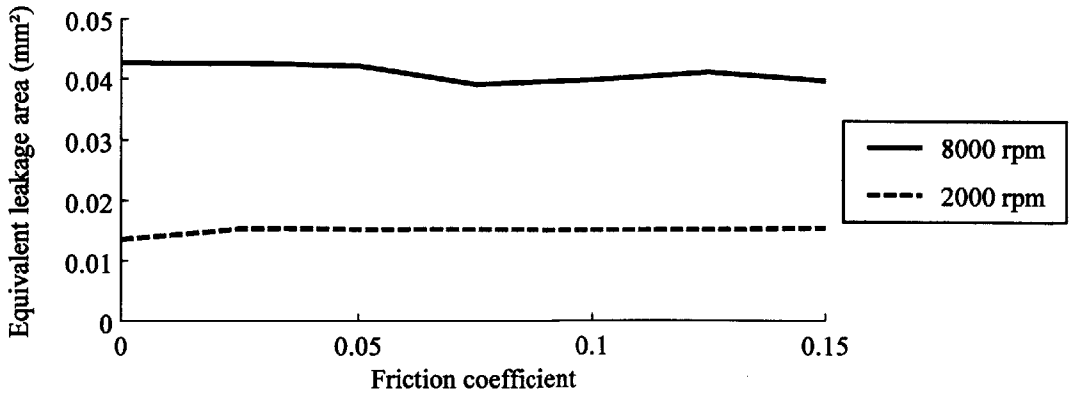

Fig. 5.30 Flank leakage for the three-piece AS as a function of the central interface friction coefficient at 2000 and 8000 rpm full-load

5.3.5 Effect of Central-Interface Outer-Piece Barrel-Shape Height

The effect of changing central-interface outer-piece barrel-shape height on leakage is shown in Fig. 5.31. For a barrel-shape height below 10 μm, the inner and outer pieces move together and act as two-piece AS leading to flank leakage similar to the two-piece AS level. Above a barrel-shape height of 10 μm, the flank leakage is roughly constant. The barrel-shape height should therefore be set as small as possible to avoid flow along the central interface clearance, while insuring it will not too small after wear down of the two pieces during the life expectancy of the engine.

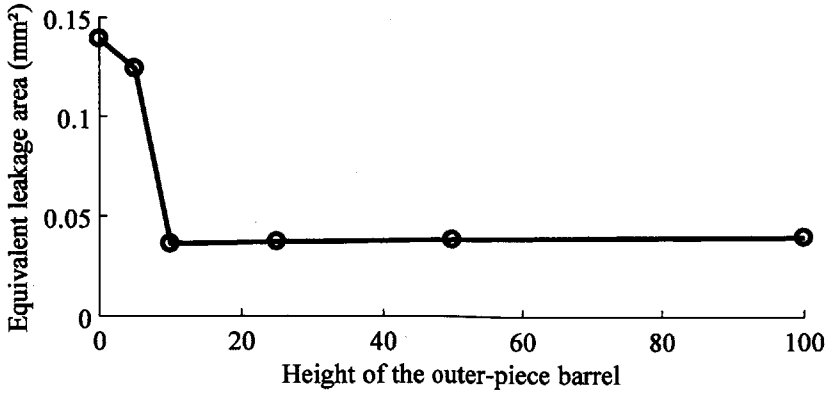

Fig. 5.31 Effective flank leakage area as a function of outer-piece barrel-shape height

5.4 Three-Piece Apex Seal Model Conclusions

The model developed is capable of predicting sealing performance of the three-piece AS, including the description of the interface between the inner and outer pieces. Model predictions lead to the following conclusions:

1. The three-piece configuration has the potential to reduce flank leakage to an acceptable level even at high speed.
2. At high speed, body force must be considered in the analysis as it changes the position of the inner piece and increases groove pressure lag under the leading AS. Flank leakage remains small, but oscillation of the inner piece could lead to durability issues.
3. Corner seal leakage remains the dominant leakage mechanism. It becomes even more important to reduce the clearance as the behavior of the seal gets better and the groove pressure lag is reduced.

Chapter 6

Side Seal Model

While side seals typically have less wear problems than apex seals, they still contribute to about 1/3 of the gas leakage from the combustion chamber. Understanding the dynamics and deformation of the side seal is therefore crucial in developing new designs to reduce leakage. Conversely to the apex seals, the deformation of the side seal is pivotal in understanding leakage and the deformable beam formulation is even more useful.

This chapter first briefly presents the model formulation differences with the apex seal model. The sealing performance of the side seal is then assessed. This chapter is concluded by showing a qualitative match between the leakage mechanisms observed in the model and with the laser-induced-fluorescence engine.

6.1 Model Formulation

The model calculates the displacements of all the side seal cross-sections due to the same forces included in the two-piece AS model: asperity contact, oil and gas pressure and shear stress on the profile, flanks and under the seal (Fig. 6.1). Additionally, the contact forces with the corner seals are added at the two ends of the side seal (Fig. 6.2).

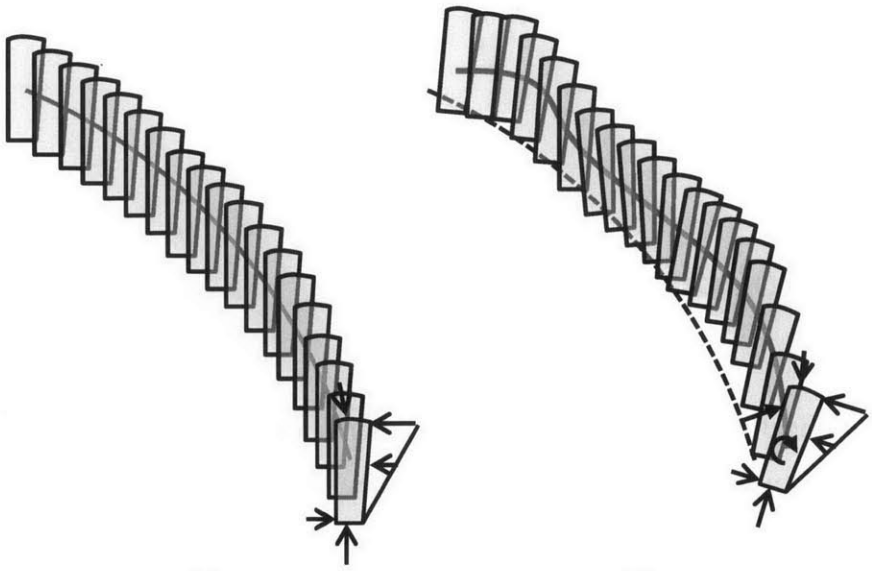

Fig. 6.1 Displacements of the side seal cross-sections due to the external forces

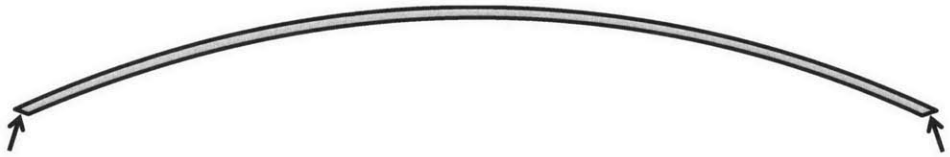

Fig. 6.2 Contact forces with the leading and trailing corner seals

A curved beam element model is used to take into account the geometry of the side seal. The beam model is adapted from a piston ring model developed by Baelden [54]. Variables used for the displacements are different from the one in the apex seal model to correspond to the piston ring model (Fig. 6.4). The lateral displacement is defined as y_g, the axial, or out-of-plane, displacement is defined as z_g, and the tilt is kept as α_g. The cross-section displacement along the circumference of the seal, x_g, is added to the piston ring displacements to calculated the clearance with the corner seals and the resulting contact force or gas leakage.

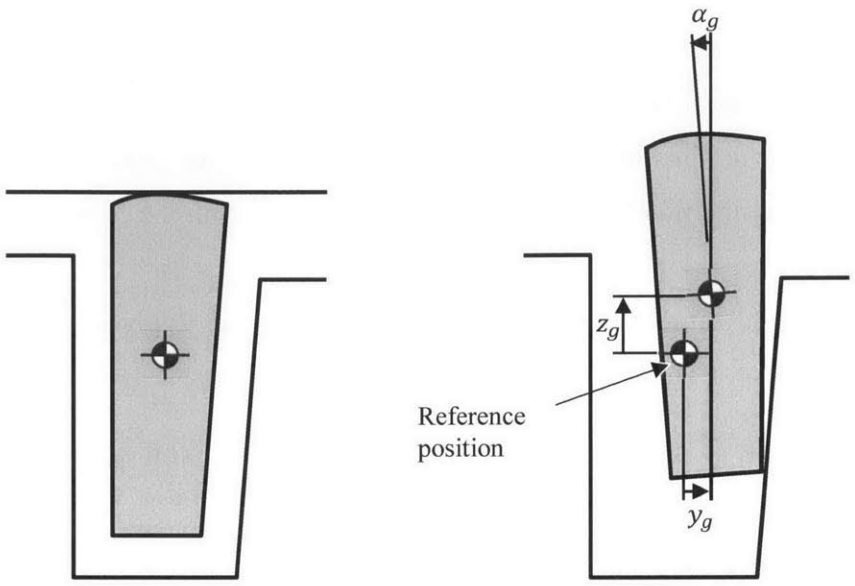

Fig. 6.3 Cross-section displacements

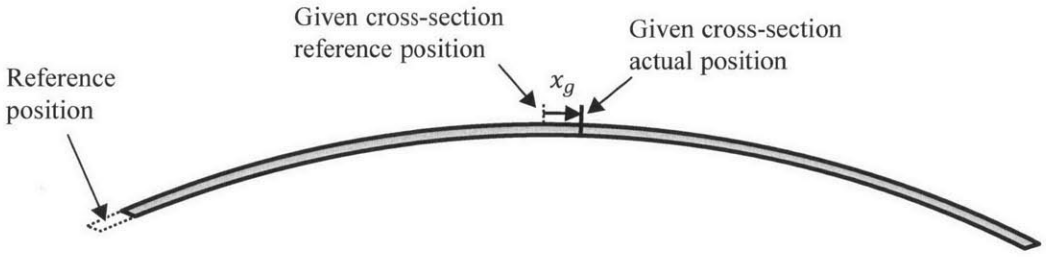

Fig. 6.4 Additional displacement along the circumference of the seal

6.1.1 Approximations

The same seven approximations used to formulate the apex seal model are used for the side seal model.

An additional approximation for the side seal is that the principal axes of the section are assumed to be aligned with the cylindrical reference frame. This means that there is no coupling between the lateral displacement of the seal and the axial displacement of the seal. This approximation is valid as the cross-section is almost symmetrical and there is only the half-keystone on one side that tilts the principal axes of a few degrees at most.

6.1.2 Seal End Forces and Moment

At both ends of the seal, the asperity contact pressure is calculated from the clearance and the Greenwood-Tripp relation. The clearance of the seal is calculated for a given number of point along the axial direction. This allows getting not only the proper reaction force, but also the reaction torque resisting the tilt of the seal end when in contact with the corner seal.

The clearance with the leading corner seal (h_m), shown in Fig. 6.5, is given by

$$h_m = \left(\frac{\Delta E}{2} + x_{gm}\right)\cos(\gamma_m) + y_{gm}\sin(\gamma_m) - z_m \sin(\gamma_m)\,\alpha_{gm} \tag{6.1}$$

in which ΔE is the initial total circumferential clearance, x_{gm}, y_{gm}, and α_{gm} are the circumferential, lateral, and rotational displacements of the seal leading end, γ_m is the angle between the leading seal end and the corner seal tangent, and z_m is the position on the leading seal end along the axial direction. Similarly, the trailing end clearance (h_n) is given by

$$h_n = \left(\frac{\Delta E}{2} - x_{gn}\right)\cos(\gamma_n) + y_{gn}\sin(\gamma_n) - z_n \sin(\gamma_n)\,\alpha_{gn} \tag{6.2}$$

in which x_{gn}, y_{gn}, and α_{gn} are the circumferential, lateral, and rotational displacements of the seal trailing end, γ_n is the angle between the trailing seal end and the corner seal tangent, and z_n is the position on the trailing seal end along the axial direction.

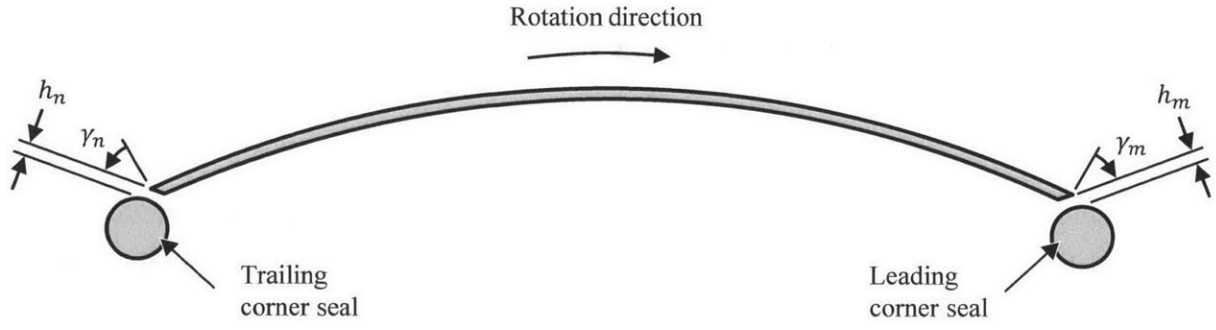

Fig. 6.5 End clearance with the leading and trailing corner seals

The asperity contact pressure is calculated from the Greenwood-Tripp relation. The forces and moment are calculated by integrating numerically the contact pressure.

6.1.3 Side Seal Gas Flow Sub-Model

The profile and flank mass flow rates (Fig. 6.6) are calculated from lubrication flow limited by isentropic flow through an orifice, as is done for the apex seal. Additionally, leakage at both ends is calculated by an isentropic flow through an orifice of the end clearance cross-sectional area (Fig. 6.7). Pressure on the outer side of the side seal is the combustion chamber pressure, while the pressure on the inner side of the side seal is taken as atmospheric.

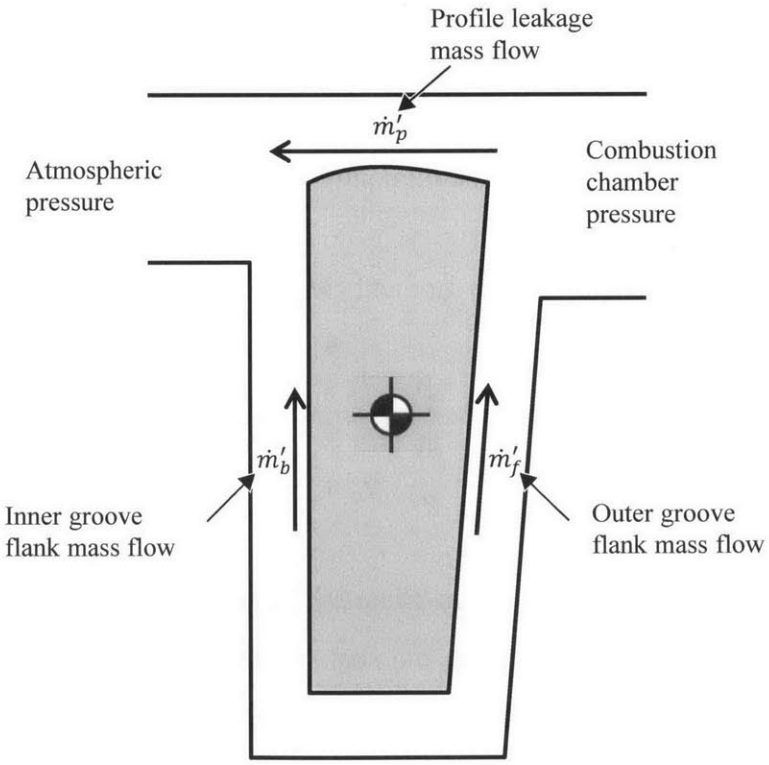

Fig. 6.6 Mass flow rate around the side seal cross-section

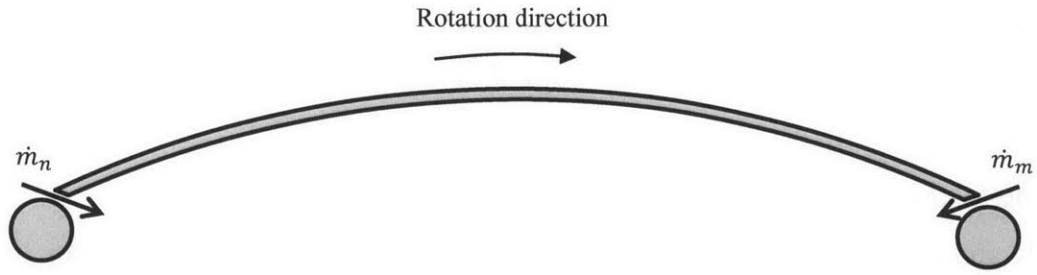

Fig. 6.7 Gas leakage though the clearance at both ends of the seal

6.1.4 Curved Beam Model

The curved beam finite element model is similar to the straight beam model used for the apex seal. It uses a few beam elements and Hermite interpolation to calculate the position of every contact points on a finer grid. The difference is the coupling between the axes due to the curvature of the seal. The twisting and bending moments are derived by Baelden [54] for small displacements, and are given here to illustrate the coupling between the axes. The complete derivation of the beam element model is given in details in Baelden's thesis [54], with the application of the model to the piston engine oil control ring.

For small displacements, in-plane bending moment (M_y) is decoupled from twisting and out-of-plane bending, and is given by

$$M_y = -\frac{EI_y}{R^2}\left(y_g + \frac{\partial^2 y_g}{\partial \phi^2}\right) \tag{6.3}$$

in which E is Young's modulus, I_y is the in-plane stiffness, R is the radius of curvature of the seal, and ϕ is the angular coordinate along the seal. To take into account the circumferential forces and displacements, the elongation energy is also included. This is the only difference from the piston ring model. For small displacement, the tension force (S) is given

$$S = \frac{EA}{R}\left(\frac{\partial x_g}{\partial \phi} + y_g\right) \tag{6.4}$$

in which A is the cross-sectional area. Actual circumferential displacement is negligible, but this approach allows inputting circumferential forces on the seal and calculating the circumferential displacement of the seal. From equations (6.3) and (6.4), it can be seen that circumferential and lateral displacements are coupled.

Because of curvature, out-of-plane bending is coupled to twisting. Out-of-plane bending moment (M_z) is given by

$$M_z = \frac{EI_z}{R^2}\left(\frac{\partial^2 z_g}{\partial \phi^2} + R\alpha_g\right) \tag{6.5}$$

in which I_z is the out-of-plane bending stiffness. The torsion moment (T) is given by

$$T = GJ_\alpha\left(\frac{\partial z_g}{\partial \phi} - R\frac{\partial \alpha_g}{\partial \phi}\right) \tag{6.6}$$

in which G is the shear modulus and J_α is the torsion constant.

From those forces and moments, potential energy can be calculated from which the stiffness matrix can be constructed. The mass matrix and load vector are the same as for the straight beam. Finally, a time-implicit globally-convergent Newton method is used to solve the seal dynamics, as is done for the apex seal.

6.1.5 Discretization

Conversely to the apex seal, the lateral deformation of the side seal plays an important role when calculating gas leakage. Furthermore, the deformation can be local as the seal is flexible in the lateral direction. It is therefore important to select a sufficient number of beam elements and number of contact points. The relative flank leakage at 2000 rpm full-load is shown in Fig. 6.8 for different number of beam elements and number of contact point per elements. For the results presented in this thesis, 10 beam elements with 20 points per beam element are selected to obtain accurate results while maintaining an adequate calculation time.

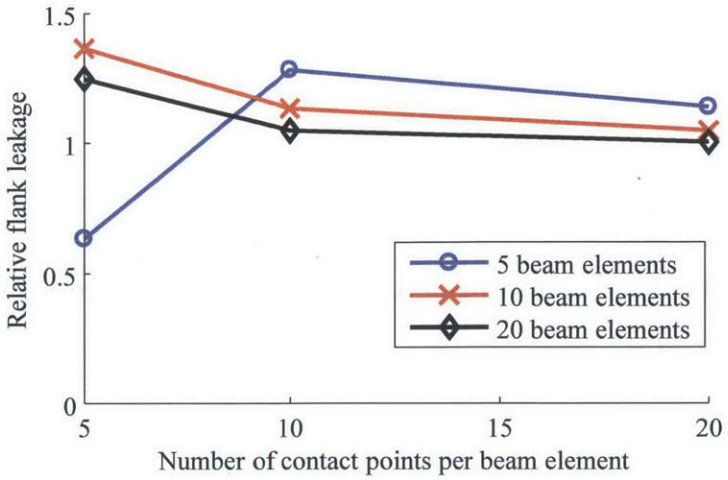

Fig. 6.8 Relative flank leakage as a function of the number of contact points per beam elements for 5, 10 and 20 beam elements

6.2 Model Predictions

The developed model is used to assess side seal performance. In order to better understand the lateral displacement and tilt of the seal, the predictions are given without hydrodynamic pressure on the profile of the seal, unless otherwise specified. The coefficient of friction is taken to be 0.1 which would be representative of the partially starved condition that the seal experience at high groove pressure when the seal motion is almost only circumferential. The effect of varying this friction coefficient is assessed toward the end of this section.

At low speed, leakage is the result of the interaction with the trailing corner seal and the gap with the leading corner seal. At high speed, body force increases seal tilt. This can seal the groove and generate inner flank leakage. Unlike the apex seal, the side seal cannot conform to the distorted side housing and profile leakage can be important, especially at high speed. Finally, the effect of varying key parameters is investigated, such as the profile friction coefficient, the contact angle with the corner seal, and the position of the minimum clearance on the profile.

6.2.1 Low-Speed Predictions

At low speed, the general dynamics of the seal is well-behaved, as long as there is pressure pushing on the outer flank. When the pressure is the same on both side of the seal, body force and profile friction dictates the position of the seal and the shape can vary greatly. However, this

is of low importance as it generates a minimal amount of leakage, wear and friction. Therefore, this section focuses on the understanding of the seal position when the outer pressure is higher than atmospheric.

At low speed, the groove pressure follows almost exactly the outer pressure (Fig. 6.9) as the outer flank is fully open along most of the seal. As soon as pressure starts increasing in the chamber, the seal is pushed towards the inner flank (Fig. 6.10). The section view shown in Fig. 6.10 is taken halfway along the seal ($x/L = 0.5$). In this case, this section view represents most of the seal, except close to the trailing corner seal. Friction pushes the seal towards the trailing corner seal and the contact angle with the corner seal creates a lateral reaction which opens the inner flank.

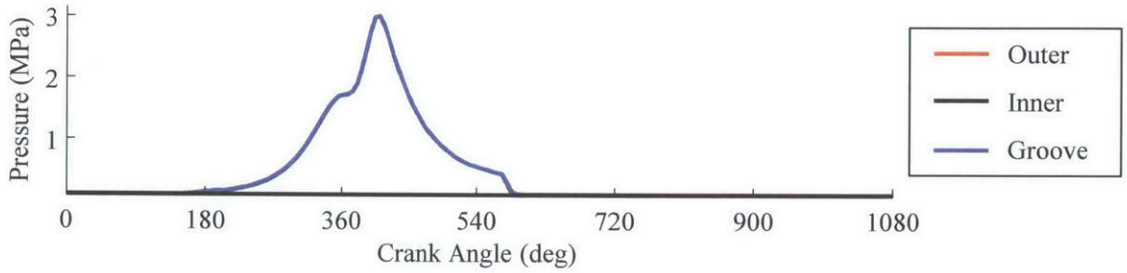

Fig. 6.9 Side seal groove pressure as a function of crank angle at 2000 rpm full-load

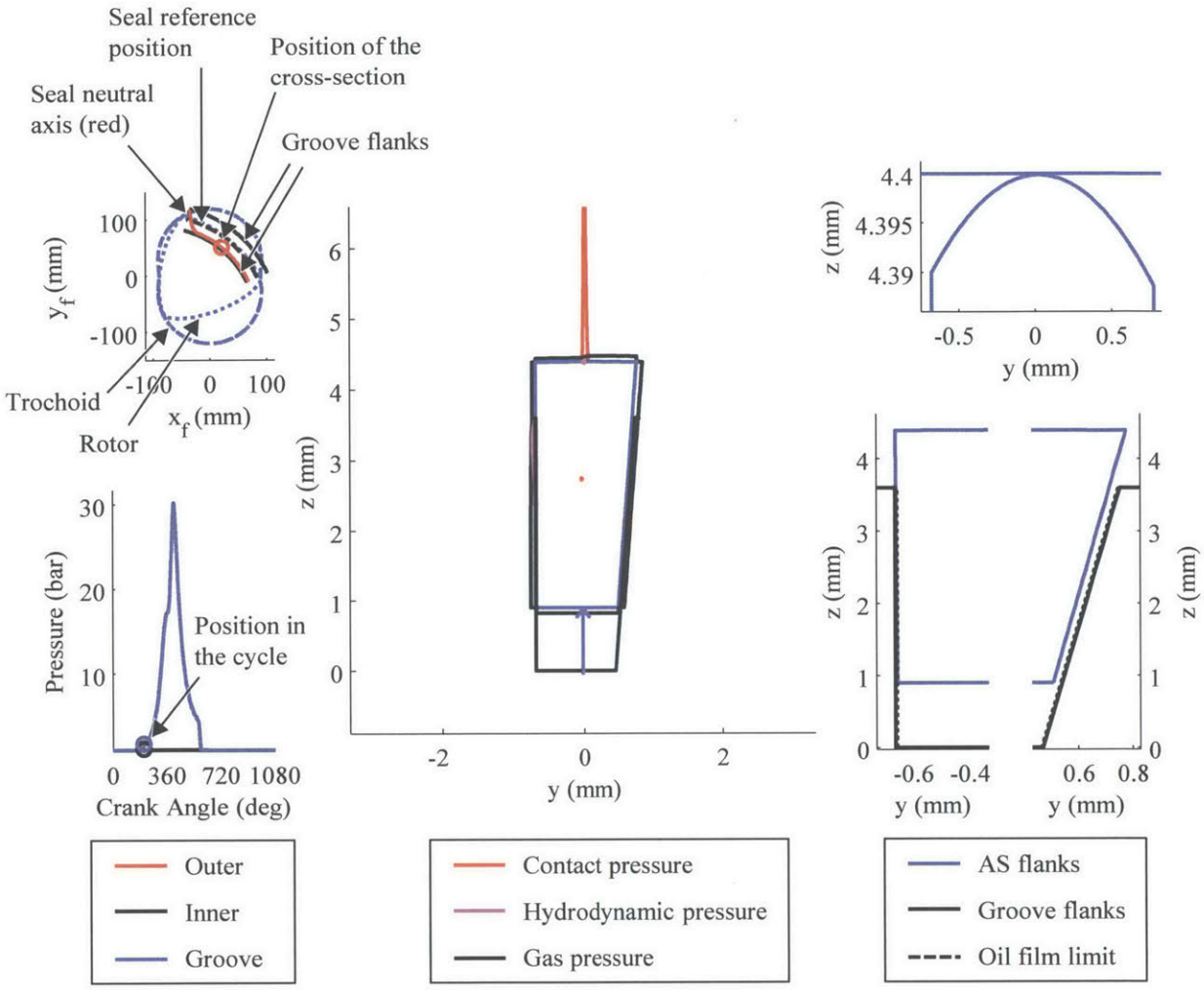

Fig. 6.10 Seal deformation and section view at x/L = 0.5 at 210 CA

The position of the seal remains similar during the entire compression stroke, except for a small tilt due to body force (Fig. 6.11). The contact with the trailing corner seal opens the inner flank which allows gas to leak from the groove to the side of the rotor (Fig. 6.12).

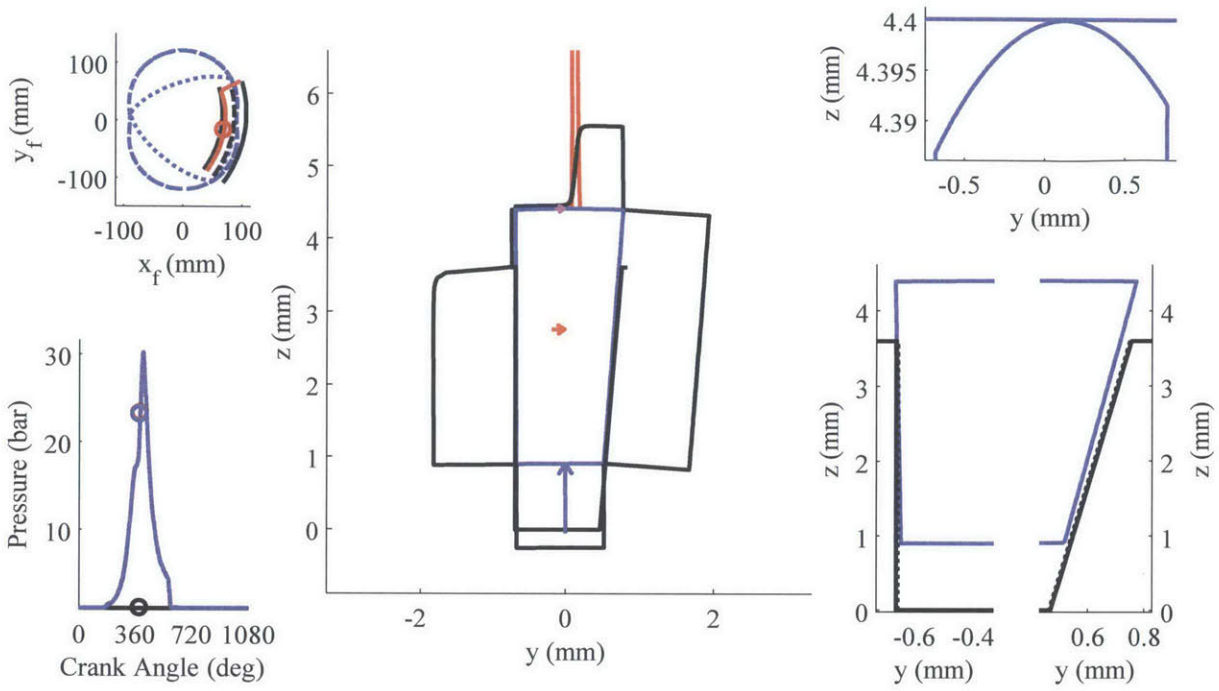

Fig. 6.11 Seal deformation and section view at x/L = 0.5 at 390 CA

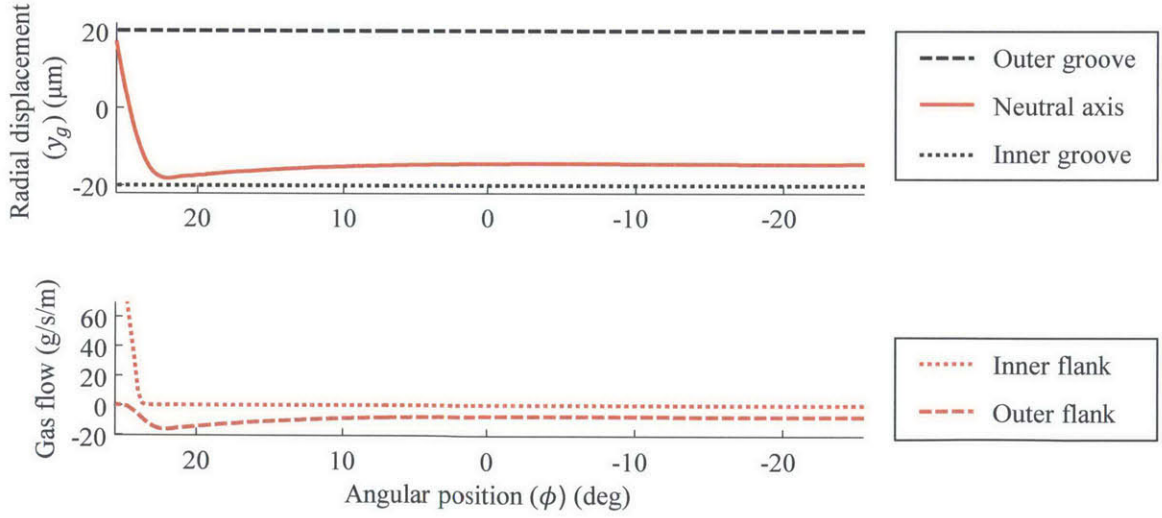

Fig. 6.12 Seal deformation and flank gas flow along the seal at 390 CA

During expansion stroke, the lateral displacement of the seal next to the corner seal reduces and comes in contact with the groove inner flank at the end of the expansion stroke (Fig. 6.13 and Fig. 6.14). The lateral displacement reduces because the housing-profile friction is not fully aligned with the seal as the velocity is partially radial and not fully circumferential. Although not

shown in the pictures, the gap between the side seal and the leading corner seal is open during the entire compression and expansions strokes.

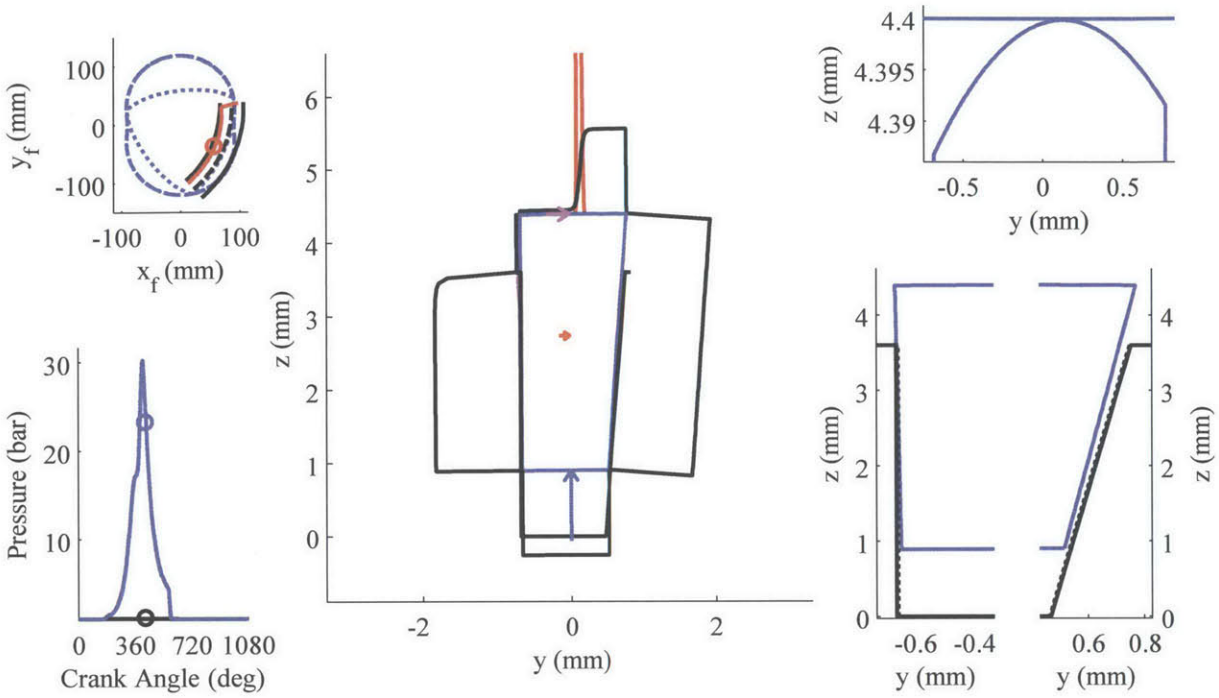

Fig. 6.13 Seal deformation and section view at x/L = 0.5 at 430 CA

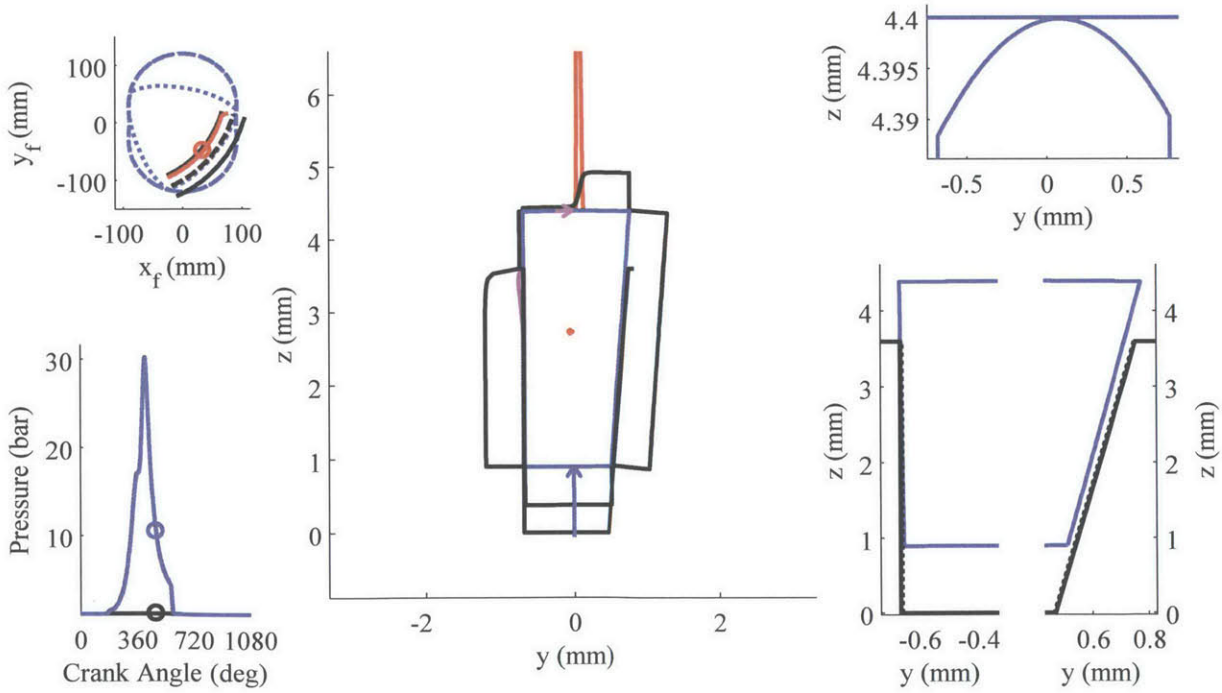

Fig. 6.14 Seal deformation and section view at x/L = 0.5 at 480 CA

Until this point, the results shown did not include rotor housing distortion. Model predictions including rotor housing distortion show that the seal cannot fully conform to the housing distortion even for high groove pressure (Fig. 6.15). This is due to the many maxima and minima caused by the numerous bolts that hold the housings together and the large temperature gradient that increases housing distortion amplitude. Housing distortion shown in Fig. 6.15 is typical of the intermediate housing, while front and rear housing distortion is smaller resulting in significantly less leakage.

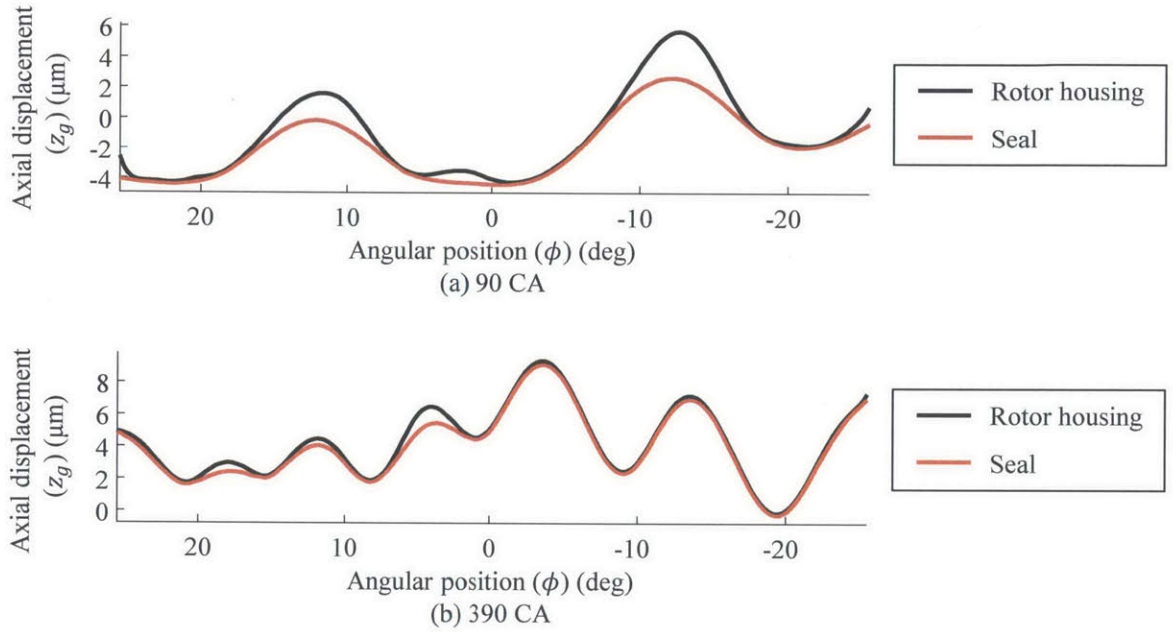

Fig. 6.15 Typical conformability of the seal to the distorted intermediate rotor housing at 2000 rpm full-load with (a) low pressure in the groove and (b) high pressure in the groove

Leakage is mainly caused by flank leakage and leading end gap leakage (Fig. 6.16 and Fig. 6.17). Leading end gap leakage follows the groove pressure, while flank leakage is larger during the compression stroke. Profile leakage, although larger than for the apex seal, remains small at low speed.

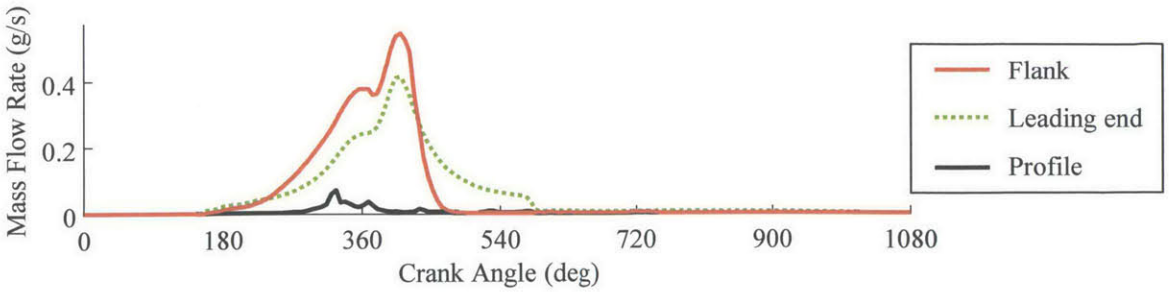

Fig. 6.16 Flank, end and profile leakage as a function of crank angle at 2000 rpm full-load

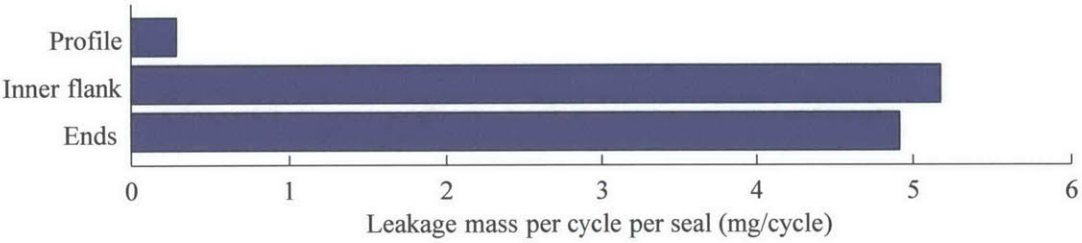

Fig. 6.17 Comparison of the total leakage for the different mechanisms at 2000 rpm full-load

As wear is typically not as critical as for the apex seal, contact pressure distribution is not assessed here. However, it can be predicted from the model as is done for the apex seal.

Friction losses are on the same order as for the apex seal. In dry conditions, predicted friction power at 2000 rpm is 81 W per side seal. With 0.5 μm of oil on the side housing, friction power is reduced to 55 W.

6.2.2 High-Speed Predictions

At high speed, body force tilts the seal in its groove, closing the outer flank gas path after chamber peak pressure. This traps the gases under the seal and groove pressure remains larger than chamber pressure until the inner flank opens (Fig. 6.18). Opening of the inner flank is the main mechanism for gas leakage at high speed.

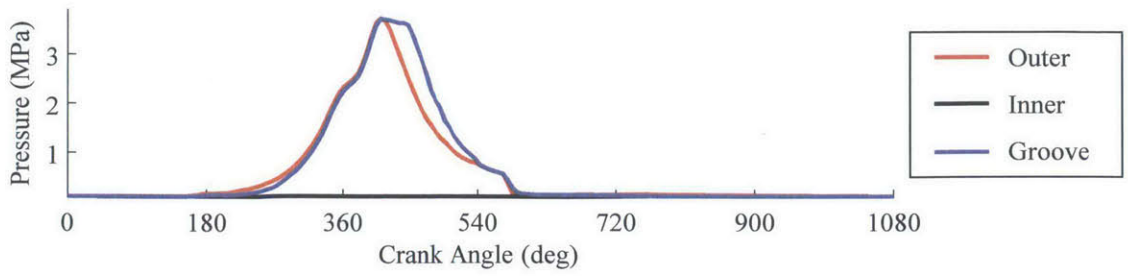

Fig. 6.18 Groove pressure as a function of crank angle at 8000 rpm full-load

At the beginning of the compression stroke, part of the seal remains pushed towards the outer groove flank due to body force (Fig. 6.19). This creates gas leakage as gas enters the groove along the leading half of the seal and exits the groove along the trailing half of the seal. Halfway in the compression stroke, the seal position is similar to the one seen at low speed with the trailing end of the seal pushed towards the outer flank of the groove (Fig. 6.20). Towards the end of the compression stroke, the lateral displacement of the trailing end is reduced because the circumferential body force balance part of the profile-housing friction force (Fig. 6.21).

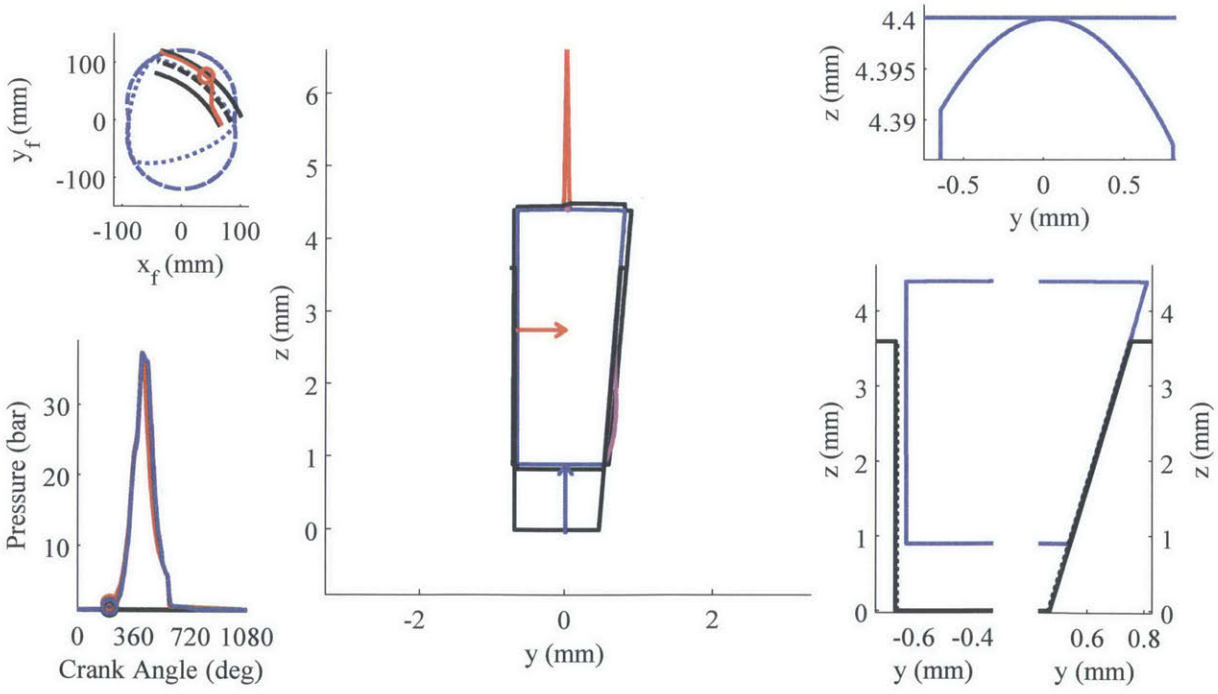

Fig. 6.19 Seal deformation and section view at x/L = 0.5 at 210 CA

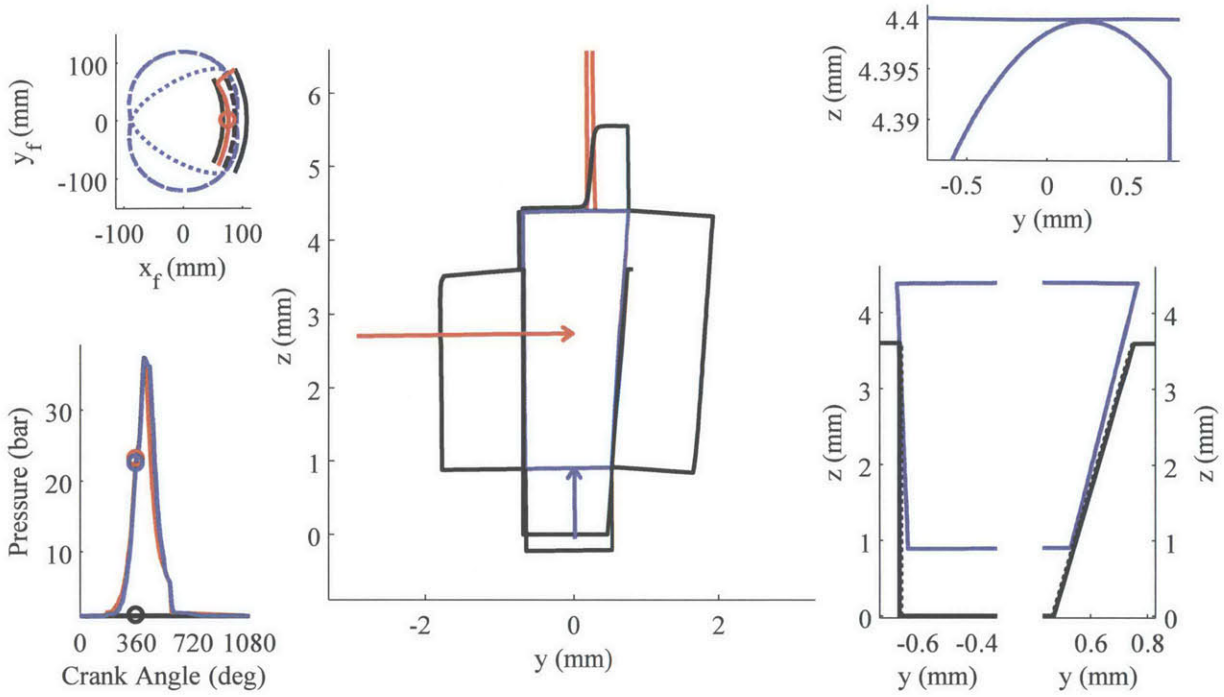

Fig. 6.20 Seal deformation and section view at x/L = 0.5 at 360 CA

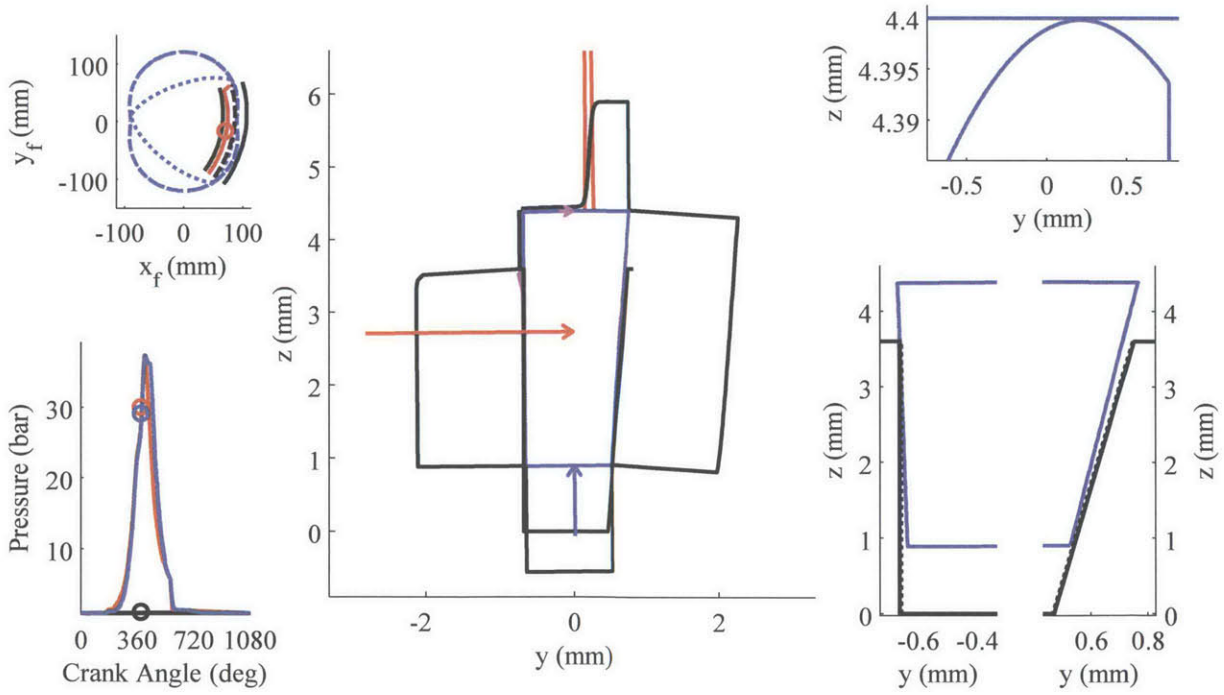

Fig. 6.21 Seal deformation and section view at x/L = 0.5 at 390 CA

When chamber peak pressure is reached, the seal tilts sufficiently to close the outer flank passage, and gases are trapped in the groove (Fig. 6.22). When the chamber pressure decreases below a certain level, the inner flank opens and gases in the groove leak to the side of the rotor (Fig. 6.23). This is the main cause of gas leakage at high speed. Towards the end of expansion stroke, circumferential body force overcomes friction and the seal is pushed against the leading corner seal (Fig. 6.24). This reverses the two ends role; the trailing end opens and the leading end is displaced laterally.

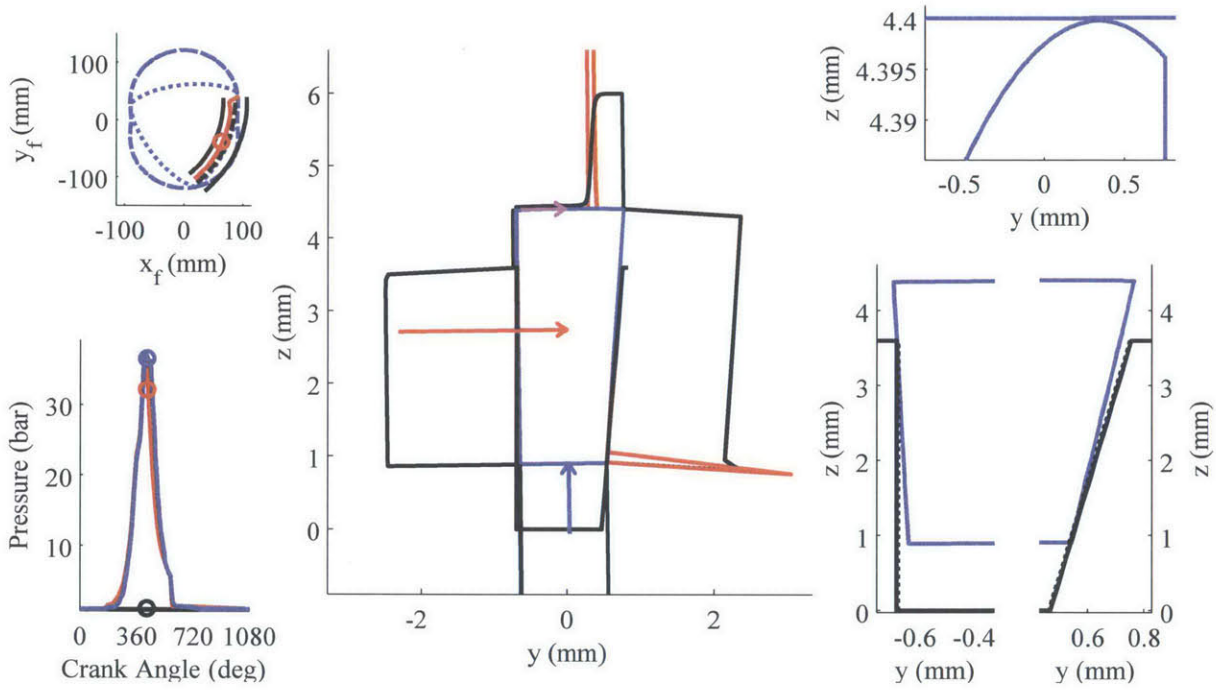

Fig. 6.22 Seal deformation and section view at x/L = 0.5 at 430 CA

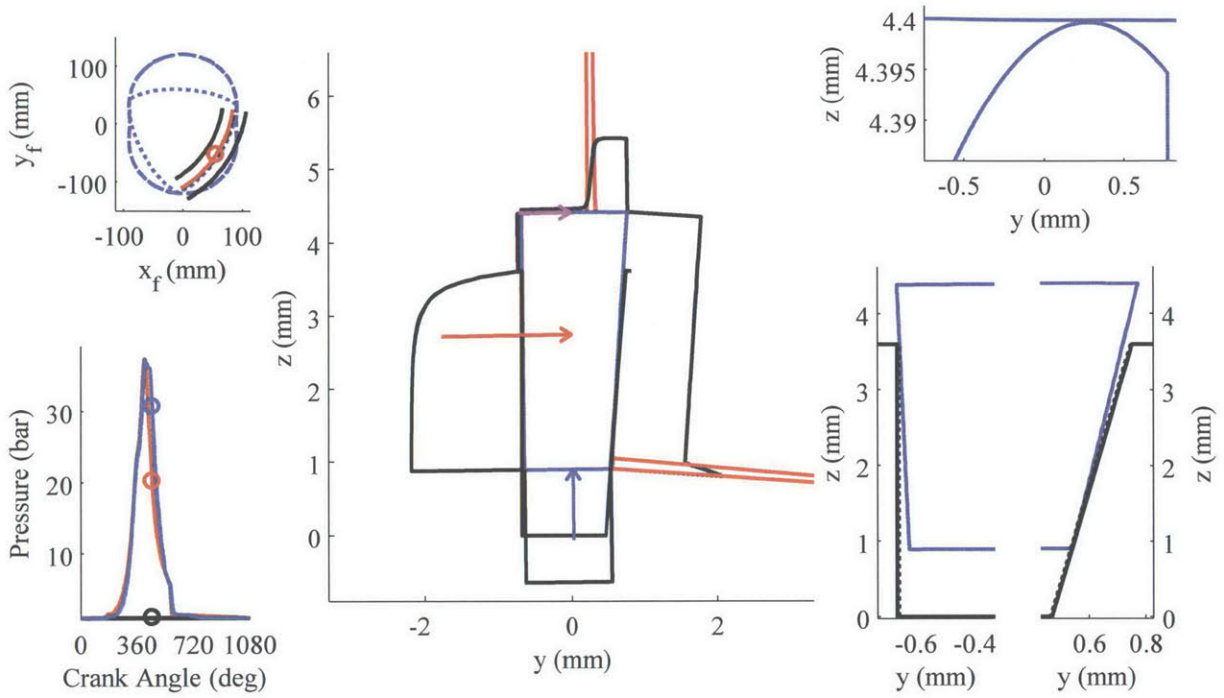

Fig. 6.23 Seal deformation and section view at x/L = 0.5 at 460 CA

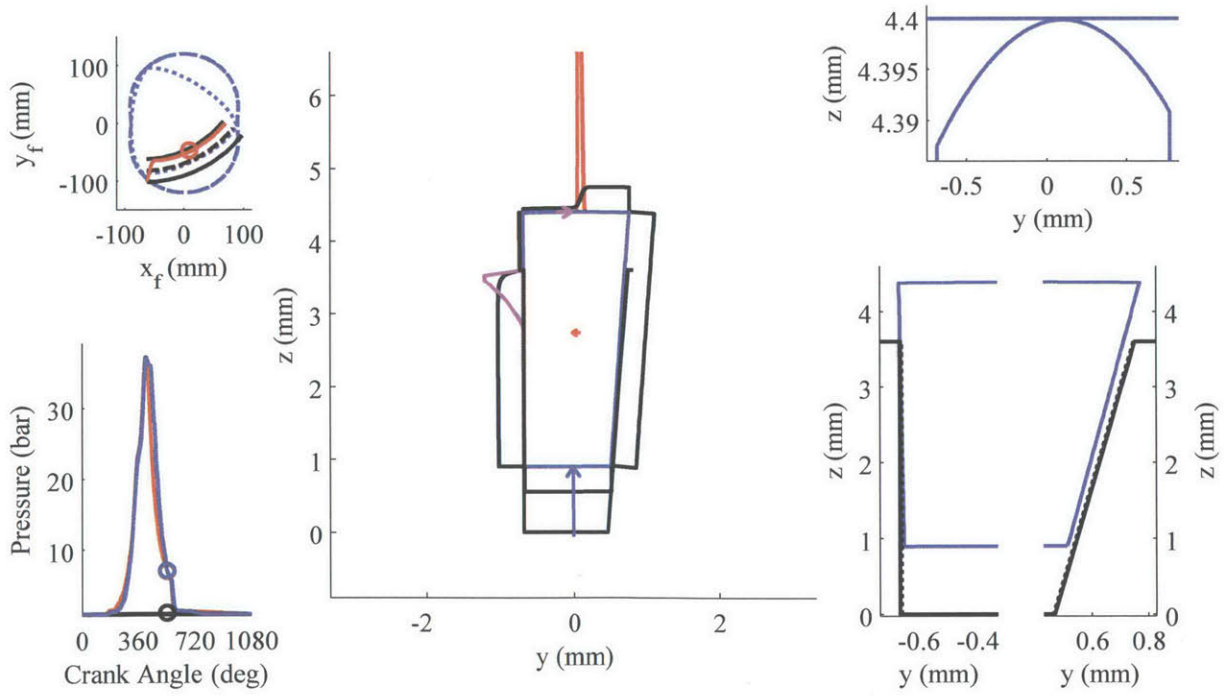

Fig. 6.24 Seal deformation and section view at x/L = 0.5 at 550 CA

The high-speed results shown up to this point did not include rotor housing distortion. As housing distortion at high speed is greater, the clearance between the seal profile and the rotor housing becomes larger even for large groove pressure (Fig. 6.25). This generates a non-negligible amount of leakage.

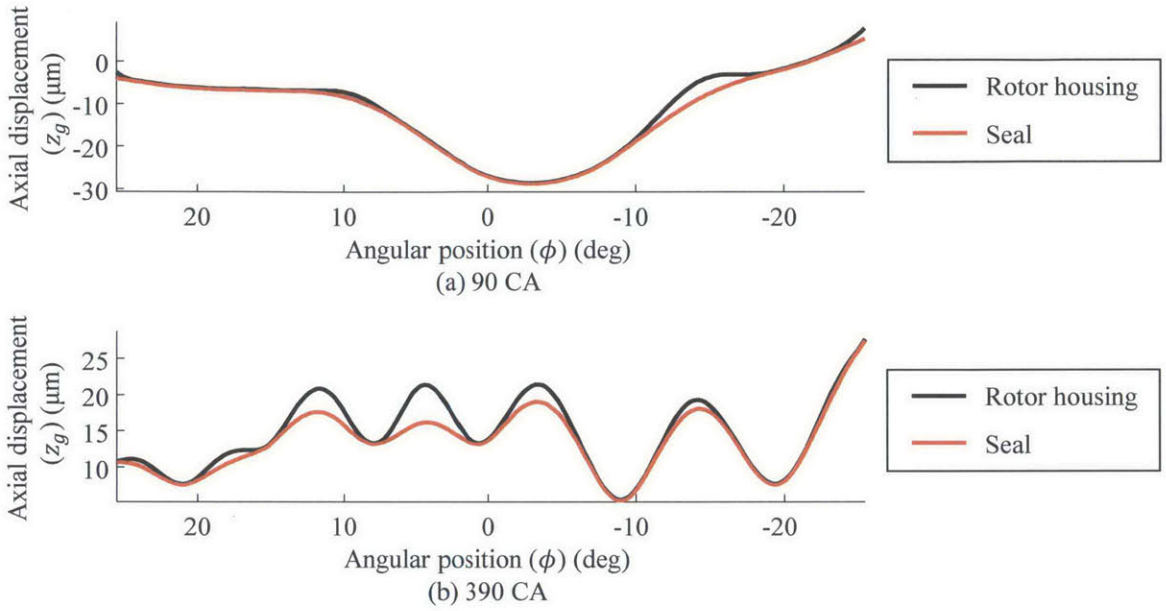

Fig. 6.25 Typical conformability of the seal to the distorted intermediate rotor housing at 8000 rpm full-load with (a) low pressure in the groove and (b) high pressure in the groove

Leakage mass flow rate as a function of crank angle is shown in Fig. 6.26 for the different mechanisms. Flank leakage between 180 and 270 CA is caused by body force maintaining part of the seal towards the outer flank. Flank leakage between 270 and 400 CA is caused by the trailing end of the seal pushed towards the outer flank because of profile friction and the corner seal contact angle. The largest portion of flank leakage happens between 450 to 540 CA when the inner flank opens to purge the gases in the groove. Profile leakage is the second most important leakage mechanism at high speed (Fig. 6.27). Profile leakage occurs when chamber pressure is high and the side seal is at the outer edge of the rotor housing where the distortion is maximal. End leakage is less important in proportion and is mainly caused by the leading end gap opening, but also the trailing end gap opening towards the end of the expansion stroke.

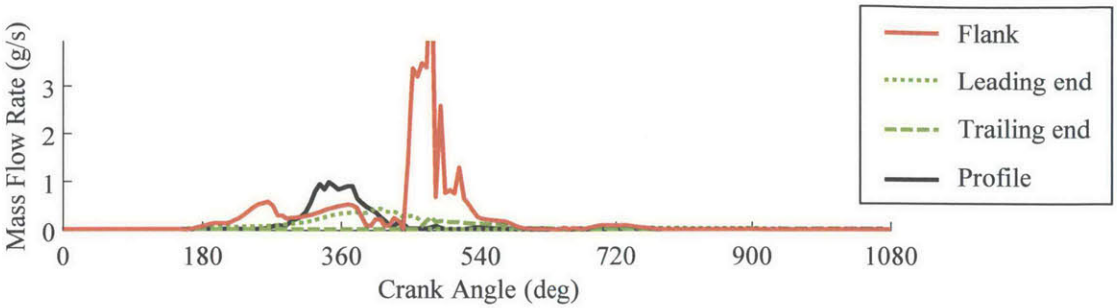

Fig. 6.26 Flank, end and profile leakage as a function of crank angle at 8000 rpm full-load

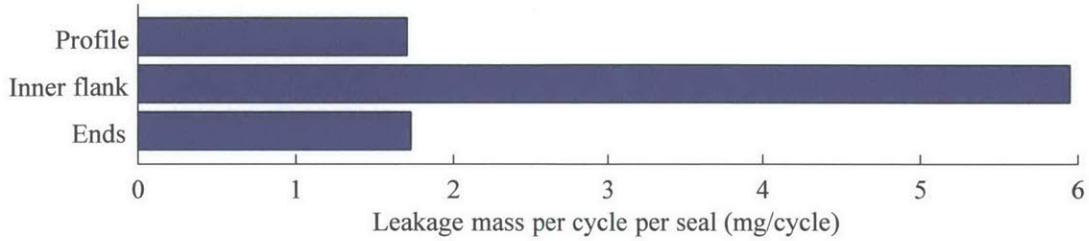

Fig. 6.27 Comparison of total leakage for the different mechanisms at 8000 rpm full-load

Finally, predicted friction power in dry condition at 8000 rpm is 394 W per side seal. With 0.5 μm of oil on the side housing, friction power is reduced to 180 W.

6.2.3 Effect of Speed on Leakage

The comparison between low and high speed can be extended to all speeds. Equivalent leakage area per chamber is used to compare all the speeds. Equivalent leakage area is defined as the area needed to obtain the same amount of leakage assuming an isentropic flow through an orifice.

Leakage from the gap at both ends of the seal is almost constant for all speeds (Fig. 6.28). On the other hand, there is a clear transition in the trend of flank leakage. For the configuration studied here, there is an important increase of flank leakage between 5000 and 6000 rpm, when body force becomes large enough to tilt the seal to close the outer flank.

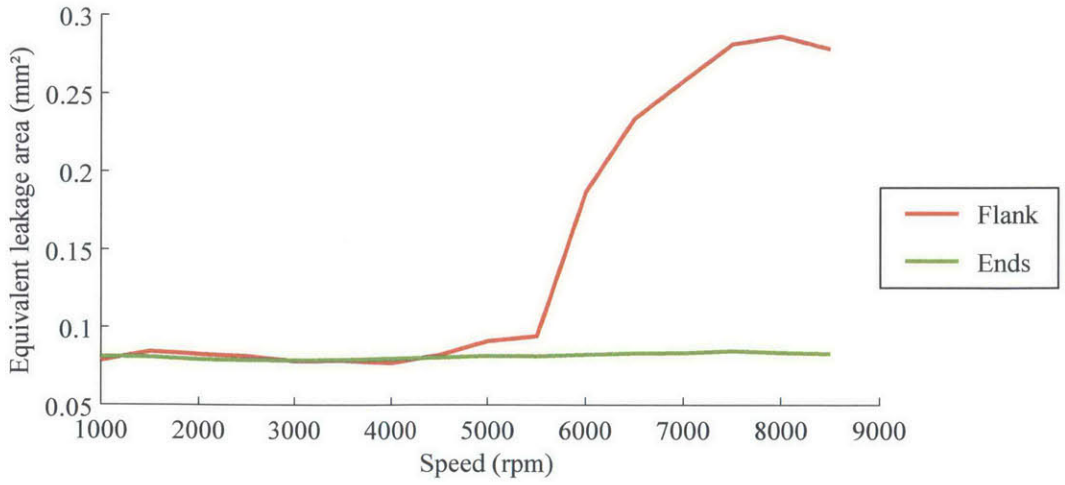

Fig. 6.28 Flank and trailing end equivalent leakage area per side seal as a function of speed at full-load

6.2.4 Effect of Profile Friction Coefficient on Leakage

Profile friction coefficient mainly changes the circumferential force on the seal. At low speed, the flank leakage is strongly dependent on the profile friction coefficient, especially as it gets above 0.1 (Fig. 6.29). On the other hand, total end leakage remains almost constant. The only difference is the leakage distribution between the leading and trailing end changes for low friction coefficient.

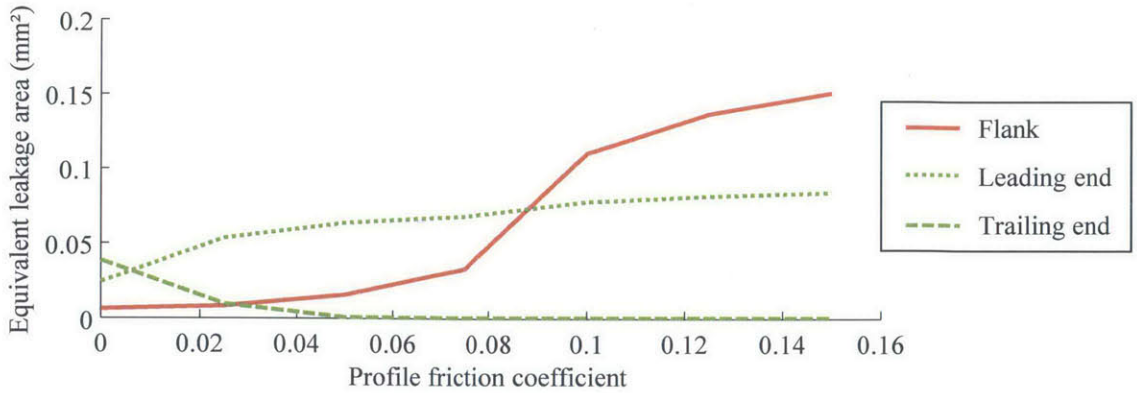

Fig. 6.29 Equivalent leakage area per side seal as a function of profile friction coefficient at 2000 rpm

At high speed, the flank leakage is more or less constant as a function of profile friction coefficient (Fig. 6.30). The variation is small because the opening of the inner flank due to CS contact angle is small compared to the opening of the inner flank due to seal tilting.

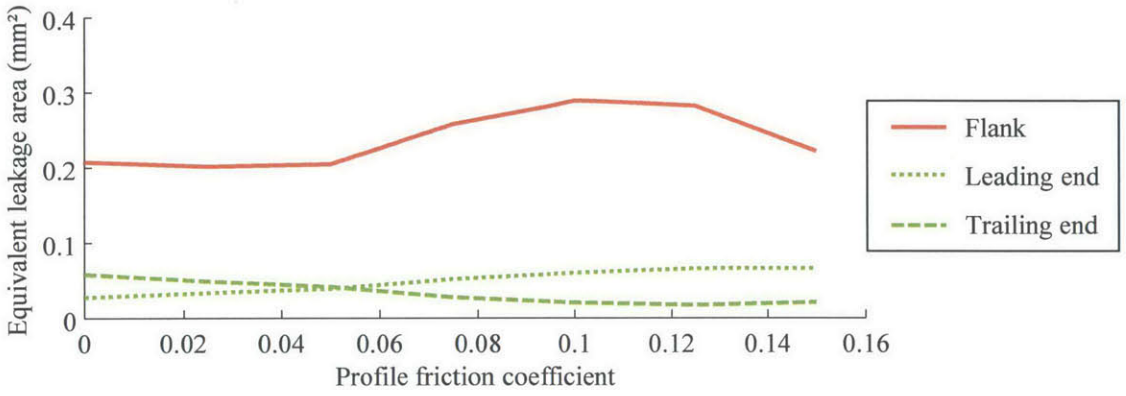

Fig. 6.30 Equivalent leakage area per side seal as a function of profile friction coefficient at 8000 rpm

6.2.5 Effect of Seal End Contact Angle on Leakage

The effect of changing the contact angle with the corner seals is investigated for different profile shapes. The profile shape is defined by the distance from the inner flank to the minimum clearance (T_{v0}) and the profile shape factor (a_v, unit m^{-1}), which determines the profile shape clearance approximated as parabolic (Fig. 6.31):

$$h_v(x_v) = a_v x_v^2 \tag{6.7}$$

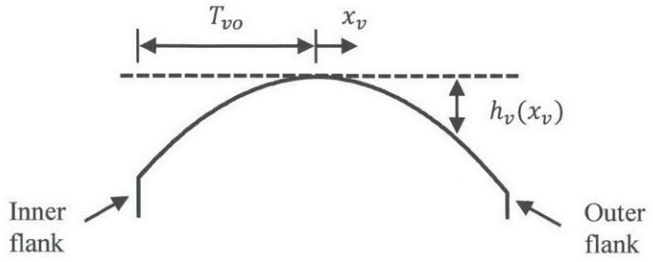

Fig. 6.31 Parabolic profile shape variables

At low speed, flank leakage varies greatly as a function of the profile shape factor and the corner seal contact angle (Fig. 6.32). For a profile shape factor of 20 and below, flank leakage is practically zero for a corner seal contact angle of zero. This is because the contact point is moving on the profile as the seal tilts, avoiding a complete tilt that would close the inner flank. Flank leakage then increases monotonically as the CS angle is increased. On the other hand, larger profile shape factor does not provide sufficient resistance to tilting and the inner flank leaks after peak pressure when the contact angle with the corner seal is small. At a critical CS contact angle, the contact with the corner seal provides additional titling resistance to the seal and the inner flank stops leaking after peak pressure, which is shown by a sudden drop in flank leakage in Fig. 6.32. As CS contact angle is increased further, flank leakage increases again because the trailing end of the seal is pushed towards the outer flank of the groove. End leakage decreases monotonically with CS contact angle as the cross-section area decreases for the same circumferential clearance.

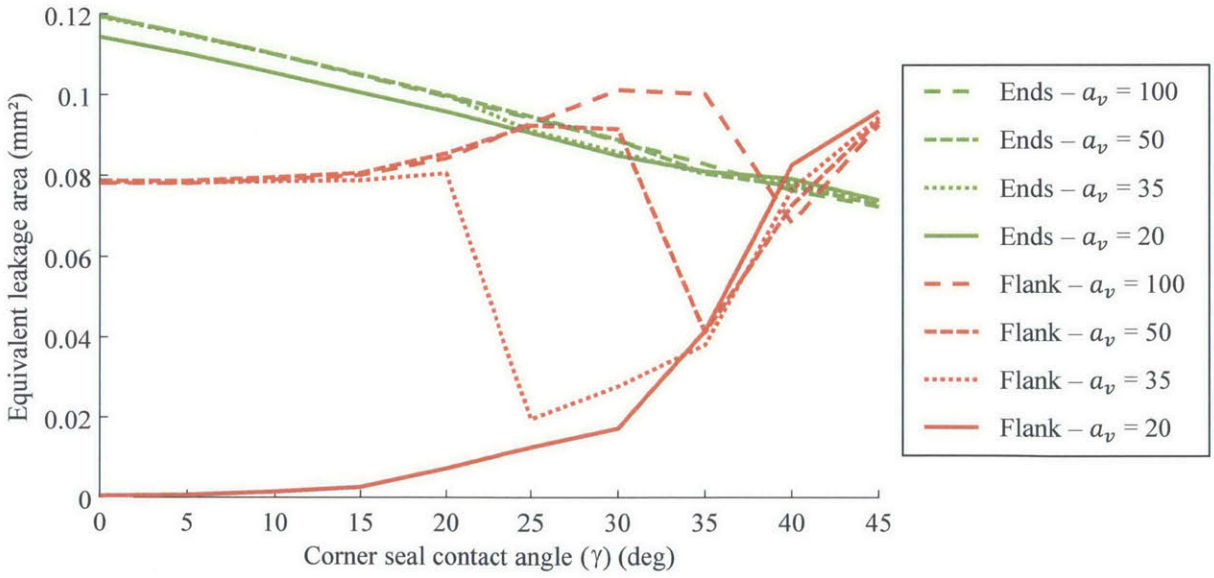

Fig. 6.32 End and flank leakage as a function of corner seal contact angle for different profiles at 2000 rpm full load

At high speed, flank leakage is more or less independent of CS contact angle (Fig. 6.33). As discussed, this is because the opening of the trailing end inner flank is not the main mechanism for flank leakage.

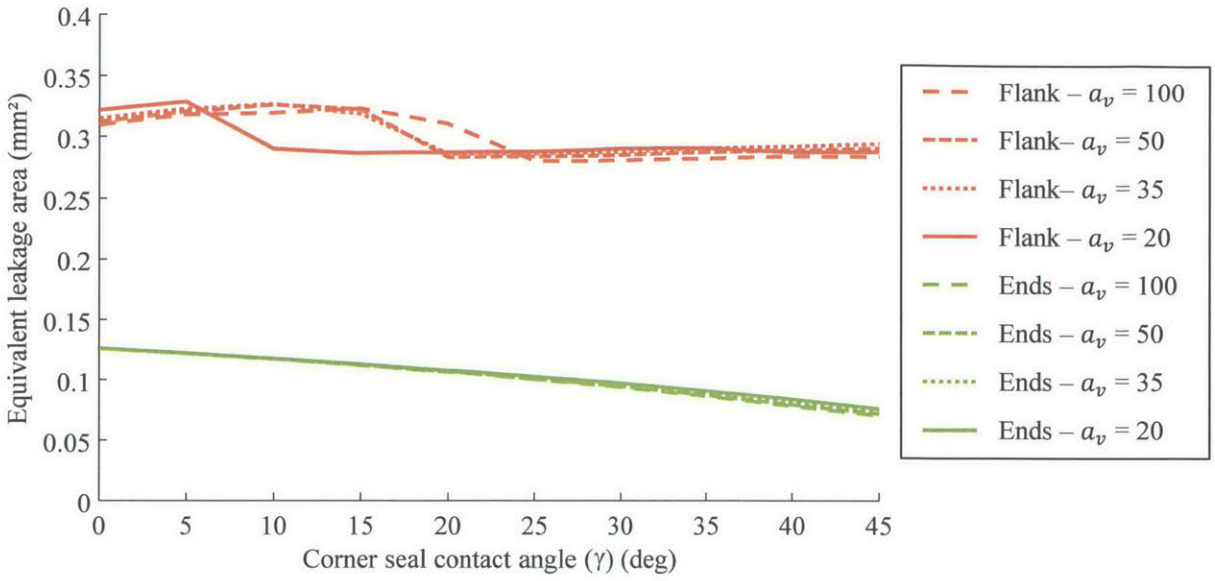

Fig. 6.33 End and flank leakage as a function of corner seal contact angle for different profiles at 8000 rpm full load

6.2.6 Effect of Position of Profile Minimum Clearance

In order to provide additional tilting resistance to the seal, the profile minimum clearance can be moved towards the outer edge of the profile. Model predictions show that this strategy works, even at high speed, especially for small profile shape factors (Fig. 6.34). The drawback of this approach is that the average gas pressure on the profile is decreased which increases the asperity contact force. This increases both side seal wear and friction. Moving the minimum clearance and reducing the contact angle to zero leads to a drastic flank leakage reduction at high speed (Fig. 6.35).

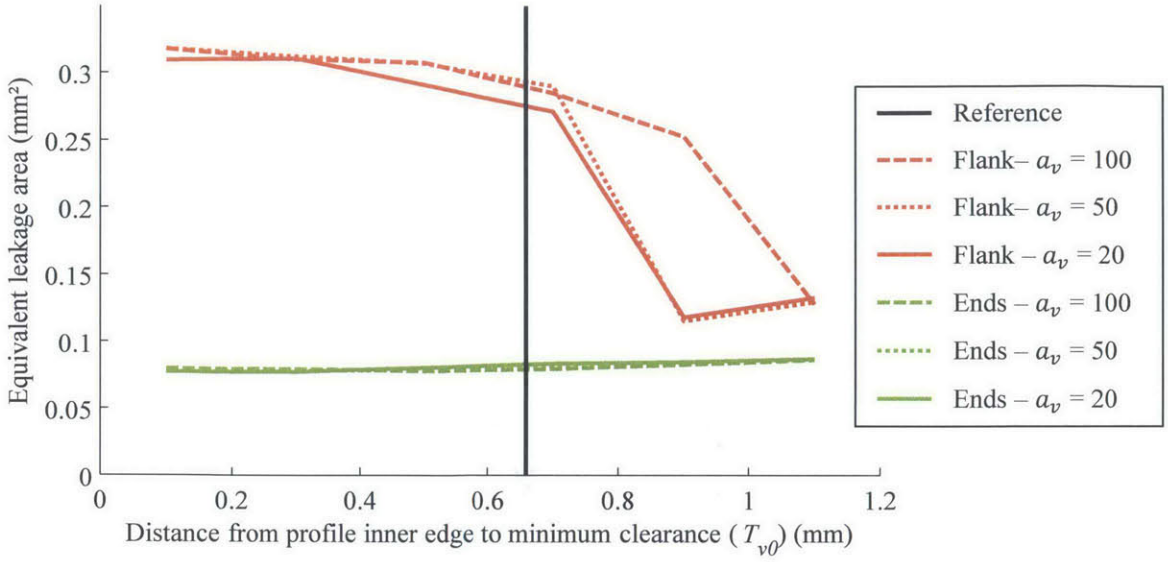

Fig. 6.34 End and flank leakage as a function of profile minimum clearance position for different profiles with CS contact angle of 40° at 8000 rpm full load

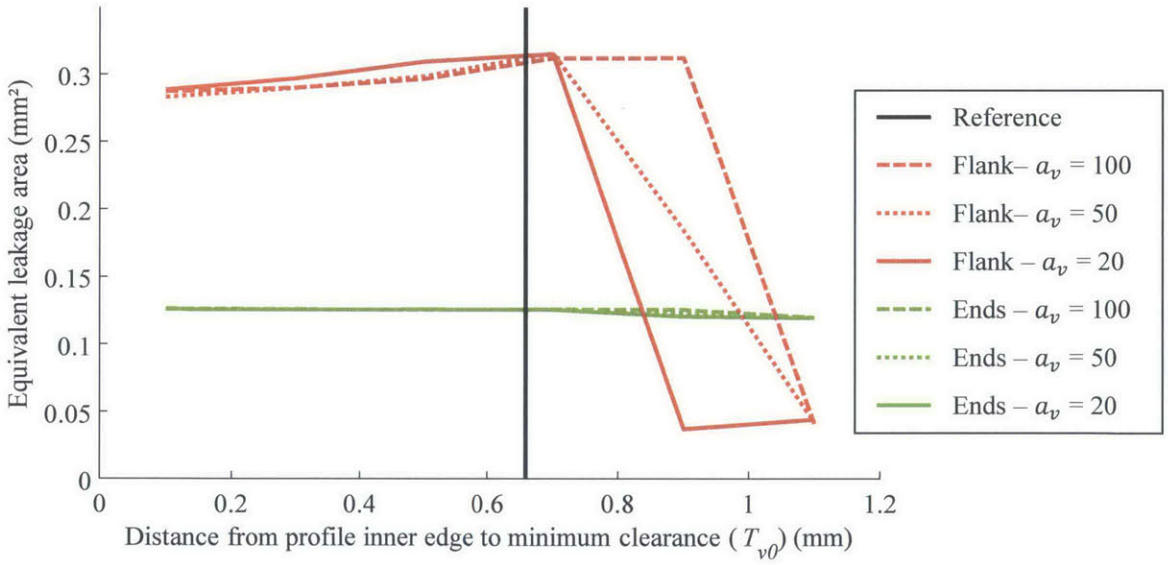

Fig. 6.35 End and flank leakage as a function of profile minimum clearance position for different profiles with CS contact angle of 0° at 8000 rpm full load

6.3 Comparison with Experiments

Experimental evidences are limited for side seal leakage. Nevertheless, it is interesting to compare with the image obtained from the 2D LIF engine. Oil patterns show that the leading end of the side seal is open which creates a narrow region where the oil is dragged inward by gas flow. At the trailing end of the side seal, the region where oil is dragged inward by gas flow is

larger. This is in agreement with the model that predicts the inner flank opening due to the contact with the corner seal.

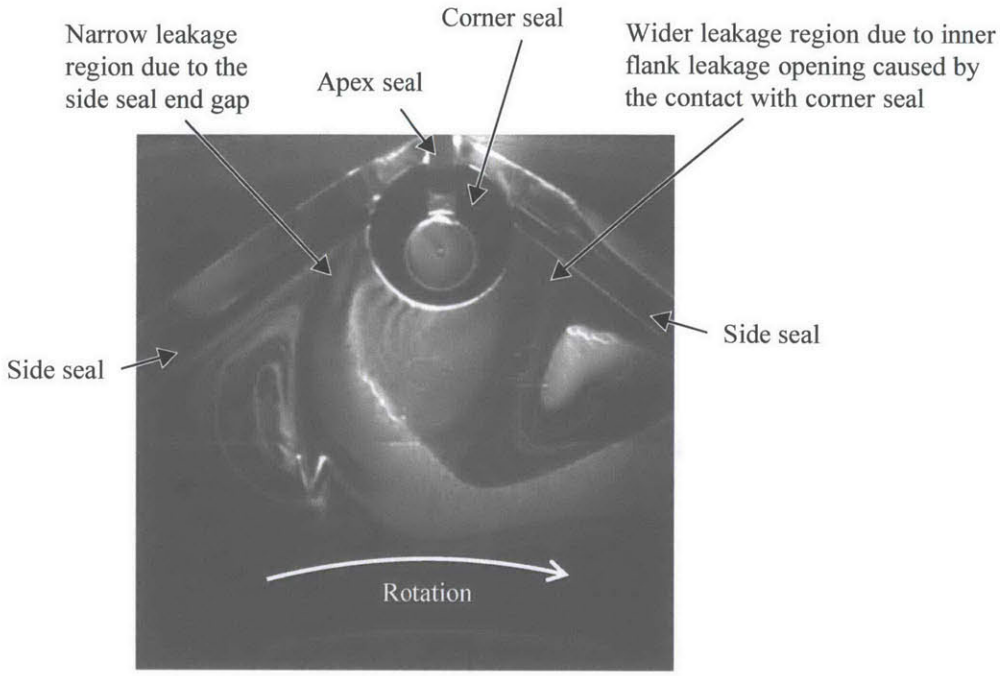

Fig. 6.36 Oil pattern around the gas seals taken with the 2D LIF engine for large injection rate

6.4 Side Seal Model Conclusions

A model to predict performance of the side seal is developed. Model formulation is similar to the apex seal model, but includes a curved beam finite element model. The model can handle the dynamics of the side seal and stiff contacts. A larger number of elements than for the apex seal are needed as the deformation of the seal can be local because the seal is more compliant. Sealing performance of the side seal is assessed from the detailed results, mainly gas leakage.

Model predictions lead to the following conclusions:

1. Flank leakage is the dominant leakage mechanism, followed by end leakage and profile leakage.
2. At low speed, flank leakage is mainly caused by the opening of the inner flank due to the contact with the trailing corner seal.

3. At high speed, flank leakage mainly occurs because of seal tilting that blocks the outer flank and forces gases to exit the groove through the inner flank.
4. End leakage area is constant and only function of the initial circumferential clearance and contact angle with the corner seal.
5. Profile leakage can be important at high speed due to the large side housing distortion. The seal is not flexible enough to conform to the distorted housing.

Chapter 7

Summary and Conclusions

Multiscale models are developed to assess the performance of the sealing grid of rotary engines. These comprehensive models can be used to seal design in order to reduce emissions and increase efficiency of rotary engines.

An internal oil consumption model is developed based on the mechanisms identified with 2D laser-induced fluorescence experiments. This model is capable of predicting oil transport through the oil seal by calculating the clearance with the side housing using a beam finite element model and tracking the oil throughout the engine cycle using a control volume approach.

A set of models are developed to calculate gas leakage and other performance indicators of the apex seals, two-piece and three-piece, as well as the side seals. Those models are capable of predicting the numerically stiff dynamics of the deformable gas seals.

7.1 Summary of the Findings

Internal oil consumption is a step-by-step process from the center of the rotor to the combustion chamber. The main mechanism leading to internal oil consumption is outward scraping of the oil seals. Once oil has passed the oil seals, there is no observed mechanism to bring the oil back to the crankcase. The cut-off seal does not provide an additional barrier to internal oil consumption and cut-off seal scraping in both directions should be avoided. Once the oil is on the rotor outside the outer oil seal, it is pushed outwards by the centrifugal acceleration toward the combustion chamber.

Outward scraping of the oil seals is due to a non-trivial combination between a lack of conformability of the seal to the distorted housing and engine kinematics. The housings have

numerous peaks and valleys, which makes it difficult for the seal to conform to the surface, leaving a clearance between the oil seals and side housing. Also, the seal orientation relative to a valley is different for the inward and outward motion because of rotor kinematics. In some regions, this leads to a large oil film thickness left on the side housing during inward motion of the oil seals that is scraped out during outward motion. This problem is complexified by the fact that, for some housing distortion shapes, increasing seal tension can increase oil consumption. The best approach in reducing internal oil consumption is to make the oil seals more compliant and to decrease housing distortion amplitude next to the intake and exhaust ports.

From the gas seal model results, gas leakage can be compiled for the entire engine considering the appropriate number of each seal type per rotor. The total leakage area obtained is 1-2 mm^2/chamber from low to high speed which is in agreement with the previous studies. At low speed, side seal leakage accounts for 30 % of the total leakage, corner seal leakage for 30 % and apex seal for 40 % (Fig. 7.1). This is similar to the previous study by Eberle and Klomp [37] that measured 1/4-1/3 of the leakage for the side seals and 2/3-3/4 for the apex seals, when accounting for the fact that the experimental apparatus used could not distinguish corner seal leakage to the rotor side from side seal leakage or corner seal leakage to the low pressure chamber from apex seal leakage.

At low speed, leakage through the spark plug holes accounts for a third of the total leakage (Fig. 7.1). The second most important leakage mechanism is the leakage through the corner seal clearance. Flanks and ends of the side seal also generate significant leakage, followed by the apex seal side piece. The distribution at high speed is changed mainly due to the increase of flank leakage for both the apex and side seals caused by the increased body force (Fig. 7.2). For the apex seal, the three-piece configuration has the potential to reduce flank leakage. For the side seal, flank leakage can be reduced by reducing the contact angle with the corner seal and moving the minimum clearance point towards the outer edge. The latter solution should be studied further as it also increases wear and friction.

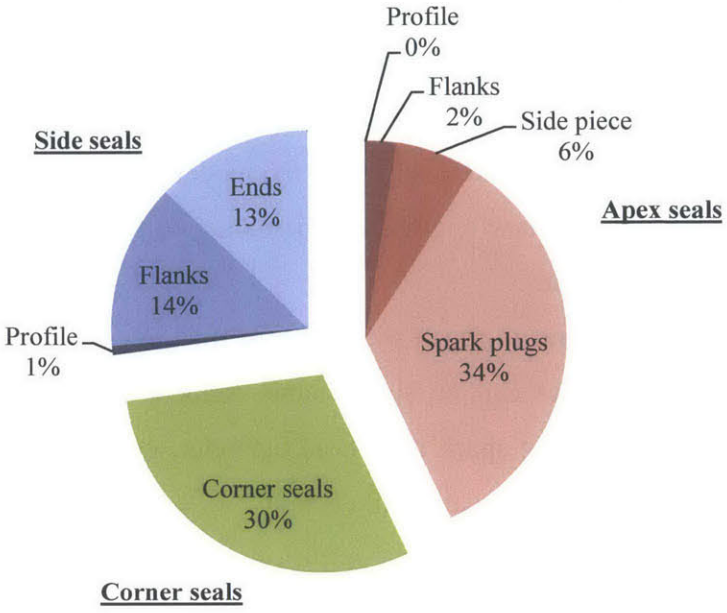

Fig. 7.1 Predicted relative gas leakage due to the different mechanisms at 2000 rpm

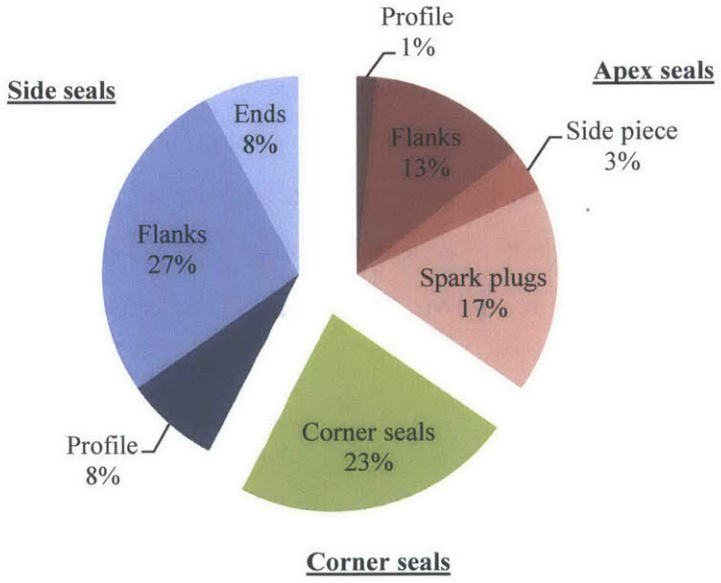

Fig. 7.2 Predicted relative gas leakage due to the different mechanisms at 8000 rpm

7.2 Conclusions

The multiscale modeling approach developed integrates local and global effects together to calculate performance indicators for rotary engine sealing, including internal oil consumption, gas leakage, wear and friction. The key take-away from the model predictions are that:

1. Internal oil consumption of rotary engines can be reduce to a low level by designing the oil seals to be more compliant.
2. Although it would be difficult to reach the low level of blow-by of piston engines, gas leakage of the rotary engines can be significantly reduced by sealing the corner seal clearance, reducing the leading spark plug hole diameter, using a three-piece apex seal configuration and modifying side seal profile design.

The comprehensive models developed are the first of their kind for rotary engines and will be valuable tools to design more efficient and environment-friendly rotary engines.

7.3 Future Work

The main goal of this work was focused at developing the models to assess sealing performance. There is still a significant amount of work to adjust the model inputs in order to obtain a better fit with experiments. In addition, it would be interesting to expand the model to take into account oil transport around the gas seals to better control the use of metered oil. Finally, as the position of the seals and gas mass flow rate are known, the model could be used to predict hydrocarbon emission trends.

References

[1] Ohkubo, M., Tashima, S., Shimizu, R., Fuse, S., and Ebino, H., 2004, "Developed Technologies of the New Rotary Engine (RENESIS)," SAE Technical Paper 2004-01-1790.

[2] Jones, C., 1979, "A Review of Curtiss-Wright Rotary Engine Developments with Respect to General Aviation Potential," SAE Technical Paper 790621.

[3] Kamiya, S., and Shirasagi, S., 1977, "Suzuki Production Rotary Engine, Model RE-5 for Powering Motorcycles," SAE Technical Paper 770190.

[4] Jones, C., 1978, "Rotary Engine Developments at Curtiss-Wright over the Past 20 Years and Review of General Aviation Engine Potential," NASA Conference Publication 2067, pp. 123–174.

[5] Jones, C., 1992, "Stratified Charge Rotary Engine Developments at JDTI from 1984 to 1991," SAE Technical Paper 920310.

[6] Yamaoka, K., Kitagawa, K., Hamada, Y., Morimoto, T., and Yamanouchi, R., 1976, "Yanmar Diesel's Rotary Engine Chain Saw," SAE Technical Paper 760642.

[7] Figart, W. T., Leisenring, R. L., and Silvestri, W. B., 1970, "The RC Engine - A New Approach to Reduce Costs," SAE Technical Paper 700273.

[8] Fraidl, G. K., Beste, F., Kapus, P. E., Korman, M., Sifferlinger, B., and Benda, V., 2011, "Challenges and Solutions for Range Extenders - From Concept Considerations to Practical Experiences," SAE Technical Paper 2011-37-0019.

[9] Huffman, B. C., 2011, "Rotary Engine Friction Test Rig Development Report," DTIC Document ARL-CR-685.

[10] Willis, E. A., and McFadden, J. J., 1992, "NASA's Rotary Engine Technology Enablement Program, 1983 Through-1991," NASA Technical Memorandum 105562.

[11] Danieli, G. A., Keck, J. C., and Heywood, J. B., 1978, "Experimental and Theoretical Analysis of Wankel Engine Performance," SAE Technical Paper 780416.

[12] Dimpelfeld, P., and Humke, A., 1987, "Heat Release Characteristics of Stratified - Charge Rotary Engines," SAE Technical Paper 870443.

[13] Norbye, J. P., 1971, *The Wankel Engine: Design, Development, Applications*, Chilton, Philadelphia, PA.

[14] Hege, J. B., 2001, *The Wankel Rotary Engine: A History*, McFarland, Jefferson, NC.

[15] Bentele, M., 1991, "The Rotary Engine Era," *Engine Revolutions: The Autobiography of Dr. Max Bentele*, Society of Automotive Engineers, Warrendale, PA, pp. 151–169.

[16] Ansdale, R. F., and Lockley, D. J., 1969, *The Wankel RC Engine*, A. S. Barnes, New York, NY.

[17] Yamamoto, K., 1981, *Rotary engine*, Sankaido, Tokyo, Japan.

[18] Jones, C., 1972, "A Survey of Curtiss-Wright's 1958-1971 Rotating Combustion Engine Technological Developments," SAE Technical Paper 720468.

[19] Shimamura, K., and Tadokoro, T., 1981, "Fuel Economy Improvement of Rotary Engine by Using Catalyst System," SAE Technical Paper 810277.

[20] Fujimoto, Y., Tatsutomi, Y., Ozeki, H., and Tadokoro, A., 1987, "Present and Prospective Technologies of Rotary Engine," SAE Technical Paper 870446.

[21] Chen, T. N., Alford, R. N., and Kim, S. S., 1986, "Detonation Characteristics of Industrial Natural Gas Rotary Engines," SAE Technical Paper 860563.

[22] Matsuura, K., Kazuo Terasaki, and Ichiro Watanabe, 1976, "The Relative Behavior of a Rotary Engine Apex Seal to the Walls of a Slot," Bulletin of the JSME, **19**(137), pp. 1367–1375.

[23] Matsuura, K., Terasaki Kazuo, and Watanabe, I., 1978, "The Behavior of a Rotary Engine Apex Seal against the Trochoidal Surface," Bulletin of the JSME, **21**(161), pp. 1642–1651.

[24] Lamping, H. D., Galliers, M. W., and Wolosin, S. M., 1974, "Rotary Combustion Engine Trochoid Coatings and Seals," SAE Technical Paper 741043.

[25] Knoll, J., Vilmann, C. R., Schock, H. J., and Strumpf, R. P., 1984, "A Dynamic Analysis of Rotary Combustion Engine Seals," SAE Technical Paper 840035.

[26] Orlandea, N. V., Welnert, M. S., and Keleher, D. B., 1987, "Computer Simulation of the Rotary Engine Apex Seal System," SAE Technical Paper 870410.

[27] Rachel, T., Schock, H., and Bartrand, T., 1991, "Analysis of Frictional Power Losses Associated With the Side and Apex Seals of a Wankel Rotary Engine," SAE Technical Paper 910626.

[28] Handschuh, R., 2010, "Analysis of apex seal friction power loss in rotary engines," NASA Technical Memorandum 2010-216353.

[29] Revankar, G. S., 1991, "The Development of a stratified charge rotary engine apex seal material," SAE Technical Paper 910627.

[30] Muroki, T., 1984, "Recent Technology Development of High-Powered Rotary Engine at Mazda," SAE Technical Paper 841017.

[31] Froede, W. G., 1968, "NSU's Double Bank Production Rotary Engine," SAE Technical Paper 680461.

[32] Bartrand, T. A., and Willis, E. A., 1990, "Performance of a supercharged direct-injection stratified-charge rotary combustion engine," NASA Technical Memorandum 103105.

[33] Rogers, T. W., Lemke, W., Lefevre, J., and Ohzawa, T., 1972, "Lubricant Studies in Rotary-combustion Engines," SAE Technical Paper 910627.

[34] Behling, R. D., and Weise, E., 1973, "Lubricant and Fuel Requirements and General Performance Data of Wankel Rotary Piston Engines," SAE Technical Paper 730048.

[35] Van Basshuysen, R., and Wilmers, G., 1978, "An Update of the Development on the New Audi NSU Rotary Engine Generation," SAE Technical Paper 780418.

[36] Shidahara, Y., Murata, Y., Tanita, Y., and Fujimoto, Y., 1985, "Development of Sliding Surface Material for Combustion Chamber of High-Output Rotary Engine," SAE Technical Paper 852176.

[37] Eberle, M. K., and Klomp, E. D., 1973, "An Evaluation of the Potential Performance Gain from Leakage Reduction in Rotary Engines," SAE Technical Paper 730117.

[38] Danieli, G. A., Ferguson, C. R., Heywood, J. B., and Keck, J. C., 1974, "Predicting the emissions and performance characteristics of a Wankel engine," SAE Technical Paper 740186.

[39] Norman, T. J., 1983, "A performance model of a spark ignition Wankel engine : including the effects of crevice volumes, gas leakage, and heat transfer," Master's Thesis, Massachusetts Institute of Technology.

[40] Roberts, J. A., Norman, T. J., Ekchian, J. A., and Heywood, J. B., 1986, "Computer Models For Evaluating Premixed and Disc Wankel Engine Performance," SAE Technical Paper 860613.

[41] Sierens, R., Baert, R., Winterbone, D. E., and Baruah, P. C., 1983, "A Comprehensive Study of Wankel Engine Performance," SAE Technical Paper 830332.

[42] Froede, W., 1965, "The Rotary Engine of the NSU Spider," SAE Technical Paper 650722.

[43] Prasse, H. F., McCormick, H. E., and Anderson, R. D., 1973, "A Critical Analysis of Rotary Engine Sealing Problem," SAE Technical Paper 730118.

[44] Muroki, T., and Miyata, J., 1986, "Material Technology Development Applied to Rotary Engine at Mazda," SAE Technical Paper 860560.

[45] Matsuda, I., Tadokoro, T., Kita, T., and Nakao, M., 1990, "New Technology Employed for the Latest 13B-Rotary Engine," SAE Technical Paper 900036.

[46] Tian, T., Noordzij, L. B., Wong, V. W., and Heywood, J. B., 1998, "Modeling Piston-Ring Dynamics, Blowby, and Ring-Twist Effects," J. Eng. Gas Turbines Power, **120**(4), pp. 843–854.

[47] Baelden, C., and Tian, T., 2014, "A Dual-Grid Curved Beam Finite Element Model of Piston Rings for Improved Contact Capabilities," SAE Technical Paper 2014-01-1085.

[48] Thirouard, B., and Tian, T., 2003, "Oil Transport in the Piston Ring Pack (Part I): Identification and Characterization of the Main Oil Transport Routes and Mechanisms," SAE Technical Paper 2003-01-1952.

[49] Picard, M., Hidaka, H., Tian, T., Nishino, T., Arai, E., and Ohkubo, M., 2014, "Visualization of the Rotary Engine Oil Transport Mechanisms," SAE Technical Paper 2014-01-1665.

[50] Thirouard, B., 2001, "Characterization and modeling of the fundamental aspects of oil transport in the piston ring pack of internal combustion engines," Ph.D. Thesis, Massachusetts Institute of Technology.

[51] Greenwood, J. A., and Tripp, J. H., 1970, "The Contact of Two Nominally Flat Rough Surfaces," Proceedings of the Institution of Mechanical Engineers, **185**(1), pp. 625 –633.

[52] Chen, H., 2011, "Modeling the Lubrication of the Piston Ring Pack in Internal Combustion Engines Using the Deterministic Method," Ph.D. Thesis, Massachusetts Institute of Technology.

[53] Parker, 2007, "Parker O-Ring Handbook ORD 5700."

[54] Baelden, C., 2014, "A Multi-Scale Model for Piston Ring Dynamics, Lubrication and Oil Transport in Internal Combustion Engines," Ph.D. Thesis, Massachusetts Institute of Technology.

[55] Liu, L., 2005, "Modeling the performance of the piston ring-pack with consideration of non-axisymmetric characteristics of the power cylinder system in internal combustion engines," Ph.D. Thesis, Massachusetts Institute of Technology.

[56] Tian, T., 1997, "Modeling the performance of the piston ring-pack in internal combustion engines," Ph.D. Thesis, Massachusetts Institute of Technology.

[57] Press, W. H., Teukolsky, S. A., Vetterling, W. T., and Flannery, B. P., 2007, "Globally Convergent Methods for Nonlinear Systems of Equations," *Numerical recipes 3rd edition: The art of scientific computing*, Cambridge university press, pp. 376–386.

[58] Juvinall, R. C., and Marshek, K. M., 2006, "Surface Damage," *Fundamentals of Machine Component Design*, John Wiley & Sons, Hoboken, NJ, pp. 348–382.

Appendix A

Adapted Deterministic Hydrodynamic Model

Hydrodynamic pressure generated by the relative motion of two surfaces is usually dominated by the macroscopic shape such as a parabolic profile. However, when the two surfaces are parallel to each other, the only pressure generated is by the surface roughness. Since this is the case for the rotary engine oil seal, it is essential to develop a method to calculate the hydrodynamic pressure.

A deterministic model has been developed by Chen [52] to calculate the pressure generated at the interface for piston rings, including cavitation. However, the motion of the piston rings is always going up and down on the liner, whereas the motion of the oil seals can be in all directions. Furthermore, the motion of the piston rings is perpendicular to the ring, whereas the motion of the rotary engine seal can be from perpendicular to parallel to itself. Those effects are to be included in the hydrodynamic pressure generation to predict their effect on oil transport.

The scope of this section is to calculate the hydrodynamic pressure generated by roughness and build a correlation that can be used in the cycle model. First, the mechanism of pressure generation by roughness is explained. The deterministic model for piston ring is then summarized and modified for the rotary engine seals. Surface orientation effect is investigated and a factor of 2 to 3 on pressure generation is observed between moving to the left and moving to the right. Seal orientation effect investigation shows mainly that the pressure drops as the motion gets parallel to the seal. Finally, correlations from the piston rings are modified to take into account both surface orientation and seal orientation.

Supply effect and friction are not studied extensively and piston ring correlations are taken directly. This subject is discussed at the end of this appendix.

A.1 Pressure Generation Mechanism

The mechanism of pressure generation is shown in Fig. A.1 for hypothetical triangular asperities on the housing. Since roughness of the seal is typically smaller than housing roughness, it usually can be neglected. If there were no cavitation, positive and negative pressure would be symmetrical and the net force would be zero (Fig. A.1a). However, if oil pressure drops below a critical pressure, cavitation occurs and pressure of this region is fixed to vapor pressure. Pressure is therefore only generated by raising wedges, and a net force is pushing the seal away from the interface (Fig. A.1b).

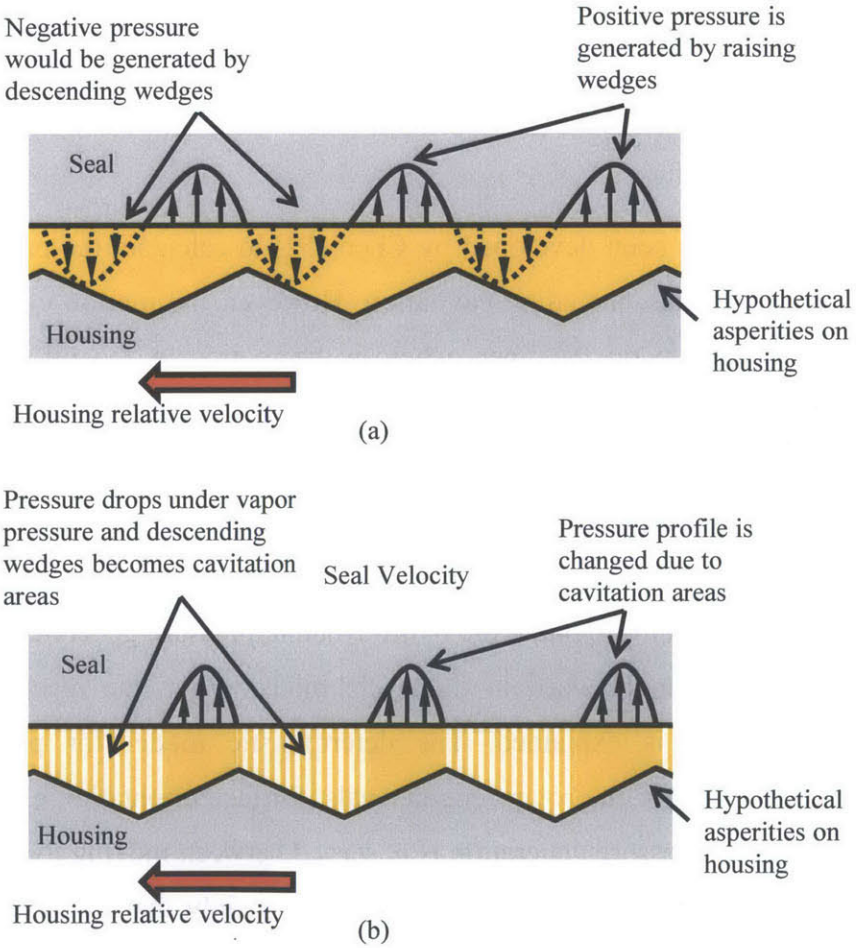

Fig. A.1 (a) Hypothetical pressure generation by asperities without cavitation, and (b) representation of actual pressure generation by asperities with cavitation

A.2 Piston Ring Current Model

In this section, a brief summary of the piston engine deterministic model is given. For a comprehensive explanation, one should read Chen's thesis [52]. The global approach is first explained. Discretization of space and time is then described followed by the equations solved in the model. Finally, correlations for the oil control ring and the top two rings are shown.

To calculate the pressure generated by the roughness, a small patch of the housing is slid under the seal contact surface, as shown in Fig. A.2. The housing is typically much rougher than the seal. The seal roughness is therefore neglected and it is assumed to be flat. The motion of the housing creates wedges that generate pressure on the seal. The pressure is solved using 2D Reynolds' equation coupled with a cavitation algorithm.

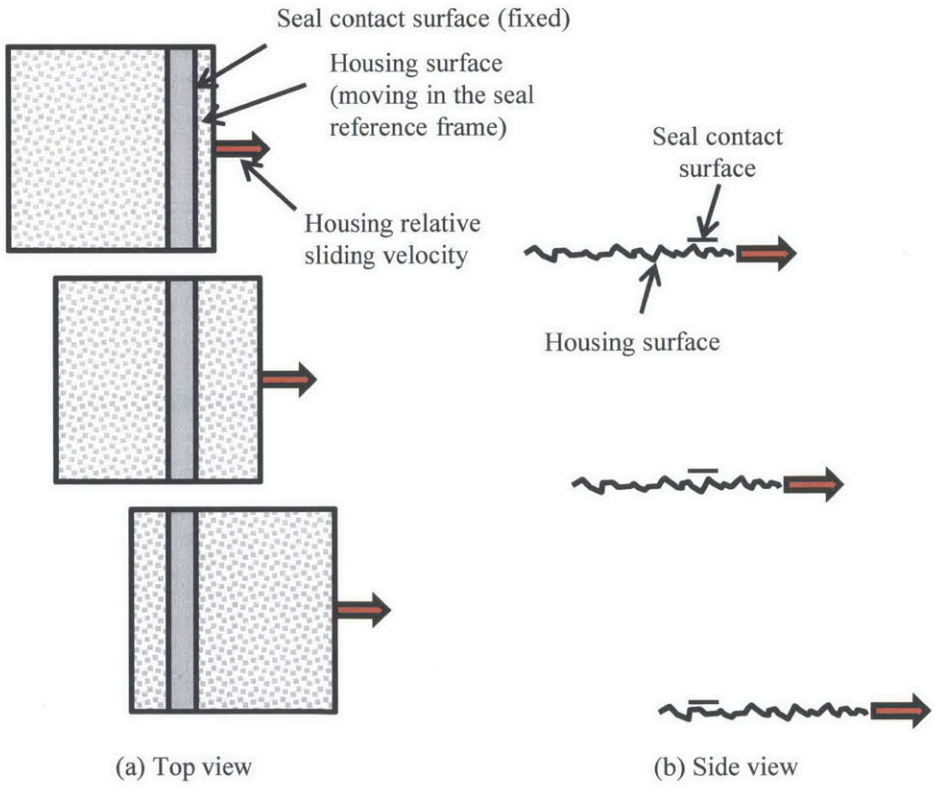

Fig. A.2 Rough housing sliding under the flat seal contact surface

A.2.1 Numerics

The seal is divided into a given number of cells. The motion of the housing under the seal is divided in a given number of time steps, chosen to match the cell length along x. Every time step (dt), the housing grid is moved of one cell (dx). This allows the housing grid to always match the seal grid. Every time step, the clearance of the cells changes, which changes the volume of the cell, as shown in Fig. A.3. Oil is then flowing into or out of the adjacent cells depending on their clearance and pressure.

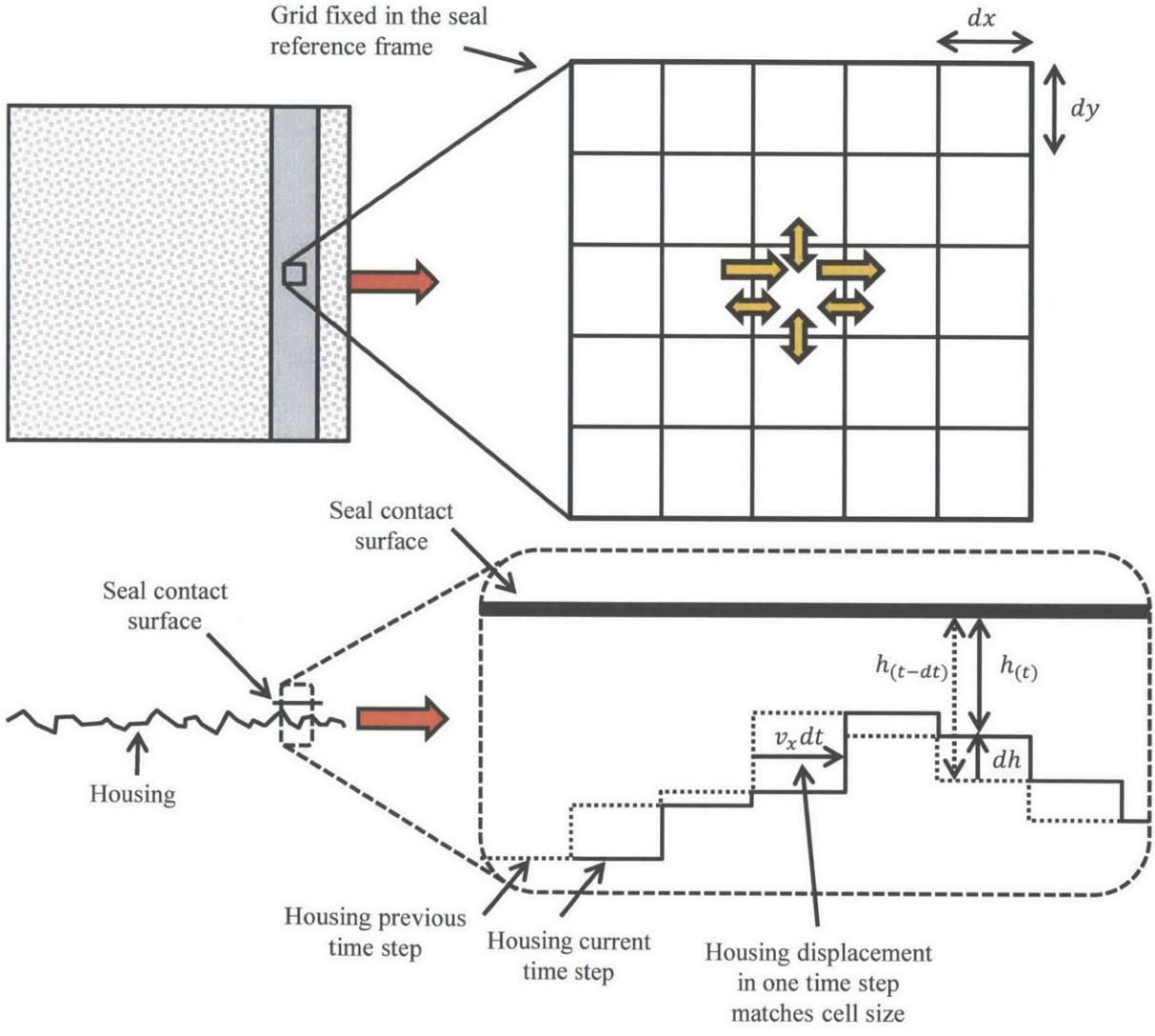

Fig. A.3 Deterministic model grid and housing displacement in a time step

A.2.2 Equations and Boundary Conditions

The governing equation solved in the model is the 2D Reynolds' equation from lubrication approximation. For the current configuration, it can be reduced to this form:

$$\frac{d}{dx}\left(\frac{\rho v_x h}{2}+\frac{\rho h^3}{12\mu}\left(-\frac{dP}{dx}\right)\right)+\frac{d}{dy}\left(\frac{\rho h^3}{12\mu}\left(-\frac{dP}{dx}\right)\right)+\frac{d}{dt}(\rho h)=0 \qquad \text{(A.1)}$$

where P is the pressure, v_x is the sliding velocity, ρ the density, μ the viscosity and h the clearance. The term including the sliding velocity (v_x) represents the shear flow, as shown in Fig. A.4. The two pressure terms represent the pressure flows. The last term represent the change in volume due to housing displacement.

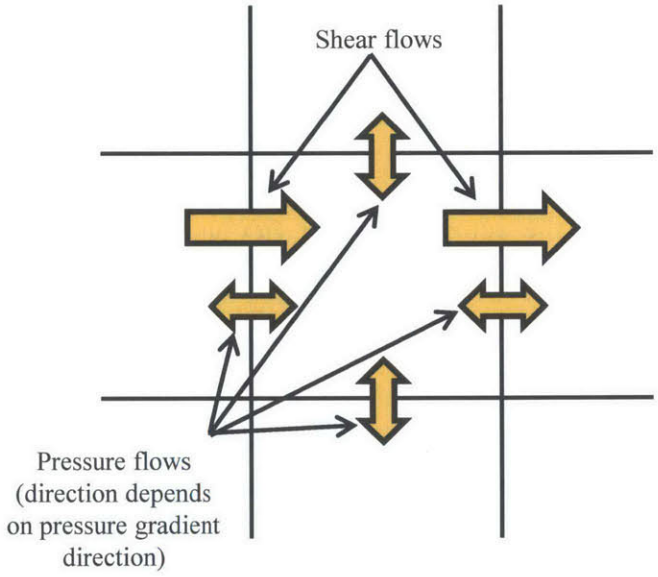

Fig. A.4 Flow between a cell and its neighbor cells

The pressure is solved with a Newton iterative method so every cell satisfies Reynolds equation. However, for the cells where the pressure is below the cavitation pressure, pressure is fixed to cavitation pressure. For those cells, the density is solved to satisfy Reynolds' equation. The density is varied by changing the ratio of vapor and liquid phases in the oil.

For the boundary conditions, the two cut ends of the seal are assumed periodic. The leading and trailing edge pressure are set to atmospheric pressure. The leading edge is assumed to be fully-flooded for the oil control ring. For the top two rings, the supply is taken from the amount of oil left from the oil control ring.

A.2.3 Oil Control Ring Correlation

The deterministic model is used to calculate the average pressure for different nominal clearance. Typically, clearances used are selected from 2 to 10 times the standard deviation of the plateau roughness (σ_p). The hydrodynamic pressure is then fitted with a power equation so it can be used in a cycle model. The form of the equation is given by:

$$P_{hydro,ocr\ @\mu_0,V_0} = P_h \left(\frac{h}{\sigma_p}\right)^{-K_h} \tag{A.2}$$

Where P_h and K_h are constants. The model is run for a reference viscosity (μ_0) and a reference velocity (V_0). Since pressure generation is directly proportional to those parameter, a term is added to take into account the actual viscosity (μ) and actual velocity (V). The correlation becomes:

$$P_{hydro,ocr} = \frac{\mu V}{\mu_0 V_0} P_h \left(\frac{h}{\sigma_p}\right)^{-K_h} \tag{A.3}$$

A.2.4 Top Two Rings Correlation

For the top two rings, the supply can vary depending on the oil left by the oil control ring on the liner. In starved condition, the hydrodynamic pressure is smaller than in fully-flooded condition. To capture this effect, a term is added to the correlation:

$$P_{hydro,piston\ engine} = P_{hydro,ocr} \left(\frac{h_s}{h}\right)^{-K_{p1}+K_{p2}\left(\frac{h_s}{\sigma_p}\right)} \tag{A.4}$$

where h_s is twice the oil film thickness left by the oil control ring, and K_{p1} and K_{p2} are constants. If the supply fills completely the clearance ($h_s \geq h$), the term added is 1 and the correlation is the same as the oil control ring. However, as the supply gets smaller, the term decreases and reduces the hydrodynamic pressure.

A.3 Rotary Engine Seal and Surface Orientation

The main limits of the piston ring model applied to the oil seals of the rotary engine are the variation in surface and seal orientation. In the piston engine, the motion is unidirectional and always perpendicular to the seal. However, the velocity of the oil seals can be in any direction. If the surface is anisotropic, this leads to a difference of hydrodynamic pressure generation between inward and outward motion. The effect of the orientation of the seal velocity on the surface needs to be studied. This angle is defined as γ, as shown in Fig. A.5, and can vary from 0 to 360°. The effect of this angle is characterized using the piston engine model and rotating the housing roughness. Macroscopically, the surface looks isotropic and the surface orientation should not have an important impact on hydrodynamic pressure. However, the model shows that the asperities are asymmetric and surface orientation can have an important impact on pressure.

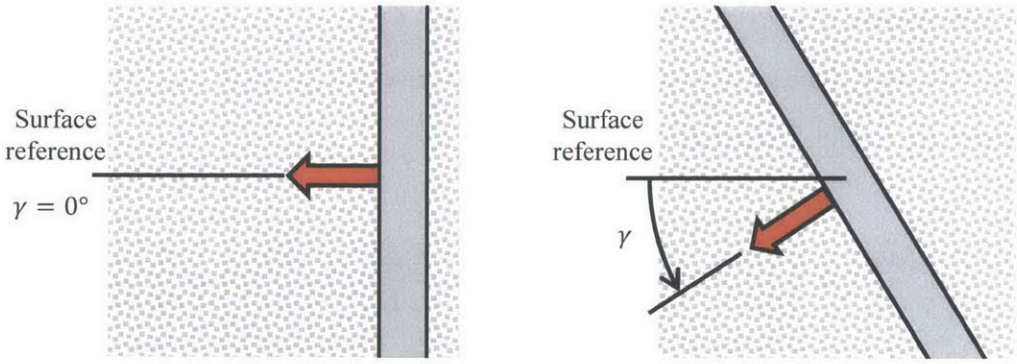

Fig. A.5 Definition of the surface orientation angle (γ)

The seal can also have a different orientation compared to its velocity, defined as β and shown in Fig. A.6. If the motion is perpendicular to the seal, like the piston engine rings, β is 0°. If the motion is parallel to the seal, β is 90°. This angle is always defined positive, from 0 to 90°. The seal orientation requires modification of the piston ring model to take into account the component of velocity parallel to the seal.

The seal orientation mainly affects the leading and trailing edge boundary conditions. If $\beta = 0°$, the behavior is the same as the piston rings. At $\beta = 90°$, the oil is pushed out of the clearance and the pressure drops to zero. From 0 to 90°, the way the pressure decreases depends on the relative clearance compared to the land width. If the clearance is very small, the boundary conditions have less influence and the pressure drops only near 90°. However, for a larger clearance, the pressure is more sensitive to boundary conditions and decreases faster.

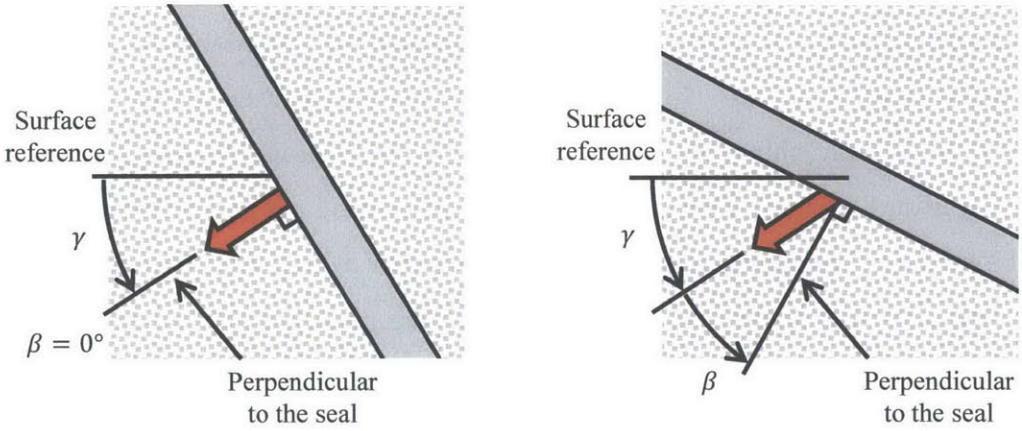

Fig. A.6 Definition of the seal orientation angle (β)

A.4 Model Modification for Seal Orientation

To take into account the seal orientation (β), the velocity parallel to the seal (v_y) is included in the deterministic model. Equation (A.1) becomes:

$$\frac{d}{dx}\left(\frac{\rho v_x h}{2} + \frac{\rho h^3}{12\mu}\left(-\frac{dP}{dx}\right)\right) + \frac{d}{dy}\left(\frac{\rho v_y h}{2} + \frac{\rho h^3}{12\mu}\left(-\frac{dP}{dx}\right)\right) + \frac{d}{dt}(\rho h) = 0 \qquad \text{(A.5)}$$

In order to have the same solution along x and y, the housing grid has to move one cell along both axis for each time step. The roughness points are remeshed depending on the velocity angle, as seen in Fig. A.7. As the angle tends to 90°, the cell aspect ratio tends to infinity. The maximum angle that can be tested with this approach is about 85°.

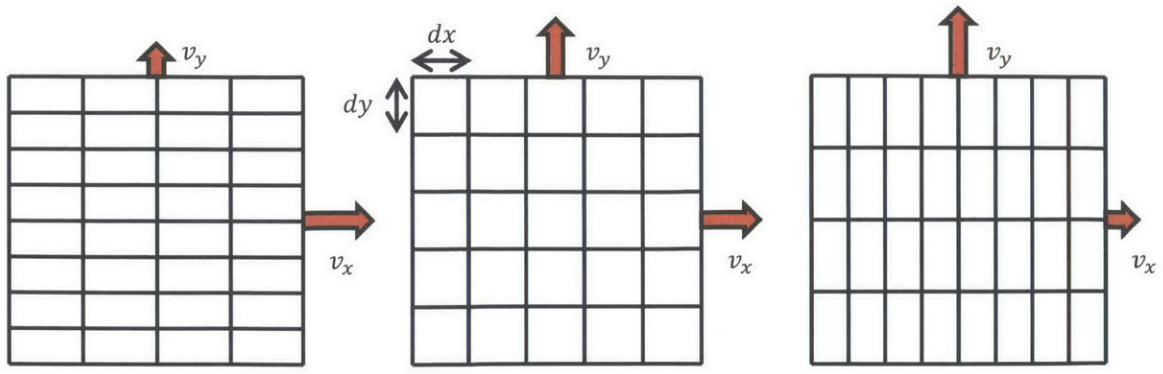

(a) $\beta = 26.6°$ (b) $\beta = 45°$ (c) $\beta = 63.4°$

Fig. A.7 Remeshing of roughness data as a function of the seal orientation angle

A.5 Results

The surface orientation (γ) is first studied, with the seal orientation (β) set to zero. It shows that the pressure generated when reversing the velocity could be different due to asperity shape. The seal angle (β) is then studied by removing the surface effect and focusing on its effect on boundary conditions. For both situations, a correction to the hydrodynamic pressure correlation is suggested. Those corrections are used in the cycle model to estimate the effect on oil consumption in section 3.2. All results presented in this section are for simulations executed with measured housing patches of about 1 mm by 1 mm and a land width of 0.2 mm.

A.5.1 Surface Orientation Effect

The effect of the surface is tested on three patches of roughness measurement from worn cast. The deterministic model is used to determine the average hydrodynamic pressure every 45°, from 0 to 315°. Hydrodynamic pressure divided by the pressure generated at $\gamma = 0°$ is plotted against the surface rotation angle in Fig. A.8.

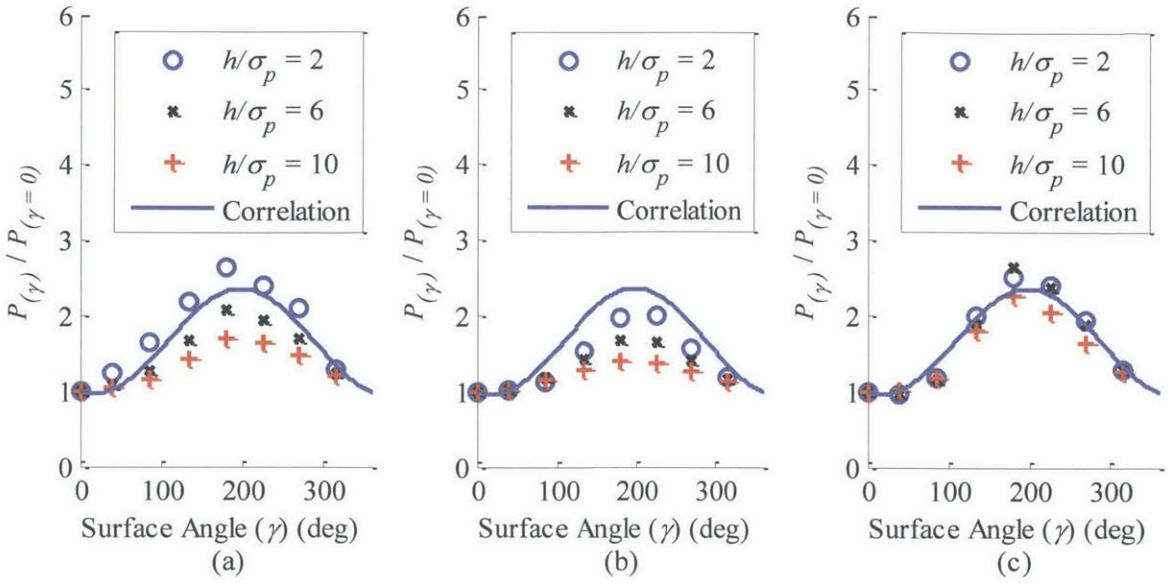

Fig. A.8 Hydrodynamic pressure divided by pressure at reference angle, for three surfaces

The pressure at 180° is about twice the pressure at the reference angle. This seems to be caused by a small tilt of the plateau parts. More investigations would be needed to validate those results and to try to relate to the manufacturing process. In the presented model, a sinusoidal term is added to the hydrodynamic correlation to capture this effect, and estimate the change in oil consumption caused by this asymmetry. For fully-flooded condition:

$$P_{hydro} = \frac{\mu V}{\mu_0 V_0}\left(P_h + P_\gamma \sin(\gamma - \phi_\gamma)\right)\left(\frac{h}{\sigma_p}\right)^{-K_h} \tag{A.6}$$

where P_γ is a constant in Pa and ϕ_γ is the phase. As shown in Fig. A.8, this correlation captures the variation of pressure due to the angle, but does not include any correction for the different heights. The constants are fitted with a least mean square method and are shown in Table A.1.

Table A.1 Constants for surface orientation hydrodynamic pressure correlation

Constant	Value
P_h	3.9×10^7 Pa
P_γ	1.64×10^7 Pa
ϕ_γ	109°
K_h	2.39

A.5.2 Seal Angle Effect

Effect of the seal angle is tested on the three same housing patches. The pressure is first corrected for remeshing the grid by running the remeshed grid at $\beta = 0°$. Maximum correction for the grid effect is about 20 %. Then, the pressure is corrected for the surface angle (γ) to isolate only the seal angle effect (β). Resulting pressures divided by the pressure at $\beta = 0°$ are shown in Fig. A.9. As expected, hydrodynamic pressure drops as β approaches 90°. Also, pressure drops faster for large clearances. It is interesting to note that the pressure increases linearly until it drops.

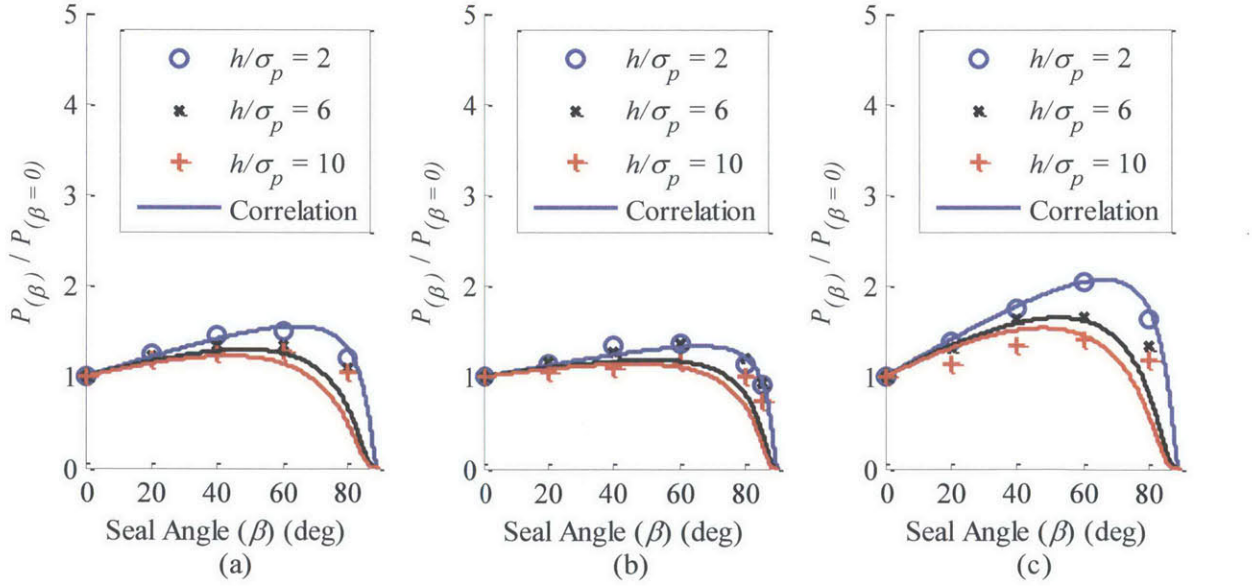

Fig. A.9 Hydrodynamic pressure divided by pressure at $\beta = 0°$, for three surfaces

The hydrodynamic correlation is corrected to take into account this effect with a linear term and a correction to the exponent:

$$P_{hydro} = \frac{\mu V}{\mu_0 V_0}\left(P_h + P_\gamma \sin(\gamma - \phi_\gamma) + P_\beta \beta\right)\left(\frac{h}{\sigma_p}\right)^{-K_h - K_\beta \tan(\beta)} \tag{A.7}$$

where P_β and K_β are constants. The exponent form is the important correction and is chosen so the pressure always drops to zero at 90°, and drops faster for the larger clearances. The linear term allows flexibility to adjust for the pressure raise from 0 to about 60°. The shape of the correlation is shown in Fig. A.9, with specific coefficients for every patch. Average coefficients are given in Table A.2.

Table A.2 Constants for seal orientation hydrodynamic pressure correlation

Constant	Value
P_β	1.06×10^7 Pa/rad
K_β	0.072

A.6 Starved Condition

Corrections for the rotary engine are developed for fully-flooded condition. However, hydrodynamic pressure is reduced if the supply of oil is insufficient to fill completely the seal-housing clearance. The term from the piston is multiplied to the rotary engine correlation:

$$P_{hydro} = P_{hydro,fully-flooded}\left(\frac{h_s}{h}\right)^{-K_{p1} + K_{p2}\left(\frac{h_s}{\sigma_p}\right)} \tag{A.8}$$

where K_{p1} and K_{p2} are constants taken directly from the piston engine liner correlation. Although the coefficients are not fitted to the housing surface, this correction allows taking into account this important effect of oil supply on hydrodynamic pressure.

A.7 Friction

The model developed for the piston rings also gives correlations for the hydrodynamic friction. Those correlations are used to calculate the friction of the oil seals, without corrections for surface orientation or seal orientation. Friction correlation used is given in section 3.1.4.2.

Coefficients for fully flooded conditions are calculated from the deterministic model for the cast iron housing. Coefficients are selected to have the best fit for all surface orientations. Coefficients for starved condition are taken directly from the piston liner correlation, as for the hydrodynamic pressure.

Those approximations are a representative estimation, since friction is dominated by the shear due to Couette flow and thus the friction coefficient variation is typically small. Further investigation using the deterministic model could be done if friction becomes the main concern for the oil seals.

A.8 Conclusion

This appendix presents a deterministic model to calculate the hydrodynamic pressure generated by housing roughness. The modifications to the piston ring deterministic model to take into account the specific kinematics of the rotary engine seals are explained. Surface orientation is shown to have an important effect on pressure and a term is added to the correlation to evaluate its effect on oil consumption. The main effect of seal orientation on pressure generation is that the pressure drops as the velocity gets parallel to the seal.